Curtis M. Zaleski *Editor*

Advances in Metallacrown Chemistry

Springer

Advances in Metallacrown Chemistry

Curtis M. Zaleski
Editor

Advances in Metallacrown Chemistry

Springer

Editor
Curtis M. Zaleski
Department of Chemistry and Biochemistry
Shippensburg University
Shippensburg, PA, USA

ISBN 978-3-031-08575-8 ISBN 978-3-031-08576-5 (eBook)
https://doi.org/10.1007/978-3-031-08576-5

This Springer imprint is published by the registered company Springer Nature Switzerland AG
The registered company address is: Gewerbestrasse 11, 6330 Cham, Switzerland

For Laura & Logan

Preface

My journey with metallacrowns began over 20 years ago. As many may know, Vince Pecoraro was my Ph.D. advisor. It all started one fateful day in the fall of 2000 as I sat in Vince's office as he rotated structures of these fascinating molecules on his computer screen and explained their properties. As a first-semester graduate student, I did not know much about coordination chemistry, but I was mesmerized by the fact that these molecules could self-assemble in a solution like Lego bricks. While I had not officially joined the research group at that point, I was hooked on metallacrowns. I completed my interviews with the other inorganic chemistry faculty members, but there was no doubt in my mind which group I wanted to join. In January of 2001, I officially joined Vince's group and started down this path exploring these metallamacrocycles.

Since my graduate school days, I have enjoyed watching the field grow as more and more scientists investigate these captivating molecules. In the early 2000s, there were other groups beyond our group investigating metallacrowns, though not as many as today. Two groups from the early 2000s stand out in my memory for their excellent contributions to the field—Prof. Dimitris Kessissoglou at the Aristotle University of Thessaloniki and Prof. Francesco Dallavalle at the University of Parma. While I was a graduate student, I had the honor of working with Prof. Kessissoglou on several different metallacrowns including an Mn_{26} metallacryptate. He and his group helped jumpstart my research concerning the magnetic properties of metallacrowns. Then in 2015, I had the pleasure of meeting Prof. Dallavalle while I was visiting Matteo Tegoni at the University of Parma. From those graduate school days, I can also vividly recall a little piece of paper that resided in Vince's lab. On one of the student cubicles, a sign was taped to a bookshelf that read "Metallacrowns—The Wave of the Future". Lab lore was that Brian Gibney, one of the first graduate students to work on the MC project, had placed the sign in the lab. [Brian is also involved in another piece of lab lore that involves the year 2056, but you will have to ask him about that one the next time you see him!] While I was in the lab, the graduate students and postdocs often joked about that little sign, but it also a bit of inspiration for the metallacrown people to try to take these molecules and find interesting applications. Personally, I also felt the MC project was a little underappreciated compared to

Vince's other projects, especially the manganese project that explored the chemistry of Photosystem II. While my fellow lab members and I were not competitive with each other and the lab was a supportive atmosphere, I always had a little "chip on my shoulder" to prove that MCs were better and deserved more recognition. Thus, it has been exciting to watch the field expand beyond just a handful of research groups to a multitude of groups that spans the globe. It has been satisfying to see the applications and properties of metallacrowns grow and diversify.

The aim of this volume on metallacrown chemistry is to highlight the interesting work being pursued by a variety of research groups and to provide inspiration for future explorations into this wonderful field. Schneider and Pecoraro begin the volume by focusing on the host–guest properties of archetypal metallacrowns, in particular, 12-MC-4 and 15-MC-5 complexes, and how these interactions could lead to applications such as molecular sensing and catalysis. Melegari and Tegoni then discuss the NMR characterization of metallacrowns and how the technique can be used to study the solution behavior of these complexes. Next, Ostrowska, Fritsky, and Gumienna-Kontecka examine the thermodynamic behavior of nickel, copper, and zinc metallacrowns and compare the solid state and solution behavior of these complexes. Following, Głuszyńska and Juskowiak explore the binding affinity of metallacrowns to various forms of DNA and discuss the analytical techniques needed to characterize these interactions. Boron then details the advancement of magnetic applications of metallacrowns including the area of single-molecule magnetism and how the MC scaffold can be used to systematically alter the magnetic behavior of the molecules. Next, Jones focuses on nonarchetypal metallacrowns in particular molecular wheels, 12-metallacrown-3 complexes, and inverse crown ether complexes, and explores the host–guest properties of each structure type. Following, Katkova and Ketkov describe several water-soluble lanthanide-copper 15-metallacrown-5 systems and their potential applications such as magnetic resonance imaging agents. Yang, Dou, and Song then discuss the use of iron, cobalt, and nickel metallacrowns as catalysts for water oxidation and carbon dioxide reduction. Lastly, Lutter and I examine the recent renaissance in the use of main group elements as the ring metal for metallacrowns. We highlight gallium-lanthanide MCs and their luminescent properties. As the topics of this volume indicate, indeed metallacrowns will one day fulfill their destiny and become that "wave of the future".

Shippensburg, USA Curtis M. Zaleski

Acknowledgments

I would like to thank the authors for without their contributions this volume would not be possible. Their hard work, willingness to meet deadlines, and toleration of my numerous e-mails were instrumental to the smooth production of the book. I would also like to thank the staff at Springer Nature for supporting this volume, in particular Angeliki Athanasopoulou for her help. Angeliki initially approached me about compiling this volume and spearheaded the effort. Moreover, Angeliki earned her Ph.D. exploring MC chemistry with mentorship from Prof. Eva Rentschler; thus, Angeliki is one of us!

Lastly, I would like to dedicate this volume to my children Laura and Logan. They inspire me than they know and because of them I strive to do better each day. This book will be a complete bore to them, but it will likely come in handy on those nights that they will just not go to bed. All that I will need to do is to start reading from page 1, and it will soon be sleepy time! Though I must admit Laura did enjoy staying up late some nights helping me make figures. She would watch as I rotated molecules to find a good angle, but I am pretty sure that she enjoyed staying up past her bedtime even more. I cannot wait to watch the two of you grow and hopefully have an appreciation for science. However, based on your current habits of climbing up household objects and penchant for jumping off the furniture, the two of you may become stunt performers in Hollywood when you grow up. Love you both!

Shippensburg, USA Curtis M. Zaleski

Contents

Contributors

Boron Thaddeus T. III Slippery Rock University, Slippery Rock, PA, USA

Dou Jianmin Shandong Provincial Key Laboratory of Chemical Energy Storage and Novel Cell Technology, College of Chemistry and Chemical Engineering, Liaocheng University, Liaocheng, P. R. China

Fritsky Igor O. Department of Chemistry, Taras Shevchenko National University of Kyiv, Kiev, Ukraine

Gumienna-Kontecka Elzbieta Faculty of Chemistry, University of Wroclaw, Wroclaw, Poland

Głuszyńska Agata Department of Bioanalytical Chemistry, Faculty of Chemistry, Adam Mickiewicz University, Poznań, Poland

Jones Leigh F. School of Sciences, University of Wolverhampton, Wolverhampton, UK

Juskowiak Bernard Department of Bioanalytical Chemistry, Faculty of Chemistry, Adam Mickiewicz University, Poznań, Poland

Katkova Marina A. G.A. Razuvaev Institute of Organometallic Chemistry RAS, Nizhny Novgorod, Russian Federation

Ketkov Sergey Yu. G.A. Razuvaev Institute of Organometallic Chemistry RAS, Nizhny Novgorod, Russian Federation

Lutter Jacob C. Department of Chemistry and Biochemistry, University of Southern Indiana, Evansville, IN, USA;
Department of Chemistry, Wayne State University, Detroit, MI, USA

Melegari Matteo Department of Chemistry, Life Sciences and Environmental Sustainability, University of Parma, Parma, Italy

Ostrowska Malgorzata Faculty of Chemistry, University of Wroclaw, Wroclaw, Poland

Pecoraro Vincent L. Department of Chemistry, University of Michigan, Ann Arbor, MI, USA

Schneider Bernadette L. Department of Chemistry, University of Michigan, Ann Arbor, MI, USA

Song You State Key Laboratory of Coordination Chemistry, Collaborative Innovation Center of Advance Microstructures, School of Chemistry and Chemical Engineering, Nanjing University, Nanjing, P. R. China

Tegoni Matteo Department of Chemistry, Life Sciences and Environmental Sustainability, University of Parma, Parma, Italy

Yang Hua Shandong Provincial Key Laboratory of Chemical Energy Storage and Novel Cell Technology, College of Chemistry and Chemical Engineering, Liaocheng University, Liaocheng, P. R. China

Zaleski Curtis M. Department of Chemistry and Biochemistry, Shippensburg University, Shippensburg, PA, USA

Host–Guest Chemistry of Metallacrowns

Bernadette L. Schneider and Vincent L. Pecoraro

Abstract Host–guest chemistry emerged as a field in the late 1960s beginning in the context of organic hosts with simple alkali metallic guests and soon expanding to more complex guests. By the 1980s metallic analogs had been developed that exhibited similar structures and interactions, but often boasted higher affinities for molecular recognition. In this article, we will describe the relationship of metallacrowns (MCs) to their organic counterparts, and discuss the importance of both ring metals and central metals for these metallic complexes to utilize noncovalent interactions to build up chemical systems of greater complexity. The focus will be on the subsets of metallacrowns known as 12-MC-4s and 15-MC-5s that bear selective recognition properties, including particular examples given for MCs with mono- and dicarboxylate guests to illustrate the selectivity of these systems. Recent efforts to develop a deeper understanding of host–guest dynamics in solution and in the solid state can inform the thoughtful design of these systems with molecular sensing, materials design, or catalytic goals in mind.

1 Molecular Recognition in Macrocycles

Molecular recognition as a concept has co-evolved with the field of host–guest chemistry as scientists have advanced in understanding the noncovalent interactions that can lead to the formation of a multimolecular complex. Molecular recognition events are ubiquitous in nature with examples such as substrate binding to an enzyme or chemical stimulus at a cell to propagate a biological signal. Such molecular docking events are often driven by selective binding of a compatible chemical motif facilitated by factors such as hydrogen bonding, coordinative or dative bonding, hydrophobic interactions, or other thermodynamic factors [1, 2]. For molecular recognition between species, compatibility in size, shape, and chemical properties are typically found to be important criteria.

B. L. Schneider · V. L. Pecoraro (✉)
Department of Chemistry, University of Michigan, 930 N. University Ave, Ann Arbor, MI 48109, USA
e-mail: vlpec@umich.edu

C. M. Zaleski (ed.), *Advances in Metallacrown Chemistry*,
https://doi.org/10.1007/978-3-031-08576-5_1

1.1 Organic Recognition Agents

Since the development of crown ethers by Charles Pedersen in 1967 [3–5], a multitude of articles have been published on synthetic organic molecular recognition agents, e.g., cryptands, calixarenes, cucurbiturils, cyclodextrins, etc. (Fig. 1), demonstrating their utility in fields such as analytical sensing, phase transfer and extraction, and drug formulation [6]. Early on, Pedersen found crown ethers could selectively bind alkali or alkaline earth metal cations via dative bonds to the oxygens of the ring under ambient conditions, and that the stability of the metal within the cavity was heavily influenced by the comparative radii of the hole of the polyether ring vs the metal ion [5, 7, 8]. Further studies revealed that complexation was strongly driven by the desolvation energy of the target cation, which led certain monovalent cations such as potassium to have a higher affinity than smaller or more highly charged cations [9, 10]. With cavity radius estimates of 12-crown-4 (12-C-4) ranging around 1.2–1.5 Å [11], 12-C-4 is selective primarily for the alkali metal cations [12, 13]. However, if the size of the metal is larger than the size of the cavity, it will sit atop the crown in a pyramidal geometry as in $Li^+(NCS^-)$[dibenzo-12-C-4], with Li^+ lying 0.95 Å above the mean plane of the crown oxygens [14] (Fig. 2), or form a sandwich complex with

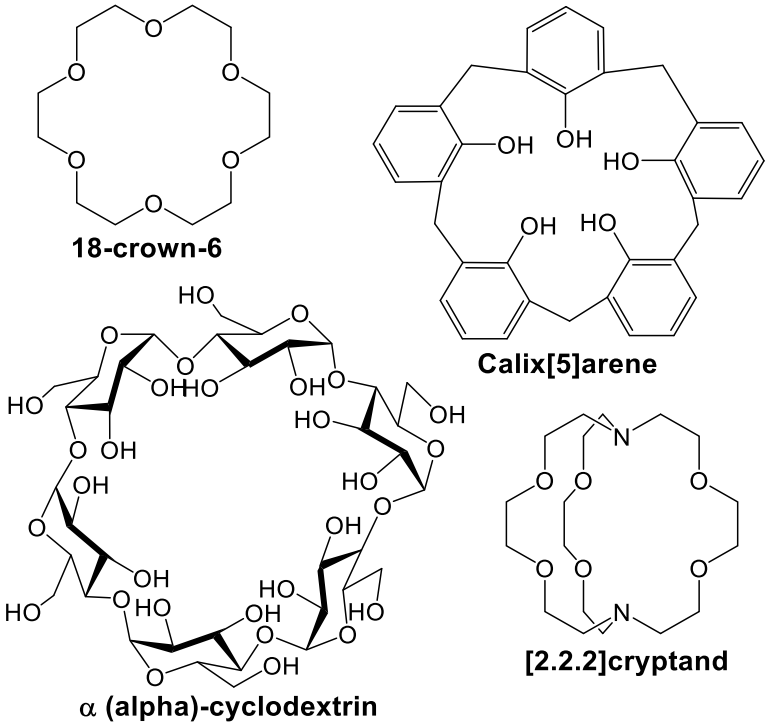

Fig. 1 A few examples of organic macrocycles and cavitands used as molecular hosts

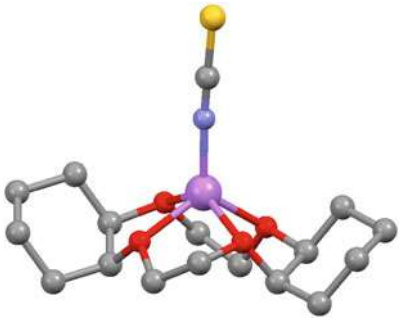

Fig. 2 Structure of [Li(dibenzo-12-crown-4)]SCN. Adapted with permission from Buchanan, G.W., Kirby, R.A., Charland, J.P., Ratcliffe, C.I.: J. Org. Chem. 56, 203–212 (1991). Copyright 1991 American Chemical Society [14]

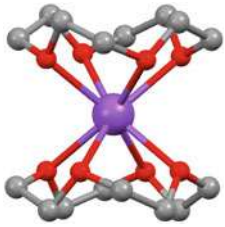

Fig. 3 Structure of $[Na(12\text{-crown-}4)_2]ClO_4$, with uncoordinated perchlorate anion not shown. Adapted with permission of the International Union of Crystallography [15]

an eight-coordinate alkali metal, for example, the bis(12-C-4) sodium perchlorate (Fig. 3) [15].

A variety of other molecular recognition agent types have been developed, including aza- and thiacrown ethers, lariat ethers, and cryptands. The diversification of the functional groups in the molecular recognition repertoire broadens the selective recognition capabilities beyond the alkali and alkaline earth metals. In the case of azacrowns and thiacrowns, at least one nitrogen or sulfur, respectively, substitutes for the oxygen of the ring of crown ethers. Replacing the harder oxygen donor atoms with softer nitrogen or sulfur heteroatoms facilitates the complexation of more polarizable ions. Nitrogen, since it is less electronegative, has a more available lone pair than oxygen making aza-macrocycles more compatible with binding many transition metals [16], whereas sulfur is particularly polarizable, enabling thiacrown sequestration of soft chalcophilic ions, such as Hg^{2+}, Pb^{2+}, Cd^{2+}, and Ag^{+} [17].

Meanwhile, both lariat ethers and cryptands form a three-dimensional cavity that enhances the entropic favorability of encapsulating ions by enabling greater desolvation of the ion. Lariat ethers include one or more pendant arms onto a macrocycle, providing a conformationally mobile axial coordination site that enhances binding capability [18, 19]. Appending the arm at the nitrogen of an azacrown (nitrogen-pivot class of lariat ethers) provides better flexibility for the arm to reach the axial site of a metal ion, as opposed to when the arm branches from a carbon (carbon-pivot), which is limited by the geometry at the carbon. If the branch ends in an ionized group such as a carboxylate, counterions become unnecessary for extraction of metal ions into an organic phase, in particular enabling sequestration of more highly charged species. Cryptands consist of one or more coordinating bridges across a macrocycle to form

a pre-organized polycyclic cavity. Cation binding occurs tightly in the crypt of the typically bis- or tris-macrocycle, which can then strongly attract anionic agents for ion transport or transfer of a cation/anion pair into an organic phase, with binding affinities higher than those of simple macrocycles [20, 21]. By moving to these more highly coordinating or chemically more diverse ligands, the range of ions that may be sequestered expands to transition ions and lanthanides, which were originally difficult to recognize with simple crown ethers. Factors affecting the complexation phenomena demonstrated by these various coordinating agents include the comparative size of the cavity and cation, ligand flexibility, configuration, and the number and type of donor atoms, as well as energies of solvation of the ligand, cation, and complex.

1.2 Metallacrowns

Discoveries of metallomacrocyclic complexes such as metallacrowns (MCs), with self-assembly driven by coordination at metal centers, soon led to investigations of their capacity as molecular hosts, as well as for various applications such as catalysis, sensing, and adsorption [22–24]. Metallacrowns in particular have proven capable of similar, rapid ion recognition chemistry as their organic cousins, the crown ethers, with stability far exceeding that of the organic crowns [25–27]. The characteristic metal–nitrogen–oxygen repeat unit of metallacrowns provides an analogous platform to the crown ether's carbon–carbon–oxygen motif for binding of a central ion within the pore of the macrocycle, with the selective recognition capabilities of metallacrowns surpassing their organic analogs (Fig. 4) [26].

1.2.1 Metallacrown Structure

Three characteristics of macrocyclic metal binding often used to draw comparisons between structures are cavity size, the distance between adjacent chelate atoms, also described as bite distance, and the distance of the bound ion to the plane formed by the ethereal or oxime oxygens of the ring. Table 1, originally compiled by Gibney et al. [28] and here updated with a few additional relevant structures, compares these parameters for some of the earliest MCs and macrocyclic analogs. The cavity radii, usually indicating the space available within the macrocycle that is not taken up by the radii of donor atoms, are often used as comparisons from one molecular structure to another. However, this approach has a wide range of values depending on assumptions that are made for the oxygen or nitrogen radii, how the orientation of these atoms is defined, and the specific geometries in question. Thus, one needs to recognize that there is a range of uncertainty in the values when comparing between structures. That being acknowledged, these measurements can still provide useful comparative information.

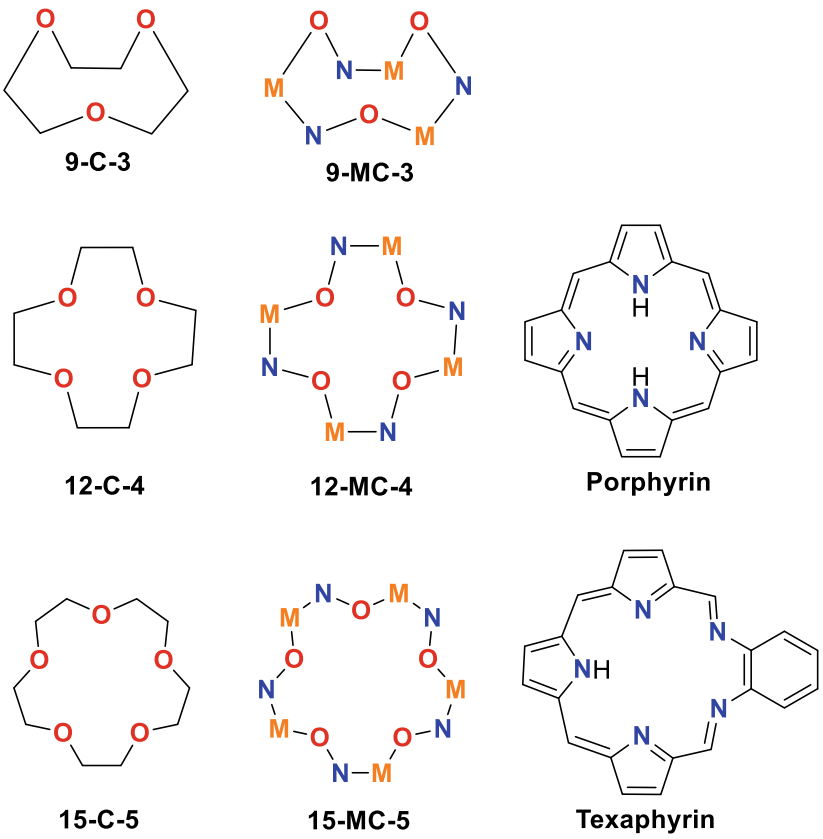

Fig. 4 Comparison of tri-, tetra-, and penta-dentate crown ether, metallacrown, and porphyrin-based macrocycles

The smallest crown ether, 9-crown-3 (9-C-3), is found vacant, as the cavity size of 0.25 Å is too small to bind any except the smallest metals. The analogous 9-MC-3 made with VO^{3+} ions and salicylhydroximate (shi) mimics the conformation of the 9-C-3 and is also found vacant [42]. By moving to Fe^{3+} ring metals, important differences are observed. The three oxygens of the ring form a cofacial coordination environment for an octahedral central metal. Additionally, the ring Fe^{3+} ions have an open coordination site (that is occupied by oxygen on VO^{3+} ions). Bridging acetates are able to fill the open coordination sites on both the central and the ring Fe^{3+} ions, stabilizing the structure [34, 43]. Notably, the cavity size of the iron and vanadium-based 9-MC-3 s at 0.25 Å and 0.35 Å, respectively, are equivalent or very similar when compared to the 9-C-3 parent. Similarly in 12-MC-4, the structural comparison indicates that although the ring metals of 12-MC-4 are larger in radius than the corresponding crown's carbons, the pore size of 12-MC-4 to 12-C-4 is again

Table 1 Structural comparison of crown ether, porphyrin, phthalocyanine, and metallacrown complexes[a,b]

Compound	Bite distance (Å)	Cavity radius (Å)[e]	Metal:host	M–O distance (Å)	M-O_{plane} (Å)	References
Crown ethers						
$[Li(12\text{-}C\text{-}4)]^+$	2.71	0.55	1:1	2.13	0.93	[29]
$[Na(12\text{-}C\text{-}4)_2]^+$	2.80	0.64	1:2	2.48	1.49	[15, 30]
$[K(12\text{-}C\text{-}4)_2]^+$	2.71	0.55	1:2	2.90	2.84	[31]
$[Na(15\text{-}C\text{-}5)]^+$	2.72	0.76	1:1	2.67	1.12	[32]
$[K(18\text{-}C\text{-}6)]^+$	2.82	1.44	1:1	2.84	0.18	[33]
Metallacrowns						
$Fe(OAc)_3[9\text{-}MC_{Fe(III)N(shi)}\text{-}3]$	2.78	0.25	1:1	2.00	1.18	[34]
$(Li)[12\text{-}MC_{Mn(III)N(shi)}\text{-}4]^+$	2.65	0.5	1:1	1.95	0.63	[28]
$(LiTFA)[12\text{-}MC_{Mn(III)N(shi)}\text{-}4]$	2.65	0.50	1:1	1.97	0.66	[28]
$(LiCl_2)[12\text{-}MC_{Mn(III)N(shi)}\text{-}4]^-$	2.66	0.51	1:1	1.97	0.64	[28]
$(NaCl)_2[12\text{-}MC_{Mn(III)N(shi)}\text{-}4]$	2.63	0.50	2:1	2.43	1.66	[25]
$(NaBr)_2[12\text{-}MC_{Mn(III)N(shi)}\text{-}4]$	2.65	0.58	2:1	2.49	1.64	[28]
$(KBr)_2[12\text{-}MC_{Mn(III)N(shi)}\text{-}4]$	2.62	0.53	2:1	2.82	2.13	[28]
$Mn(OAc)_2[12\text{-}MC_{Mn(III)N(shi)}\text{-}4]$	2.67	0.53	1:1	2.21	1.20	[35]
$Gd(NO_3)_2[15\text{-}MC_{Cu(II)N(picha)}\text{-}5]^+$	2.83	1.12	1:1	2.41	0.26	[36]
Porphyrins						
$[Li(TMPP)]^-$	2.78	0.68	1:1	2.03(M–N)	0.0	[37]
$[Na_2(OEP)]$	2.90	0.69	2:1	2.48(M–N)	1.39	[37]
$[K_2(OEP)]$	2.92	0.70	2:1	2.77(M–N)	1.85	[37]
$Gd(NO_3)[Texaphyrin\text{-}T1]^+$	2.68[c]–2.99[d]	1.02	1:1	2.46(M–N)	0.60	[38]

(continued)

Table 1 (continued)

Compound	Bite distance (Å)	Cavity radius (Å)[e]	Metal:host	M–O distance (Å)	M-O_{plane} (Å)	References
Phthalocyanines						
[Li(pc*)]	2.75	0.58	1:1	1.94(M–N)	0.0	[39]
[K_2(pc)]	2.78	0.60	2:1	2.90(M–N)	2.13	[40]

[a]TMPP, meso-tetrakis(3,4,5-trimethoxyphenyl)porphyrin dianion; OEP, octaethylporphyrin dianion; pc*, phthalocyanine dianion p-cation radical; pc, phthalocyanine dianion. Texaphyrin-T1 = 4,5- Diethyl-10,23-dimethyl-9,24-bis(3-hydroxypropyl)-16,17-(3-hydroxypropyloxy)-13,20,25,26,27-pentaazapentacyclo(20.2.1.13,6.18,11.014,19]-heptacosa-1,3,5,7,9,11(27),12,14,16,18,20,22(25),23-tridecane. [b]Adapted with permission from Gibney, B. R., Wang, H., Kampf, J. W., Pecoraro, V. L.: Inorg. Chem. 35, 6184–6193 (1996). Copyright 1996 American Chemical Society [28]. Updated with representative tri- and pentacoordinate macrocycles. [c]Average bite distance of five-membered chelate rings. [d]Average bite distance of six-membered chelate rings. [e]Most values calculated prior to this publication were likely calculated using 1.36 Å for both O in the MC ring and N in the conjugated porphyrin system. 1.36 Å is the ionic radius of a three-coordinate O^{2-} ion, according to R.D. Shannon [41]. Calculated values added for this publication used the same value

similar, at 0.5 Å vs 0.6 Å, respectively, observed for the multivalent $Mn(OAc)_2$[12-$MC_{Mn(III)N(shi)}$-4] [29, 35]. Longer M–N and M–O bond distances within the MC ring are compensated by a decrease in the M–N–O bond angles at the ring metal so that a similar cavity radius is maintained, as compared to crown ether, which is constrained by the tetrahedral geometry of carbons. A distinction from crown ethers is observed in the chelate rings formed by coordination to the central ion, which are often planar in metallacrowns but exhibit significant torsion in crown ethers due to the hybridization found around sp^3 carbon atoms. Coordinating bridges like the carboxylates observed in $Fe(OAc)_3$[9-$MC_{Fe(III)N(shi)}$-3] and $Mn(OAc)_2$[12-$MC_{Mn(III)N(shi)}$-4] and other MC species are reminiscent of the arms of lariat ethers that sport carboxylate functional groups. With minimal synthetic investment, the additional coordinating capacity increases the desolvation of guests and stabilizes the binding of higher valent ions or guests to rings that have small pore sizes. Another example where the bridging ligands are critical is $Fe(SO_4)_2$[12-$MC_{Fe(III)N(shi)}$-4]$^-$, bridged by sulfates in which the central Fe^{3+} fits snugly within the plane of the MC, a conformation that is rare among 12-MC-4 macrocycles [43, 44].

Considering the components involved in molecular recognition, the deprotonated hydroximate ligands become formally neutral when bound as part of the $[M–N–O]_n$ ring, however, when they are considered within the context of the full structure, partial negative charge spills from the oxime oxygen to interact with the central metal. In contrast, crown ethers with ethereal oxygens are fully innocent, neutral ligands, resulting in cation binding from simple Lewis adducts. The electron density at the oxygens in traditional MCs, therefore, can be considered to contribute to the strength of transition metal binding. Evidence of the MC's stronger pull on the guest cation manifests in a sandwich complex consisting of a [12-$MC_{Zn(II)N(quinHA)}$-4] plus a 12-C-4 unit sharing a Dy^{3+} ion between them, which shows the Dy–O distances are over 0.2 Å shorter to the metallacrown than to the crown ether (Fig. 5).

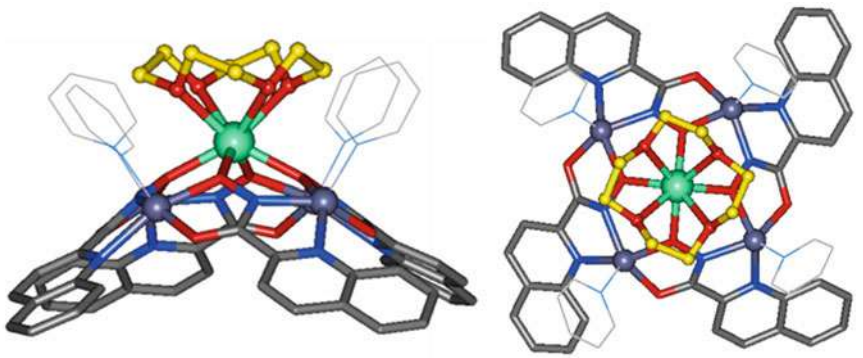

Fig. 5 Side and top images of the crystal structure of $DyZn_4(quinHA)_4$(12-crown-4)$(py)_4$. Crown is displayed oriented on top of the metallacrown. Coordinated pyridine (py) ligands are displayed as thin lines. Reprinted with permission: Joseph M. Jankolovits, Dissertation, University of Michigan, 2012 [45]

While conventional crown ethers can only bind cationic species, anion recognition can be achieved within the central cavity of the metallamacrocycle by inverting the atom connectivity to direct the metal toward the center of the cavity instead of the oxygen. These "inverse metallacrowns", first recognized in the assembly of the ligand bis(2-pyridyl) ketone oxime (Hpko) and Zn^{2+}, can then bind anionic species tightly within the central cavity [46]. Aza-metallacrowns, where the repeating unit of the ring is metal–nitrogen–nitrogen, are another variation on the metallamacrocyclic concept, several of which have also been shown to bind anions within the center, similarly termed as "inverse aza-metallacrowns" [47–50]. These are often assembled from pyrazole or triazole ligands.

An additional variation on the metallacrown archetype comes through the formation of metallacryptate structures, found with both anion and cation binding, from similar ligands and metals that form metallacrowns. For example, a metallacryptate was synthesized from bis-(2-pyridyl) ketone that converted in situ to 2,2'-dipyridylketonediolate ($pdol^{2-}$) with Mn^{2+} in alkaline methanol and was characterized as a single-molecule magnet [51, 52]. The metallacryptand housing (a three-dimensional version of a metallacrown) is comprised of four Mn^{2+} and six Mn^{3+} and 12 $pdol^{2-}$ that stores an Mn-oxide core of 16 Mn^{3+} ions (Fig. 6). Other metallacryptates may be formed with shi^{3-}-based ligands that are also common with metallacrowns. An Mn^{2+}/Mn^{3+} example with pyridyl functionalized shi forms crystalline porous structures that were characterized for gas adsorption [53]. Several shi-based metallacryptates of structure type [3.3.1] with an encapsulated lanthanide (Ln) and stoichiometry LnM_6L_9 have been synthesized, including an example with Ga^{3+} as ring metal that exhibits luminescence [54], and a family of $LnFe_6(shiH)_3(shi)_6$ metallacryptates, which were characterized for their magnetic properties, with the Dy^{3+}

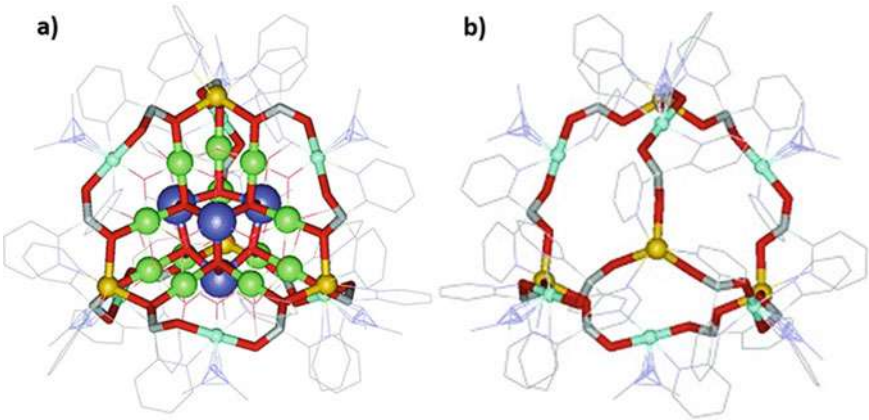

Fig. 6 **a** Structure of the metallacryptate, $[Mn^{II}_4Mn^{III}_{22}(pdol)_{12}(\mu_2\text{-}OCH_3)_{12}(\mu_3\text{-}O)_{10}(\mu_4\text{-}O)_6(N_3)_6]^+$, containing a manganese-oxide core of 16 Mn^{3+} ions. **b** The tricyclic metallacryptand macrocycle is emphasized with its inner core removed. Adapted with permission from John Wiley & Sons [51]

analog behaving as a single-molecule magnet [55]. Several species of the analogous Al^{3+} metallacryptate have also been characterized [56, 57].

1.2.2 Metallacrown Reactivity

An important feature of the analogy of metallacrowns to crown ethers is the ability to convert one species of metallacrown, e.g., M(12-$MC_{M(III)N(L)}$-4), into another species, M'(12-$MC_{M(III)N(L)}$-4), by displacing the central metal. This capability was quickly demonstrated in 1991 when $(NaCl)_2$[12-$MC_{Mn(III)N(shi)}$-4] was shown to convert to $Mn(OAc)_2$[12-$MC_{Mn(III)N(shi)}$-4] in DMF by addition of $Mn(OAc)_2$ (Fig. 7) [25].

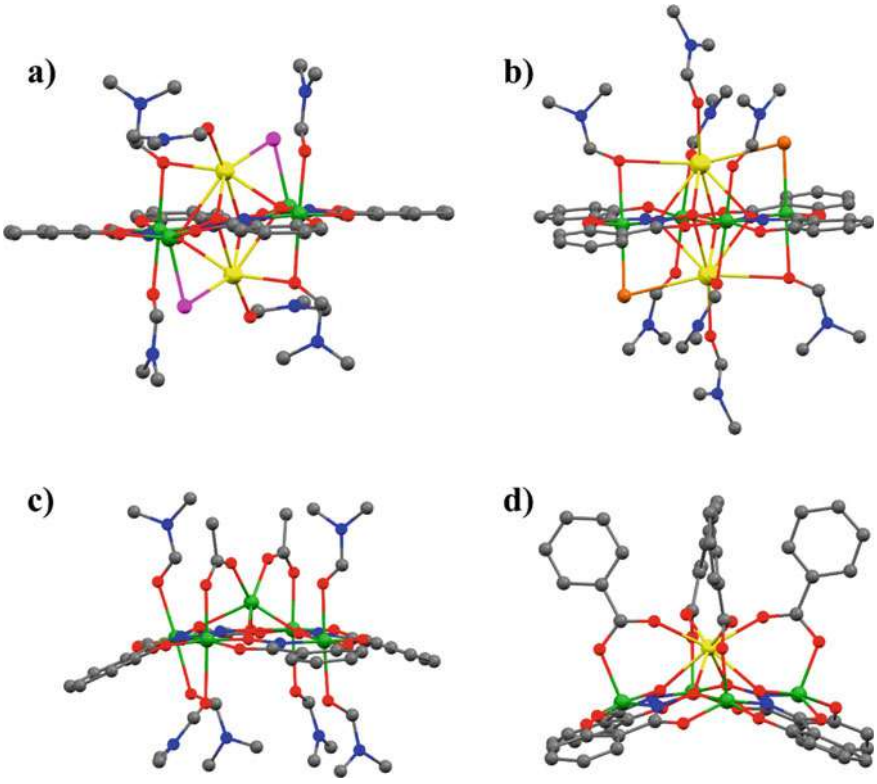

Fig. 7 Single-crystal X-ray structures of previously reported M_mX_n[12-$MC_{Mn(III)N(shi)}$-4] compounds (side views): **a** Na_2Cl_2[12-$MC_{Mn(III)N(shi)}$-4] [28]; **b** K_2Br_2[12-$MC_{Mn(III)N(shi)}$-4] [28]; **c** $Mn(OAc)_2$[12-$MC_{Mn(III)N(shi)}$-4] [35]; **d** Ca(benzoate)$_4$ [12-$MC_{Mn(III)N(shi)}$-4]$^{2-}$ [59]. Hydrogen atoms, lattice countercations, and lattice solvent molecules have been omitted for clarity. Reprinted with permission from Azar, M.R., Boron, T.T., Lutter, J.C., Daly, C.I., Zegalia, K.A., Nimthong, R., Ferrence, G.M., Zeller, M., Kampf, J.W., Pecoraro, V.L., Zaleski, C.M.: Inorg. Chem. 53, 1729–1742 (2014). Copyright 2014 American Chemical Society [60]

Establishing the capability to replace the central alkali or transition metal facilitated a great diversification in metallacrown structures. As compared to the analogous organic 12-crown-4, 12-MC-4 structures are notably more versatile at guest recognition, recognizing transition metals and rare earths as well as alkali metals. Experiments with substitution of alkali and transition metal salts with M^{n+}[12-$MC_{Mn(III)N(shi)}$-4]$^{n+}$ provided evidence that MC recognition preferred cation/anion pairs rather than simply cations or anions. That is to say, structures favored a halide or pseudohalide counter ion (e.g., chloride, thiocyanide) when an alkali metal was bound, but a carboxylate (e.g., acetate) when manganese was bound [25, 58]. Other small MCs have similarly shown cation/anion pair selectivity and have been observed to stabilize reactive species [27].

In contrast to the organic crowns and metallacrowns, nature's arguably most famous macrocycle, the porphyrin, has a notoriously slow reaction of metal incorporation into the macrocycle [61, 62]. In nature, the incorporation of the metal into the porphyrin ring is mediated by chelatase, a chaperone protein [63–65]. When these compounds are synthetically produced, the metalation step often requires elevated temperatures, long reaction times, large excess of metal reagent, or catalytic conditions to incorporate the metal in the ring [66, 67]. Additionally, porphyrin ligands are noninnocent and affect the oxidation state of the bound metal. As a result, transition metal binding to a porphyrin typically has exceptionally high stability [68, 69], and thus, the interaction traditionally is not described as host–guest chemistry. Four-coordinate porphyrins typically prefer transition metals since the pore size is too small for large metals.

1.3 Binding Larger Metals

Enhanced stability with size matching of the radii of the ring cavity and central metal's ionic radius is a unifying thread across macrocycles. Thus, larger macrocycles are typically required for the lanthanides, actinides, and other large main block metals, and the modest change in ionic radius caused by the lanthanide contraction across the period can implicate subtle differences in complex stability. Moreover, the orientation and symmetry of axially coordinated anions can influence the various structures that have been observed. While 15-crown-5 still favors the smaller alkali ions, the larger 18-crown-6 is of suitable size to selectively bind lanthanides; however, its binding conformation wraps the crown around the ion (Fig. 8) [70]. In order to achieve high kinetic stability with large metals bound to a planar porphyrin-based macrocycle, Jonathan Sessler devised an expanded porphyrin, named texaphyrins, synthesized via an easily accessible Schiff base condensation (Fig. 9) [38, 71–73]. These texaphyrins tend to have greater stability with larger lanthanides, thanks to the larger radius of the central cavity. Expanding the metallacrown ring from 12-MC-4 to 15-MC-5 is analogous to the expansion from the tetra-dentate porphyrin to the penta-dentate texaphyrin (Fig. 4).

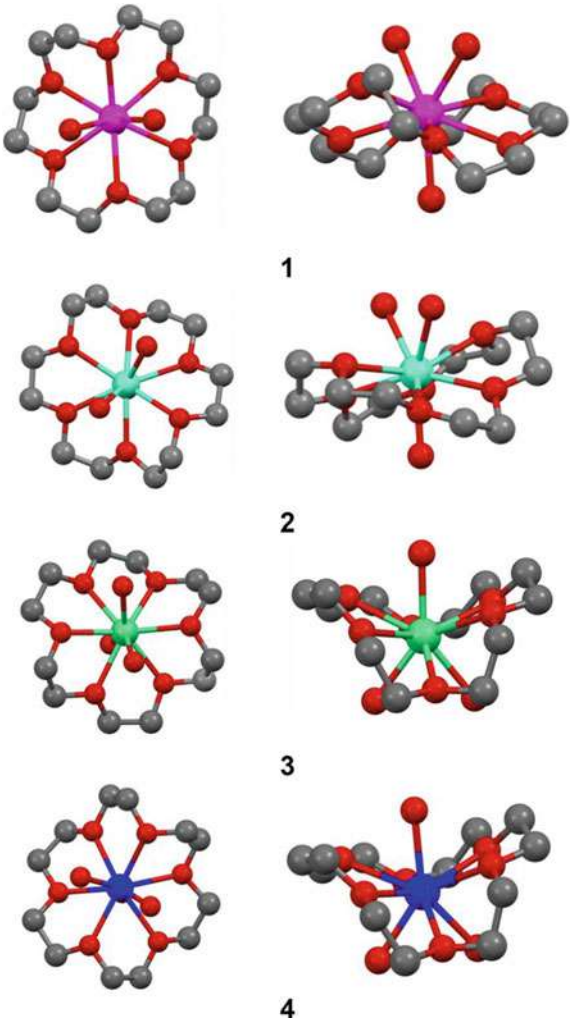

Fig. 8 Representations of the $Ln(H_2O)_3[18\text{-crown-}6](ClO_4)_3$ complexes with $Ln=Tb^{3+}$ (1), Dy^{3+} (2), Er^{3+} (3), and Yb^{3+} (4), illustrating the wrapped conformation of the 18-crown-6 macrocycle around the central ion. Reprinted with permission from Maxwell, L., Amoza, M., Ruiz, E.: Inorg. Chem. 57, 13,225–13,234 (2018). Copyright 2018 American Chemical Society [70]

Like texaphyrin, MCs exhibit size preferences for matching the ring size to the central metal within the lanthanide series. With respect to the 12-MC-4s, the heterotrimetallic $Ln^{III}Na^{I}(OAc)_4[12\text{-}MC_{Mn(III)N(shi)}\text{-}4]$ structures only formed where Ln was Pr^{3+} through Yb^{3+} [60]. These exhibit lanthanide and sodium binding to opposite faces with four acetates bridging the lanthanide to the ring Mn^{3+}. The larger lanthanides of this series cause the MC to have increased doming away from the lanthanide and increased cavity size (MC cavity radius range is 0.58–0.54 Å; Ln crystal radius is 1.15–1.03 Å; the distance of Ln to ring oxime oxygen mean plane is 1.70–1.55 Å) (Fig. 10). La, Ce, and Lu variants of the $Ln^{III}[12\text{-}MC_{Mn(III)N(shi)}\text{-}4]^{3+}$ do not form, instead yield crystals of the di-sodium species $Na_2(OAc)_2[12\text{-}MC_{Mn(III)N(shi)}\text{-}4]$. The inability to form 12-MC-4 s with the largest and smallest

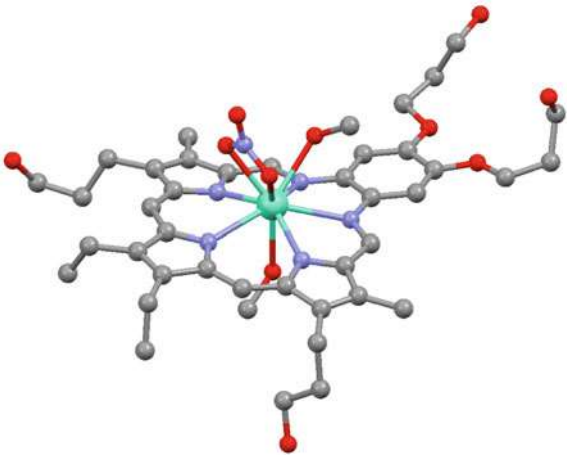

Fig. 9 Crystal structure of the water-soluble $[Gd(NO_3)(CH_3OH)_2(Texaphyrin\text{-}\mathbf{T1})]^+$. The structure illustrates the nine-coordinate Gd and planarity of the texaphyrin ring. Hydrogen, uncoordinated solvent molecules, and counter anions are omitted for clarity. (Texaphyrin-**T1**) = 4,5-Diethyl-10,23-dimethyl-9,24-bis(3-hydroxypropyl)-16,17-(3-hydroxypropyloxy)-13,20,25,26,27-pentaazapentacyclo[20.2.1.13,6.18, 11.014,19]-heptacosa-1,3,5,7,9,11(27),12,14,16,18, 20,22(25), 23-tridecane. Adapted with permission from the supporting material of Sessler, J.L., Mody, T.D., Hemmi, G.W., Lynch, V.: Inorg. Chem. 32, 3175–3187 (1993). Copyright 1993 American Chemical Society [38]

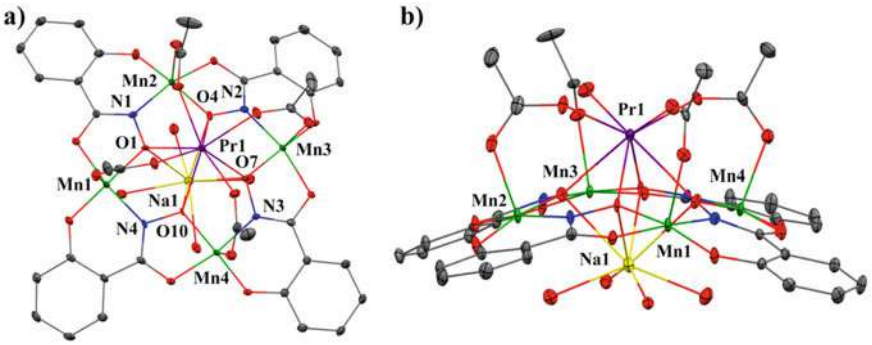

Fig. 10 Single-crystal X-ray structure of $Pr^{III}Na^{I}(OAc)_4[12\text{-}MC_{Mn(III)N(shi)}\text{-}4](H2O)_4{\cdot}6DMF$: **a** top view and **b** side view. All atoms comprising the MC ring are labeled in part a, and only the metal atoms are labeled in part b. Hydrogen atoms and the lattice solvent molecules have been omitted for clarity. Reprinted with permission from Azar, M.R., Boron, T.T., Lutter, J.C., Daly, C.I., Zegalia, K.A., Nimthong, R., Ferrence, G.M., Zeller, M., Kampf, J.W., Pecoraro, V.L., Zaleski, C.M.: Inorg. Chem. 53, 1729–1742 (2014). Copyright 2014 American Chemical Society [60]

lanthanides indicates the limits of the motif's compatibility of host pore size with guest radius.

With the 15-MC-5 motif, the central lanthanides of the series of nitrate salts of $(Ln^{III}[15\text{-}MC_{Cu(II)N(L)}\text{-}5])^{3+}$ can effectively sit within the plane of the macrocycle instead of resting atop a pyramidal structure. With L = picoline hydroxamic acid (picHA), the nine-coordinate Eu ion (1.13 Å) matches closely the radius of the cavity (1.17 Å) and is observed to fit snugly within the MC, with a slight curvature of the MC plane (induced by preferential solvent binding to one face) (Fig. 11) [36]. With L = *L*-phenylalanine hydroxamic acid (pheHA), displacement from the oxime oxygen mean plane for various polymorphs (Ln = La^{3+}–Tm^{3+}) ranges from 0.68 to 0.19 Å [74]. Additionally, the higher stability of the larger lanthanides within the $(Ln^{III}[15\text{-}MC_{Cu(II)N(L)}\text{-}5])^{3+}$ series is supported by the observation that the 15-MC-5s with the smallest lanthanides, i.e., Er^{3+} and beyond, are difficult to isolate in the solid state [74, 75]. 15-MC-5s have been synthesized with various metals indiscriminate of oxidation state including lanthanides, Y^{3+}, UO_2^{2+}, Pb^{2+}, Hg^{2+}, Ca^{2+}, Na^+, and Ag^+, as has been summarized in a review by Tegoni and Remelli [76].

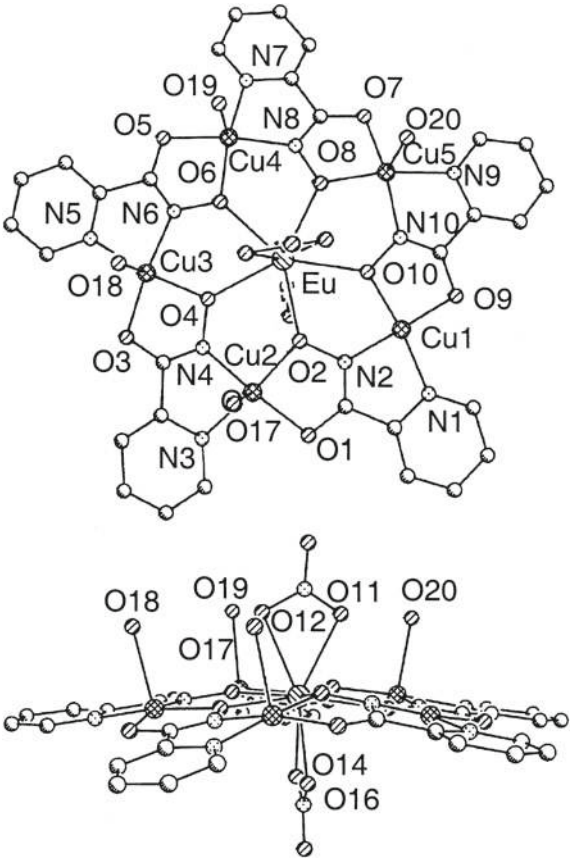

Fig. 11 Crystallographic diagram of $Eu(NO_3)_3[15\text{-}MC_{Cu(II)N(picHA)}\text{-}5]$, top and side views. Eu is observed lying within the plane of the 15-MC-5. Reprinted with permission from Stemmler, A.J., Kampf, J.W., Kirk, M.L., Atasi, B.H., Pecoraro, V.L.: Inorg. Chem. 38, 2807–2817 (1999). Copyright 1999 American Chemical Society [36]

2 Building up Systems of Greater Complexity

The versatility of hydroxamic acid ligands in coordination chemistry means that various metals can be utilized in the MC ring. Many recent studies have targeted the formation of optically transparent MCs as candidates for luminescent biological imaging, through the use of Ga^{3+} or Zn^{2+} in the ring. Similar lanthanide encapsulation as that observed with Mn^{3+}-based MCs was obtained using Ga^{3+} in the $Ln^{III}Na^{I}(OAc)_4$[12-$MC_{Ga(III)N(shi)}$-4] series (Fig. 12b). The smaller lanthanides are again favored in crystal structures, in particular, Sm^{3+} through Yb^{3+} [77]. The ring of these heterotrimetallic Ga^{3+}-based MCs were found to be of similar planarity as mixed valent $Mn^{II}(OAc)_2$[12-$MC_{Mn(III)N(shi)}$-4] and slightly more planar than their $Ln^{III}M^{I}$(benzoate)$_4$[12-$MC_{Mn(III)N(shi)}$-4] counterparts.

"Double-decker" MC complexes, sometimes abbreviated by their stoichiometry $M^{n+}{}_xGa_8L_8L'_4$, may be formed by two [12-$MC_{Ga(III)N(shi)}$-4] rings both chelating to an octa-dentate Na^+ or Ln^{3+} (Ln = Pr–Yb) and bridged by four hydroxide anions (Fig. 12a and d) [78–80]. Sometimes these complexes are also characterized as metallacryptates due to the encapsulation of a guest ion between two rings. These compounds were observed to remain intact in solutions with some exchange of the bridging OH^- groups for CH_3O^-. Larger Ga_8 complexes may be achieved by incorporating bifunctional isophthalate^{2-} anions as bridges across two [12-$MC_{Ga(III)N(shi)}$-4] rings, each ring chelating an Ln^{3+} and an Na^+ for charge balance (Fig. 12c) [81]. The bridges on this Ga_8 compound are quite stable against breaking up to

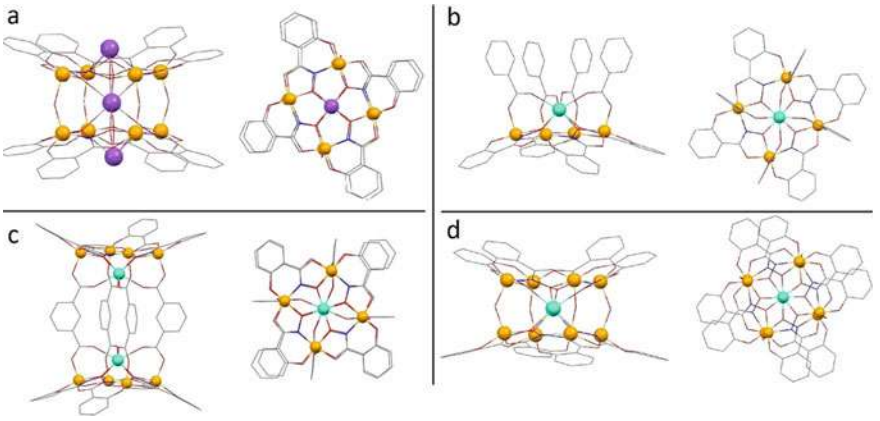

Fig. 12 Side (left) and top-down (right) views of some "double-decker" Ga^{3+}/shi MCs based on the 12-MC-4 motif. **a** [Na_3Ga_8(shi)$_8$(OH)$_4$] [78]. **b** [$DyGa_4$(shi)$_4$(benzoate)$_4$] [77]. **c** [Dy_2Ga_8(shi)$_8$(isophthalate)$_4$] [81]. (d) [$NdGa_8$(shi)$_8$(OH)$_4$] [80]. Solvents of crystallization, nonintegral counter ions, and hydrogen atoms have been omitted for clarity. Color code: Ga, orange; Na, violet; Ln, teal; O, red; N, blue; C, grey. Reprinted with permission from Salerno, E.V., Eliseeva, S.V., Schneider, B.L., Kampf, J.W., Petoud, S., Pecoraro, V.L.: J Phys Chem A. 124, 10,550–10,564 (2020). Copyright 2020 American Chemical Society [80]

form monomers, unlike smaller mono-carboxylate bridges like trimethyl acetate or benzoate, which have been observed by NMR to exchange off the ring [82].

The double-decker motif has been found as a guest itself in a complex of S_8 symmetry with an overall stoichiometry of $LnZn_{16}L_{16}$, which is described as a host (host–guest) complex, where L is picoline hydroxamic acid (picHA) [83]. The structure, synthesized from picHA, sodium hydroxide, zinc triflate, and lanthanide nitrate in methanol with added pyridine, consists of a dimer of two concave 12-MC-4s (Zn_4picHA_4) each of which is four-coordinate to the same shared guest Ln(III) ion, which is also surrounded by a belt of 24-MC-8 (Zn_8picHA_8) acting as an additional cavitand host (Fig. 13) [83]. The host–guest $Ln^{III}(Zn_4picHA_4)_2$ can be isolated inde-

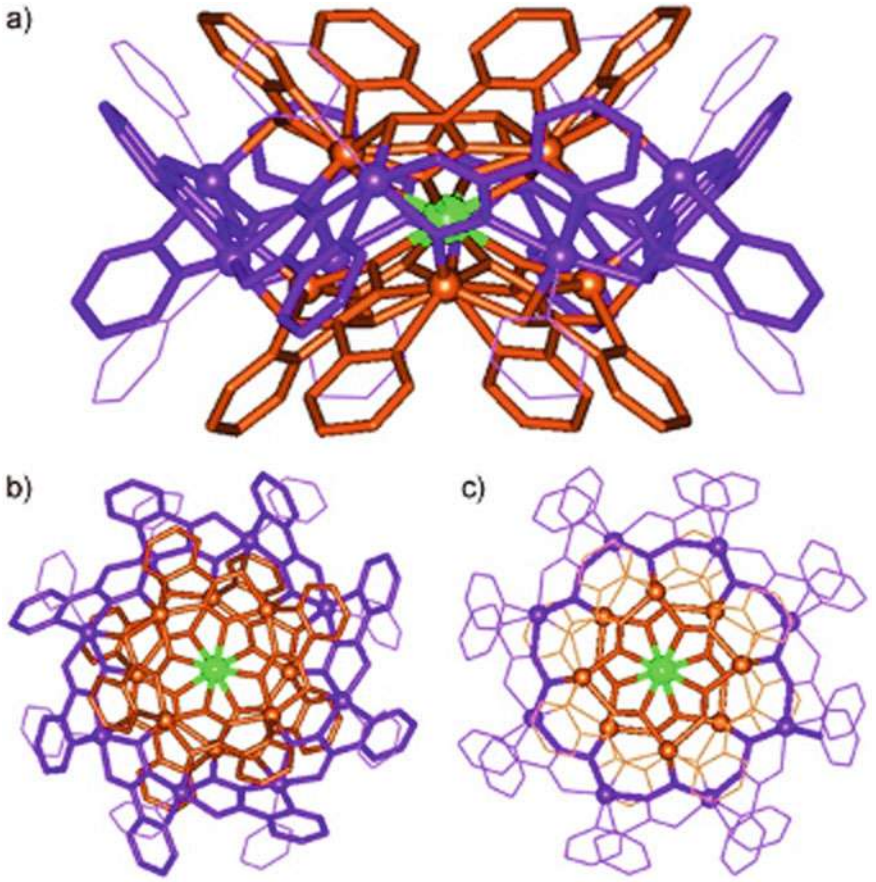

Fig. 13 X-ray crystal structure of the host (host–guest) complex, $Tb^{III}[12\text{-}MC_{Zn(II)N(picHA)}\text{-}4]_2 \subset [24\text{-}MC_{Zn(II)N(picHA)}\text{-}8]\cdot(pyridine)_8\cdot(triflate)_3$ shown **a** perpendicular to the C_4 axis, **b** down the C_4 axis, and **c** highlighting the MC macrocycle. Color scheme: bronze = [12-MC-4], purple = [24-MC-8], green = Tb^{III}. Coordinated pyridine ligands are displayed as thin purple lines. Reprinted with permission from John Wiley & Sons [83]

pendently, but the 24-MC-8 cannot be, indicating that it apparently is stabilized by its interaction with the interior structure. This Zn_{16} complex has excellent luminescent properties arising from the protection of the Ln from C–H and O–H oscillators on the ligands and from solvent molecules, but poor solubility. Lanthanides from La^{3+} to Yb^{3+} were all shown by electrospray ionization MS to be stable in solution and stable against exchange of the Ln^{3+}, indicating the Zn_{16} motif is less sensitive to lanthanide size than simple 12-MC-4 or 15-MC-5s. Interestingly, the dianionic picHA ligand has a chelating motif that typically templates two five-membered chelate rings more suitable to form a simple planar 15-MC-5 (Fig. 11), as is often found with Cu^{2+} and Ni^{2+} [36, 84]. However, with the square pyramidal Zn^{2+} ion, the 12-MC-4-based structure of the Zn_{16} becomes feasible. Under different stoichiometric proportions and crystallization conditions, these same building blocks are capable of self-assembling into the more planar 15-MC-5 complex, ruffled to accommodate the square pyramidal preference of Zn^{2+} [85].

The structural versatility of the metallacrown motif is underscored by the ability of $(Ln^{III}[15\text{-}MC_{M(II)N(picHA)}\text{-}5])^{3+}$ to achieve stable complexes, with either Ni^{2+}, Cu^{2+}, or Zn^{2+}, metals of significantly different coordination preferences (examined with the same ligand and the same central metal Eu^{3+}) [36, 85, 86]. Whereas Ni^{2+} and Cu^{2+} are octahedral or Jahn–Teller distorted, respectively, Zn^{2+} distinctly prefers a square pyramidal environment, which results in a distortion from planarity of the ring and manifests as a ruffled structure for the 15-MC-5 [85]. Remarkably, the environment of the central Eu^{3+} metal is relatively unperturbed by changing the identity of the ring metal, having similar Eu-$O_{hydroximate}$ distances in all three structures. Instead, the angles and distances of the picHA–M^{2+} bonds adjust slightly to accommodate the geometric preference of the ring metal, such that the environment of the central ion is preserved.

3 15-MC-5 Host–Guest Chemistry

Some of the most detailed host–guest and stability studies on metallacrowns have been performed using the 15-MC-5 configuration, either with picHA or with ligands derived from the chiral α-amino acids, e.g., *L*-phenylalanine hydroxamic acid (pheHA), *L*-tyrosine hydroxamic acid (tyrHA), *L*-tryptophan hydroxamic acid (trpHA), *L*-alanine hydroxamic acid (alaHA), etc., which form chiral metallacrowns. These chiral metallamacrocycles have been found, like other metallacrowns, to act as strong hosts for a central ion. Coordinating anions add additional complexity and lead to interesting solution state behavior and the formation of novel solid-state structures.

3.1 Central Ion as Guest in 15-MC-5

The 15-MC-5 motif has been examined thoroughly for its affinity for various central ions. Thermodynamic measurements, mass spectrometry, and computations suggest that a vacant 15-MC-5 can be formed using Ni^{2+} and the α-amino hydroxamic acids (alanine or valine hydroxamic acids) [87]; however, isolation of the vacant 15-MC-5 is elusive. The 15-MC-5, such as that formed using Cu^{2+} and picHA, is not stable in the absence of a central ion, instead favoring the formation of a 12-MC-4 structure with stoichiometry M_5L_4, where a fifth Cu^{2+} is encapsulated within the 12-MC-4 ring. Although pentanuclear $(Cu^{II}[12\text{-}MC_{Cu(II)N(L)}\text{-}4])^{2+}$ structures with β-alanine hydroximate [88] or 3-amino-3-hydroximinopropane hydroximate [89, 90] were published displaying a pattern of six- and five-membered chelate rings, a Cu-centered $[12\text{-}MC_{Cu(II)N(L)}\text{-}4]$ with the α-amino hydroximates that form a five–five membered chelate motif has never been crystallized, with only reported instances of the powder being isolated [91]. Tegoni et al. investigated the mechanism of formation of the $(Cu^{II}[12\text{-}MC_{Cu(II)N(L)}\text{-}4])^{2+}$ MC in a kinetic and thermodynamic study and found that dimeric $(Cu_2HL_2)^{2+}$ or dinuclear $(Cu_2L)^{2+}$ quickly forms followed by sequential incorporation of monomers of $(CuHL)^{+}$ until the 12-MC-4 crown is assembled, where L^{2-} indicates the doubly deprotonated form of *L*-alaHA [92]. The introduction of La^{3+} is understood to bind to the $(Cu^{II}[12\text{-}MC_{Cu(II)N(L)}\text{-}4])^{2+}$ likely on the opposing face of the crown from the central Cu^{2+} and then, with additional ligand, the structure rearranges to form the more stable $(La^{III}[15\text{-}MC\text{-}5])^{3+}$. The formation of the 15-MC-5 from the 12-MC-4 has been observed numerous times with the introduction of a larger metal ion (e.g., calcium, lanthanide, or uranyl ion) [93, 94]. For $(M'[15\text{-}MC_{Cu(II)N(picHA)}\text{-}5])^{n+}$, a series of ions with increasing affinity has been identified, ordered as Na^{+}, Ag^{+} $< Ln^{3+}$, Hg^{2+} $< Pb^{2+}$ [95]. The order takes into account geometric and electronic factors, preferring relatively larger central ions and those that form stronger bonds with the N and O donor atoms of the ring. Similarly, in $(Ca^{II}[15\text{-}MC_{M(II)N(picHA)}\text{-}5])^{2+}$, the Ca^{2+} is easily displaced from the central cavity by lanthanides or the uranyl ion, even in high excess of Ca^{2+} (up to ten-fold) [84], with an order of stability Ca^{2+} $< Ln^{3+}$ $< U^{VI}O_2{}^{2+}$. The binding of lanthanides to the 15-MC-5 was further explored with tyrHA and pheHA thermodynamically, and trpHA kinetically, demonstrating that the stability constant increased with lanthanide size in a direct displacement reaction of Ca^{2+} from $(Ca^{II}[15\text{-}MC_{Cu(II)N(L)}\text{-}5])^{2+}$ (Fig. 14) [96, 97]. An 18-crown-6 is unable to displace the central metal from $(M^{n+}[15\text{-}MC_{Cu(II)N(L)}\text{-}5])^{n+}$, where L is an *L*-alpha amino acid, even in a large excess of crown ether, shown for the uranyl ion [94] and for calcium and lanthanum [96]. Conversely, the 15-MC-5 is preferentially formed by extracting Ca^{2+} from a $([Ca \subset (18\text{-}C\text{-}6)](NO_3)_2)$ complex [96].

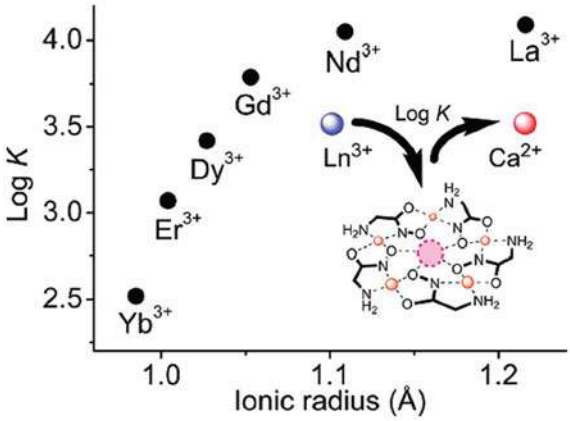

Fig. 14 Plot of the log K values of the replacement reaction $(Ca^{II}[15\text{-}MC_{Cu(II)N(trpHA)}\text{-}5])^{2+} + Ln^{3+} \rightarrow (Ln^{III}[15\text{-}MC_{Cu(II)N(trpHA)}\text{-}5])^{3+} + Ca^{2+}$ (methanol/water 99:1) as a function of the Ln^{3+} ionic radius [41]. Reprinted with permission from Tegoni, M., Furlotti, M., Tropiano, M., Lim, C.S., Pecoraro, V.L.: Inorg. Chem. 49, 5190–5201 (2010). Copyright 2010 American Chemical Society [96]

3.2 15-MC-5 Structures

The α-S-amino hydroxamic acid ligands with aromatic side chains (e.g., pheHA and tyrHA) are of particular interest due to the amphipathic quality of the resultant MCs. Due to the chirality of the amino acid-derived ligands and the directionality of the C–N–O repeating unit within the MC ring, the MCs have opposing hydrophobic and hydrophilic faces. When crystallized from aqueous solutions, these MCs form compartments like two hands facing each other, due to the influence of *pi*-stacking interactions of the aromatic side chains (Fig. 15) [75, 98]. With tyrHA, a phenolate oxygen from each MC binds directly to a Cu^{2+} of the opposing MC (Fig. 16) [98]. In contrast, when the complexes are crystallized from methanolic solutions they form resolved four-fold helical structures, with the hydrophilic faces of the MCs oriented toward the interior of the helix, which contain solvent-filled square pores approximately 11 Å across. Mirror-image helicity (P vs M) could be controlled simply by using the L or D enantiomer of the α-amino hydroximate (Fig. 17) [99].

3.3 Anion Recognition

Within the 15-MC-5 family, significant efforts have been devoted to understanding relevant anion recognition capabilities, adding an additional supramolecular level to the complexity of host–guest interactions. An early result showed that $(Gd^{III}[15\text{-}MC_{Cu(II)N(pheHA)}\text{-}5])^{3+}$, sometimes abbreviated $GdCu_5pheHA_5$, selectively binds

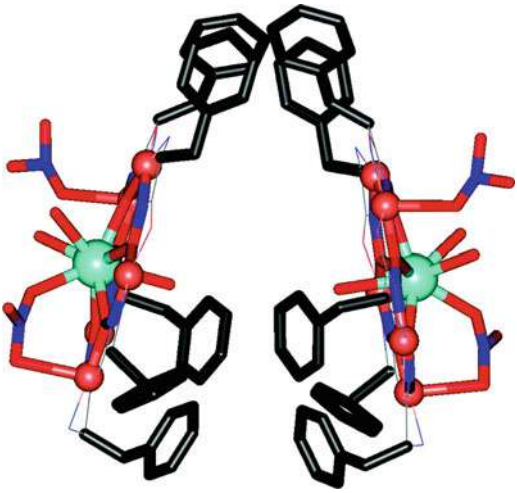

Fig. 15 Metallacrowns of $La(NO_3)_3$[15-$MC_{Cu(II)N(L\text{-pheHA})}$-5], crystallized from water, come together to form a dimer reminiscent of two hands facing each other. Copper−water bonds, hydrogen atoms, and the lattice nitrate and solvent have been removed for clarity. This figure was originally modified from the supporting material of Zaleski, C. M.; Depperman, E. C.; Kampf, J. W.; Kirk, K. M.; Pecoraro, V. L.: Inorg. Chem. 45, 10,022–10,024 (2006), [100], and reprinted with permission from Zaleski, C.M., Cutland-Van Noord, A.D., Kampf, J.W., Pecoraro, V.L.: Crys. Growth Des. 7, 1098–1105 (2007) Copyright 2007, American Chemical Society [75]

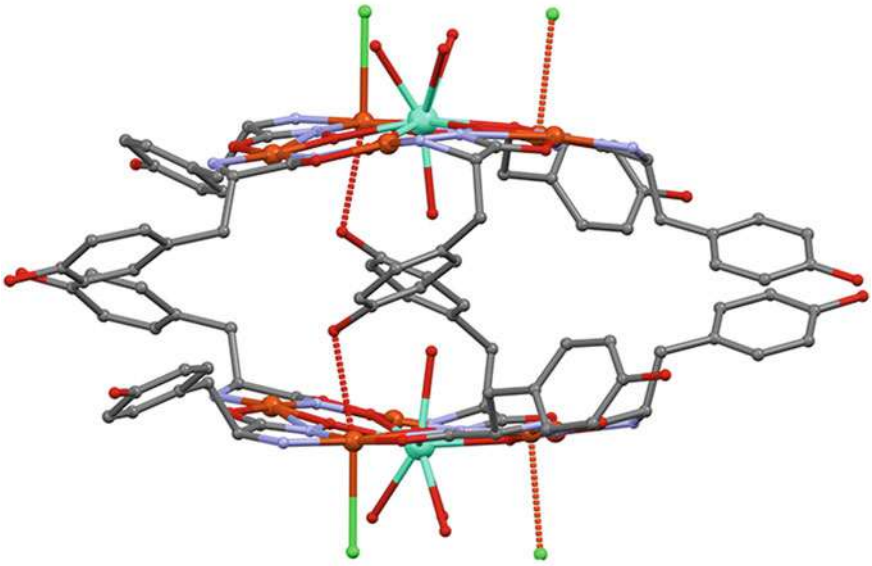

Fig. 16 Crystallographic diagram of the dimer of two MCs of Gd(Cl)[15-$MC_{Cu(II)N(L\text{-tyrHA})}$-5]$^{2+}$, demonstrating interactions between the tyrosyl oxygen and the opposing Cu ring metal to bridge the hydrophobic cavity. Figure adapted with permission from John Wiley & Sons [98]

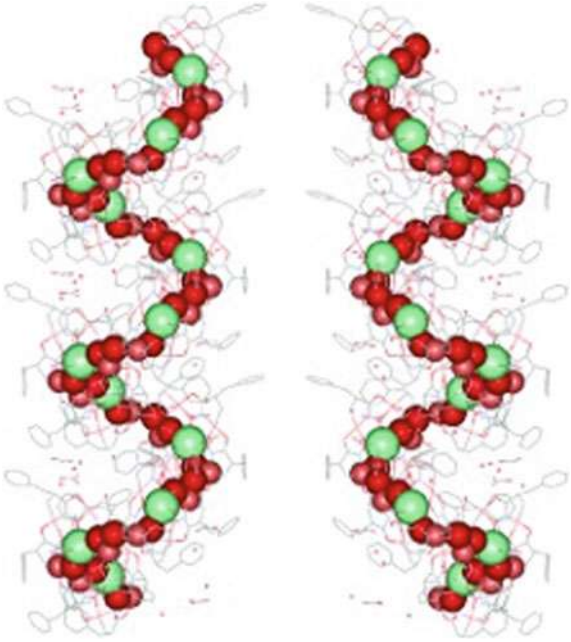

Fig. 17 Comparison of the helical structure of $Sm(NO_3)$[15-$MC_{Cu(II)N(L\text{-pheHA})}$-5]$(NO_3)_2$ and its counterpart made with *D*-pheHA with opposing helicity. The continuous chain of Cu–O-Sm–O-Cu–O through the metallacrowns is depicted as space-filled models. Reprinted with permission from John Wiley & Sons [99]

nitrate anions to its hydrophobic face and chloride anions to its hydrophilic face in the presence of both anions in the "hands-hands" dimer formation [98]. Benzoate may be precipitated selectively via binding with the MC from an aqueous solution containing sodium salts of benzoate, acetate, and trifluoroacetate. Upon the examination of binding with dicarboxylate guests, $GdCu_5pheHA_5$ was found to bind some carboxylates preferentially within the hydrophobic cavity formed by two MCs facing each other [101, 102]. The formation of a compartment was considered to occur when dimers formed with the "hand-hand" motif in a cylindrical structure, often sequestering a guest from the surrounding solvent. In consideration of which types of guests were preferred, the saturated, aliphatic dicarboxylates, adipate and glutarate were found to bridge only the hydrophilic faces in the solid state, whereas the aromatic terephthalate was found to form a continuous chain of alternating MC and guest (Fig. 18) [101]. An asymmetrical capsule with three isonicotinate guests sequestered within the hydrophobic cavity, two lying parallel to each other and the third lying antiparallel was also observed [103]. Species with one or two isonicotinates bound to an MC were observed by electrospray ionization mass spectrometry (ESI–MS), but a species with two MCs and isonicotinate was not observed, suggesting that the capsule-like species of two metallacrowns was not likely found in solution with this guest. While it was initially suspected that guest unsaturation or aromaticity was a critical factor for incorporation into the hydrophobic cavity, later calorimetric studies indicated that the length and shape of the guest were much more important [104].

Therefore, in accordance with supramolecular canon, the length of guest sequestered and the length of ligand side chains of the MC need to be compatible,

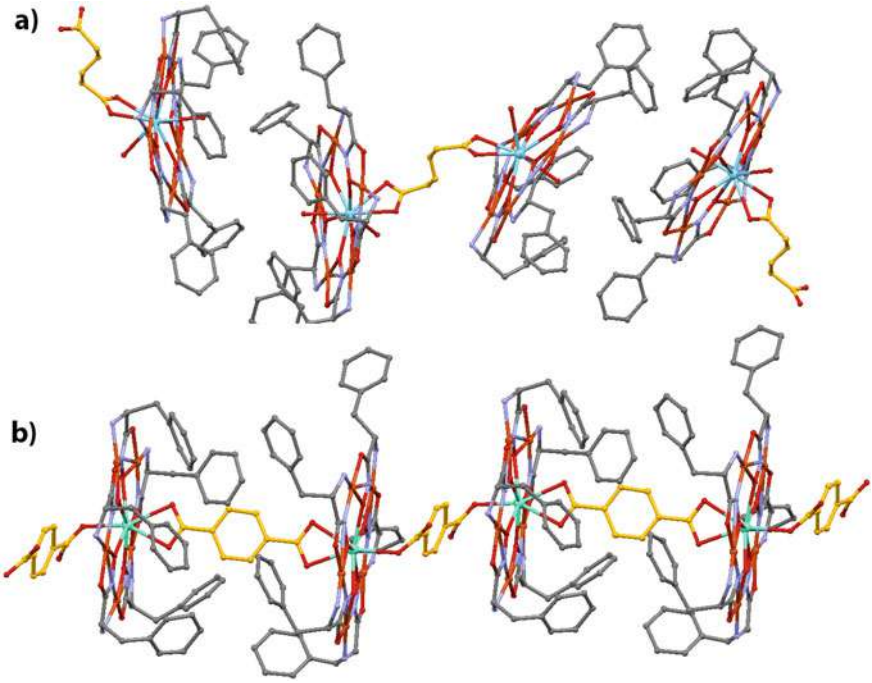

Fig. 18 Structures of metallacrown dimers linked by dicarboxylates. **a** $(La(adipate)_{0.5}[15\text{-}MC_{Cu(II)N(L\text{-}pheHA)}\text{-}5])_2$ shows metallacrowns linked by adipate across the hydrophilic faces, and **b** $(Gd(terephthalate)[15\text{-}MC_{Cu(II)N(L\text{-}pheHA)}\text{-}5])_2$ shows metallacrowns linked by terephthalate across the hydrophobic and hydrophilic faces. Adapted with permission from Cutland, A.D., Halfen, J.A., Kampf, J.W., Pecoraro, V.L.: J. Amer. Chem. Soc. 123, 6211–6212, (2001). Copyright 2001 American Chemical Society [101]

neither too long nor too short, in order to maintain the integrity of the hydrophobic cavity [102, 105, 106]. Short guests, such as fumarate, may bind at an angle, monodentate to one Gd, since they are too short to span the distance to bind the second Gd. This causes a distortion of the dimer, preventing the formation of a cylindrical compartment in the solid state. Instead, the angle of one MC is tilted and offset to one side (Fig. 19) [102]. A guest that is too long, such as naphthalene dicarboxylate, will still bind to the hydrophobic face, but interferes with the bridging *pi* interaction of the MC's side chains such that the hydrophobic compartment does not form at all [102]. Both of these disrupt the integrity of the hydrophobic cavity and increase solvent access to the interior. To form the hydrophobic cavity with these mismatched guests, longer and shorter ligands, *L*-homophenylalanine hydroxamic acid (hpheHA) and *L*-phenylglycine hydroxamic acid (pgHA) respectively, were incorporated in the MCs, with hpheHA showing the particular capacity to sequester the 9.2 Å *trans*-bithiophene dicarboxylate [106], which had been too long to form a compartment with pheHA [105].

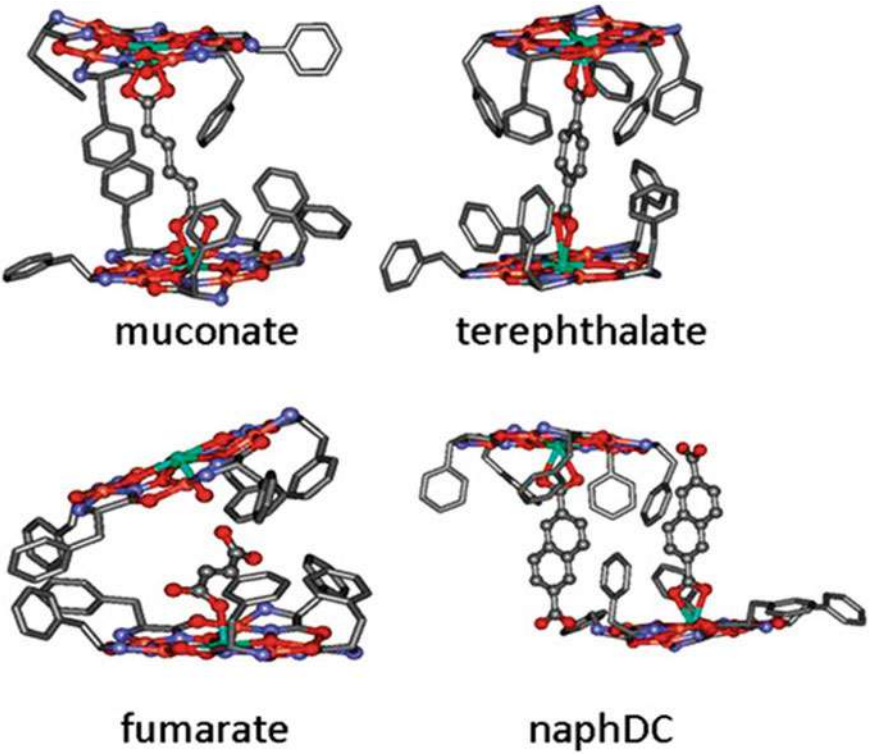

Fig. 19 Structures of muconate and terephthalate with $(Gd[15\text{-}MC_{Cu(II)N(L\text{-}pheHA)}\text{-}5])^{3+}$ show molecular compartments. However, fumarate and 2,6-naphthalenedicarboxylate (naphDC) with the same MC do not form compartments. Guests on the hydrophilic sites of both metallacrowns of all compartments were omitted. Reprinted with permission from John Wiley & Sons [102]

3.4 Porous Structures

Using the same kind of dicarboxylate and chiral amphipathic 15-MC-5 building blocks, a mesoporous solid-state assembly was obtained when the appropriate guest and lanthanide central metal was used [107]. With saturated seven- and eight-carbon aliphatic dicarboxylates and $LaCu_5pheHA_5$, each of the four oxygens of the dicarboxylate guest binds to a Cu^{2+} ring metal on the hydrophilic face of a separate adjacent MC, which draws four MCs together into a tetramer cage around the guest (Fig. 20a, b). A pair of these bowl-shaped tetramers interlock through *pi* interactions of their externally facing hydrophobic side chains to form an octamer around a hydrophilic channel (dimensions 8.9 Å × 14.6 Å) that allows access to a chamber of ~2300 $Å^3$. The packing of the crystal lattice reveals that *pi* interactions at the hydrophobic faces of the octamers (Fig. 20c) orient the MCs into a hexagonal lattice containing solvent-filled cavities more than 2.4 nm in diameter, to which access is gained through the hydrophilic channel (Fig. 20d). Although the cavity collapsed

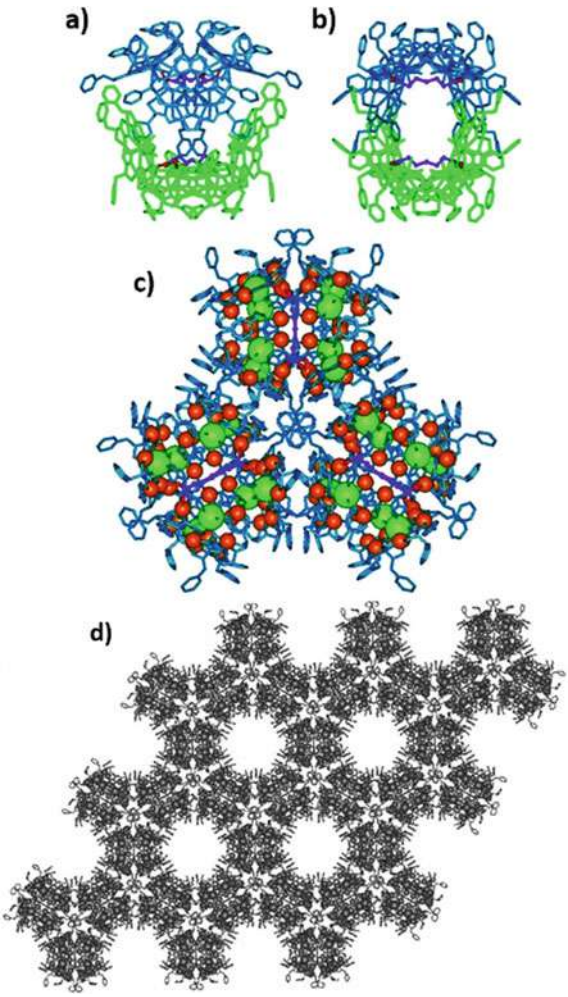

Fig. 20 Packing of the porous structure formed by the interaction of $La(NO_3)_{2.5}$[15-$MC_{Cu(II)N(L\text{-pheHA})}$-5]$(OH)_{0.5}(H_2O)_{3.5}$ with the seven carbon saturated dicarboxylate (C7DC), pimelate. **a** Two tetrameric bowls, generated by pimelate bridges, interlock yielding a hydrophilic octameric MC cavity. View (**b**) illustrates the opening to the hydrophilic cavity, which could serve as an access route for guest molecules into the structure. Color scheme: green and blue: tetrameric MC bowls dimerizing through π–π interactions; purple and red: C7DC. **c** View illustrating the hydrophobic contacts between octameric compartments that generate the packing motif observed in view (**d**). Color scheme: blue: MC framework; green: lanthanum; orange: copper; purple and red: C7DC. View (**d**) displays how six octametallacrown compartments are connected via π–π interactions on their external hydrophobic faces to generate the channel in its interior. Metal ions are displayed with their CPK radii. Water molecules and unbound guests were removed for clarity of all images. Reprinted with permission from John Wiley & Sons [107]

upon dehydration, likely indicating critical hydrogen bonding interactions from water molecules, chromophoric dye molecules could be absorbed and sequestered within the cavities [107].

Planar MC units of $LnCu_5GlyHA_5$ with *meta*- and *para*-phthalate bridges, where GlyHA is the doubly deprotonated form of glycine hydroxamic acid, have also been found to crystallize into porous structures with large void volumes [108–110]. This group of structures, synthesized by combining the sulfate salt of $LnCu_5GlyHA_5$ MCs with *m*- or *p*-benzene dicarboxylate to instigate anionic metathesis, has resulted in various structures, including 1D coordination chains, discrete multi-decker units, and coordination chains interspersed with discrete complex ionic units (Fig. 21). Structure formation exhibits dependency on the lanthanide identity. Although complete dehydration caused the structural collapse, activation could be achieved by partial drying at moderate temperature (130 °C) under vacuum. In particular, $GdCu_5GlyHA_5$ with *m*-phthalate absorbed methanol in a manner characteristic of microporous sorbents [108] while sorption studies of other structures, including the analogous Eu compound [109] and some Cu_5L_4 type MCs (with L=3-amino-3-hydroximinopropane hydroxamic acid) [89, 90] were suspected of significant structural rearrangement upon absorption of methanol or ethanol. The magnetic properties of these compounds were also studied in detail. Structural changes such as solvation effects that result in a change in magnetic behavior can provide a foundation for the development of chemical sensors.

3.5 Measuring Guest Affinities

Although the various solid-state structures provide a wealth of geometric information, the strength of guest binding must be probed in solutions via binding assays, measured for example by isothermal titration calorimetry (ITC) [111, 112], electrochemistry [113, 114], or spectroscopy [115]. Studies with monocarboxylates have indicated reversible binding, with examples ranging in the order of 10^2 M^{-1} for acetate or benzoate[113, 115], 10^3 M^{-1} for ferrocene carboxylate (Fig. 22) [113], and 10^4 M^{-1} for the fluorescent probe coumarin 343 [115], which is a carboxylated coumarin derivative. Often the strength of guest binding increases as lanthanide size decreases, primarily attributed to the increase in Lewis acidity of the lanthanide (Gd, Dy, etc.) [111, 113]. In the case of binding a second guest, the binding constant is always lower than that of the first event. When the early and late lanthanides are compared, the second binding event tends to be stronger for the early lanthanides than for the later ones [111]. This is consistent with crystal structures that show La^{3+} and Nd^{3+} as nine-coordinate, binding two guests both on the hydrophobic face (with a third possibly binding on the hydrophilic face), whereas eight-coordinate Gd^{3+} and Dy^{3+} bind the second guest on the hydrophilic face [111]. Modest enantioselectivity has been observed for *S*- over *R*-enantiomers of mandelate, but adjusting the MC side chain can lead to enhancements in selectivity, with pgHA and hpheHA both showing greater enantioselectivity than does the pheHA MC analog [112, 114]. Guests with

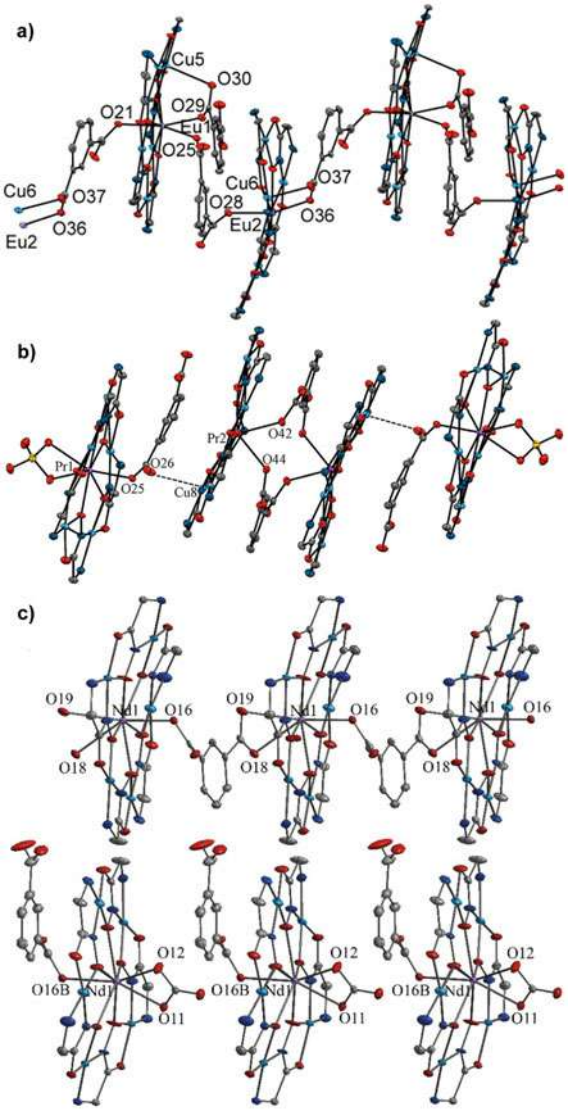

Fig. 21 Examples of assemblies formed between $(Ln^{III}[15\text{-}MC_{Cu(II)N(GlyHA)}\text{-}5])^{3+}$ and 1,3 benzene dicarboxylate (abbreviated *m*-bdc) based on X-ray structures. For clarity, hydrogen atoms and both coordinated and lattice water molecules are omitted from the figures. **a** Ln = Eu forms a one-dimensional coordination polymer. **b** Ln = Pr forms a discrete quadruple-decker unit. **c** Ln = Nd forms a 1D chain $[NdCu_5(GlyHA)_5(H_2O)_5(m\text{-}bdc)]_n^{n+}$, together with discrete complex anions $[NdCu_5(GlyHA)_5(H_2O)_4(\mu\text{-}CO_3)(m\text{-}bdc)]^-$. Adapted with permission from Pavlishchuk, A.V., Kolotilov, S.V., Zeller, M., Lofland, S.E., Thompson, L.K., Addison, A.W., Hunter, A.D.: Inorg. Chem. 56, 13,152–13,165 (2017). Copyright 2017 American Chemical Society [109]

variation of substitution at the alpha carbon (phenylalanine, phenylacetate, mandelate, etc.) allowed for a comparison of guests with variation in the electron density localized at the carboxylate binding motif [112]. A general trend in the strength of carboxylate binding is zwitterion (e.g., amino acid) < monoanion < dianion (e.g., adjacent hydroxide). The addition of an additional electron-rich atom near the Lewis acidic lanthanide site likely enhances the binding affinity.

One of the persistent challenges of host–guest chemistry with MCs has been determining whether the MC compartment, which is often observed in the solid state,

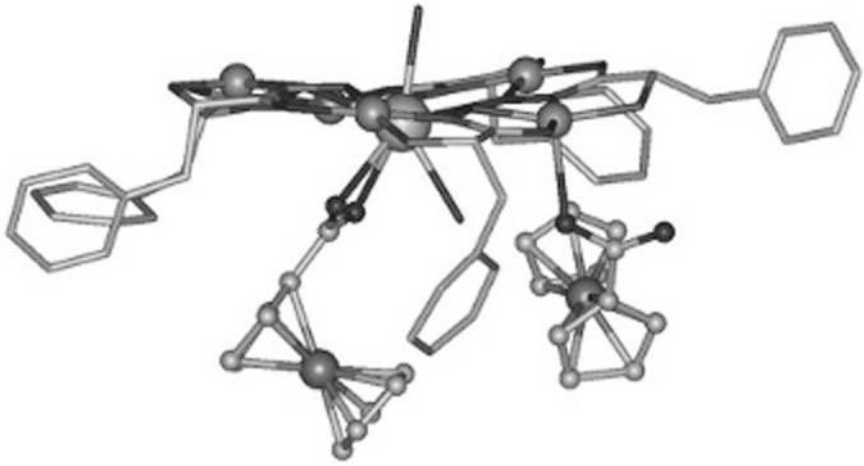

Fig. 22 Two ferrocenecarboxylate anions (FcC^-) are encapsulated in the hydrophobic cavity of $(La^{III}[15\text{-}MC_{Cu(II)N(L\text{-}pheHA)}\text{-}5])^{3+}$. One is bound monodentate to a copper ring metal with eclipsed cyclopentadienyl rings. The other is bound bidentate to lanthanum with staggered cyclopentadienyl rings. Unbound or Cu-coordinated solvent, nitrate, and hydrogens were removed for clarity. Reprinted with permission from John Wiley & Sons [113]

stays together in a solution. Measurements of the thermodynamics of dicarboxylate binding with $(Gd^{III}[15\text{-}MC_{M(II)N(L\text{-}pheHA)}\text{-}5])^{3+}$ showed that the dicarboxylate guest templates formation of the compartment in solution via an equilibrium of the dimer MC–guest–MC (2:1) compartment with the monomeric MC–guest (1:1) complex and free MC [104]. In support of earlier crystallographic evidence with short guests, guests that were too short (oxalate, maleate) were observed to only form a complex of one MC bound with one carboxylate (1:1), implying an inability to span the distance across the cavity. With longer species of suitable length (terephthalate, *trans–trans* muconate, adipate, fumarate), the free energy (ΔG) of the first complexation event to form the 1:1 species, was found to be lower than the ΔG of the second complexation event to form the 2:1, implying that a cooperative solvophobic effect drives the formation of the dimeric compartment.

Recently, a study of muconate binding to $(Ln^{III}[15\text{-}MC_{M(II)N(L\text{-}pheHA)}\text{-}5])^{3+}$ with various lanthanides has indicated the surprising result that the identity of the lanthanide influences whether or not the dimeric compartment can form. MCs with the early and late lanthanides (La, Nd, Sm, and Ho) were found only to form the 1:1 species, whereas the intermediate lanthanides (Eu, Gd, and Dy) were able to participate in the formation of the 2:1 dimeric compartment (Fig. 23) [116]. A balance of lanthanide size (which influences its placement on either face of the MC) and stability of the lanthanide within the MC ring is required for the MC to favor the formation of the 2:1 compartment. Therefore, the formation of the compartment with the Gd analog has the highest stability since the lanthanide lies reasonably well within the MC plane and the MC ring has a high affinity for Gd. In contrast

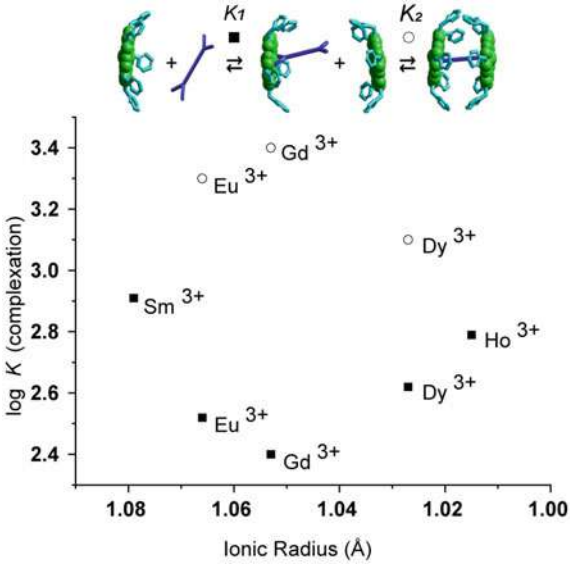

Fig. 23 Stability constants for first and second complexation events of muconate guest (Muc) with MC host according to lanthanide species ionic radius [41]. Selected lanthanides Sm^{3+} through Ho^{3+} with ionic radii of eight-coordinate species. Black squares: K_1 values to describe the equilibrium **MC** + Muc ⇄ (**MC**)Muc; Open circles: K_2 values for **MC** + (**MC**)Muc ⇄ $(\mathbf{MC})_2$Muc. Adapted with permission from John Wiley & Sons [116]

to the increasing stability observed with larger lanthanide size for simple sequestration of the lanthanide within the MC ring (Fig. 14), the preference for intermediate lanthanides in forming more complex assemblies on the supramolecular level previously had not been observed.

4 Conclusion

Various aspects of the host–guest chemistry of metallacrowns have been discussed, from structural characteristics to stability and reactivity. Metallacrowns and metallacryptates consistently have been shown to control the organization of material into supramolecular assemblies with unique properties. Different guest ions preferentially bind based on structural, electronic, and chemical considerations of the macrocyclic ring. A repeating theme is observed as simple metallacrowns can be modularly modified to build larger, more complex assemblies. Peripheral coordination sites, those that are not involved directly in bonds forming the MC ring or central metal to oxime, are utilized on both ring and central metals to obtain new structures, as has been observed for several series of metallacrowns, such as with Ga, Zn, or Cu. Complexes can take the form of a single macrocycle often with carboxylates binding or bridging the central metal and ring metals; two macrocycles can share a single central metal between them with the coordination sphere of the ring metals completed by bridging hydroxides or a belt of other stabilizing ligands; or sometimes two or more macrocycles, each binding a central metal, are bridged by longer dicarboxylates to form large assemblies. Exceptional affinities of the metallamacrocyclic

ring for the central metal can enable a higher level of supramolecular interaction, as observed in the host (host–guest) structure of the belted-dimer of $LnZn_{16}picHA_{16}$ or $(host–guest)_2$–guest interactions as in the dicarboxylate guest-induced dimerization of $LnCu_5pheHA_5$. The metallamacrocyclic hosts confine guest ions or molecules and influence their environment or spatial arrangement, which dictates physical properties, such as enhanced lanthanide luminescence through the elimination of nearby C–H, N–H, or O–H oscillators (e.g., solvent molecules that can dissipate excitation energy through nonradiative processes) as observed for Zn and Ga structures, or altered light absorption as observed when encapsulated dye molecules were shielded from the surroundings within the octameric 15-MC-5 assembly. These diverse host–guest metallacrown assemblies achieve chemistry that is not easily obtained with traditional covalent assemblies. A significant amount of recent work has built on the modularity of MCs to obtain familiar constructs that take advantage of the unique electronic and coordinative properties of lanthanides and produce insights into subtle transitions or differences across the lanthanide series. The understanding gained regarding MC stability and guest binding, both in solution and in the solid state, will continue to influence synthetic approaches to target particular supramolecular objectives, such as sensing, extraction, formulation, and catalysis.

References

1. Lehn, J.-M.: Supramolecular chemistry. Science **260**, 1762–1763 (1993). https://doi.org/10.1126/science.8511582
2. Steed, J.W., Atwood, J.L.: Supramolecular Chemistry. Wiley, West Sussex (2009)
3. Pedersen, C.J.: Cyclic polyethers and their complexes with metal salts. J. Am. Chem. Soc. **89**, 2495–2496 (1967). https://doi.org/10.1021/ja00986a052
4. Pedersen, C.J.: Macrocyclic polyethers for complexing metals. Aldrichimica Acta **4**, 1–4 (1971)
5. Pedersen, C.J.: The discovery of crown ethers (Nobel Lecture). Angew. Chem. Int. Ed. Engl. **27**, 1021–1027 (1988). https://doi.org/10.1002/anie.198810211
6. Kolesnichenko, I.V., Anslyn, E.V.: Practical applications of supramolecular chemistry. Chem. Soc. Rev. **46**, 2385–2390 (2017). https://doi.org/10.1039/C7CS00078B
7. Pedersen, C.J.: Crystalline salt complexes of macrocyclic polyethers. J. Am. Chem. Soc. **92**, 386–391 (1970). https://doi.org/10.1021/ja00705a605
8. Pedersen, C.J.: New macrocyclic polyethers. J. Am. Chem. Soc. **92**, 391–394 (1970). https://doi.org/10.1021/ja00705a606
9. Inoue, Y., Hakushi, T.: Enthalpy–entropy compensation in complexation of cations with crown ethers and related ligands. J. Chem. Soc., Perkin Trans. **2**, 935–946 (1985). https://doi.org/10.1039/P29850000935
10. Liu, Y., Han, B.-H., Chen, Y.-T.: The complexation thermodynamics of light lanthanides by crown ethers. Coord. Chem. Rev. **200–202**, 53–73 (2000). https://doi.org/10.1016/S0010-8545(99)00239-8
11. Liotta, C.L., Berkner, J.: 12-Crown-4. Encyclopedia of Reagents for Organic Synthesis (2001). https://doi.org/10.1002/047084289X.rc262
12. Pacey, G.E., Wu, Y.P.: Ion-pair extractions with 12-crown-4 and its analogues. Talanta **31**, 165–168 (1984). https://doi.org/10.1016/0039-9140(84)80043-0

13. Vögtle, F., Weber, E.: Crown ethers-complexes and selectivity. In: Patai, S., Rappoport, Z. (eds.) Crown Ethers and Analogs. Updates from the Chemistry of the Functional Groups, vol. 3, pp. 207–304. Wiley, Chichester, England, New York (1989)
14. Buchanan, G.W., Kirby, R.A., Charland, J.P., Ratcliffe, C.I.: 12-Crown-4 ethers: solid-state stereochemical features of dibenzo-12-crown-4, derived dicyclohexano-12-crown-4 isomers, and a lithium thiocyanate complex as determined via carbon-13 CPMAS nuclear magnetic resonance and x-ray crystallographic methods. J. Org. Chem. **56**, 203–212 (1991). https://doi.org/10.1021/jo00001a040
15. Mason, E., Eick, H.A.: Structure of a 1:2 complex of sodium perchlorate and 1,4,7,10-tetraoxacyclododecane (12-crown-4). Acta Crystallogr. Sect. B **38**, 1821–1823 (1982). https://doi.org/10.1107/S0567740882007316
16. Bradshaw, J.S., Krakowiak, K.E., Izatt, R.M.: Aza-Crown Macrocycles. Wiley, New York (1993)
17. Kim, S., Lindoy, L.F., Lee, S.S.: Recent developments in the thiamacrocyclic chemistry of the latter d-block elements. Coord. Chem. Rev. **280**, 176–202 (2014). https://doi.org/10.1016/j.ccr.2014.08.011
18. Gokel, G.W., Dishong, D.M., Diamond, C.J.: Lariat ethers. Synthesis and cation binding of macrocyclic polyethers possessing axially disposed secondary donor groups. J. Chem. Soc. Chem. Commun. 1053–1054 (1980). https://doi.org/10.1039/C39800001053
19. Gokel, M.R., McKeever, M., Meisel, J.W., Negin, S., Patel, M.B., Yin, S., Gokel, G.W.: Crown ethers having side arms: a diverse and versatile supramolecular chemistry. J. Coord. Chem. **74**, 14–39 (2021). https://doi.org/10.1080/00958972.2021.1878352
20. Lehn, J.-M.: Supramolecular chemistry—scope and perspectives molecules, supermolecules, and molecular devices (Nobel Lecture). Angew. Chem. Int. Ed. Engl. **27**, 89–112 (1988). https://doi.org/10.1002/anie.198800891
21. Dietrich, B., Lehn, J.M., Sauvage, J.P.: Les cryptates. Tetrahedron Lett. **10**, 2889–2892 (1969). https://doi.org/10.1016/S0040-4039(01)88300-3
22. Brown, C.J., Toste, F.D., Bergman, R.G., Raymond, K.N.: Supramolecular catalysis in metal-ligand cluster hosts. Chem. Rev. **115**, 3012–3035 (2015). https://doi.org/10.1021/cr4001226
23. Ostrowska, M., Fritsky, I.O., Gumienna-Kontecka, E., Pavlishchuk, A.V.: Metallacrown-based compounds: applications in catalysis, luminescence, molecular magnetism, and adsorption. Coord. Chem. Rev. **327**, 304–332 (2016). https://doi.org/10.1016/j.ccr.2016.04.017
24. Lutter, J.C., Zaleski, C.M., Pecoraro, V.L.: Metallacrowns: supramolecular constructs with potential in extended solids, solution-state dynamics, molecular magnetism, and imaging. In: van Eldik, R., Puchta, R. (eds.) Advances in Inorganic Chemistry, vol. 71, pp. 177–246. Academic Press, Cambridge, MA (2018)
25. Lah, M.S., Pecoraro, V.L.: A functional analogy between crown ethers and metallacrowns. Inorg. Chem. **30**, 878–880 (1991). https://doi.org/10.1021/ic00005a002
26. Pecoraro, V.L., Stemmler, A.J., Gibney, B.R., Bodwin, J.J., Wang, H., Kampf, J.W., Barwinski, A.: Metallacrowns: a new class of molecular recognition agents. In: Karlin, K.D. (ed.) Progress in Inorganic Chemistry, vol. 45, pp. 83–177. Wiley, New York (1996)
27. Mezei, G., Zaleski, C.M., Pecoraro, V.L.: Structural and functional evolution of metallacrowns. Chem. Rev. **107**, 4933–5003 (2007). https://doi.org/10.1021/cr078200h
28. Gibney, B.R., Wang, H., Kampf, J.W., Pecoraro, V.L.: Structural evaluation and solution integrity of alkali metal salt complexes of the manganese 12-metallacrown-4 (12-MC-4) structural type. Inorg. Chem. **35**, 6184–6193 (1996). https://doi.org/10.1021/ic960371+
29. Gingl, F., Hiller, W., Strähle, J., Borgholte, H., Dehnjcke, K.: [Li(12-Krone-4)]Cl: kristallstruktur und IR-spektrum. Z. Anorg. Allg. Chem. **606**, 91–96 (1991). https://doi.org/10.1002/zaac.19916060109
30. Ahle, A., Neumüller, B., Pebler, J., Atanasov, M., Dehnicke, K.: $[Na(12\text{-Krone-}4)_2]_2[Ni(Se_4)_2] \cdot DMF$; synthese, kristallstruktur und magnetisches verhalten. Z. Anorg. Allg. Chem. **615**, 131–136 (1992). https://doi.org/10.1002/zaac.19926150927
31. Kamitori, S., Hirotsu, K., Higuchi, T.: Crystal and molecular structures of double macrocyclic inclusion complexes composed of cyclodextrins, crown ethers, and cations. J. Am. Chem. Soc. **109**, 2409–2414 (1987). https://doi.org/10.1021/ja00242a026

32. Schreiner, B., Dehnicke, K., Fenske, D.: Synthese und kristallstruktur von [Na(15-Krone-5)]$_4$[Cd_4Te_{12}] · 8 DMF. Z. Anorg. Allg. Chem. **619**, 1127–1131 (1993). https://doi.org/10.1002/zaac.19936190627
33. Luger, P., Andre, C., Rudert, R., Zobel, D., Knochel, A., Krause, A.: X-ray structure of 18-crown-6-$KClO_4$ at room temperature and 20 K. Acta Crystallogr. Sect. B **48**, 33–37 (1992). https://doi.org/10.1107/S0108768191011631
34. Lah, M.S., Kirk, M.L., Hatfield, W., Pecoraro, V.L.: The tetranuclear cluster Fe^{III}[Fe^{III}(salicylhydroximato)(MeOH)(acetate)]$_3$ is an analogue of M^{3+}(9-crown-3). J. Chem. Soc. Chem. Commun. 1606–1608 (1989). https://doi.org/10.1039/C39890001606
35. Lah, M.S., Pecoraro, V.L.: Isolation and characterization of {Mn^{II}[Mn^{III}(salicylhydroximate)]$_4$(acetate)$_2$(DMF)$_6$}·2DMF: an inorganic analog of M^{2+}(12-crown-4). J. Am. Chem. Soc. **111**, 7258–7259 (1989). https://doi.org/10.1021/ja00200a054
36. Stemmler, A.J., Kampf, J.W., Kirk, M.L., Atasi, B.H., Pecoraro, V.L.: The preparation, characterization, and magnetism of copper 15-metallacrown-5 lanthanide complexes. Inorg. Chem. **38**, 2807–2817 (1999). https://doi.org/10.1021/ic9800233
37. Arnold, J., Dawson, D.Y., Hoffman, C.G.: Synthesis and characterization of lithium, sodium, and potassium porphyrin complexes. X-ray crystal structures of $Li_2(C_6H_{12}O_2)_2$TMPP, $Na_2(THF)_4$OEP, and K_2(pyridine)$_4$OEP. J. Am. Chem. Soc. **115**, 2707–2713 (1993). https://doi.org/10.1021/ja00060a020
38. Sessler, J.L., Mody, T.D., Hemmi, G.W., Lynch, V.: Synthesis and structural characterization of lanthanide(III) texaphyrins. Inorg. Chem. **32**, 3175–3187 (1993). https://doi.org/10.1021/ic00066a032
39. Sugimoto, H., Mori, M., Masuda, H., Taga, T.: Synthesis and molecular structure of a lithium complex of the phthalocyanine radical. J. Chem. Soc. Chem. Commun. 962–963 (1986). https://doi.org/10.1039/C39860000962
40. Ziolo, R.F., Guenther, W.H.H., Troup, J.M.: Planar, pleated, and saddle-shaped structures of the phthalocyanine dianion in two novel multidentate oxygen-donor complexes of dipotassium phthalocyanine. J. Am. Chem. Soc. **103**, 4629–4630 (1981). https://doi.org/10.1021/ja00405a078
41. Shannon, R.D.: Revised effective ionic radii and systematic studies of interatomic distances in halides and chalcogenides. Acta Crystallogr. Sect. A **32**, 751–767 (1976). https://doi.org/10.1107/S0567739476001551
42. Pecoraro, V.L.: Structural characterization of [VO(salicylhydroximate)(CH_3OH)]$_3$: applications to the biological chemistry of vanadium(V). Inorg. Chim. Acta **155**, 171–173 (1989)
43. Lah, M.S., Pecoraro, V.L.: Development of metallacrown ethers: a new class of metal clusters. Comments Inorg. Chem. **11**, 59–84 (1990). https://doi.org/10.1080/02603599008035819
44. Lah, M.S.: Development of metallacrowns and structural characterization of manganese chain structures. University of Michigan (1991)
45. Jankolovits, J.M.: Using the structural versatility of lanthanide metallacrowns to tune anion recognition, self-assembly, and luminescence properties. University of Michigan (2012)
46. Stemmler, A.J., Kampf, J.W., Pecoraro, V.L.: Synthesis and crystal structure of the first inverse 12-metallacrown-4. Inorg. Chem. **34**, 2271–2272 (1995). https://doi.org/10.1021/ic00113a005
47. Hulsbergen, F.B., ten Hoedt, R.W.M., Verschoor, G.C., Reedijk, J., Spek, A.L.: Synthesis, magnetic properties, and X-ray structure of *catena*-μ_3-nitrato-*O*,*O*′,*O*″-[μ_3-hydroxo-1-nitrato-1,2;1,3;2,3-tris(μ-pyrazolato-*N*,*N*′)-2,3-bis(pyrazole-N^2)tricopper(II) monohydrate]. An unusual chain of trinuclear copper clusters. J. Chem. Soc. Dalton Trans. 539–545 (1983). https://doi.org/10.1039/DT9830000539
48. Angaridis, P.A., Baran, P., Boča, R., Cervantes-Lee, F., Haase, W., Mezei, G., Raptis, R.G., Werner, R.: Synthesis and structural characterization of trinuclear Cu^{II}-pyrazolato complexes containing μ_3-OH, μ_3-O, and μ_3-Cl ligands. Magnetic susceptibility study of [PPN]$_2$[(μ_3-O)Cu_3 (μ-pz)$_3Cl_3$]. Inorg. Chem. **41**, 2219–2228 (2002). https://doi.org/10.1021/ic010670l

49. Ferrer, S., Lloret, F., Pardo, E., Clemente-Juan, J.M., Liu-González, M., García-Granda, S.: Antisymmetric exchange in triangular tricopper(II) complexes: correlation among structural, magnetic, and electron paramagnetic resonance parameters. Inorg. Chem. **51**, 985–1001 (2012). https://doi.org/10.1021/ic2020034
50. Davydenko, Y.M., Demeshko, S., Pavlenko, V.A., Dechert, S., Meyer, F., Fritsky, I.O.: Synthesis, crystal structure, spectroscopic and magnetically study of two copper(II) complexes with pyrazole ligand. Z. Anorg. Allg. Chem. **639**, 1472–1476 (2013). https://doi.org/10.1002/zaac.201300078
51. Dendrinou-Samara, C., Alexiou, M., Zaleski, C.M., Kampf, J.W., Kirk, M.L., Kessissoglou, D.P., Pecoraro, V.L.: Synthesis and magnetic properties of a metallacryptate that behaves as a single-molecule magnet. Angew. Chem. Int. Ed. **42**, 3763–3766 (2003). https://doi.org/10.1002/anie.200351246
52. Zaleski, C.M., Depperman, E.C., Dendrinou-Samara, C., Alexiou, M., Kampf, J.W., Kessissoglou, D.P., Kirk, M.L., Pecoraro, V.L.: Metallacryptate single-molecule magnets: effect of lower molecular symmetry on blocking temperature. J. Am. Chem. Soc. **127**, 12862–12872 (2005). https://doi.org/10.1021/ja050951i
53. Marzaroli, V., Spigolon, G., Lococciolo, G., Quaretti, M., Salviati, C., Kampf, J.W., Licini, G., Marchiò, L., Pecoraro, V.L., Tegoni, M.: Three-dimensional porous architectures based on $Mn^{II/III}$ three-blade paddle wheel metallacryptates. Cryst. Growth Des. **19**, 1954–1964 (2019). https://doi.org/10.1021/acs.cgd.8b01921
54. Lutter, J.C., Eliseeva, S.V., Kampf, J.W., Petoud, S., Pecoraro, V.L.: A unique $Ln^{III}\{[3.3.1]Ga^{III}$ metallacryptate$\}$ series that possesses properties of slow magnetic relaxation and visible/near-infrared luminescence. Chem. Eur. J. **24**, 10773–10783 (2018). https://doi.org/10.1002/chem.201801355
55. Athanasopoulou, A.A., Carrella, L.M., Rentschler, E.: Slow relaxation of magnetization in a Fe6Dy complex deriving from a family of highly symmetric metallacryptands. Dalton Trans. **48**, 4779–4783 (2019). https://doi.org/10.1039/C9DT00552H
56. Travis, J.R., Van Trieste III, G.P., Zeller, M., Zaleski, C.M.: Crystal structures of two dysprosium-aluminium-sodium [3.3.1] metallacryptates that form two-dimensional sheets. Acta Crystallogr. Sect. E **76**, 1378–1390 (2020). https://doi.org/10.1107/S2056989020010130
57. Rheam, R.E., Zeller, M., Zaleski, C.M.: Crystal structures of three anionic lanthanide-aluminium [3.3.1] metallacryptate complexes. Acta Crystallogr. Sect. E **76**, 1458–1466 (2020). https://doi.org/10.1107/S2056989020010725
58. Kessissoglou, D.P., Bodwin, J.J., Kampf, J., Dendrinou-Samara, C., Pecoraro, V.L.: Pseudo-halide complexation by manganese 12-metallacrowns-4 complexes. Inorg. Chim. Acta **331**, 73–80 (2002). https://doi.org/10.1016/S0020-1693(01)00755-1
59. Koumousi, E.S., Mukherjee, S., Beavers, C.M., Teat, S.J., Christou, G., Stamatatos, T.C.: Towards models of the oxygen-evolving complex (OEC) of photosystem II: a Mn_4Ca cluster of relevance to low oxidation states of the OEC. Chem. Commun. **47**, 11128–11130 (2011). https://doi.org/10.1039/C1CC13770K
60. Azar, M.R., Boron, T.T., Lutter, J.C., Daly, C.I., Zegalia, K.A., Nimthong, R., Ferrence, G.M., Zeller, M., Kampf, J.W., Pecoraro, V.L., Zaleski, C.M.: Controllable formation of heterotrimetallic coordination compounds: systematically incorporating lanthanide and alkali metal ions into the manganese 12-metallacrown-4 framework. Inorg. Chem. **53**, 1729–1742 (2014). https://doi.org/10.1021/ic402865p
61. Longo, F.R., Brown, E.M., Rau, W.G., Adler, A.D.: Kinetic and mechanistic studies of metalloporphyrin formation. In: Dolphin, D. (ed.) The Porphyrins, vol. 5, pp. 459–481. Academic Press, New York (1978)
62. Margerum, D.W., Cayley, G.R., Weatherburn, D.C., Pagenkopf, G.K.: Kinetics and mechanisms of complex formation and ligand exchange. In: Martell, A.E. (ed.) Coordination Chemistry, vol. 2. American Chemical Society, Washington, D.C. (1978)
63. Schubert, H.L., Raux, E., Wilson, K.S., Warren, M.J.: Common chelatase design in the branched tetrapyrrole pathways of heme and anaerobic cobalamin synthesis. Biochemistry **38**, 10660–10669 (1999). https://doi.org/10.1021/bi9906773

64. Wu, C.-K., Dailey, H.A., Rose, J.P., Burden, A., Sellers, V.M., Wang, B.-C.: The 2.0 Å structure of human ferrochelatase, the terminal enzyme of heme biosynthesis. Nat. Struct. Mol. Biol. **8**, 156–160 (2001). https://doi.org/10.1038/84152
65. Walker, J.C., Willows, D.R.: Mechanism and regulation of Mg-chelatase. Biochem. J **327**, 321–333 (1997). https://doi.org/10.1042/bj3270321
66. Adler, A.D., Longo, F.R., Kampas, F., Kim, J.: On the preparation of metalloporphyrins. J. Inorg. Nucl. Chem. **32**, 2443–2445 (1970). https://doi.org/10.1016/0022-1902(70)80535-8
67. Tabata, M., Tanaka, M.: A new method for the determination of the stability constant of metalloporphyrins: use of the catalytic effect of mercury(II) on metalloporphyrin formation. J. Chem. Soc. Chem. Commun. 42–43 (1985). https://doi.org/10.1039/C39850000042
68. Jiménez, H.R., Julve, M., Faus, J.: A solution study of the protonation and deprotonation equilibria of 5,10,15,20-tetra(*p*-sulphonatophenyl)porphyrin. Stability constants of its magnesium(II), copper(II) and zinc(II) complexes. J. Chem. Soc. Dalton Trans. 1945–1949 (1991). https://doi.org/10.1039/DT9910001945
69. Buchler, J.: Static coordination chemistry of metalloporphyrins. In: Smith, K. (ed.) Porphyrins and Metalloporphyrins. vol. a new edition based on the original volume by J. E. Falk, pp. 157–231. Elsevier, Amsterdam (1975)
70. Maxwell, L., Amoza, M., Ruiz, E.: Mononuclear lanthanide complexes with 18-crown-6 ether: synthesis, characterization, magnetic properties, and theoretical studies. Inorg. Chem. **57**, 13225–13234 (2018). https://doi.org/10.1021/acs.inorgchem.8b01688
71. Sessler, J.L., Murai, T., Lynch, V., Cyr, M.: An "expanded porphyrin": the synthesis and structure of a new aromatic pentadentate ligand. J. Am. Chem. Soc. **110**, 5586–5588 (1988). https://doi.org/10.1021/ja00224a062
72. Sessler, J.L., Hemmi, G., Mody, T.D., Murai, T., Burrell, A., Young, S.W.: Texaphyrins: synthesis and applications. Acc. Chem. Res. **27**, 43–50 (1994)
73. Preihs, C., Arambula, J.F., Magda, D., Jeong, H., Yoo, D., Cheon, J., Siddik, Z.H., Sessler, J.L.: Recent developments in texaphyrin chemistry and drug discovery. Inorg. Chem. **52**, 12184–12192 (2013). https://doi.org/10.1021/ic400226g
74. Zaleski, C.M., Lim, C.-S., Cutland-Van Noord, A.D., Kampf, J.W., Pecoraro, V.L.: Effects of the central lanthanide ion crystal radius on the 15-$MC_{Cu}{}^{II}{}_{(N)pheHA}$-5 structure. Inorg. Chem. **50**, 7707–7717 (2011). https://doi.org/10.1021/ic200740h
75. Zaleski, C.M., Cutland-Van Noord, A.D., Kampf, J.W., Pecoraro, V.L.: Controlling the polymorph of $Ln^{III}(NO_3)_{,3}$–x(O_H)x[15-$_{MC}{}^{Cu}I_{I\ (N)S\text{-}phe}$HA-5] complexes through solvent type and ^{LnI}II ion choice. Cryst. Growth Des. **7**, 1098–1105 (2007). https://doi.org/10.1021/cg060743h
76. Tegoni, M., Remelli, M.: Metallacrowns of copper(II) and aminohydroxamates: thermodynamics of self assembly and host–guest equilibria. Coord. Chem. Rev. **256**, 289–315 (2012). https://doi.org/10.1016/j.ccr.2011.06.007
77. Chow, C.Y., Eliseeva, S.V., Trivedi, E.R., Nguyen, T.N., Kampf, J.W., Petoud, S., Pecoraro, V.L.: Ga^{3+}/Ln^{3+} metallacrowns: a promising family of highly luminescent lanthanide complexes that covers visible and near-infrared domains. J. Am. Chem. Soc. **138**, 5100–5109 (2016). https://doi.org/10.1021/jacs.6b00984
78. Lah, M.S., Gibney, B.R., Tierney, D.L., Penner-Hahn, J.E., Pecoraro, V.L.: The fused metallacrown anion $Na_2\{[Na_{0.5}[Ga(salicylhydroximate)]_4]_2(\mu_2\text{-}OH)_4\}^-$ is an inorganic analog of a cryptate. J. Am. Chem. Soc. **115**, 5857–5858 (1993). https://doi.org/10.1021/ja00066a077
79. Athanasopoulou, A.A., Baldoví, J.J., Carrella, L.M., Rentschler, E.: Field-induced slow magnetic relaxation in the first Dy(III)-centered 12-metallacrown-4 double-decker. Dalton Trans. **48**, 15381–15385 (2019). https://doi.org/10.1039/c9dt02432h
80. Salerno, E.V., Eliseeva, S.V., Schneider, B.L., Kampf, J.W., Petoud, S., Pecoraro, V.L.: Visible, near-infrared, and dual-range luminescence spanning the 4f series sensitized by a gallium(III)/lanthanide(III) metallacrown structure. J. Phys. Chem. A **124**, 10550–10564 (2020). https://doi.org/10.1021/acs.jpca.0c08819
81. Nguyen, T.N., Chow, C.Y., Eliseeva, S.V., Trivedi, E.R., Kampf, J.W., Martinic, I., Petoud, S., Pecoraro, V.L.: One-step assembly of visible and near-infrared emitting metallacrown dimers using a bifunctional linker. Chem. Eur. J. **24**, 1031–1035 (2018). https://doi.org/10.1002/chem.201703911

82. Lutter, J.C.: Refining lanthanide luminescence in metallacrowns by systematic alteration of hydroximate ligands. University of Michigan (2018)
83. Jankolovits, J., Andolina, C.M., Kampf, J.W., Raymond, K.N., Pecoraro, V.L.: Assembly of near-infrared luminescent lanthanide host(host-guest) complexes with a metallacrown sandwich motif. Angew. Chem. Int. Ed. **50**, 9660–9664 (2011). https://doi.org/10.1002/anie.201103851
84. Stemmler, A.J., Kampf, J.W., Pecoraro, V.L.: A planar [15]metallacrown-5 that selectively binds the uranyl cation. Angew. Chem. Int. Ed. Engl. **35**, 2841–2843 (1996). https://doi.org/10.1002/anie.199628411
85. Jankolovits, J., Kampf, J.W., Pecoraro, V.L.: Insight into the structural versatility of the Ln(III)[15-metallacrown-5] platform by comparing analogs with Ni(II), Cu(II), and Zn(II) ring ions. Polyhedron **52**, 491–499 (2013). https://doi.org/10.1016/j.poly.2012.08.046
86. Seda, S.H., Janczak, J., Lisowski, J.: Synthesis and structural characterisation of nickel 15-metallacrown-5 complexes with lanthanide(III) and lead(II) ions: Influence of the central metal ion size on the spin state of peripheral nickel(II) ions. Inorg. Chem. Commun. **9**, 792–796 (2006). https://doi.org/10.1016/j.inoche.2006.04.026
87. Bacco, D., Bertolasi, V., Dallavalle, F., Galliera, L., Marchetti, N., Marchiò, L., Remelli, M., Tegoni, M.: Metallacrowns of Ni(II) with α-aminohydroxamic acids in aqueous solution: beyond a 12-MC-4, an unexpected (vacant?) 15-MC-5. Dalton Trans. **40**, 2491–2501 (2011). https://doi.org/10.1039/C0DT00832J
88. Kurzak, B., Farkas, E., Glowiak, T., Kozlowski, H.: X-Ray and potentiometric studies on a pentanuclear copper(II) complex with β-alaninehydroxamic acid. J. Chem. Soc. Dalton Trans. 163–167 (1991). https://doi.org/10.1039/DT9910000163
89. Pavlishchuk, A.V., Kolotilov, S.V., Zeller, M., Lofland, S.E., Kiskin, M.A., Efimov, N.N., Ugolkova, E.A., Minin, V.V., Novotortsev, V.M., Addison, A.W.: Supramolecular maleate adducts of copper(II) 12-metallacrown-4: magnetism, EPR, and alcohol sorption properties. Eur. J. Inorg. Chem. **2017**, 4866–4878 (2017). https://doi.org/10.1002/ejic.201700976
90. Pavlishchuk, A.V., Kolotilov, S.V., Zeller, M., Shvets, O.V., Fritsky, I.O., Lofland, S.E., Addison, A.W., Hunter, A.D.: Magnetic and sorption properties of supramolecular systems based on pentanuclear copper(II) 12-metallacrown-4 complexes and isomeric phthalates: structural modeling of the different stages of alcohol sorption. Eur. J. Inorg. Chem. **2011**, 4826–4836 (2011). https://doi.org/10.1002/ejic.201100790
91. Seda, S.H., Janczak, J., Lisowski, J.: Synthesis and reactivity of copper(II) metallacrowns with (*S*)-phenylalanine and 2-picolinehydroxamic acids. Inorg. Chim. Acta **359**, 1055–1063 (2006). https://doi.org/10.1016/j.ica.2005.11.019
92. Beccia, M.R., García, B., García-Tojal, J., Leal, J.M., Secco, F., Tegoni, M.: The mechanism of the Cu^{2+}[12-$MC_{Cu(Alaha)}$-4] metallacrown formation and lanthanum(III) encapsulation. Dalton Trans. **43**(24), 9271–9282 (2014). https://doi.org/10.1039/C4DT00557K
93. Pacco, A., Parac-Vogt, T.N., van Besien, E., Pierloot, K., Görller-Walrand, C., Binnemans, K.: Lanthanide(III)-induced conversion of 12-metallacrown-4 to 5-metallacrown-5 complexes in solution. Eur. J. Inorg. Chem. **2005**, 3303–3310 (2005). https://doi.org/10.1002/ejic.200500241
94. Parac-Vogt, T.N., Pacco, A., Görller-Walrand, C., Binnemans, K.: Pentacopper(II) complexes of α-aminohydroxamic acids: uranyl-induced conversion of a 12-metallacrown-4 to a 15-metallacrown-5. J. Inorg. Biochem. **99**, 497–504 (2005). https://doi.org/10.1016/j.jinorgbio.2004.10.023
95. Seda, S.H., Janczak, J., Lisowski, J.: Synthesis and structural characterisation of copper(II) 15-metallacrown-5 complexes with Pb^{II}, Hg^{II}, Ag^{I}, Na^{I} and Y^{III} central metal ions. Eur. J. Inorg. Chem. **2007**, 3015–3022 (2007). https://doi.org/10.1002/ejic.200600881
96. Tegoni, M., Furlotti, M., Tropiano, M., Lim, C.S., Pecoraro, V.L.: Thermodynamics of core metal replacement and self-assembly of Ca^{2+} 15-metallacrown-5. Inorg. Chem. **49**, 5190–5201 (2010). https://doi.org/10.1021/ic100315u
97. Lim, C.-S., Tegoni, M., Jakusch, T., Kampf, J.W., Pecoraro, V.L.: Clarifying the mechanism of cation exchange in Ca(II)[15-$MC_{Cu(II)Ligand}$-5] complexes. Inorg. Chem. **51**, 11533–11540 (2012). https://doi.org/10.1021/ic3013798

98. Cutland, A.D., Malkani, R.G., Kampf, J.W., Pecoraro, V.L.: Lanthanide [15]metallacrown-5 complexes form nitrate-selective chiral cavities. Angew. Chem. Int. Ed. **39**, 2689–2692 (2000). https://doi.org/10.1002/1521-3773(20000804)39:15%3c2689::AID-ANIE2689%3e3.0.CO;2-0
99. Cutland-Van Noord, A.D., Kampf, J.W., Pecoraro, V.L.: Preparation of resolved fourfold symmetric amphiphilic helices using chiral metallacrown building blocks. Angew. Chem. Int. Ed. **41**, 4667–4670 (2002). https://doi.org/10.1002/anie.200290010
100. Zaleski, C.M., Depperman, E.C., Kampf, J.W., Kirk, M.L., Pecoraro, V.L.: Using Ln^{III}[15-$MC_{Cu^{II}\ (N)(S)\text{-pheHA}}$-5]$^{3+}$ complexes to construct chiral single-molecule magnets and chains of single-molecule magnets. Inorg. Chem. **45**, 10022–10024 (2006). https://doi.org/10.1021/IC061326X
101. Cutland, A.D., Halfen, J.A., Kampf, J.W., Pecoraro, V.L.: Chiral 15-metallacrown-5 complexes differentially bind carboxylate anions. J. Am. Chem. Soc. **123**, 6211–6212 (2001). https://doi.org/10.1021/ja015610t
102. Lim, C.S., Noord, A.C.V., Kampf, J.W., Pecoraro, V.L.: Assessing guest selectivity within metallacrown host compartments. Eur. J. Inorg. Chem. **2007**, 1347–1350 (2007). https://doi.org/10.1002/ejic.200700054
103. Mezei, G., Kampf, J.W., Pan, S., Poeppelmeier, K.R., Watkins, B., Pecoraro, V.L.: Metallacrown-based compartments: selective encapsulation of three isonicotinate anions in non-centrosymmetric solids. Chem. Commun. 1148–1150 (2007). https://doi.org/10.1039/B614024F
104. Sgarlata, C., Giuffrida, A., Trivedi, E.R., Pecoraro, V.L., Arena, G.: Anion encapsulation drives the formation of dimeric Gd^{III}[15-metallacrown-5]$^{3+}$ complexes in aqueous solution. Inorg. Chem. **56**, 4771–4774 (2017). https://doi.org/10.1021/acs.inorgchem.6b03043
105. Jankolovits, J., Lim, C.-S., Kampf, J.W., Pecoraro, V.L.: Disruption of the La(III)[15-Metallacrown-5] cavity through bithiophene dicarboxylate inclusion. Z. Naturforsch. B **65**, 263–272 (2010). https://doi.org/10.1515/znb-2010-0307
106. Jankolovits, J., Lim, C.S., Mezei, G., Kampf, J.W., Pecoraro, V.L.: Influencing the size and anion selectivity of dimeric Ln^{3+}[15-Metallacrown-5] compartments through systematic variation of the host side chains and central metal. Inorg. Chem. **51**, 4527–4538 (2012). https://doi.org/10.1021/ic202347j
107. Lim, C.S., Jankolovits, J., Kampf, J.W., Pecoraro, V.L.: Chiral metallacrown supramolecular compartments that template nanochannels: self-assembly and guest absorption. Chem. Asian J. **5**, 46–49 (2010). https://doi.org/10.1002/asia.200900612
108. Pavlishchuk, A.V., Kolotilov, S.V., Zeller, M., Thompson, L.K., Addison, A.W.: Formation of coordination polymers or discrete adducts via reactions of gadolinium(III)–copper(II) 15-metallacrown-5 complexes with polycarboxylates: synthesis, structures and magnetic properties. Inorg. Chem. **53**, 1320–1330 (2014). https://doi.org/10.1021/ic401928m
109. Pavlishchuk, A.V., Kolotilov, S.V., Zeller, M., Lofland, S.E., Thompson, L.K., Addison, A.W., Hunter, A.D.: High nuclearity assemblies and one-dimensional (1D) coordination polymers based on lanthanide-copper 15-metallacrown-5 complexes (Ln^{III} = Pr, Nd, Sm, Eu). Inorg. Chem. **56**, 13152–13165 (2017). https://doi.org/10.1021/acs.inorgchem.7b01944
110. Pavlishchuk, A.V., Kolotilov, S.V., Zeller, M., Lofland, S.E., Addison, A.W.: Magnetic properties of Ln^{III}–Cu^{II} 15-metallacrown-5 dimers with terephthalate (Ln^{III} = Pr, Nd, Sm, Eu). Eur. J. Inorg. Chem. **2018**, 3504–3511 (2018). https://doi.org/10.1002/ejic.201800461
111. Lim, C.S., Kampf, J.W., Pecoraro, V.L.: Establishing the binding affinity of organic carboxylates to 15-metallacrown-5 complexes. Inorg. Chem. **48**, 5224–5233 (2009). https://doi.org/10.1021/ic9001829
112. Lim, C.S., Jankolovits, J., Zhao, P., Kampf, J.W., Pecoraro, V.L.: Gd(III)[15-metallacrown-5] recognition of chiral α-amino acid analogues. Inorg. Chem. **50**, 4832–4841 (2011). https://doi.org/10.1021/ic102579t
113. Jankolovits, J., Kampf, J.W., Maldonado, S., Pecoraro, V.L.: Voltammetric characterization of redox-inactive guest binding to Ln^{III}[15-metallacrown-5] hosts based on competition with a redox probe. Chem. Eur. J. **16**, 6786–6796 (2010). https://doi.org/10.1002/chem.200903015

114. Grant, J.T., Jankolovits, J., Pecoraro, V.L.: Enhanced guest affinity and enantioselectivity through variation of the Gd^{3+}[15-metallacrown-5] side chain. Inorg. Chem. **51**, 8034–8041 (2012). https://doi.org/10.1021/ic300110g
115. Tegoni, M., Tropiano, M., Marchio, L.: Thermodynamics of binding of carboxylates to amphiphilic Eu^{3+}/Cu^{2+} metallacrown. Dalton Trans. 6705–6708 (2009). https://doi.org/10.1039/B911512A
116. Sgarlata, C., Schneider, B.L., Zito, V., Migliore, R., Tegoni, M., Pecoraro, V.L., Arena, G.: Lanthanide identity governs guest-induced dimerization in Ln^{III}[15-$MC_{Cu^{II}N(L\text{-}pheHA)}$-5])$^{3+}$ metallacrowns. Chem. Eur. J. **27**, 17669–17675 (2021). https://doi.org/10.1002/chem.202103263

Aspects of NMR Characterization of Metallacrowns

Matteo Melegari and Matteo Tegoni

Abstract Metallacrowns (MCs) are self-assembled metallamacrocycles that confine a significant number of metal ions and organic ligands in a small molecular volume. These assembled structures present a cavity that can selectively encapsulate specific metal ions which provide MCs with peculiar spectroscopic features and reactivity. Also, MCs can bind inorganic and organic anions allowing their use in strategies of molecular recognition. For these reasons, including remarkable stability and inertness toward disassembly and the presence of paramagnetic ions in their structure, MCs possibly are among the most interesting metallamacrocyclic complexes known to date. The elucidation of dynamic processes of ligand and solvent exchange in solution is pivotal in the study of MCs as potential probes in biological imaging, as nanoshuttles for drug delivery or in molecular recognition and sensing. In this chapter, we will present and discuss representative examples of NMR investigations of metallacrowns reactivity, dynamics of assembly, and cations/anions binding. The strategies and conditions employed in the 1D NMR characterization of MCs will be discussed along with the most recent PGSE approaches. Also, we will discuss how the paramagnetic nature of these complexes opens a window into the study of their structure in solution through NMR.

1 Introduction

Metallacrowns are the inorganic analogues of organic crown ethers and are characterized by a $(M–N–O)_n$ cyclic connectivity that closely resembles the $(C–C–O)_n$ one present in the parent organic macrocycles (Fig. 1) [1–4]. The structural similarity between these two classes of molecules stands principally in the presence of an oxygen-rich cavity into which metal ions can be encapsulated. The assembly of

M. Melegari · M. Tegoni (✉)
Department of Chemistry, Life Sciences and Environmental Sustainability, University of Parma, Parco Area delle Scienze 17A, 43124 Parma, Italy
e-mail: matteo.tegoni@unipr.it

M. Melegari
e-mail: matteo.melegari@unipr.it

C. M. Zaleski (ed.), *Advances in Metallacrown Chemistry*,
https://doi.org/10.1007/978-3-031-08576-5_2

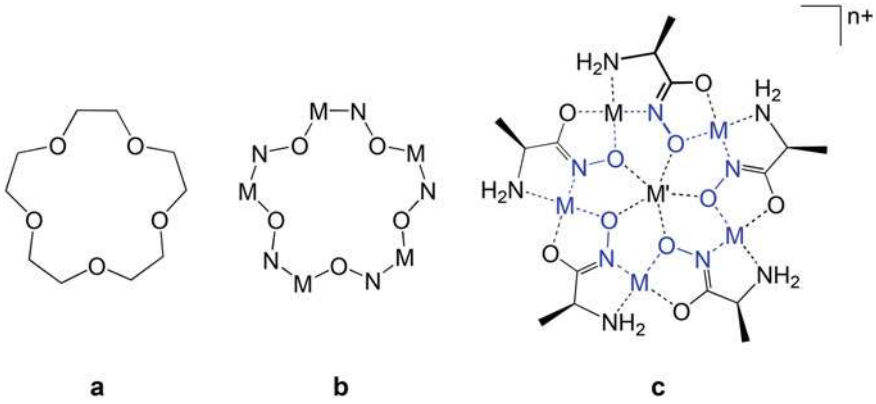

Fig. 1 **a** Scheme of a crown ether (15-C-5), **b** Scheme of a metallacrown ring (15-MC-5), **c** Scheme of a 15-MC-5 complex where the ligand and core metal are reported (L-alaninehydroxamate as ligand, the MC ring is highlighted in blue)

these molecules occurs spontaneously in solution and it requires the presence of a central (core) metal ion which templates the MC formation, and polyfunctional ligands which bridge between the (ring) metal ions (usually d-transition metals) that compose the metallamacrocyclic framework (Fig. 1c) [5, 6].

The most studied metallacrowns have been assembled using hydroxamic acid derivatives and in particular aminohydroxamic acids or salicylhydroxamic acid (Fig. 2) [1, 2, 4–7]. The use of aminohydroxamic acids and related ligands is very convenient since the completely deprotonated hydroxamate group can act as a (O, O^-) chelating group on one ring metal and it provides with the additional N^- donor atom required to form the $(M–N–O)_n$ metallacrown connectivity [4–6]. An additional donor group of the ligand (i.e., NH_2 in aminohydroxamates or a deprotonated phenolic OH in salicylhydroxamates) coordinates to a fourth equatorial coordination position of the ring metal. While the equatorial positions on the ring metals saturate upon metallacrown assembly and ring closure, axial coordination positions remain available on the metals on both sides of the metallacycle. These sites are of paramount importance to determine peculiar structural and functional properties of metallacrowns such as the coordination of anionic ancillary ligands or the formation of helicates in the solid state [6, 8–12].

Hydroxamic Ligands

α-Alaha: L-alaninehydroxamic acid; Leuha: α-L-leucinehydroxamic acid; Pheha: α-L-phenylalaninehydroxamic acid; Tyrha: α-L-tyrosinehydroxamic acid; Picha: 2-picolinehydroxamic acid; Mha: L-mandelohydroxamic acid; Trpha: α-L-tryptophanhydroxamic acid; β-Alaha: β-L-alaninehydroxamic acid; Shi: salicylhydroxamic acid; Nha: 3-hydroxy-2-naphthylhydroxamic acid; Anha: anilinehydroxamic acid.

The nature and length of the spacer between the hydroxamic function and the aminic, pyridyl or phenolic functions are the most important features determining

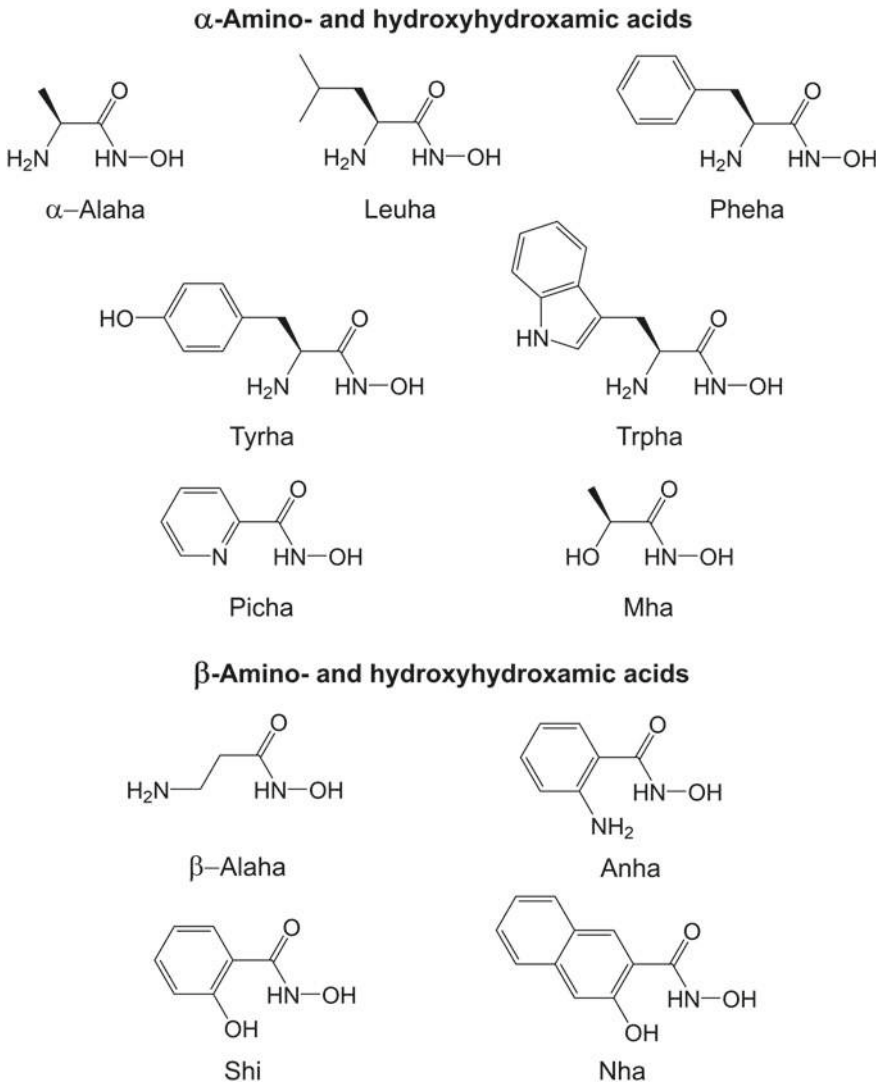

Fig. 2 Scheme of α and β-hydroxamic acids. All chiral ligands, if not otherwise stated, refer to (*S*)-isomers. Ligands are in their fully deprotonated form on the hydroxamic function when they form MC complexes

the dimension and the stability of the assembled MC architecture. In Fig. 3 is represented the principle that underlies the relationship between the dimension of the MC framework (e.g., 12-MC-4 versus 15-MC-5) and the distance between the two coordination donor groups. β-Amino- or β-hydroxohydroxamates bridge between two metal centers generating an angle between the bisectors of the chelating systems of *ca.* 90°, while this angle is close to 108° for α-hydroxamates. The result is that

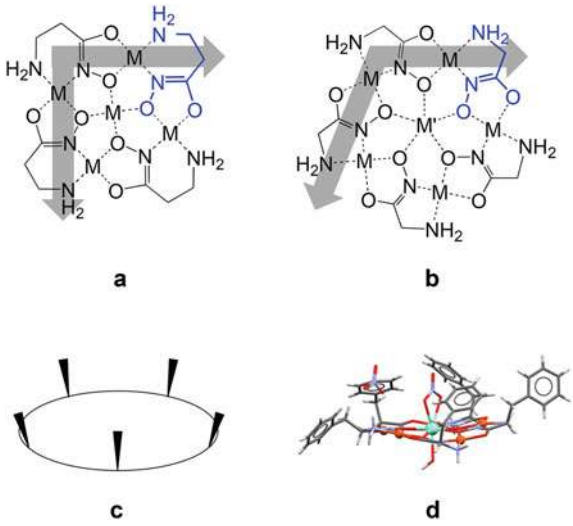

Fig. 3 Conceptual representation of the "*metallacrown structural paradigm*", **a** Four-fold axially symmetrical MC framework assembled using β-hydroxamates (*highlighted in blue*), **b** Five-fold axially symmetrical MC framework assembled using α-hydroxamates (*highlighted in blue*), **c** Conceptual representation of a *face-differentiated* MC assembly, **d** Structure of a *face–differentiated* MC: {Eu(III)(NO_3)(OH)[15-$MC_{Cu(II)Pheha}$-5]}(NO_3)

the former ligands are appropriate to assemble 12-MC-4 complexes, while the latter form planar 15-MC-5 (Fig. 3b). This principle was first rationalized by Pecoraro and coworkers in the 1990s and later named by us as the "*metallacrown structural paradigm*" [5, 6, 13].

As analogs of crown ethers, since the isolation of the first metallacrowns by Pecoraro and coworkers in the late 1980s, and early 1990s, the question related to the functional properties in a solution of these assemblies arose. On one hand, it was interesting to study the metal recognition properties of metallacrowns, in particular related to the ability of specific metal ions to template the assembly of the MC architecture [6, 14–17]. In this context, the possibility of selectively removing or substituting the core metal in favor of a different one was also explored [18, 19]. On the other hand, the isolation of *face-differentiated* metallacrown architectures characterized by bulky ligand substituents residing all on one face of the planar MC framework prompted the study of their molecular recognition properties (Fig. 3c, d). In this context, 15-MC-5 complexes and especially those assembled using Pheha proved to be extraordinary hosts for organic carboxylates, able to recognize lipophilic versus hydrophilic guests and capable of forming stable dimeric capsules [8–10, 20–25]. Further details on *face-differentiation* and its implications are provided in Sect. 2.2. Finally, it is worth to point out that in the literature other assemblies related to metallacrowns were isolated, such as aza-metallacrowns or inverted metallacrowns [1, 26, 27]. However, the studies of the structural and functional properties of these latter complexes with NMR are few. The discussion in this chapter is therefore limited to metallacrowns to give a comprehensive view of the impact of the NMR technique on the elucidation the chemistry of these compounds [1, 26, 27].

To study the above-mentioned phenomena and properties, spectroscopy techniques such as UV–visible and circular dichroism were often used. However, these

techniques could basically be applied only to MCs of open-shell d-transition metals such as copper(II), manganese(II/III) or nickel(II), or to MCs bearing specific chromophores/fluorophores [6]. Therefore, with the need to monitor processes that involve subtle structural changes in MC architecture but that often have minor effects on optical properties, NMR has also been used. From mono- to multidimensional analyses, to sophisticated pulsed-gradient techniques, NMR has been employed to analyse a number of phenomena that range from the core and ring metal substitution, to the rearrangement of the macrocyclic scaffold, and to the host–guest interaction with organic guests. These studies are the subject of this chapter.

Importantly, most of the metallacrowns studied by NMR in solution are paramagnetic. In the NMR analysis of MCs, this has been both a disadvantage and a great advantage depending on the system or on the properties under investigation. If on one hand, the fast proton relaxation in some systems made difficult or even prevented the detection of 1D, 2D or pulsed-gradient spin echo (PGSE) signals [15, 28, 29], for other MC assemblies the paramagnetic shift allowed to obtain interesting structural information in solution [30]. The latter studies have been possible in particular for metallacrowns containing heavier lanthanides, since these ions possess large magnetic anisotropies that provide with significant dipolar contributions to the chemical shifts, in turn very sensitive to the proton position in the molecular structure [31, 32].

In this chapter, we will first briefly introduce the pulsed-gradient spin echo NMR technique and some details on the theory of the relationship between the structure of Ln-containing complexes and the observed proton chemical shift. The studies of the chemistry of metallacrowns using NMR presented along this chapter will focus on the core metal substitution and molecular architecture rearrangement of MC systems containing in particular Mn(III) or Cu(II), the study of host–guest interactions between 15-MC-5 and organic carboxylates, and the study of the structure in solution of Ln(III)/Mn(III) or Ln(III)/Cu(II) metallacrowns.

Abbreviations and acronyms

MC: Metallacrown; NMR: Nuclear Magnetic Resonance; ALM: “all lanthanides” method; PGSE: Pulsed-Gradient Spin Echo; DOSY: Diffusion Ordered Spectroscopy; FID: Free Induction Decay; LIS: Lanthanide Induced Shift; ITC: Isothermal Titration Calorimetry; FAB: Fast Atom Bombardment; BzO^-: benzoate; OAc^-: acetate; TFA^-: trifluoroacetate; MeOH: methanol; DMF: dimethylformamide; DMSO: dimethylsulfoxide; TMS: tetramethylsilane.

1.1 Pulsed-Gradient Spin-Echo NMR

Pulsed-gradient spin-echo (PGSE) is an NMR experiment connected with diffusion-ordered NMR spectroscopy (DOSY) [33, 34]. The power of PGSE lies in the discrimination of the signals of different substances present in the same NMR sample on the

basis of diffusion coefficients [35, 36]. Treatment in detail of the theoretical background of this experiment can be found in the literature [34, 37]. Here we briefly describe the fundamentals of PGSE and a few aspects that are relevant for the analysis of metallacrowns.

The diffusion coefficient of a molecule depends on several factors including its effective dimension and shape, the temperature, and the solvent. The Stokes–Einstein equation relates the diffusion coefficient D of a species with its hydrodynamic or Stokes radius r_S:

$$D = \frac{kT}{c\pi\eta r_S} \tag{1}$$

where k is the Boltzmann constant, η the viscosity of the solution, and c a numerical factor (in the 4–6 interval for many medium-sized to large analytes) which depends on the size and shape of the molecule [35, 36]. As for the estimation of the c factor, Wirtz and coworkers have proposed an empirical equation which takes into account the hydrodynamic radii of both the analyte and a standard molecule of comparable size [38, 39].

A PGSE experiment (Fig. 4) starts with the excitation of nuclear spins, after which a linear gradient along the z-axis of amplitude G is applied for a time δ. Since the gradient field sums up with the external field, during the δ interval the transverse magnetization of the different spins evolves with a precession frequency that depends on its position along the z-axis. The result is that these transverse magnetizations of the spins are dephased during δ. The analytes are left diffusing in solution (for a time that may last a few hundred milliseconds) and then a spin echo 180° pulse is applied, again followed by a linear gradient along the z-axis. During this second δ interval, followed by a delay diffusion time of the same duration as the previous one, spin transverse magnetizations are rephased. Complete rephasing is obtained only if the analytes do not change their positions along the z-axis during the two Δ intervals (separation between pulses). The larger the molecule, the lower the diffusion and hence the more pronounced is the rephasing of the spin magnetizations. Conversely, the more the analytes translate along z during Δ (small molecules), the less rephasing is obtained resulting in a reduction of the detected signal (Fig. 4b). In a PGSE experiment, a series of spectra are collected by changing G and keeping constant all other acquisition parameters: by plotting the NMR signal intensities as a function of G^2 an exponential decay of the signal is observed (Fig. 4c). Since small molecules diffuse faster than larger ones, the effect of diffusion is more pronounced for the former. Indeed, the larger the size of the molecule (large r_S, small D) the less pronounced is the decay of the signal by increasing G, while the opposite is observed where the molecular size diminishes [37].

The observed intensity of the NMR signals at the end of the PGSE pulse sequence has an exponential dependence on δ, Δ and D, as follows (for a classic PGSE experiment):

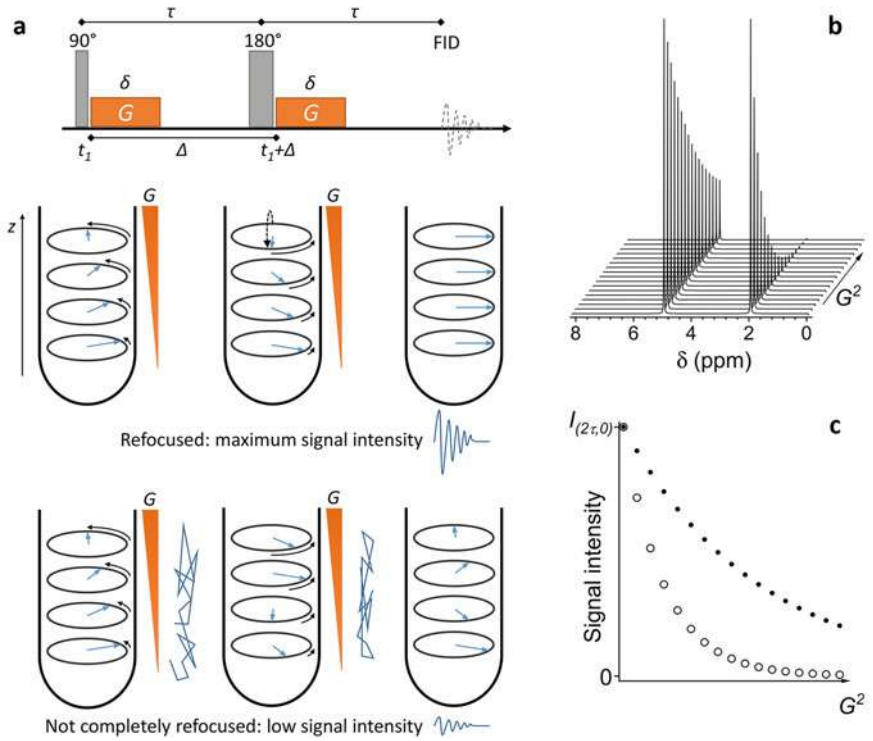

Fig. 4 **a** Representation of the PGSE pulse sequence. The effect on focused transverse magnetization of the spins along the *z*-axis in the absence and in the presence of diffusion is represented (refocused and not refocused, respectively), **b** Representation of the decay of signal intensity as a function of G^2 for a large (*left*) and a small (*right*) molecule, **c** Intensity values as a function of G^2. The exponential decay for a molecule of small dimensions (*open circles*) is more pronounced than that of a large molecule (*dots*). *G*: amplitude of pulsed-gradient; δ: duration of pulsed-gradient; Δ: separation between pulses; $I_{(2\tau,0)}$: signal intensity at the end of the PGSE pulse sequence with no gradient field applied

$$I_{(2\tau,G)} = I_{(0,0)}\exp\left(\frac{-2\tau}{T_2}\right)\exp\left(-\gamma^2 G^2\delta^2\left(\Delta - \frac{\delta}{3}\right)D\right) \tag{2}$$

where γ is the gyromagnetic ratio of the observed nuclide (see caption of Fig. 4 for the other parameters). In this equation, $I_{(0,0)}$ is the intensity of the signals after a standard 90°–Free Induction Decay (FID) pulse sequence. If a series of spectra are collected using different gradient *G* strengths and using the same acquisition parameters including Δ and δ, the equation reduces to:

$$I_{(2\tau,G)} = I_{(2\tau,0)}\exp\left(-\gamma^2\delta^2\left(\Delta - \frac{\delta}{3}\right)DG^2\right) = I_{(2\tau,0)}\exp\left(-\theta G^2\right) \tag{3}$$

The observed $I_{(2\tau,G)}$ values as a function of the gradient strength G (known for each experiment) can be fitted using $I_{(2\tau,0)}$ and θ as fitting parameters.

To calculate D of an analyte it is very convenient to use an internal standard of known hydrodynamic radius r_S. Actually, the decay of intensity $I_{(2\tau,G)}$ of both the analyte and the standard can be obtained from the same dataset, leading to the two exponential decay parameters θ_{an} and θ_{std}, respectively for the analyte and the standard (e.g., Fig. 4c). If the diffusion coefficient of the standard is known, that of the analyte can be straightforwardly obtained from the equation:

$$\frac{\theta_{an}}{\theta_{std}} = \frac{D_{an}}{D_{std}} \tag{4}$$

More importantly, if the hydrodynamic radii of the standard substance and of the solvent are known, that of the analyte can be determined from the same θ_{an} and θ_{std} parameters using an iterative process as described by Zuccaccia and Macchioni [35, 36].

It is necessary to underline a few aspects of PGSE data that are relevant in the analyses of metallacrowns. The first aspect relates to the chemical exchange effect observed when MCs were used as guests for molecular recognition. For instance, 15-MC-5 form dimeric adducts with dicarboxylates of formula $(MC)_2$(dicarboxylate), where monomers (MC) are in equilibrium with dimers under fast-exchange conditions. Under these circumstances, the observed diffusion coefficient is the average over the molar fractions of the D values of the individual monomeric and dimeric species [28]:

$$D_{obs} = \chi_{monomer} D_{monomer} + \chi_{dimer} D_{dimer} \tag{5}$$

It is worth noting that for a dimerization process (i.e., a change in molecular volume of a factor of 2) the average molecular radius and the D value are expected to vary by a factor of the cube root of 2 (=1.26). That means that to observe an r_S that increases by a factor of two the molecular volume has to increase 8 times. Assuming a reaction between an MC and a small guest such as a carboxylate, the diffusion coefficient of the metallacrown does not change to a large extent, while that of the small guest does and in the adduct it may be approximated to that of the MC host. Provided the experimental setup that allows it, it is very convenient in PGSE to examine the spins of the guest rather than those of the host, since in the former case the interaction between a small guest and the large MC host can be more easily detected [22, 28].

A second aspect important for the study of MCs relates with the attenuation of the observed signal due to relaxation, in particular for paramagnetic MCs. The intensity at zero gradient field $I_{(2\tau,0)}$ observed at the end of the PGSE sequence differs from that observed immediately after the 90° pulse of a factor $\exp(-2\tau/T_2)$ (Eqs. 2 and 3). This factor considers the transverse relaxation of the magnetization during the 2τ duration of the experiment. In standard PGSE experiments, the 2τ interval is constant while the amplitude G of the gradient is varied so that the transverse magnetization effects

are normalized along the experiment. However, the pulse sequence may often last up to hundreds of milliseconds and therefore complete signal decay due to paramagnetic relaxation may occur before the FID is even at zero G strength. This in turn may prevent the detection of signals of fast-relaxing protons [28].

A third aspect relates with the shape and size of the analyte in relationship with its hydrodynamic radius. Following Eq. 1, the larger the size of a molecule in solution the lower its diffusion coefficient D. However, even assuming a perfect spherical size for an analyte, the molecular van der Waals radius is often overestimated through the calculation of an empirical r_S. This happens because the analytes are solvated in solution and therefore they diffuse together with their solvation sphere, resulting in an r_S apparently larger than the actual one for the compound [37, 40]. This effect is more relevant for protic solvents or solvents with high polarity, for which not only the analyte–solvent but also the solvent–solvent intermolecular interactions are significant [40]. Along with this, it must be considered that the prolate or oblate shape of the molecule in terms of shape factor may impact its diffusion [35, 41, 42]. This aspect is more critical for large oblate molecules (disk-like) than for small to medium-sized prolate ones (cigar-like), and thus this effect can be relevant for planar MCs in solution. However, there are structural features of MCs observed in the solid state which may render less oblate (more spherical) the molecular architectures of metallacrowns in solution, such as the presence of anions coordinated to the two faces of the MC plane and the tendency of flexible side groups to wrap around coordinated guests [22, 43].

1.2 ^{1}H-NMR of Paramagnetic Complexes

The presence of a paramagnetic ion in a complex produces a shift in the observed proton resonances of the ligands (δ^{obs}) that is the sum of a diamagnetic and a paramagnetic contribution (δ^{dia} and δ^{para} respectively) [32]. The paramagnetic term can be further split into two contributions: the first one (pseudocontact or dipolar shift, δ^{PC}) results from the dipolar interactions between the nuclear magnetic moment of the NMR nucleus and the electron magnetic moment of unpaired electron(s). This contribution depends on the spatial position of the proton under examination with respect to the paramagnetic center. The second contribution (contact or Fermi shift, δ^{con}) results from the presence of non-zero electron density of unpaired electrons on the observed protons, an effect often referred to as through-bonds scalar coupling [44].

$$\delta^{obs}(i) = \delta^{dia}(i) + \delta^{para}(i) = \delta^{dia}(i) + \delta^{PC}(i) + \delta^{con}(i) \tag{6}$$

Both contributions to the paramagnetic shift decrease with increasing distance between the resonating nucleus and the paramagnetic center. However, in the absence of significant electron delocalization, δ^{con} is usually negligible when the probed nucleus is more than four bonds away from the paramagnetic center. The result is

that for paramagnetic centers which provide a large dipolar contribution (e.g., heavier lanthanide(III) ions), the δ^{para} term of protons far from the metal ion almost equals the δ^{PC} contribution.

The abundance of paramagnetic centers in MCs (either ring or central metals) makes NMR a unique technique in the study of the structure of those complexes and (thermo)dynamic phenomena in solution. Not all MCs could be studied in detail using this technique since some paramagnetic metal ions experience long electron relaxation rates and therefore their presence produce NMR signals that are invariably wide. However, MCs of metal ions such as manganese(III) or lanthanides(III) which have shorter electron relaxation rates could be extensively studied through NMR, as discussed in Sect. 5.

1.3 ^{1}H-NMR of Lanthanide Complexes

Due to the large spin–orbit coupling of the 4f electrons, the electron relaxation times are short for most lanthanides and this in turn allows the observation of quite sharp proton NMR resonances [45, 46]. The NMR analysis of lanthanide-containing complexes is therefore a useful method for the extraction of crucial structural information in solution. This information often pivots around the determination of the δ^{PC} contribution which is tightly related to the structure of the compounds. For this reason, lanthanides are commonly used as NMR shift reagents and as probes for the extraction of structural information of molecules of large dimensions [47].

For complexes containing one lanthanide ion as the only paramagnetic center, δ^{para} is usually reported as Lanthanide Induced Shift (LIS). In a mononuclear lanthanide complex of axial symmetry of order 3 or above, Bleaney's theory states that the δ^{PC} experienced by an observed proton *i* is related to the structure of the complex through Eq. 7 [31, 32, 48–51].

$$\delta_{Ln}^{PC}(i) = C_J(Ln) \cdot B_{Ln} \cdot G(i) = C_J(Ln) \cdot B_{Ln} \cdot \frac{3cos^2\theta_i - 1}{r_i^3} \tag{7}$$

where θ_i the angle between the principal magnetic axis of the complex and the line passing through the paramagnetic center and the *i*-proton, and r_i is the distance between the *i*-proton and the paramagnetic center (Fig. 5). The other parameters in Eq. 7 are the following: $C_J(Ln)$ is the Bleaney's constant for the lanthanide ion under examination, and B_{Ln} the lanthanide ligand field splitting parameter. The $G(i)$ term equals $3(\cos^2\theta_i\text{-}1)/{r_i}^3$ and is named geometric term.

The value of δ^{PC} depends on both the $C_J(Ln)$ and $G(i)$ parameters. In fact, $G(i)$ has a positive value if θ_i is lower than the magic angle (ca. 55°) while it has a negative value if θ_i is higher than the magic angle. Besides that, the value and sign of δ^{PC} is then determined by Bleaney's constant, which is positive for prolate Ln(III) ions (leading to δ^{PC} to have the same sign of $G(i)$) and negative for oblate ones (δ^{PC} with

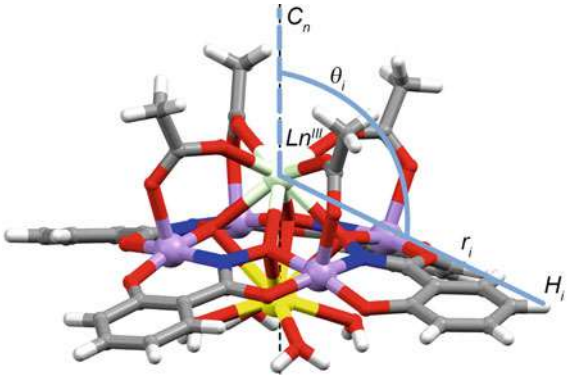

Fig. 5 Schematic representation of the geometric parameters r_i and θ_i in relation to the position of the *Ln(III)* ion and proton *i*. The principal magnetization axis coincides with the symmetry axis C_n of the metallacrown for $n > 3$. The reported structure is that of {Na(I)Pr(III)$(OAc)_4$[12-$MC_{Mn(III)Shi}$-4]$(H_2O)_4$}. *Light green*: Pr(III), *Purple*: Mn(III), *Yellow*: Na(I)

opposite sign of $G(i)$). It is therefore evident that the analysis of δ^{PC} provides data on the relative location of protons in a paramagnetic molecule, opening a window on the acquisition of structural information of the complex in solution.

Thanks to their similarity in ionic radius, lanthanide(III) ions often form isostructural complexes. Based on this property, a powerful strategy to calculate the δ^{con} and δ^{PC} contributions from δ^{para}, named "all lanthanides" method" (ALM), has been developed by Di Bari and coworkers [46]. The applicability of this method has three main requirements. First, the complexes must be axially symmetrical and have a greater than threefold symmetry [46, 52]. Second requirement is for δ^{FC} to be negligible over δ^{PC} (although ALM was applied also to cases which do not strictly fulfill this condition), while the third requirement is that a diamagnetic reference complex should be available to estimate with precision the diamagnetic contribution to the observed chemical shift (δ^{dia}). Y(III) complexes were widely used in the literature as diamagnetic references since they are usually isostructural to the lanthanide series [53, 54]. La(III) and Lu(III)-complexes are alternatives to Y(III): however, at least in MC chemistry the structure of La(III) complexes is often different from that of the other lanthanides as a consequence of its largest ionic radius in the series, and therefore Y(III) is preferred. A description of the theoretical basis and applications of the ALM can be found in the literature [30, 46], while here we just briefly remark a few key aspects relevant to MC analysis. Also, an application of this method in the analysis of MCs is reported in Sect. 5.1. Here we just put in evidence that for its nature the ALM is general in its application principles and does not depend on the reported values of the Bleaney's constants or of the crystal field parameters for the classes of compounds analysed. This is particularly important for data treatment since the Bleaney's theory and constant values have to be used with caution, as recently underlined [55].

Let us assume to have a series of isostructural MC complexes of different lanthanides including that of Y(III). If the NMR resonances are assigned to the corresponding protons in the structure, then the δ^{para} terms for each proton *i* can be calculated using the following equation:

$$\delta_{Ln}^{para}(i) \cong \delta_{Ln}^{obs}(i) - \delta_{Y}^{obs}(i) \tag{8}$$

with the δ^{para} available, ALM data treatment allows to obtain a parameter M_i which is proportional, for each i-proton position in the structures, to its $G(i)$ parameter. The following relationship between M_i and $G(i)$ applies [30, 46].

$$\frac{M_i}{M_j} = \frac{G(i)}{G(j)} \tag{9}$$

where i and j are two different proton positions in the structure. Without going into details (some of them will be described for metallacrowns in Sect. 5) it is clear from Eq. 7 that having available the information on δ^{para} and M_i means to possess a quantitative tool for the determination of the structural parameters θ_i and r_i for each proton in the structure. Possibly, more importantly, Eq. 9 can be used either way which means to obtain structural information using NMR data or to confirm the assignments of NMR resonances using known structural data. In this chapter, we will show a remarkable example present in the literature of this type of analyses. Also, we will show that in MCs containing lanthanide(III) ions and other paramagnetic transition metals the LIS is not the only contribution to the overall δ^{para}, and nevertheless, for some complexes, it could be calculated and analysed in quite detail.

Finally, one aspect related to the NMR analysis of Ln(III)-containing MCs is the presence of ring metals that can be paramagnetic. Assuming in first approximation that the ring metals are strongly coupled together, δ^{para} may be dominated by the paramagnetic features of the $[M_{ring}]_n$ system, and the effect of a core paramagnetic (i.e., lanthanide) ion may act as a second-order perturbation [15, 16, 29, 30, 56–60]. Perhaps most interesting, the coupling between two paramagnetic metals or systems results in an enhancement of the electron relaxation rate, with the consequence that relatively sharp proton NMR signals were observed for MCs containing Cu(II) and even Gd(III) [8, 16, 30, 61, 62].

2 Interaction of Metallacrowns with Inorganic and Organic Anions

Over the past three decades, elegant and often straightforward strategies based on proton NMR allowed to elucidate aspects related to the binding of anions to metallacrowns in solutions. The methodologies evolved from the use of 1D ^{1}H-NMR experiments to study the affinity for inorganic halides of Mn(III) MCs to the exploitation of PGSE techniques to study the binding of carboxylates to Cu(II) 15-MC-5 complexes and related dimerization equilibria. The most important aspects of these studies are summarized here.

2.1 Interaction of Mn(III) Metallacrowns with Anions

MC scaffolds such as [12-$MC_{Mn(III)Shi}$-4] or [12-$MC_{Mn(III)Nha}$-4] have been known for many years for their remarkable stability in solution [4, 5, 63]. These complexes can encapsulate relatively small Mn(II) and Li(I) in their cavity, while larger Na(I) and K(I) cations are coordinated side-on to the cavity rather than encapsulated. Therefore, these 12-MC-4 complexes form 1:1 adducts with Mn(II) or Li(I) cation as core metals, while with Na(I) or K(I) 2:1 core metal/MC adducts were often observed. In the latter complexes, the two core cations interact with the four-oxygen cavity on different sides of the MC plane and their structures are reported in Fig. 6 [5, 63–66].

The structure of the {Mn(II)$(OAc)_2$[12-$MC_{Mn(III)Shi}$-4]} complex is known since 1989 and is reported in Fig. 6a [66]. The two acetate anions are coordinated on the same side of the MC mean plane, acting as bidentate ligands which bridge between one ring Mn(III) and the core Mn(II). The ^{1}H-NMR spectrum of the complex presents multiple resonances in the −30 to + 60 ppm range [5, 63, 66]. With the isolation of deuterated derivatives of the Shi ligand, it was possible to clarify that the resonance of the acetate CH_3 group is at *ca.* + 50 ppm [63]. This peculiar peaks distribution (acetate protons in the downfield shifted region of the spectrum, Shi protons in the upfield region) suggested that the two sets of protons are located in space regions which experience pseudocontact shift contributions of opposite signs [5,

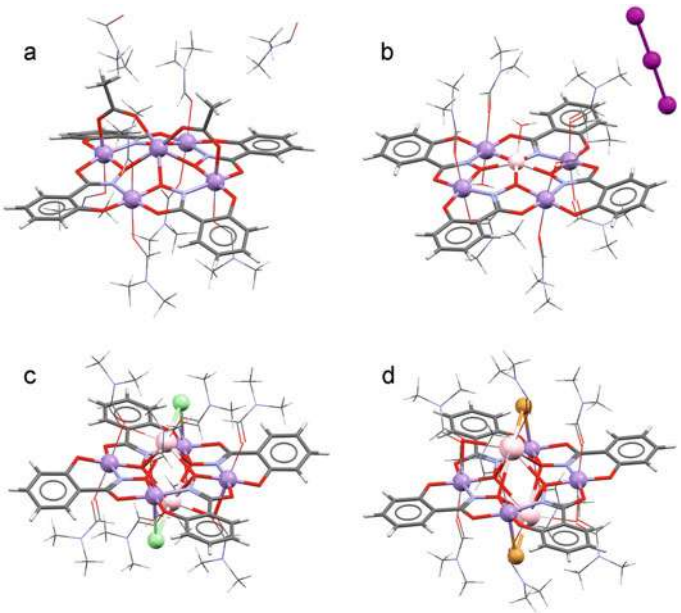

Fig. 6 Structures of **a** {Mn(II)$(OAc)_2$[12-$MC_{Mn(III)Shi}$-4]}, **b** {Li(I)[12-$MC_{Mn(III)Shi}$-4]}I_3, **c** {$(Na(I)Cl)_2$[12-$MC_{Mn(III)Shi}$-4]}, **d** {$(K(I)Br)_2$[12-$MC_{Mn(III)Shi}$-4]}. *Light violet*: Mn, *Pink*: Li/Na/K, *Purple*: I, *Green*: Cl, *Gold*: Br

63]. This qualitative analysis has been recently reexamined quantitatively [30], and it is described in Sect. 5.

Pecoraro and coworkers clarified through proton NMR experiments that $\{Mn(II)(OAc)_2[12\text{-}MC_{Mn(III)Shi}\text{-}4]\}$ in DMF solution and in the presence of sodium acetate maintains coordinated the carboxylate anions, which are however in rapid exchange with those in solution. Addition of sodium trideuteroacetate (TFA) allowed to observe the loss of the acetate signal in less than 30 s, thus leading to the conclusion that acetates are labile ancillary ligands [5, 64]. Conversely, the addition of deuterated Shi to $\{Mn(II)(OAc)_2[12\text{-}MC_{Mn(III)Shi}\text{-}4]\}$ did not exhibit any change in peak intensity, allowing to establish that the Shi ligands are not exchanged in this solvent [5]. Also, ^{1}H-NMR analysis of the $\{Mn(II)(OAc)_2(pyridine)_6[15\text{-}MC_{Mn(III)Shi}\text{-}5]\}$ complex revealed that slow but complete conversion of the 15-MC-5 framework into the 12-MC-4 one occurs in DMSO solution. This is likely due to the dissociation of the pyridine molecules around which the stability of the 15-MC-5 species pivots. In the absence of pyridine to stabilize the non-planar 15-MC-5 species, conversion to the stable 12-MC-4 was observed by proton NMR in 48 h [67].

Proton NMR experiments were used to study the relative affinity of $\{Li(I)[12\text{-}MC_{Mn(III)Shi}\text{-}4]\}^+$, $\{(Na(I))_2[12\text{-}MC_{Mn(III)Shi}\text{-}4]\}^{2+}$ and $\{(K(I))_2[12\text{-}MC_{Mn(III)Shi}\text{-}4]\}^{2+}$ for halides. These experiments were carried out by recording the ^{1}H chemical shift of the Shi protons which resonate, for all the examined MCs, in the −12 to −24 ppm window. Protons H_3, H_4 and H_5 were observed in this spectral window while the signal of proton H_6 resonates downfield of tetramethylsilane (TMS) (positive ppm), a region often covered by solvent signals (proton labels are reported in Fig. 7a) [5, 63]. The signals have a width of *ca.* 1 ppm due to the fast relaxation induced by the paramagnetic center, and nevertheless, the signals are narrow and separated enough to observe appreciable changes in the chemical shifts which for the peak of proton H_4 are of the order of 2 ppm upon anion exchange. Proton NMR spectra of $\{Li(I)[12\text{-}MC_{Mn(III)Shi}\text{-}4]\}^+$ with different anions are represented in Fig. 7 [63].

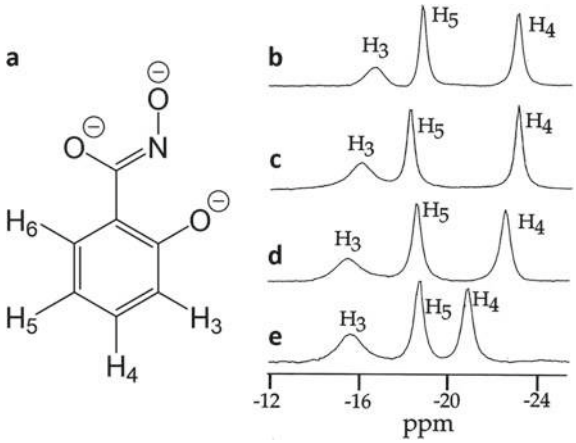

Fig. 7 **a** Scheme of the deprotonated Shi ligand (labels assigned to the protons in the NMR spectra are reported), Proton NMR spectra of Shi protons of $\{Li(I)[12\text{-}MC_{Mn(III)Shi}\text{-}4]\}^+$ with **b** I_3^-, **c** TFA^-, **d** Br^- and **e** Cl^- as counteranions. The H_6 proton resonances are not observed in this spectral window. Adapted with permission from [63]. Copyright 1996 American Chemical Society

The approach used by Pecoraro and coworkers started with the analysis of the crystal structure of $\{Li(I)[12\text{-}MC_{Mn(III)Shi}\text{-}4]\}^+$ with I_3^- as the counterion, which showed that the latter is not coordinated to the MC entity (Fig. 6b) [5, 63]. Under the reasonable assumption that triiodide anion remains uncoordinated when the complex is dissolved in DMF, ^{1}H-NMR titrations of the MC with Cl^- and Br^- obeying the following equilibria were studied:

$$\left\{Li(I)\left[12-MC_{Mn(III)Shi}-4\right]\right\}^+ + nX^- = \left\{Li(I)X_n\left[12-MC_{Mn(III)Shi}-4\right]\right\}^{(n-1)-}$$

where $X^- = Cl^-$ and Br^-, and n = 1 or 2. As a result of these binding assays, $\{Li(I)[12\text{-}MC_{Mn(III)Shi}\text{-}4]\}^+$ was found to have an affinity for chloride which is at least 3 orders of magnitude higher than that for bromide [5, 63].

The determination of the affinity for anions of disodium and dipotassium complexes of $[12\text{-}MC_{Mn(III)Shi}\text{-}4]$ could not be performed using the same strategy described above for the Li(I) MC since for Na(I) and K(I) the MC devoid of coordinated anions is not available. Therefore, to determine the relative affinity of $\{(Na(I))_2[12\text{-}MC_{Mn(III)Shi}\text{-}4]\}^{2+}$ and $\{(K(I))_2[12\text{-}MC_{Mn(III)Shi}\text{-}4]\}^{2+}$ for Cl^- and Br^- a series of ^{1}H-NMR competition experiments were carried out. In these experiments, solutions of $\{(Na(I)Br)_2[12\text{-}MC_{Mn(III)Shi}\text{-}4]\}$ and $\{(K(I)Br)_2[12\text{-}MC_{Mn(III)Shi}\text{-}4]\}$ (Fig. 6c, d) were titrated with chloride ions [5, 63]. The successive equilibria acting in these systems were:

$$\begin{aligned}&\left\{(MBr)_2\left[12-MC_{Mn(III)Shi}-4\right]\right\} + Cl^-\\ &= \left\{M_2BrCl\left[12-MC_{Mn(III)Shi}-4\right]\right\} + Br^-\\ &\left\{M_2BrCl\left[12-MC_{Mn(III)Shi}-4\right]\right\} + Cl^-\\ &= \left\{(MCl)_2\left[12-MC_{Mn(III)Shi}-4\right]\right\} + Br^-\end{aligned}$$

where M is either Na(I) or K(I). Chloride ions compete with both coordinated bromide ions, with a log K of substitution above 4 and 3.2 respectively for the first and the second anion substitution steps with M = Na(I). The log K determined for M = K(I) are only slightly lower than those of Na(I) [5, 63].

Overall, the result of these studies is two-fold: on one hand for each core cation examined, the coordination of chloride was found favored over that of bromide. Based also on the results of the crystallization trials in the presence of different anions, the relative binding order for anions to $\{Li(I)[12\text{-}MC_{Mn(III)Shi}\text{-}4]\}^+$ was found to be $Cl^- > Br^- > TFA^- > I_3^-$. Also, there is a dependence of the affinity on the core metal used, which finds sodium metallacrowns more prone to bind anions than potassium ones.

2.2 Interaction of Copper(II) 15-MC-5 with Monocarboxylates

The concept of *face-differentiation* is well established in the chemistry of metallacrowns [5, 6, 8, 9, 22, 43, 68–70]. This concept relates with the different geometric nature of the two faces of a planar MC of chiral ligands, which result in a different affinity of the two faces for guests like anions that may coordinate to the metallacrown (Fig. 3b, c). This structural concept can be visualized as follows: when chiral ligands (e.g., Pheha) are used to assemble a MC framework (e.g., that of a 15-MC-5) the ligands provide with a cyclic $(M–N–O)_n$ connectivity and therefore result iso-oriented (Fig. 3b). As a consequence, the side chains of the ligand molecules all lie on the same side of the metallacrown (Figs. 3c and 8) [4, 5, 8]. The obtained 15-MC-5 assumes the shape of a hand where the palm is the MC and the fingers are the residues. Following this simple but remarkable structural observation, the step was short into making the hypothesis that the presence of hydrophobic residues on one side of the complex could render the same side more prone to interact with lipophilic ligands such as aromatic carboxylates [8].

The first qualitative observation that benzoate ions tend to bind on the hydrophobic side of amphiphilic $\{Ln(III)[15\text{-}MC_{Cu(II)Pheha}\text{-}5]\}^{3+}$ dates back to 2001 [8, 9]. Since then, many observations of this preference for lipophilic organic anions were reported

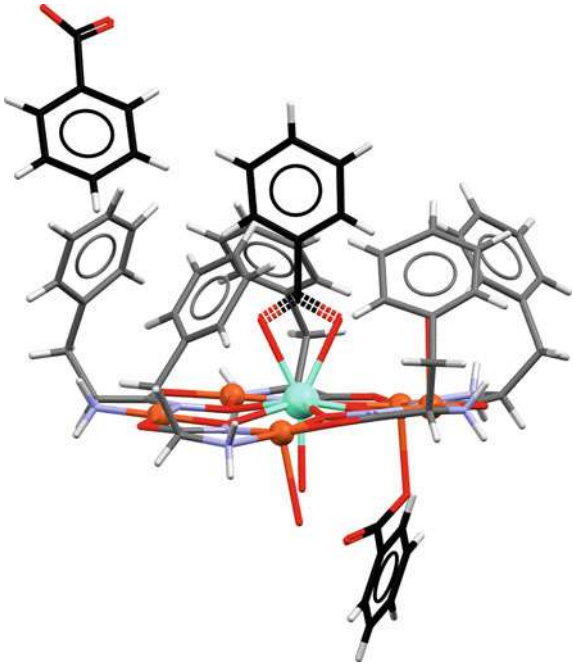

Fig. 8 Representation of *face–differentiated* $\{Eu(III)(OBz)_2[15\text{-}MC_{Cu(II)Pheha}\text{-}5]\}(OBz)$. The three benzoate anions are represented in *black*. *Orange*: Cu, *Turquoise*: Eu

[20, 25, 68–71]. In 2009, two studies appeared in which the affinity of {Ln(III)[15-$MC_{Cu(II)Pheha}$-5]}$^{3+}$ complexes for benzoate (BzO^-) and other monocarboxylates were determined (Ln = Gd and Eu) [22, 43]. In one of the two studies ^{1}H-NMR, fluorescence and UV–vis absorption were used to determine the binding constant of acetate, benzoate and coumarine 343 to {Eu(III)[15-$MC_{Cu(II)Pheha}$-5]}$^{3+}$. The binding constant of benzoate to the MC determined using ^{1}H-NMR is 363 M^{-1}, which is consistent with that determined by luminescence and absorption studies (389 and 447 M^{-1}, respectively) [22]. Also, these values compare fairly well with those determined by Pecoraro and coworkers using isothermal titration calorimetry (ITC) and cyclic voltammetry for the same MC assembly of other lanthanides as core ions which were found in the 370–760 M^{-1} range [43]. In the crystal structure of {Eu(III)$(OBz)_2$[15-$MC_{Cu(II)Pheha}$-5]}(OBz) three benzoate anions counterbalance the triple positive charge of the MC (Fig. 8): out of these, one is bidentate bound to the core Eu(III) on the hydrophobic face (possibly the primary binding site in solution), one is coordinated to a Cu(II) in axial position on the hydrophilic face, and the last one is non- coordinated [22]. ^{1}H-NMR data evidenced however that all three benzoate ions are under fast- exchange conditions in solution.

To determine the binding constant of acetate and benzoate to {Eu(III)[15-$MC_{Cu(II)Pheha}$-5]}$^{3+}$, solutions of the carboxylates (as sodium salts) in D_2O were titrated with a solution of the metallacrown up to *ca.* 1:1 molar ratio (Fig. 9). Traces of acetone were used as the internal standard for chemical shift and PGSE data [22]. The metallacrown is a paramagnetic host, and nevertheless, the benzoate and acetate proton signals could be observed during the course of the titrations despite the line broadening. For each addition of host to the guest, the chemical shift of the latter was recorded along with the PGSE decay parameters of both the guest and acetone. The change in chemical shift and the change of the ratio between the exponential parameters ($\theta_{guest}/\theta_{acetone}$) upon addition of the host were treated together by non-linear least square regression assuming fast-exchange conditions [22]. As for PGSE data the equation used was the following (see also Eq. 4):

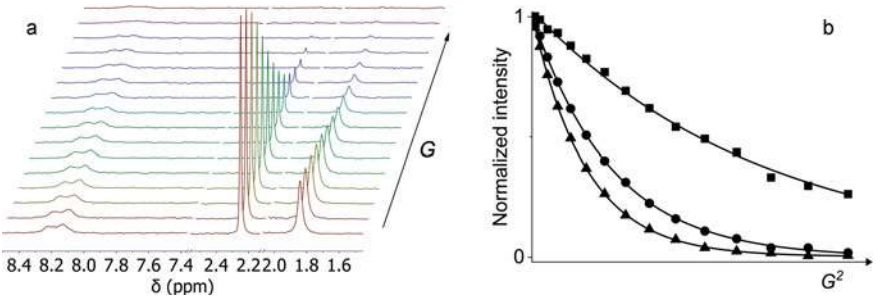

Fig. 9 The **a** PGSE spectra for the titration of acetate with {Eu(III)[15-$MC_{Cu(II)Pheha}$-5]}$^{3+}$ in D_2O, and **b** Plot of the intensities normalized over those at $G^2 = 0$. Signals of protons of benzyl groups of {Eu(III)[15-$MC_{Cu(II)Pheha}$-5]}$^{3+}$ (8.2 ppm, *squares*), of acetone (2.2 ppm, *circles*) and of acetate (1.8 ppm, *triangles*) are represented. Images drawn using original experimental dataset available from the authors [22]

$$\frac{\theta^{obs}_{guest}}{\theta^{obs}_{acetone}} = \frac{D^{obs}_{guest}}{D_{acetone}} = \frac{D^{free}_{guest}}{D_{acetone}}\chi^{free}_{guest} + \frac{D^{boundtoMC}_{guest}}{D_{acetone}}\chi^{boundtoMC}_{guest} \quad (10)$$

where θ are the experimental PGSE decay parameters at each titration point and χ the molar fractions of the free and bound guest to the MC. $D^{free}{}_{guest}/D_{acetone}$ were determined by the analysis of a solution of guest alone (acetate or benzoate). $D^{bound\ to\ MC}{}_{guest}/D_{acetone}$, although it could be considered as a fitting parameter, was put equal to $D_{EuMC}/D_{acetone}$ which was determined independently by the PGSE analysis of the metallacrown host $\{Eu(III)[15\text{-}MC_{Cu(II)Pheha}\text{-}5]\}^{3+}$ using the observable signals of aromatic protons of Pheha [22]. The procedure used led to the determination of the two binding constants that resulted 98 and 363 M^{-1} for acetone and benzoate, respectively [22].

2.3 Formation of Dimeric Capsules

The possibility of copper(II) metallacrowns to form dimeric capsules has been established a few decades ago, for both 12-MC-4 and 15-MC-5 [8, 9, 21, 24, 72–74]. This facile dimerization is allowed by the presence of out of plane coordination positions on both copper(II) and, for 15-MC-5, on the core lanthanide(III) ion which often presents a coordination number of 8 or 9. The presence of anions that may coordinate to these positions and at the same time bridge between two MC units indeed triggers the formation of dimers of MCs.

Among the first isolated dimeric capsules obtained using bifunctional organic linkers was the adduct between $\{Gd(III)[15\text{-}MC_{Cu(II)Pheha}\text{-}5]\}^{3+}$ and isonicotinate as a guest, reported in Fig. 10 [24]. In the following years, the aggregation into

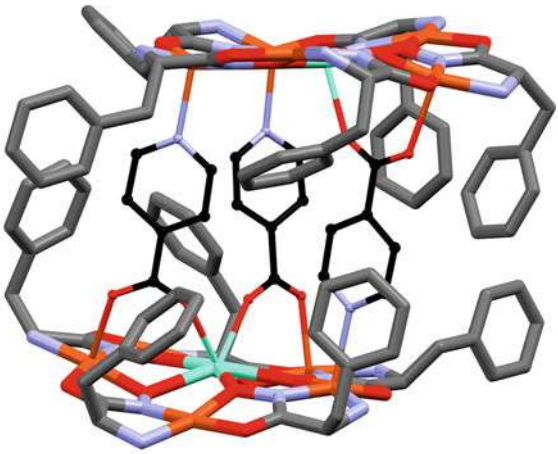

Fig. 10 Representation of the $\{(isonicotinate)_3 \subset \{Gd(III)[15\text{-}MC_{Cu(II)Pheha}\text{-}5]\}_2\}^{3+}$ adduct. The isonicotinate ions are represented in *black*. *Orange*: Cu, *Turquoise*: Gd

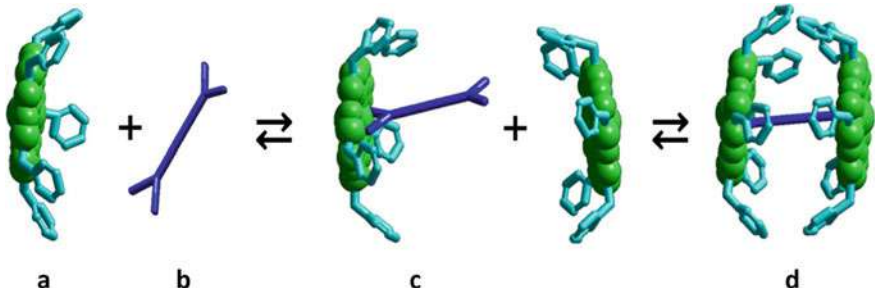

Fig. 11 Pictorial representation of the formation equilibria of capsules of **a** {Ln(III)[15-$MC_{Cu(II)Pheha}$-5]}$^{3+}$, **b** linear dicarboxylate, **c** and **d** are 1:1 and 2:1 MC:dicarboxylate adducts, respectively. Adapted with permission from [23]. Copyright 2017 American Chemical Society

dimers, trimers and even more complex superstructures was studied, exploring the possibility to use MCs as building blocks for preparing functional materials and MOF-like architectures [1, 75, 76]. The possibility to form isolated dimers remains however fascinating, since the presence of bulky side residues such as phenyl rings may lead to capsules into which guests can be accommodated and remain isolated from the environment. Ultimately, this may open the possibility to devise vessels for the delivery of pharmaceuticals or nanoreactors of dimensions of few Angstroms.

The first quantitative thermodynamic study on the speciation of dimeric compartments in solution dates back to 2017 when Pecoraro, Arena and coworkers clarified, using ITC and electrospray ionization mass spectrometry (ESI–MS), the relationship between the nature of the guest dicarboxylate and its capacity to prompt the formation of dimeric {Gd(III)[15-$MC_{Cu(II)Pheha}$-5]}$_2$(dicarboxylate)$^{4+}$ (Fig. 11) [23]. The most important result of this study was the observation that linear dicarboxylates such as terephthalate, muconate, adipate and fumarate trigger the formation of dimeric compartments with similar formation constants, although with different enthalpic and entropic parameters along with the series.

More recently, a follow-up study took into account the formation of dimeric capsules of {Ln(III)[15-$MC_{Cu(II)Pheha}$-5]}$^{3+}$ with different core metals (Ln = La, Nd, Sm, Eu, Dy, Ho) and muconate as the guest [28]. Perhaps surprisingly, ITC data revealed that only the MCs of lanthanide ions of specific dimensions (namely Eu, Gd and Dy) give rise to dimerization with muconate. To confirm this observation PGSE titrations with muconate of solutions of {Nd(III)[15-$MC_{Cu(II)Pheha}$-5]}$^{3+}$, {Sm(III)[15-$MC_{Cu(II)Pheha}$-5]}$^{3+}$ and {Eu(III)[15-$MC_{Cu(II)Pheha}$-5]}$^{3+}$ were performed using DMSO as the standard. Naked-eye examination of diffusion data revealed that the largest decrease of the diffusion coefficient of the MC (D_{MC}) is indeed observed for {Eu(III)[15-$MC_{Cu(II)Pheha}$-5]}$^{3+}$, while the diffusion coefficient for Sm(III)- and Nd(III)-containing MCs experiences a much smaller decrease. This observation fully supports the ITC finding that out of these three MCs only that of Eu(III) forms dimers. Through a quantitative data analysis, the $D'_{obs} = \theta_{MC}/\theta_{DMSO}$ values obtained from the titrations were least-square fitted using the following equation:

$$D'_{obs} = \left(D'_{monoMC} \cdot \%_{monoMC} + D'_{1:1} \cdot \%_{1:1} + D'_{2:1} \cdot \%_{2:1}\right)/100 \qquad (11)$$

where *D'* in the parentheses are D/D_{DMSO} values of the individual monomeric MC, 1:1 and 2:1 MC/muconate adducts, respectively. The molar fractions of each species at each point of the titrations were obtained from ITC speciation. Using this approach, PGSE data allowed first to calculate $D'_{1:1}$ for the {Nd(III)[15-$MC_{Cu(II)Pheha}$-5]}(muconate)$^+$ and {Sm(III)[15-$MC_{Cu(II)Pheha}$-5]}(muconate)$^+$ species, that do not form 2:1 species. In the approximation that the two latter complexes have the same *D'* of {Eu(III)[15-$MC_{Cu(II)Pheha}$-5]}(muconate)$^+$, the *D'* of the {Eu(III)[15-$MC_{Cu(II)Pheha}$-5]}$_2$(muconate)$^{4+}$ capsule could be calculated. Overall, this analysis showed that {Eu(III)[15-$MC_{Cu(II)Pheha}$-5]}$^{3+}$ experiences an increase in its diffusion coefficient of a factor of 1.14 with respect to that of the monomer, compared to the theoretical 1.26 expected for a dimerization. Solvation effects may explain this difference: actually, for the molecular volume expected for these dimeric species the hydrodynamic radii differ by only 0.07 Å, a value accounted for with the rearrangement of solvation water molecules around the MC molecules. Another possible reason for this observed behavior may reside in the fact that monomeric {Ln(III)[15-$MC_{Cu(II)Pheha}$-5]}$^{3+}$, as an oblate molecule, has a diffusion coefficient smaller than that expected for a spherical one of equivalent volume. In this perspective, the increase of hydrodynamic radius upon dimerization is apparently smaller than previewed.

Perhaps surprisingly—although they are broad—the proton signals of {Gd(III)[15-$MC_{Cu(II)Pheha}$-5]}$^{3+}$ were clearly observed. The observation of quite narrow signals is a consequence of the coupling between the ring $[Cu(II)]_5$ paramagnetic system and the core metal which results in a faster electron relaxation rate for both Gd(III) and Cu(II), and in turn into narrow NMR signals [61, 62]. Also, the PGSE experiment setup reported in this paper is almost the reverse of that previously described for the analysis of the binding of acetate or benzoate to {Eu(III)[15-$MC_{Cu(II)Pheha}$-5]}$^{3+}$. On one hand, the guest was added to the solutions of MCs in order to overcome solubility issues. On the other hand, the PGSE decay of the signals of the MC host was monitored instead of monitoring that of the guest and therefore the host needed to be present in the titrand sample. Finally, the data treatment aimed at determining the hydrodynamic radii of the individual species starting from a known speciation, rather than doing the other way around (determining *K* of binding by measuring *D* values). Overall, these aspects underline that PGSE NMR techniques can be fruitfully exploited also to study equilibria involving paramagnetic metallacrowns and to determine many of the parameters that describe these host–guest complexation processes.

3 Metal Exchange Equilibria

A metallacrown construct presents two different types of metal ions (ring and core metal), and the substitution can in principle involve either or both. NMR resonances

tightly correlate to the nature of the (paramagnetic) metals and the overall structure of the complex and therefore the exchange of either or both ring and core metal ions was found to produce significant differences in the spectra. Metal exchange reactions of MCs were therefore deeply studied through NMR and the most abundant literature is on [12-$MC_{Mn(III)}$-4] and [15-$MC_{Cu(II)}$-5] constructs, which are described here.

3.1 Metal Exchange in Manganese(II/III) 12-MC-4 Complexes

Possibly and not surprisingly the first question when looking at metallacrown structures is if they possess a functional behavior similar to those of crown ethers in terms of core metal exchange and metal ions recognition [66]. Indeed, starting as early as 1990, Pecoraro and coworkers studied in detail the capacity of the [12-$MC_{Mn(III)Shi}$-4] framework to encapsulate Li(I), Na(I), K(I) and Mn(II) [5, 63–65]. The first studies were carried out using {$(Na(I)Cl)_2$[12-$MC_{Mn(III)Shi}$-4]} which was quantitatively converted into {$Mn(II)(OAc)_2$[12-$MC_{Mn(III)Shi}$-4]} by addition of 1 eq. of manganese(II) acetate [65]. The reaction was monitored over time using ^{1}H-NMR, and representative spectra are reported in Fig. 12. Titrations of {$(Na(I)Cl)_2$[12-$MC_{Mn(III)Shi}$-4]} and {(Li(I)Cl)[12-$MC_{Mn(III)Shi}$-4]} with different couples of cations/anions also provided the first indication that MCs tend to recognize ionic pairs (anion and cation simultaneously) rather than cations or anions individually.

^{1}H-NMR and Fast Atom Bombardment (FAB) analyses showed that the cavity of [12-$MC_{Mn(III)Shi}$-4] has a stronger preference for Li(I) over Na(I) and K(I) [5, 65]. In particular, by reacting {$(AB)_2$[12-$MC_{Mn(III)Shi}$-4]} complexes with LiCl (where AB is Na(I)Cl, K(I)Cl, Na(I)Br, or K(I)Br) the product was in all cases {(Li(I)Cl)[12-$MC_{Mn(III)Shi}$-4]}. Similar experiments performed using Na(I) added to the metallacrowns encapsulating K(I) demonstrated an overall Li(I) > Na(I) > K(I) preference [5]. Furthermore, when these results were combined with the results on binding affinity for anions the order of preference of the [12-$MC_{Mn(III)Shi}$-4] framework for ionic pairs was found as follows: $Mn(II)(OAc)_2$ > $Li(I)Cl_2^-$ > $Li(I)Br_2^-$ > Li(I) > $(Na(I)Cl)_2$ > $(Na(I)Br)_2$ > $(K(I)Cl)_2$ > $(K(I)Br)_2$. As observed during anion substitution experiments (Sect. 2.1), the NMR signals of the aromatic protons were always observed in the −12 to −24 ppm region irrespective of the encapsulated cation. The H_3 and H_4 were also resolved enough to appreciate changes in their chemical shift of the order of 2–3 ppm (Figs. 13 and 7 for labels). Finally, ^{1}H-NMR titrations with 15-C-5 or 18-C-6 of Li(I), Na(I) and K(I) complexes of [12-$MC_{Mn(III)Shi}$-4] showed that only K(I) can be removed from the MC cavity and only in excess of crown ether, which allowed to assess that the affinity of [12-$MC_{Mn(III)Shi}$-4] complexes for alkali metals is higher than that of the parent organic counterparts.

In terms of the mechanism of metal exchange, FAB and ^{1}H-NMR data demonstrated that this core metal substitution proceeds by direct metal exchange and no

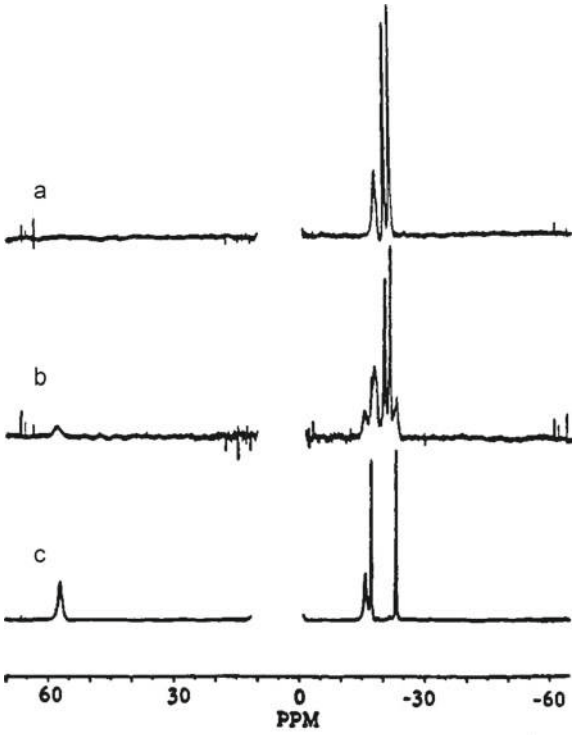

Fig. 12 ^{1}H-NMR spectra of **a** {(Na(I)Cl)$_2$[12-MC$_{Mn(III)Shi}$-4]}, **b** {(Na(I)Cl)$_2$[12-MC$_{Mn(III)Shi}$-4]} added with manganese(II) acetate, and **c** {Mn(II)(OAc)$_2$[12-MC$_{Mn(III)Shi}$-4]}. Adapted with permission from [65]. Copyright 1991 American Chemical Society

disassembly of the complex take place [5, 63]. In particular, the addition of Li(I)Cl to a mixture of {(Na(I)Cl)$_2$[12-MC$_{Mn(III)Shi}$-4]} and {(Na(I)Cl)$_2$[12-MC$_{Mn(III)Nha}$-4]} (ligands represented in Fig. 2) led to the appearance of the signals related solely to {(Li(I)Cl)[12-MC$_{Mn(III)Shi}$-4]} and {(Li(I)Cl)[12-MC$_{Mn(III)Nha}$-4]} [5]. The absence of proton NMR signals attributable to mixed ligand species confirmed FAB data that no MC disassembly occurs during these processes. Also, NMR experiments carried out in both DMF, and DMF/acetonitrile mixtures evidenced that the metal exchange process occurs in the minute time scale and in the slow-exchange regime from an NMR point of view. As a further confirmation of the inertness of the [12-MC$_{Mn(III)Shi}$-4] ring framework to ligand exchange, potassium was removed using 18-C-6 from the MC cavities of a mixture of {(K(I)Br)$_2$[12-MC$_{Mn(III)Shi}$-4]} and {(K(I)Br)$_2$[12-MC$_{Mn(III)Nha}$-4]} without observing disassembly and subsequent ligand mixing of the core metal vacant [12-MC$_{Mn(III)Shi}$-4] [5].

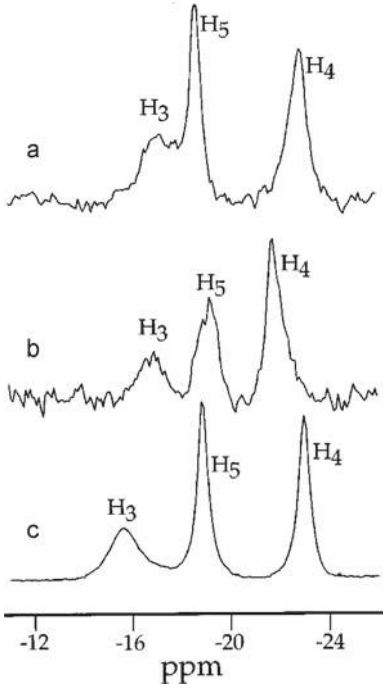

Fig. 13 ^{1}H-NMR spectra of **a** {$(K(I)Br)_2$[12-$MC_{Mn(III)Shi}$-4]}, **b** {$(Na(I)Br)_2$[12-$MC_{Mn(III)Shi}$-4]}, and **c** {$Li(I)Br_2$[12-$MC_{Mn(III)Shi}$-4]}$^{-}$. Labelling scheme is as reported in Fig. 7. The H_6 proton resonances are not observed in this spectral window. Adapted with permission from Ref. [63]. Copyright 1996 American Chemical Society

3.2 *Metal Exchange in Copper(II) 12-MC-4 and 15-MC-5 Complexes*

Cu(II)-containing MCs are possibly some of the most studied metallacrown constructs in literature [1, 4, 6, 77]. For its hard-soft behavior and its intrinsic property to form stable complexes among divalent cations (Irving–Williams series), the use of copper(II) as the ring metal is very convenient for the assembly of both 12-MC-4 and 15-MC-5 of α-hydroxamates [1, 4, 6, 63, 77]. Ni(II) has been also used to assemble structurally similar MCs, but less studies on those constructs were released in the literature [78–80]. The most common ligands used to study the processes of formation, metal substitution and framework expansion of Cu(II) metallacrowns are reported in Fig. 2, with Picha, Pheha, Tyrha and Leuha the most frequently used in these studies [5, 15, 16, 19, 23, 28, 29, 56–60, 81]. In Fig. 14a schematic summary of processes of metal exchange and framework rearrangement studied through ^{1}H-NMR on 15-MC-5 and 12-MC-4 complexes of Cu(II) are represented. The description of framework expansion processes is reported in Sect. 4.

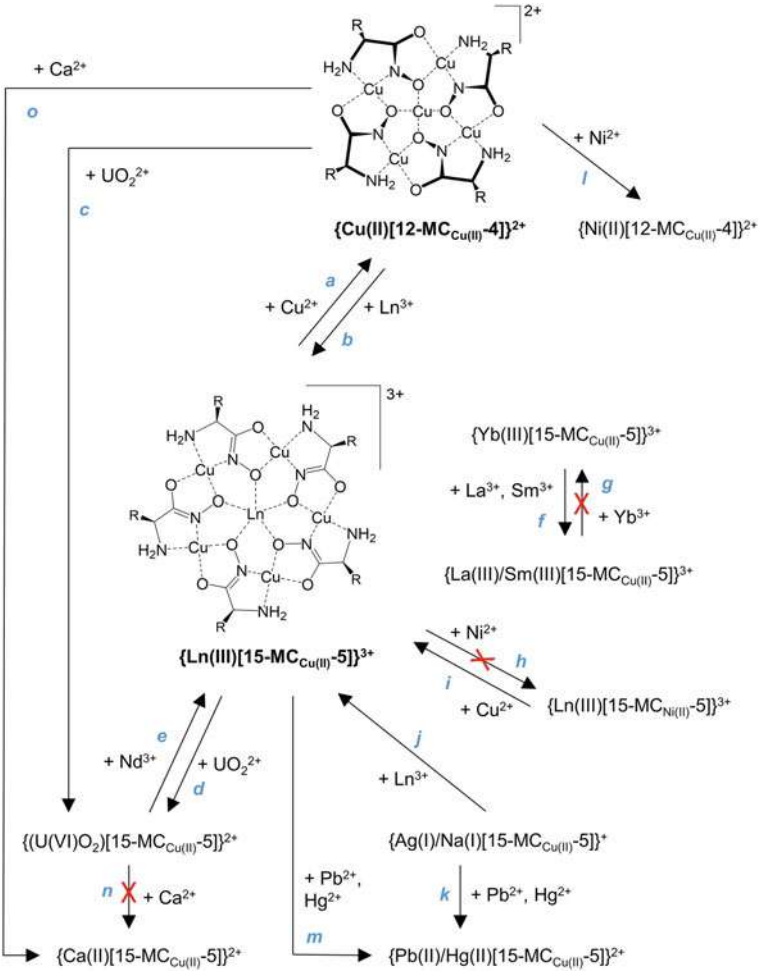

3.2.1 Ring Metal Exchange

$\{Ln(III)[15\text{-}MC_{M(II)Picha}\text{-}5]\}^{3+}$ complexes (M = Cu, Ni) can be easily isolated by reacting Picha with $Cu(NO_3)_2$ or $Ni(NO_3)_2$ in the presence of $Ln(NO_3)_3$ in a basic environment. Additions of $Ni(NO_3)_2$ to a solution of $\{Ln(III)[15\text{-}MC_{Cu(II)Picha}\text{-}5]\}$ resulted in no changes in the ^{1}H-NMR spectra in DMSO, proving that the Cu(II) MC is the most stable complex among the two [59]. Conversely, the addition of $Cu(NO_3)_2$ to a solution of $\{Sm(III)[15\text{-}MC_{Ni(II)Picha}\text{-}5]\}^{3+}$ led to the formation of $\{Sm(III)[15\text{-}MC_{Cu(II)Picha}\text{-}5]\}^{3+}$ after a month. NMR data established that the metal substitution process involves the formation of mixed $\{Sm(III)[15\text{-}MC_{Ni(II)xCu(II)5\text{-}xPicha}\text{-}5]\}^{3+}$ complexes (x = 0 − 5), and that small quantities of $\{Cu(II)[12\text{-}MC_{Cu(II)Picha}\text{-}4]\}^{2+}$

◀**Fig. 14** Representation of the processes followed by NMR regarding metal exchange reactions and framework expansions of Cu(II) 12-MC-4 and 15-MC-5- with α-hydroxamates. The experimental conditions (ligand, solvent, equivalents of metal, percentage conversion and reaction time) are also reported along with the reference to the literature. For simplicity, we reported the structure of the 12-MC-4 and 15-MC-5 complexes of an aliphatic amino-hydroxamate. Picha and Pheha, DMSO, excess Cu(II), partial conversion for Sm(III), Dy(III) and Yb(III), no conversion seen for La(III), Ce(III), and Pr(III) (*a*) [58]; Picha and Pheha, DMSO, 1 eq. of Ln(III), complete conversion after 30 days at room temperature or 2 days at 323 K (*b*) [58]; Leuha, MeOH and H_2O, 1 eq. of UO_2^{2+}, complete conversion, no signals in the starting 12-MC-4 (*c*) [15]; Leuha, MeOH, 1 eq. of UO_2^{2+}, near complete conversion (*d*) [15]; Leuha, MeOH, 1 eq. of Nd(III), 15% conversion after 2 weeks (*e*) [15]; Picha, DMSO, 1 eq. of La(II) or Sm(II), 70% conversion for La(III) and 63% for Sm(III), equilibrium after 55 days at 323 K (*f*) [60]; Picha, DMSO, 1 eq. of Yb(III), no conversion (*g*) [60]; Picha, DMSO, excess Ni(II), no conversion after 3 weeks (*h*) [59]; Picha, DMSO, 1 eq. of Cu(II), almost complete conversion with small quantities of 12-MC-4 (*i*) [59]; Picha, DMSO, 1 eq. of Ln(III), complete conversion for La(III) and Sm(III), partial conversion for Er(III) and Yb(III) with small quantities of 12-MC-4, equilibrium after 5 days at 323 K (*j*) [60]; Picha, DMSO, 1 eq. of Pb(II) or Hg(II), complete and fast conversion (15 min) (*k*) [60]; Picha and Pheha, DMSO, 3.5 or 5 eq. of Ni(II), complete conversion (*l*) [58]; Picha, DMSO, 1 eq. of Pb(II) or Hg(II), 40–70% conversion for Pb(II) depending on the starting Ln(III), partial conversion for Hg(II) (*m*) [60]; Leuha, MeOH and H_2O, 10 eq. of Ca(II), no conversion (*n*) [15]; Trpha, MeOH/H_2O 9:1, 1 eq. of Ca(II), conversion at pH > 4.5, followed through UV–vis spectroscopy (*o*) [19]

and $\{Ni(II)[12\text{-}MC_{Ni(II)Picha}\text{-}4]\}^{2+}$ are present as byproducts [59]. Perhaps expected by the Irving–Williams series, the $[15\text{-}MC_{Cu(II)Picha}\text{-}5]$ species ultimately resulted thermodynamically more stable than the analogous Ni(II) construct [82].

3.2.2 Core Metal Exchange

The first NMR study of core metal exchange reactions in MCs was performed by Lisowski and coworkers on $\{Cu(II)[12\text{-}MC_{Cu(II)Picha/Pheha}\text{-}4]\}X_2$ complexes, where and X is Cl^- in the case of Pheha and either NO_3^- or HSO_4^- for Picha [59]. From the ^{1}H-NMR spectra of the complexes in DMSO, four resonances for Picha and the eight for Pheha were indeed observable as expected for four equivalent ligands related by a four-fold axial symmetry of the complexes in solution. The addition of different amounts of $Ni(NO_3)_2$ to solutions of $\{Cu(II)[12\text{-}MC_{Cu(II)Picha/Pheha}\text{-}4]\}^{2+}$ in DMSO led to the appearance of a new set of four ^{1}H-NMR signals for Picha complexes and of eight signals for Pheha associated to $\{Ni(II)[12\text{-}MC_{Cu(II)Picha/Pheha}\text{-}4]\}^{2+}$ [58]. The presence in the solution of this species was confirmed through ESI–MS. Interestingly, these data ruled out the formation of mixed ring metal complexes (e.g., $\left\{Cu(II)\left[12-MC_{Cu(II)_xNi(II)_{4-x}Picha/Pheha}-4\right]\right\}^{2+}$, x = 0–4) (see Sect. 3.2.1). Rather, NMR and ESI data suggest that core transmetallation occurred:

$$\left\{Cu(II)\left[12-MC_{Cu(II)Picha/Pheha}-4\right]\right\}^{2+} + Ni(II) = \left\{Ni(II)\left[12-MC_{Cu(II)Picha/Pheha}-4\right]\right\}^{2+} + Cu(II)$$

Lisowski and coworkers extensively studied by ^{1}H-NMR, the transmetallation processes in Cu(II) 15-MC-5 complexes to determine the relative stabilities of the $\{M[15\text{-}MC_{Cu(II)}\text{-}5]\}^{n+}$ constructs for different M^{n+} ions. The addition of $Pb(NO_3)_2$ to solutions of $\{Ag(I)[15\text{-}MC_{Cu(II)Picha}\text{-}5]\}^+$ and $\{Na(I)[15\text{-}MC_{Cu(II)Picha}\text{-}5]\}^+$ in DMSO showed the fast appearance of a set of resonances associated to the $\{Pb(II)[15\text{-}MC_{Cu(II)Picha}\text{-}5]\}^{2+}$ complex and the disappearance of the resonances of the reactants. Conversely, the DMSO ^{1}H-NMR spectra of $\{Ln(III)[15\text{-}MC_{Cu(II)Picha}\text{-}5]\}^{3+}$ after the addition of $Pb(NO_3)_2$ showed only a 40–70% conversion to $\{Pb(II)[15\text{-}MC_{Cu(II)Picha}\text{-}5]\}^{2+}$ complex depending on the encapsulated lanthanide(III) ion. More in detail, higher yields of conversion were observed when the starting complex contained heavier lanthanides [60]. A similar behavior was observed also for Hg(II), although the low thermal stability of $\{Hg(II)[15\text{-}MC_{Cu(II)Picha}\text{-}5]\}^{2+}$ prevented the collection of accurate NMR data [60]. This different conversion yield through the lanthanide series was further explored by addition of La(III) and Sm(III) salts to solutions of $\{Yb(III)[15\text{-}MC_{Cu(II)Picha}\text{-}5]\}^{3+}$ in DMSO. The gradual growth of the ^{1}H-NMR signals of $\{La/Sm(III)[15\text{-}MC_{Cu(II)Picha}\text{-}5]\}^{3+}$ complexes could be observed in 55 days at 323 K, with final yields of conversion of 70% for La(III) and 63% for Sm(III) [60]. The reverse reactions could not be observed, showing that the stability indeed decreases through the lanthanide series due to both the lanthanide contraction and a higher Lewis acidity of the ions. Finally, further proof of the higher stability of Cu(II) 15-MC-5 complexes with lighter lanthanides was obtained by studying transmetallation processes using $\{Na/Ag(I)[15\text{-}MC_{Cu(II)Picha}\text{-}5]\}^+$ as the reactants to obtain $\{Ln(III)[15\text{-}MC_{Cu(II)Picha}\text{-}5]\}^{3+}$ species. While the complete metal exchange was observed for lighter La(III) and Sm(III) ions, the addition of Er(III) and Yb(III) resulted only in the formation of small amounts of the pentanuclear $\{Cu(II)[12\text{-}MC_{Cu(II)Picha}\text{-}4]\}^{2+}$ [60]. Overall these results consistently prove that Cu(II) 15-MC-5 are more prone to the complexation of lighter (bigger) lanthanide ions compared to heavier (smaller) ones. This behavior is in agreement with what reported in the previous experiments and was later quantitatively proved by studying the thermodynamic stability of $\{Ln(III)[15\text{-}MC_{Cu(II)Pheha}\text{-}5]\}^{3+}$ and $\{Ca(II)[15\text{-}MC_{Cu(II)Pheha/Trpha}\text{-}5]\}^{2+}$ complexes using spectrophotometric titrations [19, 58, 59].

Binnemans and coworkers finally proved through ^{1}H-NMR that $\{U(VI)O_2[15\text{-}MC_{Cu(II)Leuha}\text{-}5]\}^{2+}$ is stable against the addition of 18-C-6 (up to 10 equivalents) in MeOH and H_2O solutions, and the same behavior was observed for $\{Ca(II)[15\text{-}MC_{Cu(II)Pheha/Trpha}\text{-}5]\}^{2+}$ by Tegoni and coworkers. This in turn proved that MC assemblies are more selective than crown ethers in the complexation of uranyl ions [15, 17]. Slow core transmetallation was observed upon addition of Nd(III) to the uranyl MC resulting in 15% metal exchange for 1 equivalent of lanthanide added in MeOH solutions. Conversely, complete conversion of $\{Nd(III)[15\text{-}MC_{Cu(II)Leuha}\text{-}5]\}^{3+}$ into $\{U(VI)O_2[15\text{-}MC_{Cu(II)Leuha}\text{-}5]\}^{2+}$ could be observed by adding 1 equivalent of uranyl ions to the lanthanide complex [15]. No transmetallation was observed adding Ca(II) [15].

In conclusion, ^{1}H-NMR studies on Cu(II) MCs of α-aminohydroxamates provided with a general order of stability of the assembly with different core metals as follows:

Pb(II)/U(VI)O_2^{2+} > Hg(II), Ln(III) (lighter) > Ln(III) (heavier) > Ca(II) > Ag(I), Na(I) > K(I). Unfortunately, to date, no data has been reported on the relative stability of 15-MC-5 complexes of Pb(II) compared to that of the uranyl ion. Overall, these experiments remarkably show the versatility of 15-MC-5 species to form complexes with cations of different charges combined with fine size discrimination properties.

4 MC Rearrangements and Ligand Exchange

4.1 MC Expansion

As described in the introduction and as represented in Fig. 3, for geometric reasons β-hydroxamic acids preferentially form 12-MC-4 constructs while α-hydroxamic acids prefer to form 15-MC-5 constructs (*metallacrowns structural paradigm*). However, the formation of the latter expanded frameworks is observed only for α-hydroxamic acids in the presence of a large central metal ion capable of being encapsulated in a 5-oxygens cavity (e.g., UO_2^{2+}, Ln(III) or Ca(II)) [7, 81, 83–86]. Conversely, in the absence of a large core metal, 12-MC-4 frameworks are formed in which the core and ring metal ions are the same (i.e., $\{Cu(II)[12\text{-}MC_{Cu(II)Picha/Pheha}\text{-}4]\}^{2+}$, Figs. 3 and 14) [8, 15, 58, 72, 87–89]. β-Hydroxamic acids or their analogs (e.g., Shi and Nha) behave differently and 12-MC-4 complexes are selectively assembled in the presence of Cu(II) or Mn(II/III) ions forming $\{Cu(II)[12\text{-}MC_{Cu(II)L}\text{-}4]\}^{2-}$ and $\{Mn(II)[12\text{-}MC_{Mn(III)L}\text{-}4]\}^{2+}$ species, respectively. Although less selective, the same phenomenon was also observed with Ni(II) [87]. Here we present a summary of the most relevant studies of MC expansion and ligand exchange equilibria that have been performed using NMR.

The rearrangement process of $\{Cu(II)[12\text{-}MC_{Cu(II)Picha/Pheha}\text{-}4]\}^{2+}$ complexes into $\{M[15\text{-}MC_{Cu(II)Pheha/Picha}\text{-}5]\}^{n+}$ (n = 1–3) triggered by the addition of large core cations (Ln(III) and U(VI)O_2^{2+}) was studied by ^{1}H-NMR in DMSO or MeOH. Upon addition of 1 equivalent of Ln(III) ions to $Cu(II)[12\text{-}MC_{Cu(II)Picha/Pheha}\text{-}4]X_2$ in DMSO, where X is NO_3^- for Picha or Cl^- for Pheha, the result is the formation of $\{Ln(III)[15\text{-}MC_{Cu(II)Picha/Pheha}\text{-}5]\}^{3+}$ in 30 days at room temperature or 2 days at 323 K, according to the following reaction [58]:

$$5\left\{Cu(II)\left[12-MC_{Cu(II)Picha/Pheha}-4\right]\right\}^{2+} + 4\,Ln(III) = 4\left\{Ln(III)\left[15-MC_{Cu(II)Picha/Pheha}-5\right]\right\}^{3+} + 5\,Cu(II)$$

For Ln(III) ions like samarium(III) or heavier (i.e., Dy(III) and Yb(III)) the reaction is reversible. Actually, the addition of $Cu(NO_3)_2$ to solutions of $\{Ln(III)[15\text{-}MC_{Cu(II)Picha}\text{-}5]\}(NO_3)_3$ in DMSO produced the appearance of the signals of the starting $\{Cu(II)[12\text{-}MC_{Cu(II)Picha}\text{-}4]\}(NO_3)_2$. Conversely, this reaction did not take place when lighter lanthanides were added (La(III), Ce(III) and Nd(III)) [59].

These observations were again explained by considering that the cavity of the [15-$MC_{Cu(II)Picha}$-5] framework has a size more suitable for the encapsulation of larger lanthanide ions than smaller ones (as previously reported in Sect. 3.2.2).

The observations obtained by Binnemans and Parac-Vogt on the rearrangement of $\{Cu(II)[12\text{-}MC_{Cu(II)Tyrha}\text{-}4]\}^{2+}$ and $\{Cu(II)[12\text{-}MC_{Cu(II)Leuha}\text{-}4]\}^{2+}$ into 15-MC-5 triggered by Ln(III) and uranyl ions provided further confirmation on this behavior. However, it is interesting that differently from Picha, for both 12-MC-4 complexes of Tyrha and Leuha, no ^{1}H-NMR signals were detected [15, 29]. The reasons for these observations are still unclear. Beyond ligand exchange equilibria that may result in broad NMR signals, one possible explanation relates with the non-planar conformation of the $\{Cu(II)[12\text{-}MC_{Cu(II)}\text{-}4]\}^{2+}$ species of α-aminohydroxamates. The hypothesis is that the different nature of the side chain and the different solvents used for NMR analysis result in maybe subtly different conformations of the 12-MC-4 structure which impact the nature of the magnetic coupling of the $[Cu(II)]_4$ system of the MC ring and therefore the electron and proton relaxation rates.

Finally, NMR studies of $\{Na(I)[15\text{-}MC_{Cu(II)Picha}\text{-}5]\}^{+}$ and its analog of Ag(I) in DMSO further highlighted the ability of MCs to discriminate the size of the core metals: while $\{Ag(I)[15\text{-}MC_{Cu(II)Picha}\text{-}5]\}^{+}$ and $\{Na(I)[15\text{-}MC_{Cu(II)Picha}\text{-}5]\}^{+}$ can be isolated by addition of Ag(I) and Na(I) as nitrate salts respectively to a solution containing $\{Cu(II)[12\text{-}MC_{Cu(II)Picha}\text{-}4]\}^{2+}$, the same behavior was not observed for the larger K(I) [60]. Interestingly and accordingly with these observations, the use of NaOH as a base for the deprotonation of Picha led to the assembly of $\{Na(I)[15\text{-}MC_{Cu(II)Picha}\text{-}5]\}^{+}$ whereas the use of KOH generated the $\{Cu(II)[12\text{-}MC_{Cu(II)Picha}\text{-}4]\}^{2+}$ construct [58].

4.2 Ligand Exchange in Copper(II) Metallacrowns

The rates of ligand exchange in MC systems were observed to be very dependent on the ring metal ions involved and the dimension of the cavity. For instance, inertness towards ligand exchange reactions was earlier reported for $\{Cu(II)[12\text{-}MC_{Cu(II)Shi/Anha}\text{-}4]\}^{2+}$ complexes [90]. Conversely, the complexes of [9-$MC_{V(V)OShi/Nha}$-3] were proved to be labile in solution, possibly a consequence of the absence of a stabilizing central ion in the cavity [91].

A detailed ^{1}H-NMR study of ligand exchange processes was reported in 2005 by Binnemans and Parac-Vogt on $\{Nd(III)[15\text{-}MC_{Cu(II)Tyrha/Pheha}\text{-}5]\}^{3+}$ [16]. When mixed together in MeOH, the ^{1}H-NMR spectrum of a solution of $\{Nd(III)[15\text{-}MC_{Cu(II)Tyrha}\text{-}5]\}^{3+}$ and $\{Nd(III)[15\text{-}MC_{Cu(II)Pheha}\text{-}5]\}^{3+}$ showed signals corresponding to the two individual complexes. However, some of the peaks changed into multiplets after 2 days at 310 K [16]. To confirm that these observations are related to ligand exchange, the ^{1}H-NMR spectrum of a solution obtained by mixing Pheha and Tyrha with Cu(II) and Nd(III) ions in MeOH was recorded. The resulting spectra were indeed extremely similar to the one of the mixture of $\{Nd(III)[15\text{-}MC_{Cu(II)Tyrha}\text{-}5]\}^{3+}$ and $\{Nd(III)[15\text{-}MC_{Cu(II)Pheha}\text{-}5]\}^{3+}$ after 2 days [16]. Perhaps

more importantly, the ESI–MS analysis showed a statistical distribution of ligands in $\{Ln(III)[15\text{-}MC_{Cu(II)(Tyrha)x(Pheha)5\text{-}x}\text{-}5]\}^{3+}$ complexes (x = 0–5), in turn revealing that no ligand is preferred over the other for the formation of the metallamacrocycle and no mutual ligand recognition is expected in the construct. This observation is consistent with the crystal structures of the two homo-ligand complexes which show that no significant intramolecular interactions other than steric hindrance are observed between the ligands [16].

5 Ln(III)/Mn(III) and Ln(III)/Cu(II) MCs: Insight on Their Structure in Solution

The quantity of NMR information on MCs is vast and still, perhaps surprisingly, the potential of using ^{1}H-NMR data to extract structural information of these complexes in solution has been explored in detail only very recently [30]. We will discuss here the results of these analyses performed on Ln(III)/Mn(III) 12-MC-4 complexes, and the reasons why the same studies can not be performed straightforwardly on Ln(III)/Cu(II) 15-MC-5 complexes.

5.1 Ln(III)/Mn(III) 12-MC-4 Complexes

The ^{1}H-NMR characterization of manganese(II/III) MCs dates as early as 1989 when the first MC complexes were discovered and isolated [5, 63, 64, 66]. However, despite the large number of MCs containing different transition and rare-earth metals isolated since then, a systematic analysis aimed at correlating the structure in the solution of the MC complexes with the paramagnetic features of the assembly was reported only in 2017 by Zaleski, Tegoni and coworkers [30]. This analysis was carried out on heterotrimetallic $\{Na(I)Ln(III)(OAc)_4[12\text{-}MC_{Mn(III)Shi}\text{-}4]\}$ complexes. The study started from the isolation in the solid state of twelve isostructural $\{Na(I)Ln(III)(OAc)_4[12\text{-}MC_{Mn(III)Shi}\text{-}4](H_2O)_4\}$ complexes (Ln = Pr-Yb except Pm, and Y). The structure of the Y(III) complex is reported in Fig. 15. The analysis of proton NMR spectra of these complexes allowed to clarify the paramagnetic effects along the Ln(III) series on the protons of both Shi and acetate ligands. Although not crystallographically four-fold symmetrical in the solid state, four equivalent Shi ligands are present in the solution as a consequence of structural adaptations and fluxionality, as previously observed in the literature for Mn(III) MCs [5, 63, 64, 66]. Finally, NMR data allowed to establish that the bridging carboxylates are not dissociated in solution, being held in position by coordination to the lanthanide ions which are 8-coordinated [30].

In the ^{1}H-NMR spectra of the diamagnetic $\{Na(I)Y(III)(OAc)_4[12\text{-}MC_{Mn(III)Shi}\text{-}4]\}$ three out of the four non-equivalent Shi protons are located in the -15 to -25 ppm

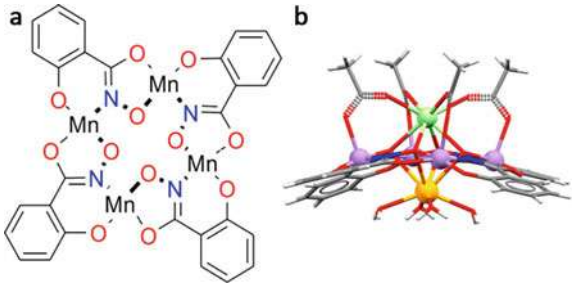

Fig. 15 **a** Representation of the [12-$MC_{Mn(III)Shi}$-4] scaffold, **b** General X-ray crystal structures of {Na(I)Ln(III)$(OAc)_4$[12-$MC_{Mn(III)Shi}$-4]$(H_2O)_4$} complexes (Ln = Pr, Nd, Sm, Eu, Gd, Tb, Dy, Ho, Er, Tm, Yb, and Y). *Green*: Ln(III); *Purple*: Mn(III); *Yellow*: Na(I). Adapted with permission from [30]. Copyright 2017 American Chemical Society

range, while the fourth proton is located downfield of TMS (Fig. 16). Also, for all compounds of the {Na(I)Ln(III)$(OAc)_4$[12-$MC_{Mn(III)Shi}$-4]} series the signals of

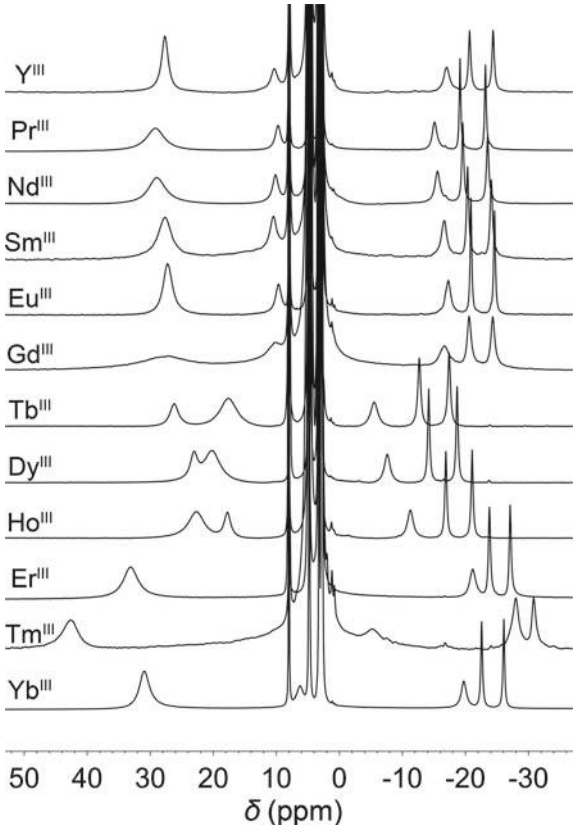

Fig. 16 ^{1}H-NMR spectra of the {Na(I)Ln(III)$(OAc)_4$[12-$MC_{Mn(III)Shi}$-4]} complexes in CD_3OD. The encapsulated lanthanide ion is indicated on the left. The spectrum of the Y(III)-MC is also reported. All spectra were recorded in CD_3OD at 298 K. Reprinted with permission from [30]. Copyright 2017 American Chemical Society

the acetate protons are also in the positive ppm window, (see Fig. 7 for labels). These signals are in the same spectral windows as those observed for the same MC framework encapsulating alkali metals [5, 63, 64, 66]. Perhaps more importantly, Fig. 16 shows that all MCs of the series present NMR spectra with the same spectral pattern, with more pronounced differences for the heavier lanthanides compared to lighter ones (Fig. 16). It is therefore evident that the paramagnetic effects provided by the $[Mn(III)]_4$ coupled system of the metallacrown impart a first order effect on the chemical shift, while the presence of the lanthanide provides a second-order perturbation. Overall, this allowed establishing naked-eye a direct correspondence between all signals along the series of spectra which simplified further data analysis (Fig. 16) [30].

The ^{1}H-NMR data analysis aimed at extracting the information on the contact and pseudocontact shift contributions was carried out through the "all lanthanides" method (ALM), using the spectral information of the MC of heavier lanthanides (Tb–Yb). In this analysis, the diamagnetic and paramagnetic shift contribution of the $[Mn(III)]_4$ system were considered constant along the lanthanide series and equal to those experienced in $\{Na(I)Y(III)(OAc)_4[12\text{-}MC_{Mn(III)Shi}\text{-}4]\}$. The analysis of the pseudocontact shift contribution showed that among the prolate ions Tb(III) provides with the greatest shift (*ca.* 15 ppm downfield on H_6), while the oblate Tm(III) shifts H_6 of ca. 16 ppm upfield.

The pseudocontact shift values were used to gain information on the structure and dynamic effects experienced by the protons of the Shi and bridging carboxylates, which we briefly described here. Although domed, the MC scaffolds deviate only slightly from planarity, and therefore all aromatic Shi protons locate at θ_i ca. 120° (direction Ln-H with respect of the pseudo-four-fold symmetry axis, Figs. 17 and 5). As a consequence, the geometric terms (see Eq. 7) present negative values which result in δ^{PC} contributions to have a sign opposite to that of the Bleaney's constant of

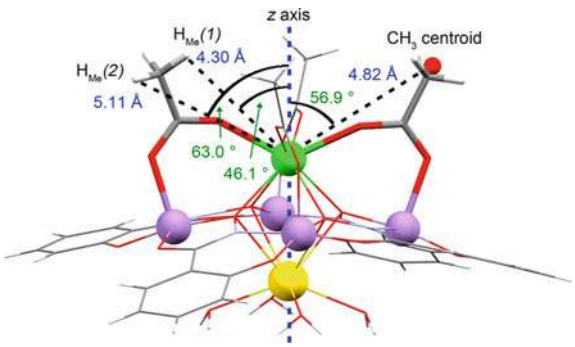

Fig. 17 Representation of $\{Na(I)Tm(III)(OAc)_4[12\text{-}MC_{Mn(III)Shi}\text{-}4](H_2O)_4\}$. The centroid of the protons of the CH_3 groups is indicated as the *red sphere*. θ_i and r_i values for the centroid and for the protons of the methyl groups are reported in *green* and *blue* respectively. The *z*-axis is approximated as coincident to the Na(I)···Ln(III) direction. *Green*: Tm(III); *Purple*: Mn(III); *Yellow*: Na(I). Copyright 2017 American Chemical Society, reprinted with permission from [30]

the Ln(III) ion under examination (Eq. 7). The chemical shifts of Shi protons agree with this interpretation.

In these complexes, for each of the heavier lanthanides, a downfield shift of the signal of the CH_3 group (compared to the Y(III)-MC) is accompanied by an upfield shift of the Shi protons signals. This phenomenon occurs as a consequence of the fast rotation of the methyl group around the C–C axis leading to the CH_3 protons averagely residing at a θ_i value lower than the magic angle. In fact, the simple evaluation of the position of the centroid of the 3 protons was not accurate enough since the θ_i value resulted higher than the magic angle. Rather, averaging over the three proton positions of the CH_3 group allowed to calculate positive $(3\cos^2\theta_i\text{-}1)/r_i^3$ terms that explain the experimental observations. The $(3\cos^2\theta_i\text{-}1)/r_i^3$ term depends on the Ln–H_i distance r_i and therefore by rotating around the C–C bonds the proton positions corresponding to θ_i value lower than the magic angle are those at a lower distance from the lanthanide. These positions dominate over the others in the calculation of the geometric term which results in a positive value.

Two interesting NMR observations were reported for these complexes. The first arose from the examination of the signals for the Gd(III) complex. Actually, in $\{Na(I)Gd(III)(OAc)_4[12\text{-}MC_{Mn(III)Shi}\text{-}4]\}$ the proton NMR signals are clearly observable and with line widths of *ca.* 10^3 Hz. Similar to what was observed for the $\{Gd(III)[15\text{-}MC_{Cu(II)Pheha}\text{-}5]\}^{3+}$ complex, the coupling between the paramagnetic $[Mn(III)]_4$ ring system and Gd(III) induces an enhancement in the electron relaxation rate of the latter. This in turn corresponds to a decrease in the electron relaxation time τ_e which has been estimated for this metallacrown into ca. 10^{-10} s, compared to $10^{-9} - 10^{-8}$ s usually reported for Gd(III) complexes [54, 92]. This enhanced electron relaxation rate results in unusually narrow proton NMR signals. The second interesting observation is that in deuterated methanol the sodium ion dissociates from the four oxygens cavity of $\{Na(I)Ln(III)(OAc)_4[12\text{-}MC_{Mn(III)Shi}\text{-}4]\}$ while the Ln(III) ion does not as it is blocked in site by the bridging acetates. Sodium dissociation has been actually proved by ^{23}Na NMR data: signal bandwidths for Y(III)-, Pr(III)-, Tb(III)-, and Yb(III)-MCs show signals with line widths between 27 and 30 Hz, which compare well with 17 Hz measured for NaCl in methanol. Conversely, much larger line widths in the range of 120 − 500 Hz were observed for Na(I) adducts with 18-C-6 and 15-C-5 demonstrating that sodium is actually non-coordinated to the scaffold [93–95].

Finally, it is worth noting that the B_0^2 parameters calculated for the complexes with heavier lanthanides should be considered only as rough estimates of the actual one, and caution has to be placed when extracting physico-chemical parameters on the basis of Bleaney's constants [55].

5.2 Ln(III)/Cu(II) 15-MC-5 Complexes

We tried to explore if the strategy of extracting structural information from pseudo-contact contributions could be applied also to $\{Ln(III)[15\text{-}MC_{Cu(II)Picha}\text{-}5]\}(NO_3)_3$

complexes, using proton NMR data reported in the literature [81]. In this series of complexes, the chemical shifts of the aromatic protons are at *ca.* 95, 37, 35 and 11 ppm for protons H_a, H_b, H_d and H_c, respectively (see Fig. 18).

We have treated the ^{1}H-NMR data of {Ln(III)[15-$MC_{Cu(II)Picha}$-5]}$(NO_3)_3$ by considering {La(III)[15-$MC_{Zn(II)Picha}$-5]}$(NO_3)_3$ as a diamagnetic reference to calculate δ^{para} shifts (reported in Fig. 19) that are to a first approximation given by the sum of the paramagnetic shifts of the $[Cu(II)]_5$ system and of the core Ln(III):

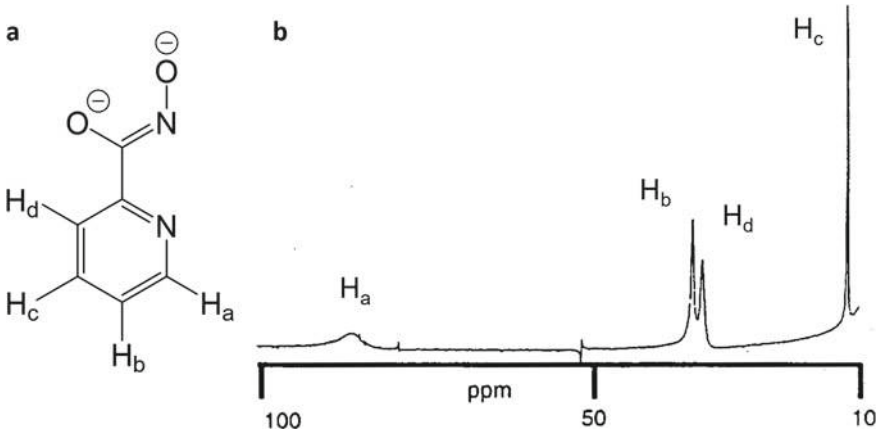

Fig. 18 The **a** Structure of the deprotonated Picha ligand (labels assigned to the protons in the NMR spectra are reported), **b** ^{1}H-NMR spectra of {La(III)[15-$MC_{Cu(II)Picha}$-5]}$(NO_3)_3$. From left to right the resonances were assigned to H_a, H_b, H_d and H_c. Adapted with permission from [81]. Copyright 1999 American Chemical Society

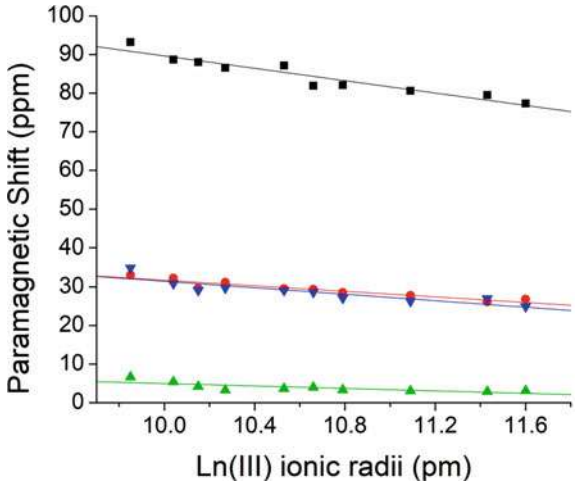

Fig. 19 Plot of the core metal radius of {Ln(III)[15-$MC_{Cu(II)Picha}$-5]}$(NO_3)_3$ (reported in picometers) *versus* the calculated δ^{para} of the four Shi protons, see Eq. 12. H_a (*black squares*), H_b (*red circles*), H_c (*green triangles*) and H_d (*blue upside-down triangles*)

$$\delta^{obs}_{Ln,Cu}(i) - \delta^{obs}_{La,Zn}(i) \cong \delta^{para}_{Ln,Cu}(i) \cong \delta^{para}_{Cu}(i) + \delta^{para}_{Ln}(i) \quad (12)$$

If we examine the plot in Fig. 19, we see that the δ^{para} shifts increase with a monotone trend along the lanthanide series, which means that there is a progressive downfield shift with decreasing ionic radius. It is therefore evident that, differently from what was observed for {Na(I)Ln(III)$(OAc)_4$[12-$MC_{Mn(III)Shi}$-4]} complexes, in {Ln(III)[15-$MC_{Cu(II)Picha}$-5]}$(NO_3)_3$ the presence of the Ln(III) paramagnetic ions almost negligibly affects the observed chemical shift values. We can therefore deduce that the contribution of the $[Cu(II)]_5$ system dominates in δ^{para} by orders of magnitude over that of the core lanthanides ion (i.e., ${\delta_{Cu}}^{para} >> {\delta_{Ln}}^{para}$).

When plotted, the δ^{para} values correlate almost linearly with the ionic radii of the Ln(III) ions (Fig. 19) [96]. This trend possibly relates either to a change in the conformation of the MC scaffold for different core metals or to a change in the magnetic coupling between the paramagnetic ions in the $[Cu(II)]_5$ system, also depending on the different core metals. On one hand, we can actually predict that the conformation of the {Ln(III)[15-$MC_{Cu(II)Pheha}$-5]} scaffold is impacted by the dimension of the coordinated core lanthanide, resulting in slightly different conformations for different Ln(III) ions and hence different geometric terms $G(i)$ [14, 19, 77]. On the other hand, a clear correlation between the Cu–Cu distances and the crystal radius of the core Ln(III) ion was observed in {Ln(III)[15-$MC_{Cu(II)Pheha}$-5]}$(NO_3)_3$ by Pecoraro and coworkers [14]. Both these structural differences likely impact the magnetic coupling in the $[Cu(II)]_5$ system, as previously stated, indeed preventing a straightforward determination of the Ln(III) pseudocontact contributions through methods such as ALM. It will be interesting in the future to deepen the study on {Ln(III)[15-$MC_{Cu(II)Tyrha}$-5]}$(NO_3)_3$ complexes to understand if some structural information can be extracted from the pseudocontact contribution to the chemical shift provided by the $[Cu(II)]_5$ system.

6 Conclusions

The use of the NMR technique has been essential in the development of the chemistry of metallacrowns. While this technique has been initially used to clarify the stability of these complexes in solutions, it turned soon clear that it could be used to study a number of the other processes that are unique to MCs. Selective encapsulation of specific metals on the basis of their dimensions and charge, or the mechanism of self-assembly and framework expansions are just examples of the processes that have been elucidated using NMR. Through NMR characterization it has also been possible to take advantage of the paramagnetic nature of MC that allowed, only quite recently, to start the study of the structure of metallacrowns in solution. For all these reasons it may be concluded not only that NMR is fully appropriate for the study of MCs, but that the latter can become paradigmatic metallamacrocycles that can be studied with a number of spectroscopic techniques, from optical methods to advanced NMR experiments.

References

1. Ostrowska, M., Fritsky, I.O., Gumienna-Kontecka, E., Pavlishchuk, A.V.: Metallacrown-based compounds: Applications in catalysis, luminescence, molecular magnetism, and adsorption. Coord. Chem. Rev. **327–328**, 304–332 (2016). https://doi.org/10.1016/j.ccr.2016.04.017
2. Nguyen, T.N., Pecoraro, V.L.: Metallacrowns: From discovery to potential applications in biomolecular imaging. In: Comprehensive Supramolecular Chemistry II. pp. 195–212. Elsevier (2017)
3. Lutter, J.C., Zaleski, C.M., Pecoraro, V.L.: Metallacrowns: supramolecular constructs with potential in extended solids, solution-state dynamics, molecular magnetism, and imaging. In: Advances in Inorganic Chemistry. pp. 177–246. Elsevier Inc. (2018)
4. Mezei, G., Zaleski, C.M., Pecoraro, V.L.: Structural and functional evolution of metallacrowns. Chem. Rev. **107**, 4933–5003 (2007). https://doi.org/10.1021/cr078200h
5. Pecoraro, V.L., Stemmler, A.J., Gibney, B.R., Bodwin, J.J., Wang, H., Kampf, J.W., Barwinski, A.: Metallacrowns: a new class of molecular recognition agents. Progress Inorgan. Chem. **45**, 83–177. Wiley (1997)
6. Tegoni, M., Remelli, M.: Metallacrowns of copper(II) and aminohydroxamates: thermodynamics of self assembly and host–guest equilibria. Coord. Chem. Rev. **256**, 289–315 (2012). https://doi.org/10.1016/j.ccr.2011.06.007
7. Kurzak, B., Kozłowski, H., Farkas, E.: Hydroxamic and aminohydroxamic acids and their complexes with metal ions. Coord. Chem. Rev. **114**, 169–200 (1992). https://doi.org/10.1016/0010-8545(92)85002-8
8. Bodwin, J.J., Cutland, A.D., Malkani, R.G., Pecoraro, V.L.: The development of chiral metallacrowns into anion recognition agents and porous materials. Coord. Chem. Rev. **216–217**, 489–512 (2001). https://doi.org/10.1016/S0010-8545(00)00396-9
9. Cutland, A.D., Halfen, J.A., Kampf, J.W., Pecoraro, V.L.: Chiral 15-Metallacrown-5 complexes differentially bind carboxylate anions. J. Am. Chem. Soc. **123**, 6211–6212 (2001). https://doi.org/10.1021/ja015610t
10. Cutland, A.D., Malkani, R.G., Kampf, J.W., Pecoraro, V.L.: Lanthanide [15] Metallacrown-5 complexes form nitrate-selective chiral cavities. Angew. Chemie Int. Ed. **39**, 2689–2692 (2000). https://doi.org/10.1002/1521-3773(20000804)39:15%3c2689::AID-ANIE2689%3e3.0.CO;2-0
11. Cutland-Van Noord, A.D., Kampf, J.W., Pecoraro, V.L.: Preparation of resolved fourfold symmetric amphiphilic helices using chiral metallacrown building blocks. Angew. Chem. Int. Ed. Engl. **41**, 4667–4670 (2002). https://doi.org/10.1002/anie.200290010
12. Jankolovits, J., Cutland Van-Noord, A.D., Kampf, J.W., Pecoraro, V.L.: Selective anion encapsulation in solid-state Ln(III)[15-metallacrown-5]3+ compartments through secondary sphere interactions. Dalton Trans. **42**, 9803–9808 (2013). https://doi.org/10.1039/c3dt50535a
13. Tegoni, M., Remelli, M., Bacco, D., Marchiò, L., Dallavalle, F.: Copper(II) 12-metallacrown-4 complexes of alpha-, beta- and gamma-aminohydroxamic acids: a comparative thermodynamic study in aqueous solution. Dalton Trans. 2693–2701 (2008). https://doi.org/10.1039/b718765c
14. Zaleski, C.M., Lim, C.-S.S., Cutland-Van Noord, A.D., Kampf, J.W., Pecoraro, V.L.: Effects of the central lanthanide ion crystal radius on the 15-MC(Cu(II)(N)pheHA)-5 structure. Inorg. Chem. **50**, 7707–7717 (2011). https://doi.org/10.1021/ic200740h
15. Parac-Vogt, T.N., Pacco, A., Görller-Walrand, C., Binnemans, K.: Pentacopper(II) complexes of α-aminohydroxamic acids: uranyl-induced conversion of a 12-metallacrown-4 to a 15-metallacrown-5. J. Inorg. Biochem. **99**, 497–504 (2005). https://doi.org/10.1016/j.jinorgbio.2004.10.023
16. Pacco, A., Parac-Vogt, T.N., Van Besien, E., Pierloot, K., Görller-Walrand, C., Binnemans, K.: Lanthanide(III)-induced conversion of 12-metallacrown-4 to 5-metallacrown-5 complexes in solution. Eur. J. Inorg. Chem. 3303–3310 (2005). https://doi.org/10.1002/ejic.200500241
17. Dallavalle, F., Remelli, M., Sansone, F., Bacco, D., Tegoni, M.: Thermodynamics of self-assembly of copper(II) 15-metallacrown-5 of Eu(III) or Gd(III) with (S)-α-alaninehydroxamic

acid in aqueous solution. Inorg. Chem. **49**, 1761–1772 (2010). https://doi.org/10.1021/ic902146d
18. Lim, C.-S., Tegoni, M., Jakusch, T., Kampf, J.W., Pecoraro, V.L.: Clarifying the mechanism of cation exchange in Ca(II)[15-MC Cu(II)Ligand -5] complexes. Inorg. Chem. **51**, 11533–11540 (2012). https://doi.org/10.1021/ic3013798
19. Tegoni, M., Furlotti, M., Tropiano, M., Lim, C.S., Pecoraro, V.L.: Thermodynamics of core metal replacement and self-assembly of Ca 2+ 15-Metallacrown-5. Inorg. Chem. **49**, 5190–5201 (2010). https://doi.org/10.1021/ic100315u
20. Lim, C.S., Jankolovits, J., Kampf, J.W., Pecoraro, V.L.: Chiral metallacrown supramolecular compartments that template nanochannels: self-assembly and guest absorption. Chem. Asian J. **5**, 46–49 (2010). https://doi.org/10.1002/asia.200900612
21. Jankolovits, J., Lim, C.-S., Mezei, G., Kampf, J.W., Pecoraro, V.L.: Influencing the size and anion selectivity of dimeric Ln 3+ [15-Metallacrown-5] compartments through systematic variation of the host side chains and central metal. Inorg. Chem. **51**, 4527–4538 (2012). https://doi.org/10.1021/ic202347j
22. Tegoni, M., Tropiano, M., Marchiò, L.: Thermodynamics of binding of carboxylates to amphiphilic Eu3+/Cu2+ metallacrown. Dalton Trans. 6705 (2009). https://doi.org/10.1039/b911512a
23. Sgarlata, C., Giuffrida, A., Trivedi, E.R., Pecoraro, V.L., Arena, G.: Anion encapsulation drives the formation of dimeric Gd III [15-metallacrown-5] 3+ complexes in aqueous solution. Inorg. Chem. **56**, 4771–4774 (2017). https://doi.org/10.1021/acs.inorgchem.6b03043
24. Mezei, G., Kampf, J.W., Pan, S., Poeppelmeier, K.R., Watkins, B., Pecoraro, V.L.: Metallacrown-based compartments: selective encapsulation of three isonicotinate anions in non-centrosymmetric solids. Chem. Commun. 1148 (2007). https://doi.org/10.1039/b614024f
25. Lim, C.-S., Jankolovits, J., Zhao, P., Kampf, J.W., Pecoraro, V.L.: Gd(III)[15-Metallacrown-5] recognition of Chiral α-Amino acid analogues. Inorg. Chem. **50**, 4832–4841 (2011). https://doi.org/10.1021/ic102579t
26. Lin, S., Liu, S.X., Chen, Z., Lin, B.Z., Gao, S.: Synthesis, structure, and magnetism of a ferric 24-Azametallacrown-8 complex. Inorg. Chem. **43**, 2222–2224 (2004). https://doi.org/10.1021/ic035145w
27. Orthmann, S., Lerch, M.: Synthesis and crystal structure of the first Sc-Nb-O-N phases. Zeitschrift für Anorg. und Allg. Chemie. **643**, 1391–1396 (2017). https://doi.org/10.1002/zaac.201700129
28. Sgarlata, C., Schneider, B.L., Zito, V., Migliore, R., Tegoni, M., Pecoraro, V.L., Arena, G.: Lanthanide identity governs guest-induced dimerization in Ln III [15-MC N(L-pheHA) -5]) 3+ Metallacrowns. Chem. Eur. J. **27**, 17669–17675 (2021). https://doi.org/10.1002/chem.202103263
29. Parac-Vogt, T.N., Pacco, A., Nockemann, P., Yuan, Y.F., Görller-Walrand, C., Binnemans, K.: Mandelohydroxamic acid as ligand for copper(II) 15-metallacrown-5 lanthanide(III) and copper(II) 15-metallacrown-5 uranyl complexes. Eur. J. Inorg. Chem. 1466–1474 (2006). https://doi.org/10.1002/ejic.200501015
30. Atzeri, C., Marzaroli, V., Quaretti, M., Travis, J.R., Di Bari, L., Zaleski, C.M., Tegoni, M.: Elucidation of 1 H NMR paramagnetic features of heterotrimetallic lanthanide(III)/Manganese(III) 12-MC-4 complexes. Inorg. Chem. **56**, 8257–8269 (2017). https://doi.org/10.1021/acs.inorgchem.7b00970
31. Bertini, I., Luchinat, C., Parigi, G., Ravera, E.: Lanthanoids and actinoids: shift and relaxation. In: Solution NMR of Paramagnetic Molecules. pp. 255–276. Elsevier (2017)
32. Bertini, I., Claudio, L.: Chapter 2 the hyperfine shift. Coord. Chem. Rev. **150**, 29–75 (1996). https://doi.org/10.1016/0010-8545(96)01242-8
33. Avram, L., Cohen, Y.: Diffusion NMR of molecular cages and capsules. Chem. Soc. Rev. **44**, 586–602 (2015). https://doi.org/10.1039/C4CS00197D
34. Johnson, C.S.: Diffusion ordered nuclear magnetic resonance spectroscopy: principles and applications. Prog. Nucl. Magn. Reson. Spectrosc. **34**, 203–256 (1999). https://doi.org/10.1016/S0079-6565(99)00003-5

35. Macchioni, A., Ciancaleoni, G., Zuccaccia, C., Zuccaccia, D.: Determining accurate molecular sizes in solution through NMR diffusion spectroscopy. Chem. Soc. Rev. **37**, 479–489 (2008). https://doi.org/10.1039/B615067P
36. Zuccaccia, D., Macchioni, A.: An accurate methodology to identify the level of aggregation in solution by PGSE NMR measurements: the case of half-sandwich diamino Ruthenium(II) salts. Organometallics **24**, 3476–3486 (2005). https://doi.org/10.1021/om050145k
37. Cohen, Y., Avram, L., Frish, L.: Diffusion NMR spectroscopy in supramolecular and combinatorial chemistry: an old parameter—new insights. Angew. Chemie Int. Ed. **44**, 520–554 (2005). https://doi.org/10.1002/anie.200300637
38. Spernol, A., Wirtz, K.: Zur Mikroreibung in Flüssigkeiten. Zeitschrift für Naturforsch. A. **8**, 522–532 (1953). https://doi.org/10.1515/zna-1953-0902
39. Gierer, A., Wirtz, K.: Molekulare Theorie der Mikroreibung. Zeitschrift für Naturforsch. A. **8**, 532–538 (1953). https://doi.org/10.1515/zna-1953-0903
40. Li, D., Kagan, G., Hopson, R., Williard, P.G.: Formula weight prediction by internal reference diffusion-ordered NMR spectroscopy (DOSY). J. Am. Chem. Soc. **131**, 5627–5634 (2009). https://doi.org/10.1021/ja810154u
41. Perrin, F.: Mouvement Brownien d'un ellipsoide (II). Rotation libre et dépolarisation des fluorescences. Translation et diffusion de molécules ellipsoidales. J. Phys. le Radium. **7**, 1–11 (1936). https://doi.org/10.1051/jphysrad:01936007010100
42. Evans, R.: The interpretation of small molecule diffusion coefficients: quantitative use of diffusion-ordered NMR spectroscopy. Prog. Nucl. Magn. Reson. Spectrosc. **117**, 33–69 (2020). https://doi.org/10.1016/j.pnmrs.2019.11.002
43. Lim, C.-S., Kampf, J.W., Pecoraro, V.L.: Establishing the binding affinity of organic carboxylates to 15-Metallacrown-5 complexes. Inorg. Chem. **48**, 5224–5233 (2009). https://doi.org/10.1021/ic9001829
44. Bertini, I., Luchinat, C., Parigi, G.: Magnetic susceptibility in paramagnetic NMR. Prog. Nucl. Magn. Reson. Spectrosc. **40**, 249–273 (2002). https://doi.org/10.1016/S0079-6565(02)00002-X
45. Blackburn, O.A., Edkins, R.M., Faulkner, S., Kenwright, A.M., Parker, D., Rogers, N.J., Shuvaev, S.: Electromagnetic susceptibility anisotropy and its importance for paramagnetic NMR and optical spectroscopy in lanthanide coordination chemistry. Dalton Trans. **45**, 6782–6800 (2016). https://doi.org/10.1039/C6DT00227G
46. Di Pietro, S., Piano, S. Lo, Di Bari, L.: Pseudocontact shifts in lanthanide complexes with variable crystal field parameters. Coord. Chem. Rev. **255**, 2810–2820 (2011). https://doi.org/10.1016/j.ccr.2011.05.010
47. Aime, S., Botta, M., Fasano, M., Terreno, E.: Lanthanide(III) chelates for NMR biomedical applications. Chem. Soc. Rev. **27**, 19–29 (1998). https://doi.org/10.1039/A827019Z
48. Bari, L.D., Pintacuda, G., Salvadori, P., Dickins, R.S., Parker, D.: Effect of axial ligation on the magnetic and electronic properties of lanthanide complexes of octadentate ligands. J. Am. Chem. Soc. **122**, 9257–9264 (2000). https://doi.org/10.1021/ja0012568
49. Fernández-Fernández, M. del C., Bastida, R., Macías, A., Pérez-Lourido, P., Platas-Iglesias, C., Valencia, L.: Lanthanide(III) complexes with a tetrapyridine pendant-armed macrocyclic ligand: 1 H NMR structural determination in solution, X-ray diffraction, and density-functional theory calculations. Inorg. Chem. **45**, 4484–4496 (2006). https://doi.org/10.1021/ic0603508
50. Valencia, L., Martinez, J., Macías, A., Bastida, R., Carvalho, R.A., Geraldes, C.F.G.C.: X-ray diffraction and 1 H NMR in solution: structural determination of lanthanide complexes of a Py 2 N 6 Ac 4 ligand. Inorg. Chem. **41**, 5300–5312 (2002). https://doi.org/10.1021/ic0257017
51. Di Bari, L., Lelli, M., Pintacuda, G., Pescitelli, G., Marchetti, F., Salvadori, P.: Solution versus solid-state structure of ytterbium heterobimetallic catalysts. J. Am. Chem. Soc. **125**, 5549–5558 (2003). https://doi.org/10.1021/ja0297640
52. Bleaney, B., Dobson, C.M., Levine, B.A., Martin, R.B., Williams, R.J.P., Xavier, A. V.: Origin of lanthanide nuclear magnetic resonance shifts and their uses. J. Chem. Soc. Chem. Commun. 791b (1972). https://doi.org/10.1039/c3972000791b

53. Ouali, N., Rivera, J.-P., Morgantini, P.-Y., Weber, J., Piguet, C.: The solution structure of homotrimetallic lanthanide helicates investigated with novel model-free multi-centre paramagnetic NMR methodsElectronic supplementary information (ESI) available: tables of structural factors Cikl, Dikl obtained for the model com. Dalton Trans. **3**, 1251–1263 (2003). https://doi.org/10.1039/b212352e
54. Rigault, S., Piguet, C.: Predictions and assignments of NMR spectra for strongly paramagnetic supramolecular lanthanide complexes: the effect of the "gadolinium break." J. Am. Chem. Soc. **122**, 9304–9305 (2000). https://doi.org/10.1021/ja000958u
55. Suturina, E.A., Mason, K., Geraldes, C.F.G.C., Kuprov, I., Parker, D.: Beyond bleaney's theory: experimental and theoretical analysis of periodic trends in lanthanide-induced chemical shift. Angew. Chemie. **129**, 12383–12386 (2017). https://doi.org/10.1002/ange.201706931
56. Parac-Vogt, T.N., Pacco, A., Nockemann, P., Laurent, S., Muller, R.N., Wickleder, M., Meyer, G., Vander Elst, L., Binnemans, K.: Relaxometric study of copper [15]Metallacrown-5 gadolinium complexes derived from α-aminohydroxamic acids. Chem. Eur. J. **12**, 204–210 (2006). https://doi.org/10.1002/chem.200500136
57. Pacco, A., Absillis, G., Binnemans, K., Parac-Vogt, T.N.: Copper(II) 15-metallacrown-5 lanthanide(III) complexes derived from l-serine and l-threonine hydroxamic acids. J. Alloys Compd. **451**, 38–41 (2008). https://doi.org/10.1016/j.jallcom.2007.04.053
58. Seda, S.H., Janczak, J., Lisowski, J.: Synthesis and reactivity of copper(II) metallacrowns with (S)-phenylalanine and 2-picolinehydroxamic acids. Inorganica Chim. Acta. **359**, 1055–1063 (2006). https://doi.org/10.1016/j.ica.2005.11.019
59. Seda, S.H., Janczak, J., Lisowski, J.: Synthesis and structural characterisation of nickel 15-metallacrown-5 complexes with lanthanide(III) and lead(II) ions: influence of the central metal ion size on the spin state of peripheral nickel(II) ions. Inorg. Chem. Commun. **9**, 792–796 (2006). https://doi.org/10.1016/j.inoche.2006.04.026
60. Seda, S.H., Janczak, J., Lisowski, J.: Synthesis and structural characterisation of copper(II) 15-metallacrown-5 complexes with Pb II, Hg II, Ag I, Na I and Y III central metal ions. Eur. J. Inorg. Chem. **2007**, 3015–3022 (2007). https://doi.org/10.1002/ejic.200600881
61. Bertini, I., Luchinat, C.: Chapter 5 magnetic coupled systems. Coord. Chem. Rev. **150**, 131–161 (1996). https://doi.org/10.1016/0010-8545(96)01245-3
62. Bertini, I., Claudio, L.: Chapter 3 relaxation. Coord. Chem. Rev. **150**, 77–110 (1996). https://doi.org/10.1016/0010-8545(96)01243-X
63. Gibney, B.R., Wang, H., Kampf, J.W., Pecoraro, V.L.: Structural evaluation and solution integrity of alkali metal salt complexes of the manganese 12-metallacrown-4 (12-MC-4) structural type. Inorg. Chem. **35**, 6184–6193 (1996). https://doi.org/10.1021/ic960371+
64. Lah, M.S., Pecoraro, V.L.: Development of metallacrown ethers: a new class of metal clusters. Comments Inorg. Chem. **11**, 59–84 (1990). https://doi.org/10.1080/02603599008035819
65. Lah, M.S., Pecoraro, V.L.: A functional analogy between crown ethers and metallacrowns. Inorg. Chem. **30**, 878–880 (1991). https://doi.org/10.1021/ic00005a002
66. Lah, M.S., Pecoraro, V.L.: Isolation and characterization of MnII[MnIII(salicylhydroximate)]4(acetate)2(DMF)6 x 2DMF: an inorganic analog of M2+(12-crown-4). J. Am. Chem. Soc. **111**, 7258–7259 (1989). https://doi.org/10.1021/ja00200a054
67. Kessisoglou, D.P., Kampf, J., Pecoraro, V.L.: Compositional and geometrical isomers of 15-metallacrowns-5 complexes. Polyhedron **13**, 1379–1391 (1994). https://doi.org/10.1016/S0277-5387(00)81704-0
68. Psomas, G., Stemmler, A.J., Dendrinou-Samara, C., Bodwin, J.J., Schneider, M., Alexiou, M., Kampf, J.W., Kessissoglou, D.P., Pecoraro, V.L.: Preparation of site-differentiated mixed ligand and mixed ligand/mixed metal metallacrowns. Inorg. Chem. **40**, 1562–1570 (2001). https://doi.org/10.1021/ic000578+
69. Jankolovits, J., Lim, C.-S., Kampf, J.W., Pecoraro, V.L.: Disruption of the La(III)[15-Metallacrown-5] cavity through bithiophene dicarboxylate inclusion. Zeitschrift für Naturforsch. B. **65**, 263-s314 (2010). https://doi.org/10.1515/znb-2010-0307

70. Lim, C., Van Noord, A.C., Kampf, J.W., Pecoraro, V.L.: Assessing guest selectivity within metallacrown host compartments. Eur. J. Inorg. Chem. 1347–1350 (2007). https://doi.org/10.1002/ejic.200700054
71. Stemmler, A.J., Pecoraro, V.L., Huang, M., Coucouvanis, D.: Syntheses of selected supramolecules. In: Inorganic Syntheses. Department of Chemistry, The Willard H. Dow Chemical Laboratories, University of Michigan, Ann Arbor, MI, USA, pp. 1–74 (2002)
72. Kurzak, B., Farkas, E., Glowiak, T., Kozlowski, H.: X-Ray and potentiometric studies on a pentanuclear copper(II) complex with β-alaninehydroxamic acid. J. Chem. Soc., Dalt. Trans. 163–167 (1991). https://doi.org/10.1039/DT9910000163
73. Pecoraro, V.L., Bodwin, J.J., Cutland, A.D.: Formation of chiral solids via a molecular building block approach. J. Solid State Chem. **152**, 68–77 (2000). https://doi.org/10.1006/jssc.2000.8670
74. Legendziewicz, J., Puchalska, M., Ciunik, Z., Wojciechowski, W.: The new decanuclear copper(II) cluster [Cu5(β-alaha)4Cl2]2·2HCl·15H2O, its structure, spectroscopy and magnetism. Polyhedron **26**, 1331–1337 (2007). https://doi.org/10.1016/j.poly.2006.11.002
75. Pavlishchuk, A.V., Satska, Y., Kolotilov, S.V., Fritsky, I.: Coordination polymers and oligonuclear systems based on oximate or hydroxamate building blocks: magnetic and sorption properties. Curr. Inorg. Chem. **5**, 5–25 (2015). https://doi.org/10.2174/1877944105666150417230637
76. Marzaroli, V., Spigolon, G., Lococciolo, G., Quaretti, M., Salviati, C., Kampf, J.W., Licini, G., Marchiò, L., Pecoraro, V.L., Tegoni, M.: Three-dimensional porous architectures based on Mn II/III three-blade paddle wheel metallacryptates. Cryst. Growth Des. **19**, 1954–1964 (2019). https://doi.org/10.1021/acs.cgd.8b01921
77. Pavlishchuk, A.V., Kolotilov, S.V., Fritsky, I.O., Zeller, M., Addison, A.W., Hunter, A.D.: Structural trends in a series of isostructural lanthanide-copper metallacrown sulfates (LnIII = Pr, Nd, Sm, Eu, Gd, Dy and Ho): hexaaquapentakis[[mu]3-glycinehydroxamato(2-)]sulfatopentacopper(II)lanthanide(III) heptaaquapentakis[[mu]3-glycinehy. Acta Crystallogr. Sect. C Cryst. Struct. Commun. **67**, m255–m265 (2011). https://doi.org/10.1107/S0108270111021780
78. Ostrowska, M., Toporivska, Y., Golenya, I.A., Shova, S., Fritsky, I.O., Pecoraro, V.L., Gumienna-Kontecka, E.: Explaining how α-hydroxamate ligands control the formation of Cu(II)-, Ni(II)-, and Zn(II)-containing metallacrowns. Inorg. Chem. **58**, 16642–16659 (2019). https://doi.org/10.1021/acs.inorgchem.9b02724
79. Marchiò, L., Marchetti, N., Atzeri, C., Borghesani, V., Remelli, M., Tegoni, M.: The peculiar behavior of Picha in the formation of metallacrown complexes with Cu(ii), Ni(ii) and Zn(ii) in aqueous solution. Dalton Trans. **44**, 3237–3250 (2015). https://doi.org/10.1039/C4DT03264K
80. Bacco, D., Bertolasi, V., Dallavalle, F., Galliera, L., Marchetti, N., Marchiò, L., Remelli, M., Tegoni, M.: Metallacrowns of Ni(ii) with α-aminohydroxamic acids in aqueous solution: beyond a 12-MC-4, an unexpected (vacant?) 15-MC-5. Dalt. Trans. **40**, 2491–2501 (2011). https://doi.org/10.1039/C0DT00832J
81. Stemmler, A.J., Kampf, J.W., Kirk, M.L., Atasi, B.H., Pecoraro, V.L.: The preparation, characterization, and magnetism of copper 15-Metallacrown-5 lanthanide complexes. Inorg. Chem. **38**, 2807–2817 (1999). https://doi.org/10.1021/ic9800233
82. Irving, H., Williams, R.J.P.: Order of stability of metal complexes. Nature **162**, 746–747 (1948). https://doi.org/10.1038/162746a0
83. Arnold, M., Brown, D.A., Deeg, O., Errington, W., Haase, W., Herlihy, K., Kemp, T.J., Nimir, H., Werner, R.: Hydroxamate-bridged dinuclear nickel complexes as models for urease inhibition. Inorg. Chem. **37**, 2920–2925 (1998). https://doi.org/10.1021/ic9711628
84. Botos, I., Scapozza, L., Zhang, D., Liotta, L.A., Meyer, E.F.: Batimastat, a potent matrix mealloproteinase inhibitor, exhibits an unexpected mode of binding. Proc. Natl. Acad. Sci. **93**, 2749–2754 (1996). https://doi.org/10.1073/pnas.93.7.2749
85. Gibney, B.R., Stemmler, A.J., Pilotek, S., Kampf, J.W., Pecoraro, V.L.: Generalizing the metallacrown analogy: ligand variation and solution stability of the VVO 9-metallacrown-3 structure type. Inorg. Chem. **32**, 6008–6015 (1993). https://doi.org/10.1021/ic00078a018

86. Stemmler, A.J., Barwinski, A., Baldwin, M.J., Young, V., Pecoraro, V.L.: Facile preparation of face differentiated, chiral 15-Metallacrown-5 complexes. J. Am. Chem. Soc. **118**, 11962–11963 (1996). https://doi.org/10.1021/ja9622968
87. Tegoni, M., Dallavalle, F., Belosi, B., Remelli, M.: Unexpected formation of a copper(ii) 12-metallacrown-4 with (S)-glutamic-γ-hydroxamic acid: a thermodynamic and spectroscopic study in aqueous solution. Dalt. Trans. **4**, 1329–1333 (2004). https://doi.org/10.1039/B316607D
88. Careri, M., Dallavalle, F., Tegoni, M., Zagnoni, I.: Pentacopper(II) 12-metallacrown-4 complexes with α- and β-aminohydroxamic acids in aqueous solution: a reinvestigation. J. Inorg. Biochem. **93**, 174–180 (2003). https://doi.org/10.1016/S0162-0134(02)00570-6
89. Dallavalle, F., Tegoni, M.: Speciation and structure of copper(II) complexes with (S)-phenylalanine- and (S)-tryptophanhydroxamic acids in methanol/water solution: a combined potentiometric, spectrophotometric. CD and ESI-MS study. Polyhedron. **20**, 2697–2704 (2001). https://doi.org/10.1016/S0277-5387(01)00886-5
90. Gibney, B.R., Kessissoglou, D.P., Kampf, J.W., Pecoraro, V.L.: Copper(II) 12-Metallacrown-4: synthesis, structure, ligand variability, and solution dynamics in the 12-MC-4 structural motif. Inorg. Chem. **33**, 4840–4849 (1994). https://doi.org/10.1021/ic00100a006
91. Pecoraro, V.L.: Structural characterization of [VO(salicylhydroximate)(CH3OH)]3: applications to the biological chemistry of vanadium(V). Inorganica Chim. Acta. **155**, 171–173 (1989). https://doi.org/10.1016/S0020-1693(00)90405-5
92. Feher, G., Scovil, H.E.D.: Electron spin relaxation times in gadolinium ethyl sulfate. Phys. Rev. **105**, 760–762 (1957). https://doi.org/10.1103/PhysRev.105.760
93. Delville, A., Stover, H.D.H., Detellier, C.: Crown ether-cation decomplexation mechanics. Sodium-23 NMR studies of the sodium cation complexes with dibenzo-24-crown-8 and dibenzo-18-crown-6 in nitromethane and acetonitrile. J. Am. Chem. Soc. 109, 7293–7301 (1987). https://doi.org/10.1021/ja00258a008
94. Lin, J.D., Popov, A.I.: Nuclear magnetic resonance studies of some sodium ion complexes with crown ethers and [2]-cryptands in various solvents. J. Am. Chem. Soc. **103**, 3773–3777 (1981). https://doi.org/10.1021/ja00403a026
95. Shamsipur, M., Popov, A.I.: Multinuclear NMR study of dibenzo-30-crown-10 complexes with sodium, potassium, and cesium ions in nonaqueous solvents. J. Am. Chem. Soc. **101**, 4051–4055 (1979). https://doi.org/10.1021/ja00509a005
96. Shannon, R.D.: Revised effective ionic radii and systematic studies of interatomic distances in halides and chalcogenides. Acta Crystallogr. Sect. A. **32**, 751–767 (1976). https://doi.org/10.1107/S0567739476001551

Influence of the Hydroxamate Ligands' Structure on the Thermodynamic Properties and Structure of Metallacrown Complexes

Malgorzata Ostrowska, Igor O. Fritsky and Elzbieta Gumienna-Kontecka

Abstract Establishing the solution stability of metallacrowns (MCs) and their selectivity for metal ions are essential for the design of functional compounds and materials based on MCs scaffolds. Optimization of ligands leading to the development of chelators forming MCs that have high stability across a broad pH range is of particular interest in the perspective of potential use of MCs when specific pH conditions are required, i.e., selective binding of anions and cations. The significance of the influence of the ligand structure, the nature of metal ions and axial ligands on the formation of the MCs with different topologies and stability are discussed on the basis of case studies of the group of aromatic hydroxamate derivatives with additional nitrogen donor atom in α-position with respect to the hydroxamate function—o-picolinehydroxamic (**PicHA**), quinolinehydroxamic acid (**QuinHA**), and pyrazylohydroxamic acid (**PyzHA**), together with β-functionalized hydroxamate derivative—ethylphosphonohydroxamic acid (**PAHEt**) and malonomonohydroxamic acid (**MACZ**). The comparison between the species isolated in solid state and those presented in solution is a valuable addition necessary to understand better the influence of the ligand structure (aromaticity, bulkiness), as well as subtle factors such as axial ligands (symmetricity of disposition vs. MC plane, denticity, size etc.) and solvation effects, on the formation of MCs.

M. Ostrowska · E. Gumienna-Kontecka (✉)
Faculty of Chemistry, University of Wroclaw, F. Joliot-Curie 14, 50-383 Wroclaw, Poland
e-mail: elzbieta.gumienna-kontecka@chem.uni.wroc.pl

M. Ostrowska
e-mail: malgorzata.ostrowska@chem.uni.wroc.pl

I. O. Fritsky
Department of Chemistry, Taras Shevchenko National University of Kyiv, Kiev 01601, Ukraine
e-mail: ifritsky@univ.kiev.ua

C. M. Zaleski (ed.), *Advances in Metallacrown Chemistry*,
https://doi.org/10.1007/978-3-031-08576-5_3

1 Introduction

Derivatives of hydroxamic acids functionalized in the α, β, or γ position with respect to the hydroxamate function are one of the most extensively studied ligands capable of forming MCs (Fig. 1) [1–3]. Among these, the aminohydroxamic acids are the most widely described in the literature (Fig. 1). Hydroxamic acids able to form MCs having donor groups other than the amino group are represented by several examples only, e.g., heterocyclic α-functionalized hydroxamic acids (**PicHA**, **QuinHA**, and **PyzHA**) or β-hydroxamic acids with not typical substituents, like carboxylic or phosphonic groups (**MACZ** or **PAHEt**, respectively) (Fig. 1) [3–8]. Moving beyond the widest group of aminohydroxamate derivatives allows us to extend knowledge about the influence of the ligand structure on the formation of MC complexes with different topologies and stability [4, 5]. A deeper understanding of the relationship between the structure of ligands and the type of metal ions in terms of the stability of MCs is important in the perspective of their use as biomedical materials, such

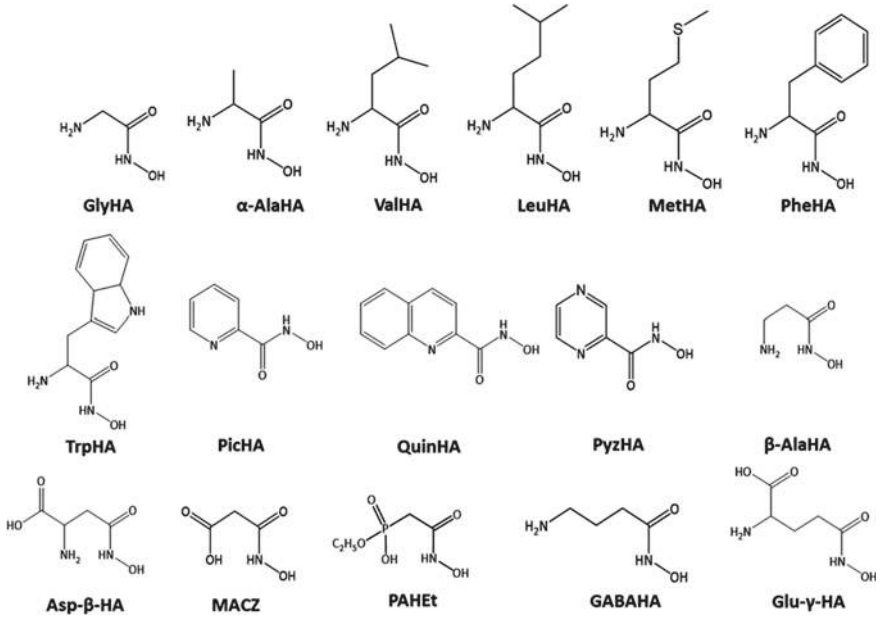

Fig. 1 Representation of α-, β- and γ-functionalized hydroxamic acids forming MC species in solution and/or in solid state. Abbreviations used: **GlyHA** = glycinehydroxamic acid, α-**AlaHA** = α-alaninehydroxamic acid, **ValHA** = valinehydroxamic acid, **LeuHA** = leucinehydroxamic acid, **MetHA** = methioninehydroxamic acid, **PheHA** = phenylalaninehydroxami acid, **TrpHA** = Tryptophanhydroxami acid, **PicHA** = picolinehydroxamic acid, **QuinHA** = quinolinehydroxamic acid, **PyzHA** = pyrazinehydroxamic acid, β-**AlaHA** = β-alaninehydroxamic acid, **Asp-β-HA** = Aspartic-β-hydroxamic acid, **MACZ** = malonomonohydroxamic acid, **PAHEt** = ethylophosphonoacetohydroxamic acid, **GABAHA** = γ-aminobutanoichydroxamic acid, **Glu-γ-HA** = glutamic-γ-hydroxamic acid

as contrast agents, selective metal ion chelators, or fluorescent probes [1, 2, 9–11]. In addition, the thermodynamic stability of MC complexes in solution and their presence in a wide range of pH is important due to the reactivity of these complexes in the processes of formation of MCs containing Ln(III) ions, which have the most promising applications [12–15]. The design of new ligand classes leading to the development of MCs with high stability over a wide pH range is of particular interest for their potential applications when specific pH conditions are required, i.e., selective binding of anions and cations [16–19].

Of course, to construct novel MCs with predictable stabilities and prearranged architectures and conformations, diverse features should be considered, among others, the size (particularly, bulkiness), geometry of the ligand molecules and their aromatic components, their basicity, the stereochemical preferences of the central ions, the nature, denticity, and size of possible apical ligands, along with the pick of solvent and effects of solvation. All the above factors influencing the inclination of the ligand to form MC complexes in solution, as well as in solid state, will be discussed herein. To illustrate the discussion we will compare selected aromatic hydroxamic acids possessing an additional nitrogen donor in α-position to the hydroxamic group—**PicHA**, **QuinHA**, and **PyzHA**, and β-functionalized hydroxamic acids—**MACZ** and **PAHEt**, to simple aminohydroxamic acids.

2 Hydroxamate Derivatives as Ligands for MCs

Hydroxamic acids may be regarded as ligands with a high binding affinity to a range of transition metal ions. Their ability to tightly bind metal ions is strongly associated with their properties: basicity, additional donor groups present in their structure, as well as geometry or aromatic character [20–22]. The broadening of knowledge explaining the influence of hydroxamate ligand structure on the formation of MCs might provide space for the design of new effective chelators.

2.1 Acid–Base Properties

Hydroxamic acids may be regarded as weak acids in which the dissociation process may proceed via several possible routes (Fig. 2a). Depending on the tautomeric form in which they are present in the solution, hydroxamic acids contain one or two easily replaceable protons. The keto tautomer, which is predominant under acidic conditions, behaves as a monobasic acid, while the enol (iminol) form, which is more stable in alkaline media, may dissociate two protons [20, 22]. While the metal is present in the solution, the second step of proton dissociation of keto form can be observed (Fig. 2a). Moreover, each of the tautomers can exist as *E* and *Z* isomers, with better stability than the first one in the solid state, and the second under aqueous conditions with stabilization by hydrogen bonds (Fig. 2b) [23–25]. The existence of

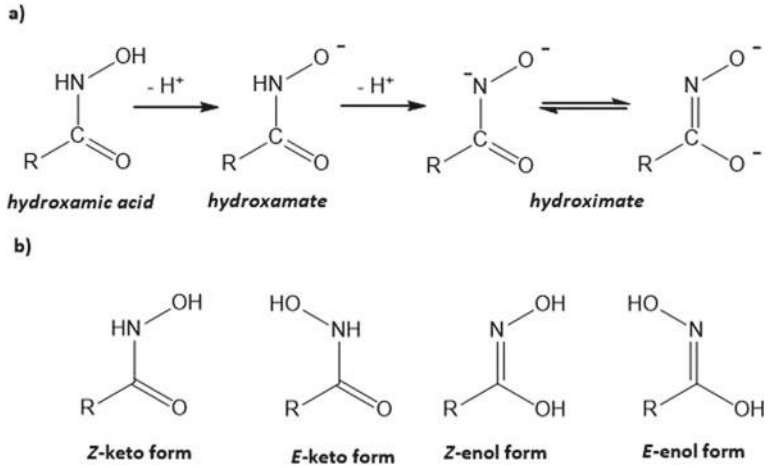

Fig. 2 Possible dissociation pathways of hydroxamic acid (**a**) with the representation of *E/Z* isomers (**b**)

several anionic forms broadens the coordination possibilities of hydroxamate ligands, however, all depend on the ligand structure [22].

Hydroxamic acids, as weak acids, typically dissociate in an aqueous solution with a pK_a value of the N–OH proton of the order 8.5–9.4. However, as it was shown through the years, this can vary depending on the ligand structure and substituents, ranging from ~7 for o-nitrobenzohydroxamic acid to ~11.3 for N-phenyl-N-butyrohydroxamic acid [26]. Starting from the simplest, monohydroxamic acids, an obvious influence of the ligand structure on the pK_a value is observed (Fig. 3, Table 1).

Modification of the simplest **AHA** via the introduction of an aromatic substituent in **BHA**, increases acidity from 9.27 to 8.69. Similarly, N-methyl substitution of **AHA** results in an enhancement of acidic properties of **MAHA** (pK_a = 8.70). The acidity of N-substituted acetohydroxamic acids can be rationalized by a network of intramolecular hydrogen bonding involving the N–H donor and CO acceptor groups,

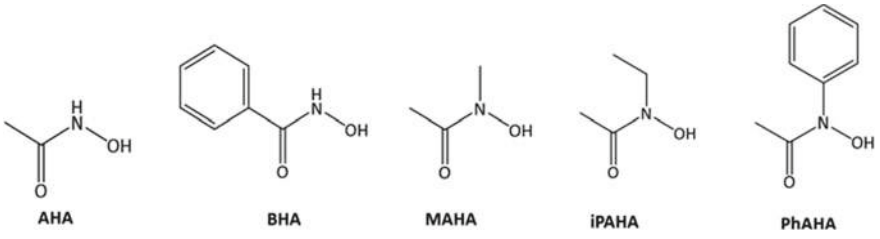

Fig. 3 Representation of monohydroxamic acids. Abbreviations used: **AHA** = acetohydroxamic acid, **BHA** = benzohydroxamic acid, **MAHA** = *N*-methylacetohydroxamic acid, **iPAHA** = *N*-propylacetohydroxamic acid, **PhAHA** = *N*-phenylacetohydroxamic acid

Table 1 Proton dissociation constants (pK_a) of selected monohydroxmic acids [27]

Ligand	AHA	BHA	MAHA	iPAHA	PhAHA
pK_a	9.27	8.69	8.70	9.26	8.47

$I = 0.2$ M KCl, T = 25 °C

additionally to hydrogen bonding between hydroxamic acid and water molecules. Elongation of the N-substituted alkyl chain by one additional $–CH_2$ group in **iPAHA** ($pK_a = 9.26$) compensates for the acidity increase observed in **MAHA** ($pK_a = 8.70$), due to an increase in the electron-donating properties of longer aliphatic chain. On the other hand, the electron-withdrawing character of N-phenyl group in **PhAHA**, affects the electron density of the hydroxamic group and increases the acidity of the ligand ($pK_a = 8.47$) (Table 1) [27].

The derivatives with an additional easily deprotonable group in the structure possess even more complicated acid–base properties. In this group, aminohydroxamic acids are the most widely studied; their acid–base behavior was comprehensively described in excellent reviews and therefore here we only mention its most important aspects [3, 22]. The simplest aminohydroxamic acids may dissociate two protons: under acidic pH, they are in fully protonated state (H_2L^+) with one proton on the amino group and one on the hydroxamate group. Because of the similar basicity of the two groups, the protons dissociate in overlapping processes (Table 2) [3, 22, 28]. The determination of dissociation macroconstants by pH-^{13}C NMR spectrometric titrations allowed us to distinguish the basicity of the two groups. Overall, in solution for most α-aminohydroxamate derivatives, the hydroxamate group is more basic than the amino group, while for β- and γ-derivatives the opposite tendency is observed (Table 2) [28–30]. The situation may be different in solid state. As was

Table 2 Proton dissociation constants (pK_a) of the selected hydroxamic acids

Ligand	GlyHA[a]	α-AlaHA[a]	ValHA[a]	LeuHA[a]	MetHA[b]	PheHA[c/d]	TrpHA[d]	PicHA[e/f]
pK_{a1}	7.42	7.33	7.21	7.30	6.87	7.18/7.05	7.35	1.85/2.07
pK_{a2}	9.18	9.15	9.22	9.16	8.87	9.83/10.75	10.82	8.29/9.64
Refs.	[29]	[32]	[29]	[29]	[33]	[34, 35]	[34]	[7, 36]

Ligand	QuinHA[f]	PyzHA[e/f]	β-AlaHA[a]	Asp-β-HA[a]	MACZ[c]	PAHEt	GABAHA[a]	Glu-γ-HA[a]
pK_{a1}	2.10	1.93/2.04	8.38	2.02	3.3	9.54	8.70	2.14
pK_{a2}	9.64	7.80/9.14	9.74	8.24	9.3		10.22	8.59
pK_{a3}				9.50				9.63
Refs.	[4]	[4]	[32]	[32]	[6]	[5]	[30]	[37]

[a] $I = 0.1$ M KCl
[b] $I = 0.2$ M KCl
[c] $I = 0.1$ $MKNO_3$
[d] $I = 0.1$ M KCl, $MeOH/H_2O$ (9/1 v/v)
[e] $I = 0.1$ M NaCl
[f] $I = 0.1$ M NaCl, $MeOH/H_2O$ (80/20 w/w), T = 25 °C

shown for the structure of **GlyHA**, the ligand isolated from a neutral solution contains a deprotonated hydroxamate group, while its amino group remains protonated [31].

For derivatives with a side-chain donor, an additional step of deprotonation may be observed, and in certain cases, this can affect the basicity of the hydroxamate group. For example, **Asp-β-HA** and **Glu-γ-HA** possess an additional carboxylic group, which deprotonates with pK_a of 2.02 and 2.14, respectively; however, this dissociation process does not influence the amino and hydroxamate groups. Similarly, in the case of β-hydroxamic acids **MACZ** and **PAHEt**, the dissociation of carboxylic and ethyl phosphonic groups, respectively, did not affect the dissociation constants of amino and hydroxamic groups which stay very close to parent hydroxamate or amino derivatives [5, 6] (Table 2). The influence of the structure of the ligand on the basicity of the hydroxamate group is much more visible in the case of aromatic hydroxamate derivatives. **PicHA**, **QuinHA**, and **PyzHA** ligands lose the first proton (from the pyridine, quinoline, and pyrazine nitrogen atoms, respectively) under acidic conditions (pK_a ~ 2). In each case, the electron-withdrawing character of the aromatic ring reduces the electron density of the hydroxamate group and facilitates the dissociation of O–H proton, resulting in a lower value of the dissociation constant of this group (pK_a = 8.29 for **PicHA** and 7.90 for **PyzHA**) (Table 2) [4, 36]. In addition, a second nitrogen in the aromatic ring of **PyzHA** reduces considerably the basicity of the ligand (**PyzHA** is ca. 3 times (0.5 log units) less basic than **QuinHA** and **PicHA**). Of importance, these ligands and their metal complexes are hardly soluble in water, and therefore were studied in MeOH/H_2O mixture. This allowed us to clearly observe and discuss the influence of the nature of solvent on the acid–base properties of the ligands. It is rather typical that MeOH/H_2O mixture affects the hydroxamic acid dissociation constants increasing their value by over 1 log unit, but it shouldn't be overlooked herein [7, 38, 39]. The same behavior was previously observed also for α-aminohydroxamic acid ligands [34].

3 Self-assembly of Metallacrown Complexes

3.1 Metallacrown Structural Paradigm

As it is widely known, MCs can be obtained by self-assembly of a proper number of coordination units of hydroxamic acids, functionalized in α, β, or γ position with respect to the hydroximate function, and metal ions [2, 3]. When designing new ligands capable of forming an MC, one should keep in mind the "*metallacrown structural paradigm*", which shows the geometrical preferences of the ligands for the formation of a given type of MC complex (Fig. 4) [9, 10]. Following the "*metallacrown structural paradigm*", ligands with an additional donor group in the β position prefer the formation of 12-MC-4, while α-hydroxamate derivatives are suitable ligands for the self-assembly of 15-MC-5. Looking at the building units of the respective MCs, one can see that the 12-MC-4 framework is based on the square

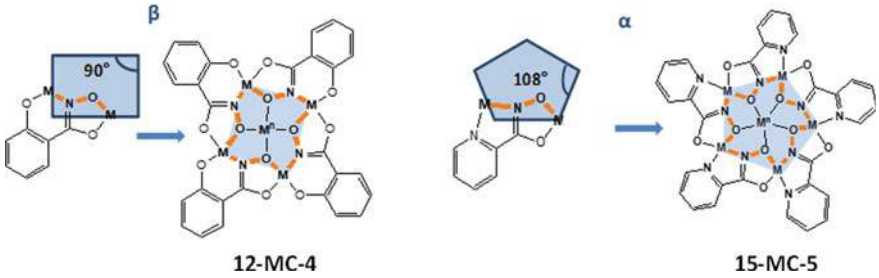

Fig. 4 Schematic representation of the building blocks of 12-MC-4 and 15-MC-5 complexes

structure, while the 15-MC-5 framework is based on the pentagon structure, which is reflected in the geometric preferences of the β- and α-hydroxamate ligands (Fig. 4).

In recent years, numerous papers indicate deviations from the paradigm, showing for example that α-hydroxamic acids, despite theoretically too short a chelating arm to form 12-MC-4, proved to form complexes of this type with Cu(II) or Zn(II) ions [3, 4, 7]. The formation of both 12-MC-4 and 15-MC-5 complexes of Ni(II) ions with α- and β-aminohydroxamic acids, specifically α-**AlaHA**, β-**AlaHA**, and **ValHA**, as well as aromatic hydroxamate derivatives **QuinHA** has also been observed [4, 40, 41]. These unexpected behaviors result probably from the balance of two main factors, the preference of metal cation to achieve an appropriate coordination environment and the tendency of α-hydroxamate to the formation of 15-MC-5 only when the cavity of MCs could be occupied by a suitable metal ion. As it was shown, when no adequate ions are present in the solution, α-hydroxamate ligands form with Cu(II) ions only 12-MC-4, not, as predicted, 15-MC-5. But, when Ca(II), Ln(III) or UO_2^{2+} cation is introduced to the solution, a rearrangement of 12-MC-4 scaffold to 15-MC-5 is observed [42–44] (Fig. 5). For heavier Ln(III) ions this process is reversible. The diversity of coordination patterns observed in isolated complexes and in thermodynamic studies confirms the potential of α- and β-hydroxamic acids and makes them very promising ligands in the coordination chemistry of MCs. The power of "*metallacrown structural paradigm*" is underlined by the thermodynamic properties of MCs (vide infra).

4 Thermodynamic Properties of Metallacrown Complexes

Thermodynamic studies on the self-assembly of MCs in solution provide a valuable set of information on the thermodynamic stability of MCs and their integrity depending on pH. These are two key points to the design and isolation of new MCs in terms of their potential functional application.

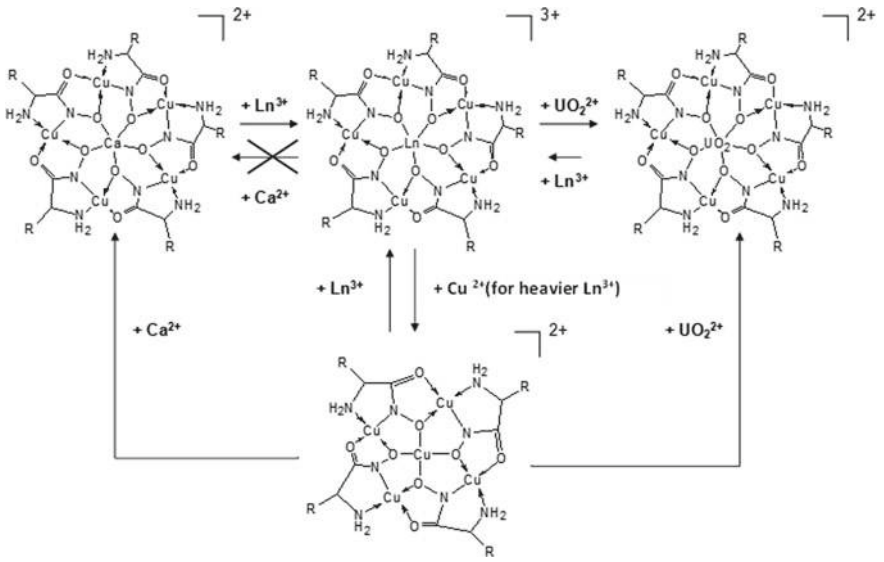

Fig. 5 Representation of the processes involving the conversion of 12-MC-4 species of α-aminohydroxamates into 15-MC-5 species. Adapted with permission from Tegoni, M., Remelli, M.: Metallacrowns of copper(II), and aminohydroxamates: Thermodynamics of self-assembly and host–guest equilibria, Coord. Chem. Rev. 256, 1–2, 289–315 (2012) [3]. Copyright 2012 Elsevier

4.1 Cu(II) Complexes

Comparison of thermodynamic stability of 12-MC-4 Cu(II) complexes of hydroxamate ligands shows that their formation is thermodynamically favored for β-derivatives, and the differences in the stability constants values reach up to 9 orders of magnitude in their favor (Table 3). The thermodynamic stability of the 12-MC-4 order is $\beta > \alpha > \gamma$, in agreement with "*metallacrown structural paradigm*" [3]. The extensive review concerning thermodynamics of self-assembly of Cu(II)/aminohydroxamate MCs was prepared by Tegoni and Remelli [3], nevertheless, to have a complete view, the most crucial issues needed for the discussion are summarized below.

Starting from α-hydroxamate ligands, stability constants ($\log\beta$) of MCs determined by potentiometric titrations in aqueous solution fall in the range of 38.78 for **MetHA** and 44.4 for **PheHA** (Table 3). The difference of almost 6 orders of magnitude between **MetHA** and **PheHA** MCs is explained by solvation effects or electronic factors related to the structure of the **PheHA**, as well as weak, or lack of interactions between thioether sulfur of **MetHA** and Cu(II) ions [35, 45]. These examples clearly visualize the influence of different functionalization of aminohydroxamates, especially the presence of aromatic function, on the stability of MCs. In addition, looking at α-hydroxamate ligands with only aliphatic side chain, e.g., α-**AlaHA**, R,S-**ValHA**, and **LeuHA**, it can be concluded that changes in the length of the non-coordinating alkyl side chain are irrelevant to the stability of MCs [30, 32]. It should be underlined

Table 3 Complex formation constants (logβ) for 12-MC-4 complexes of Cu(II) and α-, β- and γ-hydroxamic acids. Standard deviations are reported in parentheses

12-MC-4 ($[Cu_5(LH_{-1})_4]^{2+/2-}$)	Ligand	Z log β	I	References
α-hydroxamic acids				
$\{Cu(II)[12\text{-}MC_{Cu(II)N(GlyHA)}\text{-}4]\}^{2+}$	**GlyHA**	39.96(3)	0.1 M KCl	[29]
		42.75(4)	0.1 M KNO_3	[35]
$\{Cu(II)[12\text{-}MC_{Cu(II)N(\alpha\text{-}AlaHA)}\text{-}4]\}^{2+}$	**α-AlaHA**	40.16(1)	0.1 M KCl	[32]
		40.01(16)	0.2 M KCl	[45]
$\{Cu(II)[12\text{-}MC_{Cu(II)N((R,S)\text{-}ValHA)}\text{-}4]\}^{2+}$	**(*R,S*)-ValHA**	40.25(3)	0.1 M KCl	[29]
$\{Cu(II)[12\text{-}MC_{Cu(II)N(LeuHA)}\text{-}4]\}^{2+}$	**LeuHA**	39.44(3)	0.1 M KCl	[29]
$\{Cu(II)[12\text{-}MC_{Cu(II)N(MetHA)}\text{-}4]\}^{2+}$	**MetHA**	38.78(10)	0.2 M KCl	[45]
$\{Cu(II)[12\text{-}MC_{Cu(II)N(PheHA)}\text{-}4]\}^{2+}$	**PheHA**	44.42(3)	0.1 M KNO_3	[35]
		51.58(9)	0.1 M KCl, MeOH/H_2O (9/1 v/v)	[34]
$\{Cu(II)[12\text{-}MC_{Cu(II)N(TrpHA)}\text{-}4]\}^{2+}$	**TrpHA**	52.37(11)	0.1 M KCl, MeOH/H_2O (9/1 v/v)	[34]
$\{Cu(II)[12\text{-}MC_{Cu(II)N(PicHA)}\text{-}4]\}^{2+}$	**PicHA**	38.65(13)	0.1 M KCl	[36]
		44.31(5)	0.1 M NaCl, MeOH/H_2O (80:20 w/w)	[4]
$\{Cu(II)[12\text{-}MC_{Cu(II)N(QuinHA)}\text{-}4]\}^{2+}$	**QuinHA**	43.56(7)	0.1 M NaCl, MeOH/H_2O (80:20 w/w)	[4]
$\{Cu(II)[12\text{-}MC_{Cu(II)N(PyzHA)}\text{-}4]\}^{2+}$	**PyzHA**	39.4(2)	0.1 M NaCl, MeOH/H_2O (80:20 w/w)	[4]
β-hydroxamic acids				
$\{Cu(II)[12\text{-}MC_{Cu(II)N(\beta\text{-}AlaHA)}\text{-}4]\}^{2+}$	**β-AlaHA**	49.39(7)	0.1 M KCl	[32]
		46.66(6)	0.2 M KCl	[46]
$\{Cu(II)[12\text{-}MC_{Cu(II)N((R)\text{-}Asp\text{-}\beta\text{-}HA)}\text{-}4]\}^{2-}$	**(*R*)-Asp-β-HA**	50.70(3)	0.1 M KCl	[32]
$\{Cu(II)[12\text{-}MC_{Cu(II)N((R,S)\text{-}Asp\text{-}\beta\text{-}HA)}\text{-}4]\}^{2-}$	**(*R,S*)-Asp-β-HA**	50.31(16)	0.2 M KCl	[47]
$\{Cu(II)[12\text{-}MC_{Cu(II)N(MACZ)}\text{-}4]\}^{2-}$	**MACZ**	33.93(3)	0.1 M KNO_3	[6]
$\{Cu(II)[12\text{-}MC_{Cu(II)N(PAHEt)}\text{-}4]\}^{2-}$	**PAHEt**	31.18 (3)	0.1 M NaCl	[5]
γ-hydroxamic acids				
$\{Cu(II)[12\text{-}MC_{Cu(II)N(GABAHA)}\text{-}4]\}^{2+}$	**GABAHA**	36.72(6)	0.1 M KCl	[30]
$\{Cu(II)[12\text{-}MC_{Cu(II)N(Glu\text{-}\gamma\text{-}HA)}\text{-}4]\}^{2-}$	**Glu-γ-HA**	39.76(7)	0.1 M KCl	[37]

that although thermodynamic stability of Cu(II) 12-MC-4 of α-aminohydroxamate ligands can be influenced by the introduction of aromatic function to the ligand structure, it has no impact on the range of pH of MCs presence in solution. As it is shown, pH-dependent distribution diagrams of Cu(II)/α-aminohydroxamate systems are almost identical, except Cu(II)/**MetHA** system in which coexistence of dinuclear and MC species has been proposed, with 12-MC-4 species present in a narrow pH range of about 4–6 (Fig. 6).

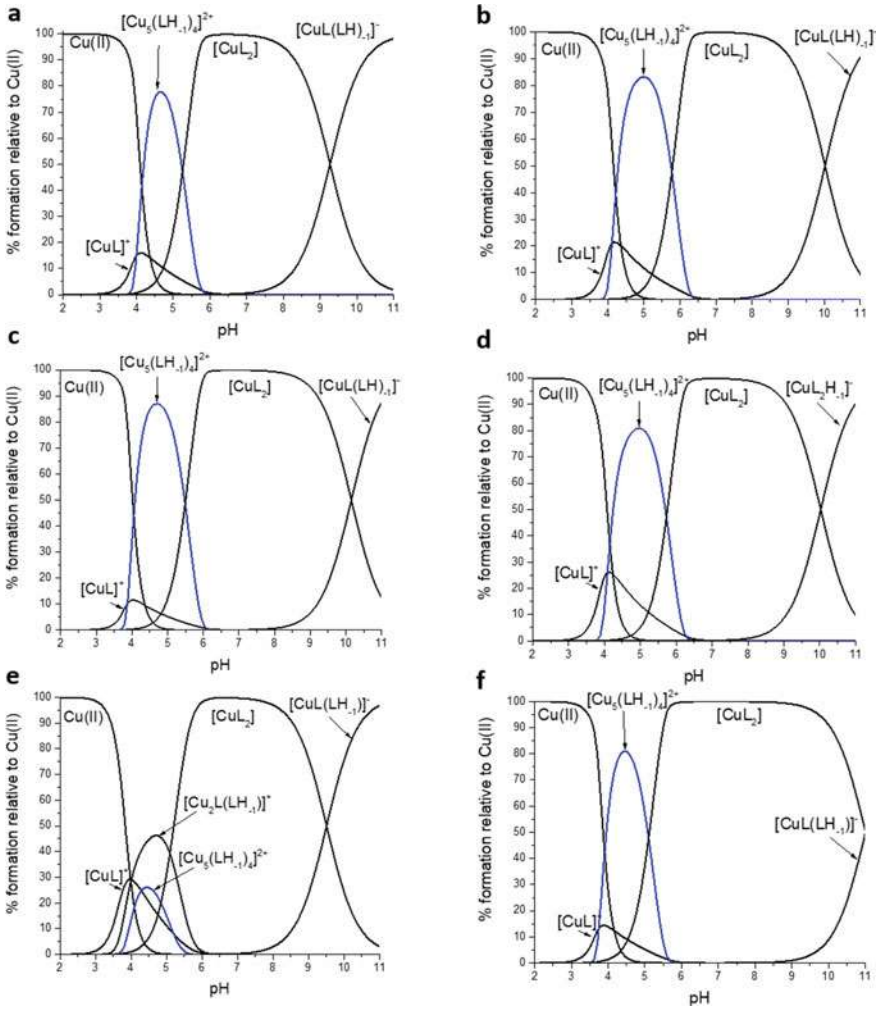

Fig. 6 Representative distribution diagram of the Cu(II)/**GlyHA** (**a**), Cu(II)/α-**AlaHA** (**b**), Cu(II)/(*R,S*)-**ValHA** (**c**), Cu(II)/**LeuHA** (**d**), Cu(II)/**MetHA** (**e**), Cu(II)/**PheHA** (**f**) systems, Cu(II):L = 1:3, [Cu(II)] = 1 mM. Drawn on the basis of potentiometric data from Refs. [29, 32, 35, 48]

When comparing the thermodynamic properties of MCs one should keep in mind the critical role of the solvent in the formation of MCs. Some of Cu(II)/α-hydroxamate systems were studied in the organic solvent to avoid precipitation of insoluble species [4, 7, 34]. The comparison of the values of MCs stability constants for **PheHA** and **TrpHA** ligands determined in MeOH/H_2O (9/1 v/v) solvent mixture, to logβs of other α-aminohydroxamic acids determined in an aqueous environment, clearly show the increase of the former by about 8–11 orders of magnitude (logβ = 51.58 for **PheHA** and 52.37 for **TrpHA**) (Table 3). The same trend of stabilization of MCs in organic solvent was observed for **PicHA** ligand; logβ values of $[Cu_5(LH_{-1})_4]$ in H_2O and in MeOH/H_2O (80/20 w/w) solutions are 38.65 and 44.31, respectively. As it was discussed by Tegoni et al., those differences can be attributed to structural and solvation effects. In contrast to **PheHA**, where despite higher thermodynamic stability of 12-MC-4 in a mixed solvent, the distribution diagrams for the systems measured in H_2O and MeOH/H_2O (80/20 w/w) are almost the same, for **PicHA** the stabilization of MC in the organic solvent is observed in a broad pH range (Fig. 7). However, the comparison of stability constants points to the higher thermodynamic stability of

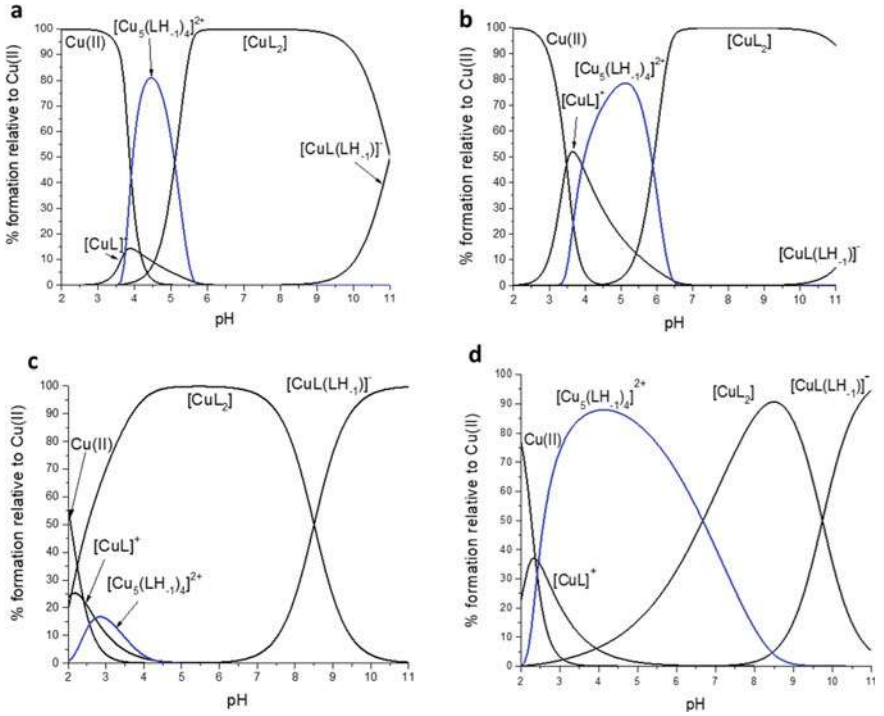

Fig. 7 Representative distribution diagram of the Cu(II)/**PheHA**, Cu(II):L = 1:3, [Cu(II)] = 1 mM, I = 0.1 M KNO_3 (**a**), I = 0.1 M KCl, MeOH/H_2O (80/20 w/w) (**b**), Cu(II)/**PicHA**, Cu(II):L = 1:3, [Cu(II)] = 1 mM, I = 0.1 M KCl (**c**), I = 0.1 M NaCl, MeOH/H_2O (80/20 w/w) (**d**). Drawn on the basis of potentiometric data from Refs. [4, 36, 34, 35]

MCs formed by α-aminohydroxamate than by heterocyclic ligand. The same trend is observed when comparing logβ values of $[Cu_5(LH_{-1})_4]$ of **PicHA** and **AlaHA** ligands in H_2O solution; they are 38.65 and 40.16, respectively. Lower stability of Cu(II) 12-MC-4 with **PicHA** in relation to **AlaHA** was ascribed to (i) the diverse nature of the donor moieties (pyridyl versus amino), and (ii) more taut structure of the heterocyclic **PicHA** 12-MC-4 than corresponding 12-MC-4 of **AlaHA**.

PicHA was the first ligand-forming MCs in such a broad range of pH, and was the inspiration for the extension of this class of ligands by the modification of its structure into **QuinHA** and **PyzHA** (Fig. 1). Comparing the stability constants of Cu(II) 12-MC-4 complexes formed by **PicHA**, **QuinHA** and **PyzHA** ligands, one can see that the stability for the first two ligands is similar with the difference in logβ values of only 0.75 units (Table 3). The stability constant of the 12-MC-4 complex formed by **PyzHA** ligand is significantly lower compared to **QuinHA** and **PicHA** (logβ difference 4.16 and 4.91, respectively) (Table 3). Lower stability of Cu(II) 12-MC-4 complexes with **PyzHA** may result from stronger π-acceptor properties of the ligand and lower basicity of the hydroxamate moiety (Table 2). The slightly lower logβ value ($\Delta\log\beta = 0.75$) for 12-MC-4 **QuinHA**, as compared to **PicHA**, may be a consequence of an additional aromatic ring in **QuinHA** structure, affecting its flexibility. Steric factors may cause smaller **PicHA** to come closer to Cu(II) ions than **QuinHA**, so that **PicHA** MC backbone may be less stressed. Though, when 12-MC-4 is formed, the aromatic rings of the four **QuinHA** ligands are likely to be more closely related compared to the complex with **PicHA**. In addition, Cu(II)/**QuinHA** is the first example of the system with the presence of only one, 12-MC-4, complex dominating in solution over the entire pH range (Fig. 8). Considering the information from speciation studies, it might be that the van der Waals interactions of π-electron clouds and hydrophobicity of the structure play a crucial role, with methanol solvent stabilizing the $[Cu_5(LH_{-1})_4]^{2+}$ complex over the entire pH range at the expense of mononuclear CuL and CuL_2 complexes [4]. As it was for **PicHA**, also **QuinHA**

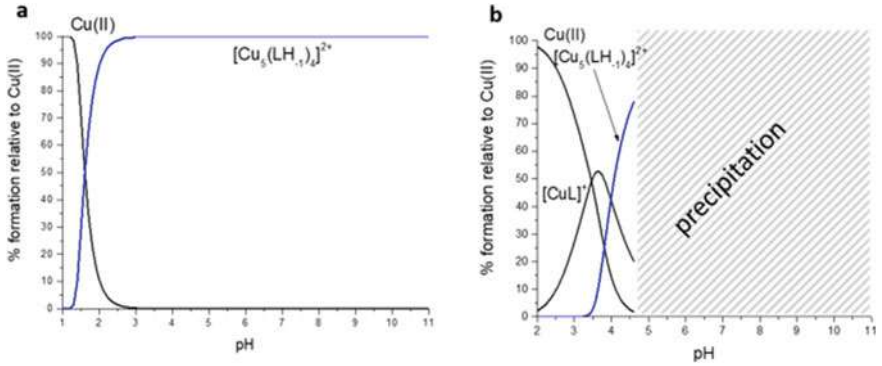

Fig. 8 Representative distribution diagram of the Cu(II)/**QuinHA**, Cu(II):L = 1:3 (**a**) and Cu(II)/**PyzHA** (**b**), [Cu(II)] = 1 mM, I = 0.1 M KCl, I = 0.1 M NaCl, MeOH/H_2O (80/20 w/w). Drawn on the basis of potentiometric data from Ref. [4]

and **PyzHA** ligands form MCs characterized by definitely lower stability constants compared to aminohydroxamate systems (Table 3) which are assigned to the different nature of both ligand groups, especially the difference in their flexibility. The location of the donor nitrogen atom in the aromatic ring decreases the flexibility of the ligand. Sp^2 hybridization of all atoms included in the ligand results in a higher tension of the 12-MC-4 backbone of **QuinHA**, **PicHA**, and **PyzHA** ligands compared to **PheHA** and **TrpHA**. When comparing the stability of the complexes formed by aromatic derivatives to the aminohydroxamate ligands, one must remember also the differences in the acid–base properties of the ligands (Table 2). The lower basicity of the donor nitrogen atoms of the aromatic rings, as compared to the amine moiety, undoubtedly influences the differences in the stability of the formed complexes.

Despite all the factors described above, which decrease the logβs of the complexes of **QuinHA**, **PicHA,** and **PyzHA** ligands, it is undeniable that the dominance of MCs for all three ligands is much wider than for the aminohydroxamate derivatives, and so far **QuinHA** is the only known ligand forming the 12-MC-4 complex with Cu(II) ions stable in the entire pH range. This may suggest that when designing ligands capable of forming MCs over a wide pH range, we do not need to look for those that will form the highest-stability MC complex expressed as logβ. The widening of the pH range of the presence of the MC in solution may result from a decrease in the stability of mononuclear complexes present at higher pH, which may cause their destabilization.

Discussing MCs of β-aminohydroxamate ligands, first one should notice higher stability of Cu(II) 12-MC-4 complexes compared to those formed by corresponding α-aminohydroxamates (Table 3). The comparison of the logβ values for α-**AlaHA** and β-**AlaHA** ligands reveals about 9 orders of magnitude difference (40.16 vs. 49.39) [32]. Considering the fact that the deprotonation constants for both derivatives are similar, the difference in the thermodynamic stability of MCs they create reflects the strength of the "*metallacrown structural paradigm*". A significant difference is also clear when analyzing the species distributions of complex forms for both ligands (Figs. 6b and 9a). Complex $\{Cu(II)[12\text{-}_{MCCu(II)N(\beta\text{-}AlaHA)}\text{-}4]\}^{2+}$ dominates the pH range 4–9, binding 100% of Cu(II) ions present in solution.

Another β-hydroxamate ligand illustrating the discussed subject is **MACZ** (Fig. 1) [6]. This is the first example of a ligand with a carboxyl group as an additional functional group at the β position instead of an amino group. The relatively low stability constant for the 12-MC-4 complex (logβ 33.93, Table 3) is a consequence of the less effective binding ability of the carboxyl group compared with an amino group present in the aminohydroxamate complexes. The thermodynamic stability of this complex is comparable to that of the 12-MC-4 complexes formed by γ-derivatives (Table 3). However, despite the low value of the stability constant of the $[Cu_5(LH_{-1})_4]^{2-}$ complex, it is present as the dominant form in solution in almost the entire pH range; because of the easily deprotonating carboxylic group, the formation of the complex begins slightly above pH 3. Similar behavior was noticed for **PAHEt** ligand, the first example was the MC forming hydroxamate ligand, having an additional ethylphosphonate group in the β-position with respect to the hydroxamate group (Fig. 1) [5]. Although the stability of the formed MC complex is relatively low (logβ =

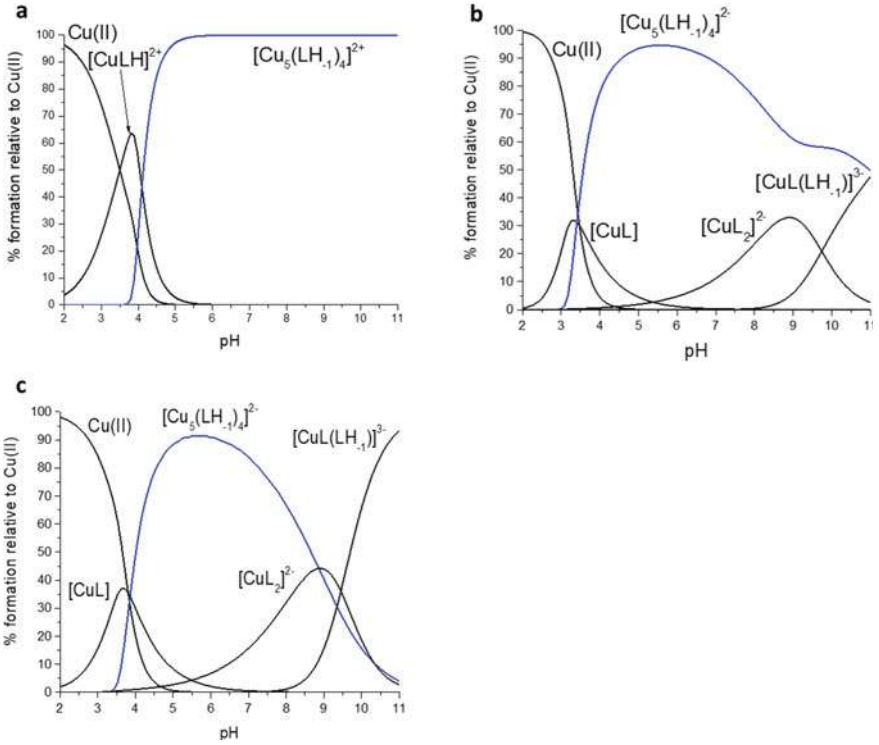

Fig. 9 Representative distribution diagram of the Cu(II)/β-**AlaHA**, $I = 0.1$ M KCl (H_2O) (**a**), Cu(II)/**MACZ**, $I = 0.1$ M KNO_3 (H_2O) (**b**) and Cu(II)/**PAHEt**, $I = 0.1$ M NaCl (H_2O) (**c**), Cu(II):L = 1:3, [Cu(II)] = 1 mM. Drawn on the basis of potentiometric data from Refs. [5, 6, 32]

31.18), **PAHEt** also offers the formation of 12-MC-4 in a broad pH range. All the above underline that the pH range of the formation of MCs and their overall stability depend on the peripheral chelating group with respect to the hydroxamate unit. When properly chosen, it can tune the thermodynamic properties of the MC assembly.

The formation of 12-MC-4 complexes by γ-aminohydroxamate ligands deviates from the "*metallacrown structural paradigm*". Elongation of the space between the hydroxamate and amino groups leads to the formation of a 7-membered chelate ring, resulting in lower stability of the resulting complexes (Table 3).

4.2 Ni(II) Complexes

The control of the geometry of the MCs scaffold through the appropriate choice of metal ions is particularly important in the context of their practical applications. Therefore, apart from the most widely researched chemistry of Cu(II) complexes,

additional attention has recently been focused on the investigation of the possibility of MCs formation with the use of other metal ions, e.g., Ni(II) and Zn(II).

Studies on the behavior of α-aminohydroxamate ligands, α-**AlaHA** and **ValHA** in the presence of Ni(II) ions have shown that under appropriate experimental conditions, both 12-MC-4 and 15-MC-5 (with no metal ion in its central cavity, the so-called "vacant" MC) are formed [41]. The formation of both types of MCs strongly depends on the metal-to-ligand molar ratio, M(II):L, and occurs when the ratio is equal to or less than 1: 2. For solutions where the molar ratio M(II):L is higher than 1:2, only the formation of mononuclear complexes is observed. Such a relationship has never been observed in the case of MCs containing Cu(II) ions. Similar behavior was recorded for β-**AlaHA** ligand, for which the formation of both Ni(II) 12-MC-4 and 15-MC-5 was also noted, both with slightly lower thermodynamic stability than for the two previous ligands, and the predomination of 15-MC-5 over the 12-MC-4, which deviates from the "*metallacrown structural paradigm*" [40] (Table 4, Fig. 10).

In the series of aromatic hydroxamate derivatives, some differences in the thermodynamic stability and MCs formation dependency on the metal-to-ligand molar ratio have been noted, depending on the ligand. The coexistence in the solution of both Ni(II) 12-MC-4 and 15-MC-5 is observed only for **QuinHA** ligand [4]. The differences in the behavior of **QuinHA**, **PicHA**, and **PyzHA** ligands in relation to Ni(II)

Table 4 Complex formation constants (logβ) for 12-MC-4 and 15-MC-5 complexes of Ni(II) and α- and β-hydroxamic acids. Standard deviations are reported in parentheses

12-MC-4 ($[Ni_5(LH_{-1})_4]^{2+}$) 15-MC-5 ($[Ni_5(LH_{-1})_5]$)	Ligand	logβ	I	References
$\{Ni(II)[12\text{-}MC_{Ni(II)N(\alpha\text{-}AlaHA)}\text{-}4]\}^{2+}$	**α-AlaHA**	15.51(5)	0.1 M KCl	[41]
$\{Ni(II)[15\text{-}MC_{Ni(II)N(\alpha\text{-}AlaHA)}\text{-}5]\}$	**α-AlaHA**	13.53(8)	0.1 M KCl	[41]
$\{Ni(II)[12\text{-}MC_{Ni(II)N(ValHA)}\text{-}4]\}^{2+}$	**ValHA**	15.57(5)	0.1 M KCl	[41]
$\{Ni(II)[15\text{-}MC_{Ni(II)N(ValHA)}\text{-}5]\}$	**ValHA**	13.9(1)	0.1 M KCl	[41]
$\{Ni(II)[12\text{-}MC_{Ni(II)N(\beta\text{-}AlaHA)}\text{-}4]\}^{2+}$	**β-AlaHA**	9.32(6)	0.1 M KCl	[40]
$\{Ni(II)[15\text{-}MC_{Ni(II)N(\beta\text{-}AlaHA)}\text{-}5]\}$	**β-AlaHA**	8.30(6)	0.1 M KCl	[40]
$\{Ni(II)[15\text{-}MC_{Ni(II)N(PicHA)}\text{-}5]\}$	**PicHA**	14.92(11)	0.1 M KCl	[36]
$\{Ni(II)[15\text{-}MC_{Ni(II)N(PicHA)}\text{-}5]\}$	**PicHA**	26.13(14)	0.1 M NaCl, MeOH/H_2O (80/20 w/w)	[4]
$\{Ni(II)[12\text{-}MC_{Ni(II)N(QuinHA)}\text{-}4]\}^{2+}$	**QuinHA**	19.35(3)	0.1 M NaCl, MeOH/H_2O (80/20 w/w)	[4]
$\{Ni(II)[15\text{-}MC_{Ni(II)N(QuinHA)}\text{-}5]\}$	**QuinHA**	20.43(7)	0.1 M NaCl, MeOH/H_2O (80/20 w/w)	[4]
$\{Ni(II)[15\text{-}MC_{Ni(II)N(PyzHA)}\text{-}5]\}$	**PyzHA**	11.73(9)	0.1 M NaCl	[4]
$\{Ni(II)[15\text{-}MC_{Ni(II)N(PyzHA)}\text{-}5]\}$	**PyzHA**	19.03(10)	0.1 M NaCl, MeOH/H_2O (80/20 w/w)	[4]

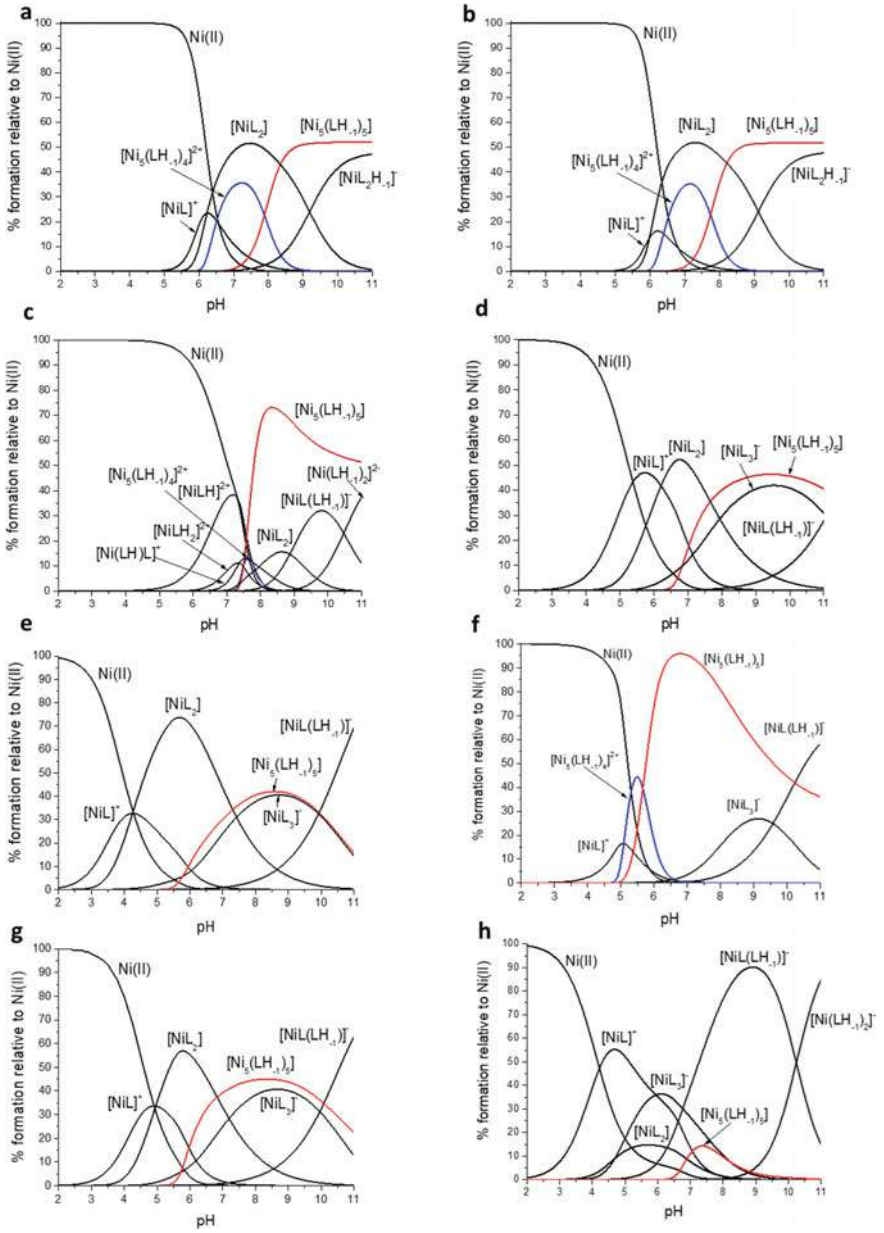

Fig. 10 Representative distribution diagrams of the Ni(II)/α-AlaHA, Ni(II):L = 1:1.5, $I = 0.1$ M KCl (H_2O) (**a**), Ni(II)/**ValHA**, Ni(II):L = 1:1.5, $I = 0.1$ M KCl (H_2O) (**b**), Ni(II)/ β-**AlaHA**, Ni(II):L = 1:1.5, $I = 0.1$ M KCl (H_2O) (**c**), Ni(II)/**PicHA**, Ni(II):L = 1:2, $I = 0.1$ M KCl (H_2O) (**d**), Ni(II)/**PicHA**, Ni(II):L = 1:2, $I = 0.1$ M NaCl, MeOH/H_2O (80:20 w/w) (**e**), Ni(II)/**QuinHA**, $I = 0.1$ M NaCl, MeOH/H_2O (80:20 w/w) (**f**), Ni(II)/**PyzHA**, Ni(II):L = 1:2, $I = 0.1$ M NaCl, MeOH/H_2O (80:20 w/w) (**g**), Ni(II)/**PyzHA**, Ni(II):L = 1:2, $I = 0.1$ M NaCl (H_2O) (**h**), [Ni(II)] = 1 mM. Drawn on the basis of potentiometric data from Refs. [4, 36, 40, 41]

ions are conditioned by many factors related to steric effects depending on the size of the ligands, the ability of π-electron clouds to interact with each other, and solvation effects. The formation of solely 15-MC-5 in the Ni(II)/**PicHA** system is rationalized by the lower flexibility of the ligand compared to aminohydroxamate derivatives, preventing the formation of 12-MC-4, as well as stabilization of the square planar Ni(II) coordination sphere, reflected by a higher logβ value compared to the 15-MC-5 complexes formed by α-**AlaHA**, **ValHA**, and β-**AlaHA** ligands (Table 4). The behavior of **PyzHA** ligand is very similar to **PicHA**, with slightly lower thermodynamic stability ensuing, with differences in the structure and acid–base properties of ligand. For both ligands, the metal-to-ligand molar ratio dependency of MCs formation is observed. Both coordination preferences of Ni(II) ions and geometry of **PicHA** and **PyzHA** disfavor the formation of 12-MC-4 species at the expense of rearrangement to most thermodynamically favored 15-MC-5. Looking at **QuinHA**, the strong preference of the ligand for the formation of MC species in solution is easy to note. A slight modification in the structure of **PicHA** results in the first example of the ligand for which the formation of MCs is observed regardless of the Ni(II):L ratio. The higher tendency of the Ni(II)/**QuinHA** pair to form MCs may be related to the higher hydrophobicity of ligand structure. Higher stability of the complex formed by **PicHA** ligand, by ~6 orders of magnitude compared to Ni(II)/**QuinHA**, may be due in part to the absence of the 12-MC-4 form in the solution of this ligand. Regardless of the higher stability of the Ni(II)/**PicHA** MC, it reaches a maximum of 40% of the Ni(II) ions present in solution, while for **QuinHA** this form makes up almost 100% which further underlines the unique tendency of **QuinHA** to form MCs (Fig. 10). In all of the present cases, the 15-MC-5 complex dominates the 12-MC-4 which is either present in a narrow pH range, or not at all. It once again demonstrates the difficulties in obtaining 12-MC-4 complexes using α-functionalized hydroxamates, and the influence of not only ligand structure but also geometrical preferences of metal ions on the type of MCs.

If one would like to compare the stability of the 12-MC-4 complexes formed by Ni(II) ions to those formed by Cu(II) ions with the described ligands, it can be seen that the Ni(II) MC complexes are definitely less stable; it can be explained by the lower affinity of Ni(II) ions for the donor O and N atoms compared to Cu(II). Moreover, Ni(II) ions prefer a square-planar geometry, while significant distortion from the plane is observed in the X-ray structures of the 12-MC-4 complexes (vide infra).

4.3 Zn(II) Complexes

Studies on the formation of Zn(II) MCs in solution are limited to just a few examples of hydroxamate ligands, i.e., α-**AlaHA**, **PicHA**, and **PyzHA** in water [36], and **PicHA**, **QuinHA,** and **PyzHA** in MeOH/H_2O (80/20 w/w) solution [4]. In water solution in all cases, 12-MC-4 complex formation has been noted. The thermodynamic stability of Zn(II) 12MC-4 is the lowest among all three discussed metal ions,

and they are present in solution in equilibrium with mononuclear complexes (Table 5, Fig. 11). Comparing stability constants (logβ) of **QuinHA** and **PicHA** 12-MC-4 complexes, one can see that they are close to each other, with the slightly lower stability of the Zn(II) complexes of the former ligand (Table 5). Therefore, unlike for the previous metal ions, the presence of the additional aromatic group in the **QuinHA** ligand structure does not seem to affect significantly the stability of the Zn(II) MC complex. More rigid structure of **PicHA** ligand compared to α-**AlaHA** results in higher thermodynamic stability of 12-MC-4, but causes the destabilization of this complex in favor of the mononuclear species (Table 5, Fig. 11). When comparing the stability constants of 12-MC-4 Zn(II)/**PyzHA** to **PicHA** α-**AlaHA** and (all in H_2O solvent) much lower stability of Zn(II)/**PyzHA** is evident. Very unusual and difficult to explain behavior has been reported for Zn(II)/**PyzHA** system in a mixed solvent, where the 15-MC-5 complex is present (Table 5) [4]. This behavior could be due to a strong influence of the solvent on the ligand and its complexes. It should be mentioned that, in absence of Ln(III) ions, Zn(II) 15-MC-5 complexes were not isolated in the solid state to date.

Table 5 Complex formation constants (logβ) for 12-MC-4 complexes of Zn(II) and α-hydroxamic. Standard deviations are reported in parentheses

12-MC-4 ($[Zn_5(LH_{-1})_4]^{2+}$) 15-MC-5 ($[Zn_5(LH_{-1})_5]$)	Ligand	log β	I	References
$\{Zn(II)[12\text{-}MC_{Zn(II)N(\alpha\text{-}AlaHA)}\text{-}4]\}^{2+}$	**α-AlaHA**	6.79(10)	0.1 M KCl	[36]
$\{Zn(II)[12\text{-}MC_{Zn(II)N(PicHA)}\text{-}4]\}^{2+}$	**PicHA**	9.63(5)	0.1 M KCl	[36]
$\{Zn(II)[12\text{-}MC_{Zn(II)N(PicHA)}\text{-}4]\}^{2+}$	**PicHA**	14.22(13)	0.1 M NaCl, MeOH/H_2O (80/20 w/w)	[4]
$\{Zn(II)[12\text{-}MC_{Zn(II)N(QuinHA)}\text{-}4]\}^{2+}$	**QuinHA**	13.94(6)	0.1 M NaCl, MeOH/H_2O (80/20 w/w)	[4]
$\{Zn(II)[12\text{-}MC_{Zn(II)N(PyzHA)}\text{-}4]\}^{2+}$	**PyzHA**	1.37(14)	0.1 M NaCl	[4]
$\{Zn(II)[15\text{-}MC_{Zn(II)N(PyzHA)}\text{-}5]\}^{2+}$	**PyzHA**	6.78(3)	0.1 M NaCl, MeOH/H_2O (80/20 w/w)	[4]

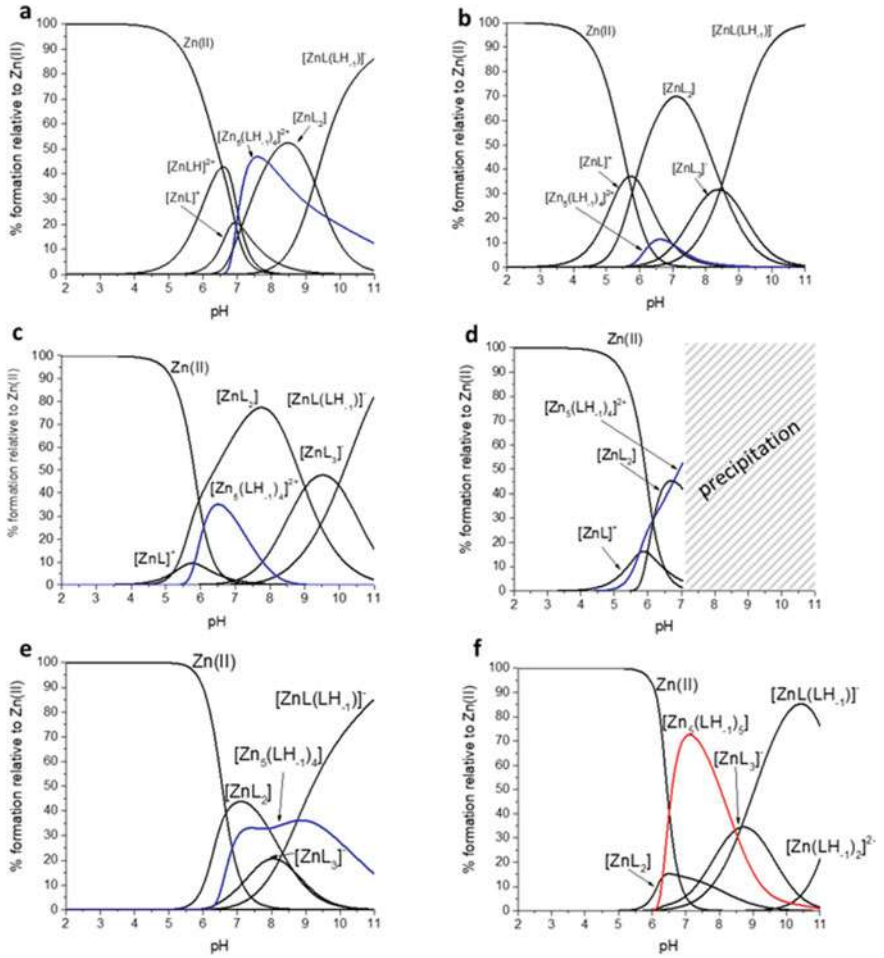

Fig. 11 Representative distribution diagrams of the Zn(II)/α-**AlaHA**, Zn(II):L = 1:3, I = 0.1 M KCl (H_2O) (**a**), Zn(II)/**PicHA**, Zn(II):L = 1:3, I = 0.1 M KCl (**b**), Zn(II)/**PicHA**, Zn(II):L = 1:3, I = 0.1 M NaCl, MeOH/H_2O (80:20 w/w) (**c**), Zn(II)/**QuinHA**, Zn(II):L = 1:3, I = 0.1 M NaCl, MeOH/H_2O (80:20 w/w) (**d**), Zn(II)/**PyzHA**, Zn(II):L = 1:3, I = 0.1 M NaCl (H_2O) (**e**), Zn(II)/**PyzHA**, Zn(II):L = 1:3, I = 0.1 M NaCl, MeOH/H_2O (80:20 w/w) (**f**), [Zn(II)] = 1 mM. Drawn on the basis of potentiometric data from Refs. [4, 36]

5 Structural Studies

5.1 MC Complexes Based on Hydroxamates Functionalized with O-Donors in β-Position

Among the reported structures of hydroxamate 12-MC-4 compounds, most were based on the ligands with an additional nitrogen-containing donor function in β-position with respect to the hydroxamic group, or on salicylhydroxamic acid [2, 49], in which the supporting function is the phenolic group. The latter represent the only examples (even though numerous) of structurally characterized 12-MCs-4 based on the hydroxamate ligands with the oxygen-containing supporting function [1, 2, 11]. Thus, the 12-MC-4 complexes with **MACZ** and **PAHEt** represent the first examples of the hydroxamate MCs containing the carboxylic or the phosphonate groups, respectively, as supporting donor functions.

According to the results of speciation studies, and in full agreement with the "*metallacrown structural paradigm*" (Fig. 4), reactions of copper(II) salts with **MACZ** and **PAHEt** with an addition of a certain amount of alkali (to ensure the target pH range favorable for MC formation) resulted in the formation of 12-MC-4 complexes. In both cases, the development of anionic MC complexes was expected. In order to obtain **MACZ**-containing MC complex, $[Cu(en)_2(H_2O)_2]^{2+}$ nitrate was added to **MACZ** reaction mixture which afforded crystallization of $[Cu(en)_2(H_2O)_2]_n[Cu(en)_2(H_2O)(\mu\text{-}H_2O)\{Cu_5(\textbf{MACZ}\text{-}3H)_4(H_2O)_3\}_2]_n \cdot 20nH_2O$ (**1**) [6]. The attempts to synthesize and isolate pentanuclear 12-MC-4 coordination compounds were performed in water or mixed solvents solutions in the pH range 4–9 (in which 12-MC-4 is dominating species, according to the results of the solution complex formation study of **PAHEt**). Various starting cupric salts were taken in 1:1 or 5:4 metal-to-ligand ratio, and both inorganic and organic bases were used. Crystals of $\{Na_4(H_2O)_6(Ac)[Cu_5(\textbf{PAHEt}\text{-}3H)_4(Ac)]\}_2 \cdot 3H_2O$ (**2**) suitable for X-ray analysis were obtained with the use of Cu(II) acetate and NaOH [5].

In the crystal structure of **1**, the pentanuclear 12-MC-4 units form double-decked 10-nuclear complex anions $[Cu_5(\textbf{MACZ}\text{-}3H)_4(H_2O)_3]_2^{4-}$ (Fig. 12a) which are linked by the $[Cu(en)_2(H_2O)_2]^{2+}$ complex cations into perpetual anionic chains $\{Cu(en)_2(H_2O)(\mu\text{-}H_2O)[Cu_5(\textbf{MACZ}\text{-}3H)_4(H_2O)_3]_2\}_n^{2n-}$ on account of the bridging coordination of the apical water molecule. The structure also contains the centrosymmetric complex cations $[Cu(en)_2(H_2O)_2]^{2+}$ (to balance the negative charge of the anionic chains) and solvate water molecules. The structure of **2** comprises 2D-coordination polymeric nets containing the dimerized bis(12-MC-4) anionic units $\{[Cu_5(\textbf{PAHEt}\text{-}3H)_4(Ac)]^{3-}\}_2$ (Fig. 12b) linked with eight Na^+ cations, two acetates and 12 water molecules partaking in Na^+ cations coordination, and water molecules of solvation [5, 6].

The decacopper complex anion $[Cu_5(\textbf{MACZ}\text{-}3H)_4(H_2O)_3]_2^{4-}$ in **1** (Fig. 12a) incorporates two pentanuclear 12-MC-4 moieties united across the faces into the double-layered dimeric structure because of coordination of the hydroxamate

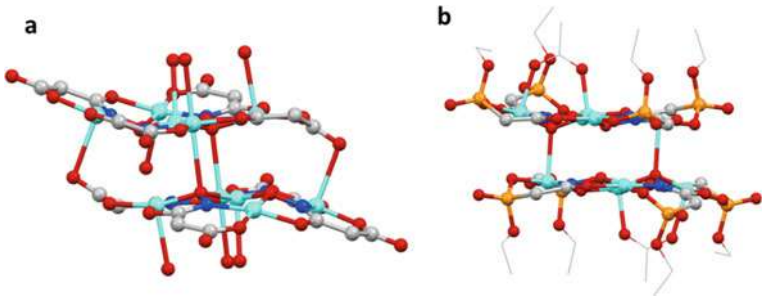

Fig. 12 Structure of decanuclear bis(12-MC-4) units in complexes with β-functionalized hydroxamates: **a** $[Cu(en)_2(H_2O)_2]_n[Cu(en)_2(H_2O)(\mu\text{-}H_2O)\{Cu_5(\textbf{MACZ}\text{-}3H)_4(H_2O)_3\}_2]_n \cdot 20H_2O$ (**1**); **b** $\{Na_4(H_2O)_6(Ac)[Cu_5(\textbf{PAHEt}\text{-}3H)_4(Ac)]\}_2 \cdot 3H_2O$ (**2**). Colour scheme: cyan = Cu, red = O, blue = N, grey = C, orange = P

and the carboxylate oxygen atoms (Cu–O = 2.731(3) and 2.613(3) Å, respectively) of one 12-MC-4 in apical positions to the metal ions of a second MC [6]. Related condensed copper MC compounds with β-alaninehydroxamate [50] and 3-hydroxyiminobutanehydroxamate [51] have been reported as well. The four Cu–O contacts between MCs fragments bring about a fairly stable dimer. In **2**, two 12-MC-4 pentacopper moieties are organized into the centrosymmetric double-decked decacopper complex anion (Fig. 12b) due to two pairs of extended due to Jahn–Teller distortion apical Cu···O bonds made by one ring and one core Cu(II) ions with two hydroximate oxygens of the translational pentacopper unit (Cu–O = 2.439(3) and 2.976(3) Å, respectively). The shortest interdeck Cu···Cu separations are 3.625(1) and 3.508(1) Å for **1** and **2**, respectively [5, 6].

The pentanuclear 12-MC-4 units in **1** and **2** (Fig. 13b, c) comprise five copper atoms and four triply charged ligand anions monodeprotonated by the carboxylic or the phosphonate groups, respectively, and doubly deprotonated by the hydroxamic function. Each anion links three copper atoms (two rings and one core ones). The binding mode of the ligand can be defined as {(N,O); (O′,μ-O″)} bis(chelating)-and-bridging. On account of the realization of (N,O)-birding mode of the hydroxamic function, a cyclic 12-MC-4 $(–Cu–N–O–)_4$ array constitutes a cavity arranged by four hydroxamic oxygens and integrates the fifth metal ion. The ligand anions are bound to two metal ions forming two condensed, six- and five-membered, chelate rings with a joint $C–N_{(hydroxamate)}$ edge. While the carboxylate and the phosphonate groups are incorporated in the six-membered chelates, the hydroxamate oxygens bind another metal ion with the formation of the five-membered chelate. In **1** and **2**, the N–O hydroxamate oxygens indicate both μ_2- and μ_3-bridging modes (in the later cases being coordinated to the metal ions of the translational pentacopper fragment within the decanuclear dimeric moieties (Fig. 12a, b)). Thus, in the case of μ_3-bridging mode, the hydroxamic oxygen atoms exhibit both out-of-plane and in-plane bridging. In **2**, the acetate co-ligand is bound in a (O,O′)-bridging fashion to two (both ring and core) metal ions. The Cu···Cu distances within the pentacopper MC modules

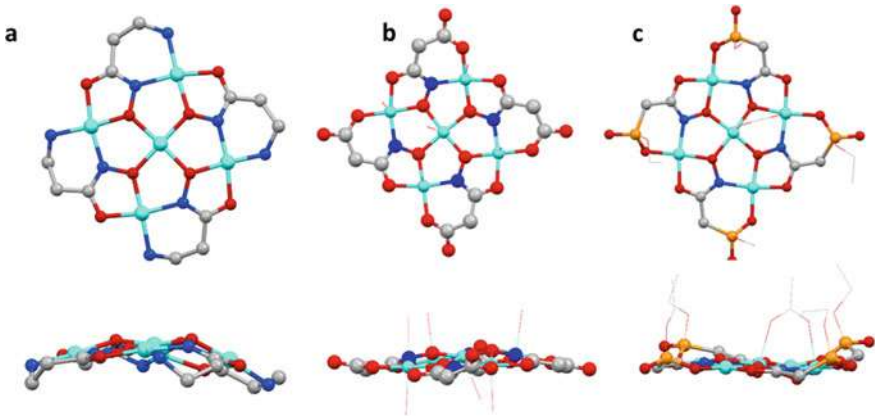

Fig. 13 Structure of pentanuclear 12-MC-4 units in complexes with β-functionalized hydroxamates in: **a** $[Cu_5(\textbf{β-AlaHA}\text{-}2H)_4](ClO_4)_2{\cdot}5H_2O$ [49]; **b** $[Cu(en)_2(H_2O)_2]_n[Cu(en)_2(H_2O)(\mu\text{-}H_2O)\{Cu_5(\textbf{MACZ}\text{-}3H)_4(H_2O)_3\}_2]_n{\cdot}20H_2O$ (**1**) [6]; **c** $\{Na_4(H_2O)_6(Ac)[Cu_5(\textbf{PAHEt}\text{-}3H)_4(Ac)]\}_2{\cdot}3H_2O$ (**2**) [5] (down-side views). Colour scheme: cyan = Cu, red = O, blue = N, grey = C, orange = P

between the core and ring metal ions are 3.2100(7)–3.3366(7) Å and 3.1657(7)–3.3115(6) Å for **1** and **2**, respectively, and these between the ring copper ions are 4.5634(7)–4.6204(7) Å and 4.5674(7)–4.6128(7) Å for **1** and **2**, respectively [5, 6].

The common feature of structures of both **1** and **2**, and earlier reported 12-MCs-4 based on β-aminohydroxamic acids, is essentially non-planar overall conformation of the metallamacrocylic molecules which differs this subgroup of 12-MCs-4 from those based on salicylhydroxamic acid showing nearly planar conformations [2]. The comparison of copper(II) 12-MC-4 complexes with **β-AlaHA**, **MACZ** and **PAHEt** revealed similar conformational features. The 12-MC-4 fragments indicate ruffled conformations in all three cases (Fig. 13). The deviations of MCs from planarity are due to dissimilar, irregular conformations of the bimetallic and the chelate rings composing the MC fragment. Thus, in **2**, two out of four six-membered chelate rings involving phosphorus atoms show almost common envelope conformation with the phosphorus atoms deviating from the chelate planes by 0.553(4) and 0.570(4) Å, respectively, while two other six-membered chelates exhibit a twist-skewed envelope conformation with oxygen and carbon atoms residing outside their chelate planes by 0.630(3) and 0.525(6) Å, respectively, by the reverse faces of the MC plane (Fig. 13c) [5]. Similar irregularities in conformations of bimetallic rings and chelates and mutual disposition of copper and hydroximate oxygen atoms are observed in $[Cu_5(\textbf{β-AlaHA}\text{-}2H)_4](ClO_4)_2{\cdot}5H_2O$ and **1** (Fig. 13a, b) [6, 49].

In **1** and **2**, the central atoms in the MC are situated in different spatial environments. In **1**, four metal ions within the MC unit indicate a distorted square-pyramidal coordination and one ring metal ion a distorted octahedral surrounding with elongated apical bonds. The equatorial plane of the core metal ion is defined by four oxygens of the hydroxamate functions indicating the bridging mode. The four-ring copper

ions have a mixed donor array in their basal environment formed by three oxygens belonging to the carboxylate and the hydroxamate functions and one hydroxamate nitrogen (Cu–N = 1.939(3)–1.953(3) Å). Of note, the Cu–O bond lengths with the hydroxamate and the carboxylate oxygen atoms (1.892(3)–1.935(3) Å) are noticeably shorter than those with the carbonyl oxygen atoms (1.949(3)–1.982(3) Å). The apical positions are occupied either by water molecules (Cu–O = 2.401(3)–2.585(3) Å) or by the out-of-plane bridging μ_3-hydroxamate or μ-carboxylate oxygens of the adjoining MC unit within the decacopper dimer (Cu–O = 2.731(3) and 2.613(3) Å, respectively) [6].

In **2**, out of four ring Cu ions, two exhibit a distorted square-planar environment, whereas the other two a somewhat distorted square-pyramidal coordination. This dissimilarity is manifested in significantly shorter basal Cu–O distances in the case of the central atoms with coordination number 4. The Cu–N and Cu–O bond distances in the equatorial planes are in the range 1.863(3)–1.955(3) Å and 1.863(3)–1.955(3) Å, respectively, and are normal for copper(II) 12-MCs-4 [1, 11]. The core copper atom is in a distorted octahedral environment of six oxygen donors. Its basal plane is defined by four hydroximato oxygens, while the apical sites are settled by the oxygen atoms of the hydroximic and acetate groups belonging to the adjoining pentacopper module [5]. The basal Cu(core)-O distances are in the range 1.881(3)–1.916(3) Å in **1**, and 1.894(3)–1.968(3) Å in **2** [5, 6]. On the whole, the geometrical characteristics observed are similar to those seen in earlier described hydroxamate 12-MCs-4 [9, 49, 51].

In **1**, the carboxylate groups are coordinated monodentately to metal ions, which makes it possible for the involvement of the second carboxylate oxygen into a copper-oxygen bond with an additional copper ion with the attainment of different bridging functions of the carboxylic group. This would open an opportunity to obtain the coordination compounds of higher nuclearity by application of the pentanuclear anionic MCs as metaloligands in reactions with metal solvato or complex cations with labile monodentate ligands. Complex **1** showcases a spectacular case of such an opportunity: a self-association resulting in the formation of the 12-nuclear anionic assemblies with their subsequent uniting into the 1D-polymeric strand [6]. This case apparently shows that the specific propensity of hydroxamates to form stable pentametallic MCs can be exploited for preparing big nuclearity assemblies, where the MC complexes themselves can be utilized as construction modules in the reactions with coordination compounds.

Due to the presence of the exo-disposed ethoxy and phosphoryl residues of the phosphoester functions in **2**, the 12-MC-4 moieties can act as metalloligands toward additional central atoms; the exo-binding of Na^+ ions results in the production of 2D-coordination polymeric network. The four Na^+ ions in the unit cell of **2** are linked with the 10-nuclear bis(MC) fragment in different fashions: (i) in a bidentate mode via the P–O and C=O functions of two adjacent **PAHEt** residues bound to the same ring copper atom thus forming CuO_2Na heterobimetallic rings, and (ii) in a monodentate mode via the phosphoryl function with accompanying coordination to the apical oxygen of the acetate ligand, thus creating CuO_2Na ring with the same copper atom as well (Fig. 14). Of note, one of the bidentately coordinated to MC Na

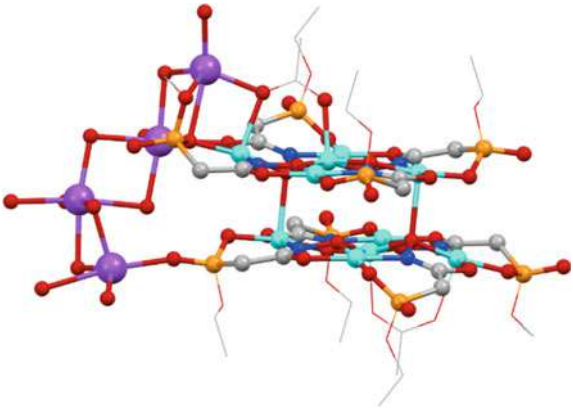

Fig. 14 Sodium cations coordination in the structure of $\{Na_4(H_2O)_6(Ac)[Cu_5(\mathbf{PAHEt}\text{-}3H)_4(Ac)]\}_2 \cdot 3H_2O$ (**2**) [5]. Colour scheme: cyan = Cu, magenta = Na, red = O, blue = N, gray = C, orange = P

cations is also monodentately bound to the neighboring decanuclear fragment via the phosphoryl group, thus uniting two bis(12-MC-4) moieties [5].

In conclusion, the introduction of the multidonor, potentially bridging, O-containing carboxylate or phosphomonoester group into β-position to the hydroxamate function has a serious impact on the thermodynamic stability (that is decreased) and pH range of existence (that is broadened) of 12-MC-4. Notwithstanding, compared to 12-MC-4 based on other known β-functionalized hydroxamic acids, it actually does not influence their structural and conformational parameters. Yet, additional donor atoms not taking part in the formation of the MC framework bring a pronounced ability for the association to the 12-MC-4 complexes thus enhancing their metal-binding ability and making them promising building blocks for higher nuclearity oligomeric and polymeric structures.

5.2 *MC Complexes Based on α-Functionalized Hydroxamates*

According to the "*metallacrown structural paradigm*" (Fig. 4), α-functionalized hydroxamates are the ligands of choice to construct 15-MCs-5 containing framework appropriate for incorporating lanthanides and other cations with large ionic radius (e.g., UO_2^{2+}, Pb^{2+}, Ca^{2+}), β-functionalized hydroxamic analogues are more convenient for the preparation of 12-MCs-4 with a cavity suitable for incorporations of smaller metal ions, e.g., 3d-metals (Fig. 15a) [2, 50]. α-functionalized hydroxamates are capable to form also 12-MC-4 having the core 3d-metal ions (Fig. 15b), such MCs are still significantly less stable as compared to the complexes based on β-aminohydroxamates as their formation occurs despite the "*metallacrown structural paradigm*"; such 12-MCs-4 are readily reorganized into 15-MCs-5 on reaction with larger metal cations [2]. Certainly, the juxtaposition of the stability constants observed for $[Cu_5(L\text{–}H)_4]^{2+}$ of β- and α-alanine hydroxamates (HL), demonstrates

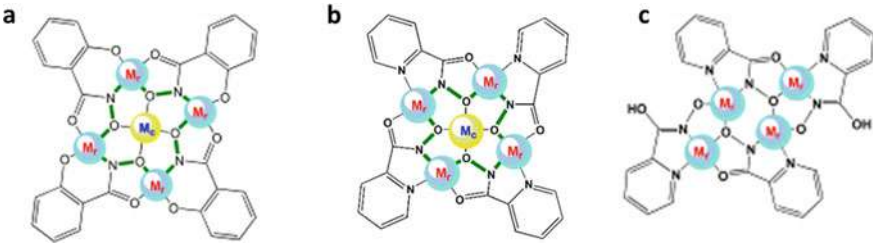

Fig. 15 12-MC-4 with α- (**a**) and β-functionalized (**b**) hydroxamates and collapsed 6-MC-2 (**c**) structures

9 orders of magnitude difference in favor of the β-functionalized derivative (49.39 vs. 40.16, Table 3) [32].

Despite numerous solution complex equilibria studies suggesting the formation of 12-MC-4 species in systems containing 3d-metal ions and α-functionalized hydroxamates (in the absence of larger cations that could serve as ring metal ions templating the formation of 15-MC-5 according to MC structural paradigm), attempts to isolate the corresponding complexes in a crystalline state and to confirm their structure by single-crystal X-ray analysis were unsuccessful for many years. Only in 2013, the first structurally characterized 3d-metals 12-MCs-4 with α-functionalized hydroxamates have been reported, namely, Zn and Ni-containing MCs with **QuinHA** and Zn MC with **PicHA** [52]. Later, Cu 12-MC-4 with **QuinHA** has been reported as well [4]. Thus, unlike 12-MC-4 3d-metals complexes with β-functionalized hydroxamates and 15-MC-5 3d-/large metal ion complexes with α-functionalized hydroxamates, having numerous reported structures, this type of MCs is represented by only a few examples of structurally characterized compounds. The difficulties with isolation in the solid state can be connected with significantly diminished stability of 12-MC-4 complexes with α-functionalized hydroxamates having 12 fused 5-membered chelate and bimetallic rings which evidently brings about significant sterical tension in the corresponding species and thus contributes to the overall decrease of thermodynamic stability. In the course of crystallization of the complexes, an equilibrium between solution and solid phases can take place that facilitates the degradation of sterically strained molecules into stable ones in the crystalline state (as it can take place on the crystallization of collapsed MCs, vide infra). Also, analysis of species distributions diagrams for 3d-metal systems with α-functionalized hydroxamates (Figs. 6, 7 and 8) reveals that 12-MC-4 species exist only in a quite narrow pH range (usually at a pH around 5) and their maximal total abundance as a rule does not exceed 80–85%. The only exception is **QuinHA**, which produces 12-MC-4 species with Cu(II) ions which are dominating and the only existing species in a wide pH range, i.e., 3–11 (Fig. 8a) [4]. As evidenced by later studies, peculiarities of ligand structure can play a critical impact on complex formation, and in the case of **QuinHA**, a bulky bicyclic aromatic moiety facilitates 12-MC-4 formation, and probably hinders the formation of other species typical for 3d-metal—α-functionalized hydroxamate systems.

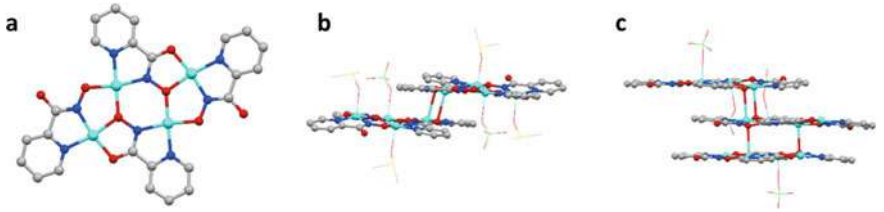

Fig. 16 Molecular structure of copper(II) complexes with **PicHA** containing collapsed metallacrowns moieties: **a** tetranuclear complex cation $[Cu_4(\mathbf{PicHA}\text{-}H)_2(\mathbf{PicHA}\text{-}2H)_2]^{2+}$ in **3**; octanuclear complex cation $[Cu_8(\mathbf{PicHA}\text{-}H)_4(\mathbf{PicHA}\text{-}2H)_4(DMSO)_4(ClO_4)_2]^{2+}$ in **4**; dodecanuclear fragment $[Cu_{12}(\mathbf{PicHA}\text{-}H)_6(\mathbf{PicHA}\text{-}2H)_6(ClO_4)_4]^{2+}$ in **5** [53]. Axial ligands are displayed as thin lines in the ball and stick diagrams for clarity. Colour scheme: cyan = Cu, red = O, blue = N, gray = C

Tegoni et al. in 2008 with the help of the DFT calculations predicted that the homometallic 3d-metals 12-MCs-4 can exist as non-planar, cap-shaped complexes [29], that should be quite strained, as they contain 12 fused five-membered chelate and bimetallic rings. It is not clear that they can retain the structure upon transfer from solution to crystalline state.

Numerous attempts to crystallize **PicHA**-based 12-MC-4 complexes in all cases resulted in obtaining of collapsed 6-MC-2 complexes or higher nuclearity structures containing collapsed 6-MC-2 motif [4, 53]. Thus, syntheses of $[Cu_5(\mathbf{PicHA}\text{-}H)]^{2+}$ followed by crystallization from various solvents (DMF, DMSO, methanol) in all cases resulted in the isolation of collapsed 6-MC-2 compounds with different degrees of self-association of tetranuclear collapsed moieties: $[Cu_4(\mathbf{PicHA}\text{-}H)_2(\mathbf{PicHA}\text{-}2H)_2](ClO_4)_2\cdot 2DMF$ (**3**), $[Cu_8(\mathbf{PicHA}\text{-}H)_4(\mathbf{PicHA}2H)_4(DMSO)_4(ClO_4)_2](ClO_4)_2\cdot 2DMSO$ (**4**), $\{[Cu_{12}(\mathbf{PicHA}\text{-}H)_6(\mathbf{PicHA}\text{-}H)_6(ClO_4)_4]\}_n(ClO_4)_{2n}\cdot 3nH_2O$ (**5**), respectively (Fig. 16) [53].

The structures of **3**, **4**, and **5** comprise the tetracopper $[Cu_4(\mathbf{PicHA}\text{-}H)_2(\mathbf{PicHA}\text{-}2H)_2]^{2+}$ (**3**), double-decked 8-nuclear $[Cu_8(\mathbf{PicHA}\text{-}H)_4(\mathbf{PicHA}\text{-}2H)_4(DMSO)_4\ (ClO_4)_2]^{2+}$ (**4**) and triple-decked 12-nuclear $[Cu_{12}(\mathbf{PicHA}\text{-}H)_6(\mathbf{PicHA}\text{-}2H)_6(ClO_4)_4]^{2+}$ (**5**) double-charged complex cations, perchlorate anions and the lattice molecules of solvents. The metal-containing cations of **5** are linked into 1D coordination polymeric strands. As the complexes **3–5** are virtually similar within the tetracopper moieties, we dwell upon a more detailed description of **3** containing isolated collapsed 12-MC-4 units.

The complex cation in **3** (Fig. 16a) adopts a virtually planar conformation, with the non-hydrogen atoms setting outside the mean plane by no more than 0.256(6) Å, and contains four copper atoms and four hydroxamic residues, arranged in such a fashion that they produce collapsed 12-MC-4 sequence. The core part of the collapsed MC involves the six-membered dicopper ring, with the Cu(2)···Cu(2A) distance of 3.909(2) Å. Six five-membered chelates, two of which contain two copper ions, are joined to the edges of the central hexagonal fragment. In the five-membered dicopper chelate rings, the two metal ions are united by two bridges: the monoatomic (–O–)

and the heterodiatomic (–N–O–), resulting in the Cu(1)···Cu(2) contact = 3.333(1) Å. The other intercopper separations in the tetranuclear complex are: Cu(1)···Cu(1A) = 7.141(2), Cu(1)···Cu(2A) = 4.693(1) Å. Each copper atom is tetracoordinated and finds itself in a distorted square-planar surrounding), as in the supramolecular packing, the shortest Cu···O intermolecular separations are >3 Å.

Two of the hydroxamic ligands in the collapsed MC moieties in **3**–**5** are doubly deprotonated by the hydroxamate N and O atoms, while two others are N-monodeprotonated. Importantly, in the latter the hydroxamic groups exhibit not the hydroxamate but in the hydroximate structure, which is manifested not only by the correspondent N–O, C–N and C–O bond distances, but also by placement of the hydrogen atoms on the carbonyl (not the oximate) oxygens. As such, the C–O bond distances in the doubly charged ligands anions in **3** (1.287(1) Å and 1.295(10)) are apparently shorter when compared with the corresponding values in the singly charged ligands (1.326(7) Å and 1.322(11)), even though the oxygens of the former are coordinated. The discrepancy in the N–O distances is even more distinct: 1.395(6)–1.418(9) Å in the (**PicHA**-2H) residues, against 1.340(5)–1.371(9) Å in the (**PicHA**-H) residues in **3**–**5**. The latter value is usual for the bridging oximate function, and the former—for the hydroxamate group. The C–N distances are also evidently distinct for the two pairs of ligand residues and are longer for the doubly deprotonated ones. Notably that doubly and monodeprotonated ligand residues are coordinated in different fashions. While the monodeprotonated residue binds one metal ion with the help of two nitrogens and connects it with another metal ion forming the (–N,O–) hydroxamate bridge, in the doubly deprotonated residue, the (–N,O–) bridging between copper atoms is accompanied by chelate formation through the C=O oxygen. Moreover, the hydroxamic oxygen in (**PicHA**-2H) exhibits μ-bridging function, so that the ligand residue bridges three metal ions. It should be mentioned the μ_2-(N,O) bridging mode of the hydroxamic function observed in (**PicHA**-H) has never been registered before in the coordination compounds with hydroxamic acids [53].

In **4**, the equatorial Cu–N and Cu–O distances are longer (sometimes by ca. 0.04 Å) as compared to the corresponding values found in **3** and **5**. This is probably due to the involvement in the dimeric structure, which causes a substantial deviation of Cu atoms from the equatorial plane towards the apically bound DMSO molecules. An additional outcome of this is a more corrugated conformation of the tetranuclear unit in **4** (the largest deviation from the mean plane is 0.452(3) Å for bridging hydroximato oxygen atom) [53].

Whereas in **3** the tetracopper collapsed MC moieties can be considered as isolated, in **4** they are associated with the double-decked dimers, and in **5**—into 1D-coordination polymeric strands featuring the tris(collapsed MC) cations. In **4**, two tetracopper collapsed MC units are joined in the double-decked octacopper complex cation due to two elongated Jahn–Teller apical contacts between copper atoms and the C=O oxygens of the adjacent tetranuclear unit (Cu···O = 2.627(3) Å). The "interdecked" Cu···Cu distance is 3.441(1) Å (Fig. 16b). The octacopper complex cations also include apically coordinated molecules of DMSO and perchlorate ions. In **5**, three planar tetracopper moieties are arranged into the triple-decked associate

on account of elongated (2.628(4)–2.777(4) Å) apical Cu···O "interdecked" bonds (Fig. 16c). Extra Cu···O apical contacts (2.989(4) and 2.864(4) Å) further unite the assembled 12-nuclear cations into the 1D-coordination polymeric strand.

Worth noting that each tetracopper collapsed MC moiety in **3–5** involves two uncoordinated O–H groups near the potentially μ_3-bridging hydroxamic oxygens, so that they both create a vacant chelating unit. In the case of α-aminohydroxamates in which the amino nitrogen atom is not involved in the cyclic fragments, such binding has been observed before in the 28-nuclear helicate complex communicated by Pecoraro et al., in which the tetracopper collapsed MC units are aggregated by copper(II) ions bound to two such (O,O′)-chelating bidentate compartments of the adjacent collapsed MC moieties [54].

Structures **3–5** represent the first cases of the solely hydroxamic-based copper(II) 12-MCs-4 with a collapse of the macrocyclic framework. The collapsed 12-MC-4 complex is produced because of sophisticated processes of decomposition of essentially tense, thermodynamically unfavorable pentacopper **PicHA**-containing 12-MC-4. Thus, the collapsed 12-MCs-4 illustrate a common, stable structural pattern that can be formed under miscellaneous conditions.

The results of structural studies of **3–5** open opportunities to study the reactivity of collapsed MC complexes which opens several attractive options: (i) formation of oligonuclear associates and MOFs proceeding due to the apical binding of the metal ions, as observed in [53]; (ii) the diversity of reorganization processes, specifically brought about by species capable to "open" the cavity of collapsed MCs (e.g., lanthanide cations); (iii) the application of the collapsed 12-MCs-4 as construction modules for preparing discrete higher nuclearity assemblies via coordination of the vacant peripheral oxygen atoms, as it was observed in the 28-nuclear helicate complex [54].

The latter possibility has been realized recently in the course of another attempt to crystallize 12-MC-4 based on **PicHA** [4]. Synthesis conducted in ethanol was followed by crystallization of the complex with the help of slow diffusion of diethyl ether vapor, which afforded isolation of the 1D-coordination polymer $[Cu_{10}(\mathbf{PicHA}\text{-}2H)_8(H_2O)_4(ClO_4)_3]_n(ClO_4)_n \cdot 4nH_2O$ (**6**) comprising decanuclear blocks (Fig. 17) [4]. Isolation of this compound as well as of collapsed MCs **3–5** (for which the

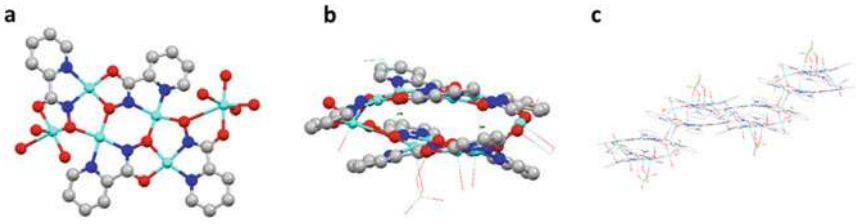

Fig. 17 Molecular structure of $[Cu_{10}(\mathbf{PicHA}\text{-}2H)_8(H_2O)_4(ClO_4)_3](ClO_4)\cdot 4H_2O$ (**6**): **a** collapsed MC unit with two exo-chelated copper(II) ions; **b** decanuclear unit; **c** 1D-polymeric motif. Apical ligands are shown as thin lines in the ball and stick diagrams for the sake of clarity. Colour scheme: cyan = Cu, red = O, blue = N, gray = C [4]

corresponding species have not been detected in solution) could result from adjusting relevant conditions of crystallization, which could not be reached in the course of solution speciation studies (neat organic solvent). This implies the presence of not only complex solvent conditioned solution equilibria (involving the penta- and tetranuclear species), but presumably also between the phase of growing crystals and solution [4].

Structure **6** is ionic and comprises decacopper complex cations $[Cu_{10}(\mathbf{PicHA}\text{-}2H)_8(H_2O)_4(ClO_4)_3]^+$, perchlorate counterions, and water molecules of solvation. The decanuclear cation, nevertheless, indicates a dimeric arrangement that is not based on a pentacopper 12-MC-4 fragments but is instead featuring two collapsed MC $Cu_4(\mathbf{PicHA}\text{-}2H)_4$ units linked by two chiral capping copper atoms exo-chelated to the external vacant (O,O′) donor compartments of each tetracopper collapsed MC unit (Fig. 17a). A related exo-coordination of a fifth copper atom to the collapsed MC fragment has been noticed in a 28-nuclear double-stranded metal helicate on the base of L-norvaline hydroxamic acid [54].

The general arrangement of the decacopper moiety can be characterized as a double-decked associate featuring two collapsed MC sheets, which are united with two edge crossbars (Fig. 17b). Remarkably, each collapsed MC unit indicates not a planar, but strikingly twisted conformation that can be described as a "canted blade". This peculiarity importantly discerns the regarded structure from those watched in copper collapsed MCs based on **PicHA** (**3**–**5**), in which substantially planar conformations of the complex cations are detected [53]. This distinctness is also manifested by an essentially twisted conformation of the core six-membered dicopper ring of each collapsed MC sheet. Two collapsed MC sheets are linked by elongated apical bonds Cu–O = 2.9038(2), 2.8633(2), and 2.7919(2) Å with μ_3-bridging coordination of the hydroxamic oxygens [4]. Evidently, this twist furnishes the required room for exo-coordination of "peripheral" copper ions.

Both "peripheral" Cu(II) ions are in the distorted octahedral surrounding. Their polyhedra are formed by six oxygen atoms, with four of them belonging to the outer (O,O′) chelating units of two different collapsed MC decks. The two remaining cis-situated coordination sites are occupied by two water molecules or by a water molecule and the carbonyl oxygen atom of the translational molecule. Such cis-bis(chelate) coordination of the terminal Cu atoms gives rise to the configuration chirality of both centers, in the basic decanuclear unit both of them indicate the Δ absolute stereochemical configuration. For both Cu(II) ions, their coordination spheres are severely distorted.

Organization of the decanuclear subunits into the 1D-coordination polymeric chains proceeds as follows. First, two chiral decanuclear subunits form a centrosymmetric dimer due to two long axial contacts Cu–O(carbonyl) = 2.7274(2) Å. Next, a similar axial interaction of the "peripheral" Cu ions between the centrosymmetrically related bis(decanuclear) dimers unites them into a 1D-polymeric motif (Cu–O(carbonyl) = 2.5623(2) Å) (Fig. 17c).

In the case of **QuinHA**, the formation of collapsed MCs is expected to be highly implausible or even impossible because of the unfavorable mutual sterical disposition of the quinoline rings and the hydroximate OH groups which in the case of planar

structure should approach very close to each other (cf. Fig. 17a, b). Here, degradation of 12-MC-4 into collapsed structure could be thermodynamically unfavorable because of an additional aromatic ring in the ligand. This can be a reason for additional stabilization of the pentanuclear 12-MC-4 structure with **QuinHA**, as the possible pathways of degradation and rearrangement into a stable planar collapsed structures are eliminated. Indeed, recent studies of isolated **QuinHA**-containing metallacrowns with 3d-metal ions revealed the formation of pentanuclear 12-MC-4 complexes; there were no reports about collapsed MCs with this ligand [4, 52] (Fig. 18).

Three 12-MC-4 complexes based on **QuinHA** have been obtained: Ni^{II}[12-$MC_{Ni}{}^{II}$,**QuinHA**-4]$(NO_3)_2$ (**7**) [52], Cu^{II}[12-$MC_{Cu}{}^{II}$,**QuinHA**-4]$(NO_3)_2$ (**8**) [4] and Zn^{II}[12-MC $_{Zn}{}^{II}$,**quinHA**-4]$(BF_4)_2$ (**9**) [52] (Fig. 19 a–c). The structures **7–9** consist of

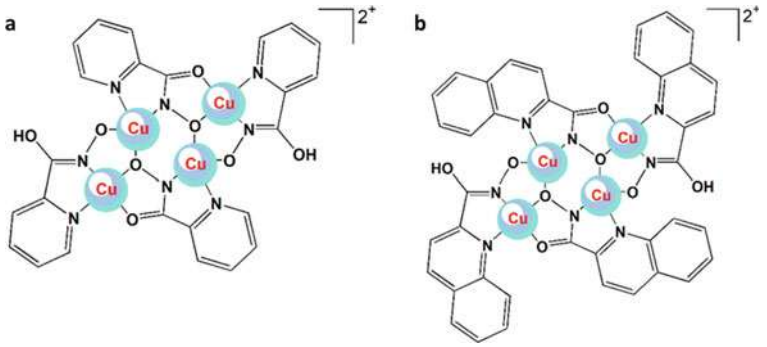

Fig. 18 Comparison of **PicHA** (**a**) and **QuinHA** (**b**) collapsed MCs

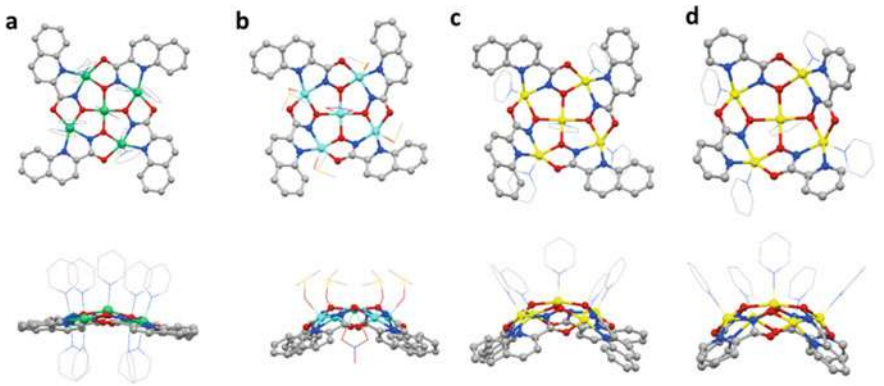

Fig. 19 Structure of pentanuclear complex cations in 12-MCs-4 with **QuinHA** and **PicHA**: **a** Ni^{II}[12-$MC_{Ni}{}^{II}$,**quinHA**-4]$(NO_3)_2$ (**7**) [52]; **b** Cu^{II}[12-$MC_{Cu}{}^{II}$,**quinHA**-4]$(NO_3)_2$ (**1**) (**8**) [4]; **c** Zn^{II}[12-MC $_{Zn}{}^{II}$,**quinHA**-4]$(BF_4)_2$ (**9**) [52]; **d** Zn^{II}[12-MC $_{Zn}{}^{II}$,**picHA**-4]$(BF_4)_2$ (**10**) [52] (downside views). Axial ligands are displayed as thin lines in the ball and stick diagrams for clarity. Colour scheme: green = Ni, cyan = Cu, yellow = Zn, red = O, blue = N, gray = C

pentanuclear complex molecules exhibiting a 12-MC-4 topology, with their metallamacrocyclic cavities formed by four ring metal ions and four doubly deprotonated **QuinHA** ligands. The centers of the cavities are occupied by the fifth core metal ion coordinated by four hydroximate oxygen atoms. As ligands forming fused 5-membered chelate rings prefer the planar pentagonal topology found in 15-MC-5 type MCs, the complexes are highly concave in order to close a cyclic system comprising 12 fused 5-membered rings. This strain leads to a significant distortion from planarity, resulting in a bowl-shaped MC conformation.

The bowl shape conformation of 12-MC-4 with copper atoms in the ring situating far above the basal ligand plane was foreseen by Tegoni et al. for {Cu(II)[12-$MC_{Cu(II),\alpha\text{-aminoHA}}$-4]} [29]. The diameter of the cupped face of **8** is almost 17.8 Å and its extent is 4.26 Å, which is close to the values noticed in zinc 12-MC-4 **9** (18.7 and 4.8 Å, respectively) but imply less noticeable indentation of copper(II) 12-MC-4. Next, the extent of the cupped face is much larger in the copper(II) and zinc 12-MCs-4 than in the nickel(II) complex (1.29 Å), the flattest in the set of 12-MCs-4 based on **QuinHA**. The core cavity radius of copper 12-MC-4 is 0.60 Å which matches properly to the ionic radius of copper(II) ion with coordination number 5 (0.65 Å), but yet smaller, so that the core copper atom is situated only insignificantly above the mean plane of the oxygen donor atoms (OMP) by 0.142(5) Å which is much smaller deviation than in the nickel(II) and zinc(II) MCs (0.38–0.39 Å). Nonetheless, the copper(II) complex is much more hollowed than the nickel(II) MC and resembles the zinc(II) complex by its conformation. This is reached by significantly shorter M_{ring}-M_{ring} distances (4.571(1) vs. 4.82–4.83 Å in nickel(II) and zinc(II) MCs) which offsets the impact of small dislocation of the core copper atom from OMP. Namely, in the case of the copper(II) complex its bowl is more obtuse than in nickel(II) and zinc(II) metallamacrocycles. On contrary, the ring copper atoms are set noticeably away from the mean planes defined by their basal donor atoms (N_2O_2) by 0.300(3) Å. The radius of the metallamacrocyclic cavity of the copper(II) complex is smaller than that of zinc(II) MC (0.65 Å), and greater than the nickel(II) complex (0.57 Å), which is in agreement with the values of ionic radii of the regarded metal ions (Table 6). The molecular structure of the copper(II) complex indicates inclinations from planarity intermediary between those of the nickel(II) and zinc MCs (Table 6, Fig. 20), accurately as foreseen, which presents direct experimental proof for the systematic bowling of the {M(II)[12-$MC_{M(II),\alpha\text{-aminoHA}}$-4]} topology [29].

Interestingly, upon similar synthetic conditions used for the preparation of **9** (methanol/pyridine solvents mixture, crystallization with the help of slow diffusion of Et_2O), **PicHA**-containing Zn(II) 12-MC-4 Zn^{II}[12-MC $_{Zn^{II},\mathbf{PicHA}}$-4]$(BF_4)_2$ (**10**) has been obtained [52]. Unlike Cu(II)—**PicHA** systems, in the case of zinc, the pentanuclear 12-MC-4 species does not undergo degradation to tetranuclear collapsed structure. The greater stability of Zn^{II}[12-MC $_{Zn^{II},\mathbf{PicHA}}$-4]$^{2+}$ relative to the Cu(II) and Ni(II) analogs were inferred and attributed to the square-pyramidal Zn(II) geometry being better complementary with the concave 12-MC-4 topology [52]. The geometrical parameters and the shape of **10** are essentially similar to those seen in **9** (Fig. 19d, Table 6). The central Zn(II) rests 0.325 Å above the OMP, noticeably less than in the case of Ni(II) and Zn(II) **QuinHA**-containing 12-MCs-4. The

Table 6 Structural parameters for Ni(II), Cu(II), and Zn(II) 12-MC-4 complexes with **QuinHA** and **PicHA** [4, 52]

	$\{Ni(II)[12\text{-}MC_{Ni(II),\mathbf{QuinHA}}\text{-}4]\}^{2+}$ (**7**)	$\{Cu(II)[12\text{-}MC_{Cu(II),\mathbf{QuinHA}}\text{-}4]\}^{2+}$ (**8**)	$\{Zn(II)[12\text{-}MC_{Zn(II),\mathbf{QuinHA}}\text{-}4]\}^{2+}$ (**9**)	$\{Zn(II)[12\text{-}MC_{Zn(II),\mathbf{PicHA}}\text{-}4]\}^{2+}$ (**10**)
M_{ring} coord. no	6	5	5	5
av M_{ring}-$O_{hydroxam}$ (Å)	1.995	1.969	2.068	2.069
av M_{ring}-$O_{carbonyl}$ (Å)	2.175	1.967	2.006	2.001
av M_{ring}-$N_{hydroxam}$ (Å	2.023	1.938	2.021	2.027
av M_{ring}-$N_{(Py)}$ (Å)	2.16	2.044	2.16	2.15
av M_{ring}-$O/N_{solvent}$ (Å)	2.138	2.74	2.041	2.044
av M_{ring}-M_{ring} (Å)	4.813	4.571	4.822	4.813
M_{ring}-OMP_{MC}[a]	0.380	0.300	0.682	0.707
av M_c-$O_{hydroxam}$(Å)	1.965	1.958	2.041	2.057
M_c-OMP_{MC}[a]	0.39	0.14	0.375	0.325
M_c coord. no	5	6	5	5
M_c ionic radius (Å)	0.63	0.65	0.68	0.68
Central cavity radius[b]	0.57	0.60	0.65	0.67

[a] Oxygen mean plane for the atoms in the central cavity

[b] Cavity radius is calculated as the average distance from the oxygen atom to the centroid of the hydroxamate oxygen atoms minus the ionic radius of an oxygen atom (1.36 Å) [52]

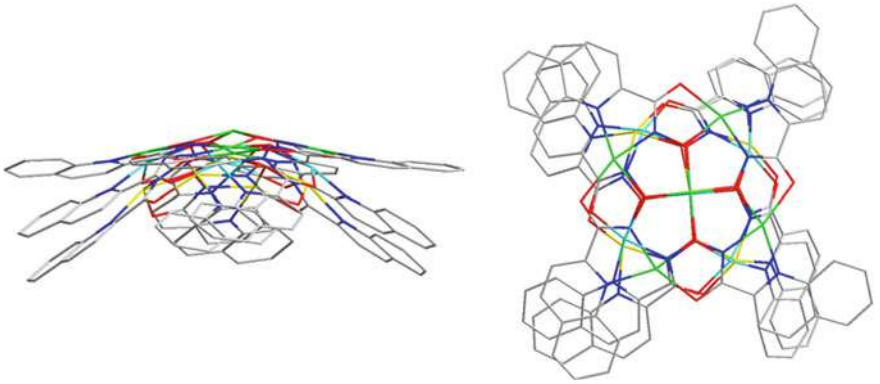

Fig. 20 Structural overlay of $\{Ni(II)[12\text{-}MC_{Ni(II),\mathbf{QuinHA}}\text{-}4]\}^{2+}$, $\{Cu(II)[12\text{-}MC_{Cu(II),\mathbf{QuinHA}}\text{-}4]\}^{2+}$ and $\{Zn(II)[12\text{-}MC_{Zn(II),\mathbf{QuinHA}}\text{-}4]\}^{2+}$. Axial ligands are omitted for clarity. Colour scheme: green = Ni, cyan = Cu, yellow = Zn, red = O, blue = N, gray = C

diameter of the concave cavity in **10** is about 14 Å which is above 4 Å less than in **9**, while its depth (4.5 Å) is comparable with that observed in **9** (4.8 Å). Due to the larger size of the **QuinHA** molecule, the concave bowl indicates larger dimensions (i.e., maximal width and depth) [52].

The most interesting observation coming from the comparison of the three structures of **QuinHA** complexes is the pronounced distinctness in the extents of concavity of their metallamacrocylic cores. Thus, nickel(II) and zinc MCs exhibit quite similar geometrical characteristics (like average M_{ring}-donor bond lengths and $M_{ring}\cdots M_{ring}$ distances, $M_{cent}\cdots$OMP separations), nevertheless, they indicate different extents of concavity. At the same time, copper(II) and zinc MCs resemble each other by their conformations but are quite distinct in geometrical characteristics (zinc MC indicates importantly longer M_{cent}-O and M_{ring}-N/O bond lengths and $M_{ring}\cdots M_{ring}$ distances). Apparently, the conformation of the most planar of nickel(II) MC is determined by the octahedral coordination of the ring nickel atoms bearing apical pyridine ligands on both faces of MC. As a result, the basal planes of the ring nickel(II) ions are essentially more flat than in the case of the pentacoordinated copper(II) and zinc ions. If Addison τ_5 parameters will be applied for the equatorial planes of the ring Ni(II) ions to estimate the degree of their inclination from the planarity ($\tau_5 = (\beta - \alpha)/60$, where $\beta > \alpha$ are the two largest valence angles for five-coordinated metal centers, this parameter allows the distinction between trigonal–bipyramidal ($\tau = 1$) and square-pyramidal geometry ($\tau = 0$) [55], the values in the range 0.008–0.027 will be received, while in the case of copper(II) and zinc ring ions $\tau_5 = 0.129$ and 0.04–0.30 (av. 0.188), respectively. Hence, almost planarly disposed basal donor atoms of nickel(II) ions comprising the 12-MC-4 sequence, accomplish substantially more planar overall geometry of the molecule. This is achieved on account of a considerable increase of the $O_{carbonyl}$–Ni^{II}–$N_{quinHA\text{-}pyridyl}$ outer bond angles values till 120.60°–123.59° (in regular octahedron they are equal to 90°) while in copper(II) and zinc complexes the corresponding angles are only 103.23° and 98.69°–102.85°,

respectively. More concave conformation of the nickel(II) MC would result in close non-covalent contacts between the adjacent apical pyridine ligands. It is likely that the pentacoordinated geometry of the core nickel(II), unusual for this ion, is induced, as the addition of an extra apical ligand on the hollow face would bring about unfavorable sterical interaction between the pyridine molecules. In the cases when the ring metal ions indicate square-pyramidal pentacoordinated coordination (Cu(II), Zn(II)) usual for these metals, the complexes adopt a convex geometry with the apical pyridine ligands placed on the protuberant face of MC frameworks due to the occupancy of two sides of the basal plane by an unequal number of apical donors.

This example illustrates the critical impact of apical ligands on MC geometry. The identical and/or symmetrical placement of apical donors in respect to the metallamacrocyclic plane promotes its more planar geometry. Asymmetric, unilateral, or opposite arrangement of the apical ligands causes declinations from planar conformation and thus boosts the degree of indentation of the MC core. Thus, adjustment of apical ligands in coordination spheres of both ring and central metals can play an important role in the realization of specific conformations of MCs. Interestingly, similar effects of disposition of axial ligands (pyridine molecules) have been observed for 15-MC-5 having Cu(II) as ring metal with different core ions (Ln(III), Ca(II), Pb(II), Hg(II)) indicating a concave conformation [56]. On the contrary, analogous complexes having Ni(II) as a ring metal with the same central metals, exhibited nearly planar conformations, as the ring Ni(II) ions indicated typical for them octahedral geometry with equal distribution of axially coordinated pyridine molecules between two sides of the MC plane [44]. While unilateral/bilateral disposition of the axial ligands coordinated to the ring metals conditions to a great extent the overall conformation of MC (planar, concave), symmetric or asymmetric disposition of the axial ligands relative to the core metal ion is responsible for its relative position with respect to the oxygen mean plane of MC (in plane disposition, “sunrise” or “partially open umbrella” conformation) [57].

One can conclude that the type of the formed MC is determined first of all by the size of the chelating unit (i.e., by location of the donor substituent in α- or β-position to the hydroxamate function) and radius of the core metal ion, non-covalent interligand interactions (imposed by the ligand structure) and solvent nature in some cases can cause a critical impact on the type of the formed MC. The position of the core metal ion in the macrocyclic cavity and overall MC conformation is determined first of all by the number and denticity of the axial ligands coordinated to both core and ring metal ions and by the nature of the latter, and only secondarily by geometrical correspondence between the ionic radius of metal ion and size of the macrocyclic cavity.

6 Metallacrowns Building Blocks

As MCs are self-assembled complexes, when the proper conditions (metal-to-ligand molar ratio, pH, etc.) are used, they do not need any precursor to form spontaneously

in solution. In 2013, Pecoraro et al. proposed a possible assembly pathway for the formation of the 12-MC-4 complex as the thermodynamically favored product, and the extension to the formation of 15-MC-5 was reported in 2019 by Ostrowska et al. (Fig. 21) [4, 52]. The presented pathway of the formation of MCs was constructed on the basis of the structural data obtained to date for Cu(II), Ni(II), and Zn(II) complexes with **PicHA**, as the most widely studied hydroxamate ligand able to form MC, as well as solution speciation studies. Starting from the appropriate amount of metal ion and ligand, the first polynuclear intermediate is the 6-MC-2 (Fig. 21b) isolated in the solid state as $\{[Zn_4(PicHA)_2](OAc)_4(DMF)_2\}$. In the next step, two more hydroxamate ligands are incorporated into the structure, leading to $[M_4(PicHA)_4]$ complex (Fig. 21c). Next, the available solution metal ion coordinates to the carbonyl oxygen of hydroxamate ligand resulting in the pentanuclear exo-coordinated non-12-MC-4 (Fig. 21d) which is then reorganized into the 12-MC-4 complex. The pentanuclear exo-coordinated non-12-MC-4 complex is probably an important participant of equilibria, and not just a transient short-lived species, whose presence depends on organic solvent content. The two last isomeric species, 21d and 21e, might not be distinguished in the solution. The rearrangement of the 12-MC-4 is the last step of the mechanism and leads to the formation of 15-MC-5 complex (Fig. 21g). Taking into account the complexity of the solution equilibrium, as well as the low activation energy of the formation and breaking of atomic bonds, the assembly of MCs could reasonably proceed through multiple pathways and consist of more intermediates (not only poly- but also mononuclear), but one could be sure that the proposed final products—12-MC-4 (in case of Cu(II) and Zn(II)) or 15-MC-5 (for Ni(II)) are the most thermodynamically stable polynuclear species characterized by the speciation studies.

Summary

In summary, in this chapter, we have showcased hydroxamic acids as very versatile and powerful ligands with a wide range of opportunities for MCs formation. The solution thermodynamic and solid-state studies discussed for selected ligands show that the formation of MC complexes, their stability, structure, topology, and conformation depend on numerous factors. Apart from the nature and geometrical preferences of the metal ions, the MCs will be influenced by the ligand structure, geometry, size, bulkiness, aromaticity, denticity, and basicity of binding groups. Of importance, even fine structural alterations in peripheral, non-donor residues of otherwise very similar hydroxamic acids can have a pronounced impact on complex formation behavior and structure of complexes crystallized in solid state. The solvents and solvation effects, as well as the nature of axial ligands cannot be neglected when designing the synthesis and isolation schemes of new MCs with pre-defined properties.

The development of this research area with many examples presented here and in the literature clearly shows that further extension of knowledge on the structure and thermodynamics of the MCs formation is awaited. A profound understanding of the correlation between the stability of the MC species, the structure of the ligands, and the type of metal ions, as well as the conditions of their formation, is especially

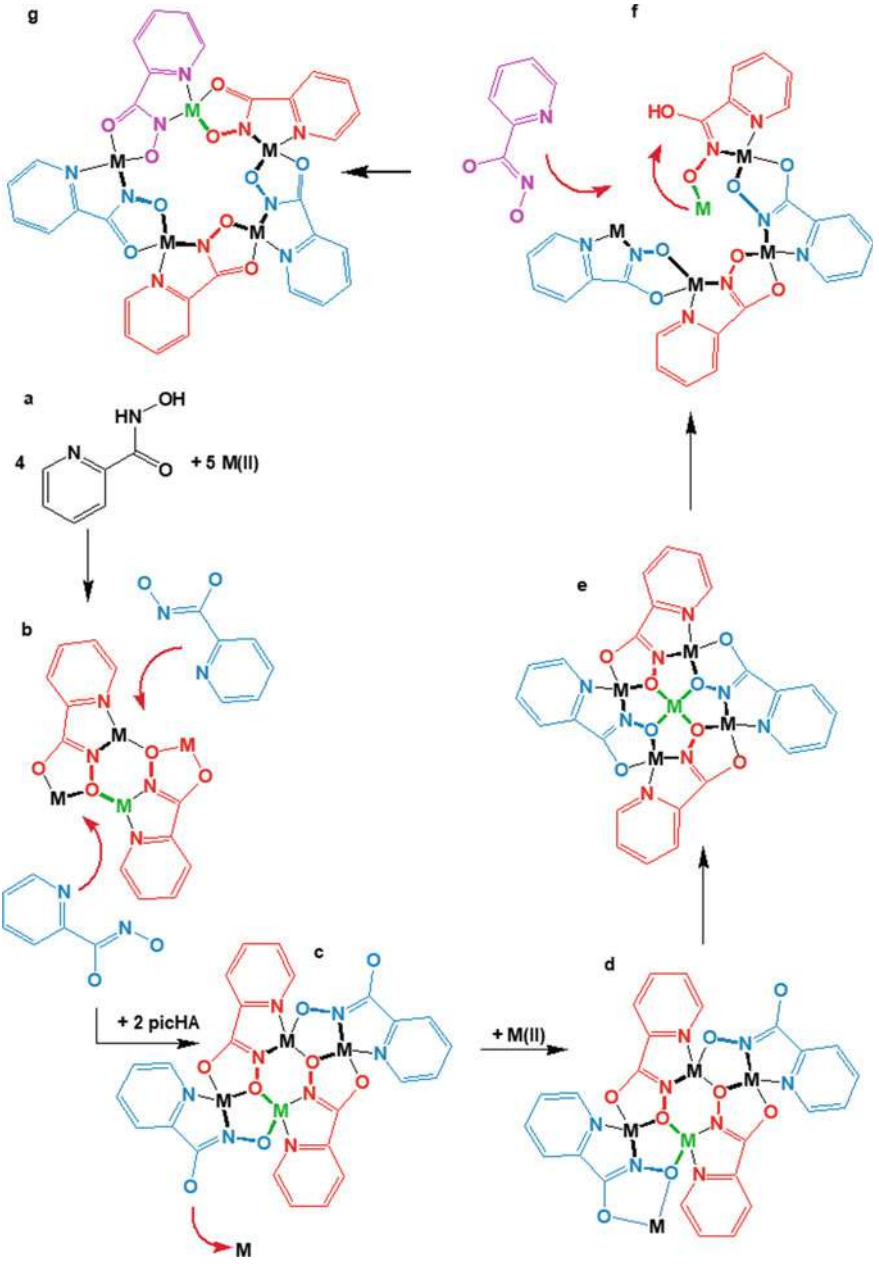

Fig. 21 Scheme of a possible assembly pathway of the formation of 12-MC-4 and 15-MC-5 complexes. The central M(II) ion is displayed in green, the core M_4L_2 ligands are displayed in red, and the exogenous ligands in the M_4L_4 are displayed in blue. Adapted with permission from Ostrowska, M., Toporivska, Y., Golenya, I.A., Shova, S., Fritsky, I.O., Pecoraro, V.L., Gumienna-Kontecka, E.: Explaining How alpha-Hydroxamate Ligands Control the Formation of Cu(II)-, Ni(II)-, and Zn(II)-Containing Metallacrowns, Inorg. Chem. 58, 24, 16,642–16,659 (2019) [4]. Copyright 2019 American Chemical Society

important to take full advantage of the potential of these refined compounds and make progress in possible applications of MCs as functional materials or their precursors.

References

1. Ostrowska, M., Fritsky, I.O., Gumienna-Kontecka, E., Pavlishchuk, A.V.: Metallacrown-based compounds: applications in catalysis, luminescence, molecular magnetism, and adsorption. Coord. Chem. Rev. **327**, 304–332 (2016). https://doi.org/10.1016/j.ccr.2016.04.017
2. Mezei, G., Zaleski, C.M., Pecoraro, V.L.: Structural and functional evolution of metallacrowns. Chem. Rev. **107**(11), 4933–5003 (2007). https://doi.org/10.1021/cr078200h
3. Tegoni, M., Remelli, M.: Metallacrowns of copper(II) and aminohydroxamates: thermodynamics of self assembly and host-guest equilibria. Coord. Chem. Rev. **256**(1–2), 289–315 (2012). https://doi.org/10.1016/j.ccr.2011.06.007
4. Ostrowska, M., Toporivska, Y., Golenya, I.A., Shova, S., Fritsky, I.O., Pecoraro, V.L., Gumienna-Kontecka, E.: Explaining how alpha-hydroxamate ligands control the formation of Cu(II)-, Ni(II)-, and Zn(II)-containing metallacrowns. Inorg. Chem. **58**(24), 16642–16659 (2019). https://doi.org/10.1021/acs.inorgchem.9b02724
5. Ostrowska, M., Golenya, I.A., Haukka, M., Fritsky, I.O., Gumienna-Kontecka, E.: Complex formation of copper(II), nickel(II) and zinc(II) with ethylophosphonoacetohydroxamic acid: solution speciation, synthesis and structural characterization. New J. Chem. **43**(26), 10237–10249 (2019). https://doi.org/10.1039/c9nj01175g
6. Gumienna-Kontecka, E., Golenya, I.A., Dudarenko, N.M., Dobosz, A., Haukka, M., Fritsky, I.O., Kozlowska-Swiatek, J.: A new Cu(II) 12 metallocrown-4 pentanuclear complex based on a Cu(II)-malonomonohydroxamic acid unit. New J. Chem. **31**(10), 1798–1805 (2007). https://doi.org/10.1039/b701600j
7. Gumienna-Kontecka, E., Golenya, I.A., Szebesczyk, A., Haukka, M., Kraemer, R., Fritsky, I.O.: Coordination diversity in mono- and oligonuclear copper(II) complexes of pyridine-2-hydroxamic and pyridine-2,6-dihydroxamic acids. Inorg. Chem. **52**(13), 7633–7644 (2013). https://doi.org/10.1021/ic4007229
8. Lago, A.B., Pasan, J., Canadillas-Delgado, L., Fabelo, O., Casado, F.J.M., Julve, M., Lloret, F., Ruiz-Pérez, C.: A three-dimensional copper(II) 12-metallacrown-4 complex with malonomonohydroxamic acid (H(3)mmh) as a ligand. New J. Chem. **35**(9), 1817–1822 (2011). https://doi.org/10.1039/c1nj20184k
9. Pecoraro, V.L., Stemmler, A.J., Gibney, B.R., Bodwin, J.J., Wang, H., Kampf, J.W., Barwinski, A.: Metallacrowns: a new class of molecular recognition agents. Prog. Inorg. Chem. **45**, 83–177 (1997). https://doi.org/10.1002/9780470166468.CH2
10. Bodwin, J.J., Cutland, A.D., Malkani, R.G., Pecoraro, V.L.: The development of chiral metallacrowns into anion recognition agents and porous materials. Coord. Chem. Rev. **216**, 489–512 (2001). https://doi.org/10.1016/s0010-8545(00)00396-9
11. Happ, P., Plenk, C., Rentschler, E.: 12-MC-4 metallacrowns as versatile tools for SMM research. Coord. Chem. Rev. **289**, 238–260 (2015). https://doi.org/10.1016/j.ccr.2014.11.012
12. Chow, C.Y., Bolvin, H., Campbell, V.E., Guillot, R., Kampf, J.W., Wernsdorfer, W., Gendron, F., Autschbach, J., Pecoraro, V.L., Mallah, T.: Assessing the exchange coupling in binuclear lanthanide(III) complexes and the slow relaxation of the magnetization in the antiferromagnetically coupled Dy-2 derivative. Chem. Sci. **6**(7), 4148–4159 (2015). https://doi.org/10.1039/c5sc01029b
13. Athanasopoulou, A.A., Carrella, L.M., Rentschler, E.: Synthesis, structural, and magnetic characterization of a mixed 3d/4f 12-metallacrown-4 family of complexes. Inorganics **6**, 3 (2018). https://doi.org/10.3390/inorganics6030066

14. Dallavalle, F., Remelli, M., Sansone, F., Bacco, D., Tegoni, M.: Thermodynamics of self-assembly of copper(II) 15-metallacrown-5 of Eu(III) or Gd(III) with (S)-alpha-alaninehydroxamic acid in aqueous solution. Inorg. Chem. **49**(4), 1761–1772 (2010). https://doi.org/10.1021/ic902146d
15. Lim, C.S., Tegoni, M., Jakusch, T., Kampf, J.W., Pecoraro, V.L.: Clarifying the mechanism of cation exchange in Ca(II) 15-MCCu(II)Ligand-5 complexes. Inorg. Chem. **51**(21), 11533–11540 (2012). https://doi.org/10.1021/ic3013798
16. Grant, J.T., Jankolovits, J., Pecoraro, V.L.: Enhanced guest affinity and enantioselectivity through variation of the Gd^{3+} 15-metallacrown-5 side chain. Inorg. Chem. **51**(15), 8034–8041 (2012). https://doi.org/10.1021/ic300110g
17. Jankolovits, J., Lim, C.S., Mezei, G., Kampf, J.W., Pecoraro, V.L.: Influencing the size and anion selectivity of dimeric Ln(3+) 15-metallacrown-5 compartments through systematic variation of the host side chains and central metal. Inorg. Chem. **51**(8), 4527–4538 (2012). https://doi.org/10.1021/ic202347j
18. Jankolovits, J., Kampf, J.W., Maldonado, S., Pecoraro, V.L.: Voltammetric characterization of redox-inactive guest binding to Ln(III) 15-metallacrown-5 hosts based on competition with a redox probe. Chem. Eur. J. **16**(23), 6786–6796 (2010). https://doi.org/10.1002/chem.200903015
19. Sgarlata, C., Giuffrida, A., Trivedi, E.R., Pecoraro, V.L., Areneite, G.: Anion encapsulation drives the formation of dimeric Gd-III 15-metallacrown-5 (3+) complexes in aqueous solution. Inorg. Chem. **56**(9), 4771–4774 (2017). https://doi.org/10.1021/acs.inorgchem.6b03043
20. Codd, R.: Traversing the coordination chemistry and chemical biology of hydroxamic acids. Coord. Chem. Rev. **252**(12–14), 1387–1408 (2008). https://doi.org/10.1016/j.ccr.2007.08.001
21. Muri, E.M.F., Nieto, M.J., Sindelar, R.D., Williamson, J.S.: Hydroxamic acids as pharmacological agents. Curr. Med. Chem. **9**(17), 1631–1653 (2002). https://doi.org/10.2174/0929867023369402
22. Kurzak, B., Kozlowski, H., Farkas, E.: Hydroxamic and aminohydroxamic acids and their complexes with metal-ions. Coord. Chem. Rev. **114**(2), 169–200 (1992). https://doi.org/10.1016/0010-8545(92)85002-8
23. Brown, D.A., Glass, W.K., Mageswaran, R., Girmay, B.: Cis-trans isomerism in monoalkylhydroxamic acids by H-1, C-13 AND N-15 NMR-spectroscopy. Magn. Reson. Chem. **26**(11), 970–973 (1988). https://doi.org/10.1002/mrc.1260261107
24. Fitzpatrick, N.J., Mageswaran, R.: Theoretical-study of hydroxamic acids. Polyhedron **8**, 18 (1989). https://doi.org/10.1016/s0277-5387(00)81252-8
25. Brown, D.A., Coogan, R.A., Fitzpatrick, N.J., Glass, W.K., Abukshima, D.E., Shiels, L., Ahlgren, M., Smolander, K., Pakkanen, T.T., Pakkanen, T. A., Perakyla, M.: Conformational behaviour of hydroxamic acids: ab initio and structural studies. J. Chem. Soc. Perkin Trans. 2 **12**, 2673–2679 (1996). https://doi.org/10.1039/p29960002673
26. Chatterjee, B.: Donor properties of hydroxamic acids. Coord. Chem. Rev. **26**(3), 281–303 (1978). https://doi.org/10.1016/s0010-8545(00)80350-1
27. Farkas, E., Kozma, E., Petho, M., Herlihy, K.M., Micera, C.: Equilibrium studies on copper(II)- and iron(III)-monohydroxamates. Polyhedron **17**(19), 3331–3342 (1998). https://doi.org/10.1016/s0277-5387(98)00113-2
28. Farkas, E., Kiss, T., Kurzak, B.: Microscopic dissociation processes of alaninehydroxamic acids. J. Chem. Soc. Perkin Trans. 2 **7**, 1255–1257 (1990). https://doi.org/10.1039/p2990001255
29. Tegoni, M., Remelli, M., Bacco, D., Marchio, L., Dallavalle, F.: Copper(II) 12-metallacrown-4 complexes of alpha-, beta- and gamma-aminohydroxamic acids: a comparative thermodynamic study in aqueous solution. Dalton Trans. **20**, 2693–2701 (2008). https://doi.org/10.1039/b718765c
30. Tegoni, M., Ferretti, L., Sansone, F., Remelli, M., Bertolasi, V., Dallavalle, F.: Synthesis, solution thermodynamics, and X-ray study of Cu-II 12 metallacrown-4 with GABA hydroxamic acid: an unprecedented crystal structure of a 12 MC-4 with a gamma-aminohydroxamate. Chem. Eur. J. **13**(4), 1300–1308 (2007). https://doi.org/10.1002/chem.200601035

31. Glowiak, T., Koralewicz, M.: Crystal and molecular-structure of glycinehydroxamic acid. J. Crystallogr. Spectrosc. Res. **15**(6), 621–628 (1985). https://doi.org/10.1007/bf01164775
32. Careri, M., Dallavalle, F., Tegoni, M., Zagnoni, I.: Pentacopper(II) 12-metallacrown-4 complexes with alpha- and beta-aminohydroxamic acids in aqueous solution: a reinvestigation. J. Inorg. Biochem. **93**(3–4), 174–180 (2003). https://doi.org/10.1016/s0162-0134(02)00570-6
33. Kurzak, B., Bogusz, K., Kroczewska, D., Jezierska, J.: Mixed-ligand copper(II) complexes with diethylenetriamine and histidine- or methioninehydroxamic acids in water solution. Polyhedron **20**(20), 2627–2636 (2001). https://doi.org/10.1016/s0277-5387(01)00860-9
34. Dallavalle, F., Tegoni, M.: Speciation and structure of copper(II) complexes with (S)-phenylalanine- and (S)-tryptophanhydroxamic acids in methanol/water solution: a combined potentiometric, spectrophotometric, CD and ESI-MS study. Polyhedron **20**(21), 2697–2704 (2001). https://doi.org/10.1016/s0277-5387(01)00886-5
35. Zyrek, M., Gumienna-Kontecka, E., Szewczuk, Z., Fritsky, I.O., Kozlowski, H.: Copper(II)-aminohydroxamate ternary complexes evidenced by mass spectrometry. ARKIVOC **3**, 145–157 (2009). https://doi.org/10.3998/ark.5550190.0010.312
36. Marchio, L., Marchetti, N., Atzeri, C., Borghesani, V., Remelli, M., Tegoni, M.: The peculiar behavior of Picha in the formation of metallacrown complexes with Cu(II), Ni(II) and Zn(II) in aqueous solution. Dalton Trans. **44**(7), 3237–3250 (2015). https://doi.org/10.1039/c4dt03264k
37. Tegoni, M., Dallavalle, F., Belosi, B., Remelli, M.: Unexpected formation of a copper(II) 12-metallacrown-4 with (S)-glutamic-gamma-hydroxamic acid: a thermodynamic and spectroscopic study in aqueous solution. Dalton Trans. **9**, 1329–1333 (2004). https://doi.org/10.1039/b316607d
38. Kornreich-Leshem, H., Ziv, C., Gumienna-Kontecka, E., Arad-Yellin, R., Chen, Y., Elhabiri, M., Albrecht-Gary, A.M., Hadar, Y., Shanzer, A.: Ferrioxamine B analogues: targeting the FoxA uptake system in the pathogenic Yersinia enterocolitica. JACS. **127**(4), 137–145 (2005). https://doi.org/10.1021/ja035182m
39. Sepehrpour, H., Fu, W.X., Sun, Y., Stang, P.J.: Biomedically relevant self-assembled metallacycles and metallacages. JACS. **141**(36), 14005–14020 (2019). https://doi.org/10.1021/jacs.9b06222
40. Remelli, M., Bacco, D., Dallavalle, F., Lazzari, E., Marchetti, N., Tegoni, M.: Stoichiometric diversity of Ni(II) metallacrowns with beta-alaninehydroxamic acid in aqueous solution. Dalton Trans. **42**(22), 8018–8025 (2013). https://doi.org/10.1039/c3dt50370d
41. Bacco, D., Bertolasi, V., Dallavalle, F., Galliera, L., Marchetti, N., Marchio, L., Remelli, M., Tegoni, M.: Metallacrowns of Ni(II) with alpha-aminohydroxamic acids in aqueous solution: beyond a 12-MC-4, an unexpected (vacant?) 15-MC-5. Dalton Trans. **40**(11), 2491–2501 (2011). https://doi.org/10.1039/c0dt00832j
42. Parac-Vogt, T.N., Pacco, A., Gorller-Walrand, C., Binnemans, K.: Pentacopper(II) complexes of alpha-aminohydroxamic acids: uranyl-induced conversion of a 12-metallacrown-4 to a 15-metallacrown-5. J. Inorg. Biochem. **99**(2), 497–504 (2005). https://doi.org/10.1016/j.jinorgbio.2004.10.023
43. Pacco, A., Parac-Vogt, T.N., van Besien, E., Pierloot, K., Gorller-Walrand, C., Binnemans, K.: Lanthanide(III)-induced conversion of 12-metallacrown-4 to 5-metallacrown-5 complexes in solution. Eur. J. Inorg. Chem. **16**, 3303–3310 (2005). https://doi.org/10.1002/ejic.200500241
44. Seda, S.H., Janczak, J., Lisowski, J.: Synthesis and structural characterisation of nickel 15-metallacrown-5 complexes with lanthanide(III) and lead(II) ions: Influence of the central metal ion size on the spin state of peripheral nickel(II) ions. Inorg. Chem. Comm. **9**(8), 792–796 (2006). https://doi.org/10.1016/j.inoche.2006.04.026
45. Kurzak, B., Kamecka, A., Bogusz, K., Jezierska, J.: Coordination modes of histidine- or methioninehydroxamic acids in copper(II) mixed-ligand complexes with ethylenediamine in aqueous solution. Polyhedron **26**(15), 4223–4227 (2007). https://doi.org/10.1016/j.poly.2007.05.024

46. Kurzak, B., Farkas, E., Glowiak, T., Kozlowski, H.: X-ray and potentiometric studies on a pentanuclear copper(II) complex with beta-alaninehydroxamic acid. J. Chem. Soc. Dalton Trans. **2**, 163–167 (1991). https://doi.org/10.1039/dt9910000163
47. Kroczewska, D., Kurzak, B., Jezierska, J.: The role of the carboxylic group in the copper(II) mixed-ligand complexes of DL-aspartic acid-beta-hydroxamic acid and polyamines. Polyhedron **25**(3), 678–686 (2006). https://doi.org/10.1016/j.poly.2005.07.043
48. Kurzak, B., Kamecka, A., Bogusz, K., Jezierska, J.: Unexpected formation of the copper(II) dinuclear mixed-ligand species in the ternary system of N, N, N′, N″, N″-pentamethyldiethylenetriamine with methionine-or histidinehydroxamic acids in aqueous solution. Polyhedron **26**(15), 4345–4353 (2007). https://doi.org/10.1016/j.poly.2007.05.033
49. Gibney, B.R., Kessissoglou, D.P., Kampf, J.W., Pecoraro, V.L.: Copper(II) 12-metallacrown-4—synthesis, structure, ligand variability, and solution dynamics in the 12-mc-4 structural motif. Inorg. Chem. **33**, 4840–4849 (1994). https://doi.org/10.1021/ic00100a006
50. Kurzak, B., Farkas, E., Glowiak, T., Kozlowski, H.: X-ray and potentiometric studies on a pentanuclear copper(II) complex with β-alaninehydroxamic acid. J. Chem. Soc. Dalton Trans. 163–167 (1991). https://doi.org/10.1039/dt9910000163
51. Song, Y., Liu, J.Ch., Liu, Y.J., Zhu, D.R., Zhuang, J.Z., You, X.Z.: Preparation, crystal structures and magnetic properties of 12-metallacrown-4 complexes with the donors on the organic periphery of molecule. Inorg. Chim. Acta **305**, 135–142 (2000). https://doi.org/10.1016/S0020-1693(00)00124-9
52. Jankolovits, J., Kampf, J.W., Pecoraro, V.L.: Isolation of elusive tetranuclear and pentanuclear M(II)-hydroximate intermediates in the assembly of lanthanide 15-metallacrown-5 complexes. Inorg. Chem. **52**(9), 5063–5076 (2013). https://doi.org/10.1021/ic302831u
53. Golenya, I.A., Gumienna-Kontecka, E., Boyko, A.N., Haukka, M., Fritsky, I.O.: Collapsed Cu(II)-hydroxamate metallacrowns. Inorg. Chem. **51**(11), 6221–6227 (2012). https://doi.org/10.1021/ic300387e
54. Johnson, J.A., Kampf, J.W., Pecoraro, V.L.: The preparation of a double metallahelicate containing 28 copper atoms. Angew. Chem. Intl. Ed. **42**, 546–549 (2003). https://doi.org/10.1002/anie.200390157
55. Addison, A.W., Rao, N.T., Reedijk, J., van Rijn, J., Verschoor, G.C.: Synthesis, structure, and spectroscopic properties of copper(II) compounds containing nitrogen–sulphur donor ligands; the crystal and molecular structure of aqua[1,7-bis(N-methylbenzimidazol-2′-yl)-2,6-dithiaheptane]copper(II) perchlorate. J. Chem. Soc. Dalton Trans. **7**, 1349–1356 (1984). https://doi.org/10.1039/dt9840001349
56. Safyanova, I.S., Golenya, I.A., Pavlenko, V.A., Gumienna-Kontecka, E., Pekhnyo, V.I., Bon, V.V., Fritsky, I.O.: Synthesis and molecular structures of Cu-II 15-metallacrown-5 complexes with encapsulated Ca-II, Pr-III and Nd-III Ions. Z. Anorg. Allg. Chem. **641**(12–13), 2326–2332 (2015). https://doi.org/10.1002/zaac.201500255
57. Seda, S.H., Janczak, J., Lisowski, J.: Synthesis and structural characterisation of copper(II) 15-metallacrown-5 complexes with Pb-II, Hg-II, Ag-I, Na-I and Y-III central metal ions. Eur. J. Inorg. Chem. **19**, 3015–3022 (2007). https://doi.org/10.1002/ejic.200600881

Metallacrowns as DNA Binders

Agata Głuszyńska and Bernard Juskowiak

Abstract tMetallacrowns (MCs) due to the enormous structural diversity have found great interest in many areas of fundamental studies and applications. One such fundamental study is research concerning the interaction of MCs with DNA in order to elucidate their potential biological activity. In the earlier reports, most studies have focused on the binding of various MCs (e.g., inverse-9-MC-3, 15-MC-5, or 36-MC-6) with double-stranded DNA. In recent years, new reports appeared about the interaction of MCs (e.g., 12-MC-4, 15-MC-5) with different structural forms of tetraplex DNA known as G-quadruplexes (G4 DNA). Published results have shown that the MC/G4 interactions are dependent on the structure and the net charge of the metallacrown as well as on the particular G4 topology. The research carried out on the group of diverse G-quadruplex structures can demonstrate whether the tested MC compounds are expected to serve in the future as agents in anticancer or gene therapy or as fluorescent probes for structural investigation of G4 DNA or for detection of trace amounts of DNA. The chapter presents the results of the investigation concerning the binding affinity of MCs to various DNA structures using several analytical techniques e.g., UV–Vis spectrophotometry, spectrofluorescence, circular dichroism spectroscopy, and gel electrophoresis.

1 DNA as a Target for Ligand Binding

Completion of the Human Genome Project has brought about great interest in the ligands entering into specific interactions with DNA, both in the bioanalytical aspect (detection and diagnosis of gene sequences or their mutant analogues) and biomedical aspect (new formulations and strategies for the treatment of cancer, viral infections or genetic diseases). Most classical ligands interact with double-stranded DNA, which often is the target for testing the activity of new drugs and compounds with potential biological properties. In recent years attention has been paid to the special role of the

A. Głuszyńska (✉) · B. Juskowiak
Department of Bioanalytical Chemistry, Faculty of Chemistry, Adam Mickiewicz University, Uniwersytetu Poznańskiego 8, 61614 Poznań, Poland
e-mail: aglusz@amu.edu.pl

C. M. Zaleski (ed.), *Advances in Metallacrown Chemistry*,
https://doi.org/10.1007/978-3-031-08576-5_4

triple-stranded DNA helix (triplex) and four-stranded DNA (quadruplex) in cellular processes [1, 2]. Intensive research devoted to developing selective ligands capable of interacting with these DNA structural forms has been initiated [3–10]. Guanine quadruplexes (G-quadruplex, G4, G4 DNA) are non-canonical, folded single- or multi-stranded nucleic acid structures formed from co-planar arrangements of four guanines (G-tetrads), which are stabilized by Hoogsteen-type hydrogen bonds in the presence of selected metal cations (Na^+, K^+) (Fig. 1). The G4 structures can be further stabilized by small organic ligands [3–10]. Depending on the number of strands forming G-quadruplexes, single-, two- or four-molecular quadruplexes can be distinguished. G-quadruplexes show a large structural polymorphism, resulting from different directionality of the strands, G-tetrad arrangement, or the orientation of the loops. Nucleotides in strand domains that do not participate in tetrads form different types of loops that connect tetrads, for example lateral, diagonal, external called propellers or loops in the shape of a V (Fig. 1a–c). All these factors influence the G-quadruplex topology, but the final topology is also affected by the type of cation and its concentration, solution pH, temperature, added solvents or ligands.

The syntheses of new ligands specifically interacting with particular DNA structural forms fit into the trend of research dealing with DNA as a molecular target in the development of anticancer and antiviral drugs, also involved in the regulation of gene expression. Investigation of the processes of such interactions and determination of mechanisms of the above processes should provide interesting experimental material

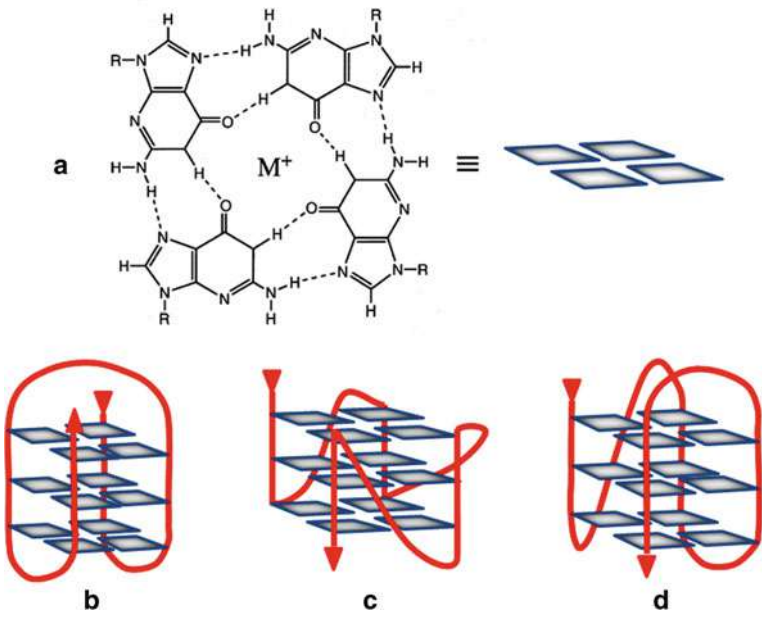

Fig. 1 Structure and schematic illustration of G-tetrad (**a**); Schematic illustrations of typical intramolecular G-quadruplex structures: antiparallel (**b**), parallel (**c**) and hybrid (**d**)

for the design of effective DNA ligands that are potentially active in anticancer or antiviral therapy. Such ligands can be useful as fluorescence probes for structural studies of DNA or detection of trace amounts of nucleic acids. Studying the interactions of ligands with DNA structures such as G-quadruplex bearing the sequence of human telomeric DNA is very important in the context of cancer research. Telomerase, an active enzyme in cancer cells that secures them an unlimited number of replications and "immortality" [11], can be inhibited by ligands interacting with G-quadruplexes [3–5]. The study of the ligand's interaction with G-quadruplexes possessing the sequences of human proto-oncogenes is also very important in the context of research on transcriptional changes by the formation of G-quadruplexes in the promoter region of genes (Fig. 2) [12–14].

The ability of the ligands to form complexes with triple- and tetra-stranded DNA is the first indication of their potential anticancer properties. Since the first literature report on the biological activity of G-quadruplexes (inhibition of human telomerase) in 1997 [16], the number and variety of "G-quadruplex" ligands with potential anticancer properties has increased significantly [3–10]. Due to the confirmation of the hypothesis about the formation of quadruplex structures in vivo, many research groups are still interested in this topic [17–20].

Small organic compounds can non-covalently interact with double-stranded DNA through minor groove binding, intercalation, or electrostatic interactions [21–23]. The structural elements of ligands that bind to the minor groove of double-stranded DNA (dsDNA) are usually non-fused aromatic rings (benzene, pyrrole, furan, pyridine, etc.) connected by single bonds, which allows free rotation of rings around them. These ligands also are able to adapt to the curvature of the small groove (e.g., DAPI, Hoechst 33,258, netropsin, distamycin, berenil) [21]. Due to the differences in the sequence of deoxyribonucleic acids, the properties of their minor grooves are not always the same. The minor groove in the region of GC-rich sequence has less

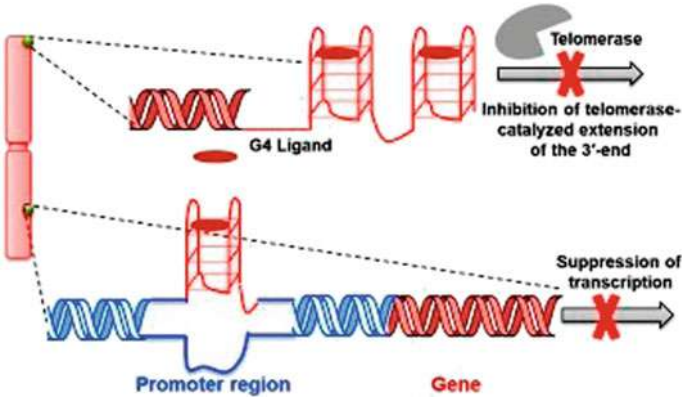

Fig. 2 Schematic representation of the inhibitory effect of G4 ligand on telomerase activity and the effect of G4 ligand on transcription, by the formation of G-quadruplex in the promoter region of the gene. Reproduced with permission from [15]

electronegative potential and is shallower and wider than that in the region of AT sequence (the amino group of guanine creates a steric hindrance in the minor groove). Therefore, the ligands that bind to the minor groove are selective for AT sequence. Another type of interaction with the double-stranded DNA is intercalation. Typical intercalators are planar fused aromatic systems with neutral or cationic substituents, allowing the insertion of ligand between neighboring base pairs. It has been reported that some compounds can bind to the minor groove of AT-rich sequences and intercalate in GC-rich ones. Such a duality of interaction has been reported for berenil, Hoechst 33,258, DAPI or lexitropsin [22, 23].

Sometimes, the ligands of structures typical for intercalating compounds (flat chromophore) bind to the minor groove of DNA rich in AT sequences forming more energetically favorable and more stable ligand-minor groove complexes than those formed by intercalation. Among the compounds showing the duality of interaction with double-stranded DNA depending on the sequence are carbazole derivatives [24].

The positively charged ions and some simple organic compounds can interact with the DNA helix, being a negatively charged polyelectrolyte, by condensing on its outer region as a result of nonspecific interactions, mainly electrostatic in nature. This type of interaction, like binding to a minor or major groove, does not require any helix conformational changes, although the ligand may induce structural changes in the complex formed.

The large structural polymorphism of G-quadruplexes creates the possibility of specific recognition of G4 by small ligands through various binding modes. Planar ligands can interact with G-quadruplex structures by π–π stacking interactions with the external G-quartet motif, comprising four guanine bases hydrogen bonded together in a very stable in-plane layout (*end-stacking*) and/or by binding to grooves or backbone of G4s by nonspecific interactions mainly of the electrostatic nature. The compact architecture of G-quadruplex DNA formed by stacking the planar G-tetrads on top of each other resulted in a stable, rigid and energetically favorable structure, the distortion of which would require a great expenditure of energy. Therefore, most ligands, potential intercalators to double-stranded DNA are unable to insert between G-tetrads and interact with the external tetrads of G4 DNA. However, there are literature reports about the possibility of creating stable intercalated complexes of G4 DNA with porphyrin molecules [25]. Some ligands may facilitate the folding and/or stabilization of G4, others may destabilize them by unfolding, which can influence various biological processes [1].

2 Analytical Techniques for Studying Ligand/DNA Interactions

Among experimental techniques used to study interactions between DNA structures and ligands, the most popular are spectroscopic techniques such as molecular absorption, fluorescence and circular dichroism spectroscopy, or less frequently used mass

spectrometry and nuclear magnetic resonance. At the same time, complementary techniques such as X-ray crystallography, surface plasmon resonance (SPR) spectroscopy, calorimetric techniques (such as differential scanning calorimetry (DSC) and isothermal titration calorimetry (ITC)), viscosity measurement or electrophoresis have found application.

UV–visible spectroscopy is a very useful instrumental method for studying interactions of DNA with ligands due to the availability of spectrophotometers and the simplicity of experiments. Since the intense absorption band of deoxyribonucleic acid occurs in the UV range (~260 nm), the analysis of DNA-ligand interactions in this region is not convenient since most ligands also absorb in the UV region. Fortunately, typically used ligands have additional long wavelength maxima of absorption, characteristic for a given chromophore. Changes in the spectra in the visible range of the ligand in the absence and the presence of DNA may be manifested by the hypo- or hyperchromic effect with a shift in the absorption maximum. The magnitude of these changes provides qualitative information about the strength of the ligand-DNA interaction, but also allows to receive quantitative data such as stoichiometries and binding constants. For the typical intercalation binding modes, red shifts (at least 15 nm) and large hypochromicities (at least 35%) are generally observed and these values are determined for long pieces of duplex DNA [26, 27].

At the same time, the course of the spectrophotometric titration experiment can provide valuable information about the equilibrium between free and DNA-complexed ligands. The appearance of a clear isosbestic point for recorded titration spectra indicates the presence of only two forms of the compound—free and bound ligand. At this point, both forms exhibit the same molar absorption coefficient. The lack of such a point may be caused by sample dilution during spectrophotometric titration or light scattering due to increasing DNA concentration. The lack of a clear point may also be the result of the complex modes of ligand-DNA interactions. Unfortunately, if the value of the molar absorption coefficient of the ligand is too low, the application of spectrophotometry to study binding equilibria and analysis of the titration results is difficult since it requires the use of high concentration of reagents (e.g., metallacrowns represent this type of ligands). In such cases, other analytical techniques, based on direct and indirect methods, should be used.

In the study of the interaction of ligands with DNA, the UV–Vis spectroscopy very often provides information about the thermal stabilization (or destabilization) of the nucleic acid structure by the ligand under investigation. Determination of thermal stability of DNA formed in the presence of each ligand is compared to that for DNA alone. Briefly, the effect of ligand can be assessed by recording melting profiles (T_m) based on changes in absorbance as a function of temperature at 260 nm for double-stranded DNA and 295 nm for G-quadruplex structures [28]. UV–Vis-monitored melting experiments are more often carried out with duplex DNA than with G4 DNA because the temperature induced hyperchromicity (at 260 nm) for duplex DNA is much higher than hyperchromicity (at 260 nm) or hypochromicity (at 295 nm) for G-quadruplex DNA. In the case of ligands stabilizing a specific DNA structure, an increase in T_m of the ligand-DNA complex is observed compared to DNA alone, while when T_m is lower, the ligand destabilizes the DNA structure.

One of the most important methods for studying interactions of DNA with ligands is fluorescence spectroscopy. Fluorescence methods are characterized by high sensitivity, accuracy and selectivity. The wide use of fluorescence is due to the possibility of studying the interactions of fluorescent ligands (direct method as e.g., titration of the ligand with DNA) and ligands that do not possess such properties (indirect methods as e.g., fluorescent intercalator displacement (FID) assays or methods for measurement of the ligand quenching effect on the Tb^{3+}/G4 luminescence). Using the fluorescence titration experiments, the binding affinity of ligands to DNA can be studied. FID is especially useful for the systems, in which ligands show no fluorescence properties, or their spectral properties are not so efficiently affected by interaction with DNA and when the ligands' molar absorptivity is low [29, 30].

Fluorescence intercalator displacement assay is a technique to study the selectivity of ligands to different structures of nucleic acids. It belongs to the family of the indicator- displacement assays (IDAs) [31]. The idea of the technique is very simple—an indicator non-covalently bound to the receptor is displaced by a more strongly binding competitive analyte introduced to the system (Fig. 3). In the FID method, it is necessary to select the appropriate dye.

The most often used are two well-known compounds: ethidium bromide (EtBr) and thiazole orange (TO). First of them is widely used to stain DNA in gel electrophoresis. This intercalating agent has carcinogenic properties, and shows a weak fluorescence quantum yield in aqueous solution and 25-fold enhancement of fluorescence upon dsDNA binding. EtBr shows high affinity to double-stranded DNA and low affinity to G-quadruplex DNA [32]. Thiazole orange (TO, free dye quantum

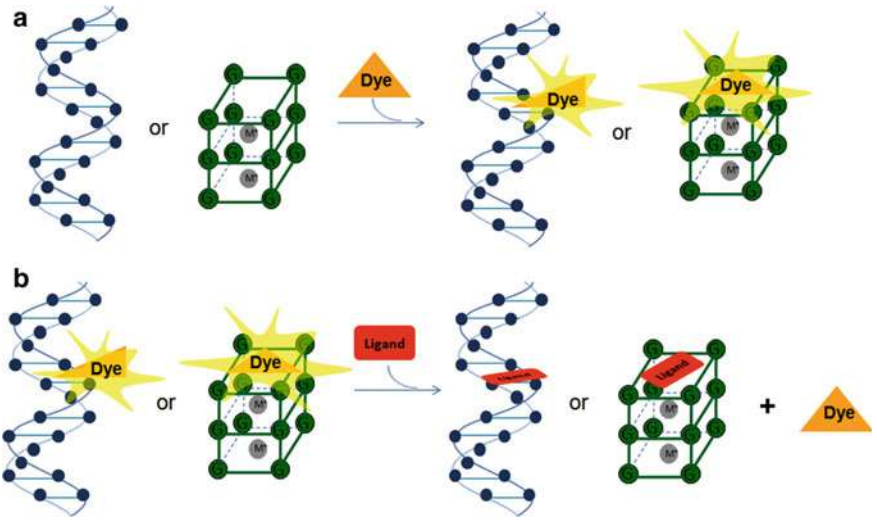

Fig. 3 The scheme of dye binding with double-stranded and G-quadruplex DNA. The fluorescence of the dye is greatly increased while bounded with DNA (**a**). In the presence of Ligand, dye is displaced from nucleic acid and the fluorescence of the system decreases (**b**)

yield 2×10^{-4} [33]) performs well as a light-up fluorescent probe in applications with higher order nucleic acids. TO binds with a much higher affinity to triplex and G-quadruplex DNA structures than to the double-stranded DNA [34]. It is generally accepted that the binding mode of TO with double-stranded DNA relies on intercalation, while with G-quadruplex via the end-stacking interaction with external guanine tetrad [35].

If during the titration experiment of the EtBr/dsDNA complex with a ligand of interest ($\lambda_{ex} = 540$ nm, $\lambda_{em} = 600$ nm) a successive lowering of this intense emission band is observed with subsequent additions of tested ligand, then one can confirm the replacement of the EtBr dye from the complex by the competitive compound [36]. Similarly, if such an effect is observed in a related experiment with the TO/G4 DNA complex ($\lambda_{ex} = 480$ nm, $\lambda_{em} = 530$ nm), it also confirms that TO is replaced by the competing analyte.

Another indirect approach is based on the quenching effect of the ligand on the luminescence of the G4/Tb^{3+} complex [37]. This lanthanide ion is able to mediate the formation of a G-quadruplex structure (binding constant of 5×10^6 M^{-1}) [37]. In aqueous solution emission of Tb^{3+} ion is very weak due to the quenching by water OH oscillators. In the presence of DNA, luminescence is enhanced as a result of the formation of the Tb^{3+}/G4 complex (shielding of Tb(III) ion). The highest luminescence is observed at a fourfold molar excess of Tb^{3+} ions [37]. The Tb^{3+} ion, being a template, is wrapped with the oligonucleotide strand. As result, it is located in the central G4 channel and is protected against quenching by water molecules. Additionally, an efficient energy transfer takes place from the nucleic bases (energy donor) to the terbium ion (acceptor) ($\lambda_{ex} = 290$ nm, $\lambda_{em} = 548$ nm). This effect increases the intensity of Tb luminescence bands and was already used in bioanalytical applications [38, 39].

Another very important technique that provides insight into DNA structural features is circular dichroism (CD) spectroscopy. CD is used to determine the absolute molecular structure of molecules (configuration), as well as to study the chiral conformation of molecules and macromolecules, in particular, peptides, proteins, and nucleic acids [40]. CD measurements are used in the study of conformational changes of DNA, such as denaturation, B/A or B/Z form transformation, and distinction of double-stranded DNA from triple- or four-stranded forms. This method has found wide application in the study of nucleic acid interactions with small molecules (ligands or drugs) containing chromophores. Circular dichroism spectroscopy provides valuable information concerning the formation, stability and topology of DNA molecules. This is also an excellent technique for the determination of ligand binding mode with duplex and G-quadruplex DNA. In most cases the studied ligands are achiral, so they do not exhibit CD activity in solution. However, when they bind to a chiral host such as DNA, CD negative or positive signals can be induced (ICD) in the long wavelength region where ligands possess absorption bands. The shape and intensity of the ICD band of the bound ligand is a valuable diagnostic of the orientation of the chromophore with respect to the longitudinal axis of the DNA base pairs. The intercalated chromophore should exhibit a negative ICD for an electron transition polarized parallel to the long axis of the base pair plane,

while a positive ICD is expected for orthogonal orientation. In many cases, the intercalation to dsDNA and end-stacking interaction to G4 DNA results in a complicated ICD spectrum. It is often the effect of the multiple binding geometries of ligands, whose low intensity positive and negative bands cancel each other out as a result of overlapping. Therefore, for such interactions, these ICD bands are invisible or only weak induced negative bands are observed. [41, 42].

A strong positive ICD band indicates ligand binding to the minor groove of the double-stranded DNA [43]. Groove binding for G4 DNA is generally indicated by the presence of a small positive induced CD signal [44]. Sometimes, G-quadruplex/ligand assemblies generate strong induced exciton CD signals, suggesting binding of aggregated ligand complex or complexes [43]. The large magnitude of such signals may also suggest complex formation in more than one groove. Therefore the lack of positive induced signals rather excludes the groove binding of ligands to double-stranded and G-quadruplex DNA structures.

In the study of the interaction of ligands with DNA, circular dichroism spectroscopy can also be used to get information about the stabilization (or destabilization) of the nucleic acid structure by the studied ligand. Determination of thermal stabilization of DNA structure formed in the presence of ligand versus that for DNA alone is realized by recording melting profiles (T_m) [45]. The melting profiles are recorded using the temperature dependence of ellipticity at the wavelength corresponding to the maximum of a CD band characteristic for a particular DNA structure: for duplex at 275 nm and for G-quadruplex depending on topology (at 265 nm for parallel structure and 295 nm for antiparallel or hybrid structures).

Another technique exploited to study DNA/ligand interaction is gel electrophoresis (GE). GE approach allows the separation of molecules according to their size, shape, and charge [46]. In DNA/ligand studies by GE, a supercoiled plasmid DNA or calf-thymus DNA (ctDNA) are often used. Carrying out a gel electrophoresis experiment for supercoiled plasmid DNA in the presence of ligand one can obtain proof for intercalation binding mode since intercalated ligand unwinds supercoiled DNA, thus producing species with different electrophoretic mobility. Additionally, such an approach may answer the question whether the compound possesses nuclease activity, i.e., is it capable of cleaving a supercoiled DNA into nicked forms. When supercoiled form [CC] of plasmid DNA (pDNA is cleaved by the ligand, additional bands on the electrophoregram appear that correspond to the relaxed (open circular, [OC]) or linear [LC] forms of plasmid DNA.

An additional technique that allows to confirm the intercalation of test compounds to DNA is viscometric titration. Intercalation requires appropriate local helix unwinding so that the planar intercalator can slip between the base pairs. This process is accompanied by an effective elongation of the DNA strand, in proportion to the number of intercalated ligand molecules. The viscosity of the biopolymer solution is directly correlated with the conformation of the polymer chain and thus with its length. Therefore, an increase in the relative viscosity of the DNA solution as a function of increasing ligand concentration is evidence of the formation of intercalation

complexes, since ligand binding to the minor groove does not change the conformation of the DNA helix. Both linear and circular DNA can be used in these measurements. The latter is based on the effect of intercalation on the super-helical structure of DNA, the process that was also exploited in GE experiments described above. Supercoiled circular DNA has a compact, quasi-linear structure. The complexation of successive intercalator molecules causes the thread to unwind and eliminate supercoils. Thus, the supercoiled DNA relaxes and changes its hydrodynamic contour. This process is accompanied by marked changes in the viscosity of the solution.

3 Metallacrown Complexes with DNA

The DNA ligands, which are small organic molecules, include a subgroup of those containing metal ions in their structure. Literature reports from recent years indicate that complex compounds of ruthenium, copper, platinum, titanium, vanadium, rhodium or cobalt interact with DNA by different binding modes [47–49]. Literature reports from the last ten years have indicated that the ligands containing the bivalent metal ions Cu(II), Pt(II), and Zn(II) in their structure showed enhanced binding affinity and selectivity to various G-quadruplexes of DNA [50–52]. Trivalent metal complexes advised as G4 ligands also showed specific binding affinities [51, 53]. Not only *d*-block metal ions are used to form G-quadruplex ligands. Also, the lanthanide metal complexes have found applications for the detection of nucleic acids and G-quadruplexes [54].

One of the groups of metal complexes are metallacrowns (MCs), inorganic analogues of organic crown ethers, consisting of metal ions (from transition (d) to lanthanide (f) elements) and bridging organic ligands. Since the discovery of the first MC by Pecoraro and Lah [55, 56], various types of metallacrowns from 8-MC-4 to 60-MC-20 have been developed, with the connections of the rings consisting of several motifs: [M–N–O], [M–N–N], [M–N–C–O], and [M–N–C–N] [57–60]. Numerous structures have been also reported, in which MCs are stacked and combined to form dimeric, one- (1D), two- (2D), or three-dimensional (3D) assemblies [60]. The structure of MC compounds with a central cavity favors encapsulation of cations or anions. This capability to form complexes with different species depends on the orientation of atoms in the metallacrown ring.

Although there are scientific reports concerning the ability of metallacrowns to bind to biomolecules such as double-stranded DNA [61–67], studies on the interaction of MCs with higher order DNA structures come only from the research group of Juskowiak [68–70].

3.1 Metallacrowns as Double-Stranded DNA Ligands

In 2003, the first literature report about the impact of four metallacrowns on plasmids pUC19 and pTZ18R isolated from *E. coli* XL1, has been published [61]. The following MCs were examined: three tetranuclear vacant metallacrowns with mixed ligand composition [12-$MC_{Ni(II)N(Hshi)2(pko)2}$-4]$(SCN)_2$(*dmf*)$(CH_3OH)$ **1**, [12-$MC_{Ni(II)N(Hshi)2(pko)2}$-4]$(NNN)_2$(*dmf*)$(CH_3OH)$ **2**, [12-$MC_{Ni(II)N(Hshi)2(pko)2}$-4]$(OCN)_2$(*dmf*)$(CH_3OH)$ **3**, and a pentanuclear mixed ligand $[Ni(AcO)_2]$[12-$MC_{Ni(II)N(shi)2(pko)2}$-4] (H_2O) **4** metallacrown (Fig. 4).

Nickel compounds have been found to show a wide spectrum of biological activity [71]. Nickel, due to its chemical nature, can form covalent bonds with DNA nucleobases through nitrogen and oxygen atoms, or through phosphate oxygens. Therefore, the authors investigated the influence of the synthesized Ni(II) MCs on the integrity and electrophoretic mobility of nucleic acids. The pentanuclear mixed $[Ni(AcO)_2]$[12-$MC_{Ni(II)N(Hshi)2(pko)2}$-4] (H_2O) **4** metallacrown did not affect the electrophoretic mobility of supercoiled or relaxed pDNA regardless of the concentration used (up to 1.2 mM). The three tetranuclear metallacrowns altered pDNA mobility to form high molecular weight concatamers (DNA molecules made of identical sections connected with each other on the head–tail principle) at low concentrations or precipitates at higher concentrations. The latter phenomenon may be related to the bridge formation between guanine–Ni(II)–guanine, because a similar effect for Ni(II) ions interacting with guanine in poly(dG-dC) even at very low concentrations (0.5 mM) has been reported [72]. In the tested metallacrowns the distance between two square planar nickel atoms of 4.8 Å (vide infra) may favor Ni (II) interaction with DNA, thereby altering pDNA mobility.

Copper is an element used both in the process of hematopoiesis and in the production of connective and bone tissue. Being a component of many enzymes, it plays an

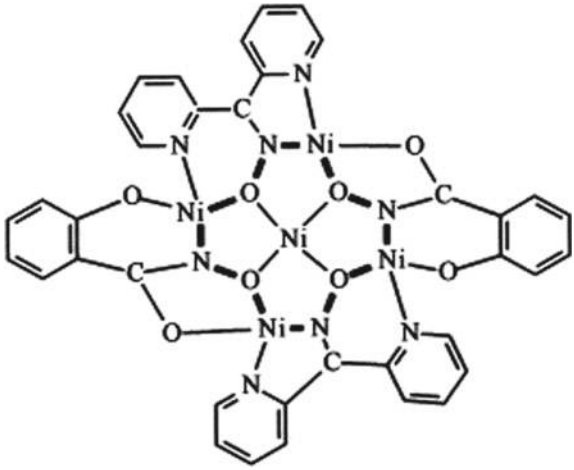

Fig. 4 Drawings showing the connectivity pattern and the arrangement around the nickel ions for the metallacrown $Ni(OAc)_2$[12-$MC_{Ni(II)N(shi)2(pko)2}$-4] **4**. Reproduced with permission from [61]

important role in lipid metabolism and the proper functioning of nervous tissue, as in the cellular respiration pathway. Copper compounds can generate the formation of reactive oxygen species (ROS), e.g., hydroxyl (OH) and superoxide (O_2^-) radicals that might damage biomolecules like DNA, proteins, and lipids. That ability of copper compounds increases significantly in the presence of oxidants, such as e.g., hydrogen peroxide [73]. The syntheses of copper inverse metallacrowns 9-MC-3: inverse-{(μ_3-OH)[9-$MC_{Cu(II)N(PhPyCNO)}$-3] (2,4,5-T)$_2$}, (2,4,5-TH = 2,4,5-trichlorophenoxyacetic acid) **5** (Fig. 5a) [74], inverse-{(μ_3-OCH_3)[9-$MC_{Cu(II)N(PhPyCNO)}$-3](Cl)(ClO_4)} **6** (Fig. 5b) [75] and inverse-{(μ_3-OH)[9-$MC_{Cu(II)N(PhPyCNO)}$-3](CH_3OH)$_2$(ClO_4)$_2$} **7** (Fig. 5c) [75] have been reported and their interaction with calf-thymus DNA has been investigated using UV–Vis spectrophotometry, fluorescence, and gel electrophoresis [62].

The inverse motif of these metallacrowns is constructed by the repeating pattern [–O–N–M–], as in the regular motif of the metallacrown ring, but the metal atoms are oriented towards the center of the cavity. Cations can be accommodated in the central cavity of regular metallacrowns, whereas the inverse metallacrowns can bind anions. The absorption band of copper complexes at ~345 nm, changed dramatically upon the addition of ctDNA, and strong hypochromicity (40–55%) with small red or blue shifts ($\Delta\lambda$ = 3–10 nm) were observed (Fig. 6). High values of hypochromicity and red shifts indicated strong stacking interactions between the aromatic chromophore and the base pairs of DNA, characteristic of intercalative binding mode [22, 23].

At the same time, for the long wavelength maxima of absorption spectra at about 650 nm, characteristic of d–d absorption band of copper complexes, the gradual hypochromism and a blue shift were observed. There was also a new band at around 980 nm with the simultaneous appearance of an isobestic point at ~910 nm (Fig. 7). It may be related to the interaction of inverse-{(OH)[9-$MC_{Cu(II)N(PhPyCNO)}$-3]}-DNA with ctDNA by intercalation leading to hydrolytic cleavage of DNA, that may be assigned to the presence of the hydroxyl group in the inverse metallacrown ring.

The indirect fluorescent method, fluorescence intercalator displacement assay (FID), with ethidium bromide (EtBr), was also used to confirm the DNA binding

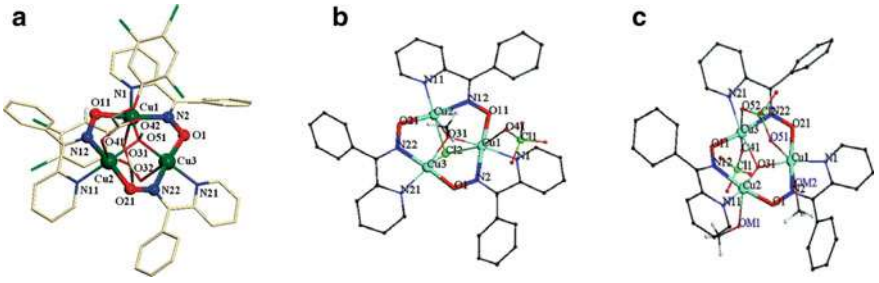

Fig. 5 X-Ray crystal structures of inverse-{(μ_3-OH)[9-$MC_{Cu(II)N(PhPyCNO)}$-3] (2,4,5-T)$_2$} **5** (**a**), inverse-{(μ_3-OCH_3)[9-$MC_{Cu(II)N(PhPyCNO)}$-3](Cl)(ClO_4)} **6** (**b**) and inverse-{(μ_3-OH)[9-$MC_{Cu(II)N(PhPyCNO)}$-3](CH_3OH)$_2$(ClO_4)$_2$} **7** (**c**). Reproduced with permission from [74] and [75]

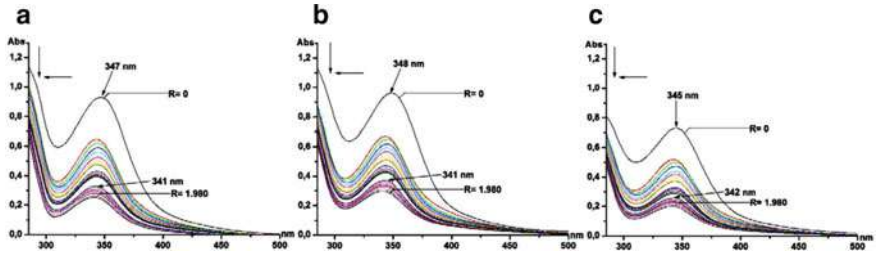

Fig. 6 Absorption spectra in the UV region of inverse-{(μ_3-OH)[9-MC$_{Cu(II)N(PhPyCNO)}$-3] (2,4,5-T)$_2$} **5** (**a**), inverse-{(μ_3-OCH$_3$)[9-MC$_{Cu(II)N(PhPyCNO)}$-3](Cl)(ClO$_4$)} **6** (**b**) and inverse-{(μ_3-OH)[9-MC$_{Cu(II)N(PhPyCNO)}$-3](CH$_3$OH)$_2$(ClO$_4$)$_2$} **7** (**c**) in the absence and presence of increasing amounts of ctDNA. [complex] = 2.5×10^{-5} M, R = [DNA]/[complex]. Arrows show the absorbance changes upon increasing ctDNA concentration. Reproduced with permission from [62]

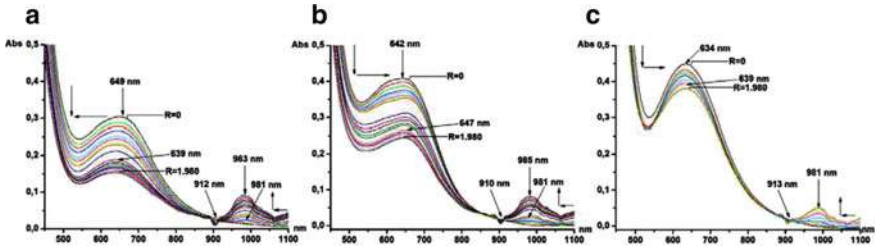

Fig. 7 Absorption spectra in the Vis region of inverse-{(μ_3-OH)[9-MC$_{Cu(II)N(PhPyCNO)}$-3] (2,4,5-T)$_2$} **5** (2) (**a**), inverse-{(μ_3-OCH$_3$)[9-MC$_{Cu(II)N(PhPyCNO)}$-3](Cl)(ClO$_4$)} **6** (**b**) and inverse-{(μ_3-OH)[9-MC$_{Cu(II)N(PhPyCNO)}$-3](CH$_3$OH)$_2$(ClO$_4$)$_2$} **7** (**c**) in the absence and presence of increasing amounts of ctDNA. [complex] = 5×10^{-4} M, R = [DNA]/[complex]. Arrows show the absorbance changes upon increasing ctDNA concentration. Reproduced with permission from [62]

of MCs. This fluorescent dye non-covalently bound to the double-stranded ctDNA was competitively displaced by all tested metallacrowns. At low molar ratios of MCs, quenching of the ctDNA-EtBr fluorescence was observed. At higher molar ratios of MCs: DNA, the enhancement of EtBr fluorescence was observed, with the shift of the emission maximum and the appearance of an additional shoulder on the emission band. Authors speculated that it may be due to the re-intercalation of EtBr between base pairs with the simultaneous formation of new DNA complexes. These results are consistent with those obtained in spectroscopic titration studies of copper(II) complexes with DNA. The quenching efficiency for each MC complex was evaluated by the Stern–Volmer constant, K_{sv}. The values of the K_{sv} constants indicate strong interaction of the complexes with DNA, which confirms the results obtained with the use of UV–Vis absorption spectroscopy. The ability of the metallacrown complexes to affect DNA cleavage was also investigated by gel electrophoresis. The nuclease activity of MCs was checked using supercoiled plasmid pET29c DNA. All MC complexes, at low cluster concentrations, were capable of binding to plasmid DNA. At higher cluster concentrations compounds showed pronounced chemical

nuclease activity causing the complete degradation of pDNA. The strong chemical nuclease activity of inverse-{(μ_3-OCH_3)[9-$MC_{Cu(II)N(PhPyCNO)}$-3](Cl)(ClO_4)} **6** and inverse-{(μ_3-OH)[9-$MC_{Cu(II)N(PhPyCNO)}$-3]($CH_3OH)_2(ClO_4)_2$} **7** may be comparable to that of enzymatic nucleases.

Other inverse-9-metallacrown-3 compounds that interact with calf-thymus DNA by intercalation were also identified: [inverse-{(μ_4-O)[9-$MC_{Cu(II)N(PhPyCNO)}$-3]}(NO_3)]$_2$, **8** (Fig. 8a) and inverse-{(μ_3-OH)-[9-$MC_{Cu(II)N(PhPyCNO)}$-3](dicl)$_2$}·MeOH·0.5H_2O **9** (Fig. 8b), accommodating $dicl^-$ (diclofenac) or NO_3^- anions.

The interaction of metallacrowns **8** and **9** with ctDNA was monitored by the use of UV–Vis and fluorescence spectroscopy, DNA viscosity measurements, and electrochemical technique [63]. The interaction was first investigated using visible absorption spectral titrations. The UV–Vis spectra of the free MCs in the range from 260 to 420 nm exhibit two absorption bands centered at about 280 and 340 nm, these bands can be assigned to the intraligand transition of the coordinated groups of the ligands [76]. Absorption titration spectra of MC complexes with increasing amounts of ctDNA were different from the initial spectra. Upon addition of ctDNA, both the bands of [inverse-{(μ_4-O)[9-$MC_{Cu(II)N(PhPyCNO)}$-3]}(NO_3)]$_2$ **8** at 288 nm and 340 nm were red-shifted (2 nm) and blue shifted (7 nm), respectively. The additional effect observed during these experiments was the slight (up 8%) and a more intense (~30%) hypochromism, respectively for the short- and long wavelength bands. In the UV spectrum of inverse-{(μ_3-OH)-[9-$MC_{Cu(II)N(PhPyCNO)}$-3](dicl)$_2$}·MeOH·0.5H_2O **9**, the band at 287 nm presents a significant hyperchromism, while the changes in the band at 347 nm are comparable to the changes of long wavelength bond of the first complex and are accompanied by blue shift and hypochromic effect.

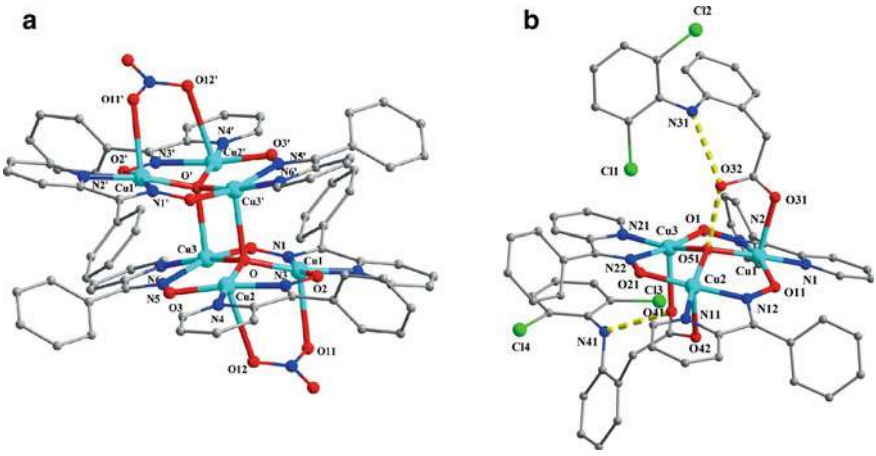

Fig. 8 The molecular structures of complexes **8** (**a**) and **9** (**b**). Primed (‘) atoms are generated by the symmetry operation: –*x*, –*y*, 1 – *z* (**a**). The dashed yellow lines indicate intramolecular hydrogen bonds (**b**). Hydrogen atoms are omitted for clarity. Reproduced with permission from [63]

The investigation of MC-DNA interaction was also monitored using the FID method with ethidium bromide as a fluorescent dye. To the EtBr-DNA complex, showing an intense fluorescence emission band at 592 nm, metallacrown portions were added. The observed quenching (up to 79.8% for **8** and 61.5% for **9**) suggested that complexes **8** and **9** could displace EtBr from EtBr–DNA complex, indicating an interaction with double-stranded DNA by intercalation (Fig. 9).

The fluorescence quenching data were also analyzed by the Stern–Volmer equation [36]. A linear Stern–Volmer plot with MCs proved the displacement of EtBr from EtBr–DNA complex by each tested compound. The viscosity of ctDNA solution in the presence of subsequent additions of the MC complexes significantly increased. This change in viscosity due to the increase in the DNA length confirmed the interaction of MCs with ctDNA by intercalation. Cyclic voltammetry was also used to study the interaction of inverse-9-metallacrown-3 compounds with ctDNA. This technique works well for studies on the electroactive ligands with DNA. When a metal complex intercalates between DNA base pairs, the electrochemical potential will show a positive shift, while in the case of electrostatic interaction the potential will turn in a negative direction. Simultaneous occurrence of negative and positive shifts of two independent potentials shows that the molecule can bind to DNA in two modes—through intercalation and electrostatic interactions [77, 78]. The additions of ctDNA to the MC complexes resulted in a decrease in the current intensity, which may indicate the existence of an equilibrium mixture of free and DNA bound complexes on the electrode surface. Increasing amounts of ctDNA caused a positive shift of the cathodic and the anodic potentials. Thus, all conducted experiments have shown that most likely there is an intercalation mode of interaction between the MC complexes and ctDNA.

The inverse-[9-MC-3]-metallacrowns manganese complexes were also reported to interact with double-stranded DNA [64]. The hexanuclear complexes

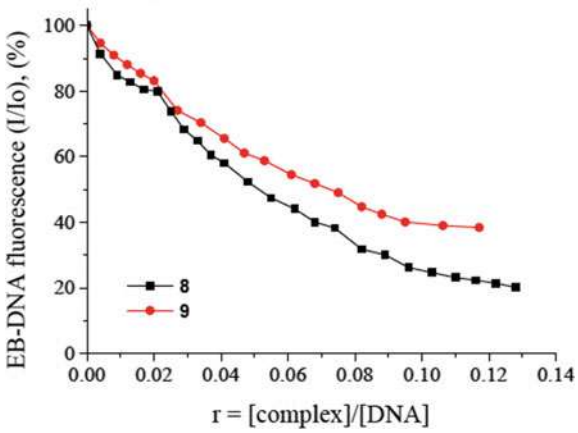

Fig. 9 Plot of EB relative fluorescence intensity at λ_{em} = 592 nm (%) versus r (r = [complex]/[DNA]) (150 mM NaCl and 15 mM trisodium citrate at pH = 7.0) in the presence of complexes **8** and **9** (up to 20.2% of the initial EtBr–DNA fluorescence intensity for **8** and 38.5% for **9**). Reproduced with permission from [63]

[inverse-{(μ_3-O)[9-$MC_{Mn(III)N(sao)}$-3](dicl)$_2$}$(CH_3OH)_6]_2$, **10** and [inverse-{(μ_3-O)[9-$MC_{Mn(III)N(sao)}$-3](indo)$_2$}$(H_2O)_4]_2$, **11** [79], with the non-steroidal antiinflammatory drugs (NSAIDs) as ring ligands: sodium diclofenac (Nadicl) and indomethacin (Hindo) and in the presence of salicylaldoxime (H_2sao), have been synthesized and studied as potential intercalators to double-stranded DNA (Fig. 10).

Manganese was chosen as the metal whose complexes show biological activity: anticancer, antimicrobial, antifungal, or antioxidant [64]. CtDNA was chosen as the molecular target and the interactions with Mn MCs were studied using UV–Vis spectroscopy, competitive studies with ethidium bromide and DNA-viscosity measurements. The maxima of absorption spectra at ~290 and ~380 nm, characteristic for intraligand transitions of the coordinated groups of NSAID ligands, changed dramatically upon the addition of ctDNA, and the bathochromic shifts ($\Delta\lambda = 2$–8 nm) and hypochromicity (17–35%) were observed. The bathochromic shifts occurred only for $\lambda_{max} = 289$ nm and 314 nm, respectively for complexes **10** and **11**, because the long wavelength maxima of absorption at ~380 nm disappeared during the titration experiments. Generally, similar changes were observed in the UV–Vis spectra of both complexes upon the addition of ctDNA with less pronounced hypochromism for complex **11**. The observed spectral changes—hypochromism and red shifts, indicated π-π stacking interaction between DNA bases and the aromatic chromophore of MC complexes that is, probably interaction by intercalation. The values of DNA-binding constants (K_b) for the DNA-MCs were calculated by the Wolfe-Shimer equation [80]. The obtained binding parameters were relatively high. The K_b constant for complex DNA/**11** (1.10 (±0.08) × 10^6 M^{-1}) was 20-times higher than K_b constant for complex DNA/**10** (5.34 ± 0.11 × 10^4 M^{-1}) and 10-times higher than the K_b constant calculated for classical intercalator EtBr (1.23 ± 0.07 × 10^5 M^{-1}) [81]. The indirect competitive studies for complexes of **10** and **11** with ethidium bromide

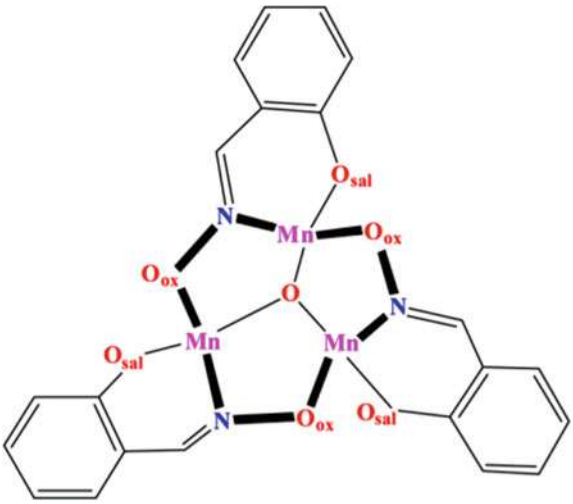

Fig. 10 [9-MC-3] metallacrown ring found in the structures of complexes **10** and **11**. Reproduced with permission from [79]

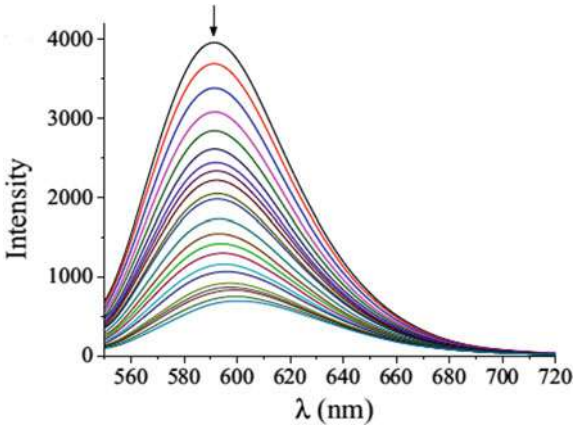

Fig. 11 Fluorescence emission spectra (λ_{ex} = 540 nm) for EB-DNA ([EB] = 20 μM, [DNA] = 26 μM) in buffer solution in the absence and presence of increasing amounts of complex **10** (up to the value of $r = 0.22$). The arrow shows the changes of intensity upon increasing amounts of **10**. Reproduced with permission from [64]

were performed in order to examine whether the MCs interact with ctDNA by intercalation binding mode. The addition of each non-fluorescent compound to ctDNA-EtBr conjugate caused quenching of EtBr fluorescence, which was related to the displacement of EtBr from the MC complexes (Fig. 11).

Another method used to clarify the binding mode of MCs was viscosity measurements. The addition of the tested compounds to the DNA solution resulted in a significant increase in the relative DNA viscosity. Such changes are associated with an increase in the overall DNA length due to intercalation. Thus, the results obtained using three different analytical techniques suggested that intercalation was the most possible DNA binding mode for these manganese MCs.

Metallacrowns with the 15-MC-5 structure have also been tested as potential intercalators in the interaction with ctDNA. The six complexes {La(III)(OAc)$(H_2O)_2$[15-$MC_{Cu(II)N(glyha)}$-5]$(H_2O)_4$}·2NO_3·5H_2O **12** (Fig. 12), {Gd(III)(OAc)(H_2O)[15-$MC_{Cu(II)N(glyha)}$-5]$(H_2O)_3$}·2NO_3·5H_2O **13**, {Tb(III)(OAc)(H_2O)[15-$MC_{Cu(II)N(glyha)}$-5]$(H_2O)_4$}·2NO_3·4H_2O **14**, {Pr(III)$(NO_3)(H_2O)_2$[15-$MC_{Cu(II)N(glyha)}$-5]10(H_2O)}·2NO_3·8H_2O **15**, {Nd(III)$(NO_3)(H_2O)_2$[15-$MC_{Cu(II)N(glyha)}$-5]$(H_2O)_2$}·2NO_3·7H_2O **16** and {Sm(III)$(NO_3)(H_2O)_2$[15-$MC_{Cu(II)N(glyha)}$-5]$(H_2O)_2$}·2NO_3·6H_2O **17** (glyha^{2-} = dianion glycinehydroxamic acid) were investigated by fluorescence and circular dichroism (CD) spectroscopy [65].

The studies showed that all examined MCs displaced EtBr from the EtBr-DNA system, which is manifested by the quenching of the system's fluorescence and proved the intercalation of metal complexes to DNA. The data were also analyzed through the Stern–Volmer equation and the obtained values of K_{sv} for tested complexes suggest a strong intercalation interaction [82], compared to other complexes [62]. The complexes showed comparable DNA binding ability except for the {Tb(III)(OAc)(H_2O)[15-$MC_{Cu(II)N(glyha)}$-5]$(H_2O)_4$}·2NO_3·4H_2O **14** compound. Among the examined MCs, Tb(III) complex presents higher rigidity and bigger steric hindrance, because of the smallest radius of Tb(III) ion. It is a disadvantage for the intercalation DNA binding because the compound is not flat, contrary to

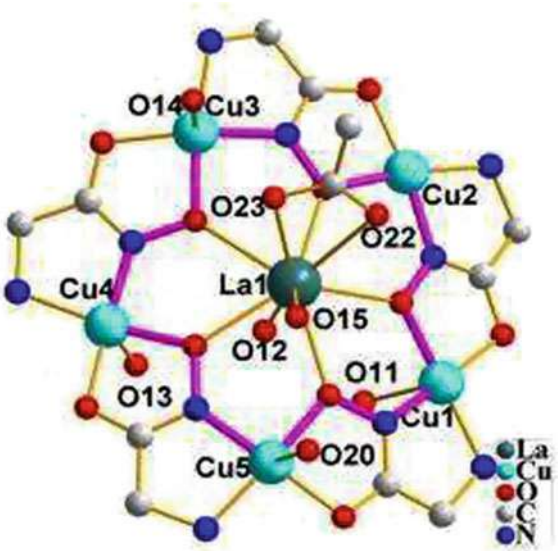

Fig. 12 The molecular structure of complex **12**. Reproduced with permission from [65]

well-known intercalators. CD spectroscopy has been used to clarify the effect of the complexes on the double-stranded DNA helix. The CD spectrum of ctDNA in Tris HCl buffer (pH 7.2) is dominated by a strong positive band at 275 nm and a strong negative at 245 nm, due to base stacking and right-handed helicity of B-DNA form [83]. In general, the addition of ligand does not affect the positions of CD peaks, but a decrease in the intensity of CD signals suggests ligand-dependent perturbation of DNA structure (Fig. 13). Such effects were observed for tested MCs and these changes suggested that the DNA helix conformation was disturbed by intercalation binding of MC complexes to ctDNA [84, 85].

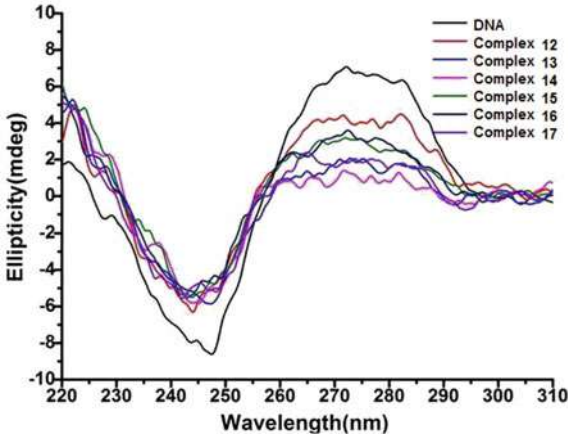

Fig. 13 CD spectra of 100 μM ctDNA in the absence and presence of 0.2 μM complexes **12–17**. Reproduced with permission from [65]

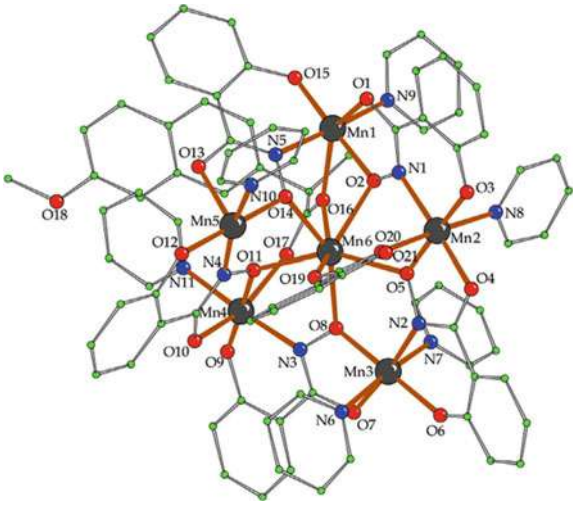

Fig. 14 Molecular structure of complex **18**. Hydrogen atoms are omitted for clarity. Reproduced with permission from [66]

With ctDNA also interact manganese15-MC-5 metallacrowns hosting tolfenamic acid (Htolf) and naproxen (Hnap) as anionic ligands (belonging to NSAIDs family). Metallacrowns $\{Mn(II)(tolf)_2[15\text{-}MC_{Mn(III)N(shi)}\text{-}5](py)_6\}$ **18** (Fig. 14) and $\{Mn(II)(nap)(Hsal)[15\text{-}MC_{Mn(III)N(shi)}\text{-}5](py)_6\}$ **19**, (where H_2sal = salicylic acid) were synthesized and studied in the presence of DNA [66].

DNA-binding studies of these hexanuclear complexes with the use of UV–vis spectroscopy, viscosity measurements, and EtBr-based competitive FID were carried out. For these MCs, the results of UV–Vis spectroscopy did not provide conclusive evidence of binding mode to DNA. In the UV–Vis spectra, the band at $\lambda_{max} = 258$ nm derived from ctDNA changed slightly with the increasing concentration of MCs. Authors speculated that this may indicate the formation of new associates between DNA and complexes as a result of their interaction [86]. Changes in the intraligand bands of the compounds were also observed. For complex **18**, a hyperchromism at 294 and 340 nm was observed in the presence of ctDNA, but for complex **19** only very low hypochromism was visible. The K_b constants of the complexes were calculated by the Wolfe-Shimer equation and their values were in the range reported for other metal-NSAID complexes. However, it was necessary to use other methods in order to clarify the DNA-binding mode [87]. The DNA viscosity measurements of ctDNA solution in the presence of increasing amounts of the complexes were conducted. The addition of complex **19** resulted in a significant increase in the relative DNA-viscosity, while the changes of DNA-viscosity in the presence of compound **18** were not so intense (Fig. 15a).

The observed changes in the DNA viscosity under the influence of complex **19** may be related to the intercalation of this compound between the ctDNA base pairs. Probably complex **18** interacted with DNA via, for example, DNA grove-binding or electrostatic interaction, because in the case of such interactions the relative DNA-viscosity may be decreased or remain unchanged [88]. Another method used for

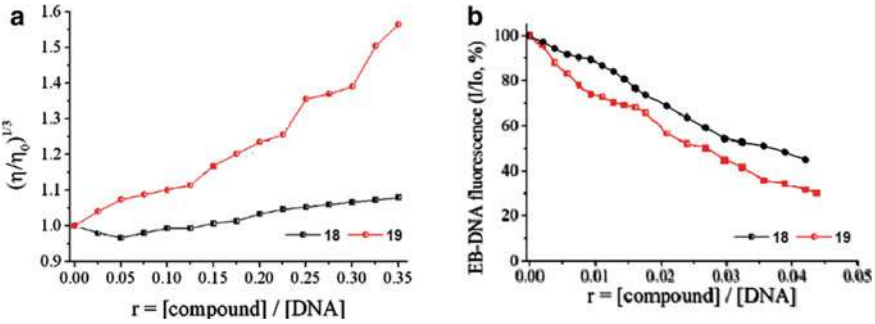

Fig. 15 Relative viscosity $(\eta/\eta_o)^{1/3}$ of ctDNA (0.1 mM) in buffer solution (150 mM NaCl and 15 mM trisodium citrate at pH 7.0) in the presence of compounds **18** and **19** at increasing amounts (r = [complex]/[DNA]) (**a**). Plot of EtBr-DNA relative fluorescence intensity at λ_{em} = 592 nm (I/I_o, %) versus r (r = [complex]/[DNA]) in buffer solution (150 mM NaCl and 15 mM trisodium citrate at pH 7.0) in the presence of compounds **18** and **19** (quenching up to 44.8% of the initial EB-DNA fluorescence for **18**, 30.6% for **19**) (**b**). Reproduced with permission from [66]

interaction studies between MC and ctDNA was the FID method with EtBr as a fluorescent indicator (Fig. 15b). The observed magnitude of the quenching of the EtBr-DNA conjugate band at 592 nm was higher for compound **19** and less intense for complex **18**, which confirmed the DNA-viscosity measurements.

Also 36-metallacrown-6 complex $Cu(II)(CN)_2)(PF_6)[36\text{-}MC_{Cu(II)N(L)}\text{-}6]\cdot 0.5H_2O$ **20** (Fig. 16) (L = 1,4,7-triisopropyl-1,4,7-triazacyclononane) interacts with double-stranded ctDNA as reported by Yang et al. [67].

The interaction between the MC and ctDNA was first investigated using spectrophotometric titration. The UV spectrum of the free MC exhibited two absorption bands at 232 nm and 298 nm assigned to the intraligand π–π* transitions. Upon

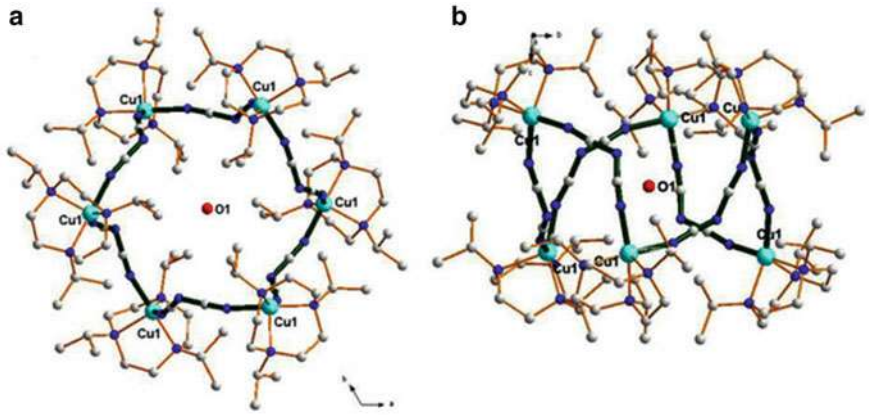

Fig. 16 Diagram showing the perspective view of complex **20** with atom labels (**a**) from *c* axis and (**b**) from *a* axis. Reproduced with permission from [67]

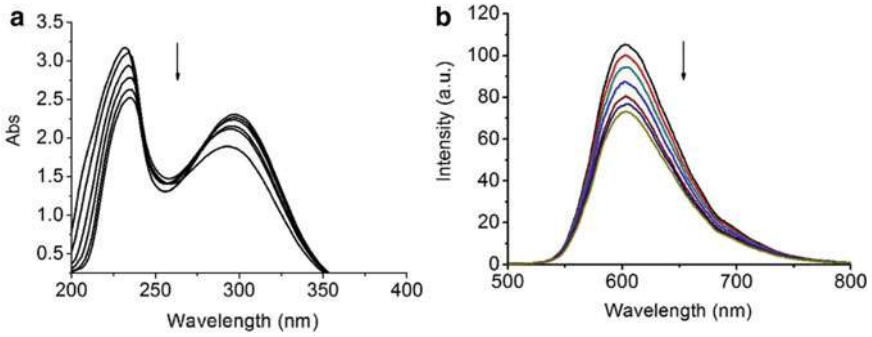

Fig. 17 Absorption spectra of complex **20** with increasing calf-thymus DNA (ctDNA). The arrow shows the absorbance changes with increasing DNA concentration. The concentration of the compound was 20 μM, r = [ctDNA]/[compound] = 0–0.6 (**a**). Fluorescence emission spectra (excited at 305 nm) of the ctDNA–EtBr system (2.5 μM EtBr, 100 μM ctDNA) in the absence and presence of complex **20** with increasing concentrations of complex—0 to 4 μM (from top to bottom) (**b**). Reproduced with permission from [67]

addition of ctDNA, the bands were red-shifted (7–12 nm) and 20% hypochromism was observed (Fig. 17a). Such spectral changes were attributed to the intercalation with DNA. This speculation was confirmed by the fluorescence titration of the ctDNA-EtBr system with MC complex. The emission intensity of EtBr was quenched with an increasing concentration of MC, suggesting that metallacrown can displace DNA-intercalated EtBr molecules (Fig. 17b).

3.2 Metallacrowns as G4 DNA Ligands

Studies on the interactions of metallacrown compounds with higher order DNA structures were started only a few years ago. The idea of using metallacrowns as G-quadruplex ligands were based on the structural fitting of planar or almost planar compounds to the external G-quartet of the G-quadruplex.

The interactions of two pentacoordinate lanthanide (III) metallacrown complexes containing phenylalanine hydroxamic acid (pheHA) and copper(II) ions Eu(III)[15-$MC_{Cu(II)N(pheHA)}$-5] **21** and Tb(III)[15-$MC_{Cu(II)N(pheHA)}$-5] **22** with human telomeric G-quadruplex DNA (G4 22HT) were investigated at first. A variety of direct and indirect analytical techniques were used in the research, such as CD, UV–Vis and fluorescent spectroscopy (Fig. 18) [68].

Circular dichroism spectroscopy is a powerful method for the determination of binding modes of ligands to nucleic acid structures. The application of this method provided valuable information on the influence of the examined MCs on the structure of the telomeric G-quadruplex (G4 22HT). Typically, in studies of ligand-G4 interactions, ligands have no optical activity, so they do not exhibit CD activity in solution. However, in this case, the incorporation of chiral hydroxamic acid molecules into a

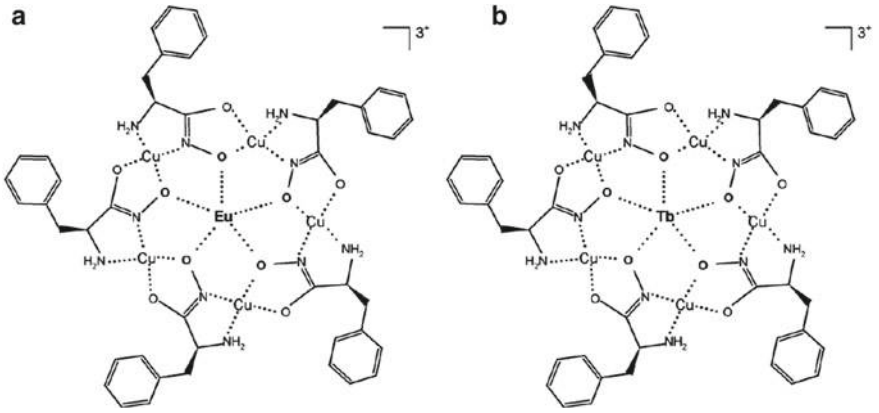

Fig. 18 Schematic representation of studied metallacrowns Eu(III)[15-MC$_{Cu(II)N(pheHA)}$-5] **21** and Tb(III)[15-MC$_{Cu(II)N(pheHA)}$-5] **22**. Reproduced with permission from [68]

metallacrown skeleton, caused the tested compounds to exhibit CD activity. Therefore, the metallacrown reference CD spectra were subtracted from those for MC/G4 systems. The G4 22HT in sodium solution showed a positive signal at about 290 nm and a negative signal at 260 nm, which suggested a typical antiparallel G-quadruplex structure [89]. The successive decrease of both signals was observed after the addition of both MC ligands, leading to the complete reduction of CD bands at a higher G4:MC concentration ratio (1:10) (Fig. 19). However, it was excluded that observed spectral changes were caused by residual copper ions. Copper(II) exhibited a noticeable decrease in CD signals in the G4 spectrum at a much higher concentration than that resulting from possible dissociation or destruction of MC compounds.

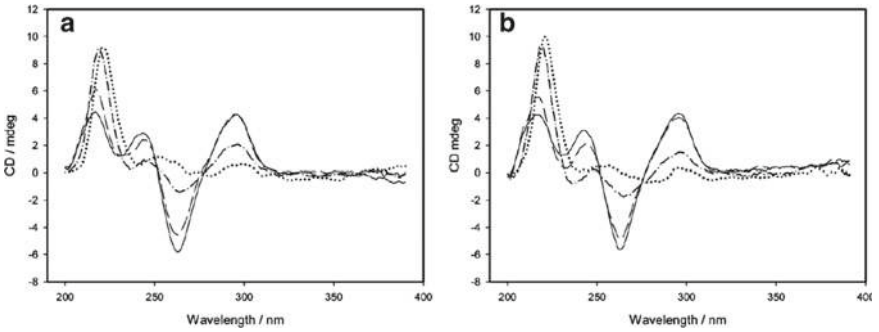

Fig. 19 CD differential spectra of 22HT titrated with Eu(III)[15-MC$_{Cu(II)N(pheHA)}$-5] **21** (**a**) and Tb(III)[15-MC$_{Cu(II)N(pheHA)}$-5] **22** (**b**) in 10 mM cacodylate buffer, pH 7.2 and 100 mM NaCl. Ratio DNA/MC equals 1:0 (solid line), 1:2.3 (long dash), 1:6.8 (dash-dot line), 1:10 (dotted line). Reproduced with permission from [68]

Reasonable thermal stability of free MCs in an aqueous solution was proved in the wide temperature range using UV–Vis spectroscopy. This allowed us to carry out G-quadruplex melting experiments. Determination of thermal stabilization of G4 22HT DNA formed in the presence of each MC, compared to that of G4 DNA alone, confirmed the results of CD titration experiments. The investigated MC compounds destabilized the 22HT G-quadruplex structure ($\Delta T_m = -16$ and -20 °C, respectively for compounds **21** and **22**). This effect could be caused by the destabilizing action of free Cu(II) ions in solution and/or by unfavorable steric interactions of large MC planes with external G-tetrads. Because the tested MCs do not possess spectral properties necessary for direct monitoring of binding interactions with nucleic acids (they have low molar absorption coefficients and are non-fluorescent), the indirect fluorescence competition methods were used. One of them was the FID assay based on changes in emission of a G4-bound fluorescent dye thiazole orange (TO). TO molecules undergo replacement from the G4-TO complex with MC competing compound and fluorescence of the system decreases [35]. During the experiments, fluorescence quenching of the G4 22HT-TO system was observed under the influence of subsequent MCs additions (Fig. 20). A small difference in binding affinity for compounds **21** and **22** was noticed. This indicates that the nature of the central lanthanide ion in metallacrown core is not the key factor influencing the MC–DNA interactions.

In the case of FID experiments, the obtained results should be analyzed very carefully, since a potential cause of TO fluorescence disappearance may not only be caused by simple ligand replacement. Also, other processes could affect the fluorescence intensity of TO that are not considered by most researchers. One can mention fluorescence quenching of bound TO molecules by MC or free copper ions, as well as the destabilizing effect of metallacrowns on the G4 structure. The end-stacking interaction of MC with external guanine tetrad was postulated as shown from thiazole orange replacement in these FID experiments. To study the binding of DNA ligands containing metal cations in their structure a new Tb^{3+}–G4 luminescence quenching

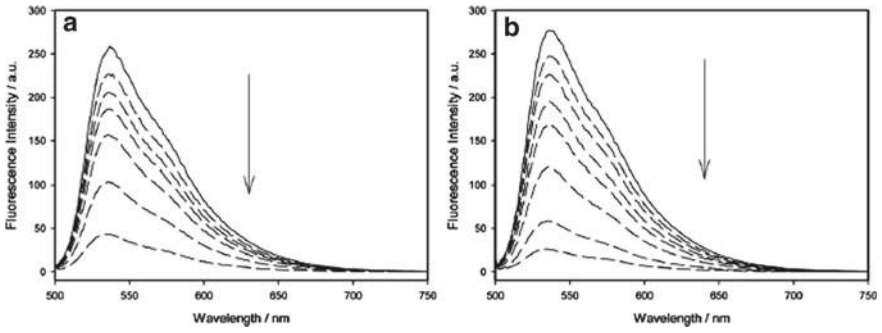

Fig. 20 Fluorescence spectra recorded in FID experiment for metallacrowns **21** (**a**) and **22** (**b**). Arrows indicate increasing concentration of particular metallacrown. Reproduced with permission from [68]

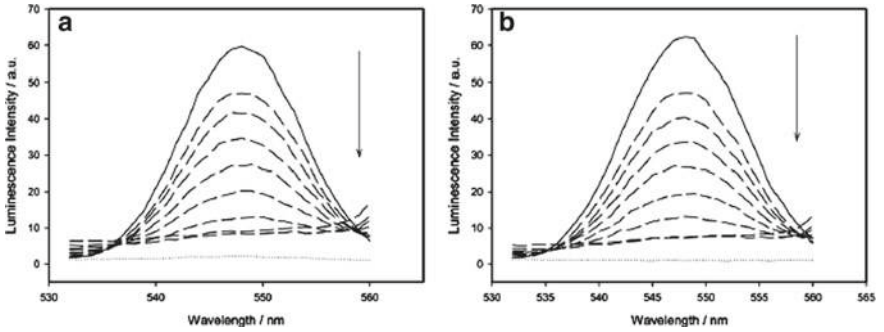

Fig. 21 Quenching effect of MC **21** (**a**) and MC **22** (**b**) on the emission band for Tb(III)-22HT quadruplex (λ_{ex} = 290 nm, λ_{em} = 548 nm). Arrows indicate increasing concentration of metallacrown. Reproduced with permission from [68]

assay was proposed and evaluated. The quenching effect of MCs on the emission band for Tb(III)-G4 22HT system was observed (λ_{em} = 548 nm). (Fig. 21).

Decreased emission of terbium luminescence with subsequent additions of MC can be caused by the quenching effect of metallacrown bound to the G4–Tb(III) complex, as well as the unfolding of the G4 structure induced by metallacrown binding. Fluorescence quenching Stern–Volmer plots were also analyzed, and the Stern–Volmer quenching constants (K_{sv}), which can be interpreted as the association constants (K_{as}) were calculated (3.9×10^5 M^{-1} and 4.6×10^5 M^{-1} for MCs **21** and **22**, respectively). The obtained quenching parameters can be regarded as association constants because the association of MC to G4–Tb(III) luminophore causes quenching of Tb luminescence according to a static mechanism. These values were higher by ca. 50% than the K_{MC} values obtained from the FID assay, and the differences between Kas and K_{MC} were explained by different experimental conditions used in both assays.

Interactions of a human telomeric (22HT) G-quadruplex as the molecular target with the luminescent Sm(III)[12-$MC_{Ga(III)N(shi)}$-4] **23** (Hshi–salicylhydroxamic acid) metallacrown was recently examined (Fig. 22).

Miscellaneous approaches were used in this study: CD spectroscopy (CD titrations and CD melting profiles), fluorescence spectroscopy (fluorescence titration of Sm(III)[12-$MC_{Ga(III)N(shi)}$-4] with G4/Na^+, fluorescence competition (FID assay and the method based on Tb^{3+}/G4 luminescence quenching by MC) [69]. The 12-MC-4 type complex has structural features (the size, shape, and bonding of cations) that make it an excellent candidate for precise molecular recognition of G4s. Sm(III)[12-$MC_{Ga(III)N(shi)}$-4] metallacrown **23** possesses a nearly planar geometry with four benzoate anions, which are perpendicular to the ring plane [90]. This creates the opportunity for the interaction of the opposite side of the Sm(III)[12-$MC_{Ga(III)N(shi)}$-4] with the external G-tetrad of G4. Although achiral reagents were used for the synthesis of this metallacrown, weak negative bands at about 230 and 310 nm were observed in the CD spectrum of MC, which was consistent with the position of the

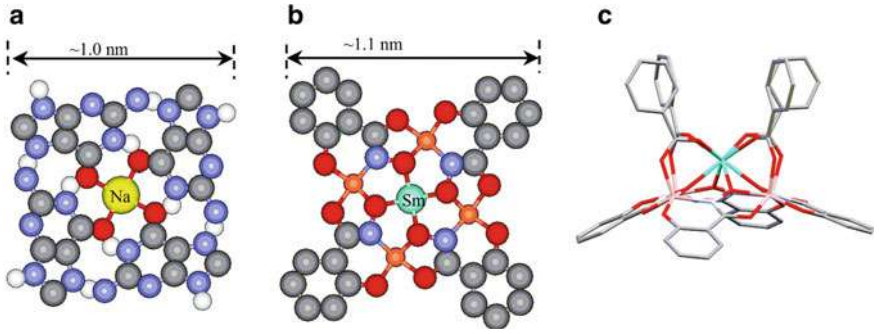

Fig. 22 A ball and stick model of a G-tetrad with Hoogsteen-type base pairing and Na^+ cation coordinated in a central cavity (**a**). A simplified molecular structure of Sm(III)[12-$MC_{Ga(III)N(shi)}$-4] **23** (**b**). A side view of the Sm(III)/(benzoate)$_4$[12-$MC_{Ga(III)N(shi)}$-4]. The metallacrown encapsulates a central samarium ion with four gallium ions (ring metal), four salicylhydroxamates (shi^{3-}), and four benzoate bridges (**c**). Reproduced with permission from [69]

absorption bands in the UV spectrum of MC. This peculiarity was explained by the existence of the SmMC complex in two optical isomeric forms caused by the order of joining of atoms in the ring (A isomer: the M–N–O–M–N–O– linkage and C isomer: the M–O–N–M–O–N–linkage). Therefore, to accurately assess the interactions of MC with G4, the subtraction of metallacrown CD spectrum was applied to obtain adifferential CD spectra. The decrease of a strong positive band at 290 nm and a negative one at 260 nm up to 30–40%, characteristic for antiparallel G-quadruplex structure, was observed after the addition of metallacrown at higher concentration (6.9 and 12.4 MC equiv.) (Fig. 23a).

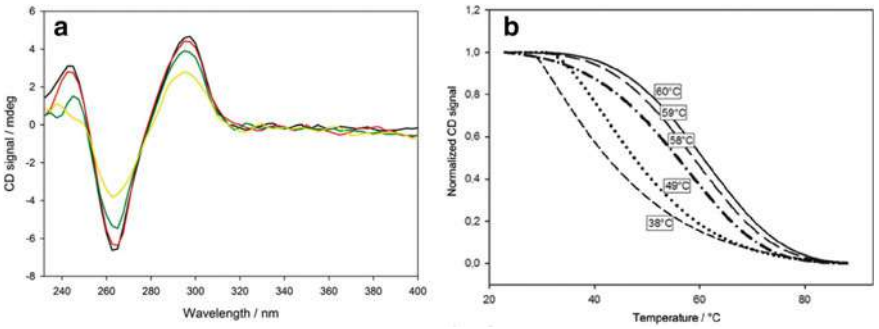

Fig. 23 CD spectra of G-quadruplex 22HT with increasing concentration of Sm(III)[12-$MC_{Ga(III)N(shi)}$-4] (equivalents of **23**: 0—black line, 2.3—red line, 6.9—green line and 12.4—yellow line) (**a**). Normalized melting profiles of G-quadruplex in the absence (solid line) and in the presence of 1 equiv. (long dash line), 2.3 equiv. (dash-dot line), 6.9 equiv. (dotted line), and 12.4 equiv. (short dash line) of MC **23**. Profiles were plotted using normalized CD signals at 295 nm vs. temperature (**b**). Conditions: 10 mM sodium cacodylate buffer, pH 7.2, 100 mM NaCl (**a**, **b**). Reproduced with permission from [69]

It should be emphasized that the G4 DNA showed much higher stability in the presence of Sm(III)[12-$MC_{Ga(III)N(shi)}$-4] **23** compared to Ln15-MC-5 complexes: Eu(III)[15-$MC_{Cu(II)N(pheHA)}$-5] **21** and Eu(III)[15-$MC_{Cu(II)N(pheHA)}$-5] **22** [68]. This is probably a consequence of a better fit of the G4 tetrad and 12-MC-4 plane, especially if one takes into account the high positive charge (+3) of Ln15-MC-5, which favors destabilizing electrostatic interactions with the negatively charged DNA molecule. To determine the thermal stability of G4 22HT DNA formed in the presence of metallacrown, CD melting measurements were taken. At lower ratios of MC (1 and 2.3 equiv.), the T_m values of G4 were slightly lower compared to the T_m of free 22HT/Na^+ quadruplex.

In the case of higher concentrations of Sm(III)[12-$MC_{Ga(III)N(shi)}$-4] **23** (6.9 and 12.4 equiv.), the melting temperature decreased by 11 °C and 22 °C, respectively (Fig. 23b). The hysteresis between the melting and annealing curves was observed, which suggested the presence of irreversible or very slow processes connected with the folding of the G4/Sm(III)[12-$MC_{Ga(III)N(shi)}$-4] system. However, in this case, the metallacrown emission spectra confirmed, that disruption of the **23** complexes at higher temperature appeared to be irreversible. It should be noted apparent discrepancies in the results obtained from CD melting study. The melting temperature of G-quadruplex with 6.9 equiv. of MC has decreased by 11 °C, while no such large changes were observed in the CD spectra. Authors speculated that increased temperature caused the loss of benzoates from the MC complex. When the **23** is in excess, the generation of highly positive charged MC form (after benzoate dissociation) inhibits the appropriate G-quadruplex folding. It seems very likely that at the higher molar ratio of MC, when the external quartets of G4 DNA have been saturated (end-stacking binding mode), the interactions between the DNA phosphate groups and MC complexes may result in another external binding mode, which may destabilize the antiparallel structure of G4.

Fluorescence titration experiments of Sm(III)[12-$MC_{Ga(III)N(shi)}$-4] **23** with G4 DNA were possible to be carried out because Ga^{3+} ions do not disturb the luminescence transitions of samarium ions, thanks to fully occupied 3d orbitals of gallium ion. In addition, the spatial structure of MC **23** protects the samarium ion from CH and OH oscillator quenching, giving a strong luminescence enhancement effect (Fig. 24). However, the emission spectra of **23** (1 μM) in buffer solution showed a gradual increase in the emission band of shi ligand and a simultaneous decrease in the luminescence bands of samarium.

This observation indicated that Sm(III) luminescence is associated with energy transfer from the shi ligand to the central samarium ion. Luminescence quenching effect of the Sm(III)[12-$MC_{Ga(III)N(shi)}$-4] **23** may be caused by the release of benzoate ligands and an attack of water molecules. The release of shi is presumably mediated by excitation of shi that activates bond oscillation in the coordination sphere of Sm(III). The obtained results showed that the photo-induced dissociation processes in **23** were partially reversible, which ruled out the possibility of total destruction of the metallacrown. This is in line with previous reports, which showed that coordinated anions may dissociate from 12-MC-4 complexes, whereas the metallacrown ring and centrally trapped metal ions are resistant to dissociation or decomposition [91–94,

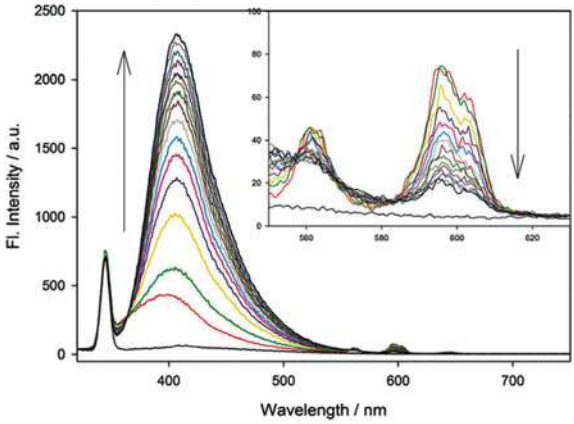

Fig. 24 Spectra of 1 μM Sm(III)[12-$MC_{Ga(III)N(shi)}$-4] **23** in buffer (λ_{ex} = 309 nm) recorded in 4 min time intervals. Arrows indicate intensity changes in emission bands with time. The inset shows detailed changes in the spectral region of samarium luminescence. Reproduced with permission from [69]

94]. The shi ligand-focused photoreaction likely affects coordination bonds around Sm(III) and enables quenching of Sm luminescence by water molecules.

Therefore, the direct fluorescent titration method could not be used for the quantitative binding study of samarium MC with nucleic acids and provided only qualitative evidence for the interaction between Sm(III)[12-$MC_{Ga(III)N(shi)}$-4] and G4 DNA. To confirm the interaction of **23** with G-quadruplex DNA the use of indirect fluorescent methods was necessary. One of them was a method based on the quenching effect of the ligand on the luminescence of the G4/Tb^{3+} system. The G4/Tb^{3+} system was titrated with an increasing concentration of **23**. Initially the strong Tb^{3+} luminescence band at 540 nm gradually decreased under the influence of successive portions of MC, which was the evidence for the interaction of the metallacrown with the G4/Tb^{3+} complex (Fig. 25).

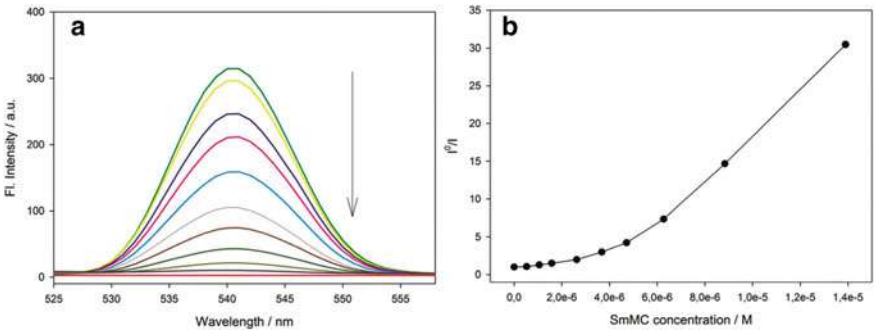

Fig. 25 Quenching of the Tb(III) emission band of the G4–Tb^{3+} system by consecutive additions of Sm(III)[12-$MC_{Ga(III)N(shi)}$-4] **23**. Experimental conditions: [G4] = 1 μM, [Tb^{3+}] = 4 μM, [MC] = 0–14 μM; 10 mM Tris–HCl buffer, pH 7.0; λ_{ex} = 290 nm. Arrows indicate increasing concentration of metallacrown (**a**). Plot of I_0/I versus increasing concentration of metallacrown **23** (**b**). Reproduced with permission from [69]

The Stern–Volmer plot showed an upward curvature. The positive deviation of the quenching plot was observed at higher concentration ratios and the G4 destabilizing effect has been confirmed by the CD titration experiments. The fluorescence quenching data were analyzed by the Stern–Volmer equation and $K_{sv} = 3.9 \pm 0.3 \times 10^5\ M^{-1}$ was calculated considering only the rectilinear range of the S–V plot. This value was close to those obtained for 15-MC-5 compounds—$3.9 \times 10^5\ M^{-1}$ and $4.6 \times 10^5\ M^{-1}$ for Eu(III) **21** and Tb(III) **22** [15-$MC_{Cu(II)N(pheHA)}$-5], respectively. Similar values of the G4 binding constants for both the 12-MC-4 and 15-MC-5 complexes may suggest the same type of binding mode, which is unlikely. The pentacoordinate lanthanide (III) metallacrown copper complexes have a charge of +3, which promotes electrostatic interactions with negatively charged DNA. In the case of the Sm(III)[12-$MC_{Ga(III)N(shi)}$-4] **23**, which is a monoanion, the expected effect is repulsion from DNA. The fact that a trivalent cationic MC complex binds to G4 with a similar affinity as a monoanionic MC indicates that the mechanism of the interaction is not just charge-based. It is highly probable that this difference stems from the perfect match of the Sm 12-MC-4 **23** shape and size to those of the G-tetrad, which results in binding to G4 by an end-stacking mode. On the other hand, the polycationic Ln 15-MC-5 **21** and **22** probably interact with the negatively charged phosphate groups by Coulombic forces.

The second indirect method applied to study Sm(III)[12-$MC_{Ga(III)N(shi)}$-4]-DNA interactions was the G-quadruplex FID assay. The replacement of TO from TO/G4 complex by the competing **23** was observed (Fig. 26).

The metallacrown concentration required to reduce the TO/G4 fluorescence signal by 50% (MC50%) was estimated to be $5.3 \pm 0.3\ \mu M$. This value was used to calculate the binding constant for the **23**/G4 complex of $1.3 \pm 0.2 \times 10^5\ M^{-1}$, suggesting a moderate binding affinity. Simultaneously, this binding constant is lower than that obtained by Tb^{3+}/G4 luminescence quenching that can be explained by different experimental conditions in both assays.

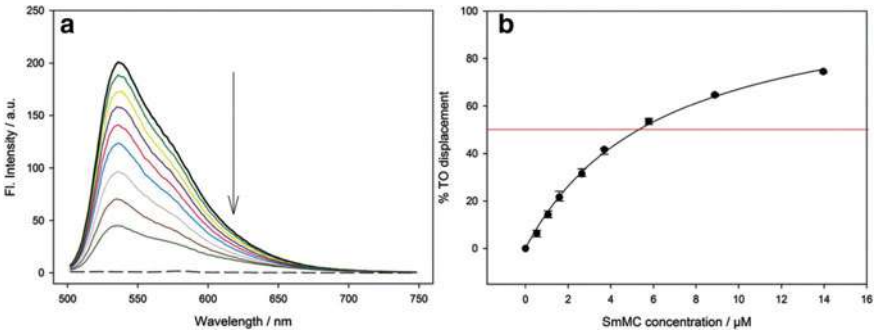

Fig. 26 Spectra of 0.25 μM G4 containing 0.5 μM TO in the presence of increasing concentrations of MC **23** in 10 mM sodium cacodylate buffer, pH 7.2 and 100 mM NaCl (**a**). Plot of the TO displacement percentage against concentration of the metallacrown (**b**). Reproduced with permission from [69]

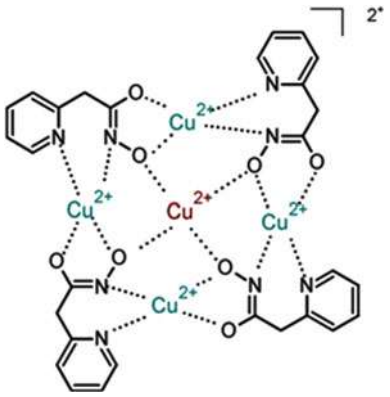

Fig. 27 Molecular structure of Cu(II)[12-$MC_{Cu(II)N(PyrAcHA)}$-4] **24**. Reproduced with permission from [70]

Another 12-MC-4 metallacrown Cu(II)[12-$MC_{Cu(II)N(PyrAcHA)}$-4] **24** was reported to show very interesting properties, causing conformational rearrangements of G-quadruplex topology (Fig. 27) [70].

The dianionic ligand (2-pyridylacetylohydroxamate) and divalent copper(II) ions form a 12-MC-4 ring with a neutral charge that incorporates a central Cu(II) cation giving an overall charge of 2+ to the MC complex. The Cu(II)[12-$MC_{Cu(II)N(PyrAcHA)}$-4] **24** metallacrown adopts a quasi-planar conformation that is reminiscent of the porphyrin ring structure, known as the G-quadruplex ligand. These structural features favor interactions with negatively charged G-tetrads. This MC does not possess any fluorescence properties and is inactive in CD spectroscopy. As the molecular targets, G-quadruplexes formed by oligonucleotides with the sequence of human telomeric DNA (22HT) and human proto-oncogene c-MYC were chosen. Telomeric DNA sequence forms G-quadruplex with different topologies depending on the used monovalent cation, sodium or potassium. In Na^+-containing buffer the nuclear magnetic resonance (NMR) spectroscopy confirmed the creation of an antiparallel basket-type G-quadruplex structure possessing two lateral and one diagonal loops [95]. The CD spectrum shows the major positive signal at 295 nm with a negative signal at 265 nm and a smaller positive signal at 240 nm. In K^+-containing solution, depending on the analysis method used, two entirely different structures for the same sequence were obtained. The crystallographic investigations of the solid sample obtained in the presence of K^+ showed a parallel structure [95], while the solution study with the use of NMR spectroscopy in presence of K^+ buffer showed the existence of two so-called hybrid-1 and hybrid-2 G-quadruplex structures [96, 97]. The typical CD spectrum characteristic of a mixed-type hybrid structure (one sidewise loop and two lateral loops) shows a strong positive band at 293 nm, a shoulder at ~270 nm, and a weak negative band at ~240 nm[96].

The CD spectrum of G-quadruplex c-MYC in K^+ solution is dominated by a strong positive band at 260 nm and a smaller negative band at 240 nm, typical for the parallel G-quadruplex structure with three sidewise loops [40].

The CD titrations of these three pre-folded G-quadruplexes with Cu(II)[12-$MC_{Cu(II)N(PyrAcHA)}$-4] **24** metallacrown indicated different interactions with particular G4 topologies. In the case of antiparallel G4 (22HT/Na^+), even at large excess of MC (18-fold) the G-quadruplex was not destroyed as indicated by the unaffected characteristic positive band at 295 nm (Fig. 28a). The CD profile of G4 22HT recorded in K^+ solution revealed that the addition of metallacrown increased marginally with the main CD band at 295 nm and creates a negative band at 265 nm (Fig. 28b). These changes suggested the transformation of the hybrid G4 structure to the antiparallel G-quadruplex. A comparison of CD spectra of MC/G4 22HT complexes in the sodium and potassium environments indicates that both have a very similar structure. The influence of the metallacrown on the third of the examined G4 topologies was also noticeable. Additions of MC decreased the strong positive band at 265 nm (up to 75% at 18 equiv.), and to a lesser extent influenced the small negative band at 240 nm characteristic for the parallel topology (Fig. 28c). The obtained results indicated strong structure-dependent interactions of Cu(II)[12-$MC_{Cu(II)N(PyrAcHA)}$-4] **24** with G4s. The examined metallacrown binds specifically to the telomeric sequence, with stabilization of the antiparallel G4 topology and destabilization of the parallel c-MYC G4 structure.

Thermal stabilization of G4s DNA formed in the presence of metallacrown ligand was also tested. The temperature-dependent changes in the CD spectra were very interesting. Melting was monitored at the wavelength of 295 nm (characteristic positive CD signal antiparallel and hybrid G-quadruplex telomeric structures) and at 265 nm where the positive band of parallel topology occurs. The melting temperature of antiparallel G-quadruplex has grown up to the maximum already in the presence of 1 equivalent of MC (ΔT_m of +14 °C) and higher MC excesses improve this effect only by +1 °C (Fig. 29a). The reversibility of the spectral changes was observed in melting experiments, both upon heating and cooling runs (Fig. 29b).

Interestingly, addition of Cu(II)[12-$MC_{Cu(II)N(PyrAcHA)}$-4] to the hybrid G-quadruplex resulted in a decrease in melting temperature monitored at 295 nm by 6 and 5 °C in the presence of 1 and 6.9 equivalents of MC, respectively (Fig. 30a).

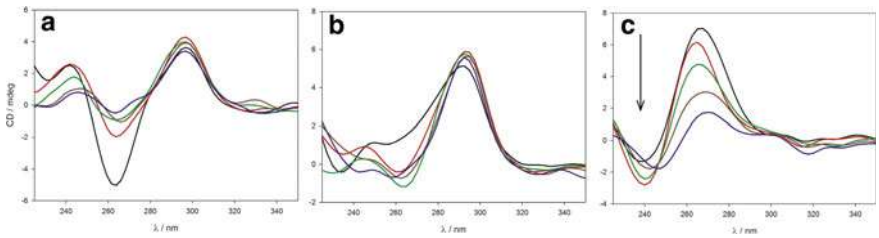

Fig. 28 CD spectra of 2 μM 22HT/Na^+ (**a**), 2 μM 22HT/K^+ (**b**) and 2 μM c-MYC/Na^+ (**c**) in the presence of increasing concentration of Cu(II)[12-$MC_{Cu(II)N(PyrAcHA)}$-4] **24**. Conditions: 100 mM of salt, 10 mM sodium cacodylate buffer, pH 7.2. DNA/MC ratio: 1:0 (black line), 1:2.3 (red line), 1:6.7 (green line), 1:12 (brown line), 1:18 (blue line). Reproduced with permission from [70]

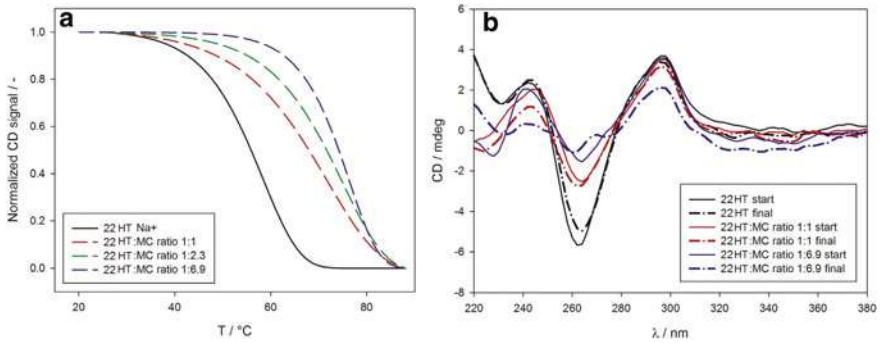

Fig. 29 Normalized CD melting profiles for 22HT/Na^+ [2 μM] in the presence of Cu(II)[12-$MC_{Cu(II)N(PyrAcHA)}$-4] **24** registered in the heating mode. DNA:MC ratio: 1:0 (black line), 1:1 (red dashed), 1:2.3 (green dashed), 1:6.9 (blue dashed) (**a**). CD spectra recorded at 25 °C before (long lines) and after (dash-dot lines) full melting experiment (heating and cooling cycles) for 22HT/Na^+ [2 μM] in the presence of metallacrown at different ratios (**b**). Conditions to all: 10 mM cacodylate buffer, pH 7.2, 100 mM NaCl. Reproduced with permission from [70]

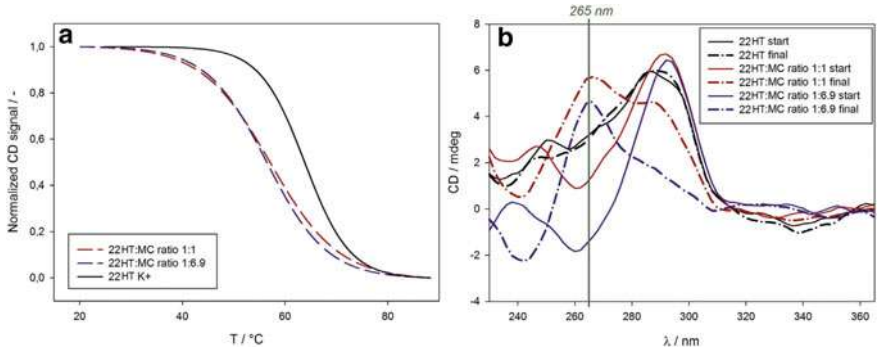

Fig. 30 Normalized CD melting profiles for 22HT/K^+ [2 μM] in the presence of Cu(II)[12-$MC_{Cu(II)N(PyrAcHA)}$-4] **24** registered in the heating mode. DNA:MC ratio: 1:0 (black line), 1:1 (red dashed), 1:6.9 (blue dashed) (**b**) CD spectra before (solid lines) and after (dash-dot lines)melting temperature experiment for 22HT/K^+ [2 μM] in the presence of different G4:MC ratios (**a**). Conditions to all: 10 mM cacodylate buffer, pH 7.2, 100 mM KCl. Reproduced with permission from [70]

The opposite effect was observed for the melting plot recorded at 265 nm, which indicated the transformation of the hybrid form into a parallel structure with an increase in T_m by 16 °C. This conformational transformation of the MC **24**-G4 22HT/K^+ system appeared to be irreversible upon cooling (Fig. 30b). Moreover, this transformation was kinetically controlled since the MC caused this topological change not only upon heating but a similar effect was observed after longtime incubation (13 days, 312 h) of the sample at room temperature (Fig. 31).

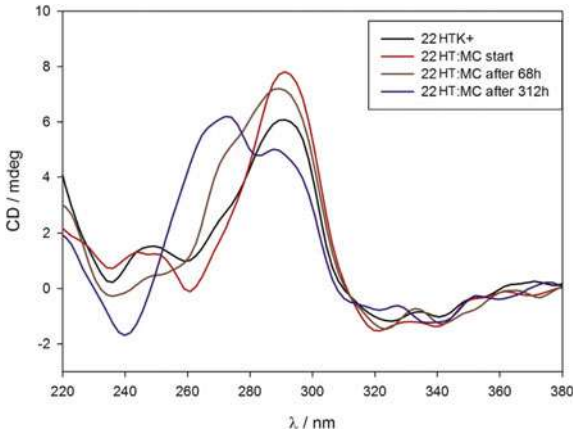

Fig. 31 Conformational changes of the hybrid structure (G4 22HT/K^+) in the presence of Cu(II)[12-$MC_{Cu(II)N(PyrAcHA)}$-4] **24** (1:1 ratio) with ongoing time of incubation at room temperature. Conditions: 10 mM cacodylate buffer, pH 7.2, 100 mM KCl. Reproduced with permission from [70]

The stabilizing effect of **24** on the parallel structure of G4 DNA was confirmed by the MC **24**/parallel G4 complex of c-MYC, for which T_m appeared to be quite high and was estimated as above 80 °C. The obtained value was more than 27 °C higher compared to the T_m of 52.5 °C calculated for c-MYC G4 in the absence of MC.

Due to the poor spectroscopic properties of **24** metallacrown (very low molar absorptivity and lack of fluorescence), the G4 FID assay was used for the study of interactions of Cu(II)[12-$MC_{Cu(II)N(PyrAcHA)}$-4] with telomeric G4 DNA in sodium solution (Fig. 32). Each addition of metallacrown **24** decreased the fluorescence intensity of the TO-G4 complex as a result of the displacement of thiazole orange from the complex (Fig. 32a). The concentration of Cu(II)[12-$MC_{Cu(II)N(PyrAcHA)}$-4]

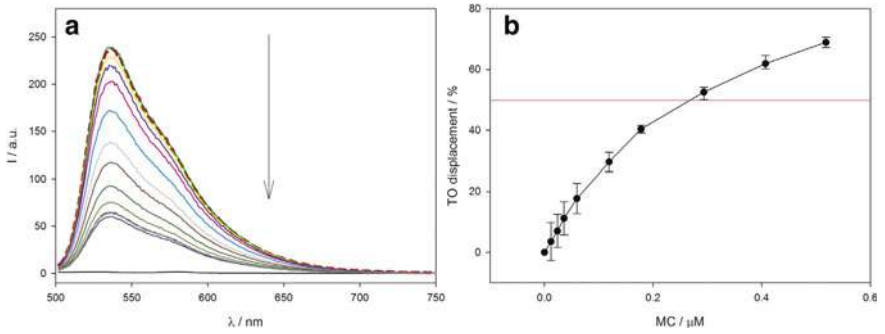

Fig. 32 Fluorescence spectra of G4:TO complex in the presence of increasing concentration of Cu(II)[12-$MC_{Cu(II)N(PyrAcHA)}$-4] **24**. Conditions: 0.25 μM G4, 0.5 μM TO, 10 mM sodium cacodylate buffer, pH 7.2 and 100 mM NaCl (**a**). Plot of TO displacement percentage from G4:TO complex by metallacrown. Red line indicates 50% decrease of TO emission (**b**). Reproduced with permission from [70]

required to decrease the emission of thiazole orange by 50% was determined as 0.26 μM (Fig. 32b).

Assuming a 1:1 stoichiometry for both G4-TO and G4-MC complexes, the binding constant (K_{MC}) of $3.9 \pm 0.4 \times 10^6$ M^{-1} was calculated for the complex between 22HT/Na^+ G-quadruplex and Cu(II)[12-$MC_{Cu(II)N(PyrAcHA)}$-4]. Although the copper(II) ions with unfilled d orbitals present in MC structure were suspected to quench the fluorescence of TO in FID assay by electron transfer (charge transfer complexes), this effect was neglected since no new CT band nor spectral band shifts were observed in FID experiment. Thus, the changes in fluorescence intensity should be ascribed to the release of thiazolium orange from the G-quadruplex. To further prove the strong interaction of Cu(II)[12-$MC_{Cu(II)N(PyrAcHA)}$-4] with antiparallel 22HT G4 structure, an additional indirect method based on MC effect on the Tb(III)-G4 luminescence was applied [68]. Luminescence of the G4:Tb^{3+} system titrated with Cu(II)[12-$MC_{Cu(II)N(PyrAcHA)}$-4] was quenched after each addition of MC that suggested the interaction between MC **24** and G4 (Fig. 33).

Using the Stern–Volmer equation, the association constant of **24** to G4 was calculated as $K_{as} = 6.4 \pm 0.5 \times 10^5$ M^{-1}. Binding results for Cu(II)[12-$MC_{Cu(II)N(PyrAcHA)}$-4] indicated slightly higher affinity to 22HT G-quadruplex than those reported for other metallacrowns: Ln (III) 15-MC-5 **21** Eu(III)[15-$MC_{Cu(II)N(pheHA)}$-5] and **22** Tb(III)[15-$MC_{Cu(II)N(pheHA)}$-5] ($3.9 - 4.6 \times 10^5$ M^{-1}) [68] and Sm(III)[12-$MC_{Ga(III)N(shi)}$-4] **23** ($3.9 \pm 0.3 \times 10^5$ M^{-1}) [69]. The difference in binding affinity between Sm(III) **23** and Cu(II) **24** 12-MC-4 complexes can be explained by the different structural features of both MCs. Copper metallacrown **24** possesses a planar

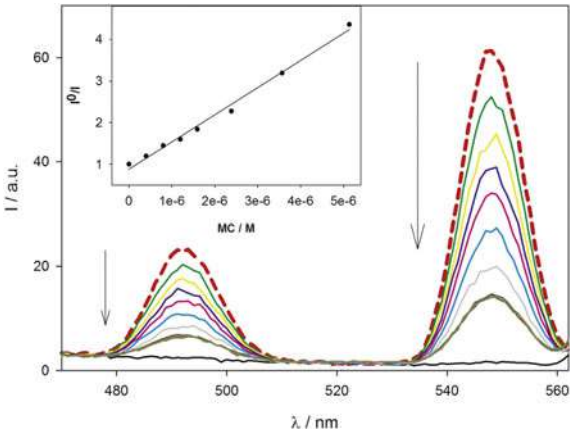

Fig. 33 Quenching of the luminescence bands of Tb^{3+}/G4 complex by consecutive additions of Cu(II)[12-$MC_{Cu(II)N(PyrAcHA)}$-4] **24**. Conditions: [22HT] = 1 μM, [Tb^{3+}] = 4 μM, [MC] = 0–9.4 μM; 12 mM Tris–HCl buffer, pH 7.0, λ_{ex} = 290 nm. Arrow indicates increasing concentration of metallacrown. Inset: Plot of I0/I vs. increasing concentration of MC. Reproduced with permission from [70]

square shape structure [91], while Sm(III) 12-MC-4 **23** exhibits a bowl-shaped structure [90]. Most probably, this bowl-like geometry somehow limits the MC/G-tetrad interactions in the case of the last one. Concluding, the differences arise from the structural features of the MC compounds and the positive net charge of the metallacrown facilitates the interaction with negatively charged G-tetrad of G4 DNA via electrostatic interaction. The ligands interact with G4s DNA via π–π stacking and groove/loop interactions. Although the main binding mode of the ligands seems to be the π–π stacking with external G-tetrads, other interactions like electrostatic ones and H-bonds also play a substantial role. The effectiveness of *end-stacking* interactions is demonstrated for the ligands having a large flat aromatic surface. The introduction of a positive charge on the ring system of the chromophore improves the binding affinity to the anionic backbone and/or to the negative central channel of the G-quadruplex. In the case of metal complexes, the arrangement of metal over the central channel of G4 can additionally improve electrostatic stabilization. In addition, the positive net charge of the ligands may be associated with the side chains of the cationic substituents that bind to the grooves and loops through electrostatic interactions, contributing to the improvement of G4 DNA/ligand stability.

4 Conclusions

The development of DNA binding compounds gives opportunities to manipulate and tune cellular processes. Through ligand-DNA interactions, one can affect replication, transcription, regulation of gene expression, or other processes. The advantages of introducing metal ions inside an organic skeleton to get DNA-interacting ligands such as metallacrowns are miscellaneous. Metal chelation may cause the following effects: (i) impart certain specific chemical or physical properties to the ligand, (ii) cause ligand flattening, thus facilitating intercalation to dsDNA and increasing the affinity to an external G-quartet of G-quadruplex, (iii) improve the interaction with the negatively charged biopolymer by introducing additional charge into the ligand molecule, or (iv) reduce the electron density of the surrounding aromatic system.

Many different techniques have been used to study the interactions of compound with DNA structures. These methods are simple or complicated, they have their own advantages and disadvantages. Usually, more than one method is needed to obtain complete information about ligand/DNA interactions. However, it is important to remember that various disturbing processes may accompany the observed effects of the experiments. For example, in the case of FID experiments not only the simple ligand replacement should be considered as a potential cause of dye fluorescence disappearance. Also, other processes such as fluorescence quenching of bound dye molecules by MC or free metal ions, as well as the destabilizing effect of metallacrowns on the DNA structure, could affect the fluorescence intensity of the dye. The participation of quenching phenomena is especially important for studying ctDNA (multiple binding) but is not considered by most researchers. Although variety of conventional techniques was used to study MC/DNA interactions, still there is a need

to implement more advanced techniques for this purpose. One can advise the development of new DNA/MC binding protocols based on mass spectrometry (ESI MS, MALDI TOF MS), isothermal titration calorimetry (ITC), surface plasmon resonance (SPR), quartz microbalance (QCM), or microscale thermophoresis (MST).

Unquestionably, metallacrowns display a great biomedical potential and surely further study will be focusing on the biotechnology and medical applications.

References

1. Rhodes, D., Lipps, H.J.: G-quadruplexes and their regulatory roles in biology. Nucleic Acids Res. **43**, 8627–8637 (2015). https://doi.org/10.1093/nar/gkv862
2. Ruggiero, E., Richter, S.N.: G-quadruplexes and G-quadruplex ligands: targets and tools in antiviral therapy. Nucleic Acids Res. **46**, 3270–3283 (2018). https://doi.org/10.1093/nar/gky187
3. De Cian, A., Lacroix, L., Douarre, C., Temime-Smaali, N., Trentesaux, C., Riou, J.-F., Mergny, J.-L.: Targeting telomeres and telomerase. Biochemie **90**, 131–155 (2008). https://doi.org/10.1016/j.biochi.2007.07.011
4. Ou, T., Lu, Y., Tan, J., Huang, Z., Wong, K., Gu, L.: G-quadruplexes: targets in anticancer drug design. Chem. Med. Chem. **3**, 690–713 (2008). https://doi.org/10.1002/cmdc.200700300
5. Monchaud, D., Teulade-Fichou, M.-P.: A hitchhiker's guide to G-quadruplex ligands. Org. Biolol. Chem. **6**, 627–636 (2008). https://doi.org/10.1039/B714772B
6. Asamitsu, S., Bando, T., Sugiyama, H.: Ligand design to acquire specificity to intended G-quadruplex structures. Chem. Eur. J. **25**, 417–430 (2019). https://doi.org/10.1002/chem.201802691
7. Dhamodharan, V., Pradeepkumar, P.I.: Specific recognition of promoter G-quadruplex DNAs by small molecule ligands and light-up probes. ACS Chem. Biol. **14**, 2102–2114 (2019). https://doi.org/10.1021/acschembio.9b00475
8. Carvalho, J., Mergny, J.L., Salgado, G.F., Queiroz, J.A., Cruz, C.: G-quadruplex, friend or foe: the role of the G-quartet in anticancer strategies. Trends Mol. Med. **26**, 848–861 (2020). https://doi.org/10.1016/j.molmed.2020.05.002
9. Savva, L., Georgiades, S.N.: Recent developments in small-molecule ligands of medicinal relevance for harnessing the anticancer potential of G-quadruplexes. Molecules **26**, 27 (2021). https://doi.org/10.3390/molecules26040841
10. Alessandrini, I., Recagni, M., Zaffaroni, N., Folini, M.: On the road to fight cancer: the potential of G-quadruplex ligands as novel therapeutic agents. Int. J. Mol. Sci. **22**, 23 (2021). https://doi.org/10.3390/ijms22115947
11. Blackburn, E.H.: Structure and function of telomeres. Nature **350**, 569–573 (1991). https://doi.org/10.1038/350569a0
12. Huppert, J.L., Balasubramanian, S.: Prevalence of quadruplexes in the human genome. Nucleic Acids Res. **35**, 406–413 (2007). https://doi.org/10.1093/nar/gki609
13. Bay, D.H., Busch, A., Lisdat, F., Iida, K., Ikebukuro, K., Nagasawa, K., Karube, I., Yoshida, W.: Identification of G-quadruplex structures that possess transcriptional regulating functions in the *Dele* and *Cdc6* CpG islands BMC Mol. Biol. **18**, 17 (2017). https://doi.org/10.1186/s12867-017-0094-z
14. Wu, G., Xing, Z., Tran, E.J., Yang, D.: DDX5 helicase resolves G-quadruplex and is involved in MYC gene transcriptional activation. Proc. Natl. Acad. Sci. U. S. A. **116**, 20453–20461 (2019). https://doi.org/10.1073/pnas.1909047116
15. Ramos, C.I.V., Almeida, S.P., Lourenço, L.M.O., Pereira, P.M.R., Fernandes, R., Faustino, M. Amparo F., Tomé, J.P.C., Carvalho, J., Cruz, Neves, M. Graça P.M.S.: Multicharged phthalocyanines as selective ligands for G-quadruplex DNA structures. Molecules **24**, 733 (2019). https://doi.org/10.3390/molecules24040733

16. Sun, D., Thompson, B., Cathers, B.E., Salazar, M., Kerwin, S.M., Trent, J.O., Jenkins, T.C., Neidle, S., Hurley, L.H.: Inhibition of human telomerase by a G-quadruplex-interactive compound. J. Med. Chem. **40**, 2113–2116 (1997). https://doi.org/10.1021/jm970199z
17. Biffi, G., Tannahill, D., McCafferty, J., Balasubramanian, S.: Quantitative visualization of DNA G-quadruplex structures in human cells. Nat. Chem. **5**, 182–186 (2013). https://doi.org/10.1038/nchem.1548
18. Salgado, G.F., Cazenave, C., Kerkour, A., Mergny, J.-L.: G-quadruplex DNA and ligand interaction in living cells using NMR spectroscopy. Chem. Sci. **6**, 3314–3320 (2015). https://doi.org/10.1039/C4SC03853C
19. Laguerre, A., Hukezalie, K., Winckler, P., Katranji, F., Chanteloup, G., Pirrotta, M., Perrier-Cornet, J.-M., Wong, J.M.Y., Monchaud, D.: Visualization of RNA-quadruplexes in live cells. J. Am. Chem. Soc. **137**, 8521–8525 (2015). https://doi.org/10.1021/jacs.5b03413
20. Zhang, S., Sun, H., Wang, L., Liu, Y., Chen, H., Li, Q., Guan, A., Liu, M., Tang, Y.: Real-time monitoring of DNA Gquadruplexes in living cells with a small-molecule fluorescent probe. Nucleic Acids Res. **46**, 7522–7532 (2018). https://doi.org/10.1093/nar/gky665
21. Strekowski, L., Wilson, B.: Noncovalent interactions with DNA: an overview. Mutat. Res. **623**, 3–13 (2007). https://doi.org/10.1016/j.mrfmmm.2007.03.008
22. Wilson, W.D., Tanious, F.A., Ding, D., Kumar, A., Boykin, D.W., Colson, P., Houssier, C., Bailly, C.: Nucleic acid interactions of unfused aromatic cations: evaluation of proposed minor-groove, major-groove, and intercalation binding modes. J. Am. Chem. Soc. **120**, 10310–10321 (1998). https://doi.org/10.1021/ja981212n
23. Colson, P., Houssier, C., Bailly, C.: Use of electric linear dichroism and competition experiments with intercalating drugs to investigate the mode of binding of Hoechst 33258, Berenil and DAPI to GC sequences. J. Biomol. Struct. Dyn. **13**, 351–366 (1995). https://doi.org/10.1080/07391102.1995.10508845
24. Tanious, F.A., Wilson, W.D., Patrick, D.A., Tidwell, R.R., Colson, P., Houssier, C., Tardy, C., Bailly, C.: Sequence-dependent binding of bis-amidine carbazole dications to DNA. Eur. J. Biochem. **268**, 3455–3464 (2001). https://doi.org/10.1046/j.1432-1327.2001.02242.x
25. Haq, I., Trent, J.O., Chowdhry, B.Z., Jenkins, T.C.: Intercalative G-tetraplex stabilization of telomeric DNA by a cationic porphyrin. J. Am. Chem. Soc. **121**, 1768–1779 (1999). https://doi.org/10.1021/ja981554t
26. Wilson, W.D., Tanious, F.A., Barton, H.J., Jones, R., Strekowski, L., Boykin, D.W.: Binding of 4',6-diamidino-2-phenylindole (DAPI) to GC and mixed sequences in DNA: intercalation of a classical groove-binding molecule. J. Am. Chem. Soc. **111**, 5008–5010 (1989). https://doi.org/10.1021/ja00195a080
27. Czarny, A., Boykin, D.W., Wood, A.A., Nunn, C.M., Neidle, S., Zhao, M., Wilson, W.D.: Analysis of van der Waals and electrostatic contributions in the interactions of minor groove binding benzimidazoles with DNA. J. Am. Chem. Soc. **117**, 4716–4717 (1995). https://doi.org/10.1021/ja00121a034
28. Mergny, J.L., Lacroix, L.: Analysis of thermal melting curves. Oligonucleotides **13**, 515–537 (2003). https://doi.org/10.1089/154545703322860825
29. Tran, P.L.T., Largy, E., Hamon, F., Teulade-Fichou, M.-P., Mergny, J.-L.: Fluorescence intercalator displacement assay for screening G4 ligands towards a variety of G-quadruplex structures. Biochimie **93**, 1288–1296 (2011). https://doi.org/10.1016/j.biochi.2011.05.011
30. Monchaud, D., Allain, C., Bertrand, H., Smargiasso, N., Rosu, F., Gabelica, V., De Cian, A., Mergny, J.-L., Teulade-Fichou, M.-P.: Ligands playing musical chairs with G-quadruplex DNA: a rapid and simple displacement assay for identifying selective G-quadruplex binders. Biochimie **90**, 1207–1223 (2008). https://doi.org/10.1016/j.biochi.2008.02.019
31. Nguyen, B.T., Anslyn, E.V.: Indicator–displacement assays. Coord. Chem. Rev. **250**, 3118–3127 (2006). https://doi.org/10.1016/j.ccr.2006.04.009
32. Koeppel, F., Riou J-F., Laoui A., Mailliet P., Arimondo P.B., Labot D., Petitgenet O., Hélène C., Mergny J-L.: Ethidium derivatives bind to G-quartets, inhibit telomerase and act as fluorescent probes for quadruplexes. Nucleic Acids Res. **29**, 1087–1096 (2001). https://doi.org/10.1093/nar/29.5.1087

33. Nygren, J., Svanvik, N., Kubista, M.: The interactions between the fluorescent dye thiazole orange and DNA. Biopolymers **46**, 39–51 (1998). https://doi.org/10.1002/(SICI)1097-0282(199807)46:1%3c39::AID-BIP4%3e3.0.CO;2-Z
34. Lubitz, I., Zikich, D., Kotlyar, A.: Specific high-affinity binding of thiazole orange to triplex and G-quadruplex DNA. Biochemistry **49**, 3567–3574 (2010). https://doi.org/10.1021/bi1000849
35. Monchaud, D., Allain, C., Teulade-Fichou, M.-P.: Development of a fluorescent intercalator displacement assay (G4-FID) for establishing quadruplex-DNA affinity and selectivity of putative ligands. Bioorg. Med. Chem. Lett. **16**, 4842–4845 (2006). https://doi.org/10.1016/j.bmcl.2006.06.067
36. Lakowicz, J.R.: Principles of fluorescence spectroscopy, 3rd edn. Springer, Boston, MA, USA (2006)
37. Galezowska, E., Gluszynska, A., Juskowiak, B.: Luminescence study of G-quadruplex formation in the presence of Tb^{3+} ion. J. Inorg. Biochem. **101**, 678–685 (2007). https://doi.org/10.1016/j.jinorgbio.2006.12.013
38. Worlinsky, J.L., Basu, S.: Detection of quadruplex DNA by luminescence enhancement of lanthanide ions and energy transfer from lanthanide chelates. J. Phys. Chem. B **113**, 865–868 (2009). https://doi.org/10.1021/jp8100464
39. Xu, H., Zhang, H., Qu, X.: Interactions of the human telomeric DNA with terbium–amino acid complexes. J. Inorg. Biochem. **100**, 1646–1652 (2006). https://doi.org/10.1016/j.jinorgbio.2006.05.015
40. Vorlíčková, M., Kejnovská, I., Sagi, J., Renčiuk, D., Bednářová, K., Motlová, J., Kypr, J.: Circular dichroism and guanine quadruplexes. Methods **57**, 64–75 (2012). https://doi.org/10.1016/j.ymeth.2012.03.011
41. Czerwinska, I., Sato, S., Juskowiak, B., Takenaka, S.: Interactions of cyclic and non-cyclic naphthalene diimide derivatives with different nucleic acids. Bioorg. Med. Chem. **22**, 2593–2601 (2014). https://doi.org/10.1016/j.bmc.2014.03.034
42. Głuszyńska, A., Juskowiak, B., Kuta-Siejkowska, M., Hoffmann, M., Haider, S.: Carbazole ligands as c-myc G-quadruplex binders. Int. J. Biol. Macromol. **114**, 479–490 (2018). https://doi.org/10.1016/j.ijbiomac.2018.03.135
43. White, E.W., Tanious, F., Ismail, M.A., Reszka, A.P., Neidle, S., Boykin, D.W., Wilson, W.D.: Structure-specific recognition of quadruplex DNA by organic cations: influence of shape, substituents and charge. Biochem. Phys. **126**, 140–153 (2007). https://doi.org/10.1016/j.bpc.2006.06.006
44. Dash, J., Shirude, P.S., Hsu, S.-T.D., Balasubramanian, S.: Diarylethynyl amides that recognize the parallel conformation of genomic promoter DNA G-quadruplexes. J. Am. Chem. Soc. **130**, 15950–15956 (2008). https://doi.org/10.1021/ja8046552
45. Głuszyńska, A., Juskowiak, B., Kuta-Siejkowska, M., Hoffmann, M., Haider, S.: Carbazole derivatives binding to c-KIT G-quadruplex DNA. Molecules **23**, 1134 (2018). https://doi.org/10.3390/molecules23051134
46. Lopez-Gomollon, S., Nicolas, F.E.: Purification of DNA oligos by denaturing polyacrylamide gel electrophoresis (PAGE). Methods Enzymol. **529**, 65–83 (2013). https://doi.org/10.1016/B978-0-12-418687-3.00006-9
47. Pages, B.J., Ang, D.L., Wright, E.P., Aldrich-Wright, J.R.: Metal complex interactions with DNA. Dalton Trans. **44**, 3505–3526 (2015). https://doi.org/10.1039/C4DT02700K
48. Li, F., Chen, W., Tang, C., Zhang, S.: Recent development of interaction of transition metal complexes with DNA based on biosensor and its applications. Talanta **77**, 1–8 (2008). https://doi.org/10.1016/j.talanta.2008.06.011
49. Komor, A.C., Barton, J.K.: The path for metal complexes to a DNA target. Chem. Commun. **49**, 3617–3630 (2013). https://doi.org/10.1039/C3CC00177F
50. Bhattacharyya, D., Arachchilage, G.M., Basu, S.: Metal cations in G-quadruplex folding and stability. Front. Chem. **4**, 38 (2016). https://doi.org/10.3389/fchem.2016.00038
51. Dejeu, J., Lavergne, T., Nora, J.D., Defrancq, E., Pratviel, G.: Binding of metalloporphyrins to G-quadruplex DNA: the role of the central metal. Inorg. Chim. Acta **452**, 98–103 (2016). https://doi.org/10.1016/j.ica.2016.02.007

52. He, L., Meng, Z., Xie, Y., Chen, X., Li, T., Shao, F.: Aza-bridged bisphenanthrolinyl Pt(II) complexes: efficient stabilization and topological selectivity on telomeric G-quadruplexes. J. Inorg. Biochem. **166**, 135–140 (2017). https://doi.org/10.1016/j.jinorgbio.2016.11.011
53. Lin, S., Lu, L., Liu, J.-B., Liu, C., Kang, T.-S., Yang, C., Leung, C.-H., Ma, D.-L.: A G-quadruplex-selective luminescent iridium(III) complex and its application by long lifetime. Biochim. Biophys. Acta BBA Gen. Subj. **1861**, 1448–1454 (2017). https://doi.org/10.1016/j.bbagen.2016.08.022
54. Zhao, C., Sun, Y., Ren, J., Qu, X.: Recent progress in lanthanide complexes for DNA sensing and targeting specific DNA structures. Inorg. Chim. Acta **452**, 50–61 (2016). https://doi.org/10.1016/j.ica.2016.04.014
55. Lah, M.S., Pecoraro, V.L.: Isolation and characterization of $\{Mn^{II}[Mn^{III}(salicylhydroximate)]_4(acetate)_2(DMF)_6\}\cdot 2DMF$: an inorganic analog of M^{2+}(12-crown-4). J. Am. Chem. Soc. **111**, 7258–7259 (1989). https://doi.org/10.1021/ja00200a054
56. Pecoraro, V.L.: Structural characterization of [VO (salicylhydroximate)$(CH_3OH)]_3$: applications to the biological chemistry of vanadium (V). Inorg. Chim. Acta **155**, 171–173 (1989). https://doi.org/10.1016/S0020-1693(00)90405-5
57. Mezei, G., Zaleski, C.M., Pecoraro, V.L.: Structural and functional evolution of metallacrowns. Chem. Rev. **107**, 4933–5003 (2007). https://doi.org/10.1021/cr078200h
58. Tegoni, M., Remelli, M.: Metallacrowns of copper(II) and aminohydroxamates: thermodynamics of self assembly and host–guest equilibria. Coord. Chem. Rev. **256**, 289–315 (2012). https://doi.org/10.1016/j.ccr.2011.06.007
59. Happ, P., Plenk, C., Rentschler, E.: 12-MC-4 metallacrowns as versatile tools for SMM research. Coord. Chem. Rev. **289–290**, 238–260 (2015). https://doi.org/10.1016/j.ccr.2014.11.012
60. Ostrowska, M., Fritsky, I.O., Gumienna-Kontecka, E., Pavlishchuk, A.V.: Metallacrown-based compounds: applications in catalysis, luminescence, molecular magnetism, and adsorption. Coord. Chem. Rev. **327–328**, 304–332 (2016). https://doi.org/10.1016/j.ccr.2016.04.017
61. Alexiou, M., Tsivikas, I., Dendrinou-Samara, C., Pantazaki, A.A., Trikalitis, P., Lalioti, N., Kyriakidis, D.A., Kessissoglou, D.P.: High nuclearity nickel compounds with three, four or five metal atoms showing antibacterial activity. J. Inorg. Biochem. **93**, 256–264 (2003). https://doi.org/10.1016/S0162-0134(02)00591-3
62. Afrati, T., Pantazaki, A.A., Dendrinou-Samara, C., Raptopoulou, C., Terzis, A., Kessissoglou, D.P.: Copper inverse-9-metallacrown-3 compounds interacting with DNA. Dalton Trans. **39**, 765–775 (2010). https://doi.org/10.1039/B914112J
63. Tarushi, A., Raptopoulou, C.P., Psycharis, V., Kontos, C.K., Kessissoglou, D.P., Scorilas, A., Tangoulis, V., Psomas, G.: Copper(II) inverse-[9-metallacrown-3] compounds accommodating nitrato or diclofenac ligands: structure, magnetism, and biological activity. Eur. J. Inorg. Chem. **2016**, 219–231 (2016). https://doi.org/10.1002/ejic.201500769
64. Geromichalos, G.D., Tarushi, A., Lafazanis, K., Pantazaki, A.A., Kessissoglou, D.P., Psomas, G.: In vitro and in silico study of the biological activity of manganese(III) inverse-[9-MC-3]-metallacrowns and manganese(II) complexes with the anti-inflammatory drugs diclofenac or indomethacin. J. Inorg. Biochem. **187**, 41–55 (2018). https://doi.org/10.1016/j.jinorgbio.2018.07.007
65. Meng, Y.-X., Yang, H., Li, D.-C., Zeng, S.-Y., Cheng, G.-F., Li, S.-L., Dou, J.-M.: Synthesis, crystal structure, DNA-binding and magnetism of copper 15-metallacrown-5 complexes based on glycinehydroxamic acid ligand. RSC Adv. **6**, 47196–47202 (2016). https://doi.org/10.1039/C6RA05239H
66. Tarushi, A., Zampakou, M., Perontsis, S., Lafazanis, K., Pantazaki, A.A., Hatzidimitriou, A.G., Geromichalos, G.D., Psomas, G.: Manganese(II) complexes of tolfenamic acid or naproxen in polymeric structures or encapsulated in [15-MC-5] manganese(III) metallacrowns: structure and biological activity. Inorganica Chim. Acta **483**, 579–592 (2018). https://doi.org/10.1016/j.ica.2018.09.001
67. Yang, Y.-S., Liu, L.-J., Ju, H.-Y., Liu, X.-Y., Li, Y.-G., Yan, S.-P.: Dicyanamide bridged Cu(II)36-metallacrown-6 complex with 1,4,7-triisopropyl-1,4,7-triazacyclononane

and binding properties with DNA. Molecules **23**, 1269 (2018). https://doi.org/10.3390/molecules23061269
68. Rajczak, E., Gluszynska, A., Juskowiak, B.: Interaction of metallacrown complexes with G-quadruplex DNA. J. Inorg. Biochem. **155**, 105–114 (2016). https://doi.org/10.1016/j.jinorgbio.2015.11.025
69. Rajczak, E., Pecoraro, V.L., Juskowiak, B.: Sm(III)[12-$MC_{Ga(III)shi}$-4] as a luminescent probe for G-quadruplex structures. Metallomics **9**, 1735–1744 (2017). https://doi.org/10.1039/c7mt00232g
70. Rajczak, E., Juskowiak, B.: Conformational rearrangements of G-quadruplex topology promoted by Cu(II) 12-$MC_{Cu(II)PyrAcHA}$-4 metallacrown. Int. J. Biol. Macromol. **156**, 1258–1269 (2020). https://doi.org/10.1016/j.ijbiomac.2019.11.163
71. Paison, F., Su, B., Pan, D., Yan, T., Wu, J.: The study of biological activities of various mixed ligand complexes of Nickel(II). Austin Biochem. **5**, 1025 (2020)
72. Abrescia, N.G.A., Huynh-Dinh, T., Subirana, J.A.: Nickel-guanine interactions in DNA: crystal structure of nickel-d$[CGTGTACACG]_2$ J. Biol. Inorg. Chem. **7**, 195–199 (2002). https://doi.org/10.1007/s007750100286
73. Cervantes-Cervantes, M.P., Calderón-Salinas, J.V., Albores, A., Muñoz-Sánchez, J.L.: Copper increases the damage to DNA and proteins caused by reactive oxygen species. Biol. Trace Elem. Res. **103**, 229–248 (2005). https://doi.org/10.1385/BTER:103:3:229
74. Afrati, T., Dendrinou-Samara, C., Raptopoulou, C., Terzis, A., Tangoulis, V., Tsipis, A., Kessissoglou, D.P.: Experimental and theoretical study of the antisymmetric magnetic behavior of copper *inverse*-9-metallacrown-3 compounds. Inorg. Chem. **47**, 7545–7555 (2008). https://doi.org/10.1021/ic8003257
75. Afrati, T., Dendrinou-Samara, C., Raptopoulou, C., Terzis, A., Tangoulis, V., Kessissoglou, D.P.: Copper inverse-9-metallacrown-3 compounds showing antisymmetric magnetic behaviour. Dalton Trans. 5156–5164 (2007). https://doi.org/10.1039/B708767E
76. Long, E.C., Barton, J.K.: On demonstrating DNA intercalation. Acc. Chem. Res. **23**, 271–273 (1990). https://doi.org/10.1021/ar00177a001
77. Psomas, G.: Mononuclear metal complexes with ciprofloxacin: synthesis, characterization and DNA-binding properties. J. Inorg. Biochem. **102**, 1798–1811 (2008). https://doi.org/10.1016/j.jinorgbio.2008.05.012
78. Carter, M.T., Rodriguez, M., Bard, A.J.: Voltammetric studies of the interaction of metal chelates with DNA. 2. Tris-chelated complexes of cobalt (III) and iron (II) with 1,10-phenanthroline and 2,2′-bipyridine. J. Am. Chem. Soc. **111**, 8901–8911 (1989). https://doi.org/10.1021/ja00206a020
79. Tarushi, A., Hatzidimitriou, A.G., Estrader, M., Kessissoglou, D.P., Tangoulis, V., Psomas, G.: Toward multifunctional materials incorporating stepladder manganese(III) inverse-[9-MC-3]-metallacrowns and anti-inflammatory drugs. Inorg. Chem. **56**, 7048–7057 (2017). https://doi.org/10.1021/acs.inorgchem.7b00655
80. Wolfe, A., Shimer, G., Meehan, T.: Polycyclic aromatic hydrocarbons physically intercalate into duplex regions of denatured DNA. Biochemistry **26**, 6392–6396 (1987). https://doi.org/10.1021/bi00394a013
81. Dimitrakopoulou, A., Dendrinou-Samara, C., Pantazaki, A.A., Alexiou, M., Nordlander, E., Kessissoglou, D.P.: Synthesis, structure and interactions with DNA of novel tetranuclear, $[Mn_4(II/II/II/IV)]$ mixed valence complexes. J. Inorg. Biochem. **102**, 618–628 (2008). https://doi.org/10.1016/j.jinorgbio.2007.10.005
82. Raja, D.S., Bhuvanesh, N.S.P., Natarajan, K.: DNA binding, protein interaction, radical scavenging and cytotoxic activity of 2-oxo-1,2-dihydroquinoline-3-carbaldehyde(2′-hydroxybenzoyl)hydrazone and its Cu(II) complexes: a structure activity relationship study. Inorg. Chim. Acta **385**, 81 (2012). https://doi.org/10.1016/j.ica.2011.12.038
83. Sarkar, D., Das, P., Basak, S., Chattopadhyay, N.: Binding interaction of cationic phenazinium dyes with calf thymus DNA: a comparative study. J. Phys. Chem. B **112**, 9243–9249 (2008). https://doi.org/10.1021/jp801659d

84. Mahadevan, S., Palaniandavar, M.: Spectroscopic and voltammetric studies on copper complexes of 2,9-dimethyl-1,10-phenanthrolines bound to calf thymus DNA. Inorg. Chem. **37**, 693–700 (1998). https://doi.org/10.1021/ic961066r
85. Li, G.Y., Du, K.J., Wang, J.Q., Liang, J.W., Kou, J.F., Hou, X.J., Ji, L.N., Chao, H.: Synthesis, crystal structure, DNA interaction and anticancer activity of tridentate copper(II) complexes. J. Inorg. Biochem. **119**, 43–53 (2013). https://doi.org/10.1016/j.jinorgbio.2012.09.019Get
86. Zhang, Q., Liu, J., Chao, H., Xue, G., Ji, L.: DNA-binding and photocleavage studies of cobalt(III) polypyridyl complexes: $[Co(phen)_2IP]^{3+}$ and $[Co(phen)_2PIP]^{3+}$. J. Inorg. Biochem. **83**, 49–55 (2001). https://doi.org/10.1016/S0162-0134(00)00132-X
87. Pratviel, G., Bernadou, J., Meunier, B.: DNA and RNA cleavage by metal complexes. Adv. Inorg. Chem. **45**, 251–262 (1998). https://doi.org/10.1016/S0898-8838(08)60027-6
88. García-Giménez, J.L., González-Álvarez, M., Liu-González, M., Macías, B., Borrás, J., Alzuet, G.: Toward the development of metal-based synthetic nucleases: DNA binding and oxidative DNA cleavage of a mixed copper(II) complex with *N*-(9*H*-purin-6-yl)benzenesulfonamide and 1,10-phenantroline. Antitumor activity in human Caco-2 cells and Jurkat T lymphocytes. Evaluation of *p*53 and *Bcl-2* proteins in the apoptotic mechanism. J. Inorg. Biochem. **103**, 923–934 (2009). https://doi.org/10.1016/j.jinorgbio.2009.04.003
89. Balagurumoorthy, P., Brahmachari, S.K.: Structure and stability of human telomeric sequence. J. Biol. Chem. **269**, 21858–21869 (1994). https://doi.org/10.1016/S0021-9258(17)31882-3
90. Chow, C.Y., Eliseeva, S.V., Trivedi, E.R., Nguyen, T.N., Kampf, J.W., Petoud, S., Pecoraro, V.L.: Ga^{3+}/Ln^{3+} metallacrowns: a promising family of highly luminescent lanthanide complexes that covers visible and near-infrared domains. J. Am. Chem. Soc. **138**, 5100–5109 (2016). https://doi.org/10.1021/jacs.6b00984
91. Gibney, B.R., Kessissoglou, D.P., Kampf, J.W., Pecoraro, V.L.: Copper (II) 12-metallacrown-4: synthesis, structure, ligand variability, and solution dynamics in the 12-MC-4 structural motif. Inorg. Chem. **33**, 4840–4849 (1994). https://doi.org/10.1021/ic00100a006
92. Gibney, B.R., Wang, H., Kampf, J.W., Pecoraro, V.L.: Structural evaluation and solution integrity of alkali metal salt complexes of the manganese 12-metallacrown-4 (12-MC-4) structural type. Inorg. Chem. **35**, 6184–6193 (1996). https://doi.org/10.1021/ic960371+
93. Kessissoglou, D.P., Bodwin, J.J., Kampf, J., Dendrinou-Samara, C., Pecoraro, V.L.: Pseudohalide complexation by manganese 12-metallacrowns-4 complexes. Inorg. Chim. Acta **331**, 73–80 (2002). https://doi.org/10.1016/S0020-1693(01)00755-1
94. Zaleski, C.M., Tricard, S., Depperman, E.C., Wernsdorfer, W., Mallah, T., Kirk, M.L., Pecoraro, V.L.: Single molecule magnet behavior of a pentanuclear Mn-based metallacrown complex: solid state and solution magnetic studies. Inorg. Chem. **50**, 11348–11352 (2011). https://doi.org/10.1021/ic2008792
95. Atzeri, C., Marzaroli, V., Quaretti, M., Travis, J.R., Bari, L.D., Zaleski, C.M., Tegoni, M.: Elucidation of ^1H NMR paramagnetic features of heterotrimetallic lanthanide(III)/manganese(III) 12-MC-4 complexes. Inorg. Chem. **56**, 8257–8269 (2017). https://doi.org/10.1021/acs.inorgchem.7b00970
96. Wang, Y., Patel, D.J.: Solution structure of the human telomeric repeat d[AG3(T2AG3)3] G-tetraplex. Structure **4**, 263–282 (1993). https://doi.org/10.1016/0969-2126(93)90015-9
97. Parkinson, G.N., Lee, M.P.H., Neidle, S.: Crystal structure of parallel quadruplexes from human telomeric DNA. Nature **417**, 876–880 (2002). https://doi.org/10.1038/nature755
98. Ambrus, A., Chen, D., Dai, J., Bialis, T., Jones, R.A., Yang, D.: Human telomeric sequence forms a hybrid-type intramolecular G-quadruplex structure with mixed parallel/antiparallel strands in potassium solution. Nucleic Acids Res. **34**, 2723–2735 (2006). https://doi.org/10.1093/nar/gkl348
99. Dai, J., Carver, M., Punchihewa, C., Jones, R.A., Yang, D.: Structure of the Hybrid-2 type intramolecular human telomeric G-quadruplex in K^+ solution: Insights into structure polymorphism of the human telomeric sequence. Nucleic Acids Res. **35**, 4927–4940 (2007). https://doi.org/10.1093/nar/gkm522

Magnetic Metallacrowns: From Randomness to Rational Design

Thaddeus T. Boron III

Abstract Early single-molecule magnets (SMMs) featured *3d* metal ions and mixed 3*d*/4*f* ions in interesting geometric arrangements. While these coordination compounds had interesting molecular magnetic behaviors, they lacked structural predictability, making it difficult to systematically control their physical properties. Metallacrowns allow for the rational design of SMMs by selecting appropriate metal ions and ligands with predictable coordination environments. This design strategy allows chemists to systematically vary multiple physical properties, including the number of magnetic centers, pseudo-symmetries, and connectivity between magnetic centers. Additionally, the cavity of metallacrowns offers a unique opportunity to systematically investigate how structural deformations, pseudo-symmetries, and intrinsic magnetic properties of different metal ions affect the overall magnetic properties. In this chapter, we will explore the progression of the use of metallacrowns as SMMs from the first known Mn–lanthanide "pseudo"-metallacrown in 2004 to "true" metallacrowns recently reported. The progression from early pseudo-metallacrowns to "true" metallacrowns follows a general trend of minimizing the number of magnetic centers and controlling the overall geometry of the structure. This geometric control and selective modification to the structure have allowed chemists to explore the roles that the intrinsic properties of lanthanides, structural distortions around lanthanide ions, and ligand-choice have on the overall magnetic behavior.

1 Introduction

In the 1980s and 1990s, interest in the properties of molecular magnets began to grow with the discovery of a manganese-containing coordination compound that showed unique magnetic properties [1–3]. The manganese-containing compound, $[Mn_{12}O_{12}\text{-(caboxylato)}_{16}]$, often referred to as $Mn_{12}(OAc)$, (OAc = acetate), demonstrated magnetic behavior that originated from the molecule, rather than from bulk-magnetic properties, providing physicists and chemists with an opportunity to study

T. T. Boron III (✉)
Slippery Rock University, Slippery Rock, PA, USA
e-mail: Thaddeus.Boron@sru.edu

C. M. Zaleski (ed.), *Advances in Metallacrown Chemistry*,
https://doi.org/10.1007/978-3-031-08576-5_5

the transition from nano-to bulk properties [2]. This compound is generally recognized as the first single-molecule magnet (SMM). It was realized that SMMs, or their single-chain and single-ion analogues, could be utilized to build a new generation of spintronic devices, capable of high-density information storage, quantum computing, or magnetic refrigeration [4].

1.1 Molecular Magnetism

Molecular magnets, such as single-molecule magnets (SMMs), single-ion magnets (SIMs), or single-chain magnets (SCMs), show superparamagnetic behavior that originates from the individual molecule (or ion)'s overall spin and Ising-type magnetoanisotropy [5, 6]. Superparamagnetism is similar to paramagnetism in that it originates from the magnetic moments of residual unpaired electrons in a compound. The key difference between paramagnetism and superparamagnetism is the size of the magnetic domain, that is, the region of space where magnetic moments align to minimize the energy of repulsion. In superparamagnets, the size of the magnetic domain is comparable to the size of the individual molecule, where in paramagnets—the magnetic domain is significantly larger [6].

Unlike paramagnetism, however, below a critical temperature, superparamagnets display "blocked" magnetic behavior. This blocked behavior results from the Ising-type magnetoanisotropy, which typically only allows one of two different magnetic moment orientations that are anti-parallel to each other. This orientation preference creates an energy barrier that separates the two different orientations. To overcome this energy barrier, either thermal energy or a coercive field must be applied. The time required for the relaxation over the energy well is described by the Arrhenius equation:

$$\tau = \tau_0 e^{\frac{KV}{k_B T}} \tag{1}$$

where τ is the relaxation time, τ_0 is a length of time characteristic to the material, K is the molecule's magnetic anisotropy, V is the molecule's volume, k_B is the Boltzmann constant, and T is the temperature of relaxation [6].

The KV term in the equation above is also directly related to a molecule's spin and anisotropy. In many manuscripts, the magnetic properties of an SMM are described by a spin Hamiltonian:

$$\widehat{H} = g\beta \vec{\boldsymbol{H}}\, \widehat{\boldsymbol{S}} + D\widehat{S}_z^{\,2} + E\left(\widehat{S}_x^{\,2} - \widehat{S}_y^{\,2}\right) \tag{2}$$

where g is the Landé factor, β is the Bohr magneton, $\vec{\boldsymbol{H}}$ is the applied external magnetic field, $\hat{\boldsymbol{S}}$ is the spin operator, D is the axial anisotropy eigenvalue, $\hat{S}_z$ is the

spin operator along the z-axis, E is the equatorial anisotropy eigenvalue, and $\hat{S}_x$ and $\hat{S}_y$ are the spin operators along the x and y-axes, respectively. The full equation can be derived and the interested reader is invited to read Chapter 2 of Gatteschi, Sessoli, and Villain's *Molecular Nanomagnets* [6] or Girerd and Journaux's Chapter 7 on molecular magnetism in Que's *Physical Methods in Bioinorganic Chemistry* [7]. For axially symmetric cases in zero-field, the spin Hamiltonian can be simplified to

$$\widehat{H} = g\beta \vec{\boldsymbol{H}} \widehat{\boldsymbol{S}} + D\hat{S}_z^2 \tag{3}$$

The reader may notice that the first term is the Zeeman splitting Hamiltonian. Thus, for a molecular magnet with Ising-type anisotropy, the Hamiltonian may be reduced to

$$\widehat{H} = D\hat{S}_z{}^2 \tag{4}$$

with a corresponding eigenvalue U_{eff} of

$$U_{eff} = -DM_s{}^2 \tag{5}$$

$$U_{eff} = -D\left(M_s{}^2 - \frac{1}{4}\right) \tag{6}$$

for integer and non-integer spins, respectively, and where M_s is the microspin state values from the $\hat{S}_z$ operator. The overall sign of the magnetoanisotropy eigenvalue D must be negative to ensure that the spin states with the largest magnitude have the lowest overall energy values. A positive D eigenvalue correlates to easy-plane anisotropy and would give the smallest magnitude microspin states as the lowest overall energy.

This splitting of the magnetic spin states creates bistable ground states separated by the eigenvalue U_{eff}. This eigenvalue U_{eff} is the effective height of the energy barrier to spin reversal (Fig. 1). Thus, the earlier equation describing the time required to scale the energy barrier can be modified to correlate to the energy of the barrier:

$$\tau = \tau_0 e^{\frac{U_{eff}}{k_B T_c}} \tag{7}$$

where T_c now specifies a critical temperature, in Kelvin, related to the thermal relaxation over the energy barrier described by U_{eff}. Unlike paramagnets, superparamagnets (and specifically SMMs, SIMs, and SCMs for our interests) will maintain a magnetic orientation below this critical temperature. This energy barrier and the size of the particles involved is what makes molecular magnets so intriguing as potential data storage devices. If a single molecule could maintain its magnetic orientation at a high temperature, then the particle could potentially be used to store information

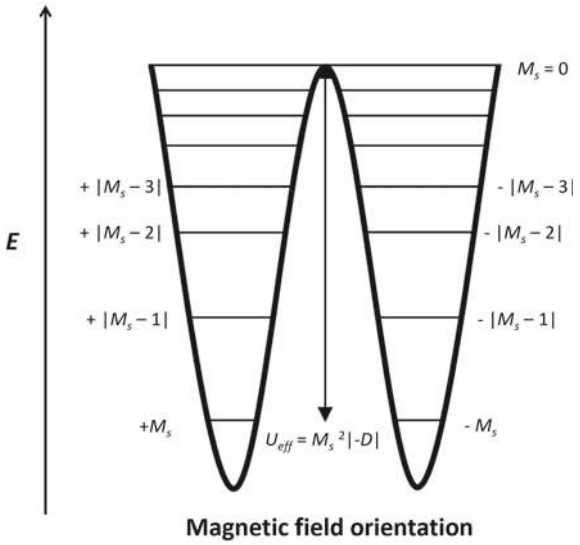

Fig. 1 The effective energy barrier, U_{eff}, separates the spin states of the molecular magnet. The height of the energy barrier is dependent on the overall spin of the molecule, M_s, and the anisotropy of the molecule, D

based on the spin orientation. Because of the small size of the particle, a significantly larger amount of information could be stored in the same overall space.

1.2 Synthetic Strategies for Preparing Molecular Magnets

Two synthetic strategies exist for preparing molecular magnets. The first approach is a "top-down" approach, where one employs a bulk material with known magnetic behavior and attempts to sufficiently shrink the material such that the crystalline size and the magnetic domain size are similar. A second approach, a "bottom-up" approach, attempts to prepare new materials that have the potential to display the desired properties. In 1998, Aromi and co-workers discussed four advantages of the bottom-up approach. These included that since the magnetic materials are synthesized and isolated from the solution, they often produce a particle with a single, well-defined size. As the molecules are often prepared from ionic salts, the peripheral ligands can potentially be modified easily by changing the identity of the starting materials. Due to the fact that they are often isolated from common organic solvents, they can potentially be processed in common solvents, making them ideal candidates for future applications, such as deposition and preparing of films. Lastly, molecular magnets prepared from a bottom-up approach are sub-nanoscale [8]. This sub-nanoscale can also lead to mono-disperse particles, that reduce potential intermolecular interactions [9]. The compounds that we will discuss below, including metallacrowns, feature a bottom-up synthetic scheme.

Regardless if a "top-down" or "bottom-up" approach is pursued for molecular magnets, it is relatively apparent that the synthetic strategy should attempt to maximize the spin, M_s, and/or the magnetoanisotropy, D, in Eqs. 5 and 6. While increasing spin seems to be the obvious solution to quickly increasing the energy barriers of molecular magnets, computational chemists have suggested that this increase does not have the desired effect. In 2007, Waldmann proposed that earlier efforts to increase the spin values of molecular magnets, the so-called "golden rule" of SMM development, were misdirected [10]. Additionally, Waldmann proposed that in cases of strongly coupled spin and anisotropy values, such as the case for lanthanide ions, Eq. 5 would also fail. So while it seems apparent that increasing the spin value M_s in Eq. 5 will lead to an exponential increase in the thermal energy barrier, Waldmann found that because the projection coefficients of the zero-field-splitting tensor D (and therefore D itself) scale with spin as M_s^{-2}, the energy barrier seemed to increase linearly with spin [10]. Instead, Waldmann suggested that SMM properties could be improved by either increasing the number of magnetic centers in the molecule or to focus on the anisotropy term.

In 2009, Ruiz, Neese, Kortus, and co-workers used density functional theory (DFT) to examine the magnetoanisotropy of mononuclear transition metal compounds [11]. The authors looked at the zero-field splitting parameters of trigonal Jahn–Teller distortions, Bailar twists, Berry pseudorotations, and planarization of tetrahedral compounds. The authors found that Jahn–Teller distortions, such as those found in high-spin Mn^{III}, produced relatively large D values, with the sign determined by the contraction/elongation of the octahedral coordination environment. Bailar twists of d^5 ions with trigonal prismatic geometry also produced large, negative D values. A Berry pseudorotation of d^5 ions led to either positive (tetragonal pyramid) or close to zero D values for trigonal bipyramidal compounds. Lastly, during the conversion of tetrahedral compounds to square planar for d^5 ions, a maximum negative anisotropy value was obtained in the middle of the pathway. Ruiz, Neese, and Kortus also suggested that it could be possible to link multiple magnetic centers, ensuring that their Jahn–Teller axes were parallel to one another. However, the authors cautioned that this strategy was most efficient for smaller molecules (trinuclear) versus larger molecules (pentanuclear) [11].

1.3 Single-Molecule, Single-Ion, and Single-Chain Magnets

Single-molecule, single-ion, and single-chain magnets, in principle, behave as superparamagnets. There are, however, a few distinguishing features that warrant discussion. Briefly, we will outline key differences between the three before giving some representative examples of each.

Single-molecule magnets tend to serve as the "archetype" of molecular nanomagnets, and it is often easier to identify how single-ion or single-chain magnets differ from SMMs. A single-ion magnet possess a residual charge typically due to a difference in charge between the magnetic ion and ligands present. Single-ion magnets

are governed by similar relaxation pathways as SMMs. The key difference is that SMMs are molecular in nature, while SIMs are ionic in nature.

Single-chain magnets have two key distinguishing features. First, single-chain magnets must behave as a one-dimensional Ising-type ferro- or ferrimagnet and the ratio between intra- and inter-chain interactions must be larger than 10^4 [12, 13]. Second, because single-chain magnets possess multiple magnetic centers and the environment of the spin-centers differs based on location, different relaxation modes exist for SCMs and these modes are best modeled by Glauber dynamics [14]. When a relaxation process begins in an SCM, it can occur at either the end of the chain or within the chain. A magnetic center at the end of the chain only interacts with one other magnetic center and will have half the barrier-to-reversal when compared to a magnetic center located within the chain. A magnetic center located within the chain has two neighbors with which it interacts, doubling the energy barrier as the reversal process must overcome both coupling interactions. Once a spin flips, the relaxation process can propagate throughout the chain in a zero-energy fashion or it will reverse, i.e., return to the original orientation, if there is not enough energy to overcome the magnetic coupling between neighbors. A third relaxation pathway for SCMs also exists. In this pathway, the magnetization of the entire chain reverses in a single step, rather than in a cascade. This collective reversal is only observed for small chains at low temperature.

1.3.1 Mn_{12} Acetate, the Archetypical Single-Molecule Magnet

Perhaps the most well-studied SMM is the Mn_{12}(OAc) and its derivatives. First identified in 1980 by Lis (Fig. 2) [15], its utility as an SMM was expounded upon by Caneschi, Gatteschi, and Sessoli, beginning in 1991 [1, 16]. The compound is

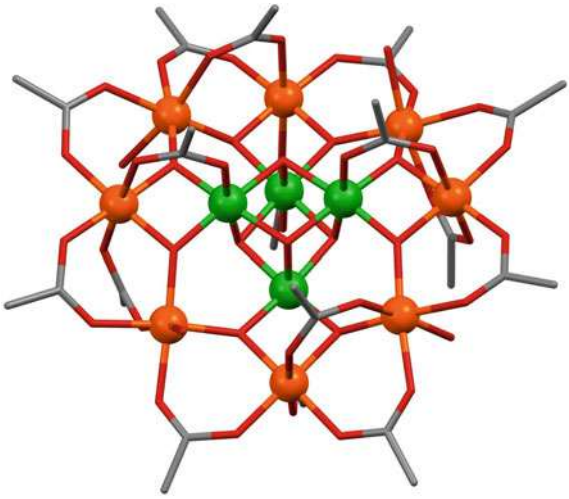

Fig. 2 Mn_{12}(OAc) was the first identified single-molecule magnet. Color scheme: orange—Mn^{III}; green—Mn^{IV}; red—oxygen; gray—carbon. Hydrogen atoms excluded for clarity

composed of eight Mn^{III} ions surrounding a Mn^{IV}-oxo cubane core. The magnetic properties have been well-studied for this compound and the interested reader is invited to read one of the many original manuscripts, reviews, or books on the compound [5, 6, 17, 18]. In subsequent years, the effect of modifying the carboxylate bridges has been examined [19, 20] as well as deposition onto surfaces [21, 22]. It was found from out-of-phase magnetic susceptibility measurements that the effective barrier to energy relaxation was 68 K, with a spin value $M_s = \pm 10$ and an magneto anisotropy D of $-0.47\ cm^{-1}$ [17]. However, due to tunneling [18, 23, 24] and other relaxation pathways, the functional energy barrier was actually closer to 7 K [20]. Remarkably, despite being the first synthetically prepared SMM, $Mn_{12}OAc$ was the highest performing SMM in terms of blocking temperature for the next decade.

1.3.2 Bis(Phthalocyaninato)-Terbium Compounds and Lanthanide-Containing Polyoxometalates as Representative Single-Ion Magnets

Bis(phthalocyaninato)-lanthanide compounds are relatively well-known, and in the 1990s were considered possible candidates for a diverse range of material applications, including electrochromic display materials [25], molecular semiconductors, [26] or non-linear optical applications [27]. In 2003, Ishikawa and co-workers reported the magnetic properties, finding that the tetrabutylammonium bis(phthalocyaninato)-terbium(III) ($[Pc_2Tb^{III}]^-TBA^+$) and the dysprosium(III) analog ($[Pc_2Dy^{III}]^-TBA^+$) displayed frequency-dependent slow-magnetic relaxation, a hallmark of single-molecule magnetism (Fig. 3a) [28–30]. As the only magnetic site in the compound was the lanthanide ion, these bis(phthalocyaninato)-lanthanide compounds ushered in a new area within the broader field of molecular magnetism, the area of single-ion magnetism. The terbium(III) analog, excitingly, showed a functional energy barrier of about 40 K at 997 Hz. The calculated barrier height for the terbium compound was about 230 cm^{-1}, while it was only 28 cm^{-1} for the dysprosium analog [28]. In subsequent studies, Ishikawa proposed

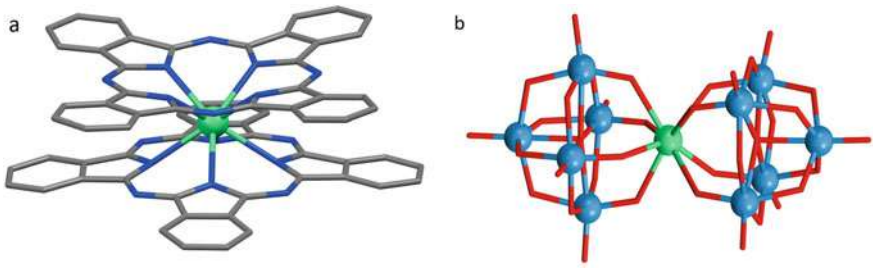

Fig. 3 $[Pc_2Er]^-$ **a** and $[Er(W_5O_{18})_2]^{9-}$ **b** are shown. Hydrogen atoms are omitted for clarity in both structures. In addition, for $[Er(W_5O_{18})_2]^{9-}$, potassium ions are omitted for clarity. Color scheme: teal—Er^{III}; red—oxygen; blue—nitrogen; light blue spheres—W; gray—carbon

that the ligand field around the lanthanide affected the stability of the ground states [29]. This was further supported by a 2007 report published by Takamatsu on the bonding/anti-bonding properties relationship between the ligand and the metal [31], helping confirm that the magnetic properties were molecular in nature and not due to intermolecular interactions.

Coronado, studying lanthanide-containing polyoxometalates (POMs), further developed the new branch of molecular magnets. Examining different lanthanide POMs where the POM itself contained diamagnetic ions, Coronado and co-workers found that deviations from an ideal square anti-prism (idealized D_{4d} symmetry) and the separation between ligand-planes coordinated to the lanthanide affected the magnetic properties [32, 33]. Coronado measured the skew angle, the angle between the square ligand plane above and below the central lanthanide ion, as well as the separation between the two ligand planes. When Coronado compared the structural properties of analogous POMs and phthalocyaninato compounds. For the $[Er(W_5O_{18})_2]^{9-}$ POM (Fig. 3b), the axially compressed square anti-prism with a skew angle of 44.2° displayed SMM-like behavior, while the $[Pc_2Er]^-$ analog, with an elongated anti-prism and a skew angle of 41.4°, did not show SMM-behavior [33].

Rinehart and Long summarized the effect structural modifications had on lanthanide SIM behavior in an excellent 2011 *Chemical Science* manuscript. Rinehart and Long summarized that terbium(III), dysprosium(III), and holmium(III) ions had an electron cloud best described as short, but wide (oblate), while erbium(III), thulium(III), and ytterbium(III) ions had taller, narrow electron density clouds (prolate) (Fig. 4). For oblate ions, maximum anisotropy occurred when the ligand field was above or below the electron cloud, while for prolate ions, ligands located equatorially maximized anisotropy [34]. Tong and co-workers continued the investigation of symmetry and crystal field played on lanthanide SMMs in a 2018 *Chemical Society Review* [35]. The review highlights specific point groups that may help suppress quantum tunneling of magnetization by removing transverse crystal field parameters.

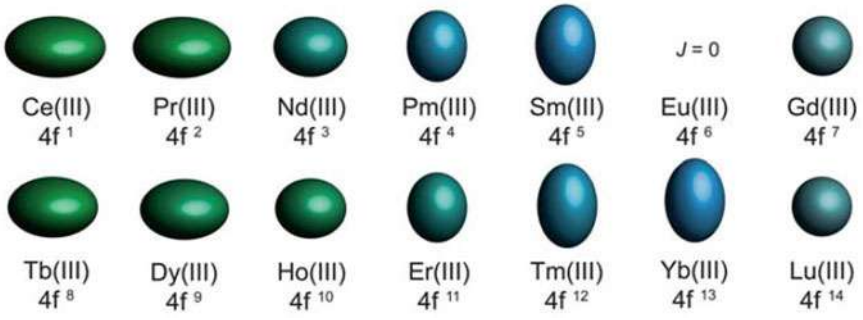

Fig. 4 Predicted shapes of the lanthanides. Reproduced with permission from the Royal Society of Chemistry, Rinehart and Long [34]

1.3.3 Cobalt-Radical Chains, the First Single-Chain Magnets

Caneschi and co-workers identified the first single-chain magnet in 2001, roughly 48 years after Glauber hypothesized their existence [36]. The first reported SCM was a one-dimensional chain made of a coordinated cobalt(II) ion and an antiferromagnetically coupled organic radical. The compound, [Co(hfac)$_2$(NITPhOMe)], where hfac$^-$ is hexalfuoroacetylacetonate and NITPhOMe is 4′-methoxy-phenyl-4,4,5,5-tetramethylimidazoline-1-oxyl-3-oxide, had alternating Co(hfac)$_2$ and NITPhOMe subunits [37, 38]. The chain showed frequency-dependent behavior below 17 K with a calculated energy barrier of relaxation of 154 K.

2 Metallacrowns

Metallacrowns are the inorganic analogs of crown ethers [39]. Using multidentate ligands to coordinate multiple-metal ions, metallacrowns (MCs) are macrocyclic structures that can be easily modified by metal or ligand choice, affording a wide range of regular, polygon-shaped structures [40, 41]. If a hydroxamic acid is utilized as the ring ligand, an [M–N–O] repeat unit is formed. The oxygen atoms from the hydroximate face toward the center of the ring, forming an oxygen-rich cavity that is capable of participating in electrostatic interactions with cations and serving as a Lewis base.

The naming convention used for MCs closely mimics that of crown ethers. Coordinated metals and ligands are listed first, followed by the total ring size are numerically identified, then MC for metallacrown and the elements or ligands found in the MC ring, and finally followed by the number of oxygen atoms in the ring. The general nomenclature is M_cX[12-MC$_{M,rZ(L)}$-4M_cX[12-MC$_{MrZ(L)}$-4]Y, where M_c is the central metal, X is an anion serving as a bridge between the ring metal and the central metal, M_r is the ring metal, Z is the non-oxygen heteroatom in the ring, L is the ring ligand, and Y is any uncoordinated anion necessary for charge balance of the MC. This may sometimes be abbreviated as [12-MC-4], MX[12-MC-4], or M[12-MC-4] for the sake of simplicity. Derivatives where the ring-oxygen atoms are substituted for nitrogen atoms exist and are known as azametallacrowns (aza-MCs) [42–44]. If the ring metal faces the central cavity, rather than the oxygen atoms, the central area becomes Lewis acidic, allowing for anion recognition, and is classified as an “inverse metallacrown” [45].

2.1 Structural Control of Metallacrowns

Formation of MCs depends on a number of factors, including ligand choice, metal choice, solvent, overall stoichiometry, crystallization conditions, and central metal identity. Of these factors, ligand/metal choice and stoichiometry are often the easiest

to understand and provide a good "starting point" when thinking of preparing new MCs. When considering the many different possibilities for ring ligands and ring metals, it is often useful to consider the charges that the ligand and metal ion will take upon coordination. For instance, selecting a trivalent cation and trivalent anion will allow a neutral MC-ring to be isolated. However, it should be noted that this is not a "hard and fast" rule; copper(II) has been found to form MCs with trivalent ring ligands [39]. Next, considering the angle between the chelating atoms of the ring ligand and the preferred geometry of the ring metal can help predict the final shape of the MC. Ring metals that prefer planar or octahedral geometries tend to coordinate better with ligands that have binding sites that are also planar. The presence of axial elongation via a Jahn–Teller axis may also promote MC formation or provide selectivity for axial ligands that coordinate the ring metal to the central ligand.

Two common magnetic metallacrowns have a 12-MC-4 or a 15-MC-5 geometry and serve as excellent archetypes for MC structure and nomenclature (Fig. 5). If the target metallacrown is a 12-MC-4, one would want to select a ring ligand and ring metals that encourage completing a full circle in four repeat units. A classic example is M 12-$MC_{Mn^{III}(N)shi}$-4, a 12-membered ring with Mn^{III} and salicylhydroximate as the ring ligand [46]. Salicylhydroxamic acid (H_3shi) is a triprotic ligand and the fully deprotonated ligand possesses two binding pockets, one a six-membered ring formed by the phenolate oxygen and the imine nitrogen and the other a five-membered ring from the hydroximate oxygen and a carbonyl oxygen. These two pockets are orthogonal to each other, creating a 90° internal angle. If a metal that prefers a square planar or octahedral geometry is used, such as manganese(III), given the correct stoichiometries (1 central metal:4 ring ligand:4 ring metal), a relatively square-shaped 12-MC-4 can be formed by repeating the ligand—ring metal subunit four times. On the other hand, a ligand that creates two binding sites 108° apart, such as the hydroxamic acid derivative of *S*-tyrosine [47] or the hydroxamic acid derivative of phenylalanine [48], and a ring metal such as copper(II) may produce a 15-membered ring with 5 repeat units. Thus, if one equivalent of gadolinium(III) nitrate ($Gd(NO_3)_3$) is added to a dimethylformamide solution of five equivalents of copper(II) acetate and picoline hydroxamic acid (picHA), $Gd(NO_3)_3$[15-$MC_{Cu^{II}(N)picHA}$-5] can be isolated in a 76% yield [49]. It has been found that the stoichiometric ratios between the metals and ligands or the presence of multiple coordinating solvents can affect the identity of the isolated metallacrown. Under certain conditions, lanthanides can interrupt the ring formation of the MC and lead to unexpected structures. Modifying ligand/metal stoichiometry or doping the solution with an additional coordinating solvent can lead to the formation of different MCs. For instance, using H_3shi, which often yields 12-MC-4 structures, has been shown to yield 9-MC-3 [50], 14-MC-5 [51], or 15-MC-5 [52] geometries depending on the stoichiometry of the ligand, ring, and central metals or the presence of a competing coordinating solvent. Additionally, non-traditional MC-types, such as 28-MC-10 [53] or 22-MC-8 [54], have also been produced despite using solvents and metal/ligand stoichiometries previously shown to produce more "traditional" MC architectures. We will discuss some of these structures in more depth as we investigate the SMM properties of different MC structures.

The magnetic properties of a metallacrown originate from the metal ions used in its construction. When selecting metal ions, recall that at least one metal ion should have unpaired electrons to impart magnetic behavior on the entire ring. Therefore, it merits discussing some of the more commonly used metal ions and why these ions may be of interest. We will differentiate between ring metal ions and the central metal ion. It should also be noted that the ligands used affect the magnetic coupling between the metal ions. The impact of ligand choice on SMM behavior will be specifically addressed in the section on M 12-$MC_{Mn^{III}(N)shi}$-4 properties as the magnetic coupling is not simply a ligand-controlled property, but a structural property as well.

2.1.1 Common Ring Metal Ions Used in Single-Molecule Magnetic Metallacrowns

Ring metal ions used for magnetic metallacrowns can fall into one of two categories—paramagnetic ring ions or diamagnetic ring ions. Paramagnetic ions may include high spin Mn^{III}, [51, 55–59] Fe^{III}, [60] and Cu^{II} [49, 60]. Manganese(III) is of particular interest due to its relatively high intrinsic anisotropy, a relatively large spin value (for a *d*-group element), and its directional abilities due to the presence of a Jahn–Teller axis. Copper(II) is also of interest due to its magnetic directing abilities as well as its intrinsic anisotropy and directional abilities arising from a Jahn–Teller axis. Some commonly used diamagnetic ions include Ga^{III} and Zn^{II} [61, 62]. Some ions, such as Co^{III} have been used as the ring metal for magnetic MCs. Co^{III} is unique because depending on the ligand environment, it may be high spin or low spin, an application used in many spin-crossover materials [13]. When salicylhydroxamic acid was employed as a ring ligand, Co^{III} adopted a low spin diamagnetic state [60].

While it may seem advantageous to use anisotropic paramagnetic ions, such as Mn^{III} or Cu^{II} as the ring metal, antiferromagnetic coupling through the ring ligands can lead to an overall diamagnetic contribution from the ring. For instance, in 12-MC-4 rings, it has been found that the ring metals are antiferromagnetically coupled regardless of the metal or ligand used [55, 58, 63–66]. Thus, while one may attempt to introduce paramagnetic metals into the 12-MC-4 framework, the orthogonality of the ligands and magnetic orbitals often counteracts the intended increase in spin. One potential pathway to avoid the cancelation of spin is to use the magnetic director approach. Happ and co-workers utilized Cu^{II} as a central metal in a Cu^{II} 12-$MC_{Fe^{III}(N)shi}$-4 system. Happ reported that because Cu^{II} has a $d_{x^2-y^2}$ magnetic orbital, experienced strong antiferromagnetic coupling with the ring metals, and is located within the MC plane, it was able to enforce a high spin ground state through enhanced radial proportion interactions [67]. Another way that a diamagnetic ground state may be minimized is by employing MC rings that have an uneven rotational element. For instance, in a recently reported inverse 9-MC-3, strong antiferromagnetic coupling was found within the Cu^{II} triangles, leading to spin frustration in the overall compound [68].

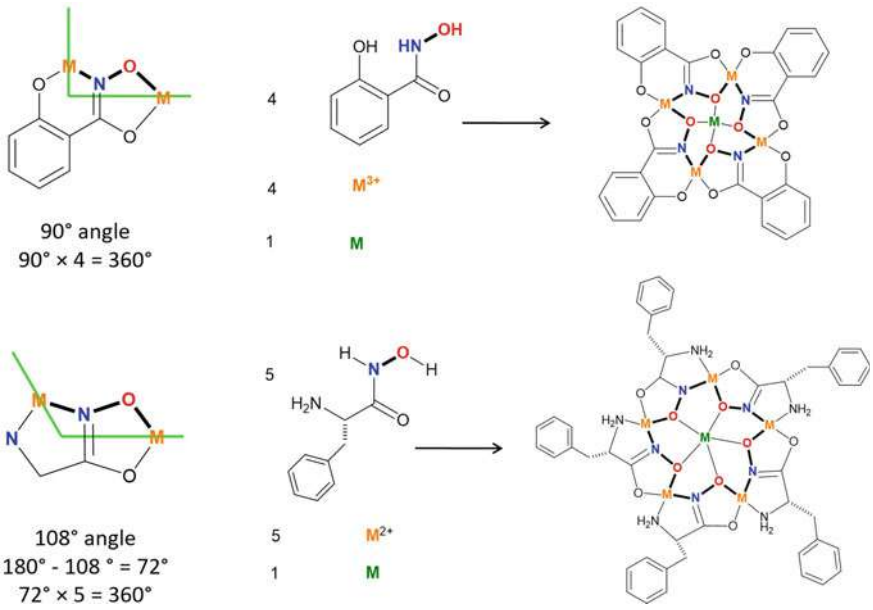

Fig. 5 Careful selection of the ring ligands and metals allows for the predictable formation of metallacrowns

2.1.2 Common Central Metal Ions Used in Single-Molecule Magnetic Metallacrowns

One of the unique possibilities offered by metallacrowns is the ability to systematically vary a single component without dramatically changing the structure (Fig. 6). In the 12-$MC_{Mn^{III}(N)shi}$-412-$MC_{Mn^{III}N(shi)}$-4 system, numerous alkali [69], alkaline earth [70, 71], transition metals [46, 58], and lanthanides [57, 59, 70, 72] have been encapsulated in the central cavity. In each of the cited cases, the structure of the 12-$MC_{Mn^{III}N(shi)}$-4 remains relatively constant, perhaps only "ruffling" or "doming", depending on the size of the central ring. For instance, when a larger ion, such as Ca^{II}, Y^{III}, or a lanthanide(III) is present, the MC ring tends to dome slightly such that the oxygen atoms of the ring are directed towards the central atom. The degree of "doming" also was affected by the alkali counteraction. For instance, the $Dy^{III}Na(OAc)_4$ 12-$MC_{Mn^{III}(N)shi}$-4 was slightly less domed than the $Dy^{III}K(OAc)_4$ 12-$MC_{Mn^{III}(N)shi}$-4, reflecting the steric interactions between the MC ring and the counteraction [59]. For many of the di-alkali compounds, the two alkali metals on either side of the MC ring lead to identical attractive forces on both sides of the MC ring. This equal attraction results in the MC itself remaining relatively planar. These structural changes in the ring are a direct result of the central metal that has been selected as the constituents of the ring remain constant. These slight structural changes can lead to perturbations to the magnetic coupling within the ring due to slight changes in the orbital overlap. Unfortunately, this is not an area that has been studied in significant depth.

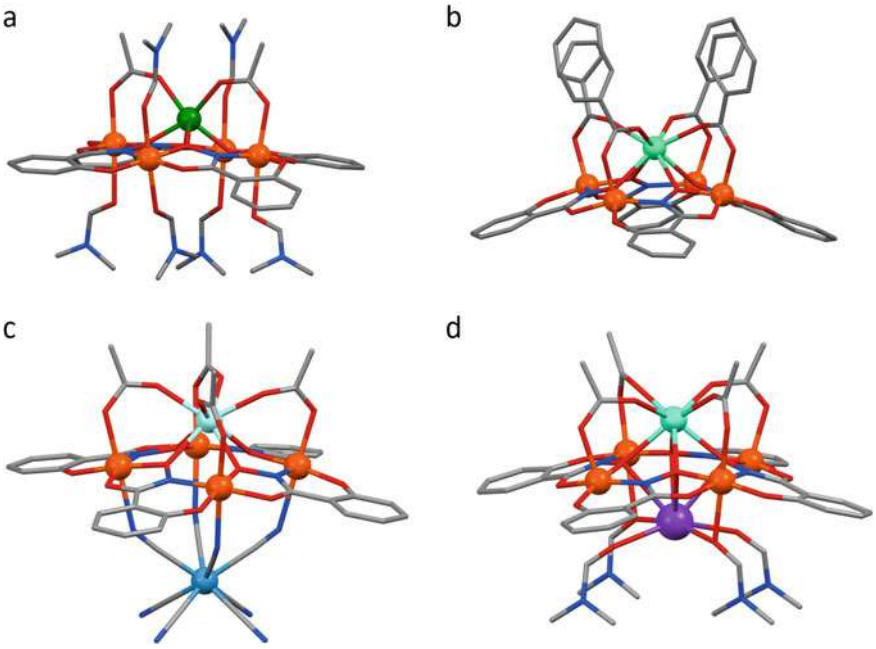

Fig. 6 Four different 12-$MC_{Mn^{III}(N)shi}$-4 are shown. a) $Mn(OAc)_2$ 12-MC-4; b) $Ca(OBz)_4$ 12-MC-4; c) $Y(OAc)_4(WO_8)$ 12-MC-4; d) $Dy(OAc)_4$ K 12-MC-4. Color scheme: orange—Mn^{III}; green—Mn^{II}; light green—Ca^{II}; light blue—W^{V}; aqua—Y^{III}; teal—Dy^{III}; gray—carbon; red—oxygen; blue—nitrogen. Hydrogen atoms and solvent molecules omitted for clarity

In recent years, there has been an increased interest in using lanthanides in molecular magnets. Lanthanide ions, in general, have large magneto-crystalline anisotropy values, making them ideal candidates for SMMs [73]. Unlike *d*-block elements, where the spin and orbital momentum quantum values can be separated from one another, in *f*-block elements it is best to consider the spin–orbit quantum number *J* rather than the total number of unpaired electrons. This coupling also makes it more difficult to use the simple assumptions that are often employed with *d*-elements [34].

In the case of lanthanides, the crystal field tends to perturb the spin–orbit quantum number, as opposed to the opposite as found in transition elements. For instance, in the phthalocyaninato lanthanide sandwich complexes, the Tb^{III} analog showed SMM behavior but when Tb^{III} was used in a polyoxometalate, the resulting compound did not show SMM behavior. The Tb^{III} ion has a significant anisotropy value, but as a non-Kramers doublet ground state (i.e., even value for *J*), it requires rigorous axial symmetry to produce a bistable ground state [74]. When Tb^{III} was employed in the axially elongated ligand environment found in the phthalocyaninato compound, the crystal field environment created by the phthalocyanine ligands was conducive to SMM behavior. This was because the electron density of the Tb^{III} ion is oblate and the

ligand field of the phthalocyanine ligands was located above and below the Tb^{III} *xy*-plane [34]. When Tb^{III} was introduced in a relatively compressed ligand environment found in the polyoxometalate framework, this crystal field inhibited SMM behavior. However, when a prolate ion, Er^{III} was introduced into the polyoxometalate, the compressed crystal field led to the observation of SMM behaviors [33].

3 Pseudo-Metallacrowns with Single-Molecule Magnetic Properties

Here, we will outline some important pseudo-metallacrowns that show single-molecule magnetic behavior. We differentiate between "true" MCs and "pseudo-MCs" based on whether the structure follows the M–N–O or M–N–N repeat of traditional MCs and aza-MCs. The first reported Mn-*4f* compound to show single-molecule magnetic properties was a pseudo-metallacrown identified by Zaleski and co-workers in 2004 [53]. These pseudo-MCs continue to be of interest to the field, as they have shown interesting magnetic properties.

3.1 28-MC-10: $Dy^{III}{}_6Mn^{III}{}_4Mn^{IV}{}_2$, the First Mn-4f Single-Molecule Magnet

In 2003, Osa and co-worker reported the first *3d/4f* SMM, using copper(II), terbium(III), and dysprosium(III) as the metals [75, 76]. These tetranuclear compounds showed out-of-phase AC magnetic susceptibility, but did not have magnetic hysteresis. In 2004, Zaleski and co-workers reported the first Mn-*4f* single-molecule magnet, attempting to harness the large, intrinsic magnetoanisotropy associated with Mn^{III} ions and *4f* ions [53]. Using ligands commonly used in MCs, Zaleski prepared a 28-MC-10 with the chemical formula $[Ln^{III}{}_6Mn^{III}{}_4Mn^{IV}{}_2(H_2shi)_4(Hshi)_2(shi)_{10}(CH_3OH)_{10}(H_2O)_2]\cdot 9CH_3OH\cdot 8H_2O$, where Ln^{III} was Gd^{III}, Tb^{III}, or Dy^{III} (Fig. 7). The MC ring was comprised of six Ln^{III}, four Mn^{III}, and two Mn^{IV} ions. While an M–N-O repeat unit is present in the ring, the lanthanide ions are connected through oxygen atoms, and due to a pseudo-inversion center in the molecule, the M–N–O pattern is not a repeated cycle. Also, there is no central ion in the compound, rather six Ln^{III} ions that are connected through oxo-bridges from $Hshi^{2-}$ ligands in a chair configuration analogous to the chair confirmation of cyclohexane. The oxidation states of the Mn ions were determined through charge balance and bond length considerations—the Mn^{III} ions possessed clear Jahn–Teller axes while the Mn^{IV} ions were relatively symmetric. Two of the Ln^{III} ions were eight-coordinate while a third was nine-coordinate. The shape of the lanthanide ions were not described in the text.

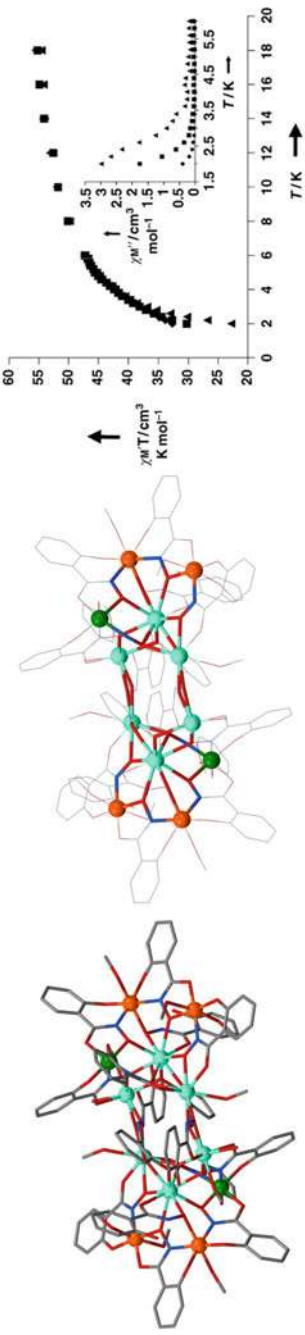

Fig. 7 $Dy^{III}_6Mn^{III}_4Mn^{IV}_2$ was the first Mn/4f SMM reported. The MC structure is highlighted. Color scheme: orange—Mn^{III}; green—Mn^{IV}; aqua—Dy^{III}; red—oxygen; blue—nitrogen; gray—carbon. Hydrogen atoms and solvent molecules omitted for clarity. Ac susceptibility plot used from Wiley with permission Zaleski et al. [53]

The authors compared the properties of the Dy^{III} and Tb^{III} analogs, finding that only the Dy^{III} version showed slow magnetic relaxation. Though not mentioned in the manuscript, researchers have hypothesized that the Kramers doublet (i.e., non-integer) ground state possessed by the spin–orbit quantum number *J* of Dy^{III} makes it an ideal lanthanide to use for SMMs. Dysprosium(III), by virtue of a Kramers double ground state, always has a degenerate ground state, while non-Kramers doublets, such as Tb^{III}, must have strictly axial crystal field symmetry to produce a degenerate ground state [34].

3.2 22-MC-8: $Dy^{III}{}_4Mn^{III}{}_6$ Displays Slow Magnetic Relaxation

If the filtrate from the preparation of $Ln^{III}{}_6Mn^{III}{}_4Mn^{IV}{}_2$ described above was allowed to sit longer, a "daughter" compound, $[Ln^{III}{}_4Mn^{III}{}_6(H_2shi)_2(shi)_6(sal)_2(O_2CCH_3)_4(OH)_2(CH_3OH)_8]\cdot 4CH_3OH$, where Ln^{III}=Dy^{III} or Ho^{III}, sal^{2-}=salicylate, which was derived in situ from the hydrolysis of salicylhydroxamic acid (Fig. 8) [54]. The molecule possesses an inversion center, with two unique Ln^{III} and three unique Mn^{III} ions. In this compound, all Ln^{III} ions were eight-coordinate and the Mn^{III} ions possessed clear Jahn–Teller distortions. The compound looks as if a 12-MC-4 was being formed before one of the Ln^{III} ions and the third Mn^{III} interrupted the M–N–O repeat pattern. The result is that a pseudo-MC with two unique planes of metal ions—three Mn^{III} and two Ln^{III} ions sit on one plane and the other metal ions sit on a symmetry-generated plane.

It was found that both $Ho^{III}{}_4Mn^{III}{}_6$ and $Dy^{III}{}_4Mn^{III}{}_6$ showed slow magnetic relaxation in the solid phase, but only $Dy^{III}{}_4Mn^{III}{}_6$ retained slow magnetic relaxation in a frozen solution. This implied that the Dy^{III} analog was an SMM while the Ho^{III} analog was possibly a spin glass or magnetic ordering in the solid phase due to intermolecular interactions. This observation also agrees with the observation that Kramers doublets often show SMM-like behavior while non-Kramers doublet ions do not show SMM behavior unless oriented in the appropriate geometry.

3.3 16-MC-6: $Dy^{III}{}_4Mn^{III}{}_4$ Displays Slow Magnetic Relaxation

Recently, Lutter and co-workers published a $Dy^{III}{}_4Mn^{III}{}_4$ compound that showed slow-magnetic relaxation [77]. The compound, $[Dy^{III}{}_4Mn^{III}{}_4(OH)_2(O_2C_2H_3)_3(shi)_4(H_2shi)_4(Hsal)_3(DMF)_4]\cdot 3DMF$ (Fig. 9), was structurally similar to the $Dy^{III}{}_4Mn^{III}{}_6$ compound discussed above. The molecule possesses an inversion center, with two symmetry generated $Mn^{III}{}_2/Dy^{III}{}_2$ planes. The two Mn^{III} ions begin to form an MC, using the prerequisite M–N–O connectivity

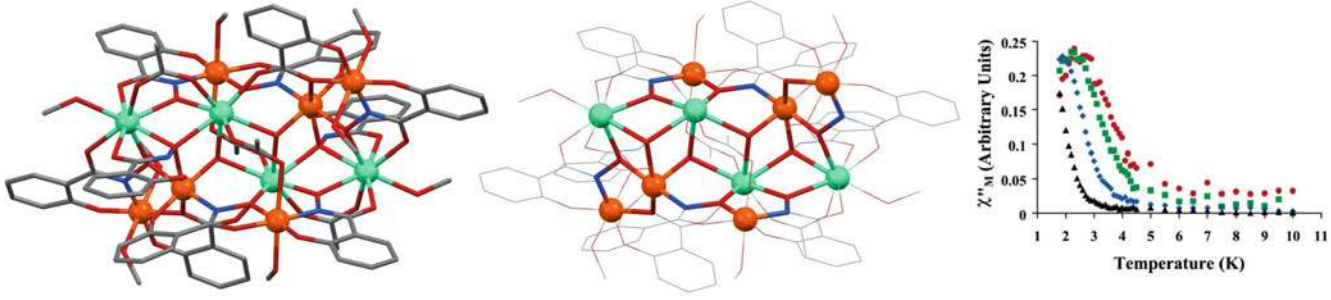

Fig. 8 The crystal structure of $Ho^{III}_4Mn^{III}_6$ is isostructural to $Dy^{III}_4Mn^{III}_6$. The MC structure is highlighted. Color scheme: orange—Mn^{III}; aqua—Ho^{III}; red—oxygen; blue—nitrogen; gray—carbon. Hydrogen atoms and solvent molecules omitted for clarity. The frozen DMF out-of-phase ac susceptibility for $Dy^{III}_4Mn^{III}_6$ is shown at varying frequencies (1000; 500; 100; 10 Hz). Ac susceptibility data reprinted with permission from Zaleski; J. W. Kampf; T. Mallah; M. L. Kirk; V. L. Pecoraro. Assessing the Slow Magnetic Relaxation Behavior of $Ln^{III}_4Mn^{III}_6$ Metallacrowns. Inorg. Chem. 2007, 46, 1954–1956. © 2007 American Chemical Society [54]

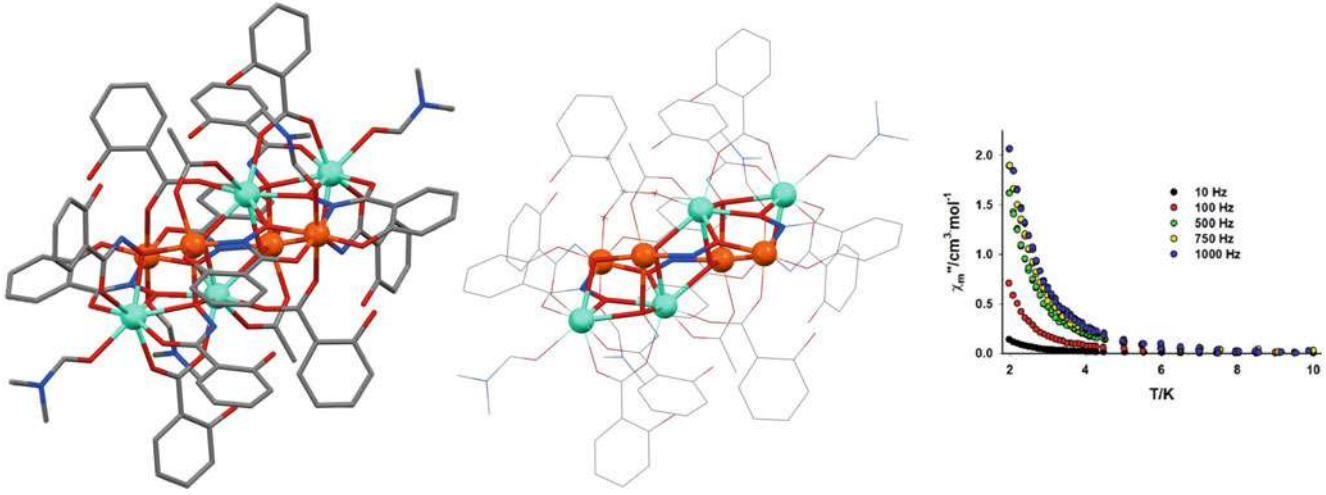

Fig. 9 $Dy^{III}_4Mn^{III}_4$ showed slow mangetic relaxation. The MC framework is highlighted. Color scheme: orange—Mn^{III}; aqua—Dy^{III}; red—oxygen; blue—nitrogen; gray—carbon. Hydrogen atoms and solvent molecules excluded for clarity. The ac susceptibility plot was used with permission from Polyhedron, 202, J. C. Lutter, T. T. Boron, III, K. E. Chadwick, A. H. Davis, S. Kleinhaus, J. W. Kampf, C. M. Zaleski, V. L. Pecoraro, "Identification of slow magnetic relaxation and magnetocoolant capabilities of heterobimetallic lanthanide-manganese metallacrown-like compounds", 115,190, Copyright (2021) with permission from Elsevier [77]

with a Dy^{III} encapsulated in the center. However, the second Dy^{III} ion is incorporated into the ring, interrupting the Mn–N–O repeat pattern, but rather creating a Dy^{III}–O–Mn^{III}–N–O–Mn^{III}–N–O repeat pattern. Both Dy^{III} ions are eight-coordinate and the two Mn^{III} ions are six-coordinate with a Jahn–Teller distortion. The encapsulated Dy^{III} ions formed a $Dy^{III}_2(\mu_3\text{-OH})_2$ core. The Ln^{III}–O–Mn^{III}–N–O–Mn^{III}–N–O-repeat pattern found in the $Dy^{III}_4Mn^{III}_4$ compound is remarkably similar to that found in the Ln^{III}–O–Mn^{III}–N–O–Mn^{III}–N–O-repeat pattern found in $Ln^{III}_4Mn^{III}_6$.

Indeed, the main difference between the metal connectivity of the two seems to be the absence of two Mn^{III} ions. This is also manifested in the magnetic susceptibility: the dc magnetic susceptibility of the $Dy^{III}_4Mn^{III}_4$ is about 6 cm^3 K mol^{-1} smaller (two idealized high spin d^4 centers) than the $Dy^{III}_4Mn^{III}_6$ compound. Similar to $Dy^{III}_4Mn^{III}_6$, $Dy^{III}_4Mn^{III}_4$ showed slow-magnetic relaxation, and in the solid state did not show a maximum in the susceptibility versus temperature out-of-phase ac susceptibility plot. A diluted frozen solution ac susceptibility measurement was not taken on the $Dy^{III}_4Mn^{III}_4$ compound.

3.4 26-MC-8: Lanthanide Choice Leads to Different Magnetic Responses

In the same paper, Lutter and co-workers reported that using $LnCl_3$, $Mn(OAc)_2$, H_3shi, and salicylic acid in DMF led to the formation of $[Ln^{III}_6Mn^{III}_2Mn^{IV}_2(shi)_6(Hshi)_4(H_2shi)_2(Hsal)_4(DMF)_8]$, where Ln^{III} may either be Gd^{III} or Dy^{III} (Fig. 10) [77]. This compound featured a [Ln^{III}–O–Ln^{III}–O–N–C–O–Mn^{III}–N–O–Mn^{IV}–N–O] connectivity that was repeated twice, producing a 26-MC-8 that encapsulated two Ln^{III} ions. The encapsulated Gd^{III} ion was found to be nine-coordinate, while the two Gd^{III} ions found in the ring were eight-coordinate. These six lanthanide ions were bridged by oxygen atoms, leaving the lanthanides in a pseudo-six-membered chair configuration, analogous to that found in the $Ln^{III}_6Mn^{III}_4Mn^{IV}_2$ compound cited above. Both manganese ions were six-coordinate, but one pair possessed a clear axial elongation, helping the authors to assign them as high spin Mn^{III} and the other pair, because of the similar bond lengths as Mn^{IV}.

The $Dy^{III}_6Mn^{III}_2Mn^{IV}_2$ compound showed slow-magnetic relaxation, but did not display a maximum above 2 K. This was similar to $Dy^{III}_6Mn^{III}_4Mn^{IV}_2$, the first Dy/Mn SMM reported [53]. Unlike the $Dy^{III}_4Mn^{III}_4$/$Dy^{III}_4Mn^{III}_6$ pair, the dc magnetic susceptibility of $Dy^{III}_6Mn^{III}_2Mn^{IV}_2$ was not simply two high spin Mn^{III} ions smaller than $Dy^{III}_6Mn^{III}_4Mn^{IV}_2$, suggesting that other factors were affecting the magnetic behavior. These possible factors include slight differences in the geometry/connectivities of the metals, leading to different coupling constants between the metal ions.

While not a major topic in this chapter, it is worth mentioning that $Gd^{III}_6Mn^{III}_2Mn^{IV}_2$ showed magnetocoolant properties through the magnetocaloric effect [78, 79]. Briefly, the magnetocaloric effect is a thermal equilibrium that exists

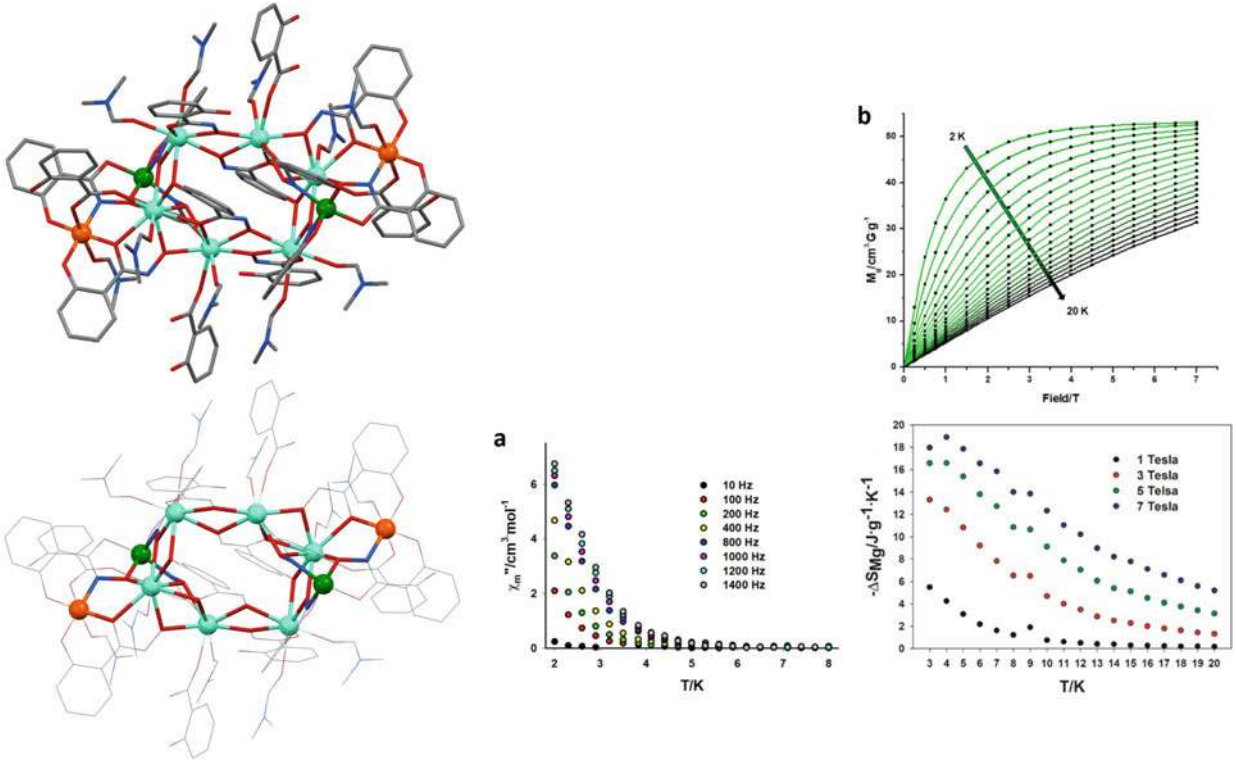

Fig. 10 The crystal structure of $Gd^{III}_6Mn^{III}_2Mn^{IV}_2$ is isostructural with $Dy^{III}_6Mn^{III}_2$ Mn^{IV}_2. The MC framework is highlighted. Color scheme: orange—Mn^{III}; aqua: Gd^{III}; red—oxygen; blue—nitrogen; gray—carbon. Hydrogen atoms and solvent molecules omitted for clarity. $Dy^{III}_6Mn^{III}_2$ Mn^{IV}_2 demonstrates frequency-dependent out-of-phase magnetic susceptibility, while the $Gd^{III}_6Mn^{III}_2Mn^{IV}_2$ shows behavior consistent with a magnetic refrigerant. Reprinted from Polyhedron, 2021, J. C. Lutter, T. T. Boron, III, K. E. Chadwick, A. H. Davis, S. Kleinhaus, J. W. Kampf, C. M. Zaleski, V. L. Pecoraro, "Identification of slow magnetic relaxation and magnetocoolant capabilities of heterobimetallic lanthanide-manganese metallacrown-like compounds", 115,190, Copyright (2021) with permission from Elsevier [77]

Table 1 A comparison of magnetocaloric effect behaviors of Mn/Gd containing compounds. Reprinted from Polyhedron, 2021, J. C. Lutter, T. T. Boron, III, K. E. Chadwick, A. H. Davis, S. Kleinhaus, J. W. Kampf, C. M. Zaleski, V. L. Pecoraro, "Identification of slow magnetic relaxation and magnetocoolant capabilities of heterobimetallic lanthanide-manganese metallacrown-like compounds", 115,190, Copyright (2021) with permission from Elsevier [77]

Compound description	$-\Delta S_{mg}$ [J kg^{-1} K^{-1}]	Theoretical maximum, $-\Delta S_{mg}$ [J kg^{-1} K^{-1}]	Percentage (%) of ideal magnetic entropy	Conditions
$Gd^{III}_4Mn^{III}_4$ calix[4]arene	19.0	37.1	51	4 K, 7 T
$Gd^{III}_9Mn^{II}_9$ phosphonate cage	28.0	57.0	49	3 K, 7 T
$Gd^{III}_6Mn^{II}_4$ phosphonate cage	33.7	41.8	81	3 K, 7 T
$Gd^{III}Mn^{III}_2$ cluster[a]	13.5	45.79	29	3 K, 9 T
$Gd^{III}Mn^{III}_2$ cluster[a]	20.39	37.91	54	3 K, 9 T
$Gd^{III}Mn^{III}_2$ cluster[a]	19.73	36.64	54	3 K, 9 T
$Gd^{III}Mn^{III}_2$ cluster[a]	31.75	38.14	83	3 K, 9 T
$Gd^{III}Mn^{III}_2$ cluster[a]	19.0	44.48	43	3 K, 9 T
$Gd^{III}_6Mn^{III}_2Mn^{IV}_2$ compound	18.89	35.66	53	4 K, 7 T

[a]*based on computational magnetic coupling values*

between the heating/cooling of a material and an applied magnetic field. In magnetocoolants, an external magnetic field is applied to a magnetic sample, causing the magnetic moments to align with the field. The sample then absorbs heat from the surroundings, causing the magnetic moments to become randomly oriented due to entropy [80, 81]. Interestingly, the qualities that make good magneto coolants often conflict with the desirable qualities of an SMM. For instance, magnetocoolants benefit from easily accessible excited states and metal ions that are isotropic [78]. Thus, it is relatively rare for a family of compounds to show both SMM and magnetocoolant behavior. Lutter and co-workers reported that the $Gd^{III}_6Mn^{III}_2Mn^{IV}_2$ had a maximum gravimetric magnetic entropy change of 18.89 J kg^{-1} K^{-1} at 7 T, which was about 53% of its maximum theoretical value (35.66 J kg^{-1} K^{-1}). This percentage performance has only been bested by two other Gd/Mn compounds reported at that time (Table 1) [77].

3.5 14-MC-5: The Development of Planar Metallacrowns as SMMs

The above MCs showed interesting magnetic properties but were not highly efficient in regards to performance to metal count. That is, while the above compounds contained numerous magnetic centers, some with large intrinsic anisotropy values, the resulting compounds did not have high blocking temperatures. It has been

proposed that, unfortunately, large compounds "accidentally" cancel the anisotropy tensors of the magnetoanisotropy ions [82]. Alternatively, with many magnetic ions present, the compounds lack a large separation between the ground and excited spin states [77].

Inspired by Waldmann's hypothesis and recognizing that MCs offered a unique opportunity to control the structures of the resulting SMMs, Boron, and Pecoraro attempted to design planar MCs with the intention of aligning magnetoanisotropy vectors of the final product. The resulting compound was a newly identified type of pseudo-planar MC, the $Ln^{III}(OAc)(NO_3)_2$ 14-$MC_{Mn^{III}Ln^{III}(\mu\text{-}O)(\mu\text{-}OH)N(shi)}$-5 compound, where Ln^{III} was Y^{III}, Gd^{III}, Tb^{III}, Dy^{III}, and Ho^{III} (Fig. 11) [51]. The Ln 14-MC-5 was structurally interesting because it closely mimics a traditional MC; there was an [Ln^{III}–O–N–Mn^{III}–O–N–Mn^{III}–O] repeat in the compound. However, rather than a rotational axis as found in "true" MCs, there was a mirror plane running down the middle of the molecule. There was also an encapsulated Ln^{III} ion. The Mn ions possessed clear axes of elongation, suggesting a Jahn–Teller distortion. These axes all pointed roughly parallel to one another and perpendicular to the MC plane. The Ln^{III} ion in the ring was slightly tilted out of the plane of the MC, while the encapsulated Ln^{III} was seven-coordinate, forming a pentagonal bipyramid. Note that the geometries of these two Ln^{III} differ from the geometries found in the bis-phthalocyaninato lanthanide and lanthanide polyoxometalate compounds discussed above. Therefore, it is difficult to predict how the coordination environment perturbed the magnetic properties.

It was found that the anisotropic lanthanides, i.e., Tb^{III}, Dy^{III}, and Ho^{III} all showed frequency-dependent slow magnetic relaxation, with Dy^{III} having an energy barrier above 2 K. Using Y^{III} 14-MC-5, Boron and co-workers demonstrated that the Mn^{III} ions were strongly antiferromagnetically coupled, though a coupling constant could not be calculated. The lack of SMM-like behavior in the Y^{III} 14-MC-5 compound suggested that the Mn^{III} ions in the ring were not sufficient for providing the SMM behavior on their own. Adding an isotropic but high spin Gd^{III} ion did not produce SMM-like properties either, suggesting that the SMM properties of the Ln^{III} 14-MC-5 required a magnetoanisotropic lanthanide to confer the desired properties. It was found that Dy^{III} 14-MC-5 had an effective energy barrier of 16.7 K and $\tau_0 = 4.9 \times 10^{-8}$ s while the Tb^{III} and Ho^{III} analogs, while having frequency-dependence, did not have a maximum above 2 K.

In a 2014 *Journal of the American Chemical Society* article, Deb and co-workers utilized magnetic Compton scattering to probe the spin structure and orbital interactions of the Y^{III} 14-MC-5, Gd^{III} 14-MC-5, and Dy^{III} 14-MC-5 compounds [83]. Magnetic Compton scattering allowed for a direct investigation of the spin-polarized orbitals and was the first known application of magnetic Compton scattering to molecular materials. Deb and co-workers were able to determine the contributions each metal ion orbital made to the overall magnetic properties of the respective 14-MC-5. The results suggested that there was a small orbital contribution, and subsequently, a small molecular anisotropy contribution, to the magnetic moment of the Y^{III} 14-MC-5 compound. This suggests that while aligning the Ising-type anisotropy vectors of the Mn^{III} occurred due to the planar geometry of the 14-MC-5, the anisotropy vectors

were not additive. Investigating the Gd^{III} 14-MC-5 compound revealed ferromagnetic exchange between the Mn^{III} ions and the central Gd^{III} ion which competed with weak antiferromagnetic coupling between the Mn^{III} ions themselves. The Dy^{III} 14-MC-5 compound featured a spin-only moment dominated by the Dy^{III} contributions while the Mn^{III} contribution was smaller than that found in the Gd^{III} 14-MC-5 analog. The total magnetic moment of Dy^{III} 14-MC-5 was significantly larger than the spin-only contribution, which suggested a major contribution from the Dy^{III} orbital magnetic moment [83].

Song and co-workers reported a [Ln^{III} 14-MC-5]$_2$ dimer, that is, two Ln^{III} 14-MC-5 compounds that were bridged by two oxo-groups and two methoxy groups, where Ln^{III} were Eu^{III}, Gd^{III}, Tb^{III}, and Dy^{III} (Fig. 12) [56]. The resulting dodecanuclear compounds retained the Ln^{III}–O–N–Mn^{III}–O–N–Mn^{III}–O repeat unit, with a Ln^{III} encapsulated in the central cavity. The oxidation states of the Mn^{III} were assigned based on the presence of a Jahn–Teller distortion and bond valence sum calculations. Both Ln^{III} ions in the [Ln^{III} 14-MC-5]$_2$ dimers were eight coordinates. The compounds showed long-range ordering, forming a one-dimensional network through π-π stacking. When Song compared the [Ln^{III} 14-MC-5]$_2$ dimer to the comparable monomer, it was found that the ring Ln^{III} was further out of the MC plane in the monomer than in the dimer (1.734 Å versus 0.113 Å), while the central Ln^{III} ions were more comparable (0.300 Å and 0.402 Å, respectively). Additionally, the dimer showed a higher planar structure than the monomer.

The magnetic properties of the [Ln^{III} 14-MC-5]$_2$ dimer compounds showed that the measured dc susceptibility values were lower than the expected susceptibility, but were roughly twice as much as the comparable 14-MC-5 compounds. Only the [Dy^{III} 14-MC-5]$_2$ dimer showed slow-magnetic relaxation, but unlike the Dy^{III} 14-MC-5 compound the dimer did not have a maximum in the out-of-phase ac susceptibility measurement. This prevented the calculation of an energy barrier. However, the [Dy^{III} 14-MC-5]$_2$ dimer had a circular best-fit for the Cole–Cole plot of the in-phase versus out-of-phase AC susceptibility, a hallmark of SMM behavior. Song and co-workers suggested that the difference in magnetic behavior between the monomer and the dimer was the planarity of the MC and its effects on the magnetic coupling within the ring. The monomer Ln^{III} 14-MC-5 was slightly less planar than the dimer, which could possibly weaken the antiferromagnetic coupling between the metal ions. They also suggested that antiferromagnetic coupling between the two 14-MC-5 units could reduce the SMM behavior of the dimer [56].

3.6 12-MC-4, 16-MC-6, and 20-MC-7: Using Diamagnetic Ring Metals to Probe Lanthanide Coupling

In 2015, Chow and co-workers published a $Ln^{III}{}_2Ga^{III}{}_4$ 16-MC-6 using salicylhydroxamic acid, $Ga(NO_3)_3$, $Ln(NO_3)_3$, where Ln^{III} = Gd^{III}, Tb^{III}, Dy^{III}, Er^{III}, Y^{III}, and a diluted $Y^{III}{}_{0.9}Dy^{III}{}_{0.1}$ stoichiometry, and a mixed methanol/pyridine solvent [84].

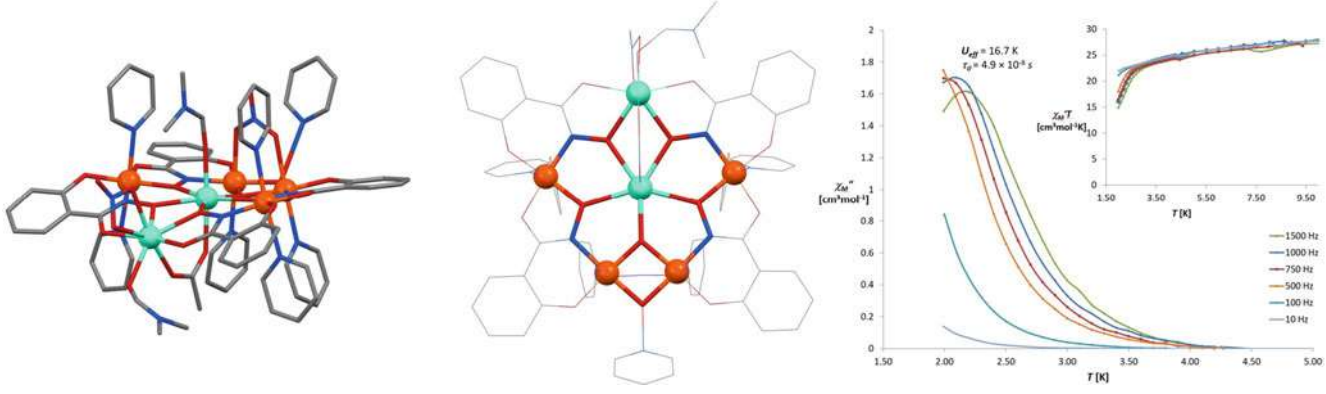

Fig. 11 Dy^{III} 14-MC-5 showed slow magnetic relaxation with an U_{eff} of 16.7 K. Color scheme: orange—Mn^{III}; aqua—Dy^{III}; red—oxygen; blue—nitrogen; gray—carbon. Hydrogen atoms and solvent molecules omitted for clarity. Adapted with permission from T. T. Boron, III, J. W. Kampf, V. L. Pecoraro. A Mixed 3d-4f 14-Metallacrown-5 Complex that Displays Slow Magnetic Relaxation through Geometric Control of Magnetoanisotropy. Inorg. Chem. 2010, 49, 9104–9106. © 2010 American Chemical Society [51]

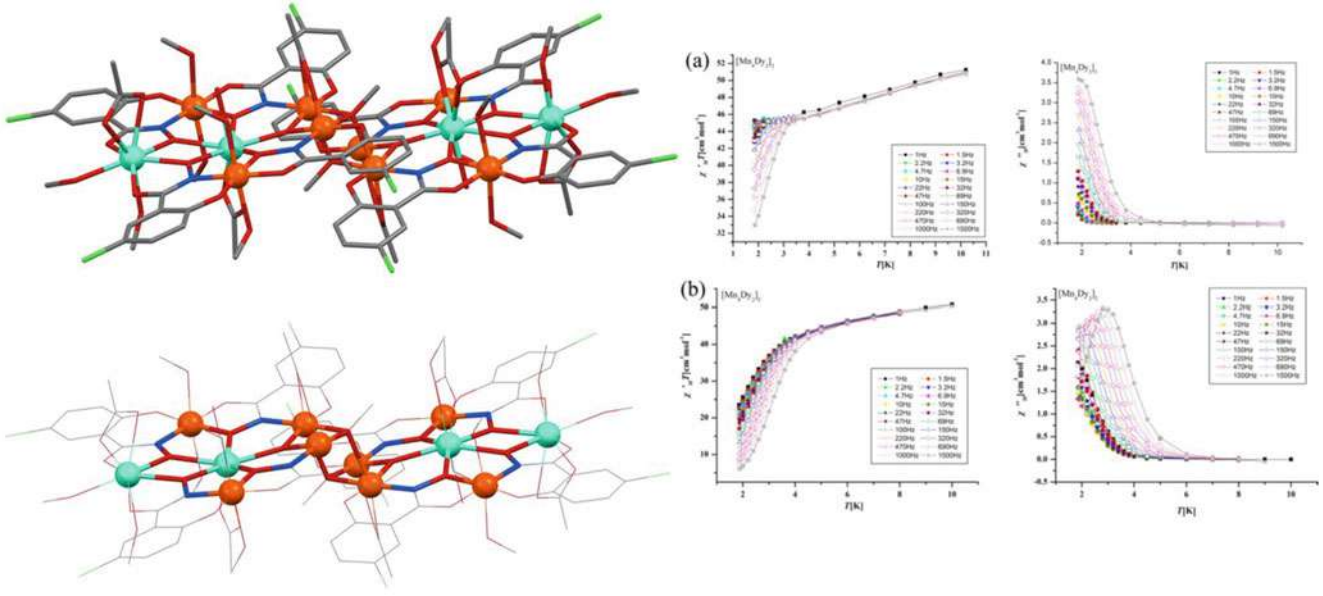

Fig. 12 The $[Dy^{III}$ 14-MC-5$]_2$ dimer showed slow magnetic relaxation. Color scheme: orange—Mn^{III}; aqua—Dy^{III}; red—oxygen; blue—nitrogen; gray—carbon; lime—chlorine. Hydrogen atoms and solvent molecules omitted for clarity. The AC susceptibility showed frequency dependence in 0 Oe applied dc field **a** and with 2000 Oe DC applied field **b**. Reprinted with permission from Cao, F.; Wang, S; Li, D.; Zeng, Z.; Niu, M.; Song, Y.; Dou, J. Family of Mixed 3d–4f Dimeric 14-Metallacrown-5 Compounds: Syntheses, Structures, and Magnetic Properties. Inorg. Chem. 2013, 52, 10,747- 10,755. © 2013 American Chemical Society [56]

The compound featured a Ga^{III}–N–O–Ga^{III}–O–Ln^{III}–O–N–Ga^{III} repeat unit with no encapsulated Ln^{III} ions (Fig. 13). The Ga^{III} and Ln^{III} ions form a pseudo-chair configuration. Gallium^{III} is a diamagnetic, isotropic metal ion and adopts octahedral geometries in the compound. The Ln^{III} ions are eight-coordinate in a trigonal dodecahedral geometry. Chow and Pecoraro hoped that the Ga^{III} ions would serve to isolate the Ln^{III} and reduce intermolecular dipolar interactions.

Examining the dc magnetic properties, it was found that for Gd^{III}, Tb^{III}, and Dy^{III} displayed antiferromagnetic dipolar interactions between the Ln^{III} ions while the Er^{III} analog showed ferromagnetic dipolar interactions. In an attempt to understand why Er^{III} differed from the other Ln^{III} ions, Chow and co-workers determined the Natural Spin Orbitals for the magnetic axes. These orbitals allowed them to predict how the magnetization for a given direction of the magnetic field. The authors found that there was a 10 times stronger overlap of the Natural Spin Orbitals for the $Dy^{III}{}_2Ga^{III}{}_4$ compound compared to the $Er^{III}{}_2Ga^{III}{}_4$, but admitted it was difficult to provide a much

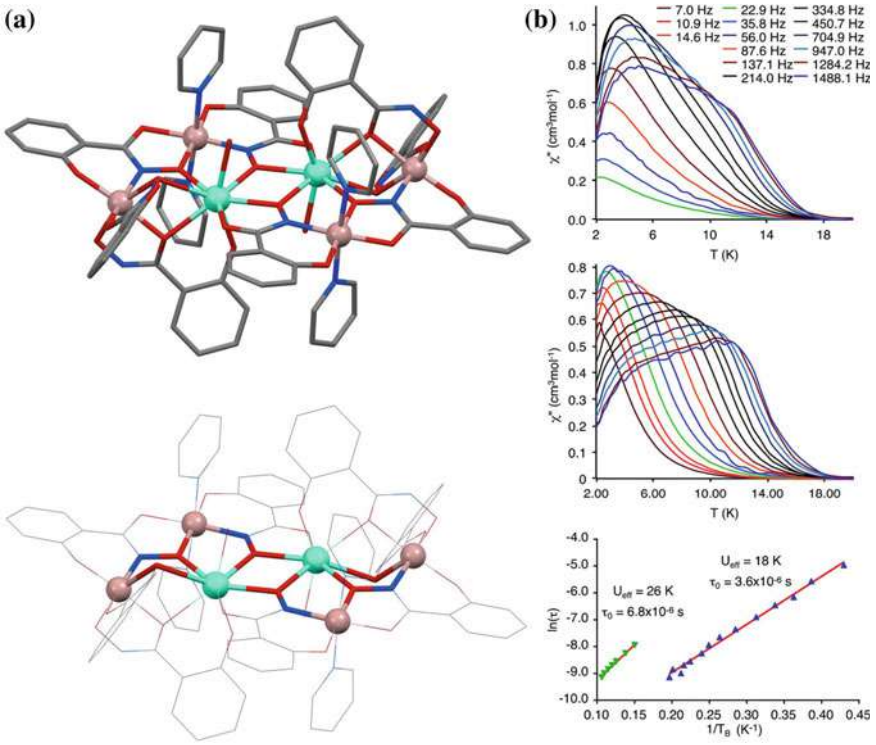

Fig. 13 A $Ln^{III}Ga^{III}{}_6$ metallacryptand with visible/near-infrared luminescence and slow-magnetic relaxation. The MC-type ring is highlighted. Color scheme—beige—Ga^{III}; aqua—Tb^{III}; red—oxygen; blue—nitrogen; gray—carbon. Hydrogen atoms and solvent molecules omitted for clarity. The out-of-phase AC susceptibility showed frequency-dependent slow magnetic relaxation in the presence of a 750 Oe applied DC field. AC susceptibility data reproduced from John Wiley and Sons with permission, Lutter et al. [62]

more quantitative conclusion. The authors also noted that the Dy^{III} and Tb^{III} analogs had easy-axis magnetic orientations while the Er^{III} analog had an easy plane.

When looking for SMM behavior, Chow and co-workers found that the $Dy^{III}{}_2Ga^{III}{}_4$ compound had an opening in the hysteresis curve at zero field. Lowering the sweep rate led to the observation of quantum tunneling. The authors noted that an opening in the hysteresis loop at low temperatures has not been observed in antiferromagnetic coupled binuclear Dy^{III} compounds before. The authors posited that a few residual molecules were in a ferromagnetic excited state even at the lowest temperature. The authors also noted that two unique relaxation pathways in the $Dy^{III}{}_2Ga^{III}{}_4$ compound existed, with two different thermal energy barriers. One of the relaxation pathways was due to an excited state that existed at lower temperatures with a thermal energy barrier of 18 K and $\tau_0 = 3.6 \times 10^{-6}$ s. The second pathway was assigned to isolated Dy^{III} ions with a relaxation barrier of 26 K and $\tau_0 = 6.8 \times 10^{-6}$ s.

This work led to a study of a $Ln^{III}Ga^{III}{}_6$ metallacryptand where $Ln^{III} = Pr^{III}$, Nd^{III}, Sm^{III}–Yb^{III}, which could be considered a 20-$MC_{Ga^{III}N(shi)}$-720-$MC_{Ga^{III}N(shi)}$-7 (Fig. 14) [62]. The metallacryptand featured a Ga^{III}-N-O repeat with an encapsulated Ln^{III} ion. Lutter and co-workers reported that the key differentiating factor between the metallacryptand and other Ga/H_3shi-based MCs was the stoichiometry. Using a gallium to lanthanide to salicylhydroximate ratio of 6:1:9 yielded the desired metallacryptand. Two of the Ga^{III} ions were five-coordinate square pyramidal while the other four adopted distorted octahedral geometries. Two of the Ga^{III} ions adopted a Λ-chirality while the other two adopted a Δ-chirality in an alternating fashion. Alternating stereochemistry is not unprecedented in MCs; a variety of metals, ligands, and MC shapes have been identified [52, 85, 86]. The central Ln^{III} is nine-coordinate and best described as a tricapped trigonal prism.

By using Ga^{III}, a diamagnetic metal ion and a Ln^{III} ion, Lutter et al. were able to create a bi-functional material, as lanthanide compounds are known to be luminescent [87–89]. Diamagnetic metal ions have been shown to be effective in increasing the quantum yield of luminescent materials [88, 89], while many Ln-based polyoxometalate SIMs have utilized diamagnetic ions for structural rigidity. The $Dy^{III}Ga^{III}{}_6$ compound showed slow magnetic relaxation in an out-of-phase AC susceptibility experiment with a maximum above 2 K at the examined frequencies. The compound had an effective energy barrier of 12.7 K and a τ_0 of 3.6×10^{-6} s [62].

While not employing diamagnetic metal ions, Rentschler and co-workers prepared an analogous $Ln^{III}Fe_6$ [3.3.1] metallacryptand, ($Ln^{III} = Gd^{III}$, Dy^{III}, Tb^{III}, and Y^{III}) [90]. According to the authors, this was the first reported Fe/Ln/shi^{3-} metallacryptand and only the second Fe/Ln/shi^{3-} MC reported [91]. Using charge balance, BVS (bond valence sum), and bond lengths, the six Fe ions were assigned a 3+ oxidation state. These six Fe^{III} ions were in distorted octahedral environments. The $Dy^{III}Fe^{III}{}_6$ analog showed frequency-dependence below 5 K, consistent with SMM behavior, but no maxima in the χ'' susceptibility versus temperature plot were observed. The application of an 800 Oe external applied field allowed the group to collect sufficient data to fit the Debye function and extract an effective energy barrier of 10.4 K and a τ_0 of 2.08×10^{-6} s. These data were not appreciably better than the $Dy^{III}Ga^{III}{}_6$

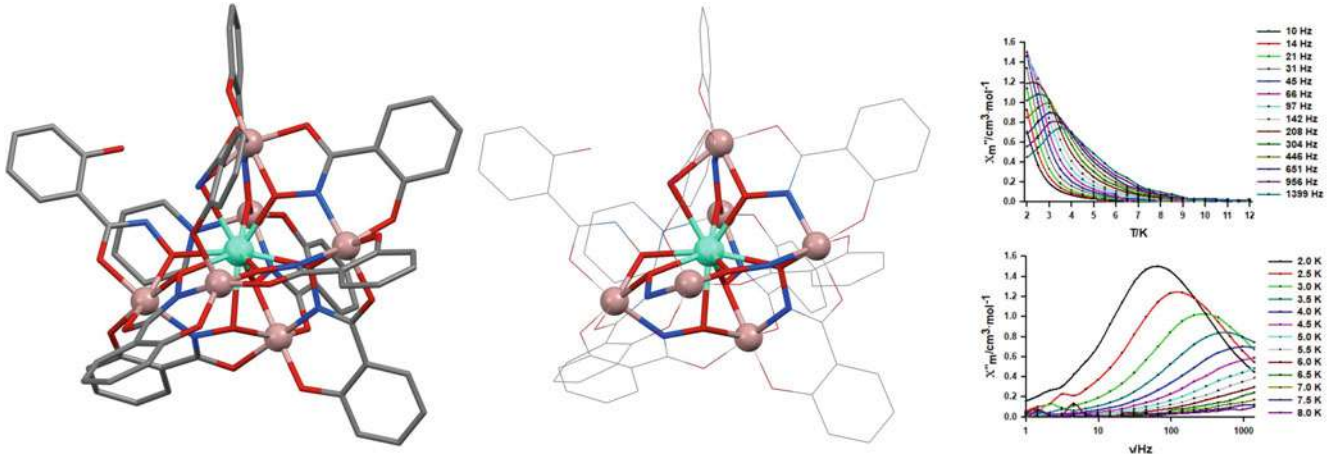

Fig. 14 $Dy^{III}_2Ga^{III}_4$ 16-MC-6 possesses a unique connectivity and is relatively planar. Color scheme: beige—Ga^{III}; aqua—Dy^{III}; red—oxygen; blue—nitrogen; gray—carbon. Hydrogen atoms and solvent molecules omitted for clarity. The $Dy^{III}_2Ga^{III}_4$ showed frequency-dependent ac susceptibility behavior in **a** 0 Oe applied dc field and in **b** 2000 Oe applied dc field. The Arrhenius plot for the low temperature and high-temperature relaxation processes are shown. AC susceptibility plots reprinted with permission from the Royal Society of Chemistry, Chow et al. [84]

metallacryptand reported by Lutter et al., suggesting the presence of the paramagnetic ring metals may not appreciably improve SMM performance.

4 Single-Molecule Magnetic Metallacrowns

Like pseudo-metallacrowns, employing traditional MCs has proven useful for advancing the field of 3*d*/4*f* SMMs. In this section, we will focus on some key traditional MCs that have been used in the SMM field. Many of these compounds were originally published in the 1990s and later reexamined for SMM properties. Additionally, many of these compounds have been investigated concurrently with pseudo-MCs or metallacryptands. That is to say, traditional MCs have not "phased out" pseudo-MCs. Rather, we separate pseudo—from traditional MCs strictly for issues of clarity.

4.1 12-MC-4s

Many different 12-MC-4s have been investigated as potential SMMs. For the interest of clarity, we will break down the 12-MC-4 family into two categories: manganese-based 12-MC-4s and cobalt-based 12-MC-4s. These 12-MC-4s could also be broken down into *d*-metal only MCs and *d,4f*-MCs. We will explore some of these different MCs and highlight key properties.

4.1.1 Manganese-Based 12-MC-4s

The following 12-MC-4s discussed feature Mn^{III} ions in the MC ring. The ring ligand will be salicylhydroxamic acid (H_3shi). When deprotonated, the shi^{3-} ligand is ideal for constructing a relatively planar 12-MC-4 ring—the two binding pockets associated with shi^{3-} are orthogonal. The ring ligand also favors the formation of a tri-cation that can adopt either an octahedral or square pyramidal geometry, which is complementary to a Mn^{III} ion.

$[Mn(OAc)_2$ 12-$MC_{Mn^{III}N(shi)}$-4$](DMF)_6$

One of the first MCs identified, $[Mn(OAc)_2$ 12-$MC_{Mn^{III}N(shi)}$-4] was identified as an SMM in a *Chemical Review* in 2007 [40], with the properties further detailed in a 2011 *Inorganic Chemistry* article [55]. The Mn 12-MC-4 compound features four high spin Mn^{III} ions in the MC ring and an encapsulated Mn^{II} ion in the central cavity. The four Mn^{III} ions possess Jahn–Teller axes. These axes seem to be roughly parallel to one another and perpendicular to the MC ring. The central Mn^{II} is also in

an unusual trigonal prismatic geometry rather than an octahedral. The Mn 12-MC-4 compound seems to check the boxes related to the desired properties of an SMM with high anisotropy values as detailed by Waldmann and Ruiz, Neese, and Kortus above: a relatively small molecule using four highly isotropic metals where there is a high probability of aligning their magnetoanisotropy vectors.

Zaleski and co-workers studied the solid and solution phase properties of Mn 12-MC-4. They found that the ring Mn^{III} ions were antiferromagnetically coupled to one another ($J = -6.3\ cm^{-1}$) and the ring Mn^{III} ions were weakly antiferromagnetically coupled to the central Mn^{II} ion ($J' = -4.2\ cm^{-1}$) (Fig. 15). This led to a ground spin state of $M_s = 1/2$ with an excited state $M_s = 3/2$ that was 2 cm^{-1} higher in energy. The anisotropy values for Mn^{II} and Mn^{III} were calculated from the field-dependent magnetization data and fitted to different local spin Hamiltonians using the above coupling constants J and J'. The calculated anisotropy parameter for Mn^{II} was $D = +1\ cm^{-1}$ with $g = 2.0\ cm^{-1}$ and the calculated anisotropy parameter for Mn^{III} was $D = -3.0\ cm^{-1}$ and $g = 1.98\ cm^{-1}$. The magneto anisotropy value for Mn^{III} was well within the expected parameters [92, 93], but the magneto anisotropy value for Mn^{II} was higher than expected (typical D values for an octahedral Mn^{II} is 0.1–0.2 cm^{-1}) [94]. This was attributed to the fact that the Mn^{II} ion was in a trigonal prismatic geometry rather than a typical octahedral geometry [95].

It was hoped that the presence of anisotropic ring Mn^{III} ions and an unexpectedly anisotropic central Mn^{II} ion would lead to SMM behaviors. The solid-state out-of-phase AC magnetic susceptibility data showed weak frequency dependency, a hallmark of SMM behavior. However, there was no maximum above 3 K. A single crystal of Mn 12-MC-4 was mounted to a micro-SQUID. The micro-SQUID allowed the authors to investigate the low-temperature properties of the Mn 12-MC-4 as a function of the direction of the applied external field. Zaleski and co-workers reported a small hysteresis below 1 K with a sweep rate of 0.07 T/s.

Knowing that the 12-$MC_{Mn^{III}N(shi)}$-4 structural type had previously shown structural integrity in solution, Zaleski and co-workers dissolved Mn 12-MC-4 in DMF and froze the resulting solution. The hope was that by dissolving and freezing the compound, any intermolecular interactions between MCs would be minimized. The results of this experiment were that maxima in the ac susceptibility versus temperature frequency-dependent studies were observed above 2 K at multiple frequencies, allowing the authors to identify the thermal energy barrier (14.7 cm^{-1}) and a τ_0 of 1.4×10^{-7} s. Using a $Li\{Li(Cl)_2$[12-MC-4]$\}$ complex, where one Li^+ is encapsulated rather than Mn^{II} revealed that the observed magnetic behavior was not exclusively from the ring. The ring exhibited antiferromagnetic coupling ($J = -4.0\ cm^{-1}$) between the Mn^{III} ions, no coupling to the central Li^+, and a g value of 1.9. Additionally, no frequency-dependent AC magnetic susceptibility responses were observed, suggesting that the central Mn^{II} was responsible for the observed SMM properties.

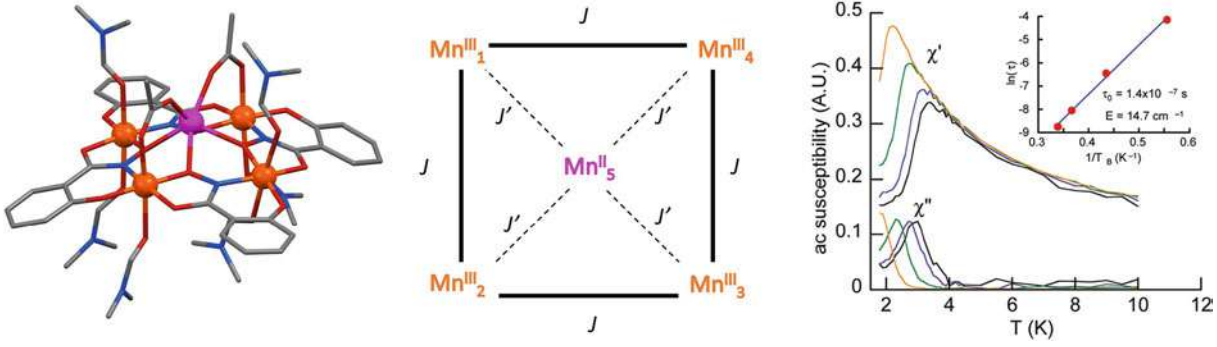

Fig. 15 $Mn(OAc)_2$12-MC-4 features four Mn^{III} ions in the ring and one Mn^{II} in the central cavity. Color scheme: orange—Mn^{III}; magenta—Mn^{II}; red—oxygen; blue—nitrogen; gray—carbon. Hydrogen and solvent molecules omitted for clarity. The magnetic coupling scheme of $Mn(OAc)_2$ 12-MC-4 features antiferromagnetic coupling between the ring Mn^{III} (J) and the central Mn^{II} (J′). The frozen DMF solution ac magnetic susceptibility data showed frequency-dependent behavior consistent with a SMM. Reprinted with permission from C. M. Zaleski, S. Tricard, E. C. Depperman, W. Wernsdorfer, T. Mallah, M. L. Kirk, V. L. Pecoraro. "Single Molecule Magnet Behavior of a Pentanuclear Mn-Based Metallacrown Complex: Solid State and Solution Magnetic Studies. Inorg. Chem. 2011, 50, 11, 348–11, 352. © 2011 American Chemical Society [55]

[$Ln(OAc)_4$ M 12-$MC_{Mn}{}^{III}{}_{N(shi)}$-4]

In an effort to expand the known central metal ions encapsulated in the 12-$MC_{Mn}{}^{III}{}_{N(shi)}$-4 framework, Azar, Pecoraro, Zaleski, and co-workers published a study on the preparation and structural characterization of 12 $Ln^{III}(OAc)_4$ Na^+ 12-$MC_{Mn^{III}N(shi)}$-412-$MC_{Mn}{}^{III}{}_{N(shi)}$-4 containing compounds, where Ln^{III} = Pr^{III}, Sm^{III}, Eu^{III}, Gd^{III}, Tb^{III}, Dy^{III}, Ho^{III}, Er^{III}, Tm^{III}, Yb^{III}, and Y^{III} and an additional $Dy^{III}(OAc)_4$ K^+ 12-$MC_{Mn^{III}N(shi)}$-4 [57]. Like the previously reported 12-$MC_{Mn^{III}N(shi)}$-4 compounds, the MC ring remained charge neutral. However, the inclusion of a trivalent Ln ion and four acetate counterions resulted in a negatively charged moiety. The inclusion of a monovalent alkali metal produced a charge-neutral compound as well as the first reported heterotrimetallic MCs.

Azar and co-workers determined that the 12-MC-4 retains a relatively domed shape with four Jahn–Teller distorted Mn^{III} ring metal ions (Fig. 16). The encapsulated central lanthanide caused slight changes to the size of the MC cavity and the degree of "doming" of the MC. Larger Ln^{III} ions, such as Pr^{III}, caused the central cavity to be slightly larger (0.58 Å) and a larger axial coordination angle for the ring Mn^{III} ions (103.95°) as opposed to the slightly smaller Yb^{III} ion, which had a smaller cavity radius (0.54 Å) and axial coordination angle for the ring Mn^{III} ion (101.69°). Substituting K^+ for Na^+ did not appreciably change the cavity radius (0.56 Å), as it fell within the observed range for the other Ln^{III} Na^+ 12-MC-4 compounds. This substitution did result in a slightly more planar 12-MC-4 compound as measured by the axial coordination angle of the ring Mn^{III} ions. When K^+ was bound on the face opposite of the Dy^{III} ion, the angle about the Mn^{III} ions was on average 101.35° while the angle was 102.40° for the Na^+ compound. Additionally, the K^+ ion was further from the oxime O MC mean plane than the Na^+ ion (2.21 Å versus 1.90 Å), as may be expected for a larger cation [57]. Azar and co-workers also reported that the encapsulated Ln^{III} ion was in a distorted square antiprismatic geometry, similar to those found in the bis(phthalocyaninato) terbium and lanthanide polyoxometalate compounds discussed above, suggesting that these compounds *may* have interesting magnetic properties to be investigated.

$(Bu_4N)[Y(OAc)_4$ 12-$MC_{Mn}{}^{III}{}_{N(shi)}-4(MeOH)_4]$
and $(Et_4N)_5[Y(OAc)_4[W^V(CN)_8]$ 12-$MC_{Mn}{}^{III}{}_{N(shi)}-4](WO_4)_{0.5}$

In 2016, Song, Dou, and co-workers published two Y^{III}-containing 12-$Mn_{Mn}{}^{III}{}_{N(shi)}$-4 compounds, $(Bu_4N)[Y(OAc)_4$ 12-MC-4$(MeOH)_4]$ and $(Et_4N)_5[Y(OAc)_4[W^V(CN)_8]$ 12-MC-4$](WO_4)_{0.5}$ [58]. These two compounds featured Y^{III} coordinated in the center of the 12-MC-4 ring with four acetate bridges between the central atom and the ring Mn^{III} ions. One compound had four methanol groups coordinated on the ring Mn^{III} opposite the acetate groups while the other included an octacyanotungstate $[W^V(CN)_8]$ in place of four coordinated solvent methanol ligands, producing $[Y(OAc)_4[W^V(CN)_8]$ 12-MC-4$](WO_4)_{0.5}$. The 12-MC-4s maintained their "bowl" shape and [Mn–N–O] connectivity, but there

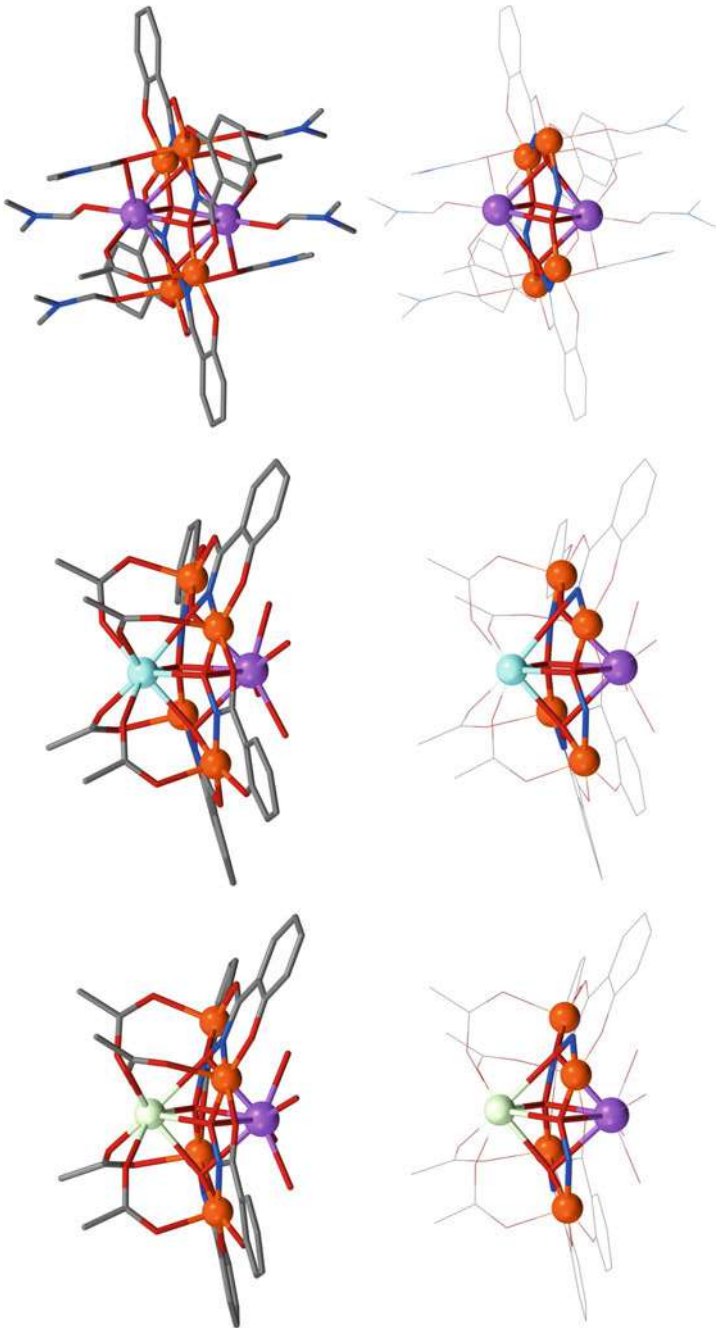

Fig. 16 A M Na 12-MC-4 may undergo slight changes in ring shape due to the central cation. From left to right: $Pr(OAc)_4$ Na 12-MC-4, $Y(OAc)_4$ Na 12-MC-4, $Na_2(OAc)_2$ 12-MC-4. The $Pr(OAc)_4$ Na 12-MC-4 and $Y(OAc)_4$ Na 12-MC-4 feature a domed shape, where the $Na_2(OAc)_2$ 12-MC-4 features a ruffled shape. Color scheme: orange—Mn^{III}; lime: Pr^{III}; aqua: Y^{III}; purple: Na^{I}; red—oxygen; blue—nitrogen; gray—carbon. Hydrogen atoms and solvent molecules omitted for clarity

were slight changes in the MC planarity (Fig. 17). In both compounds, a Jahn–Teller distortion was identified for each ring Mn ion. The average distance between the ring Mn^{III} ions was approximately the same for the two compounds (4.639 Å) and the separation between the encapsulated Y^{III} ion and the Mn^{III} mean plane (1.851 Å) was also nearly identical. The only major deviation observed was in the Mn-N–O-Mn torsion angle: the torsion angle of the octacyanotungstate was 4.59° *larger* than the Y^{III}-only containing MC [58]. Comparing the three $Y(OAc)_4$ M 12-MC-4 compounds, one can see that the three compounds are relatively bowl-shaped, but the $Y(OAc)_4$ $W(CN)_8$ 12-MC-4 appears slightly less concave compared to the other two, presumably due to the size of the $W(CN)_8$ anion.

At the end of the 2011 Mn 12-MC-4 paper, Zaleski and co-workers stated that alternate ground states were available if the coupling between the magnetic ions could be perturbed [55]. Song, Dou, and co-workers identified a potentially interesting manipulation; using the competition between the two coupling constants J and J' to bring about a spin-frustrated system. As before, the coupling between the Mn^{III} ions was represented by J and the coupling between the ring Mn^{III} and the W^{V} ion was represented by J'. Computational studies suggested that a very strong J' value compared to J would lead to a ferromagnetically polarization of the spin values, creating a stabilized ground state with a large S value (Fig. 18). Song et al. proposed that because the four-ring metal ions were antiferromagnetically coupled, the central metal would become spin-frustrated due to the divergent coupling pattern with the ring. Testing this hypothesis, the authors found that the $[Y(OAc)_4$ 12-MC-$4]^-$ retained antiferromagnetic coupling between the ring Mn^{III} ions and did not display SMM behavior. However, the introduction of the $[W^{V}(CN)_8]$ resulted in ferromagnetic coupling between the Mn^{III} ions. The authors proposed that this was due to the coupling of the Mn^{III} ions and the paramagnetic W^{V} ion, creating a spin frustrated compound with a M_s ground spin state of 11/2. This in turn led to SMM behavior in the $Y(OAc)_4[W^{V}(CN)_8]$ 12-MC-4 compound. The same group also demonstrated that the octacyanotungstate anion could be used to prepare single-chain magnets, albeit these SCMs were not MC-based [96].

$[DyX_4M$ 12-$MC_{Mn^{III}N(shi)}$-4]

Also in 2016, Boron, Pecoraro, and Zaleski published the synthesis and structural and magnetic properties of a family of $[DyX_4M$ 12-$MC_{Mn^{III}N(shi)}$-4] compounds, which were X = acetate, salicylate, benzoate, or trimethylacetate, and M = Na^+ or K^+ [59]. The authors, inspired by their earlier work with $Ln(OAc)_4$ M 12-MC-4 and $Mn(OAc)_2$ 12-MC-4, hoped that by selecting the Kramers doublet Dy^{III} ion and modifying the counteranion, they could modify the SMM properties.

Structurally, these compounds were similar to those previously reported by Azar et al. The ring Mn^{III} ions possessed Jahn–Teller axes that were roughly perpendicular to the MC plane. The benzoate-containing MCs had a more ruffled shape, whereas the acetate and salicylate-based MCs had a more bowl shape (Fig. 19). This ruffling or bowling can be observed in the angle of the Jahn–Teller axes, where the angle of the

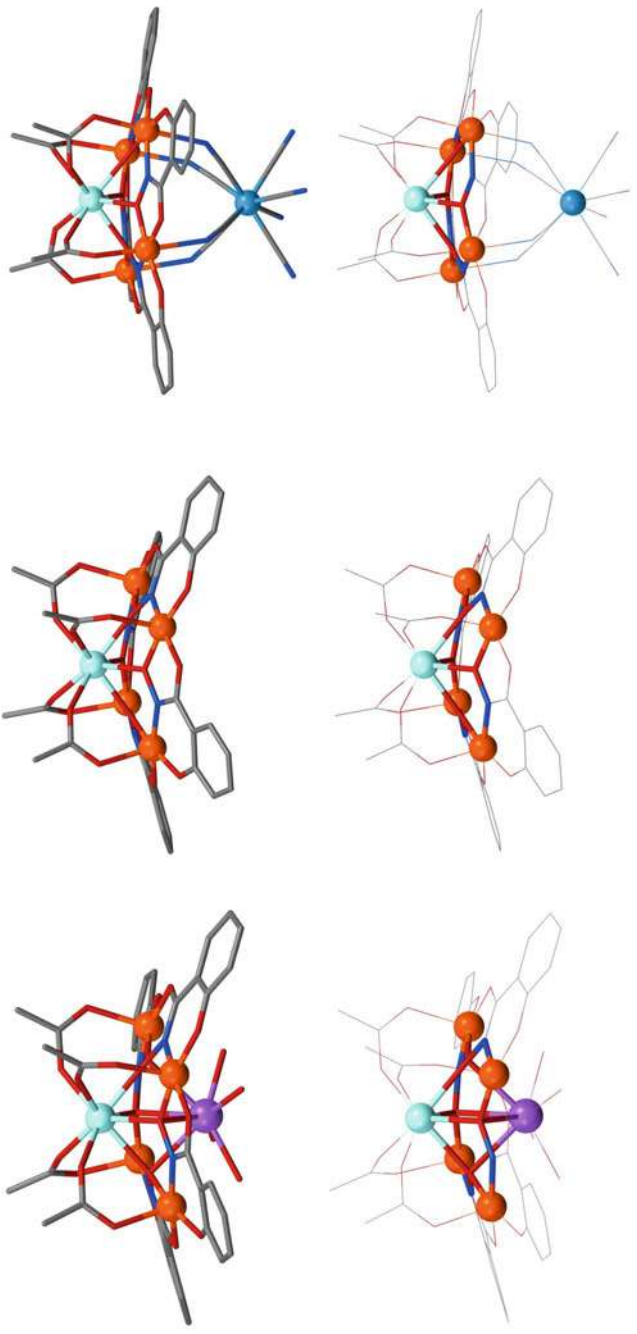

Fig. 17 From left to right, $Y(OAc)_4Na$ 12-MC-4, $Y(OAc)_4$ 12-MC-4, and $Y(OAc)_4[W(CN)_8]$ 12-MC-4 demonstrate the unique binding possibilities available from the 12-MC-4 framework. Color scheme: orange—Mn^{III}; aqua—Y^{III}; purple—Na^{I}; light blue—W^{V}; red—oxygen; blue—nitrogen; gray—carbon. Hydrogen and solvent molecules omitted for clarity

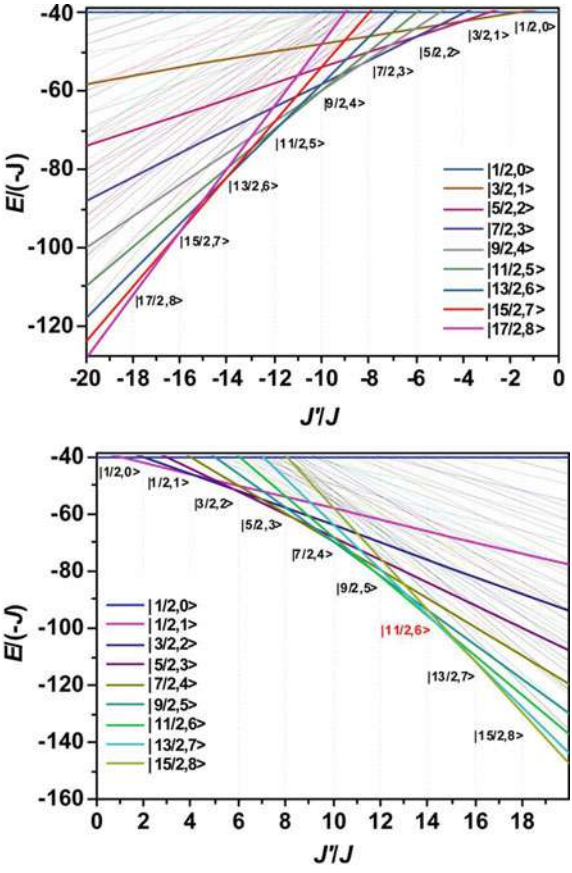

Fig. 18 Cao and co-workers studied the ratio of J' to J, finding that when J′ value was very large, a large spin state ground state could be stabilized in $Y(OAc)_4[W(CN)_8]$ 12-MC-4. The top plot shows a J'/J ratio with ferro-/antiferromagnetic coupling constants, while the bottom shows J'/J ratios with the antiferro-/antiferromagnetic coupling constants. Reprinted with permission from F. Cao; R.-M. Wei; J. Li; L. Yang; Y. Han; Y. Song; J.-M. Dou. Ferromagnetic Polarization: The Quantum Picture of Switching On/Off Single-Molecule Magnetism. Inorg. Chem. 2016. 55, 5914–5923. © 2016 American Chemical Society [58]

axis that coincides with the Jahn–Teller distortion is on average larger in the benzoate MCs compared to the other MCs. Regardless of the distortions to the MC ring, the central Dy^{III} ions were encapsulated in a slightly compressed square antiprism with roughly 45° angles between the upper and lower oxygen ligand planes (Table 2). The distance separating the central Dy^{III} ion from the oxime MC mean plane was highly dependent on the identity of the bridging ligand, ranging from 1.51 Å to 1.63 Å, with acetate being the furthest from the plane (1.63 Å or 1.59 Å, Na^+ and K^+, respectively) and salicylate being closest (1.51 Å or 1.53 Å, Na^+ and K^+, respectively).

Exploring the magnetic behavior, all of the compounds had similar DC magnetic susceptibility and dc magnetization responses, as one may expect from compounds composed of the same magnetic centers. The observed dc susceptibility at 300 K was very close to the anticipated magnetic susceptibility of four independent Mn^{III} ions and one Dy^{III} ion. However, only the $Dy(Hsal)_4$ M 12-MC-4 compounds showed frequency out-of-phase ac susceptibility behavior. The authors ruled out that structural changes in the Dy^{III} ion were responsible, as the compression ratio (distance separating ligand planes created by the two MC oxime oxygen planes divided by the

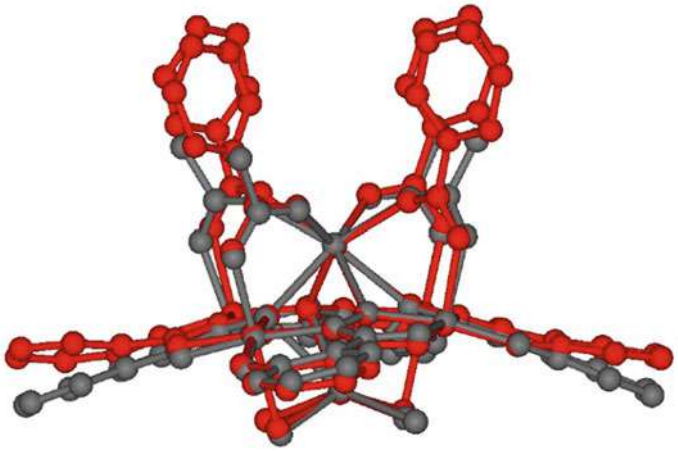

Fig. 19 $Dy(ben)_4$ Na 12-MC-4 (red) is overlaid on $Dy(OAc)_4$ 12-MC-4 (gray), highlighting the slight difference between bowling and ruffling of the MC ring. The position of the oxime planes has been minimized between the structure. Figure reprinted with permission from T. T. Boron, III; J. C. Lutter; C. I. Daly; C. Y. Chow; A. H. Davis; R. Nimthong; M. Zeller; J.W. Kampf; V. L. Pecoraro. The Nature of the Bridging Anion Controls the Single-Molecule Magnetic Properties of DyX_4M 12-Metallacrown-4 Complexes. Inorg. Chem. 2016. 55, 10,597–10,607. © 2016 American Chemical Society [59]

Table 2 The ratio of the distance separating the two ligand planes above and below the central Dy^{III} to the average oxime ligand square edge length are relatively consistent across the series. Table adapted with permission from T. T. Boron, III; J. C. Lutter; C. I. Daly; C. Y. Chow; A. H. Davis; R. Nimthong; M. Zeller; J.W. Kampf; V. L. Pecoraro. The Nature of the Bridging Anion Controls the Single-Molecule Magnetic Properties of DyX_4M 12-Metallacrown-4 Complexes. Inorg. Chem. 2016. 55, 10,597–10,607. © 2016 American Chemical Society [59]

$Dy(Hsal)_4$ K/$Dy(Hsal)_3(OAc)$K 12-MC-4	Compression ratio
$Dy(Hsal)_4$Na 12-MC-4	0.98
$Dy(OAc)_4$ K 12-MC-4	0.98
$Dy(OAc)_4$ K 12-MC-4	0.98
$Dy(OAc)_4$Na 12-MC-4	0.96
$Dy(ben)_4$Na 12-MC-4	0.99
$Dy(ben)_4$ K 12-MC-4	0.98
Dy(trimethylacetate)$_4$Na 12-MC-4	0.97

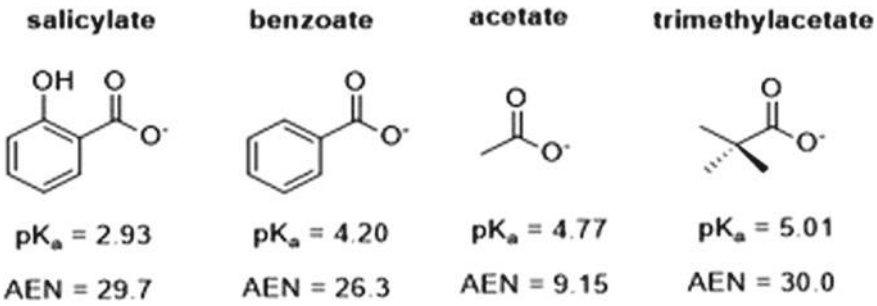

Fig. 20 Bridging ligand pK_a values for DyX_4M 12-MC-4 seem to correlate with SMM behavior: the lowest pK_a values led to SMM behavior. Figure reprinted with permission from T. T. Boron, III; J. C. Lutter; C. I. Daly; C. Y. Chow; A. H. Davis; R. Nimthong; M. Zeller; J.W. Kampf; V. L. Pecoraro. The Nature of the Bridging Anion Controls the Single-Molecule Magnetic Properties of DyX_4M 12-Metallacrown-4 Complexes. Inorg. Chem. 2016. 55, 10, 597–10, 607. © 2016 American Chemical Society [59]

average edge-length of the oxygen ligand planes) about the Dy^{III} ion remained relatively constant across the series (Table 2). Recall that this compression ratio along with the skew angles had been found to be important in understanding the magnetic behaviors of the $[Pc_2Ln]^-$ and Ln POM SIMs described earlier.

The authors proposed that the onset (or loss) of SMM-like behavior correlated to the pK_a of the bridging ligands (Fig. 20). Boukhvalov and co-workers had suggested that the electronic properties of bridging ligands in Mn_{12} derivatives could modify resulting SMM behaviors. Boukhvalov used accumulated electronegativity values (AEN) to quantify the structural changes of the ligand through various substitutions to different carboxylates studied [19]. However, AEN fails to account for the induction effect nor electronic effects of aromatic compounds. The result was that for the DyX_4M 12-MC-4 series, AEN did not properly describe the SMM behaviors. However, using pK_a as a measure of electron density from the ligand did seem to correlate to the perturbations in magnetic behavior. The ligand with the lowest pK_a, salicylate, showed the strongest SMM properties. As the pK_a increased and the electron-withdrawing ability of the ligand changed, SMM properties were lost. The countercation, then seemed to "fine-tune" the SMM behavior, likely by affecting the electron density in the MC oxime oxygen ring, as the K^+ analog showed slightly stronger frequency dependence than the Na^+ compound (Fig. 21).

Combining the findings of the $Y(OAc)_4[W(CN)_8]$ 12-MC-4 and DyX_4M 12-MC-4, one can see that slight modifications to the composition of the MC can affect the overall magnetic behavior. One can modify the coupling constants between the magnetic centers by careful selection of the bridging ligand or countercation. If lanthanides exhibited a stronger magnetic exchange with other elements, extrapolating the findings of Song et al. one may have expected a more dramatic change in the magnetic properties of the DyX_4M 12-MC-4 compounds. However, lanthanides, due to their contracted *f*-orbitals are not tremendously efficient at magnetically coupling

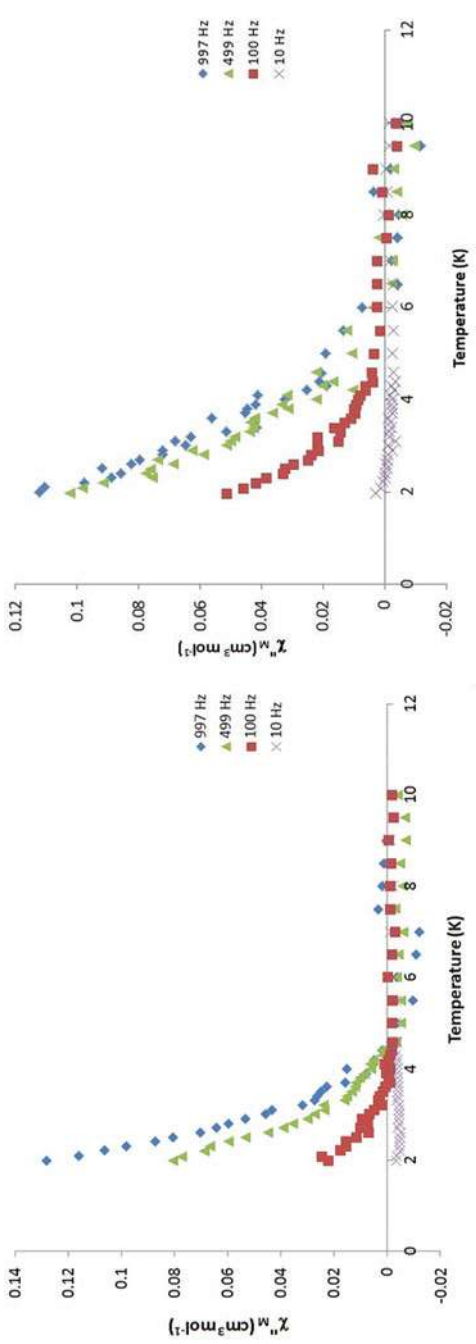

Fig. 21 $Dy(OAc)_4$ K 12-MC-4 (left) and $Dy(OAc)_4Na$ 12-MC-4 (right) showed frequency-dependent out-of-phase magnetic susceptibility. Figure adapted with permission from T. T. Boron, III; J. C. Lutter; C. I. Daly; C. Y. Chow; A. H. Davis; R. Nimthong; M. Zeller; J.W. Kampf; V. L. Pecoraro. The Nature of the Bridging Anion Controls the Single-Molecule Magnetic Properties of DyX_4M 12-Metallacrown-4 Complexes. Inorg. Chem. 2016. 55, 10,597–10,607. © 2016 American Chemical Society [59]

to other ions. However, it is becoming apparent that lanthanides can, and do, magnetically couple to other ions, especially under conditions commonly encountered in SMM research.

Liu and Tong continued the work of Dy 12-MC-4 compounds by utilizing the MCs as "building blocks", creating a double layer and trimeric triangular assemblies [97]. The MC subunits were connected via bidentate dicarboxylate ligands. These connector ligands coordinated the ring Mn^{III} and central Ln^{III} ion on two different MCs. By using bridging ligands with a 120° bite angle (isophthalic acid, 4,4′-oxybis(benzoic acid)), the group was able to produce a double-layer dimer. When the bridging ligand was modified to have a bite angle of 180° (terephthalic acid, [1,1′-biphenyl]-4,4′-dicarboxylic acid), a trimeric triangular compound was isolated. As was observed in the DyX_4M 12-MC-4 structures, antiferromagnetic exchange dominated the interactions between the Mn^{III} ions. The AC magnetic susceptibility did not show frequency dependence without an applied external DC field. Upon the application of a 1000 Oe applied field, only the oxybis(benzoic acid) bridged $(Dy[12\text{-}MC\text{-}4])_2$ showed frequency-dependent out-of-phase behavior. No maxima in the out-of-phase susceptibility were observed above 2 K, but using the Debye model, the effective energy barrier could be estimated to be between 25.5 and 30.9 K with $\tau_0 = 1.2 \times 10^{-8}$ to 4.7×10^{-8} s. The authors hypothesized that the asymmetry of the charge distribution and the angles between the ligands accounted for the difference in the magnetic behavior of the $(Dy[12\text{-}MC\text{-}4])_x$ compounds compared to $[LnPc_2]^-$ compounds [97]. While the authors did not comment on the differences in magnetic behavior compared to other $DyX_4$12-MC-4 compounds, it is possible that because the linkers placed the individual MCs either directly across from one another or on vertices of an equilateral triangle, the anisotropy of each individual MC was effectively canceled by the other MCs in the system.

4.1.2 Cobalt-Based 12-MC-4s

Cobalt-based metallacrowns are a developing field, but an interesting field for molecular magnetism. Cobalt is able to stabilize different oxidation states, and under certain conditions, different spin states (high-spin/low-spin) states, making them interesting materials for spin-crossover compounds [13]. Cobalt(II)-containing compounds have shown slow-magnetic relaxation in a variety of geometries and in the presence of many different heteroatoms commonly used as MC ligands (nitrogen and oxygen), making them intriguing candidates as molecular magnets. Rentschler and co-workers published an in-depth review on cobalt-based 12-MC-4s in a 2015 *Coordination Chemistry Reviews* article [60]. We will briefly summarize some of these key developments and encourage the interested reader to refer to this review and included references.

Rentschler and co-workers found that using a $[Co^{II}_2(H_2O)(piv)_4(HPiv)_4]$ precursor, where piv^- is pivalate, with the appropriate stoichiometric ratios of salicylhydroxamic acid and either pyridine or 3-picoline, various $12\text{-}MC_{Co^{III}N(shi)}\text{-}4$ compounds could be isolated. These compounds featured Co^{III} in the ring with a

[Co^{III}–N–O] repeat unit. The ring Co^{III} ions are all octahedral; four coordination sites along the equator of the Co^{III} ions come from two different shi^{3-} ligands. The remaining two positions on Co^{III} are along an axis and are trans to one another. For two of these Co^{III} ions, both axial positions are occupied by solvent molecules. The remaining two ring Co^{III} ions have one coordination site occupied by a solvent molecule and the other by a bridging carboxylate. The bridging ligand can occupy one side of the MC, like the ligands found in $Mn(OAc)_2$ 12-$MC_{Mn^{III}N(shi)}$-4 in a pseudo-C_2-rotation fashion, or may be in a new fashion and trans to one another through a pseudo-inversion center through the encapsulated Co^{II} central atom.

The geometry of the central Co^{II} ion varied from example to example. $Co^{II}(piv)_2$ 12-$MC_{Co^{III}N(shi)}$-4 has one shi^{3-} ligand perpendicular to the MC plane and the remaining three shi^{3-} ligands in the MC plane. The two bridging pivalate ligands are trans to one another and on the same face of the MC ring in a *trans-syn* arrangement. The result is that the central Co^{II} ion is in what is best described as a distorted trigonal prism. In $Co^{II}(boa)_2$ 12-$MC_{Co^{III}N(shi)}$-4, the bridging 2-benzoxazolinate ligand (boa) ligands from the ring Co^{III} atoms in a *trans-anti* fashion for the Co^{II}, resulting in a slightly elongated octahedral geometry for the central Co^{II}. The equatorial ligands on the Co^{II} are the oxime oxygens from the MC ring.

The authors also identified that for this family of MCs, the two bridging ligands could be different (Fig. 22). A Co^{II}(boa)(piv) 12-$MC_{Co^{III}N(shi)}$-4 compound featured both pivalate and 2-benzoxazolinate ligands in a *syn-cis* geometry. One of the shi^{3-} ligands is almost perpendicular to the MC ring, while the remaining ligand lies along the MC plane. The central Co^{II} adopts a distorted octahedral geometry. A $Co^{II}(NO_2)$(piv) 12-$MC_{Co^{III}N(shi)}$-4 again had one shi^{3-} almost perpendicular to the MC ring with the remaining three roughly in the MC plane. The bridging nitrite and pivalate ligands are on the same face of the MC and are trans to one another, giving a *syn-cis* arrangement. The central Co^{II}, coordinated to four oxime ligands from the MC ring and the nitrite oxygen and pivalate carboxylate take on a strongly distorted trigonal prism. In the [$Li[Co^{II}(\mu_2$-Piv)(Piv)[12-$MC_{Co^{III}N(shi)}$-4](pip)$_5$]]$_2$ compound, the bridging pivalate anions are on adjacent Co^{III} ions. This arrangement, along with an additional pivalate anion bridging a Co^{III} ion to a Li^{I} cation (which bridges to another MC) results in a non-planar MC geometry. The central Co^{II} is best described as a strongly distorted octahedron, with two pivalate bridges and four oxime oxygens.

These MCs are unique in that one of the shi^{3-} ligands in four of the five reported MCs is pointed out of the plane. In other 12-MC-4 compounds prepared with the shi^{3-}, the four ligands were all roughly in the same plane. The authors noted that the ring Co^{III} ions were in the low spin d^6 configuration and there was no Jahn–Teller distortion present in the MC ring. Thus, the orientation of the one shi^{3-} ligand likely is due to a minimization of Coulombic repulsions.

Examining the magnetic susceptibility of the Co^{II}(boa)(piv) 12-$MC_{Co^{III}N(shi)}$-4, $Co^{II}(NO_2)$(piv) 12-$MC_{Co^{III}N(shi)}$-4 and [$Li(Co^{II}(\mu_2$-piv)(piv)[12-$MC_{Co^{III}N(shi)}$-4]] compounds, the authors found that the DC magnetic susceptibility was relatively consistent for a mononuclear high spin Co^{II} compound. The compounds revealed a partially unquenched orbital moment, meaning that the observed room temperature susceptibility was almost double that expected of an $S = 3/2$ spin center ($\chi_M T = 3.03$,

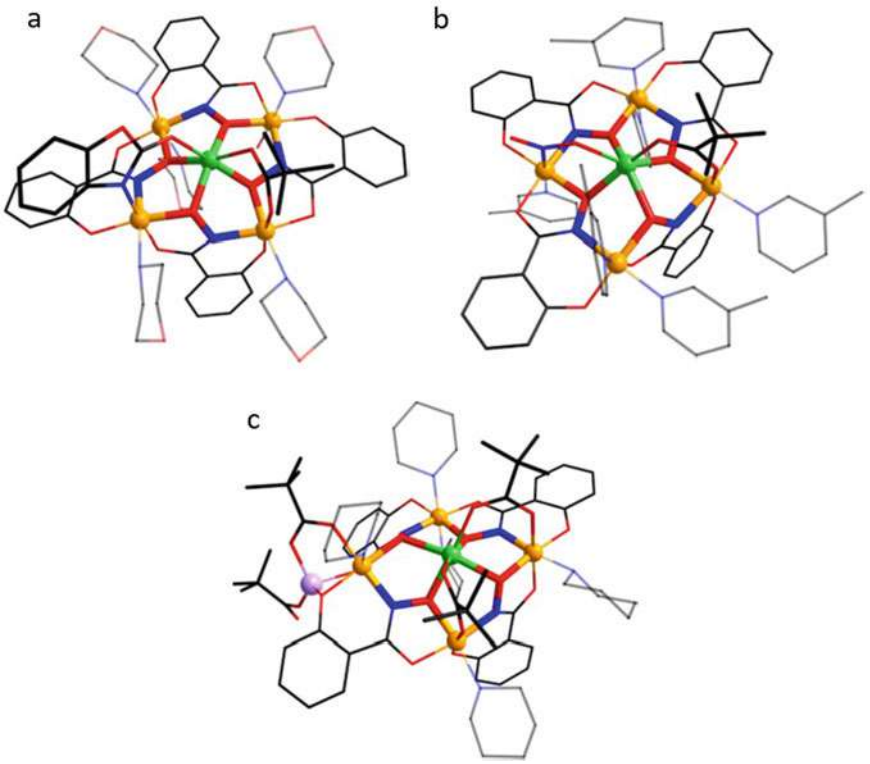

Fig. 22 Five unique Co^{II} 12-$MC_{Co^{III}N(shi)}$-4 compounds were identified but only three were magnetically characterized, **a** Co^{II}(piv)(boa) 12-MC-4; **b** $Co^{II}(NO_2)$(piv) 12-MC-4; and **c** $Li[Co^{II}(\mu_2\text{-piv})(piv)$ 12-MC-4]. Color scheme: orange—Co^{III}; light green—Co^{II}; lavender—Li^{I}; red—oxygen; blue—nitrogen; gray—carbon. Hydrogen atoms and solvent molecules omitted for clarity. Structures republished with permission from Happ et al. [60]

3.23, and 3.15 cm^3 K mol^{-1}, expected $\chi_M T = 1.876$ cm^3 K mol^{-1}). Additionally, trigonal prismatic Co^{II} ions are known to have large, negative magnetoanisotropy values [98, 99]. Therefore, these three cobalt-based MCs seemed to be excellent candidates to study for SMM behavior. The Co(boa)(piv) and $Co(NO_2)$(piv) analogs showed frequency-dependence in the out-of-phase ac magnetic susceptibility, though they did not display a maxima. Applying a weak DC field (1500 Oe) resulted in all three compounds displaying frequency-dependent behavior. The magnetic behavior was compared to other Co^{II} SMMs and the observed behavior of the three MCs was consistent with the behavior of other Co^{II}-based SMMs [98, 100, 101].

4.1.3 Other 12-MC-4 Structures of Interest

Before moving on from this interesting architecture, we should pause to mention that there are other 12-MC-4 structures using different metal ions that have been investigated as SMMs. These include SMMS or SIMs utilizing zinc(II) or copper(II) as ring metals.

Zinc-Based 12-MC-4 Structures

In 2015, Tong and co-workers reported two Yb^{III} 12-$MC_{Zn^{II}N(quinHA)}$-4 "half-sandwich" SMMs, where quinHA is quinaldichydroxamic acid. The main structural differences between the two were the use of either pyridine or isoquinoline as a crystallization solvent [61]. The compound was deemed a half-sandwich because previous work by Jankolovits and co-workers had prepared and characterized an $LnZn_{16}$ compound where a lanthanide ion was sandwiched between two (12-$MC_{Zn^{II}N(picHA)}$-4)$_2$ metallacrowns, which was further wrapped by a 24-$MC_{Zn^{II}N(picHA)}$-8 host [87]. Later, Trivedi and co-workers reported the quinHA analogs of the $LnZn_{16}$ compounds (though no magnetic data was presented) [88]. Jankolovits et al. also prepared an Ln 12-$MC_{Zn^{II}N(picHA)}$-4 double-decker or "sandwich" compound where two 12-MC-4 rings encapsulated the central lanthanide and Ln 12-$MC_{Zn^{II}N(picHA)}$-4 half-sandwich compounds [102]. For the Yb^{III} 12-$MC_{Zn^{II}N(quinHA)}$-4 "half-sandwich" compounds, the Yb^{III} ions were encapsulated by eight oxygen ligands, four from the oxime oxygens in the MC ring and another four from coordinated DMF solvent molecules, in a slightly distorted, axially compressed square antiprism. The 12-MC-4 ring featured a [Zn–N–O] repeat unit, in a bowl shape (Fig. 23).

Recall from Long and Rinehart that this environment should be optimal for later lanthanide ions to show SMM behavior. The room-temperature DC magnetic susceptibility of the two compounds was consistent with a single, isolated Yb^{III} ion. Both compounds showed frequency-dependent out-of-phase AC magnetic susceptibility in the presence of a 600 Oe applied dc field. The applied DC field was required to avoid magnetic quenching due to quantum tunneling. The group found that the isoquinoline analog had an effective energy barrier of 22.7 K and a pre-exponential factor of 3.90×10^{-7} s, while the pyridine structure had an energy barrier of 12.6 K and τ_0 of 3.92×10^{-7} s. No reason was given for the difference in observed U_{eff} for the compounds and it was noted that the observed energy barriers were several times smaller than the energy gaps calculated from the emission spectra [61].

Gallium(III)-Based 12-MC-4s

In 2019, Rentshcler and co-workers reported a Dy^{III}(n-Bu_4N) (μ-$OH)_4$[12-$MC_{Ga^{III}N(shi)}$-4]$_2$ sandwich compound, where two 12-$MC_{Ga^{III}N(shi)}$-4 metallacrowns encapsulated a Dy^{III} ion (Fig. 24). Four hydroxide ligands were

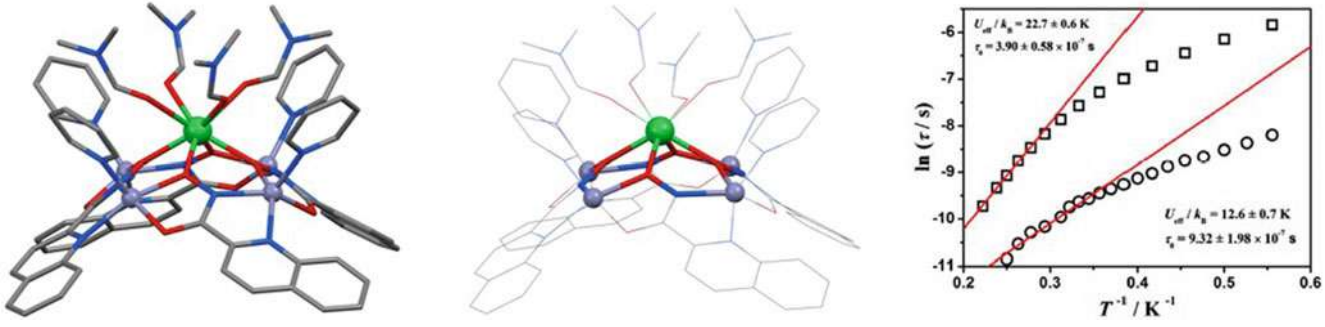

Fig. 23 Yb^{III} 12-$MC_{Zn^{II}N(quinHA)}$-4 showed slow magnetic relaxation in the presence of a 600 Oe applied dc field. The crystal structure of the pyridine analog is shown. Color scheme: purple—Zn^{II}; green—Yb^{III}; red—oxygen; blue—nitrogen; gray—carbon. Hydrogen atoms and solvent molecules omitted for clarity. AC susceptibility data shown for the isoquiniline analog (squares) and pyridine (circles) shown. Susceptibility plot reproduced with permission from Li et al. [61]

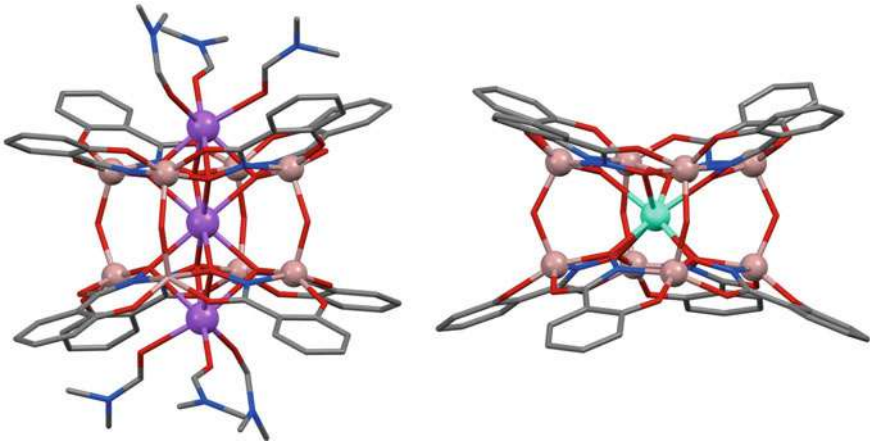

Fig. 24 The $Na_3(\mu\text{-}OH)_4$ [12-$MC_{Ga^{III}N(shi)}$-4]$_2$ (left) and $Dy(\mu\text{-}OH)_4$ [12-$MC_{Ga^{III}N(shi)}$-4]$_2$ (right) are structurally similar. The inclusion of a Dy^{III} ion removed the requirement of external Na^+ cations for charge balance as well as introducing interesting magnetic and optical properties. Color scheme: beige—Ga^{III}; aqua—Dy^{III}; purple—Na^+; red—oxygen; blue—nitrogen; gray—carbon. Hydrogen atoms and solvent molecules omitted for clarity

coordinated to the Ga^{III} ions on the two MC rings. A *n*-Bu_4N^+ cation was present for charge balance [103]. This compound was structurally similar to a $Na_3((CH_3)_2NCHO)_6(\mu\text{-}OH)_4$ [12-$MC_{Ga^{III}N(shi)}$-4]$_2$ MC reported by Pecoraro and co-workers in 1993 [104]. Unlike the earlier reported MC, the Dy^{III} [12-MC-4]$_2$ featured a paramagnetic central metal. The Ga^{III}-based 12-MC-4s acted as a magnetic diluter, helping to isolate the Dy^{III} ions from each other. Rentshcler and co-workers investigated the coordination environment of the Dy^{III} ion, looking at the skew angles and degree of compression/elongation of the square antiprism. The Dy^{III} ion was encapsulated in an 8-coordinate square antiprism. The coordination environment was slightly elongated and the skew angle between the ligand planes averaged 36.40°, consistent with a distorted square antiprism.

Long and Rinehart suggested that elongated square antiprisms would provide an ideal environment for the oblate Dy^{III} ion. In their investigation, Rentschler and co-workers used the computer program SIMPRE to calculate the population percentages of the magnetic microstates. They reported that the ground-state wave function consisted mainly of the $|\pm 11/2\rangle$ microstate (79%) pointed along the easy axis with a large contribution from the next excited state ($|\pm 13/2\rangle$). This distribution was similar to those reported in other D_{4d} Dy^{III}-based SIMs, such as Pc_2Dy [105] and $Dy(W_5O_{18})_2]^{9-}$ [106]. The application of a 1000 Oe field led to an observed U_{eff} of 39.00 ± 0.04 K and a relaxation time $\tau_0 = 2.3(5) \times 10^{-8}$ s [103] (Fig. 25).

In another 2019 paper, Shao and co-workers described the preparation and isolation of a Dy 12-$MC_{Ga^{III}N(nha)}$-4 that featured a non-planar MC ring. The group used 3-hydroxy-2-napthanoic hydroxamic acid, a triprotic ligand similar to salicylhydroxamic acid, in a 4:4:1 stoichiometric ratio with gallium(III) nitrate and dysprosium(III)

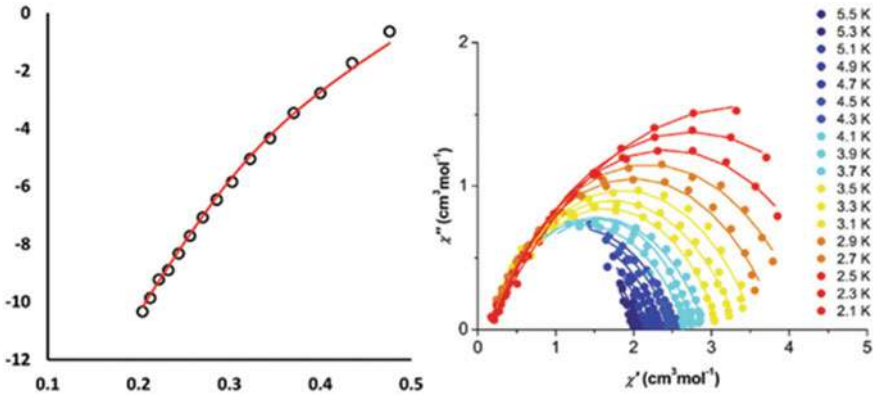

Fig. 25 The Arrhenius plot under an applied dc field of 1000 Oe and the Cole–Cole plot for Dy(μ-OH)$_4$ [12-MC$_{Ga^{III}N(shi)}$-4]$_2$ reveal SMM behavior. Reproduced with permission from the Royal Society of Chemistry, Anthanasopoulou A et al. [103]

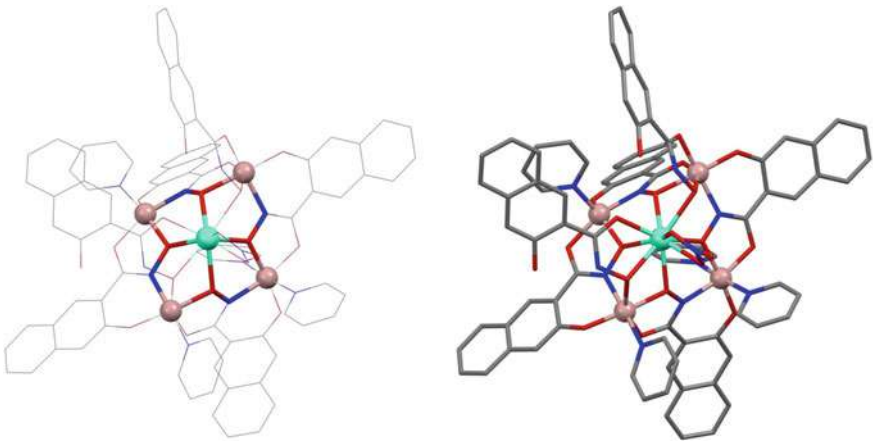

Fig. 26 Dy 12-MC-4 had an extremely bowled geometry. Color scheme: beige - Ga^{III}; aqua—Dy^{III}; red—oxygen; blue—nitrogen; gray—carbon. Hydrogen atoms and solvent molecules omitted for clarity

nitrate in a methanol, pyridine, water solvent system (Fig. 26) [107]. The resulting metallacrown was bowled, with the six-coordinate Ga^{III} ions being crystallographically inequivalent. The compound had pseudo-D_3 symmetry with the central Dy^{III} ion being approximately 1.814 Å above the Gd$_4$ plane.

Examination of the magnetic properties revealed that Dy 12-MC$_{Ga^{III}N(nha)}$-4 underwent three different relaxation pathways depending on temperature. At high temperatures, the relaxation process corresponded to an activated mechanism, or an Orbach process. At low temperatures, the magnetic relaxation was temperature-independent, probably corresponding to quantum tunneling of magnetization, and the third process

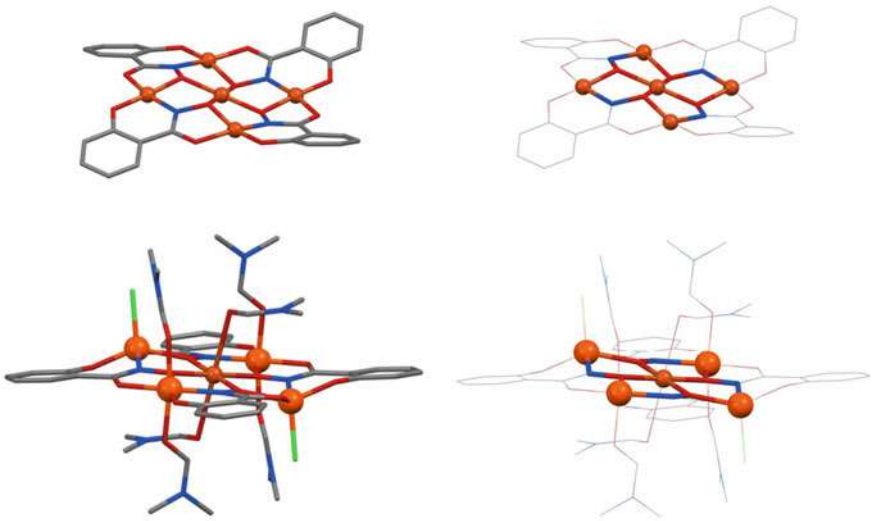

Fig. 27 Cu^{II} 12-$MC_{Cu^{II}N(shi)}$-4 (top) and $Cu^{II}Cl_2$ 12-$MC_{Fe^{III}N(shi)}$-4 (bottom) are ruffled MCs. Color scheme: orange—Fe^{III}; copper—Cu^{II}; red—oxygen; blue—nitrogen; gray—carbon; green—chlorine. Hydrogen atoms and solvent molecules omitted for clarity

at intermediate temperatures that were not fully identified [107]. Fitting the high-temperature relaxation pathway, Shao and co-workers reported an effective energy barrier of 26.4 K and a τ_0 of 2.2×10^{-6} s, while if the whole process is fitted, the U_{eff} became 26.2 K and the relaxation time τ_0 was 2.97×10^{-6} s. Recall that the energy barrier of the Dy(μ-OH)$_4$ [12-$MC_{Ga^{III}N(shi)}$-4]$_2$ was 39.0 K and the relaxation time was two orders of magnitude smaller (2.3×10^{-8} s). One possible explanation is that in the Dy 12-$MC_{Ga^{III}N(nha)}$-4 compound, the Dy^{III} anisotropy vector was not aligned with the threefold axis of the molecule, though the authors indicate that additional studies are required to better understand the anisotropy properties or to further expound on the magnetic properties of Dy 12-$MC_{Ga^{III}N(nha)}$-4 [107].

12-MC-4s with Other Paramagnetic Ring Metals

In 2016, Elmers published a study on Cu^{II} 12-$MC_{MN(shi)}$-4, where M=Cu or Fe, that showed potential as SMMs [108]. Copper and iron MCs with salicylhydroxamic acid are relatively well-known [39, 50], but their SMM potential has not been extensively examined. Structurally, these MCs have a similar connectivity to their 12-$MC_{Mn^{III}N(shi)}$-4 cousins, with an [M–N–O] repeat unit (Fig. 27). In the $Cu^{II}Cl_2$ 12-$MC_{Fe^{III}N(shi)}$-4, the ring Fe^{III} ions are relatively planar. Two of the Fe^{III} ions are six-coordinate, with four equatorial positions occupied by nitrogen or oxygen atoms from two different shi^{3-} ligands, with the axial positions occupied by two DMF solvent molecules. These two six-coordinate Fe^{III} ions are *trans* to one another. The

remaining two Fe^{III} ions are five-coordinate square pyramidals. Again, the equatorial positions are occupied by the heteroatoms of two different shi^{3-} ligands. The fifth position (axial) is a chloride anion in a *trans-anti* arrangement.

Elmers and co-workers examined the magnetic properties of the $Cu^{II}Cl_2$ 12-$MC_{Fe^{III}N(shi)}$-4 and $Cu^{II}Cl_2$ 12-$MC_{Cu^{II}N(shi)}$-4 compounds using X-ray magnetic circular dichroism spectroscopy and SQUID magnetometry. From an earlier study, Happ and Rentschler had found that the Fe^{III} ions preferred to be in a high spin state at room temperature. Lowering the temperature led to an increase until 40 K, before the susceptibility began to decrease. Happ and Rentschler suggested that this decrease could potentially be due to significant zero-field splitting values associated with the square pyramidal Fe^{III} ions present, though intermolecular interactions between adjacent MCs could not be ruled out [67]. Interestingly, strong antiferromagnetic coupling between the central Cu^{II} and ring Fe^{III} forces the ring Fe^{III} ions to behave in a ferromagnetic fashion [108]. When examining the AC susceptibility, the group did not report any frequency-dependent behavior, but hoped that subtle changes in the MC framework could lead to SMM behavior.

In 2021, Rentschler and co-workers prepared, isolated, and characterized a Tb $[12\text{-}MC_{Ni^{II}N(shi)}\text{-}4]_2$ dimer compound (Fig. 28) [109]. This MC was analogous to the $[Pc_2Tb]^-$ compound first described by Ishikawa and co-workers in 2003. The two 12-MC-4 units formed an almost ideal square antiprism about the central Tb^{III} ion. The two 12-MC-4 rings were relatively planar and separated by 3.321 Å. The Tb^{III} ion sat slightly closer to one MC ring (1.35 Å) than the other (1.63 Å). This could be because the closer MC ring had a piperidine ligand coordinated to two Ni^{II} ions, while the other MC was in close, but non-coordinating interactions, with acetate and piperidine ligands, affecting the electron density associated with each MC ring. Because the Ni^{II} ions are either square planar or square pyramidal in geometry, there is no need for a bridging ligand, such as hydroxide, as found in many of the analogous Ga^{III}-based sandwich 12-MC-4 compounds.

Investigation of the magnetic properties revealed fast quantum tunneling of magnetization under zero-field conditions. Fitting the susceptibility data to the Arrhenius equation and taking into consideration quantum tunneling and Raman relaxation pathways, the authors reported an effective energy barrier of 346 K and a τ_0 of 2.53×10^{-8} s. When an external magnetic field was applied to suppress this quantum tunneling, an effective energy barrier of 585 K and $\tau_0 = 3.11 \times 10^{-10}$ s was observed. The authors noted that there were two unique molecules in the crystal structure that could potentially impact the magnetic response. They also note that this result presents an interesting pathway for additional ligand modification to adjust the magnetic properties of the Ni^{II}-based 12-MC-4 sandwich compounds [109].

4.2 15-MC-5s

The 15-MC-5 architecture was first recognized by Kessisoglou in 1994 [52]. In 1999, Stemmler and co-workers described the creation of planar 15-MC-5 s using

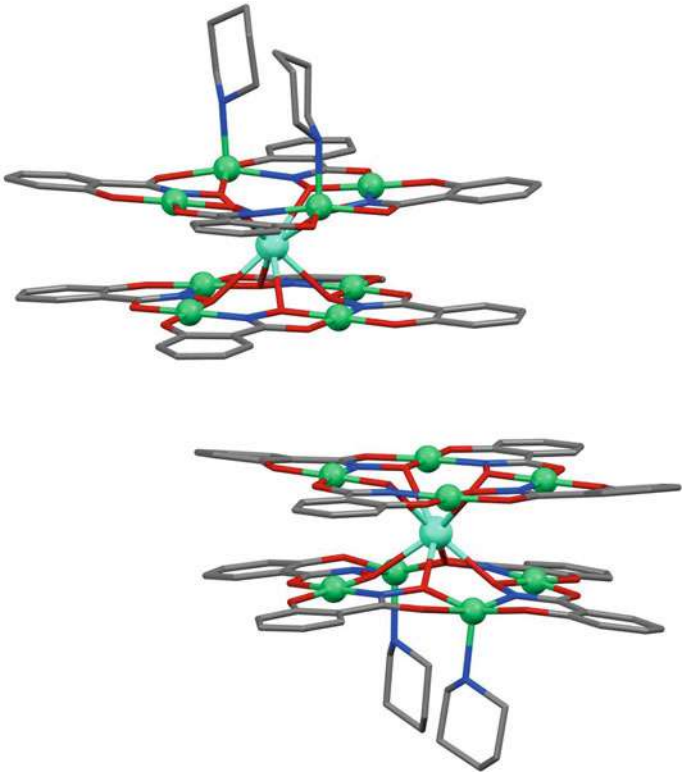

Fig. 28 The $Gd(NO_3)$ 15-$MC_{Cu^{II}N(picHA)}$-5 was the first planar 15-MC-5. Color scheme: copper—Cu^{II}; aqua—Gd^{III}; red—oxygen; blue—nitrogen; gray—carbon. Hydrogen atoms and solvent molecules omitted for clarity

Cu^{II} as ring metals and α-amino hydroxamic acids (Fig. 28). These 15-$MC_{Cu^{II}N}$-5 compounds were capable of binding lanthanides in the central cavity [49]. Because of the odd number of atoms in the ring, there would be a distinct possibility of observing spin-frustration from the ring should antiferromagnetic coupling be the dominant coupling force. Indeed, in the $La(NO_3)_3$ 15-$MC_{Cu^{II}N(picHA)}$-5 compound, a low-temperature magnetic susceptibility correlating to an $S = ½$ was observed. The $Gd(NO_3)_3$ 15-$MC_{Cu^{II}N(picHA)}$-5 showed ferromagnetic coupling between the central Gd^{III} and the ring Cu^{II} ions.

In a follow-up paper in 2006, Zaleski and co-workers studied the Ln 15-$MC_{Cu^{II}N(S-pheHA)}$-5 structures as potential SMMs [110]. Interestingly, depending on the solvent, the authors reported isolating dimers of 15-MC-5 in a "hand-holding" formation, creating a hydrophobic pocket, or in a helix that resulted from a carbonyl oxygen atom from one MC binding to a Cu^{II} ring ion of an adjacent MC (Fig. 29) [47, 111]. Using a chiral α-amino hydroxamic acid afforded a chiral helix, with the ligand chirality affecting the helix's pitch—the *S*-pheHA affording the (+) pitch and

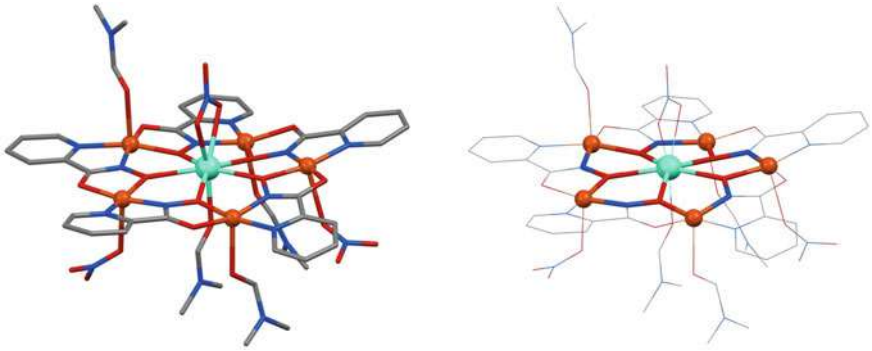

Fig. 29 The $Tb^{III}[12\text{-}MC_{Ni^{II}N(shi)}\text{-}4]_2$ dimer compound suggests a promising future for Ni^{II}-based MC sandwich compounds. Color scheme: green—Ni^{II}; aqua—Tb^{III}; red-oxygen; blue—nitrogen; gray—carbon. Hydrogen atoms, solvent piperidine, and acetate ligands omitted for clarity

the *R*-pheHA producing the (–) pitch. Zaleski noted that the MC geometry allowed the five Cu^{II} ions, regardless of solvent, to be roughly planar with one another and allowed their Jahn–Teller axes to align perpendicular to the MC plane [110]. The authors also noted that in 2006 there were only a few examples of chiral SMMs [112, 113], providing an opportunity to further expand on chiral SMMs and to explore the magnetochiral effect first observed in 1997 [114].

Zaleski and co-workers noted that the susceptibility of the Dy 15-MC-5 and Ho 15-MC-5 showed decreases from room temperature to 5 K, which they contribute to the depopulation of higher spin states and not magnetic exchange, as the large spin–orbit coupling values of the studied lanthanides made it difficult to extract exchange constants. Both the dimers and the helices of Dy 15-MC-5 and Ho 15-MC-5 polymorphs showed frequency-dependence below 4.5 and 6.0 K, respectively, at the studied frequencies. To rule out spin-glass behavior, the dimers were dissolved in methanol. Mass spectrometry had previously supported that the MCs retained their connectivity, but that the helices were only a solid-state packing effect and the structure was lost in solution. The Dy 15-MC-5 retained frequency-dependent behavior, but the Ho 15-MC-5 analog did not, suggesting that the observed solid-state behavior was likely due to spin glass behavior and/or magnetic ordering. Zaleski and co-workers noted that the helical Dy 15-MC-5 did not show enhanced AC susceptibility properties, suggesting that the helical Dy 15-MC-5 should be considered a chain of SMMs rather than an SCM [115].

Since 2006, numerous papers have presented the magnetic properties of other 15-MC-5-based compounds. In the interest of balancing the competing interests of brevity with covering the topic with some degree of completeness, we will focus on a few of the more recent examples of Ln encapsulated $15\text{-}MC_{Cu^{II}}\text{-}5$ compounds. We would like to point to some potentially interesting review articles on the magnetic properties of 15-MC-5s in general that can help supplement this text [116, 117].

Several of the 15-MC-5 s that we will discuss utilize Cu^{II} as a ring metal. Copper(II) prefers octahedral or square pyramidal geometry, allowing for relative

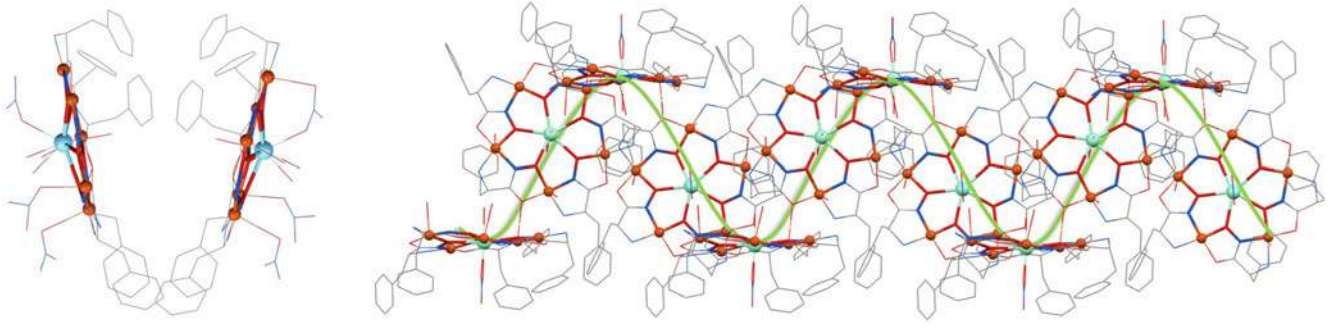

Fig. 30 Eu [15-$MC_{Cu^{II}N(quinHA)}$-5] has a ruffled geometry. Color scheme: copper—Cu^{II}; aqua—Eu^{III}; red—oxygen; blue—nitrogen; gray—carbon. Hydrogen atoms and solvent molecules omitted for clarity

planar pentagonal MCs employing amino-acid-based hydroxamic acid ring ligands. This geometry has been exploited for other applications, such as molecular recognition [87, 118, 119]. The use of Cu^{II} provides a paramagnetic ring metal (d^9) that due to the odd number of metals in a pentagonal arrangement is forced into a spin-frustrated coupling situation with the other Cu^{II} ions. Additionally, the 15-MC-5 framework of planar Cu^{II}-based MCs is ideal for encapsulating a lanthanide ion in the central cavity [120–122].

4.2.1 Ln 15-$MC_{Cu^{II}N(quinHA)}$-5s

In 2018, Liu and co-workers published the magnetic studies on a $Dy^{III}(sal)_2$[15-$MC_{Cu^{II}N(quinHA)}$-5](pyridine)$_5$, where sal = the deprotonated salicylaldehyde anion compound [123]. The MC was slightly ruffled, with a Dy^{III} ion encapsulated in the 15-MC-5 ring. Two salicylaldehydes coordinate to either face of the Dy^{III} ion through the phenoxide groups while the equatorial planar features five donor atoms from the ring ligand hydroximate groups. The authors noted that the strong axial crystal field around the central Dy^{III} provided a large Ising-type magnetoanisotropy value.

Investigating the magnetic properties with the isostructural Y^{III} analog, the group observed relatively strong antiferromagnetic coupling between neighboring Cu^{II} ions; –44 cm^{-1} for the interactions between adjacent Cu^{II} ions with coordinated pyridine ligands on the same face and –68 cm^{-1} for adjacent Cu^{II} ions with coordinated pyridine ligands on opposite faces. It was determined that the ring had an $S = ½$ ground state with an excited ½ state separated by approximately 51 cm^{-1}. The Dy^{III} ion had a weak ferromagnetic coupling with the ring Cu^{II} ions (+0.88 cm^{-1}). The Dy^{III} 15-MC-5 compound showed interesting single-molecule magnetic behavior. Three unique relaxation pathways were identified. A true Orbach relaxation pathway for the crystal field states of Dy^{III} ion led to a U_{eff} of 623 cm^{-1}. Meanwhile, the second and third relaxation pathways matched the relaxation from the first and second excited states predicted by the exchange pathway calculations (5.2 and 38.7 cm^{-1}, respectively).

In a follow-up 2019 Dalton Transactions article, the group investigated the magnetic properties of a structurally similar $Eu^{III}(sal)_2$[15-$MC_{Cu^{II}N(quinHA)}$-5](pyridine)$_5$ compound (Fig. 31) [124]. Structurally, the compound was very similar to other Ln [15-MC-5] compounds, including the Dy^{III} analog described above. Investigating the magnetic properties of the MC, the authors reported similar Cu coupling parameters as described above, while the coupling between the central Eu^{III} and the ring Cu^{II} ions was set to 0 cm^{-1}. The compound showed frequency-dependent out-of-phase magnetic susceptibility with an U_{eff} of 14.8 cm^{-1} and a τ_0 of 1.2×10^{-7} s, which was smaller than the calculated energy difference between the ground and the first excited state. Therefore, the authors assigned the relaxation pathway to a Raman-like process, suggesting that the relaxation process in the MC was based solely on the Cu_5 MC ring.

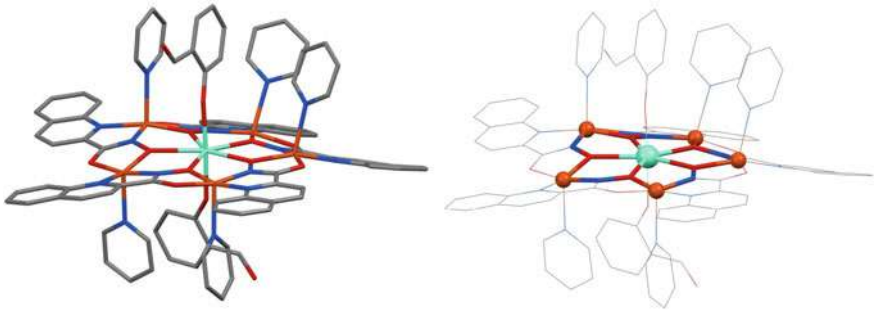

Fig. 31 The $Sm(NO_3)_3$ 15-$MC_{Cu^{II}N(pheHA)}$-5 was able to form different crystal structure types depending on solvent conditions—a "clasped hands" structure (left) and a helix (right). Color scheme: copper—Cu^{II}; aqua—Sm^{III}; red—oxygen; blue–nitrogen; gray—carbon. Hydrogen atoms, nitrate counter ions, and solvent molecules were omitted for clarity. A light green guideline is added to help demonstrate the helix

In 2021, Liu, Chilton, and Tong described a process of using a single hydroxide linker to bridge two Dy^{III} [15-$MC_{Cu^{II}N(quinHA)}$-5 compounds [125]. The Dy^{III} ions were in compressed pentagonal bipyramidal geometries, while all but one Cu^{II} ion had a square pyramidal geometry. The unique Cu^{II} ion belonged to the sandwich compound and was square planar. The authors hypothesized that the Dy^{III} anisotropy vector of the Dy^{III} ion was perpendicular to the MC plane and that by using a single hydroxide bridge, they could potentially ferromagnetically couple the two units together and align the anisotropy vectors of the Dy^{III} ions in the same direction.

Both the monomer and the dimer compounds showed antiferromagnetic coupling between the ring Cu^{II} ions and depopulation of the Dy^{III} Stark levels. Below 28 K, there was evidence of ferromagnetic coupling between the Dy^{III} and Cu^{II} ion in the monomer. Below 40 K, there appeared to be ferromagnetic coupling between the two Dy^{III} ions in the dimer. The monomer compound showed butterfly-shaped magnetic hysteresis while the dimer compound showed open magnetic hysteresis without a loss of magnetization at zero field. The authors proposed that this was due to the axial dimerization, as the anisotropy vectors of the Dy^{III} ions were roughly colinear. The effective energy barrier of the monomer Dy[15-$MC_{Cu^{II}N(quinHA)}$-5] was 625 cm^{-1} and a $\tau_0 = 2.0 \times 10^{-11}$ s with no applied external field. For the dimer, (Dy[15-$MC_{Cu^{II}N(quinHA)}$-5])$_2$, the U_{eff} decreased to 582 cm^{-1} and $\tau_0 = 5 \times 10^{-11}$ s. The authors indicated that these are the largest observed for *d-f* SMMs [125].

4.2.2 Ln 15-$MC_{Cu^{II}N(pyzHA)}$-5s

A similar compound, $Tb(H_2O)_3$ [15-$MC_{Cu^{II}N(pyzHA)}$-5]$(H_2O)_3$, was prepared and characterized in 2019, where pyzHA is pyrazine hydroxamic acid [126]. The MC again had three Cu^{II} ions in square pyramidal geometries and two Cu^{II} ions in square planar geometries. The Tb^{III} ion was encapsulated in the metallacrown and featured

two water molecules on one face and an additional water molecule coordinated on the other face (Fig. 32). Interestingly, two adjacent 15-MC-5 are connected through a hydrogen-bonding network. The hydrogen adjacent to a nitrogen atom in the pyrazine hydroxamic acid ligand is close enough to interact with a non-coordinated triflate ion. This triflate ion can then hydrogen bond with another hydrogen atom on a new 15-MC-5's pyrazine hydroxamic acid ligand. These complicated interactions led to a 1-dimensional network.

The authors found that upon cooling the sample, antiferromagnetic coupling between the ring Cu^{II} ions could be observed until approximately 6 K. Below 6 K, a rapid increase in $\chi_M T$ was observed likely due to depopulation of the Tb^{III} Stark levels or ferromagnetic coupling between the Tb^{III} and Cu^{II} ions. Investigating the out-of-phase magnetic susceptibility, Zhang and co-workers found that the compound showed frequency-dependent out-of-phase magnetic susceptibility. However, there was no observed maximum above 2 K, which the authors contribute to the presence of quantum tunneling of magnetization. To minimize the impact of tunneling, the group applied an external dc field of 1000 Oe, allowing them to observe an effective energy barrier of 5.42 K and a pre-exponential τ_0 of 8.09×10^{-7} s.

Continuing their work, but now employing Gd^{III} and Dy^{III} in addition to Tb^{III}, the authors explored the possibilities of creating 2- and 3-dimensional frameworks (Fig. 33). These structures were the first reported 2- and 3-dimensional [15-$MC_{Cu^{II}N(pyzHA)}$-5] networks presented in the literature [127]. The authors reported that the five Cu^{II} ions remained square pyramidal in geometry. Three of the Cu^{II} ions coordinated solvent methanol molecules while the other two were coordinated to a nitrogen atom on a neighboring metallacrown's pyrazine ring ligand. The central Ln^{III} ion was found to be eight coordinate with five atoms from the MC ring and the remaining three ligands from H_2O ligands. The coupling between the Gd^{III}[15-MC-5] rings created two voids—one large (7.3569 Å × 20.2994 Å) with "irregular symmetry" [127] and one smaller (7.1598 Å × 7.1428 Å). The size of the larger void was found to vary across the series. Nitrogen sorption isotherm studies suggest that despite having two voids in the crystal structure, these compounds are not microporous solids.

Investigation of the magnetic properties suggested weak antiferromagnetic coupling between adjacent Cu^{II} ions in a single MC subunit around 14 K. Slight increases in susceptibility for the Tb^{III} and Dy^{III} 15-MC-5 units below 14 K were also observed, as was observed in the Tb^{III} [15-MC-5] compound discussed above [126]. It was found that the compounds all displayed weak intermetallic ferromagnetic coupling at low temperatures. It was hypothesized that this interaction might be due to Ln^{III}-Cu^{II} magnetic coupling. The Tb^{III} and Dy^{III} structures both displayed frequency-dependent out-of-phase magnetic susceptibility, but neither showed a maximum above 2 K. Under a 1000 Oe applied magnetic field, all three showed slow magnetic relaxation. The authors suggested that in the case of the Gd^{III} structure the change in magnetic behavior suggest that the 2-dimensional network changes the magnetic behavior as other monomers Gd^{III} 15-MC-5 compounds have not shown SMM-like behavior [49, 128].

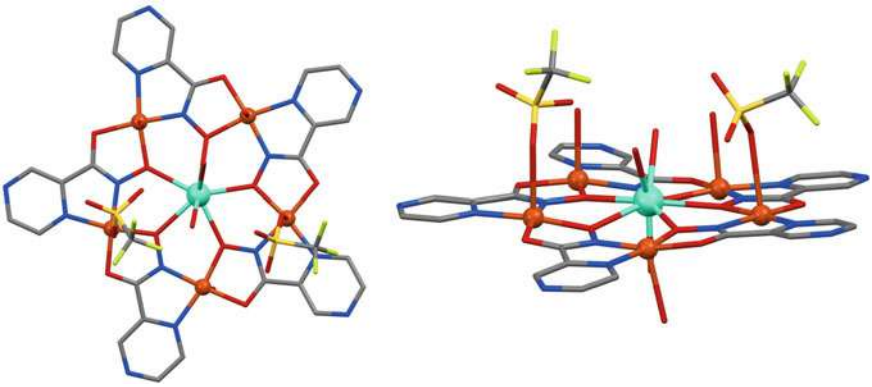

Fig. 32 $Tb(H_2O)_3$ [15-$MC_{Cu^{II}N(pyzHA)}$-5] demonstrated a frequency-dependent relaxation pathway with an effective energy barrier or 5.42 K and τ_0 of 8.09×10^{-7} s. Color scheme: copper—Cu^{II}; aqua—Tb^{III}; red—oxygen; blue—nitrogen; gray—carbon—yellow—sulfur; lime—fluorine. Hydrogen atoms, solvent molecules, and non-coordinated triflate groups are omitted for clarity

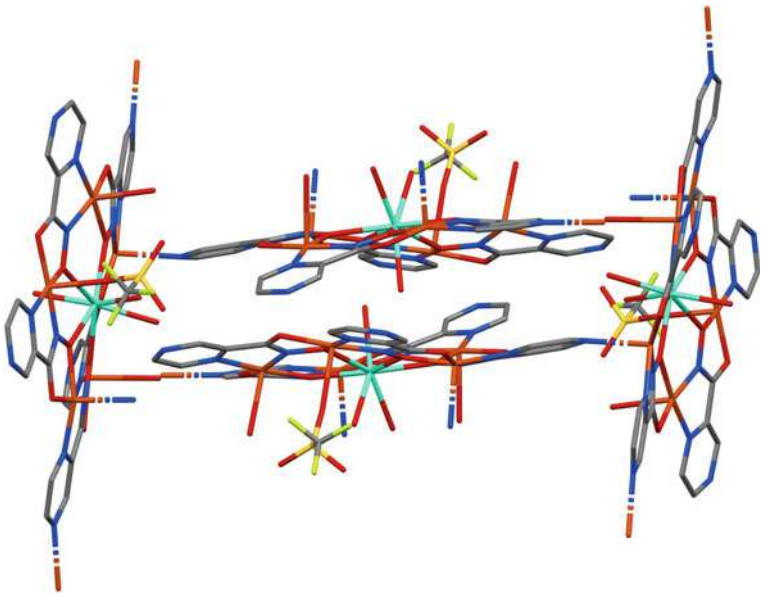

Fig. 33 Dy [15-$MC_{Cu^{II}N(pyzHA)}$-5] forms a network solid. Two voids are formed, with the larger one shown. Due to the irregular shape of the cavity, it is not an efficient microporous solid. Color scheme: copper—Cu^{II}; aqua—Dy^{III}; red—oxygen; blue—nitrogen; gray—carbon; yellow—sulfur; lime—fluorine. Hydrogen atoms, solvent molecules, and non-coordinated triflate ions have been removed for clarity. Dotted lines indicate connections to neighboring MCs

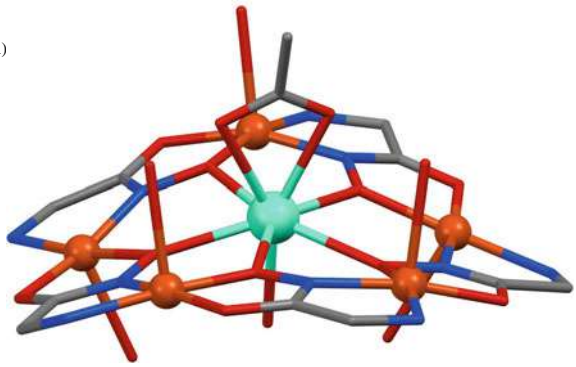

Fig. 34 $Dy(OAc)(H_2O)$[15-$MC_{Cu^{II}N(glyHA)}$ has an interesting bell-shaped geometry. Color scheme: copper—Cu^{II}; aqua—Dy^{III}; red—oxygen; blue—nitrogen; gray—carbon. Hydrogen atoms, solvent molecules, and non-coordinated nitrate ligands were omitted for clarity

4.2.3 Ln 15-$MC_{Cu^{II}N(glyHA)}$-5*s*

When glycine hydroxamic acid was used as the ring ligand, Li and Dou reported a bell-shaped $Dy(OAc)(H_2O)$15-$MC_{Cu^{II}N(glyHA)}$-5 compound (Fig. 34) [129]. The five Cu^{II} ions were five-coordinate square pyramidal. The four planar positions were coordinated by the glycinehydroxamic acid ligands while the axial position was coordinated by a water molecule. The orientation of the axial ligand switched with the neighboring Cu^{II} ion having the water molecule pointing in the opposite direction. The Dy^{III} ion remained in the middle of the 15-MC-5 ring and was 8-coordinate. Five of the coordination sites were occupied by donors from the MC ring. Two coordination sites were from an acetate ligand. On the opposite face was a single water molecule. The presence of hydrogen bonding led to a 2-dimensional network.

Investigation of the magnetic properties suggested antiferromagnetic coupling between the ring Cu^{II} ions upon cooling at room temperature. A sharp decrease between 18 and 4 K was attributed to the strong spin–orbit coupling of the Dy^{III} ion as well as the depopulation of the Stark levels. Below 4 K, a slight increase is observed, which was assigned to the ferromagnetic coupling between the Cu^{II} and the Dy^{III} ion. In an ac magnetic field, the compound showed frequency-dependent out-of-phase magnetic susceptibility, but no maxima were observed both with and without an applied external magnetic field up to 2000 Oe [129].

Song and Dou showed that Ln [15-$MC_{Cu^{II}N(glyHA)}$-5] compounds could be linked via diamagnetic $[Fe(CN)_5NO]^{2-}$ linkers, creating new dimer and coordination polymers [120]. These heterotrimetallic compounds were able to be prepared and isolated in a one-pot procedure. Whether a dimer or coordination polymer was isolated depended on the size of the encapsulated Ln—the larger La^{III}, Pr^{III}, and Nd^{III} producing the dimers, while Sm^{III}, Gd^{III}, Tb^{III}, Dy^{III}, and Ho^{III} gave coordination polymers. As was previously shown by $Ln(OAc)_4$ M [12-$MC_{Mn^{III}N(shi)}$-4], $Y(OAc)_4(WO_8)$ [12-$MC_{Mn^{III}N(shi)}$-4], and $Y(OAc)_4[W(CN)_8]$[12-$MC_{Mn^{III}N(shi)}$-4], metallacrowns are capable of producing heterotrimetallic compounds using metallic linkers [57, 58]. Perhaps one of the unique benefits of the MC architecture compared

to other coordination compounds is its ability to form predictable compounds from mixtures of metals.

Regardless, this utilization of trimetallic 15-MC-5 building blocks linked by diamagnetic connectors is a relatively unexplored area and one that could potentially be of interest to the field. Song and Dou suggested that diamagnetic linkers can mediate superexchange interactions and modify the magnetic properties, such has been observed in Prussian blue [130]. Indeed, the authors report that the inclusion of the $[Fe(CN)_5NO]^{2-}$ linker sufficiently modified the geometry of the Dy^{III} ion to induce ferromagnetic interactions between the Dy^{III} and Cu^{II} ions. Of the eight compounds produced, the Tb^{III} and Dy^{III} 15-MC-5 polymers were tested for SMM behavior. Only the Dy^{III} 15-MC-5 polymer demonstrated frequency-dependent out-of-phase magnetic susceptibility, albeit in the presence of a 2000 Oe external field, likely due to quantum tunneling of magnetization. The observed effective energy barrier for the Dy^{III} 15-MC-5 chain under an applied 2000 Oe external field was 9.14 K and the pre-exponential term, $\tau_0 = 3.69 \times 10^{-6}$ s.

Closing Remarks

Since the first reports of SMMS almost 30 years ago, the field of single-molecule magnets has grown exponentially. Some of the most consequential findings in the field are related to metallacrowns. From the first Ln-Mn SMM to systematic approaches, MCs have served a major role, demonstrating unique adaptability within the field. Most reported SMMs have been "one-offs", where the compound is serendipitously prepared and shows interesting properties. However, the fields of polyoxometalates, metallowheels, and metallacrowns have shown that a systematic approach can provide the field with a deeper, richer understanding of the origin of the underlying phenomenon. Indeed, the work on the bisphthalocyaninato-lanthanide, lanthanide-containing polyoxometalates, and metallacrowns have revealed the importance of the coordination environment around the lanthanide.

In the past 30 years, the idea that lanthanides are relatively magnetically exchange inert due to their contracted *f*-orbitals has been dispelled, at least at the low temperatures studied in the field of molecular magnetism [73]. This richer understanding of lanthanide chemistry can pay major dividends in the design of new SMMs and other functional materials. Chemists should now consider the connectivity around lanthanide ions and *if* an exchange pathway may exist between the relevant magnetic orbitals. Predicting a priori the exchanges and the properties will likely remain difficult due to spin–orbit coupling found in lanthanides, the *S* term is not a "pure" quantum number, and is better understood as a *J*-term [73].

Metallacrowns have demonstrated the ability to control the structure and orientation of magnetic centers. The works of Waldmann, Ruiz, Neese, and Kortus suggested that a rational design approach for SMMs could lead to improved magnetic behavior. Waldmann suggested that increasing the number of magnetic centers, rather than improving the observed magnetic behavior would have a minimal effect. Instead, Waldmann suggested focusing on improving the anisotropy SMMs [10]. Ruiz, Neese, and Kortus suggested linking anisotropy vectors, such as Jahn–Teller axes, could lead to an increase in molecular magnetoanisotropy. They also suggested that this coupling

would be most efficient in smaller molecules, such as trinuclear compounds [11]. Metallacrowns are uniquely equipped to examine these theoretical predictions.

Metallacrowns' ability to take on predictable geometries allows researchers to prepare compounds with a set number of magnetic centers and to arrange those magnetic centers in a predefined orientation. This has provided researchers the ability to study how geometric control can affect coupling and magnetic properties. It has been observed that some of the best SMM-MCs are those that have highly anisotropic metal ions, such as lanthanides and manganese(III) ions in a planar geometry. This planarity allows the possibility to align the anisotropy vectors. Researchers have also shown that they can fine-tune the properties of these magnetic properties by slightly varying ligand environments. Zaleski and co-workers showed how placing a normally isotropic metal ion (Mn^{II}) in a distorted orientation can lead to exciting magnetic properties [55]. Song and co-workers showed how introducing a paramagnetic W^{V} ion to the 12-$MC_{Mn^{III}N(shi)}$-4 could turn a molecule with a diamagnetic ground state and antiferromagnetic coupling between ring Mn^{III} ions into an SMM with ferromagnetically coupled ring Mn^{III} ions by changing the ratio between coupling constants [58]. Boron and co-workers demonstrated that changing the bridging ligand between the central Dy^{III} ion and ring Mn^{III} ions in the 12-$MC_{Mn^{III}N(shi)}$-4 could affect observed SMM behavior but have little effect on the magnetization or magnetic susceptibility [59]. Employing diamagnetic metal ions, such as Zn^{II} or Ga^{III} coupled with lanthanide ions provides an opportunity to prepare SIM-like magnets [61, 62, 84].

Larger MCs still have an interest in the field. The first observed Ln^{III}/Mn SMM was a member of the extended MC family. Recently, it was shown that by substituting Gd^{III} for Dy^{III} in an $Ln^{III}{}_6Mn^{III}{}_2Mn^{IV}{}_2$ could turn a molecule with SMM behavior into a magnetic refrigerant [77]. These MCs indicate that in the future, potentially multifunctional MCs could be easily prepared by simply modifying one component.

We have attempted to provide a background on the work of researchers in the field and provide a rationale for some of the decisions or directions taken by researchers. We hope that we have inspired the reader to continue to examine the field of MC-based SMMs. We believe that the future of magnetic MCs is bright with the field only being limited by access to starting materials and the creativity and time of the researcher. New ligands can be prepared to create new geometries and orientations of MCs. These ligands could also potentially modify the coupling between magnetic centers. Numerous paramagnetic ions could be introduced as either ring metals or as central ions. Linking MCs into chains of SMMs or into larger geometries could lead to interesting magnetic behaviors. Using diamagnetic ring metals and paramagnetic central ions could lead to interesting SIM compounds or nonlinear optical materials. Fundamental studies of magnetic exchange pathways between Ln ions and *d*-group metals can also be undertaken. New spectroscopic techniques for the field can be tested with MC-based SMMs, allowing for a deeper understanding of the source of magnetic behaviors.

References

1. Sessoli, R., Gatteschi, D., Caneschi, A., Novak, M.A.: Nature **365**, 141 (1993)
2. Gatteschi, D., Caneschi, A., Pardi, L., Sessoli, R.: Science **265**, 1054 (1994)
3. Gatteschi, D.: Adv. Mater. **6**, 635 (1994)
4. Long, J.R.: Chem. Nanostruct. Mater. **291** (2003).
5. Villain, J., Hartman-Boutron, F., Sessoli, R., Rettori, A.: Eur. Lett **27**, 159 (1994)
6. Gatteschi, D., Sessoli, R., Villain, J.: Molecular Nanomagnets. Oxford University Press, New York (2006)
7. Girerd, J.J., Journaux, Y.: Physical Methods Bioinorganic Chemistry. In: Que, L. (eds.) 1st edn, pp. 321–374. University Science Books, Sausalito (2000)
8. Aromí, G., Aubin, S.M.J., Bolcar, M.A., Christou, G., Eppley, H.J., Folting, K., Hendrickson, D.N., Huffman, J.C., Squire, R.C., Tsai, H.L., Wang, S., Wemple, M.W.: Polyhedron **17**, 3005 (1998)
9. Gómez-Segura, J., Veciana, J., Ruiz-Molina, D.: Chem. Comm. 3699 (2007)
10. Waldmann, O.: Inorg. Chem. **46**, 10035 (2007)
11. Cirera, J., Ruiz, E., Alvarez, S., Neese, F., Kortus, J.: Chem. A Eur. J. **15**, 4078 (2009)
12. Glauber, R.J.: J. Math. Phys. **4**, 294 (1963)
13. Brooker, S., Kitchen, J.A.: J. Chem. Soc., Dalton Trans. 7331 (2009)
14. Bogani, L., Vindigni, A., Sessoli, R., Gatteschi, D.: J. Mater. Chem. **18**, 4750 (2008)
15. Lis, T.: Acta Cryst. **36**, 2042 (1980)
16. Caneschi, A., Gatteschi, D., Sessoli, R., Barra, A.L., Brunei, L.C., Guillot, M.: J. Am. Chem. Soc. **113**, 5873 (1991)
17. Hill, S., Perenboom, J.A.A.J., Dalal, N.S., Hathaway, T., Stalcup, T., Brooks, J.S.: Phys. Rev. Lett. **80**, 2453 (1998)
18. Mertes, K.M., Suzuki, Y., Sarachik, M.P., Myasoedov, Y., Shtrikman, H., Zeldov, E., Rumberger, E.M., Hendrickson, D.N., Christou, G.: Solid State Commun. **127**, 131 (2003)
19. Boukhvalov, D.W., Dobrovitski, V.V., Kögerler, P., Al-Saqer, M., Katsnelson, M.I., Lichtenstein, A.I., Harmon, B.N.: Inorg. Chem. **49**, 10902 (2010)
20. Sessoli, R., Gatteschi, D., Tsai, H.L., Hendrickson, D.N., Schake, A.R., Wang, S., Vincent, J.B., Christou, G., Folting, K.: J. Am. Chem. Soc. **115**, 1804 (1993)
21. Salman, Z., Chow, K.H., Miller, R.I., Morello, A., Parolin, T.J., Hossain, M.D., Keeler, T.A., Levy, C.D.P., MacFarlane, W.A., Morris, G.D., Saadaoui, H., Wang, D., Sessoli, R., Condorelli, G.G., Kiefl, R.F.: Nano Lett. **7**, 1551 (2007)
22. Coronado, E., Gatteschi, D.: J. Mater. Chem. **16**, 2513 (2006)
23. Gatteschi, D., Sessoli, R.: Angew. Chem. Int. Ed **42**, 268 (2003)
24. Hendrickson, D.N., Christou, G., Ishimoto, H., Yoo, J., Brechin, E.K., Yamaguchi, A., Rumberger, E.M., Aubin, S.M.J., Sun, Z., Aromí, G.: Polyhedron, pp. 1479–1488 (2001)
25. Nicholson, M.M.: Phthalocyanines Properties and Applications. Wiley-VCH Verlag, New York (1993)
26. Petit, P., André, J.-J.: Le J. Phys. Colloq. **49**, C8 (1988)
27. Shirk, J.S., Lindle, J.R., Bartoli, F.J., Boyle, M.E., Shirk, J.S., Lindle, J.R., Bartoli, F.J., Boyle, M.E.: J. Phys. Chem. **96**, 5847 (1992)
28. Ishikawa, N., Sugita, M., Ishikawa, T., Koshihara, S.Y., Kaizu, Y.: J. Am. Chem. Soc. **125**, 8694 (2003)
29. Ishikawa, N., Sugita, M., Okubo, T., Tanaka, N., Iino, T., Kaizu, Y.: Inorg. Chem. **42**, 2440 (2003)
30. Ishikawa, N., Sugita, M., Ishikawa, T., Koshihara, S.Y., Kaizu, Y.: J. Phys. Chem. B **108**, 11265 (2004)
31. Takamatsu, S., Ishikawa, T., Koshihara, S.Y., Ishikawa, N.: Inorg. Chem. **46**(7250), 42 (2007)
32. AlDamen, M.A., Clemente-Juan, J.M., Coronado, E., Martí-Gastaldo, C., Gaita-Ariño, A.: J. Am. Chem. Soc. **130**, 8874 (2008)
33. AlDamen, M.A., Cardona-Serra, S., Clemente-Juan, J.M., Coronado, E., Gaita-Ariño, A., Martí-Gastaldo, C., Luis, F., Montero, O.: Inorg. Chem. **48**, 3467 (2009)

34. Rinehart, J.D., Long, J.R.: Chem. Sci. **2**, 2078 (2011)
35. Liu, J.L., Chen, Y.C., Tong, M.L.: Chem. Soc. Rev. **47**, 2431 (2018)
36. Caneschi, A., Gatteschi, D., Lalioti, N., Sangregorio, C., Sessoli, R., Venturi, G., Vindigni, A., Rettori, A., Pini, M.G., Novak, M.A., Gatteschi, D., Caneschi, A., Lalioti, N., Sangregorio, C., Sessoli, R., Venturi, G., Vindigni, A., Rettori, A., Pini, M.G., Novak, M.A.: Angew. Chem. Int. Ed. Engl **40**, 1085 (2001)
37. Caneschi, A., Gatteschi, D., Lalioti, N., Sessoli, R., Sorace, L., Tangoulis, V., Vindigni, A.: Chem. A Eur. J. **8**, 286 (2002)
38. Caneschi, A., Gatteschi, D., Lalioti, N., Sangregorio, C., Sessoli, R., Venturi, G., Vindigni, A., Rettori, A., Pini, M.G., Novak, M.A.: Eur. Lett **58**, 771 (2002)
39. Gibney, B.R., Kessissoglou, D.P., Kampf, J.W., Pecoraro, V.L.: Inorg. Chem. **33**, 4840 (1994)
40. Mezei, G., Zaleski, C.M., Pecoraro, V.L.: Chem. Rev. **107**, 4933 (2007)
41. Chow, C.Y., Trivedi, E.R., Pecoraro, V.L., Zaleski, C.M.: Comments Inorg. Chem. **35**, 214 (2015)
42. Hulsbergen, F.B., ten Hoedt, R.W.M., Verschoor, G.C., Reedijk, J., Spek, A.L.: J. Chem. Soc., Dalton Trans. 539 (1983)
43. Bovio, B., Bonati, F., Banditelli, G.: Inorganica Chim. Acta **87**, 25 (1984)
44. Raptis, R.G., Fackler, J.P., Raptis, R.G., Fackler, J.P.: Inorg. Chem. **27**, 4179 (1988)
45. Stemmler, A.J., Kampf, J.W., Pecoraro, V.L.: Inorg. Chem. **34**, 2271 (1995)
46. Lah, M.S., Pecoraro, V.L.: J. Am. Chem. Soc. **111**, 7258 (1989)
47. Cutland, A.D., Malkani, R.G., Kampf, J.W., Pecoraro, V.L.: Angew. Chem. Int. Ed. **39**, 2689 (2000)
48. Cutland-Van Noord, A.D., Kampf, J.W., Pecoraro, V.L.: Angew. Chem. Int. Ed **41**, 4668 (2002)
49. Stemmler, A.J., Kampf, J.W., Kirk, M.L., Atasi, B.H., Pecoraro, V.L.: Inorg. Chem. **38**, 2807 (1999)
50. Lah, M.S., Kirk, M.L., Hatfield, W., Pecoraro, V.L.: J. Chem. Soc. Chem. Commun. 1606 (1989)
51. Boron, III, T.T., Kampf, J.W., Pecoraro, V.L.: Inorg. Chem. **49**, 9104 (2010)
52. Kessisoglou, D.P., Kampf, J., Pecoraro, V.L.: Polyhedron **13**, 1379 (1994)
53. Zaleski, C.M., Depperman, E.C., Kampf, J.W., Kirk, M.L., Pecoraro, V.L.: Angew. Chem., Int. Ed. **43**, 3911 (2004)
54. Zaleski, C.M., Kampf, J.W., Mallah, T., Kirk, M.L., Pecoraro, V.L.: Inorg. Chem. **46**, 1954 (2007)
55. Zaleski, C.M., Tricard, S., Depperman, E.C., Wernsdorfer, W., Mallah, T., Kirk, M.L., Pecoraro, V.L.: Inorg. Chem. **50**, 11348 (2011)
56. Cao, F., Wang, S., Li, D., Zeng, S., Niu, M., Song, Y., Dou, J.: Inorg. Chem. **52**, 10747 (2013)
57. Azar, M.R., Boron, III, T.T., Lutter, J.C., Daly, C.I, Zegalia, K.A., Nimthong, R., Ferrence, G.M, Zeller, M., Kampf, J.W., Pecoraro, V.L., Zaleski, C.M.: Inorg. Chem. **53**, 1729 (2014)
58. Cao, F., Wei, R.-M., Li, J., Yang, L., Han, Y., Song, Y., Dou, J.-M.: Inorg. Chem. **55**, 5914 (2016)
59. Boron, III, T.T., Lutter, J.C., Daly, C.I., Chow, C.Y., Davis, A.H., Nimthong-Roldán, A., Zeller, M., Kampf, J.W., Zaleski, C.M., Pecoraro, V.L.: Inorg. Chem. **55**, 10597 (2016)
60. Happ, P., Plenk, C., Rentschler, E.: Coord. Chem. Rev. **238**, 289–290 (2015)
61. Li, Q.W., Liu, J.L., Jia, J.H., Chen, Y.C., Liu, J., Wang, L.F., Tong, M.L.: Chem. Comm. **43**(51), 10291 (2015)
62. Lutter, J.C., Eliseeva, S.V., Kampf, J.W., Petoud, S., Pecoraro, V.L.: Chem. Eur. J. **24**, 10773 (2018)
63. Lago, A.B., Pasán, J., Cañadillas-Delgado, L., Fabelo, O., Casado, F.J.M., Julve, M., Lloret, F., Ruiz-Pérez, C.: New J. Chem. **35**, 1817 (2011)
64. Song, Y., Liu, J.C., Liu, Y.J., Zhu, D.R., Zhuang, J.Z., You, X.Z., Zhuang, J.Z., You, X.Z.: Inorganica Chim. Acta **305**, 135 (2000)
65. Legendziewicz, J., Puchalska, M., Ciunik, Z., Wojciechowski, W.: Polyhedron **26**, 1331 (2007)

66. Pavlishchuk, A.V., Kolotilov, S.V., Zeller, M., Thompson, L.K., Fritsky, I.O., Addison, A.W., Hunter, A.D.: Eur. J. Inorg. Chem. **2010**, 4851 (2010)
67. Happ, P., Rentschler, E.: Dalton Trans. **43**, 15308 (2014)
68. Das, L.K., Drew, M.G.B., Diaz, C., Ghosh, A.: Dalton Trans. **43**, 7589 (2014)
69. Gibney, B.R., Wang, H., Kampf, J.W., Pecoraro, V.L.: Inorg. Chem. **35**, 6184 (1996)
70. Meelich, K., Zaleski, C.M., Pecoraro, V.L.: Philos. Trans. R. Soc. B Biol. Sci. **363**, 1271 (2008)
71. Koumousi, E.S., Mukherjee, S., Beavers, C.M., Teat, S.J., Christou, G., Stamatatos, T.C.: Chem. Comm. **47**, 11128 (2011)
72. Travis, J.R., Zeller, M., Zaleski, C.M.: Polyhedron **114**, 29 (2016)
73. Benelli, C., Gatteschi, D.: Chem. Rev. **102**, 2369 (2002)
74. Hewitt, I.J., Tang, J., Madhu, N.T., Anson, C.E., Lan, Y., Luzon, J., Etienne, M., Sessoli, R., Powell, A.K.: Angew. Chem. Int. Ed. **49**, 6352 (2010)
75. Kido, T., Ikuta, Y., Sunatsuki, Y., Ogawa, Y., Matsumoto, N., Re, N.: Inorg. Chem. **42**, 398 (2003)
76. Osa, S., Kido, T., Matsumoto, N., Re, N., Pochaba, A., Mrozinski, J.: J. Am. Chem. Soc. **126**, 420 (2004)
77. Lutter, J.C., Boron, T.T., Chadwick, K.E., Davis, A.H., Kleinhaus, S., Kampf, J.W., Zaleski, C.M., Pecoraro, V.L.: Polyhedron **202**, 115190 (2021)
78. Romero Gómez, J., Ferreiro Garcia, R., De Miguel Catoira, A., Romero Gómez, M.: Renew. Sustain. Energy Rev. **17**, 74 (2013)
79. Sessoli, R.: Angew. Chem. Int. Ed. **51**, 43 (2012)
80. Pecharsky, V.K., Gschneidner, K.A.: Ref. Modul. Mater. Sci. Mater. Eng. Encycl. Condens. Matter Phys. In: Bassani, F., Liedl, G.L., and P. B. T.-E. of C. M. P. Wyder (eds.). Elsevier, Oxford, pp. 236–244 (2005).
81. Mozharivskyj, Y.B.: Ref. Modul. Chem. Mol. Sci. Chem. Eng. Elsevier (2016)
82. Waldmann, O., Ako, A.M., Güdel, H.U., Powell, A.K.: Inorg. Chem. **47**, 3486 (2008)
83. Deb, A., Boron, III, T.T., Itou, M., Sakurai, Y., Mallah, T., Pecoraro, V.L., Penner-Hahn, J.E.: J. Am. Chem. Soc. **136**, 4889 (2014)
84. Chow, C.Y., Bolvin, H., Campbell, V.E., Guillot, R., Kampf, J.W., Wernsdorfer, W., Gendron, F., Autschbach, J., Pecoraro, V.L., Mallah, T.: Chem. Sci. **6**, 4148 (2015)
85. Afrati, T., Dendrinou-Samara, C., Zaleski, C.M., Kampf, J.W., Pecoraro, V.L., Kessissoglou, D.P.: Inorg. Chem. Commun. **8**, 1173 (2005)
86. Jin, L., Yu, H., Wu, S., Xiao, F.: Dalton Trans. 197 (2009)
87. Jankolovits, J., Andolina, C.M., Kampf, J.W., Raymond, K.N., Pecoraro, V.L.: Angew. Chem., Int. Ed. **50**, 9660 (2011)
88. Trivedi, E.R., Eliseeva, S.V., Jankolovits, J., Olmstead, M.M., Petoud, S., Pecoraro, V.L.: J. Am. Chem. Soc. **136**, 1526 (2014)
89. Chow, C.Y., Eliseeva, S.V., Trivedi, E.R., Nguyen, T.N., Kampf, J.W., Petoud, S., Pecoraro, V.L.: J. Am. Chem. Soc. **138**, 5100 (2016)
90. Athanasopoulou, A.A., Carrella, L.M., Rentschler, E.: Dalton Trans. **48**, 4779 (2019)
91. Lou, T., Yang, H., Zeng, S., Li, D., Dou, J.: Crystals **8**, 229 (2018)
92. Bonadies, J.A., Kirk, M.L., Lah, M.S., Kessissoglou, D.P., Hatfield, W.E., Pecoraro, V.L.: Inorg. Chem. **28**, 2037 (1989)
93. Barra, A.L., Gatteschi, D., Sessoli, R., Abbati, G.L., Cornia, A., Fabretti, A.C., Uytterhoeven, M.G.: Angew. Chem., Int. Ed. Engl. **36**, 2329 (1997)
94. Krzystek, J., Ozarowski, A., Telser, J.: Coord. Chem. Rev. **250**, 2308 (2006)
95. Pichon, C., Mialane, P., Rivière, E., Blain, G., Dolbecq, A., Marrot, J., Sécheresse, F., Duboc, C.: Inorg. Chem. **46**, 7710 (2007)
96. Wei, R.-M., Cao, F., Li, J., Yang, L., Han, Y., Zhang, X.-L., Zhang, Z., Wang, X.-Y., Song, Y.: Sci. Rep. **6**, 24372 (2016)
97. Wang, J., Lu, G., Liu, Y., Wu, S.-G., Huang, G.-Z., Liu, J.-L., Tong, M.-L.: Cryst. Growth & Des. **19**, 1896 (2019)

98. Zhu, Y.-Y.Y., Cui, C., Zhang, Y.-Q.Q., Jia, J.-H.H., Guo, X., Gao, C., Qian, K., Da Jiang, S.-D., Wang, B.-W.W., Wang, Z.-M.M., Gao, S.: Chem. Sci. **4**, 1802 (2013)
99. Gomez-Coca, S., Cremades, E., Aliaga-Alcalde, N., Ruiz, E.: J. Am. Chem. Soc. **135**, 7010 (2013)
100. Yang, E.-C., Hendrickson, D.N., Wernsdorfer, W., Nakano, M., Zakharov, L.N., Sommer, R.D., Rheingold, A.L., Ledezma-Gairaud, M., Christou, G.: J. Appl. Phys. **91**, 7382 (2002)
101. Chandrasekhar, V., Dey, A., Mota, A.J., Colacio, E.: Inorg. Chem. **52**, 4554 (2013)
102. Jankolovits, J., Kampf, J.W., Pecoraro, V.L.: Inorg. Chem. **53**, 7534 (2014)
103. Athanasopoulou, A.A., Baldoví, J.J., Carrella, L.M., Rentschler, E.: Dalton Trans. **48**, 15381 (2019)
104. Lah, M.S., Gibney, B.R., Tierney, D.L., Penner-Hahn, J.E., Pemraro, V.L.: The Fused Metallacrown Anion Na2[Na0.5(Salicylhydroximate)4]2(m-OH)4]-Is an Inorganic Analogue of a Cryptate. Springer-Verlag (1993)
105. Marx, R., Moro, F., Dörfel, M., Ungur, L., Waters, M., Jiang, S.D., Orlita, M., Taylor, J., Frey, W., Chibotaru, L.F., van Slageren, J.: Chem. Sci. **5**, 3287 (2014)
106. Baldoví, J.J., Clemente-Juan, J.M., Coronado, E., Duan, Y., Gaita-Ariño, A., Giménez-Saiz, C.: Inorg. Chem. **53**, 9976 (2014)
107. Jiang, X.-F., Chen, M.-G., Tong, J.-P., Shao, F.: New J. Chem. **43**, 8704 (2019)
108. Happ, P., Sapozhnik, A., Klanke, J., Czaja, P., Chernenkaya, A., Medjanik, K., Schuppler, S., Nagel, P., Merz, M., Rentschler, E., Elmers, H.J.: Phys. Rev. B **93** (2016)
109. Rauguth, A., Kredel, A., Carrella, L.M., Rentschler, E.: Inorg. Chem. **60**, 14031 (2021)
110. Zaleski, C.M., Depperman, E.C., Kampf, J.W., Kirk, M.L., Pecoraro, V.L.: Inorg. Chem. **45**, 10022 (2006)
111. Cutland, A.D., Halfen, J.A., Kampf, J.W., Pecoraro, V.L.: J. Am. Chem. Soc. **123**, 6211 (2001)
112. Domingo, N., Gerbier, P., Gómez, J., Ruiz-Molina, D., Amabilino, D.B., Tejada, J., Veciana, J.: Polyhedron **22**, 2355 (2003)
113. Gerbier, P., Domingo, N., Gómez-Segura, J., Ruiz-Molina, D., Amabilino, D.B., Tejada, J., Williamson, B.E., Veciana, J.: J. Mater. Chem. **14**, 2455 (2004)
114. Rikken, G.L.J.A., Raupach, E.: Nature **390**, 493 (1997)
115. Yoo, J., Wernsdorfer, W., Yang, E.-C.C., Nakano, M., Rheingold, A.L., Hendrickson, D.N.: Inorg. Chem. **44**, 3377 (2005)
116. Ostrowska, M., Fritsky, I.O., Gumienna-Kontecka, E., Pavlishchuk, A.V.: Coord. Chem. Rev. **327–328**, 304 (2016)
117. Alhassanat, A., Gamer, C., Rauguth, A., Athanasopoulou, A.A., Sutter, J., Luo, C., Ryll, H., Radu, F., Sapozhnik, A.A., Mashoff, T., Rentschler, E., Elmers, H.J.: Phys. Rev. B **98**, 64428 (2018)
118. Lim, C.S., Jankolovits, J., Zhao, P., Kampf, J.W., Pecoraro, V.L.: Inorg. Chem. **50**(4832), 45 (2011)
119. Grant, J.T., Jankolovits, J., Pecoraro, V.L.: Inorg. Chem. **51**, 8034 (2012)
120. Yang, H., Meng, Y.-X., Tian, H.-Q., Li, D.-C., Zeng, S.-Y., Song, Y., Dou, J.-M.: Dalton Trans. **49**, 1955 (2020)
121. Tegoni, M., Furlotti, M., Tropiano, M., Lim, C.S., Pecoraro, V.L.: Inorg. Chem. **49**, 5190 (2010)
122. Lim, C.S., Tegoni, M., Jakusch, T., Kampf, J.W., Pecoraro, V.L.: Inorg. Chem. **51**, 11533 (2012)
123. Li, Q.W., Wan, R.C., Wang, J., Chen, Y.C., Liu, J.L., Reta, D., Chilton, N.F., Wang, Z.X., Tong, M.L. ArXiv E-Prints arXiv:1804.05818 (2018)
124. Wang, J., Ruan, Z.-Y., Li, Q.-W., Chen, Y.-C., Huang, G.-Z., Liu, J.-L., Reta, D., Chilton, N.F., Wang, Z.-X., Tong, M.-L.: Dalton Trans. **48**, 1686 (2019)
125. Wang, J., Li, Q.-W., Wu, S.-G., Chen, Y.-C., Wan, R.-C., Huang, G.-Z., Liu, Y., Liu, J.-L., Reta, D., Giansiracusa, M.J., Wang, Z.-X., Chilton, N.F., Tong, M.-L.: Angew. Chem. Int. Ed. **60**, 5299 (2021)
126. Zhang, H., Yang, H., Yang, J., Li, D., Dou, J.: Inorganica Chim. Acta **495**, 119014 (2019)
127. Zhang, H.-G., Yang, H., Sun, L., Li, D.-C., Dou, J.-M.: Eur. J. Inorg. Chem. **2019**, 2839 (2019)

128. Pavlishchuk, A.V., Kolotilov, S.V., Zeller, M., Thompson, L.K., Addison, A.W.: Inorg. Chem. **53**, 1320 (2014)
129. Yang, H., Liu, Z., Meng, Y., Zeng, S., Li, Y., Li, D., Dou, J.: J. Mol. Struct. **1221**, 128822 (2020)
130. Herren, F., Fischer, P., Ludi, A., Haelg, W.: Inorg. Chem. **19**, 956 (1980)

Beyond the Metallacrown: Controlling First- and Second-Order Coordination Spheres Towards Discrete and Extended Architectures

Leigh F. Jones

Abstract The global aim of this review chapter is to highlight how synthetic chemists are able to manipulate pre-selected metallacrowns at both their first and second-order coordination spheres towards the production of novel discrete host–guest complexes. We will begin by discussing how the flexible functionality afforded to metallacrowns allows a degree of control with respect to their second-order coordination spheres and strongly encourages complementary interactions with target substrates towards the production of discrete host–guest complexes. We will show how these findings have led to a plethora of interesting new materials with applications in (for example) molecular sensing, molecular magnetism and quantum computing. We will also discuss the strategic first-order coordination sphere modulation of select 12-$MC_{Cu(II)}$-4 metallacrowns towards the construction of pre-determined extended architectures.

1 An Introduction to Discrete Host–guest Assemblies Centred on Metallacrown Host Units

This chapter aims to provide evidence on the importance and versatility of metallacrown complexes as host units in both discrete and more elaborate host–guest architectures. Discussions are centred around four distinct but related areas of work beginning with the role of F^- bridges in metallacrowns (Sect. 6.1) before progressing to the elegant manipulation of trinuclear organometallic 12-$MC_{M(III)}$-3 (M = Ru, Rh, Ir) host metallacrowns and their remarkably selective Na^+, Li^+ and F^- ion sensing in solution (Sect. 6.2). Section 6.3 focuses on the selective sequestration of environmentally relevant anions using host metallacrowns before turning the spotlight onto the strategic replacement of labile ligands to form pre-designed extended network architectures comprising 12-$MC_{Cu(II)}$-4 metallacrown building blocks. We conclude by highlighting (and distinguishing between) the rise of inverse metallacrown and

L. F. Jones (✉)
School of Sciences, University of Wolverhampton, Wolverhampton WV1 1LY, UK
e-mail: Leigh.Jones@wlv.ac.uk

C. M. Zaleski (ed.), *Advances in Metallacrown Chemistry*,
https://doi.org/10.1007/978-3-031-08576-5_6

Inverse Crown Ether (ICE) complexes. We will also discuss the evolution of their anionic siblings, Metal Anionic Crowns (MACs). Upon close inspection of the structures described here, it will become apparent that although traditional metallacrowns comprising –[M–N-O]$_n$– linkages are presented (e.g. the [M(II)$_5$] (M = Cu, Ni) 12-MC$_{Cu(II)}$-4 metallacrowns in Sect. 6.3), the majority of architectures discussed in this chapter are best described as non-archetypal MCs. For instance, the metal centres within the Inverse Crown Ether complexes described in Sect. 6.4 are bridged by just one atom, while the cavitands and homo- and heterometallic wheels described in Sect. 6.1 require a combination of one-atom F-bridges and –[M–N-N]$_n$– (azametallacrowns) or –[M–O–C–O]$_n$—linkages (wheels). In a similar vein, –[Cu–N-N]$_n$ – (aza-MC) pathways are observed within the 18-MC$_{Cu(II)}$-6 (Sect. 6.3.1) and triple-decker inverse 12-MC$_{Cu(I)\text{-}pz}$-4 complexes (Sect. 6.4.1). Likewise, the organometallic 12-MC$_{M(III)}$-3 (M = Ru, Rh, Ir) metallacrown host complexes of Sect. 6.2 each exhibit –[M–N–C–O]$_n$– bridges and therefore also represent non-traditional MC topologies. It should also be noted here that the metallacrowns (and non-archetypal analogues) discussed in this chapter are by no means exhaustive and were selected to represent a wide variety of different species with disparate physical properties. With these thoughts in mind, it would be remiss not to mention the pioneering metal coronate work of Saalfrank and co-workers [1]. Likewise, the solid-state hosting abilities of the family of *pseudo* metallocalix[6]arene [M$_7$] (M = Ni(II) [2a]), Zn(II) [2b] and Co(II/III) [2c] complexes, whose body-centred hexagonal core topologies could easily be described as body-centred metallacrowns, would not look out of place in this work [2].

2 Fluoro-Centred Host Metallacrowns and Their Guest Enticing Abilities

We begin by looking at the vital role μ-F$^-$ ions play as building blocks in metallacrown host units, not only in preserving their structure but in their ability to partake in strong intermolecular interactions with various guest moieties towards producing novel host–guest architectures. Discussions predominantly centre on two disparate families of complexes; hexanuclear [Cu(II)$_6$] azametallacrowns and homo- and heterometallic 'ring'/metallacrown complexes.

2.1 Hexacopper Fluoro Azametallacrown Cavitands as Hosts for Cationic Guests

In 2007, Halcrow and co-workers demonstrated that the reaction of anhydrous CuF_2 and the ligand 3{5}-(pyrid-2-yl)-5{3}-(*tert*-butyl)pyrazole (LH) along with *n*Bu$_4$OH gave rise to the complex [Cu(II)$_6$(μ-F)$_6$(μ-L)$_6$(H$_2$O)$_2$]·8CH$_2$Cl$_2$, whose crystal

structure revealed a planar ring-like $\{Cu(II)_6(\mu\text{-}F)_6\}^{6+}$ core (Fig. 1a) [3]. Each of the distorted square pyramidal Cu(II) centres connect through $\eta^1{:}\eta^1{:}\eta^1\text{-}\mu$ bridging L^- moieties (resulting in $-[Cu–N–N]_n-$ linkages) to give rise to the azametallacrown (or double-bowl) topology observed in $[Cu(II)_6(\mu\text{-}F)_6(\mu\text{-}L)_6(H_2O)_2]\cdot 8CH_2Cl_2$. The inward pointing positioning of the F^- bridging anions along with the absence of a centrally bound guest moiety made this complex an ideal host candidate for various

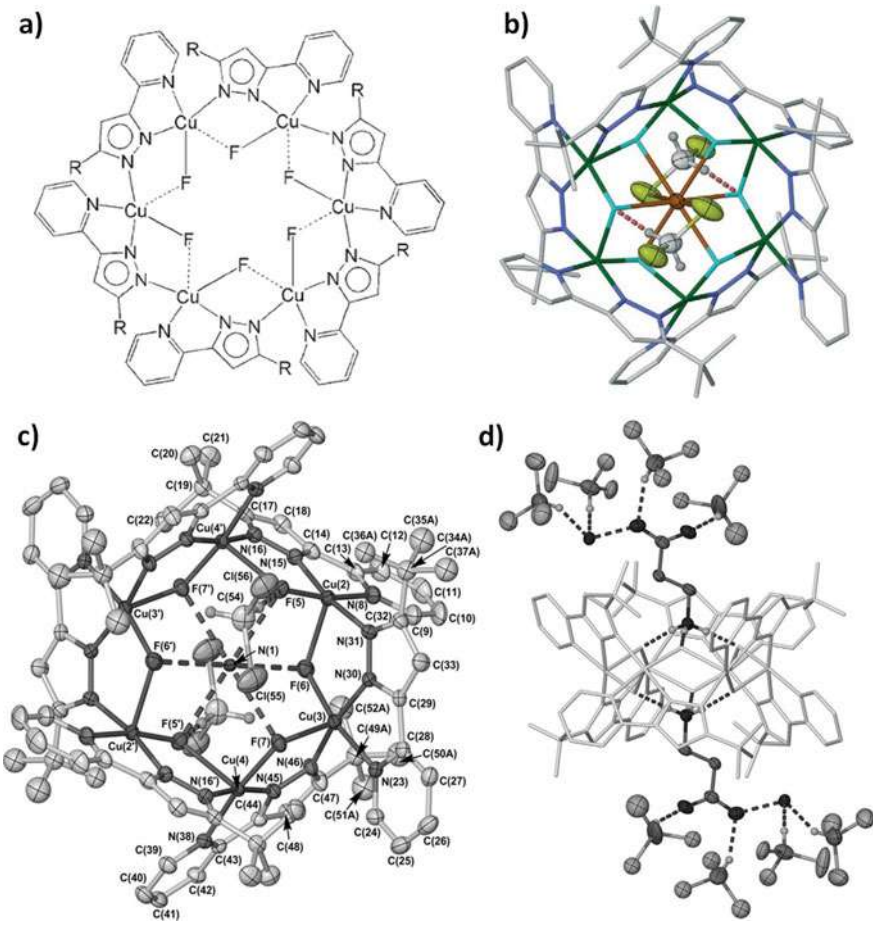

Fig. 1 **a** ChemDraw representation of the $[Cu(II)_6(\mu\text{-}F)_6(\mu\text{-}L)_6]$ azametallacrown (R = tert-butyl). The dashed lines represent the longer apical Cu-F bonds at the metal centres. Crystal structures of the azametallacrown complexes **b** [K ⊂ $Cu(II)_6(\mu\text{-}F)_6(\mu\text{-}L)_6(CH_2Cl_2)_2]F_{0.6}(HF_2)_{0.4}\cdot 3.5CH_2Cl_2$ (Colour code: light blue (Cu), dark blue (N), brown (K), green (Cl) and grey (C)); **c** [(NH_4) ⊂ $Cu(II)_6(\mu\text{-}F)_6(L)_6(CH_2Cl_2)_2]\cdot HF_2\cdot 5.6CH_2Cl_2\cdot 0.4((C_2H_5)_2O)$ and **d** [$(H_3N(CH_2)_6NHCO_2)_2$ ⊂ $Cu(II)_6(\mu\text{-}F)_6(\mu\text{-}L)_6]\cdot 1.6H_2O\cdot 3.8CHCl_3$ (L = *N*-(6-aminohexyl)carbamic acid). Figures **a** and **b** reproduced with permission from [3]. Copyright 2007 John Wiley and Sons. Figures **c** and **d** reproduced with permission from [4]. Copyright 2008 John Wiley and Sons

guest units. To this end, the replacement of base nBu$_4$OH with NaOH and KOH give rise to the azametallacrown cavitands [(Na) ⊂ Cu(II)$_6$(μ-F)$_6$(μ-L)$_6$(CH$_2$Cl$_2$)$_2$]HF$_2$·3.2CH$_2$Cl$_2$·0.66((C$_2$H$_5$)$_2$O) and [(K) ⊂ Cu(II)$_6$(μ-F)$_6$(μ-L)$_6$(CH$_2$Cl$_2$)$_2$]F$_{0.6}$(HF$_2$)$_{0.4}$·3.5CH$_2$Cl$_2$, respectively. In both cases the alkali metal ions lie at the centre of the host molecule and are bound through six Na$^+$/K$^+$···F electrostatic interactions (Fig. 1b). Attempts at the incorporation of Li$^+$ and Cs$^+$ guests were fruitless and highlight that Na$^+$ and K$^+$ ions represent the optimal spatial fit with respect to the [Cu(II)$_6$(μ-F)$_6$(μ-L)$_6$(H$_2$O)$_2$]·8CH$_2$Cl$_2$ host molecule. The double-bowl molecular cavities in all three complexes showed similar dimensions (base × rim × height): 2.1(1) × 5.6(6) × 6.5(2) Å ([Cu(II)$_6$]), 1.9(1) × 5.0(4) × 6.8(2) Å ([(Na) ⊂ Cu(II)$_6$]) and 2.2(1) × 4.7(2) × 6.4(1) Å ([(K) ⊂ Cu(II)$_6$]).

It was predicted that the positioning of the inward facing bridging F$^-$ anions within the host planar molecular wheel was deemed primed to aid the molecular docking of H-donor guest species through H···F interactions. This was proven correct when further investigations into the hosting dexterity of the [Cu(II)$_6$(μ-F)$_6$(L)$_6$(H$_2$O)$_2$]0.8CH$_2$Cl$_2$ azametallacrown revealed an ability to accommodate both NH$_4^+$ (in [(NH$_4$) ⊂ Cu(II)$_6$(μ-F)$_6$(L)$_6$(CH$_2$Cl$_2$)$_2$] ·HF$_2$·5.6CH$_2$Cl$_2$·0.4((C$_2$H$_5$)$_2$O) and MeNH$_3^+$ (in [(CH$_3$NH$_3$)$_2$ ⊂ Cu(II)$_6$(μ-F)$_6$(L)$_6$]Cl$_2$·0.67H$_2$O·3CH$_2$Cl$_2$) along with the zwitterionic forms of the amino acids glycine, L-alanine and β-alanine in the form of the complexes: [(gly)$_2$ ⊂ Cu(II)$_6$(μ-F)$_6$(μ-L)$_6$]·2H$_2$O·6CH$_2$Cl$_2$, [(L-ala)$_2$ ⊂ Cu(II)$_6$(μ-F)$_6$(μ-L)$_6$]·5H$_2$O·3CH$_2$Cl$_2$ and [(β-ala)$_2$ ⊂ Cu(II)$_6$(μ-F)$_6$(μ-L)$_6$]·2H$_2$O·8CHCl$_3$, respectively [4]. Attempts at linking the [Cu(II)$_6$(μ-F)$_6$(μ-L)$_6$] azametallacrown host units through the introduction of 1,6-diaminohexane (towards producing a $^+$NH$_3$(CH$_2$)$_6$NH$_3^+$ dicationic connector unit) gave a surprising result in the form of the complex [(H$_3$N(CH$_2$)$_6$NHCO$_2$)$_2$ ⊂ Cu(II)$_6$(μ-F)$_6$(μ-L)$_6$]·1.6H$_2$O·3.8CHCl$_3$. Here, the *N*-(6-aminohexyl)carbamic acid guest moieties were produced in situ via atmospheric CO$_2$ fixation and observed in their zwitterionic form (Fig. 1d).

Variable temperature magnetic susceptibility measurements on [Cu(II)$_6$(μ-F)$_6$(μ-L)$_6$(H$_2$O)$_2$]·3CH$_2$Cl$_2$, [(Na) ⊂ Cu(II)$_6$(μ-F)$_6$(μ-L)$_6$(CH$_2$Cl$_2$)$_2$]HF$_2$·CH$_2$Cl$_2$ and [(K) ⊂ Cu(II)$_6$(μ-F)$_6$(μ-L)$_6$(CH$_2$Cl$_2$)$_2$]F$_{0.6}$(HF$_2$)$_{0.4}$ each exhibited relatively weak antiferromagnetic exchange between the Cu(II) metal centres and $S = 0$ ground spin states (J-values in the −15.0(1) to −13.5(1) cm^{-1} range). X-band EPR spectra obtained between 115 and 293 K from all siblings were identical (a broad isotropic peak centred at $g = 2.13$) and typical for a magnetically coupled hexametallic copper complex. Moreover, these findings confirmed that guest accommodation has no discernible effect on the magnetic structure of the original [Cu(II)$_6$(μ-F)$_6$(μ-L)$_6$(H$_2$O)$_2$]·8CH$_2$Cl$_2$ host azametallacrown.

2.1.1 Mixed Valence Cobalt Azametallacrown Anion Hosts

Halcrow and co-workers then began investigations into the cobalt coordination chemistry of the ligand 3{5}-(pyrid-2-yl)-5{3}-(*tert*-butyl)pyrazole (LH) and these studies gave rise to a family of mixed valent hexacobalt azametallacrowns of general

formulae $[(X)_2 \prime\ Co(III)_3Co(II)_3(\mu\text{-}OH)_6(\mu\text{-}L)_6](X)$ $\left(X = ClO_4^- \text{ or } CF_3SO_3^-\right)$ and $[(Y)_2 \prime\ Co(III)_2Co(II)_4(\mu\text{-}OH)_6(\mu\text{-}L)_6]\cdot_n H_2O$ $\left(Y = BF_4^-, PF_6^- \text{ or } SbF_6^-;\ n \rangle\ 2\right)$ [5], whose structures bore similarities with the previously reported fluoro azametallacrown cavitands (previous section). For instance, the core in each complex comprised a planar hexagonal array of a combination of distorted octahedral (Co(III)/Co(II)) and distorted tetrahedral (Co(II)) cobalt centres linked by a combination of $\eta^1{:}\eta^1{:}\eta^1$ μ-bridging L^- ligands (to give $-[Co–N–N]_n-$ linkages) and μ-bridging OH^- ions (as opposed to $\mu\text{-}F^-$ anions). Likewise, the pyrazole ligands sit alternately above and below the $\{Co(II/III)_6(\mu\text{-}OH)_6\}^{m+}$ plane to produce the double-bowl aza-12-$MC_{Co(II/III)}$-6 metallacrown topology with dimensions commensurate with their F-bridged hexacopper counterparts (~2.1 (base) × ~5.5 (rim) × ~6.0 Å (height)) (Fig. 2a). The H-acceptor counter anions employed in this work (e.g. ClO_4^- and SbF_6^-) were specifically selected to interact with the $\mu\text{-}OH^-$ ions lying within the anion host azametallacrown and this was proven to be the case, giving hydrogen bond distances commensurate with literature values (e.g. $O–H\cdots O\text{-}ClO_3$ = 1.97–2.08 Å in $[(ClO_4)_2 \prime\ Co(III)_3Co(II)_3(\mu\text{-}OH)_6(\mu\text{-}L)_6](ClO_4)$ and $O–H\cdots F\text{-}SbF_5$ = 1.95 Å in $[(SbF_6)_2 \prime\ Co(III)_2Co(II)_4(\mu\text{-}OH)_6(\mu\text{-}L)_6]\cdot 2H_2O$).

The metal oxidation states in $[Co(III)_3Co(II)_3(\mu\text{-}OH)_6(\mu\text{-}L)_6](X)_3$ $(X = ClO_4^- \text{ or } CF_3SO_3^-)$ and $[Co(III)_2Co(II)_4(\mu\text{-}OH)_6(\mu\text{-}L)_6](Y)_{2n}H_2O$ $(Y = BF_4^-, PF_6^- \text{ or } SbF_6^-;\ n \rangle\ 2)$ were assigned using a combination of Bond Valence Sum (BVS) analyses (giving values of ~2 and ~3–3.5 for the 4- and 6-coordinate cobalt centres, respectively), charge balancing considerations and variable temperature magnetic susceptibility measurements ($\chi_M T$ vs. T; Fig. 2c) (vide infra). From this data, Halcrow and co-workers were able to confirm the presence of weak antiferromagnetic coupling between the four paramagnetic Co(II) centres in the sibling complexes $[Co(III)_2Co(II)_4(\mu\text{-}OH)_6(\mu\text{-}L)_6](Y)_{2n}H_2O$ $(Y = BF_4^-, SbF_6^-;\ n \rangle\ 2)$ and extremely weak/negligible exchange between the paramagnetic Co(II) centres in analogues $[Co(III)_3Co(II)_3(\mu\text{-}OH)_6(\mu\text{-}L)_6](X)_3$ $(X = ClO_4^- \text{ or } CF_3SO_3^-)$; as expected due to their separation induced by the alternating $\{–Co(II)\text{-}Co(III)–\}_3$ array observed in their molecular structure. In all cases, the rapid decline in $\chi_M T$ product at lower temperatures was indicative of zero-field splitting effects as expected when observing high spin Co(II) centres [5].

ESI–MS, NMR and UV/Vis/NIR solution studies on siblings $[(X)_2 \prime\ Co(III)_3Co(II)_3(\mu\text{-}OH)_6(\mu\text{-}L)_6](X)$ $(X = ClO_4^- \text{ or } CF_3SO_3^-)$ registered the sole presence of their cationic $\{Co(III)_3Co(II)_3(\mu\text{-}OH)_6(\mu\text{-}L)_6\}^{3+}$ units but more than one significant component was observed in each $[(Y)_2 \prime\ Co(III)_2Co(II)_4(\mu\text{-}OH)_6(\mu\text{-}L)_6]_nH_2O$ $(Y = BF_4^-; PF_6^-; SbF_6^-;\ n \rangle\ 2)$ solution. Cyclic voltammetry studies were undertaken for all species using MeCN as a solvent and the $[n Bu_4N]BPh_4$ (0.1 M) base electrolyte. An irreversible $\{Co(II/III)_6\}^{3+}/\{Co(II/III)_6\}^{2+}$ reduction was observed at $E_{pc} = -1.09 \pm 0.06$ V (vs. Fc/Fc^+; $\nu = 100\ mVs^{-1}$) for just the $[(X)_2 \prime\ Co(III)_3Co(II)_3(\mu\text{-}OH)_6(\mu\text{-}L)_6](X)$ $(X = ClO_4^- \text{ or } CF_3SO_3^-)$ species, while a second irreversible reduction was observed for all five siblings at $E_{pc} = -1.40 \pm 0.05$ V (Fig. 2d). The $[n Bu_4N]X$ $(X = ClO_4^-; CF_3SO_3^-)$ and $[nBu_4N]Y$ $(Y = BF_4^-; PF_6^-; SbF_6^-)$ base electrolytes were subsequently employed in a secondary CV study of the $[(X)_2 \prime\ Co(III)_3Co(II)_3](X)$ $(X = ClO_4^- \text{ or } CF_3SO_3^-)$ and $[(Y)_2 \prime\ Co(III)_2Co(II)_4$

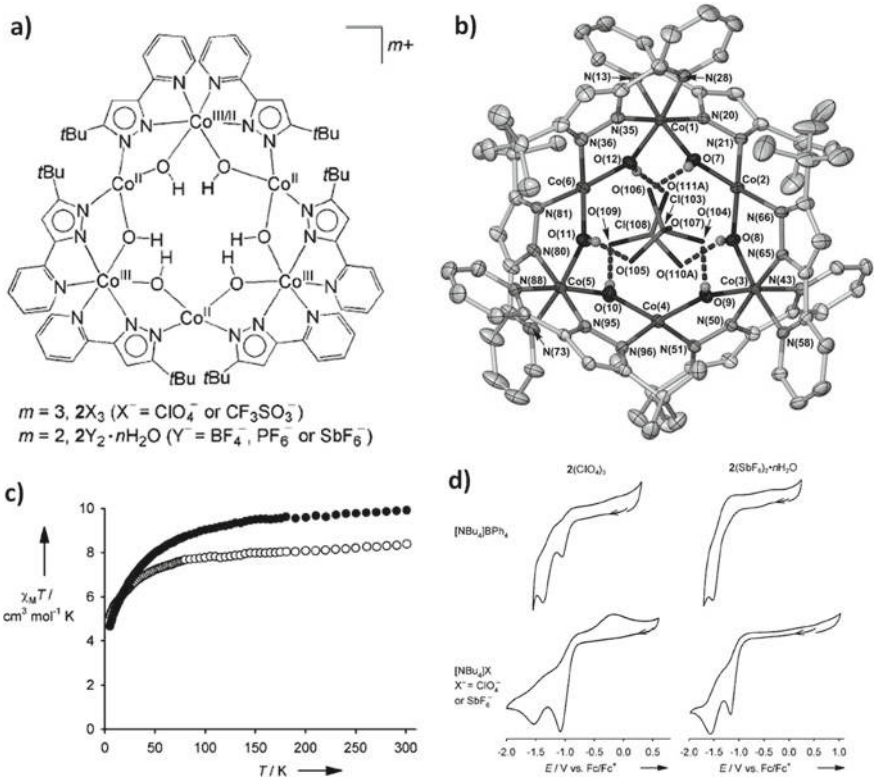

Fig. 2 **a** Schematic of the 12-$MC_{Co(II/III)}$-6 anion host azametallacrown. **b** Crystal structure of the cation $[(ClO_4)_2 \subset Co(III)_3Co(II)_3(\mu\text{-}OH)_6(\mu\text{-}L)_6]^+$. Dashed lines represent H-bonding interactions between the guest ClO_4^- ions and the anionic host (e.g. O8(H8)···O110A = 2.06 Å, O9(H9)···O104 = 2.08 Å and O10(H10)···O109 = 1.97 Å). **c** Plots of variable temperature magnetic susceptibility ($\chi_M T$) studies on azametallacrowns $[(ClO_4)_2 \subset Co(III)_3Co(II)_3(\mu\text{-}OH)_6(\mu\text{-}L)_6](ClO_4)$ (○) and $[(SbF_6)_2 \subset Co(III)_2Co(II)_4(\mu\text{-}OH)_6(\mu\text{-}L)_6]\cdot 2H_2O$ (●). **d** Cyclic voltammograms of the compounds $[(ClO_4)_2 \subset Co(III)_3Co(II)_3(\mu\text{-}OH)_6(\mu\text{-}L)_6](ClO_4)$ and $[(SbF_6)_2 \subset Co(III)_2Co(II)_4(\mu\text{-}OH)_6(\mu\text{-}L)_6]\cdot 2H_2O$ carried out in MeCN solutions at room temperature (0.1 M base electrolyte; $\nu = 100\,mV\,s^{-1}$). Figures reproduced with permission from [5]. Copyright 2009 John Wiley and Sons

$]\cdot_n H_2O$ (Y = BF_4^-, PF_6^-; SbF_6^-; n ⟩ 2) siblings (0.1 M conc. in MeCN). Two irreversible reductions were also observed in these experiments but pertinently, all five siblings exhibited a first reduction at $E_{pc} = -1.13 \pm 0.05$ V and was subsequently attributed to the $[Co(II/III)_6]^{3+}/[Co(II/III)_6]^{2+}$ couple. Although the $[(X)_2 \subset Co(III)_3Co(II)_3](X)$ (X = ClO_4^- or $CF_3SO_3^-$) complexes exhibited a strong $\{Co(III)_3Co(II)_3\}^{3+}/\{Co(III)_3Co(II)_3\}^{2+}$ reduction under both experimental conditions, it became clear that the $[(Y)_2 \subset Co(III)_2Co(II)_4]$ (Y = BF_4^-, SbF_6^-) complexes only exhibited this first reduction process in the presence of excess anion; that is, when the [$n$$Bu_4$N]Y base electrolyte was employed. These findings implied that the $[Co(III)_2Co(II)_4]^{3+}$ species was stabilised by in-cavity anion binding. Halcrow and co-workers further

concluded that there was a clear trend that the more strongly associating anions (ClO_4^- and $CF_3SO_3^-$) give rise to the formation of the $[Co(III)_3Co(II)_3(\mu\text{-}OH)_6(\mu\text{-}L)_6]^{3+}$ azametallacrown unit whereas the less strongly interacting anions (BF_4^-; PF_6^-; SbF_6^-) support $[Co(III)_2Co(II)_4(\mu\text{-}OH)_6(\mu\text{-}L)_6]^{2+}$ assembly. Such observations were supported on the grounds that the coordination of anions within $\{Co(II/III)_6\}^{m+}$ azametallacrown cavities would stabilise the higher + 3 charge (Coulombic considerations).

2.2 *Guest Binding Within F-bridged Octametallic 16-$MC_{Cr(III)}$-8 [Cr_8] Metallacrowns*

The cyclic structure in $[Cr(III)_8(\mu\text{-}F)_8(O_2\text{-}C^tBu)_{16}]$ (Fig. 3a) was formed from the reaction of $CrF_3{\cdot}4H_2O$ and pivalic acid and was first determined, along with a detailed electron density distribution map (EDD), from synchrotron X-ray structure factors collected at 16(5) K [6]. The ring structure was shown to comprise eight Cr(III) metal ions (each of distorted octahedral geometries) connected through a combination of μ-bridging F^- and $^-O_2\text{-}C^tBu$ carboxylate ligands, whose positions alternated above and below the $\{Cr(III)_8\}$ plane to form an 16-$MC_{Cr(III)}$-8 metallacrown topology (see Figs. 3 and 4). Using the previously garnered EDD data, electrostatic potential (EP) distribution calculations on $[Cr(III)_8(\mu\text{-}F)_8(O_2\text{-}C^tBu)_{16}]$ showed that there was

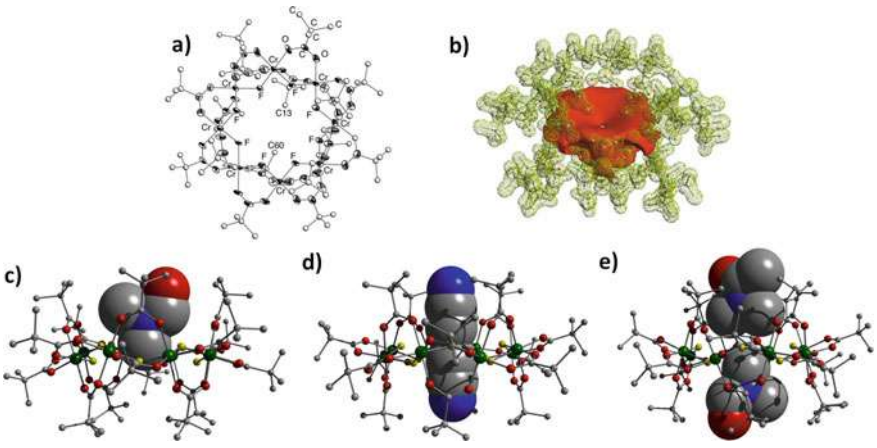

Fig. 3 **a** Crystal structure of the complex $[Cr(III)_8(\mu\text{-}F)_8(O_2\text{-}C^tBu)_{16}]$. **b** Isosurface plot of the electrostatic potential in $[Cr(III)_8(\mu\text{-}F)_8(O_2\text{-}C^tBu)_{16}]$. Surface at -0.54 ea^{-1} (red) and -0.3 ea^{-1} (yellow). Crystal structures of [(DMF)$_2$ $Cr(III)_8(\mu\text{-}F)_8(O_2\text{-}C^tBu)_{16}$] (**c**), [$(MeCN)_2$ $Cr(III)_8(\mu\text{-}F)_8(O_2\text{-}C^tBu)_{16}]{\cdot}$THF (**d**) and [(DMF)(DMA) $Cr(III)_8(\mu\text{-}F)_8(O_2\text{-}C^tBu)_{16}]{\cdot}4t$BuOH (**e**) reproduced by the author. The guest molecules are Space-fill represented. Colour code: green (Cr), blue (N), red (O), yellow (F) and grey (C). Figures reproduced with permission from [6]. Copyright 2002 John Wiley and Sons

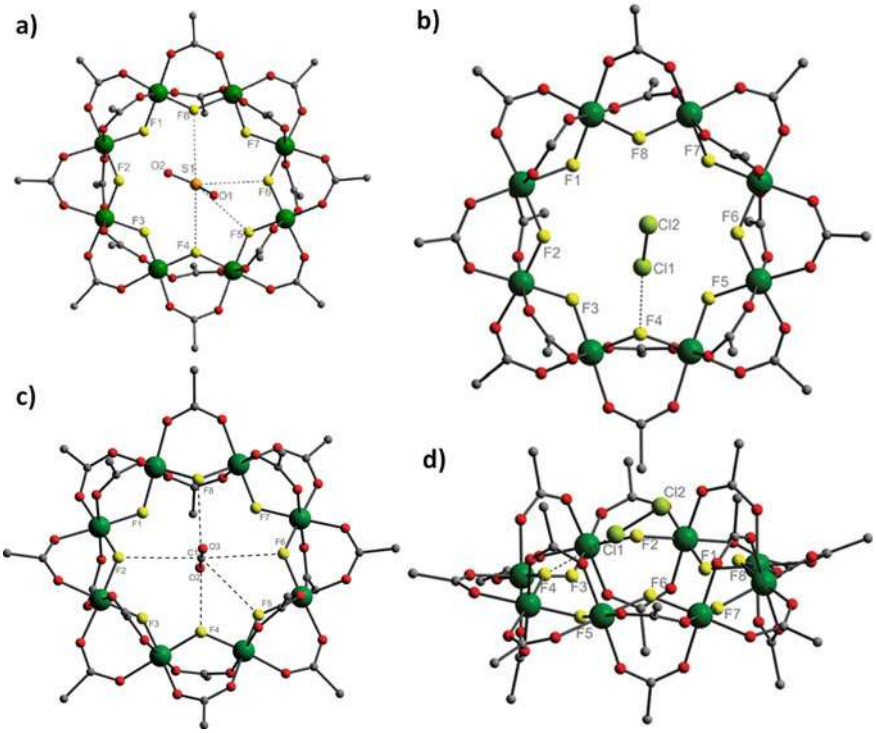

Fig. 4 Crystal structures of the host–guest adducts $[(SO_2)_{0.85} \prime \ [Cr(III)_8(\mu\text{-}F)_8(O_2\text{-}C^tBu)_{16}]$ (**a**), $[(Cl_2) \prime \ [Cr(III)_8(\mu\text{-}F)_8(O_2\text{-}C^tBu)_{16}]$ (**b** and **d**) and $[(CO_2)_{0.79} \prime \ [Cr(III)_8(\mu\text{-}F)_8(O_2\text{-}C^tBu)_{16}]$ (**c**). Colour code: green (Cr), red (O), yellow (F), orange (S), pale green (Cl) and grey (C). Dashed lines represent various host–guest interactions as discussed in the main text. Figure **a** reproduced with permission from [12]. Copyright 2019 Royal Society of Chemistry. Figures **b** and **d** reproduced with permission from [9]. Copyright 2018 Royal Society of Chemistry. Figure **c** reproduced with permission from [7]. Copyright 2017 John Wiley and Sons

a funnel shaped region of negative electrostatic potential as illustrated by the red region in Fig. 3b. The connotations of these findings were discussed in great detail and concluded that accurate predictions could be made with respect to suitable guest candidates for inclusion within the 16-$MC_{Cr(III)}$-8 metallacrown host. To this end it was anticipated that neutral molecules would not bind strongly but an extended linear molecule with a permanent dipole would be stabilised at both ends of the molecule through asymmetric placement within the molecular cavity, where the positive and negatively charged electrostatic regions sit inside and outside the cavity, respectively. Likewise, small positive cations were predicted to be stabilised upon cavity ingression however no such adducts were obtained experimentally.

To probe these forecasts a series of solvent accommodated complexes were synthesised in the form of $[(DMF) \prime \ Cr(III)_8(\mu\text{-}F)_8(O_2\text{-}C^tBu)_{16}]$ (DMF = dimethylformamide), $[(DMA) \prime \ Cr(III)_8(\mu\text{-}F)_8(O_2\text{-}C^tBu)_{16}]$ (DMA = dimethylacetamide;

Fig. 3c), [(DMF)(DMA) ⊂ $Cr(III)_8(\mu\text{-}F)_8(O_2\text{-}C^tBu)_{16}]\cdot 4^tBuOH$ (Fig. 3e) and [$(MeCN)_2$ ⊂ $Cr(III)_8(\mu\text{-}F)_8(O_2\text{-}C^tBu)_{16}]\cdot THF$ (MeCN = acetonitrile; THF = tetrahydrofuran; Fig. 3d). Before we discuss these complexes in detail, we must revisit the crystal structure of the original host. Upon closer inspection of the 16-$MC_{Cr(III)}$-8 metallacrown, Larsen and co-workers found there was effectively an open side of the molecule (with a minimum entry distance of 7.273(4) Å) and a more sterically hindered (closed) side with a minimum entry gap of 4.027(4) Å (measures as the C···C distance of adjacent pivalate methyl carbon atoms). More pertinently and through close inspection of the siblings $[(sol)_xCr(III)_8(\mu\text{-}F)_8(O_2\text{-}C^tBu)_{16}]$ (x = 1–2; sol = DMF, DMA, MeCN), it was found that the more screened side of the molecule could be opened through methyl group rotation to produce a more strained host structure and was proposed to be compensated for via improved host–guest and host-solvent interactions. For instance, it was found that the DMF guest in [(DMF) ⊂ $Cr(III)_8(\mu\text{-}F)_8(O_2\text{-}C^tBu)_{16}$] sat at the open end of the metallacrown with slight changes to the opening diameters (open side = 7.45 Å; closed side = 3.95 Å). Moreover, the DMF was found to be positioned perfectly for stabilisation by the nucleophilic cavity. The larger DMA guest were located further away from the mean $\{Cr(III)_8\}$ plane in [(DMA) ⊂ $Cr(III)_8(\mu\text{-}F)_8(O_2\text{-}C^tBu)_{16}$] when compared to its DMF counterpart, while the presence of the extra methyl group results in a different docked orientation.

Interestingly, the 16-$MC_{Cr(III)}$-8 metallacrown host was found to have significantly distorted in order to accommodate the DMF and DMA guests in [(DMF)(DMA) ⊂ $Cr(III)_8(\mu\text{-}F)_8(O_2\text{-}C^tBu)_{16}]\cdot 4^tBuOH$. Here the DMA and DMF moieties were located at the open and closed sides of the host molecule, respectively. More specifically, the DMA and DMF methyl groups were found to be 2.83 Å and 1.03 Å above and below the $\{Cr(III)_8\}$ plane, respectively (Fig. 3e). The host distortions were manifested by an expanded closed side (shortest C^α-C^α cross-opening distance of 8.907(5) Å; C^α = alpha pivalate C atoms) and a similar opening size for the open side of the molecule (shortest C^α-C^α cross-opening distance = 9.126(5) Å). As shown in Fig. 3d and postulated by Larsen and co-workers, the guest acetonitrile molecules in [$(MeCN)_2$ ⊂ $Cr(III)_8(\mu\text{-}F)_8(O_2\text{-}C^tBu)_{16}]\cdot THF$ entered the cavity from both sides with the positively polarised CH_3– ends of the MeCN guests sitting within the metallacrown cavity at a distance of only 0.56 Å above the $\{Cr(III)_8\}$ plane. The disordered THF solvents of crystallisation were located interstitially.

In a similar vein although over a decade later (2017–2019), the Winpenny group undertook elaborate studies concerning the potential solid-state encapsulation of various neutral guest molecules within the 16-$MC_{Cr(III)}$-8 metallacrown $[Cr(III)_8(\mu\text{-}F)_8(O_2\text{-}C^tBu)_{16}]$. The first example of their success came in the form of the CO_2 absorbed complex [$(CO_2)_{0.79}$ ⊂ $Cr(III)_8(\mu\text{-}F)_8(O_2\text{-}C^tBu)_{16}$], which was produced when crystals of the host species were exposed to CO_2 at 290 K for 2 h [7]. Single-crystal X-ray diffraction studies on the resultant material confirmed successful molecular cavity docking of the guest substrate, albeit situated slightly away from its centre. More specifically, the CO_2 carbon atom sits 1.31 Å above the $\{Cr(III)_8\}$ mean plane and is bound through numerous C···F interactions (see dashed lines in Fig. 4c), all of which are situated on the same side of the ring. DFT studies confirmed the

origin of these interactions to be electrostatic between the μ-F^- anions (partial −ve charge) and the central CO_2 carbon atom (partial +ve charge) and provided C-F interactions commensurate to those obtained via X-ray diffraction studies (3.224–3.352 Å vs. 3.19–3.39 Å, respectively). Thermogravimetric analysis (TGA) on [$(CO_2)_{0.79}$ ⊂ $Cr(III)_8(\mu\text{-}F)_8(O_2\text{-}C^tBu)_{16}$] further confirmed CO_2 absorption by showing a gradual mass loss of 1.96% (in the 52–200 ºC range) consistent with the loss of 1 × CO_2 per [$Cr(III)_8$] metallacrown. Moreover, combined TGA and Differential Scanning Calorimetry (DSC) studies produced a CO_2 binding energy (heat of absorption) value of 45(1) kJ mol^{-1}, a value commensurate to that observed elsewhere and indicative of significant host–guest binding [8]. An absorption isotherm study on [$Cr(III)_8(\mu\text{-}F)_8(O_2\text{-}C^tBu)_{16}$] ($N_2$; 77 K) confirmed this material to be classified as non-porous by exhibiting a saturation capacity of 17 cm^3 g^{-1} at a partial pressure (P/P_0) of 0.9. A comparative adsorption study (1 bar; 288 K) showed that the 16-$MC_{Cr(III)}$-8 metallacrown absorbs 12 times as much CO_2 than N_2. It was also noted that a minimum pressure of 0.04 bar was required to activate CO_2 absorption, as often observed for non-porous materials.

These extremely promising results were rapidly followed up by the successful absorption of the halogens Cl_2, Br_2 and I_2 in the form of the host–guest complexes [(Cl_2) ⊂ $Cr(III)_8(\mu\text{-}F)_8(O_2\text{-}C^tBu)_{16}$], [$(Br_2)$ ⊂ $Cr(III)_8(\mu\text{-}F)_8(O_2\text{-}C^tBu)_{16}$] and [$(I_2)$ ⊂ $Cr(III)_8(\mu\text{-}F)_8(O_2\text{-}C^tBu)_{16}$] (Fig. 4b, d) [9]. Again, these complexes were formed through exposing crystals of the host 16-$MC_{Cr(III)}$-8 metallacrown to the required halogen albeit under different conditions (Cl_2 and Br_2 = 16 h at rt.; I_2 = 1 week at 50 ºC). Single crystal X-ray diffraction studies showed successful (albeit disordered) guest molecular cavity ingression in all three complexes, giving rise to the shortest X···F distances of 2.852(3) Å (X = Cl), 2.78(1) Å (X = Br) and 2.84(1) Å (X = I). The X_2 bond distances when encapsulated were found to be 1.889(5) Å (Cl_2), 2.185(10) Å (Br_2) and 2.576(4) Å (I_2) and were each shorter than X_2 gas phase distances (Cl_2 = 1.99 Å; Br_2 = 2.28 Å and I_2 = 2.67 Å) [10, 11]. Halogen occupation was further evidenced through Raman spectroscopy, giving peaks at 495 cm^{-1} ((Cl_2) ⊂ $Cr(III)_8$) (red-shifted from 540 cm^{-1}), 554 cm^{-1} ((Br_2) ⊂ $Cr(III)_8$) (red-shifted from 611 cm^{-1}) and 212 cm^{-1} ((I_2) ⊂ $Cr(III)_8$) (slight red-shifted from 214.5 cm^{-1}). The red shift was attributed to the donation of electron density from the μ-F^- anions to the halogen when partaking in X···F host–guest interactions. Halide release rates for all three complexes were measured using single crystal X-ray diffraction by measuring guest halogen occupancy changes during heating (350 K) and cooling cycles (collected at 200 K). It was found that the release rate was dominated by the size of the guest molecule ([Cl_2 ⊂ $Cr(III)_8$] > [Br_2 ⊂ $Cr(III)_8$]) > ([I_2 ⊂ $Cr(III)_8$]). That is, the smaller the guest molecule, the faster its release.

By 2019, Vitórica-Yrezábal and co-workers had successfully demonstrated the reversible uptake of SO_2 and H_2S within the host 16-$MC_{Cr(III)}$-8 complex, giving rise to the species [$(SO_2)_{0.85}$ ⊂ $Cr(III)_8(\mu\text{-}F)_8(O_2\text{-}C^tBu)_{16}$] (Fig. 4a) and [$(H_2S)_{0.79}$ ⊂ $Cr(III)_8(\mu\text{-}F)_8(O_2\text{-}C^tBu)_{16}$] [12]. Subsequent heating of these materials brought about guest release with no change in crystallinity (or quality of single crystals), despite the toxic nature of both guest molecules. Akin to the siblings [(X_2) ⊂ $Cr(III)_8(\mu\text{-}F)_8(O_2\text{-}C^tBu)_{16}$] (X = Cl, Br and I), the guest SO_2 and H_2S moieties showed

crystallographic disorder (over three and two sites around the S atom, respectively). In the crystal structure of $[(SO_2)_{0.85} \prime \ Cr(III)_8(\mu\text{-}F)_8(O_2\text{-}C^tBu)_{16}]$ all three different guest SO_2 positions had the S atom lying 1.78 Å above the mean plane of the $[Cr(III)_8]$ metallacrown. The shortest S···F distances were found at distances varying from 3.326(3) to 3.786(4) Å. Likewise, the S···F distances in $[(H_2S)_{0.79} \prime \ Cr(III)_8(\mu\text{-}F)_8(O_2\text{-}C^tBu)_{16}]$ ranged from 3.667(1) to 4.077(2) Å, while the central S atom was located 2.517 Å above the $[Cr(III)_8]$ mean plane. Both sets of S···F distances were found to be longer than the sum of their van der Waals and indicated negligible S···F interactions in both cases. These weak interactions were corroborated when experimental binding energies (using DSC experiments) of 26 kJ mol^{-1} ($[(SO_2) \prime \ Cr(III)_8]$) and 14 kJ mol^{-1} ($[(H_2S) \prime \ Cr(III)_8]$) were obtained.

DFT studies centred on the modelling of both complexes showed excellent agreement with their crystal structure data, including the off-centre positions of both guest molecules with respect to their host cavities (unlike the central position taken up by CO_2 in $[(CO_2)_{0.79} \prime \ Cr(III)_8(\mu\text{-}F)_8(O_2\text{-}C^tBu)_{16}]$) (Fig. 4c). For instance, the displaced SO_2 positions were attributed to an energy penalty that the guest O atom would have to compensate when crossing the partially negative electrostatic potential region at the centre of the 16-$MC_{Cr(III)}$-8 metallacrown, as previously postulated by the Larsen group when discussing guest solvent (DMF, DMA and MeCN) positions within the $[Cr(III)_8(\mu\text{-}F)_8(O_2\text{-}C^tBu)_{16}]$ host [6]. A similar scenario was attributed to the off-set H_2S positions, this time concerning the energy penalty required for the partially negative guest S atom to infiltrate the central metallacrown cavity.

2.3 *Heterometallic [Cr(III)$_7$M(II)] (M = Mn, Fe, Co, Ni, Zn, Cd and Mg) Metallacrowns (and Variations on the Theme)*

The magnetic data obtained from the now well studied $[Cr(III)_8(\mu\text{-}F)_8(O_2\text{-}C^tBu)_{16}]$ metallacrown was indicative of antiferromagnetic exchange between the Cr(III) metal centres and an inevitable $S = 0$ ground spin state. It was proposed by Winpenny and co-workers that the successful replacement of a single Cr(III) metal centre in $[Cr(III)_8(\mu\text{-}F)_8(O_2\text{-}C^tBu)_{16}]$ with a metal ion with a different spin would produce a new ring structure with a non-zero ground state. These aspirations were soon realised when the family of analogues $[R_2NH_2][Cr(III)_7\,M(II)(\mu\text{-}F)_8(O_2\text{-}C^tBu)_{16}]$ (where M = Mn, Fe, Cd; R = Me, Et, *n*Pr, *n*Bu, *n*-octyl) were successfully synthesised using two different synthetic routes [13]. Further investigations rapidly gave rise to a vast family of homo- and heterometallic rings of general formula $[R_2NH_2][Cr_7M(\mu-F)_8(O_2-CR')_{16}]$(M = Mn, Fe, Co, Ni, Zn, Cd, Mg; R = Et, ^{n}Pr and R′ = various (circa 14) carboxylates) along with analogous {V(III)$_7$M(II)} (M = Zn and Ni; R = ^{n}Pr; R′ = ^{t}Bu) and {Fe(III)$_7$M(II)} (M = Mn, Fe, Co, Ni, Zn, Cd; R = Et, ^{n}Pr; R′ = ^{t}Bu, CMe_2Et, CH_2C^tBu) assemblies [14]. As well as allowing charge neutrality, the secondary ammonium counter cations are routinely located within the 16-$MC_{Cr(III)}$-8 metallacrown

and are held in position through multiple hydrogen bonding interactions in conjunction with the inner cavity μ-F^- bridging anions. Interestingly, the heterometallic 16-MC-8 metallacrown $[H_3N^nPr\,/\,Cr(III)_7Co(II)(\mu\text{-}F)_8(O_2\text{-}C^tBu)_{16}]$ was found to selectively extract Cs^+ ions (over Na^+, K^+ and Rb^+ species) from water into an organic dichloromethane layer to give $[Cs\,/\,Cr(III)_7Co(II)(\mu\text{-}F)_8(O_2\text{-}C^tBu)_{16}]$ [15].

2.3.1 Linking $[Cr(III)_7Ni(II)]$ Metallacrowns Towards Dimers and Beyond

Building upon their recent findings concerning the facile introduction of guest alkylammonium species within heterometallic host rings, the Winpenny group soon confirmed that the coupling of $[Cr(III)_7M(II)]$ units could be achieved through the utilisation of diamine counter cations. The first successful example required the incorporation of 1,8-diaminooctane ($1,8\text{-daoH}_2$) into the structure of $[1,8\text{-daoH}_2][Cr(III)_7Ni(II)(\mu\text{-}F)_8(O_2\text{-}C^tBu)_{16}]_2$ (Fig. 5a). Since this breakthrough more elaborate ways of coupling have been successfully

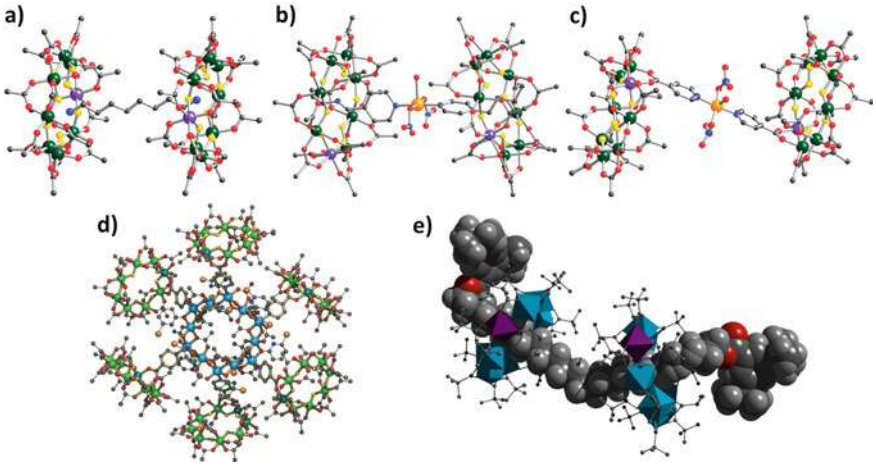

Fig. 5 Crystal structures of the linked 16-MC-8 homo- and heterometallic metallacrowns **a** $[1,8\text{-daoH}_2][Cr(III)_7Ni(II)(\mu\text{-}F)_8(O_2\text{-}C^tBu)_{16}]_2$, **b** $\{[EtNH_2CH_2py][Cr(III)_7Ni(II)\ (\mu\text{-}F)_8(O_2C^tBu)_{16}]\}_2\ [Cu(II)(NO_3)_2(H_2O)]$ and **c**) $\{[NH_2Pr_2][Cr(III)_7Ni(II)(\mu\text{-}F)_8\ (O_2C^tBu)_{15}\ (Nic)]\}_2\{Cu(II)(NO_3)_2(H_2O)\}]$. **d** The sixty-metal ring of rings complex $[Ni(II)_{12}(chp)_{12}\ (O_2CMe)_{12}(H_2O)_6\ \{[NH_2Pr_2][Cr(III)_7Ni(II)(\mu\text{-}F)_8(O_2C^tBu)_{15}(Nic)]\}_6]$ (chpH = 6-chloro- -hydroxypyridine) comprising two heterometallic ring complexes threaded onto an organic axle. Colour code: green (Cr), purple (Co), lilac (Ni), orange (Cu), red (O), blue (N), yellow (F), brown (Cl), dark grey (C) and light grey (H). Many H-atoms have been omitted for clarity. **e** A [3]-rotaxane comprising a space-fill represented organic thread running through two $[Cr(III)_7Co(II)(\mu\text{-}F)_8(O_2C^tBu)_{16}(H_3O)]$ rings. Colour code: light blue (Cr), purple (Co), red (O), blue (N), yellow (F), dark grey (C) and light grey (H). Figures **a–c** reproduced with permission from [18]. Copyright 2011 John Wiley and Sons. Figure **d** reproduced with permission from [17]. Copyright 2013 John Wiley and Sons. Figure **e** reproduced with permission from [23]. Copyright 2009 Springer Nature

explored by the Winpenny group. For example, using the ammonium cation $EtNH_2CH_2py$ to template $[Cr(III)_7Ni(II)]$ formation also allows the external facing pyridine functional group to connect to mono- (e.g. -{$Cu(II)(NO_3)_2(H_2O)$}-); bi- (e.g. -{$Cu_2(O_2CtBu)_4$}-); tri- (e.g. -{$Fe(III)_2Co(II)(\mu_3\text{-}O)(O_2C^tBu)_6$}-) or hexametallic (e.g. -{$Mn(II)_4Mn(III)_2(\mu_4\text{-}O)_2(O_2C^tBu)_{10}$}-) nodes towards the extended oligomeric complexes {$[EtNH_2CH_2py][Cr(III)_7Ni(II)(\mu\text{-}F)_8(O_2C^tBu)_{16}]$}$_2[Cu(II)(NO_3)_2(H_2O)]$ (Fig. 5b), {$[EtNH_2CH_2py][Cr(III)_7Ni(II)(\mu\text{-}F)_8(O_2C^tBu)_{16}]$}$_2[Cu(II)_2(O_2C^tBu)_4]$, [16], $[Fe(III)_2Co(II)(\mu_3\text{-}O)(O_2C^tBu)_6${$[NH_2Pr_2][Cr(III)_7Ni(II)(\mu\text{-}F)_8(O_2C^tBu)_{15}(O_2C\text{-}C_5H_4N)]$}$_3]$ and [{$Mn(II)_4Mn(III)_2(\mu_4\text{-}O)_2(O_2C^tBu)_{10}$}{$[NH_2Pr_2][Cr(III)_7Ni(II)(\mu\text{-}F)_8(O_2C^tBu)_{15}(O_2CC_5H_4N)]$}$_4$] [17].

A tandem investigation focusing on other ways to link $[Cr(III)_7(M(II)]$ rings found a successful route centred along their connection through their bridging carboxylate ligands located at the periphery of the rings. Indeed this was successful and although forcing conditions were required, the monosubstitution of a pivalate ligand within $[Cr(III)_7Ni(II)(\mu\text{-}F)_8(O_2\text{-}C^tBu)_{16}]$ metallacrowns was indeed realised to give complexes of general formula $\{[NH_2Pr_2][Cr(III)_7Ni(II)(\mu\text{-}F)_8(O_2C^tBu)_{15}(O_2CR)]$. The inert nature of the Cr(III) centres means that this substitution is regioselective and occurs only at the M(II) metal site as required. For instance, substituting with isonicotinic acid (NicH) allows a pyridine functional group to protrude away from the ring while being attached to the mainframe. From here, Winpenny and co-workers were able to employ mono- and bimetallic bridging metal units in the dimerization of the 16-MC-8 metallacrowns. This is exampled in Fig. 5c, with the complex {$[NH_2{}^nPr_2][Cr(III)_7Ni(II)(\mu\text{-}F)_8(O_2C^tBu)_{15}(Nic)]$}$_2${$Cu(II)(NO_3)_2(H_2O)$}] [18]. Using the same general synthon, an even more elaborate aggregation of six $[Cr(III)_7Ni(II)]$ rings connected to a single $[Ni(II)_{12}(chp)_{12}(O_2CMe)_{12}(H_2O)_6(THF)_6]$(chpH=6-chloro-2-hydroxypyridine) wheel to give the ring of rings structure $[Ni\,(II)_{12}(chp)_{12}(O_2CMe)_{12}(H_2O)_6${$[NH_2Pr_2][Cr(III)_7Ni(II)(\mu\text{-}F)_8(O_2C^tBu)_{15}(Nic)]$}$_6$] (Fig. 5d). Here, the six terminal THF molecules were simply substituted by the isonicotinate N-donor atoms of the six $[Cr(III)_7Ni(II)]$ metallacrowns to give the final extended architecture [17].

2.3.2 Heterometallic $[Cr(III)_7Ni(II)]$ Metallacrowns as Qubits Towards Quantum Information Processing (QIP)

While classical computers rely on the manipulation of binary units (bits; where 0 is 'off' and 1 is 'on'), quantum computers require the use of quantum bits (qubits), each representing a superposition of 0 and 1. These qubits can take the form of (for example) electron spin or the polarisation of a photon and when grouped together into more complex arrays (quantum entanglement), these superpositions can be used to solve complex mathematical problems and effectively process information (Quantum Information Processing). With these thoughts in mind, Winpenny and co-workers decided that their $\{Cr(III)_7Ni(II)\}$ ring system was an ideal candidate as a molecular qubit due to its: (1) two-tiered $S = ½$ ground spin state ($m_s = \pm 1/2$), (2) high chemical stability [13] and (3) ability to be chemically integrated into more complex multi-qubit architectures as introduced in Sect. 6.3.1 [18].

Weak magnetic communication between the spins (from each S = ½ {$Cr(III)_7$ Ni(II)} qubit) is a prerequisite for quantum entanglement and thus quantum information processing. Indeed, such inter-ring interactions have been observed experimentally (using elegant EPR measurements) on a number of architectures where the individual {$Cr(III)_7Ni(II)$} qubits are connected through a variety of inorganic and organic moieties including {Cu(II)} (itself a qubit) and {$Cu(II)_2$} units [16], {$Co(II)(terpy)_2$} units [19], boronic acid-capped clathrochelate complexes [20] and divergent diimines (e.g. 4,4′-bipyridine) [21]. Despite initial concerns that coherence times would be reduced due to hyperfine interactions within each {$Cr(III)_7Ni(II)$} qubit, pulsed EPR measurements on $[NH_2{}^nPr_2][Cr(III)_7Ni(II)(\mu\text{-}F)_8(O_2C{}^tBu)_{16}]$ proved these fears unfounded with (for instance) extremely competitive phase-coherence times (T_2) of 0.55 μs (at 1.8 K) and 3.8 μs (at 1.8 K) for its perdeuterated analogue [22]. Indeed, more recent studies on a number of related architectures, each comprising {$Cr(III)_7Ni(II)$} qubit building blocks, have also demonstrated long spin coherence times (e.g. T_m ~ 800 ns in the inorganic–organic hybrid [3]-rotaxane $\{[H_2R][Cr(III)_7Ni(II)(\mu\text{-}F)_8(O_2C{}^tBu)_{16}]_2\}$ (R = Ph-CH_2-CH_2-NH-CH_2-$(C_6H_4)_3$-CH_2-NH-CH_2-CH_2-Ph; see Sect. 6.3.3 below) [20]) and an ability to control and fine tune inter-qubit interactions as required when assembling useful QIP components. Indeed, in 2016 Ferrando-Soria and co-workers successfully integrated {$Cr(III)_7$ Ni(II)} qubits into assemblies deemed suitable for either CNOT or $\sqrt{}$iSWAP quantum logic gates, depending on the choice of linker employed to attach the individual ring moieties [19].

2.3.3 *Threading the Needle: Heterometallic Rings as Components in Rotaxanes and Molecular Shuttles*

In 2009, a fruitful collaboration between the Leigh and Winpenny groups led to a family of elegant organic–inorganic rotaxanes centred around employing organic axles that allow the templation and therefore threading of $[Cr(III)_7Co(II)(\mu\text{-}F)_8(O_2\text{-}C{}^tBu)_{16}]$ and $[Cr(III)_{10}Cu(II)_2(\mu\text{-}F)_8(O_2\text{-}C{}^tBu)_{16}]$ rings to produce the targeted rotaxane superstructures [23]. Each dumbbell shaped organic molecular axle was specifically equipped with bulky end groups to prevent de-threading while the number of inorganic rings incorporated was readily directed by the number of templating dialkylammonium groups integrated into the organic moieties. The result was the impressive generation of a number of rotaxanes comprising varying numbers of axles and threads as depicted by (for instance) the multi-ring (2 × {$Cr(III)_7Co(II)$}) [3]-rotaxane in Fig. 5e, the 1 × ring ({$Cr(III)_7Co(II)_2$}) 1 × axle [2]-rotaxane in Fig. 6a and the double axled multi-ring (2 × {$Cr(III)_{10}Cu(II)_2$}) [4]-rotaxane shown in Fig. 6b. In the solid state, each ring was found to partake in short F· · · H-N interactions (~2.0 Å) with the ammonium functional groups of the molecular axles situated at the centre of their cavities. NMR studies on two members of this family confirmed structural preservation in a number of solution (e.g. $CDCl_3$, $C_2D_2Cl_4$) and rapid ring rotation about their molecular axles. Remarkably, significant chemical shifts (up to 45 ppm) of the organic axle protons were observed and attributed to the paramagnetic

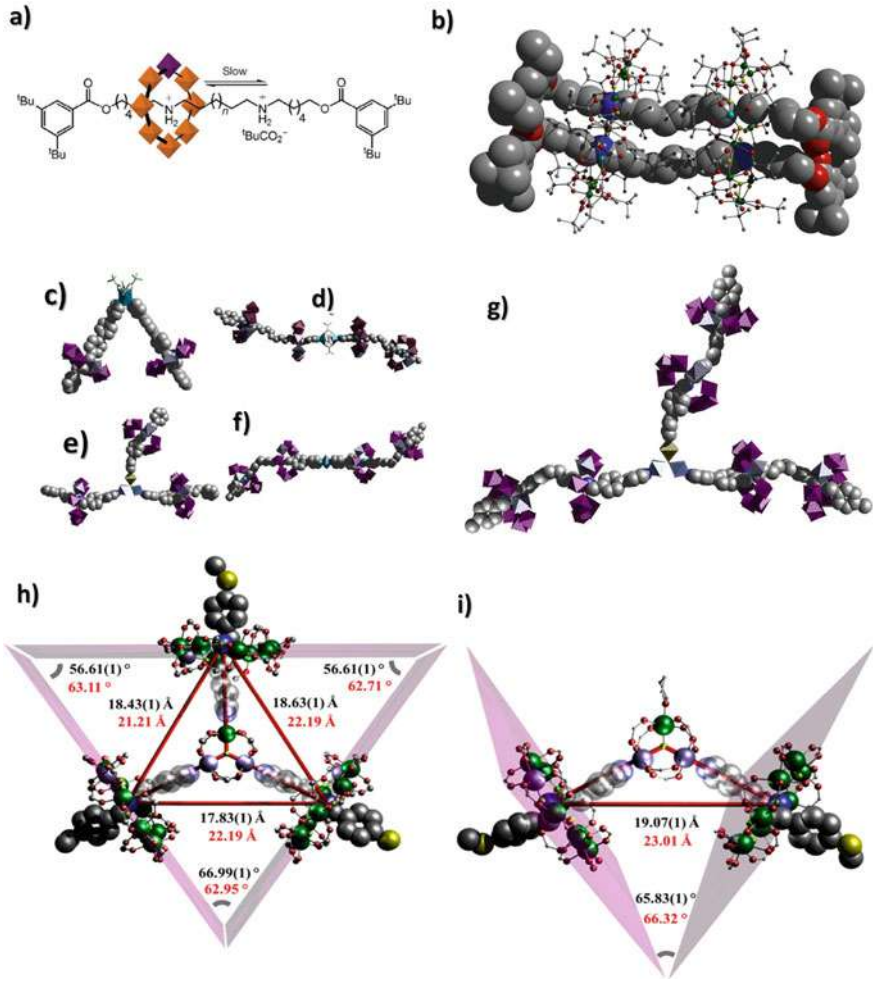

Fig. 6 **a** Schematic of a [2]-rotaxane comprising one organic axle and one {Cr(III)$_7$Co(II)} ring. **b** Crystal structure of a multi-ring double-axle [4]-rotaxane represented in wire-stick ({Cr(III)$_{10}$Cu(II)$_2$} rings) and space-fill mode (organic axles). Crystal structure of the [3]-rotaxane [*cis*-{Cu(II)(hfacac)$_2$}**A**H$_2${Cr(III)$_7$Ni(II)(μ-F)$_8$(O$_2$C*t*Bu)$_{16}$}$_2$] (**c**); the [5]-rotaxanes [{Cu(II)(O$_2$C^{t}Bu)$_2$}**D**H$_2${Cr(III)$_7$Ni(II)(μ-F)$_8$(O$_2$C^{t}Bu)$_{16}$}$_2$]$_2$ (**d**); the [4]-rotaxane [Fe(III)$_2$Co(II)(μ$_3$-O)(O$_2$C^{t}Bu)$_6${BH$_2${Cr(III)$_7$Ni(II)(μ-F)$_8$(O$_2$C^{t}Bu)$_{16}$}$_3$] (**e**) and [{Cu(II)(NO$_3$)$_2$}{**C**H$_2${Cr(III)$_7$Ni(II)(μ-F)$_8$(O$_2$C^{t}Bu)$_{16}$}$_2$}$_2$] (**f**) along with the proposed structure of the [7]-rotaxane [{Fe(III)$_2$Co(II)(μ$_3$-O)(O$_2$C^{t}Bu)$_6$}{**C**H$_2${Cr(III)$_7$Ni(II)(μ-F)$_8$(O$_2$C^{t}Bu)$_{16}$}$_2$}$_3$] (**g**; determined using SAXS). (**h**) Crystal structure of the [4]-rotaxane [Cr(III)Ni(II)$_2$(μ$_3$-F)(O$_2$C^{t}Bu)$_6$]{(**B**H)[Cr(III)$_7$Ni(II)(μ-F)$_8$(O$_2$C^{t}Bu)$_{16}$]}$_3$ and (**i**) the [3]-rotaxane [Cr(III)Ni(II)$_2$(μ$_3$-F)(O$_2$C^{t}Bu)$_6$(THF)]{(**B**H)[Cr(III)$_7$Ni(II)(μ-F)$_8$(O$_2$C^{t}Bu)$_{16}$]}$_2$. Figures **a** and **b** reproduced with permission from [23]. Copyright 2009 Springer Nature. Figures and **c-g** reproduced with permission from [25]. Copyright 2016 Springer Nature. Figures **h** and **i** were reproduced with permission from [24]. Copyright 2010 American Chemical Society

Co(II) ions present within the {Cr(III)$_7$Co(II)} rings. Similarly, NMR studies on the [2]-rotaxane depicted in Fig. 6a, comprising a single heterometallic {Cr(III)$_7$Co(II)} ring threaded onto an axle containing two dialkylammonium binding sites, showed slow back and forth shuttling (between the two binding sites) when compared to the more rapid ring rotation about the thread axle. Subsequent 2-D exchange spectroscopy experiments derived a rate of exchange of 1.2 ± 0.5 s^{-1} (at 330 K in $C_2D_2Cl_4$), corresponding to a shuttling free energy of activation of $\Delta G^{\ddagger} = 19.3 \pm 0.2$ kcal mol^{-1}, a value found to be at least 10 kcal mol^{-1} higher than the free energy activation associated to the spinning of the heterometallic ring about the molecular thread [23]. These observations were attributed to the fact that for these heterometallic rings to simply spin around the axle, they only require the partial breaking of existing NH$\cdots$F hydrogen bonds before forming the next interaction with a neighbouring μ-F^- ion (i.e. moving from a short NH$\cdots$F bond to a longer interaction). However, for the ring to move along the organic axle requires complete disassociation of all ring$\cdots$axle NH$\cdots$F interactions before translation towards the second binding site further along the thread. A natural extension to this work was reported in 2010 when Ballesteros and co-workers successfully threaded new heterometallic [Cr(III)$_7$ M(II)(μ-F)$_8$(O_2-C^{t}Bu)$_{16}$] (M = Mn, Fe, Co, Ni, Cu) rings to produce a library of hybrid organic–inorganic [2]-rotaxanes and pseudo rotaxanes using improved synthetic efficiency [24].

Apart from the elegant synthesis, aesthetic beauty and molecular shuttle behaviour of such hybrid inorganic–organic rotaxanes, it was not lost on Winpenny and co-workers that they have also forged a viable approach towards the controlled self-assembly of multiple qubits in the form of their $S = ½$ {Cr(III)$_7$M(II)} moieties. This was indisputably proven with the design and implementation of new organic axles (e.g. 2-phenyl-*N*-{[4′-(pyridin-4-yl)-(1,1′-biphenyl)-4-yl]methyl}ethanamine (**A**) and 4-phenyl-*N*-(4-(pyridin-4-yl)benzyl)butan-1-amine (**B**)), this time comprising a pyridyl functional group at one end of their structures. This vital addition allowed the association of multiple threaded axles using connecting metal complex nodes as exampled by the three qubit assemblies [*cis*-{Cu(II)(hfacac)$_2$}**A**H$_2${Cr(III)$_7$Ni(II)(μ-F)$_8$(O_2C*t*Bu)$_{16}$}$_2$] (Fig. 6c) and [Fe(III)$_2$Co(II)(μ$_3$-O)(O_2C^{t}Bu)$_6${**B**H$_2${Cr(III)$_7$Ni(II)(μ-F)$_8$(O_2C^{t}Bu)$_{16}$}}$_3$] (Fig. 6e) [25]. Moreover, by employing the elaborate organic threads N^1-(4-(methylthio)benzyl)-N^{12}-(4-(pyridin-4-yl)benzyl)dodecane-1,12-diamine (**C**) and N^1-(4-(methylthio)benzyl)-N^{12}-(pyridin-4-ylmethyl)dodecane-1,12-diamine (**D**), Fernandez and co-workers were able to congregate four and five qubit systems in the form of the [5]-rotaxanes [{Cu(II)(NO$_3$)$_2$}{**C**H$_2${Cr(III)$_7$Ni(II)(μ-F)$_8$(O_2C^{t}Bu)$_{16}$}$_2$}$_2$] (Fig. 6f) and [{Cu(II)(O_2C^{t}Bu)$_2$}**D**H$_2${Cr(III)$_7$Ni(II)(μ-F)$_8$(O_2C^{t}Bu)$_{16}$}$_2$]$_2$ (Fig. 6d). Almost 7 nm in length, both architectures were constructed to comprise four {Cr$_7$(Ni(II)} rings threaded onto an extended axle forged from the connection of two **C**/**D** units using a Cu(II) moiety ({Cu(II)$_2$(O_2C^{t}Bu)$_4$} and {Cu(II)(NO$_3$)$_2$}, respectively). This work reached a crescendo upon the successful combination of seven potential qubits in the form of the [7]-rotaxane [{Fe(III)$_2$Co(II)(μ$_3$-O)(O_2C^{t}Bu)$_6$}{CH$_2${Cr(III)$_7$Ni(II)(μ-F)$_8$(O_2C^{t}Bu)$_{16}$}$_2$}$_3$] (Fig. 6g). Although no crystal structure was obtained, Small-Angle X-ray Scattering (SAXS) was subsequently employed to confirm its

production by producing a model comprising a central triangular {Fe(III)$_2$Co(II)} unit connected at each of the three metal sites by six doubly threaded {Cr(III)$_7$ Ni(II)} rings. Pulsed EPR measurements on these multi-qubit assemblies showed no detrimental effect on the phase memory. Double Electron–Electron Resonance Spectroscopy (DEER) was then employed to successfully demonstrate that the qubit$\cdots$qubit interactions were deemed suitable for the propagation of two-qubit quantum logic gates. More recent investigations by Lockyer and co-workers have shown how a family of [2]-rotaxane {Cr(III)$_7$Ni(II)}-Cu(II) assemblies may be considered candidate elementary units as building blocks towards larger assemblies for quantum information processing [26]. Here, the {Cr(III)$_7$Ni(II)} heterometallic rings would represent a processing unit ($S = ½$) while the Cu(II) units (through their $I = 3/2$ nuclear spin) would embody the quantum memory and introducing quantum error correction; a prerequisite in the operation of a quantum computer.

2020 saw Lockyer and co-workers divulge the successful design and synthesis of even more elaborate rotaxane architectures in the form of the [4]-rotaxane [Cr(III)Ni(II)$_2$(μ_3-F)(O$_2$C^{t}Bu)$_6$]{(**B**H)[Cr(III)$_7$Ni(II)(μ-F)$_8$(O$_2$C^{t}Bu)$_{16}$]}$_3$ and the [3]-rotaxane [Cr(III)Ni(II)$_2$(μ_3-F)(O$_2$C^{t}Bu)$_6$(THF)]{(**B**H)[Cr(III)$_7$Ni(II)(μ-F)$_8$(O$_2$C^{t}Bu)$_{16}$]}$_2$ (where **B** = py-CH$_2$CH$_2$NHCH$_2$C$_6$H$_4$SCH$_3$) (Fig. 6h, i) [27]. The [3]- and [4]-rotaxane assemblies each comprises a central {Cr(III)Ni(II)$_2$(μ_3-F)(O$_2$C^{t}Bu)$_6$} unit connected to three and two [2]-rotaxane [Cr(III)$_7$Ni(II)(μ-F)$_8$(O$_2$C^{t}Bu)$_{16}$] moieties, respectively. Continuous wave Electron Paramagnetic Resonance studies on both assemblies confirmed internal antiferromagnetic coupling and S = ½ ground states for both {Cr(III)Ni(II)$_2$} and {Cr(III)$_7$Ni(II)} components and thus discounted scrambling of the metal ions within both polymetallic units (in each case). A combination of Atomistic Molecular Dynamic Simulations (AMDS), SAXS studies and DEER measurements (the latter revealing {Cr(III)$_7$Ni(II)$\cdots$Cr(III)$_7$ Ni(II)} interactions) were then employed to prove the solution stability of both supramolecular architectures. Both the [3]- and [4]-rotaxanes showed more extended calculated structures and attributed to longer inter-ring distances than observed in the solid state. These observations were found to be more pronounced for the [4]-rotaxane [Cr(III)Ni(II)$_2$(μ_3-F)(O$_2$C^{t}Bu)$_6$]{(BH)[Cr(III)$_7$Ni(II)(μ-F)$_8$(O$_2$C^{t}Bu)$_{16}$]}$_3$.

3 Organometallic 12-MC$_{M(III)}$-3 (M = Ru, Rh, Ir) Metallacrown Hosts

We present in this section a body of work emanating (predominantly) from the Severin group concerning the design and synthesis of a family of 12-MC$_{M(III)}$-3 (M = Ru, Rh, Ir) metallacrown host complexes, whose molecular cavities demonstrate selective accommodation of cations (Na^+/Li^+) and F^- anions in the solid and solution state as evidenced below.

3.1 Redox Responsive 12-$MC_{M(III)}$-3 (M = Ru, Rh) Metallacrown Li^+ and Na^+ Receptors

This work began in 2001 when Piotrowski and co-workers discovered that reaction of $[(cymene)_2Ru(III)_2Cl_4]$, 3-hydroxy-2-pyridone ($C_5H_5NO_2$) and a suitable base ($Cs_2CO_3$ or K_2CO_3) brought about the self-assembly of the trimetallic complex $[(cymene)_3Ru(III)_3(C_5H_3NO_2)_3]$ [28]. The structure comprised a triangular core topology where the distorted tetrahedral $\{(cymene)Ru(III)\}^{2+}$ centres were connected by $\eta^1{:}\eta^1{:}\eta^1$ μ-bridging doubly deprotonated $C_5H_3NO_2{}^{2-}$ ligands to forge a core topology comprising $-[Ru(III)-N-C-O]_n-$ linkages (Fig. 7a). The result was a structure best described as a metallamacrocycle whose O_{phen} donor atoms positioned above the plane of the macrocyclic ring provided the perfect platform for the accommodation of cationic guests. Indeed this was found to be the case when treatment of $[(cymene)_3Ru(III)_3(C_5H_3NO_2)_3]$ with excess LiCl or NaCl (in methanol followed by extraction from $CHCl_3$) produced the 12-$MC_{Ru(III)}$-3 metallacrown complexes $[(MCl) \prime\ (cymene)_3Ru(III)_3(C_5H_3NO_2)_3]$ (M = Li, Na) (Fig. 7b) in quantitative yields. X-ray crystallographic studies on both complexes confirmed the docking of the metal chloride guests at the three juxtaposed O_{phen} donor atoms of the bridging pyridonate ligands, giving Li–O and Na–O bond distances of 1.95 Å and 2.23 Å, respectively along with M-Cl values of 2.42 Å (M = Li) and 2.53 Å (M = Na). Both the $[(LiCl) \prime\ (cymene)_3Ru(III)_3(C_5H_3NO_2)_3]$ and $[(NaCl) \prime\ (cymene)_3Ru(III)_3(C_5H_3NO_2)_3]$ complexes were found to be highly stable in non-polar organic solvents (such as benzene) and this stability was quantified using competition experiments with crown ethers. For instance, it was shown that despite the use of a large excess (tenfold) of 18-crown-6; Na^+ ions preferentially complexed to the 12-$MC_{Ru(III)}$-3 $[(cymene)_3Ru(III)_3(C_5H_3NO_2)_3]$ receptor and indicated a stability over 3 orders of magnitude higher than that of the [Na ⁄ crown-ether] adduct in $CDCl_3$. Likewise, similar results were obtained using 18-crown-6 and 12-crown-4 with each losing out to the 12-$MC_{Ru(III)}$-3 host when competing for Li^+ ions. Similar studies (again in $CDCl_3$) using the 2,2,1- and 2,1,1-cryptands (affinities with Na^+ and Li^+ ions, respectively) indicated dominant $[(LiCl) \prime\ (cymene)_3Ru(III)_3(C_5H_3NO_2)_3]$ and $[(NaCl) \prime\ (cymene)_3Ru(III)_3(C_5H_3NO_2)_3]$ complexation. The Li^+ and Na^+ affinity of the $[(cymene)_3Ru(III)_3(C_5H_3NO_2)_3]$ metallamacrocycle was further evidenced by its ability to successful extract LiCl and NaCl from water (2 M), giving the resultant host–guest complexes in quantitative yield. Furthermore, the ionophore behaviour of the 12-$MC_{Ru(III)}$-3 host complex was observed electrochemically by producing a shift in the peak potential (450 ± 50 mV in anodic direction) upon metal chloride binding thus highlighting potential use as an ion-selective sensor (Fig. 7c).

This work expanded rapidly with the formation of a family of analogous $[(arene)_3M(III)_3(C_5H_3NO_2)_3]$ (M = Ru, Rh; arene = C_6H_6, C_6Me_6, $C_6H_3Et_3$ and Cp*) complexes with structures differing in the type of arene ligand employed and/or metal centre selected. Akin to the solid and solution state behaviour of the original 12-$MC_{Ru(III)}$-3 metallacrown $[(cymene)_3Ru(III)_3(C_5H_3NO_2)_3]$, these trimetallic metallacrown architectures allowed the guest coordination of various metal halides

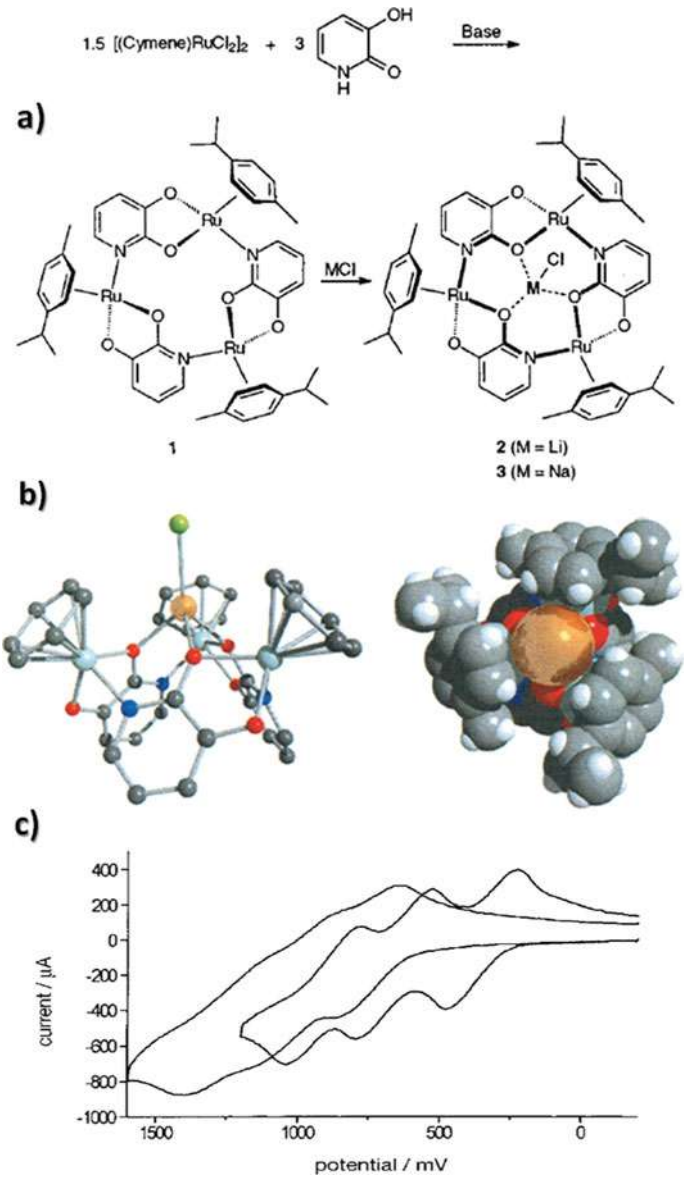

Fig. 7 **a** ChemDraw representation of the synthetic route towards the incorporation of MCl (M = Li, Na) within a host 12-$MC_{Ru(III)}$-3 metallacrown. **b** and **c** Two perspectives of the crystal structure of the [(NaCl)$_3$(cymene)$_3$Ru(III)$_3$($C_5H_3NO_2$)$_3$] adduct. Colour code: light blue (Ru), red (O) dark blue (N) and grey (C). Hydrogen atoms omitted for clarity. **d** Cyclic voltammograms (in 1:1 CH_2Cl_2/MeCN) of the 12-$MC_{Ru(III)}$-3 host metallacrown [($C_6H_3Et_3$)$_3$Ru(III)$_3$($C_5H_3NO_2$)$_3$] (Ag/AgCl reference electrode and glassy carbon working electrode; v = 4015 mV sec^{-1}) along with the corresponding Li^+ bound [(LiCl)($C_6H_3Et_3$)$_3$Ru(III)$_3$($C_5H_3NO_2$)$_3$] adduct. A significant shift of the first peak potential was observed upon Li^+ binding. Figures **a** and **b** were reproduced with permission from (2001) [28]. Copyright 2001 American Chemical Society. Figure **c** reproduced with permission from [29]. Copyright 2001 John Wiley and Sons

(e.g. [(MX) ⊂ $(C_6H_6)_3Ru(III)_3(C_5H_3NO_2)_3$] (MX = LiCl, NaCl, NaBr and NaI and [(LiCl) ⊂ $(Cp^*)_3Rh(III)_3(C_5H_3NO_2)_3$], amongst others) and exhibited solution state affinities for Li^+ and/or Na^+ ions that were in-line with those of cryptands. Such binding affinities were again assessed using competition and extraction experiments along with cyclic voltammetry and (rather neatly) differentiated using colourimetric studies [29].

3.2 The Accommodation of F-containing Guests Within 12-$MC_{M(III)}$-3 (M = Ru, Rh, Ir) Metallacrowns

The Severin groups expanded their investigations into the binding abilities of their 12-$MC_{M(III)}$-3 (M = Ru(III), Rh(III)) metallacrown host units by successfully synthesising the Ir(III) analogue [$(Cp^*)_3Ir(III)_3(C_5H_3NO_2)_3$] [30]. It became apparent that unlike the Rh(III) analogue, the Li^+ complexation reaction was slow (over 1 h to form [(LiCl) ⊂ $(Cp^*)_3Ir(III)_3(C_5H_3NO_2)_3$] with a pseudo first-order rate constant of $k = 5.8 \times 10^{-4}$ s^{-1}) when compared to the rather rapid (<8 min) formation of [(LiCl) ⊂ $(Cp^*)_3Rh(III)_3(C_5H_3NO_2)_3$]. It was therefore proposed that [$(Cp^*)_3Ir(III)_3(C_5H_3NO_2)_3$] may be employed as a F^- sensor. To this end, the guest encapsulation of LiF in the form of [(LiF) ⊂ $(Cp^*)_3Ir(III)_3(C_5H_3NO_2)_3$] was successfully executed via anion exchange of [(LiCl) ⊂ $(Cp^*)_3Ir(III)_3(C_5H_3NO_2)_3$] and KF (Fig. 8a, b). Representing the first structurally characterised complexation of molecular LiF, the

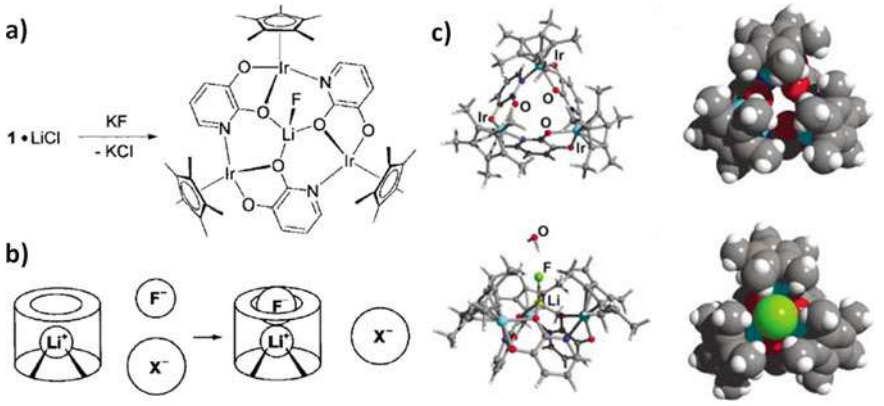

Fig. 8 **a** Schematic description of the anion exchange route towards the target [(LiF) ⊂ $(Cp^*)_3Ir(III)_3(C_5H_3NO_2)_3$] 12-$MC_{Ir(III)}$-3 metallacrown. **b** Schematic representation of a typical F^- ion receptor with a Li^+ ion binding site. **c** Various viewing angles of the crystal structure and associated space-fill representations of host complex [$(Cp^*)_3Ir(III)_3(C_5H_3NO_2)_3$] (top) and the host–guest complex [(LiF) ⊂ $(Cp^*)_3Ir(III)_3(C_5H_3NO_2)_3$] (bottom). Colour codes: light blue (Ir), red (O), dark blue (N), green (F), Grey (C), white (H). Figures reproduced with permission from [30]. Copyright 2002 John Wiley and Sons

Li-F unit is bound within the cavity using three O_{phen} donor atoms sitting above the plane of the macrocyclic ring and provide the perfect platform for the accommodation of the Li^+ centre to give Li–O distances of 1.97–2.02 Å and a Li-F distance of 1.76 Å. The resultant F^- position at the cavity opening allows the occurrence of four short C-$H_{arene}\cdots$F contacts (range = 2.15–2.28 Å) that no doubt enhance the stability of the resultant host–guest adduct (Fig. 8c). In order to establish whether a Li^+ bound 12-$MC_{Ir(III)}$-3 metallacrown would be a F^- sensor candidate, the complex $[(LiBF_4)\subset(Cp^*)_3Ir(III)_3(C_5H_3NO_2)_3]$ was successfully synthesised towards subsequent receptor experiments (replacing loosely bound BF_4^- with F^- ions). Indeed, ^{1}H NMR studies on this complex showed that the BF_4^- ion was not Li^+ coordinated in solution and thus the more likely $[(Li^+)\subset(Cp^*)_3Ir(III)_3(C_5H_3NO_2)_3(solv)_x]BF_4$ species was proposed in solution (solvent = $CDCl_3/CD_3CN$). These observations allowed the authors to test F^- receptor selectivity through competition experiments with $[(LiBF_4)\subset(Cp^*)_3Ir(III)_3(C_5H_3NO_2)_3]$, NBu_4X ($X = Cl^-, Br^-, I^-, NO_3^-$) and $NBu_4F{\cdot}3H_2O$ in a ratio of 1:100:2. Despite the large excess of X^- in solution, ^{1}H and ^{7}Li NMR studies indicated exclusive formation of $[(LiF)\subset(Cp^*)_3Ir(III)_3(C_5H_3NO_2)_3]$ in all cases (with selectivity $>1.6 \times 10^3$).

Differential pulse voltammetry studies on a solution comprising $[(LiBF_4)\subset(Cp^*)_3Ir(III)_3(C_5H_3NO_2)_3]$ gave rise to a first oxidation peak potential of 890 (±3) mV (against Ag/AgCl in 0.1 M $^tBu_4NBF_4$). The introduction of a five-fold excess of NBu_4F brought about a marked difference in the first oxidation peak potentials of $\Delta E = -203$ mV (in $CHCl_3$:CH_3CN (2:1)) and $\Delta E = -191$ mV (in $CHCl_3$:CH_3CN:CH_3OH (4:2:1)). Identical experiments using an excess of NBu_4X ($X = F^-$, Cl^-, Br^-, NO_3^-, HSO_4^- and ClO_4^-) showed no significant differences in the resultant peak potentials, thus demonstrating a viable signal output for F^- binding and a fluoride sensor compatible with protic solvents. Lehaire and co-workers then went on to further demonstrate the facile incorporation of both molecular LiF and LiFHF within the host–guest complexes $[(LiF)\subset(cymene)_3Ru(III)_3(C_5H_3NO_2)_3]{\cdot}H_2O$ (**a**), $[(LiFHF)\subset(cymene)_3Ru(III)_3(C_5H_3NO_2)_3]$ (**b**), $[(LiF)\subset(Cp^*)_3Rh(III)_3(C_5H_3NO_2)_3]$ H_2O (**c**) and $[(LiFHF)\subset(Cp^*)_3Ir(III)_3(C_5H_3NO_2)_3]$ (Fig. 9) [31]. Once again, these target complexes required in-situ production through the initial isolation of the precursors $[(LiBF_4)\subset(cymene)_3Ru(III)_3(C_5H_3NO_2)_3]$ and $[(LiBF_4)\subset(Cp^*)_3M(III)_3(C_5H_3NO_2)_3]$ (M = Rh, Ir) followed by F^-/FHF^- anion exchange (using KF and $[Et_4N]FHF$, respectively). As observed in the previously discussed 12-$MC_{Ir(III)}$-3 metallacrown, the location of the O_{phen} macrocyclic ring donor atoms within this family were show to form adept docking station for the guest $LiBF_4$, LiF and LiFHF molecules.

Following on from these successes, the Severin group then focused their attentions on the successful stabilisation and subsequent solid state incorporation of the poorly soluble Na_2SiF_6 to give the $[(Na_2SiF_6)\subset\{(cymene)_3Ru(III)_3(C_5H_3NO_2)_3\}_2]$ complex (Fig. 10b) [32]. The low solubility of Na_2SiF_6 necessitated the initial isolation of the complex $[(NaBF_4)\subset(cymene)_3Ru(III)_3(C_5H_3NO_2)_3]$ (Fig. 10a) followed by replacement of the weakly bound BF_4^- anions with SiF_6^{2-} (using $(Et_4N)_2SiF_6$) through a salt metathesis reaction. The complex $[(Na_2SiF_6)\subset\{(cymene)_3Ru(III)_3$

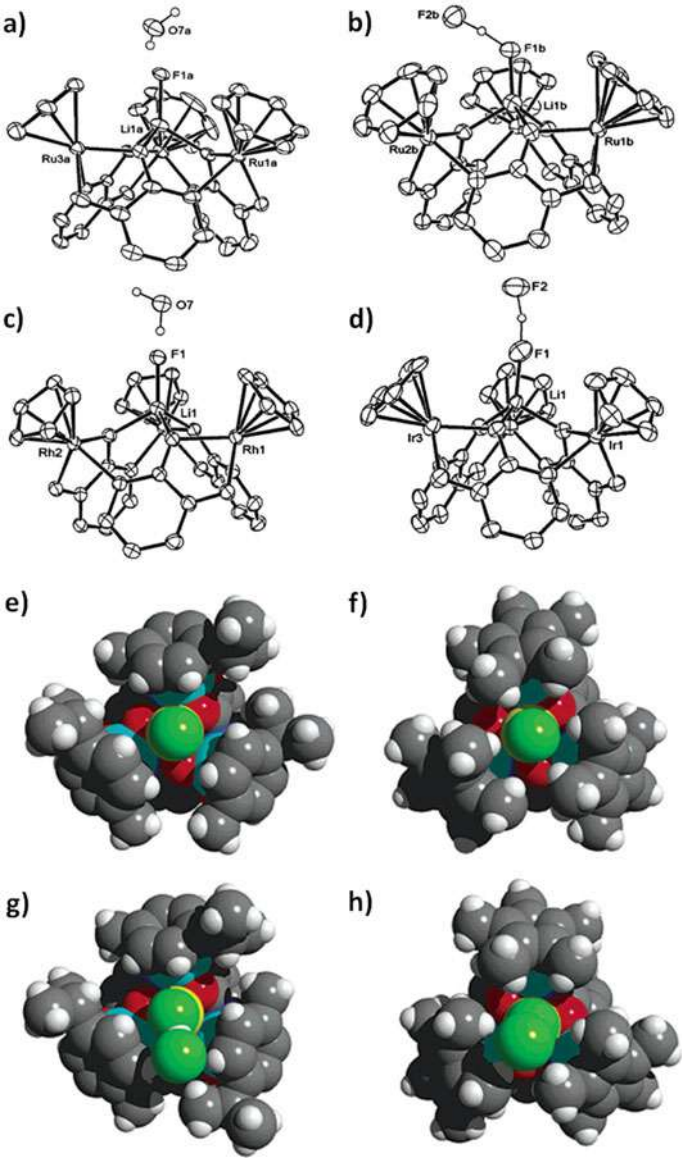

Fig. 9 Crystal structures of the 12-$MC_{M(III)}$-3 (M = Rh(III) and Ir(III)) metallacrowns [(LiF) ′ (cymene)$_3$Ru(III)$_3$($C_5H_3NO_2$)$_3$]·H_2O (**a**), [(LiFHF) ′ (cymene)$_3$Ru(III)$_3$($C_5H_3NO_2$)$_3$] (**b**), [(LiF) ′ (Cp*)$_3$Rh(III)$_3$($C_5H_3NO_2$)$_3$]·H_2O (**c**) and [(LiFHF) ′ (Cp*)$_3$Ir(III)$_3$($C_5H_3NO_2$)$_3$] (**d**) along with their corresponding space-fill representations (**e**–**h**, respectively). Colour codes: light blue (Ir), red (O), dark blue (N), green (F), grey (C), white (H). Figures reproduced with permission from [31]. Copyright 2002 American Chemical Society

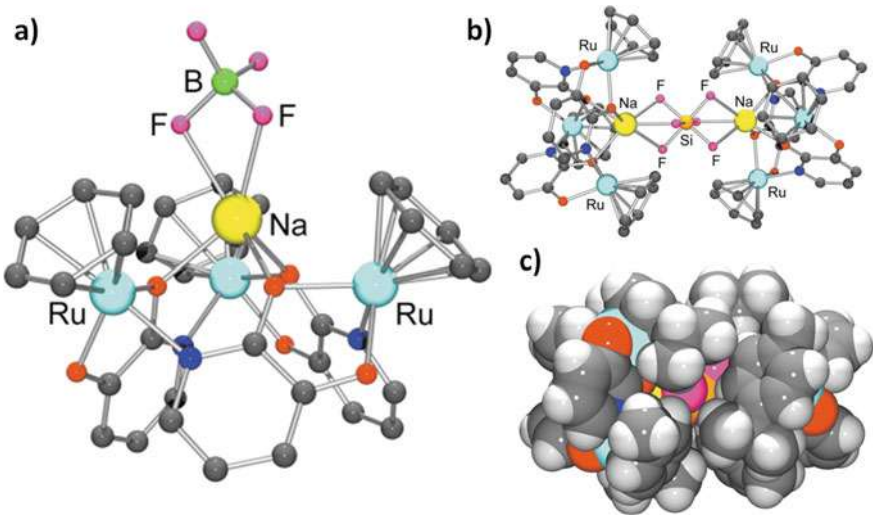

Fig. 10 Molecular structures of $[(NaBF_4)\prime\ (cymene)_3Ru(III)_3(C_5H_3NO_2)_3]$ (**a**) and $[(Na_2SiF_6)\prime\ \{(cymene)_3Ru(III)_3(C_5H_3NO_2)_3\}_2]$ (**b**). **c** Space-fill representation of the complex $[(Na_2SiF_6)\prime\ \{(cymene)_3Ru(III)_3(C_5H_3NO_2)_3\}_2]$. Hydrogen atoms and arene ligand side-chains were omitted for clarity in Figure **a**. Colour codes: light blue (Ru), red (O), dark blue (N), green (B), yellow (Na), pink (F) grey (C), white (H). Figures reproduced with permission from [32]. Copyright 2002 Royal Society of Chemistry

$(C_5H_3NO_2)_3\}_2]$ was characterised using a combination of NMR studies (^{19}F, ^{13}C, ^{1}H) and single-crystal X-ray diffraction.

The Severin group then went on to fine tune structural aspects of their trinuclear $[M(III)_3]$ (M = Ru, Rh, Ir) 12-$MC_{M(III)}$-3 host complexes. More specifically and in order to improve solubility of the target metallacrowns, a piperidino group was attached to the original trimetallic metallacrown forming ligand (3-hydroxy-2-pyridone) to give the new ligand 3-hydoxy-4-piperidino-methyl-2-(1*H*)-pyridone (LH_2) (Fig. 11a). Indeed, it was subsequently shown that reaction of LH_2 with $[(arene)M(III)Cl_2]_2$ (where arene = C_6H_6, *p*-$MeC_6H_4{}^iPr$, $C_6H_5CO_2Et$ and Cp*) under neutral pH conditions (phosphate buffer employed) produced the novel complexes $[(C_6H_6)_3Ru(III)_3(L)_3]$ (Fig. 11b), $[(p\text{-}MeC_6H_4{}^iPr)_3Ru(III)_3(L)_3]$, $[(C_6H_5CO_2Et)_3Ru(III)_3(L)_3]$ and $[(Cp^*)_3Ir(III)(L)_3]$ in >95% yields [33]. As expected, the introduction of the piperidino group did not impinge on the formation of the target metallamacrocyclic structures (under neutral conditions) and was found to be significant in promoting selective Li^+ complexation in water under the same conditions with respect to siblings $[(C_6H_6)_3Ru(III)_3(L)_3]$, $[(p\text{-}MeC_6H_4{}^iPr)_3Ru(III)_3(L)_3]$ and $[(C_6H_5CO_2Et)_3Ru(III)_3(L)_3]$ (no alkali metal ion complexation was observed for $[(Cp^*)_3Ir(III)(L)_3]$). Although all three complexes showed admirable affinities for Li^+ ions, most impressive was the performance of $[(p\text{-}MeC_6H_4{}^iPr)_3Ru(III)_3(L)_3]$ when it was shown (through ^{1}H NMR studies) to have a Li^+ binding constant 3 orders of magnitude higher than classic crown ethers ($K = 2.3 \times 10^3\ M^{-1}$) and

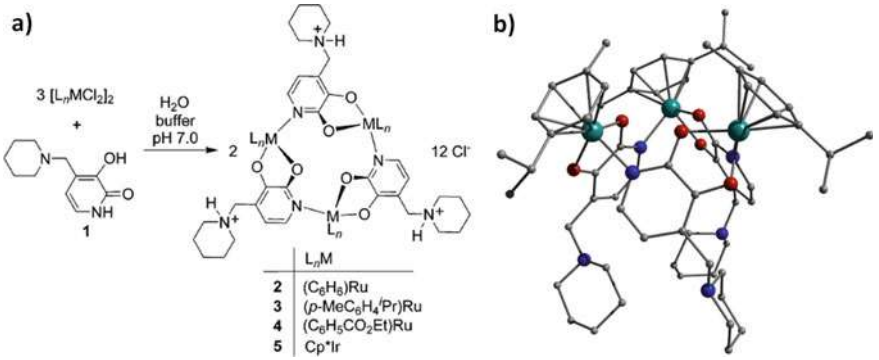

Fig. 11 **a** Schematic description of the general synthetic route employed to form the target 12-$MC_{M(III)}$-3 (M = Ru, Ir) metallacrown host receptors. **b** Crystal structure of the metallacrown [(*p*-MeC6H4^{i}Pr)$_3$Ru(III)$_3$(L)$_3$] (where LH_2 = 3-hydoxy-4-piperidino-methyl-2-(1*H*)-pyridone). Colour code light blue (Ru), red (O), dark blue (N) and grey (C). All hydrogen atoms have been omitted for clarity. Figures reproduced with permission from (2003) [33]. Copyright 2003 American Chemical Society

an extremely competitive Li^+/Na^+ selectivity of 10,000:1, making this complex one of the most selective Li^+ ionophores around. The authors proposed that substrate binding was enhanced via the two-electron donating alkyl side-chains belonging to the arene ligands in [(*p*-$MeC_6H_4{}^{i}Pr)_3Ru(III)_3(L)_3$]. Indeed, subsequent computational studies carried out on the 12-$MC_{Ru(III)}$-3 complex [$(C_6H_6)_3Ru(III)_3(C_5H_3NO_2)_3$] and the original 12-crown-3 (crown ether) found that the O-donor atoms of the 12-MC-3 complex were in possession of a higher negative charge than their crown ether counterparts, thus supporting their proficient cation (Li^+ and Na^+) binding ability. Moreover, analysis of the complex [$(cymene)_3Ru(III)_3(C_5H_2ClNO_2)_3$] (where $C_5H_2ClNO_2$ = 5-chloro-2,3-dihydroxypyridine) showed that the introduction of a chloro electron withdrawing group effectively reduced Li^+ and Na^+ affinity by approximately 2-orders of magnitude [34]. Interestingly, none of the receptors was able to bind K^+ or Cs^+, thus highlighting the how their receptor site cavities are ideal in terms of size and shape for Li^+ and to a lesser extent, Na^+ ions.

3.3 Selective Li^+ Ion Detection in Water and Serum

Following on from these successes, it was decided that the incorporation of fluorescent dihydroxypyridine ligands within such trimetallic 12-$MC_{M(III)}$-3 hosts would allow an alternative physical 'handle' towards producing a fluorescent Li^+ chemosensor. To this end, Rochat and co-workers, using extensive synthetic efforts (6 steps in total), successfully integrated pyrene, dansyl and methoxycoumarin functional groups within the 3-hydroxy-2-pyridone framework and synthesised the target host metallacrowns [$(cymene)_3Ru(III)_3(pyrene\text{-}C_5H_3NO_2)_3$], [$C_6H_5CH_2NMe_2H)_3$

$Ru(III)_3$(dansyl-$C_5H_3NO_2)_3$] and [$(C_6H_5CH_2NMe_2H)_3Ru(III)_3$(methoxycoumarin-$C_5H_3NO_2)_3$] (Fig. 12a, b) [35]. The first complex showed strong indicators for Li^+ binding, however its poor solubility in polar solvents hampered its progress. Indeed, these findings catalysed the introduction of the arene tertiary amine groups (to improve solubility) and the dansyl- and methoxycoumarin-dihydroxypyridine groups (to reduce lipophilicity). The subsequent results made for pleasant reading when ^1H NMR studies on aqueous solutions of [$(C_6H_5CH_2NMe_2H)_3Ru(III)_3$(dansyl-$C_5H_3NO_2)_3$] and [$(C_6H_5CH_2NMe_2H)_3Ru(III)_3$(methoxycoumarin-$C_5H_3NO_2)_3$] in the presence of various concentrations of LiCl both indicated strong Li^+ affinities, while further studies provided association constants (K_a) of $5.0 \pm (0.5)\ 10^3$ and $8.3 \pm (0.3)\ 10^2\ M^{-1}$, respectively. Importantly in biological terms, similar studies using NaCl solutions gave rise to a K_a value of $6 \pm (3)\ 10^{-1}\ M^{-1}$, thus pointing to a significant Li^+ selectivity over Na^+ (3 orders of magnitude).

Fluorescence studies on [$(C_6H_5CH_2NMe_2H)_3Ru(III)_3$(dansyl-$C_5H_3NO_2)_3$] showed significantly quenching when compared to the free dansyl-hydroxypyridine

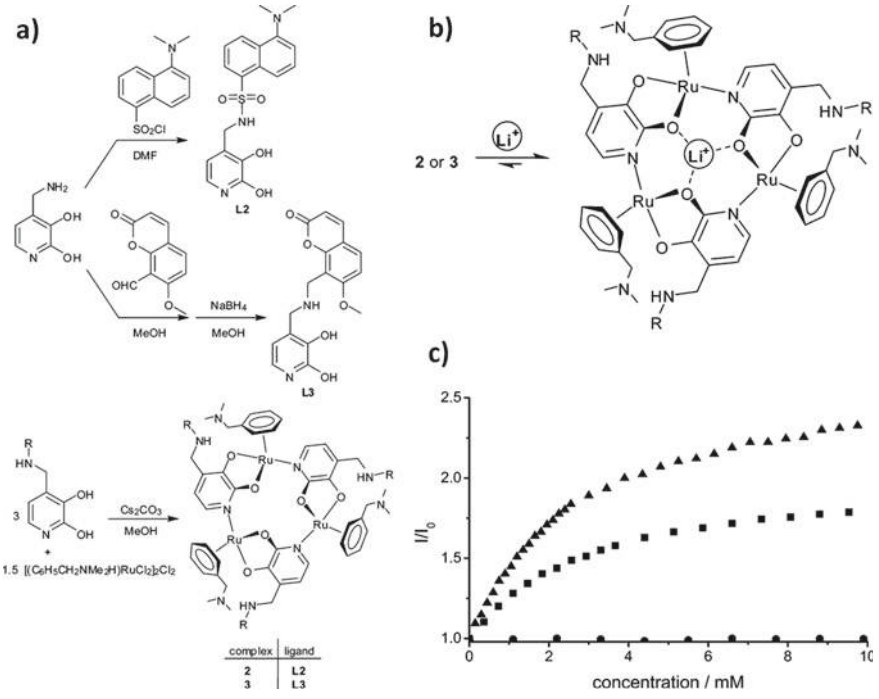

Fig. 12 **a** General synthetic routes to the fluorescent dansyl- and methoxycoumarin-dihydroxypyridine ligands. **b** Schematic representation of the Li^+ binding within the 12-$MC_{Ru(III)}$-3 host metallacrown. **c** Relative fluorescence studies for solutions of [$C_6H_5CH_2NMe_2H)_3Ru(III)_3$(methoxycoumarin-$C_5H_3NO_2)_3$] with various amounts of LiCl (■ and ▲) and NaCl (●). Data shown as ■ and ● were obtained in water (100 mM phosphate buffer, pH 8.0). The data represented by the ▲ symbols were obtained in serum (proteins removed prior to analysis). Figures reproduced with permission from [35]. Copyright 2009 Royal Society of Chemistry

ligand as expected upon Ru(III) complexation. Despite this, the observed signal (centred on 547 nm; λ_{ex} = 360 nm) increased in intensity upon Li^+ addition. However, due to its limited solubility in water, it was decided that the more water soluble $[C_6H_5CH_2NMe_2H)_3Ru(III)_3$(methoxycoumarin-$C_5H_3NO_2)_3]$ complex would be carried forward for more detailed fluorescence measurements. Indeed, an increase in the fluorescence signal (centred on 480 nm; λ_{ex} = 382 nm) was observed upon LiCl addition and kinetic data was fitted using a 1:1 binding model using the WinEQNMR fitting program, giving a K_a value (7.4 ± (0.6) 10^2 M^{-1}) in good agreement with NMR studies (Fig. 12c) [36]. As previously mentioned, the striking selectivity for Li^+ over Na^+ ions allowed the possibility of employing $[(C_6H_5CH_2NMe_2H)_3Ru(III)_3$(methoxycoumarin-$C_5H_3NO_2)_3]$ as a Li^+ ion chemosensor in biological samples. Indeed, this turned out to be the case when fluorescence studies in serum (once large proteins were removed to avoid signal masking) showed concentration dependent increases in fluorescence in the biologically relevant (0–3 mM) concentration range. Subsequent fitting of the data gave an extremely competitive association constant (K_a) of 8.3 ± (0.6) 10^2 M^{-1}.

Due to the difficult and time-consuming efforts required to produce the aforementioned 12-$MC_{Ru(III)}$-3 Li^+ fluorometric chemosensors, Gao and co-workers decided to investigate the non-covalent incorporation of fluorescent moieties in order to side-step such synthetic hurdles. Here the 12-$MC_{Ru(III)}$-3 metallacrown $[(cymene)_3Ru(III)_3(L)_3]$ (where LH_2 = 4-(2-hydroxyethyl)piperazine-1-ethanesulfonic acid) was successfully employed as a ditopic receptor in conjunction with both a Li^+ ion and a fluorescent dye (8-hydroxy-1,3,6-pyrenetrisulfonate; HPTS) (Fig. 13a, b). It was predicted that any communication between the two guests would modulate fluorescence properties. Remarkably, this was proven to be the case when addition of Li^+ ions to an aqueous solution comprising the host 12-$MC_{Ru(III)}$-3 metallacrown: HPTS adduct (bound at the arene ligands) resulted in a change in fluorescence. Fitting of these data using a 1:1 binding model gave a K_a value of 2.3 ± (0.2) × 10^3 M^{-1}, a value commensurate with the aqueous Li^+ binding event with $[(cymene)_3Ru(III)_3(L)_3]$ (LH_2 = 4-(2-hydroxyethyl)piperazine-1-ethanesulfonic acid) alone (Fig. 13c). Similar fluorescence enhancement effects were obtained using mixtures of deproteinized serum and buffered water (3:1) in the biologically relevant 0.5–1.5 nM concentration range (K_a = 1.2 ± (0.1) × 10^3 M^{-1}) [37].

Recent (2018) studies by Katsuka and co-workers on the structurally related 12-$MC_{Ru(III)}$-3 complex $[(3,5\text{-dimethylanisole})_3Ru(III)_3(2,3\text{-pyridinediolate})_3]$ devised an efficient Extraction-Spectrophotometric methodology for Li^+ quantification in saline water [38]. It was found that sub-ppm Li^+ extraction was enhanced through the use of the picrate anion (other anions were also investigated) and actioned through the complexation of the ion-pair, thus forming the $[(Li\text{-pic})\prime\ (3,5\text{-dimethylanisole})_3Ru(III)_3(2,3\text{-pyridinediolate})_3]$ complex.

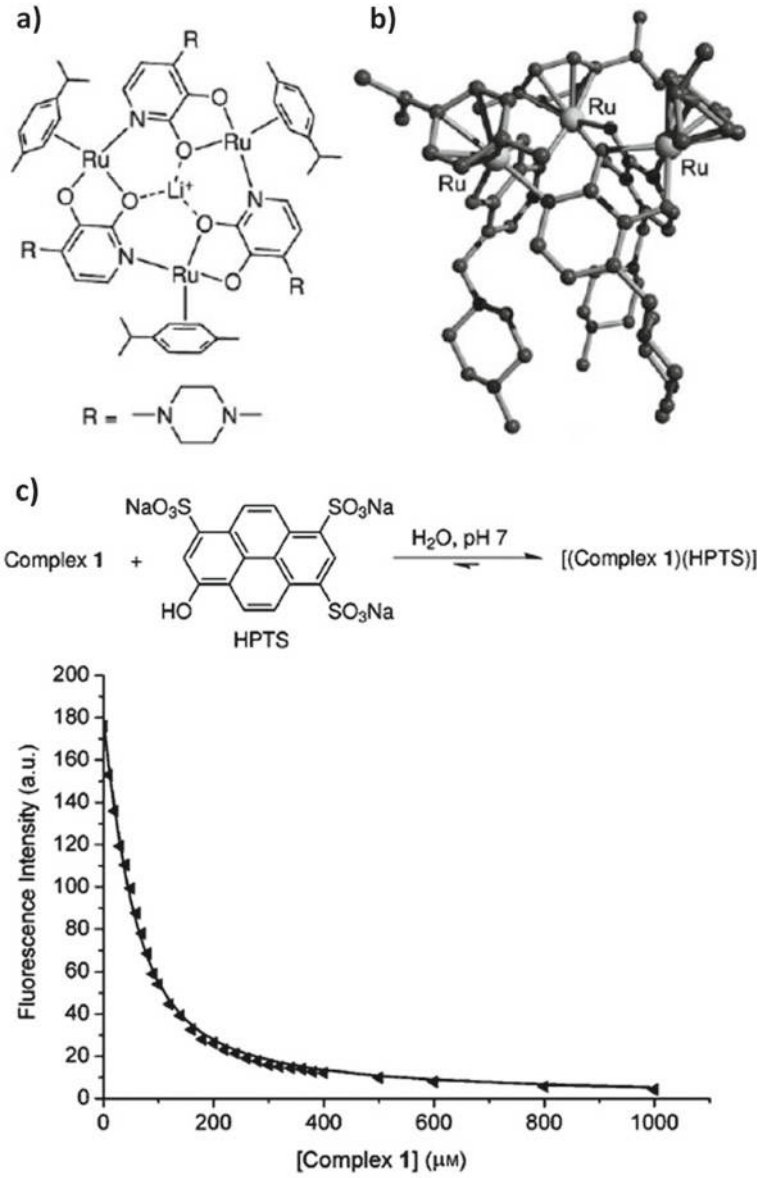

Fig. 13 **a** ChemDraw schematic of the Li^+ bound adduct of $[(cymene)_3Ru(III)_3(L)_3]$ (where LH_2 = 4-(2-hydroxyethyl)piperazine-1-ethanesulfonic acid) (Complex 1). **b** Crystal structure of $[(cymene)_3Ru(III)_3(L)_3]$. **c** Plot of fluorescence emission (at 510 nm) versus [12-$MC_{Ru(III)}$-3] addition (0–1000 μM) on a 50 μM solution of HPTS (λ_{ex} = 462 nm). The solid line is the best-fit using a 1:1 binding model. Figures reproduced with permission from [37]. Copyright 2010 John Wiley and Sons

3.4 *The Role of a 16-Membered Metallacrown in the Interconversion of Two Nanocages*

In 2012, Kilbas and co-workers employed the 16-membered metallacrown $[(cymene)_2Ru(III)_2(L_1)_2(MeCN)_2]$ (L_1H_2 = 3,4-dimethoxyfuran-2,5-dicarboxylic acid) in conjunction with the N-donor ligand tetra(4-pyridylphenyl)ethylene (L_2) towards the self-assembly of two coordination cages in the form of the octanuclear $[(cymene)_8Ru(III)_8(L_1)_8(L_2)_2]\cdot 23CHCl_3$ and the tetranuclear $[(cymene)_4Ru(III)_4(L_1)_4(L_2)]\cdot 4CH_2Cl_2$ complexes (Fig. 14). Furthermore, it was found that these complexes were interconvertible through solvent-induced rearrangements using two closely related solvents ($CHCl_3$ and CH_2Cl_2) to give the octanuclear and tetranuclear species, respectively. It was proposed that these observations were due to the incorporation of the $\{(cymene)_2Ru(III)_2(L_1)_2\}$ metallacrown building blocks (10.14a), whose ability to provide solvent specific binding sites allowed such nanostructure interconversion [39].

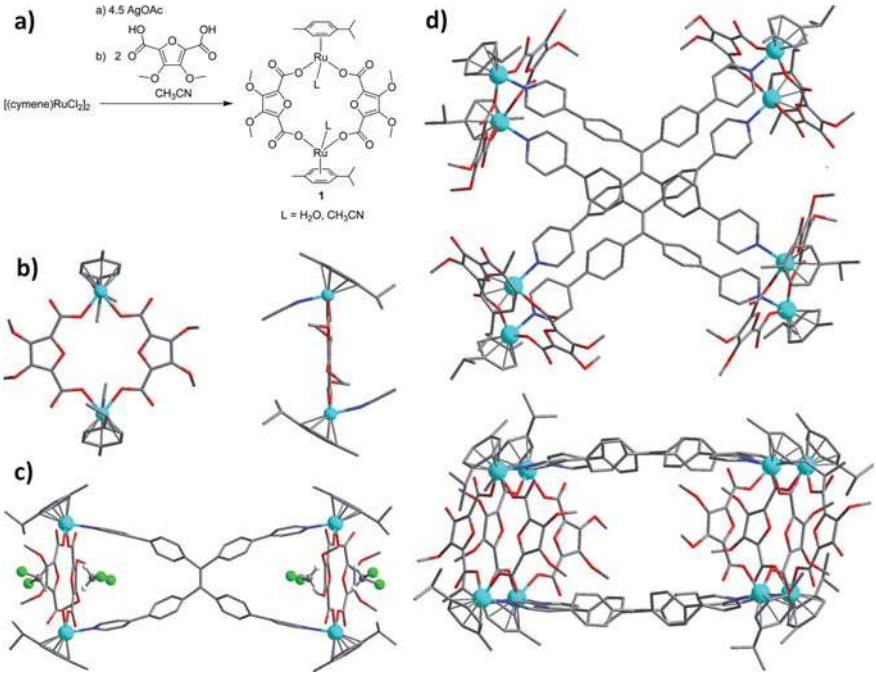

Fig. 14 **a** Schematic describing the synthesis of the 16-membered macrocycle $[(cymene)_2Ru(III)_2(L_1)_2(sol)_2]$ (sol = H_2O/MeCN; LH_2 = 3,4-dimethoxyfuran-2,5-dicarboxylic acid) along with its resultant crystal structure (**b**). Crystal structures of the interconvertible nanocages $[(cymene)_4Ru(III)_4(L_1)_4(L_2)]\cdot 4CH_2Cl_2$ (**c**) and $[(cymene)_8Ru(III)_8(L_1)_8(L_2)_2]\cdot 23CHCl_3$ (**d**). Colour codes: light blue (Ru), red (O), grey (C), green (Cl). Figures reproduced with permission from [39]. Copyright 2012 Royal Society of Chemistry

4 Controlling the First Coordination Sphere Towards Selective Binding and Topology Control

The ability to control the first coordination sphere of any molecule opens up endless possibilities in terms of the design and construction of more complex hierarchies whose physical properties may be inherited from their building blocks towards targeted physical behaviour. We present here examples of how such endeavours can be implemented with respect to metallacrown units towards (for example) the self-assembly of 1- and 2-D extended networks or their employment as anion scavengers.

4.1 Hexametallic 18-$MC_{Cu(II)}$-6 Pertechnetate and Perrhenate Scavengers

In 2016, Vázquez-López and co-workers demonstrated the versatile anion binding ability of an aza-[18-$MC_{Cu(II)\text{-}N(2ph)}$-6] framework. More specifically, it was found that reaction of a number of Cu(II) salts in the presence of 2-piconyl hydrazine (2phH) and a suitable solvent gave rise to the corresponding solid-state host–guest complexes of general formula $[Cu(II)_6(2ph)_6(sol)_x(anion)_y]^{(6-y)+}$ (sol = H_2O, DMF; anion = ClO_4^-, BF_4^-, NO_3^-, SiF_6^{2-} and SO_4^{2-}) (Fig. 15) [40]. The metal centres within the $[Cu(II)_6(2ph)_6]^{6+}$ structure are connected through the $\eta^1{:}\eta^1{:}\eta^1{:}\eta^1$ μ-bridging $2ph^-$ ligands and results in repeating –[Cu–N–N]$_n$– units within the ring-like topology that is ideal for the incorporation of guest species through a combination of direct metal coordination and H-bonding interactions. These findings encouraged investigations

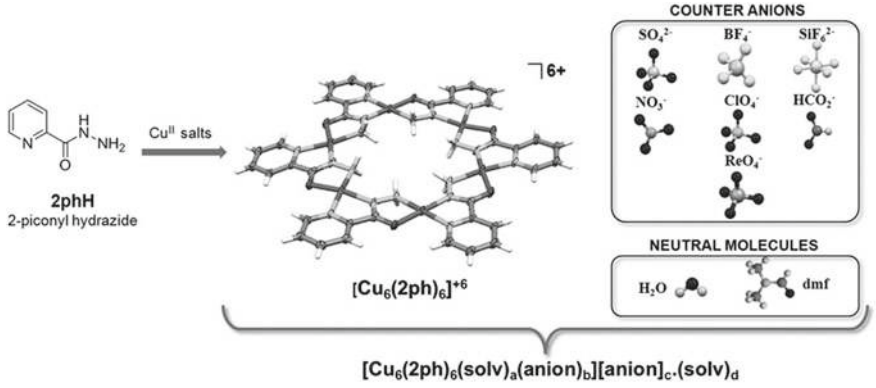

Fig. 15 General schematic of the hexametallic [18-$MC_{Cu(II)\text{-}N(2ph)}$-6] azametallacrowns first published by Rodríguez-Hermida and co-workers. The additional ligands (solvents and anions) have been omitted from the central figure for clarity. Figure reproduced with permission from [40]. Copyright 2016 John Wiley and Sons

into the anion trapping of the pertechnetate (TcO_4^-) and perrhenate (ReO_4^-) species. Indeed, strong evidence of their successful adsorption was obtained after aqueous 24 h mixing of $[Cu(II)_6(2ph)_6](BF_4)_6$ or $[Cu(II)_6(2ph)_6](NO_3)_6{\cdot}5H_2O$ when the resultant precipitates were isolated and assessed using IR, EDS (energy-dispersive X-ray) and pXRD (for ReO_4^-) or ^{99}Tc NMR (for TcO_4^-). Although similar studies using MnO_4^- and CrO_4^- showed no evidence of trapping behaviour, the ability to successfully immobilise the environmentally sensitive species ReO_4^- and TcO_4^- promoted these hexametallic complexes as potentially viable functional materials.

4.2 Pentanuclear 12-$MC_{Cu(II)}$-4 Metallacrowns as Building Blocks Towards 1- and 2-D Extended Networks

In 2013, McDonald and co-workers synthesised the pentanuclear 12-$MC_{Cu(II)}$-4 metallacrowns $[Cu(II)_5(L_1)_4(MeOH)_4](ClO_4)_2$ (Fig. 16a) and $[Cu(II)_5(L_2)_4(MeOH)_4](ClO_4)_2{\cdot}H_2O$ using the hydroxamate ligands 2-(dimethylamino)phenylhydroxamic acid (L_1H_2) and 2-(amino)phenylhydroxamic acid (L_2H_2) [41]. Both complexes exhibited a planar body-centred square array of Cu(II) centres comprising a combination of distorted square planar and distorted square-based pyramidal geometries, depending on the number of terminal MeOH ligands bound to the metallacrown. The singly deprotonated L_1^- and L_2^- hydroxamates were found to connect the outer Cu(II) centres to one another through the $\eta^1{:}\eta^1{:}\eta^2{:}\eta^1$ μ_3-bonding motif while their O_{oxime} donor atoms stabilised the central metal site. Upon close inspection of these structures, it soon became clear that there were opportunities to take advantage of the coordinative flexibility and/or vacant coordination sites of the Cu(II) ions along with the potential for substitution of the terminally bound methanol ligands. This was indeed the case when through introduction of pyridine (1 cm^3; 12.4 mmol) to the synthon gave rise to the analogous complex $[Cu(II)_5(L_1)_4(py)_2](ClO_4)_2{\cdot}py$ (Fig. 16b), while the addition of excess pyridine (5 cm^3; 62.0 mmol) produced the 12-$MC_{Cu(II)}$-4 metallacrown $[Cu(II)_5(L_1)_4(py)_6](ClO_4)_2$ (Fig. 16c). The successful conservation of the $\{Cu(II)_5(L_1)_4\}^{2+}$ 12-$MC_{Cu(II)}$-4 core upon addition of pyridine to give products $[Cu(II)_5(L_1)_4(py)_2](ClO_4)_2{\cdot}py$ and $[Cu(II)_5(L_1)_4(py)_6](ClO_4)_2$ was by no means a formality as exampled by Lisowski and co-workers, when they found that the addition of pyridine to the 12-$MC_{Cu(II)}$-4 complex $[Cu(II)_5(picha)_4](NO_3)_2$ (where picha = 2-picolinehydroxamic acid) resulted in a change in topology in the form of the linear trinuclear complex $[Cu(II)_3(picha)_2(py)_5(NO_3)_2]$ [42].

ESI–MS and UV–vis studies on each of these discrete 12-$MC_{Cu(II)}$-4 metallacrowns demonstrated solution stability with respect to their $\{Cu(II)_5(L_{1\text{-}2})_4\}^{2+}$ cores (Fig. 17a). Taking advantage of this solution stability and building upon the initial success in manipulating the primary coordination spheres of the Cu(II) centres, McDonald and co-workers correctly predicted that the self-assembly of larger extended architecture comprising pentametallic 12-$MC_{Cu(II)}$-4 nodes could

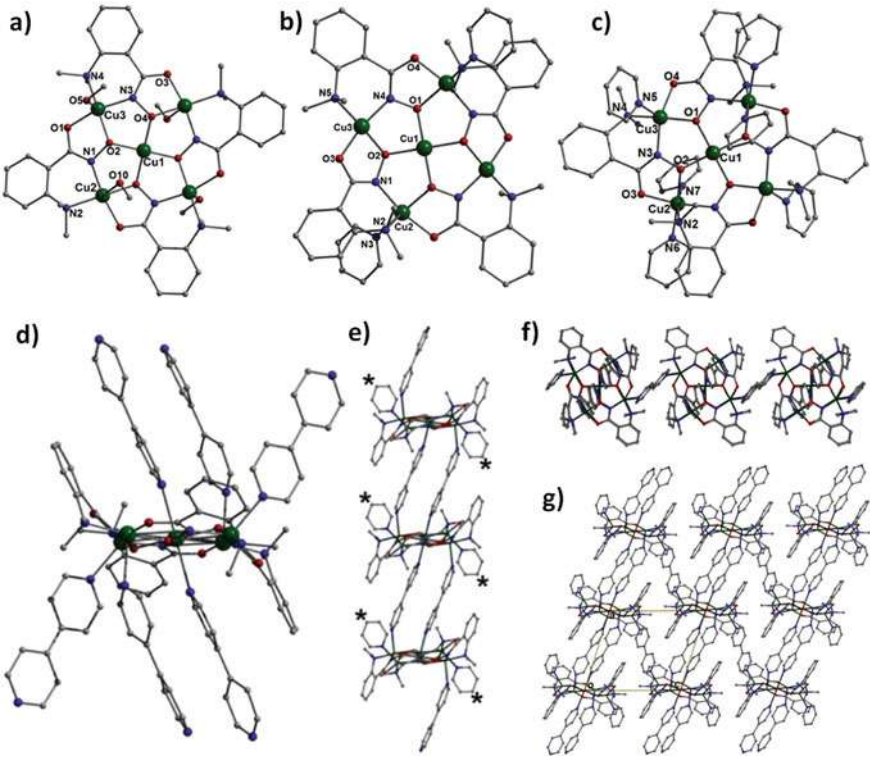

Fig. 16 Crystal structures of the 12-$MC_{Cu(II)}$-4 metallacrowns $[Cu(II)_5(L_1)_4(MeOH)_4](ClO_4)_2$ (**a**), $[Cu(II)_5(L_1)_4(py)_2](ClO_4)_2{\cdot}py$ (**b**) and $[Cu(II)_5(L_1)_4(py)_6](ClO_4)_2$ (**c**). **d** Crystal structure of a single $\{Cu(II)_5\}$ node within the extended network $\{[Cu(II)_5(L_1)_4(4,4'\text{-bipy})_3](ClO_4)_2{\cdot}(H_2O)\}_n$. **e** Structure of three $\{Cu(II)_5\}$ nodes linked into 1-D arrays by 4,4′-bipyridine linkers. The * symbol shows the points at which the 1-D rows are connected (via 4,4′-bipy ligands) to form the 2-D sheets in $\{[Cu(II)_5(L_1)_4(4,4'\text{-bipy})_3](ClO_4)_2{\cdot}(H_2O)\}_n$. Hydrogen atoms, counter anions and solvent molecules have been omitted for clarity. **f** Top-view and perpendicular **g** views of a single 2-D sheet of $\{Cu(II)_5\}$ nodes connected into an [4,4] grid array in $\{[Cu(II)_5(L_1)_4(4,4'\text{-bipy})_3](ClO_4)_2{\cdot}(H_2O)\}_n$. H-atoms, counter anions and solvent molecules have been omitted for clarity. Colour code: green (Cu), red (O) dark blue (N) and grey (C). Figures reproduced with permission from [41]. Copyright 2013 Royal Society of Chemistry

be achieved through the simple addition of suitable linear connector ligands. This was soon realised when the introduction of the ditopic ligands 4,4′-bipyridine (4,4′-bipy) and 4,4′-azopyridine (4,4′-azp) to the synthon employed to form the discrete complex $[Cu(II)_5(L_1)_4(MeOH)_4](ClO_4)_2$ formed the 2-D extended network $\{[Cu(II)_5(L_1)_4(4,4'\text{-bipy})_3](ClO_4)_2{\cdot}(H_2O)\}_n$ and the 1-D coordination polymer $\{[Cu(II)_5(L_1)_4(4,4'\text{-azp})_2(MeOH)_2](ClO_4)_2\}_n$. Likewise, the reaction of pyrazine (pz) in conjunction with $[Cu(II)_5(L_2)_4(MeOH)_4](ClO_4)_2{\cdot}H_2O$ gave rise to the 1-D chain $\{[Cu(II)_5(L_2)_4(pz)_2(MeOH)_3](ClO_4)_2{\cdot}MeOH\}_n$. The extended architecture observed in $\{[Cu(II)_5(L_1)_4(4,4'\text{-bipy})_3](ClO_4)_2{\cdot}(H_2O)\}_n$ comprises chains of

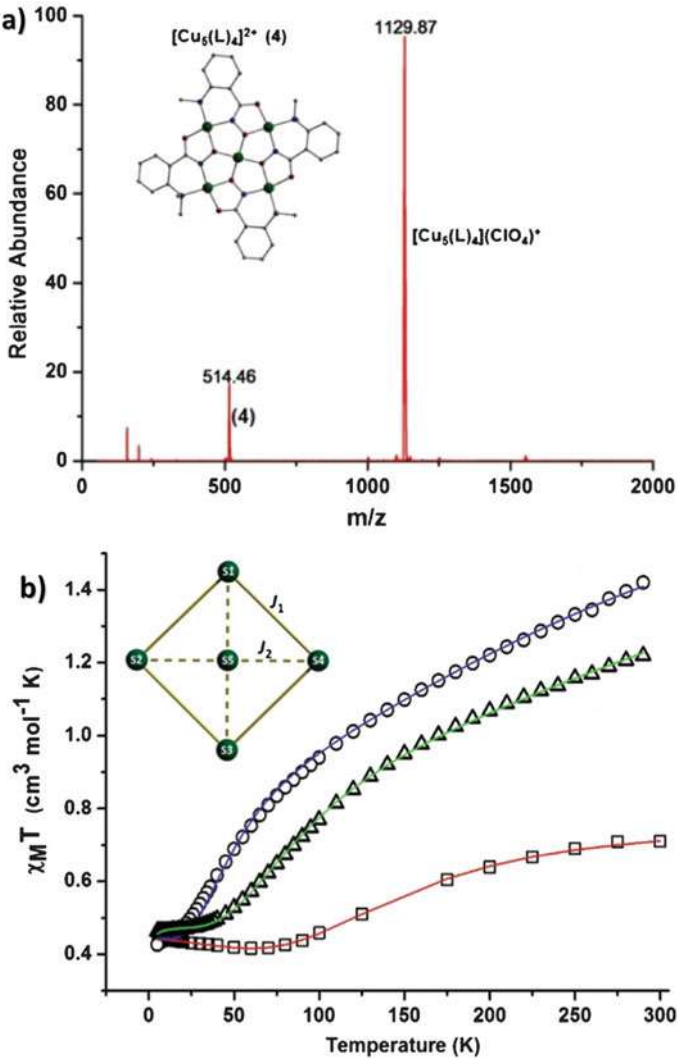

Fig. 17 **a** TOF–MS-ES$^+$ spectrum of $\{[Cu(II)_5(L_1)_4(4,4'\text{-bipy})_3](ClO_4)_2\cdot(H_2O)\}_n$ using a H_2O–MeCN solvent matrix. The peaks at $m/z = 514.46$ and 1129.87 correspond to the $\{Cu(II)_5(L_1)_4\}^{2+}$ and $[\{Cu(II)_5(L_1)_4\} + \{ClO_4\}]^+$ species, respectively. **b** Magnetic susceptibility ($\chi_M T$) data obtained for complexes $[Cu(II)_5(L_1)_4(MeOH)_4](ClO_4)_2$ (□), $\{[Cu(II)_5(L_1)_4(4,4'\text{-bipy})_3](ClO_4)_2\cdot(H_2O)\}_n$ (○) and $\{[Cu(II)_5(L_2)_4(pz)_2(MeOH)_3](ClO_4)_2\cdot MeOH\}_n$ (Δ). The solid lines represent the best-fits for the data using the spin-Hamiltonian in Eq. 1 and the model given inset. Figures reproduced with permission from [41]. Copyright 2013 Royal Society of Chemistry

{Cu(II)$_5$} units each connected by two axially bound ditopic 4,4′-bipyridine ligands. A third dipyridyl ligand then connects these individual chains to form covalent 2-D sheets of [4,4] grid topology (Fig. 16g). The ClO_4^- counter anions act as molecular mortar by connecting the disparate 2-D sheets and are locked in position through extensive hydrogen bonding. Replacing 4,4′-bipyridine with 4,4′-azopyridine (4,4′-azp) allowed the self-assembly of the 1-D coordination polymer {[Cu(II)$_5$(L$_1$)$_4$(4,4′-azp)$_2$(MeOH)$_2$](ClO$_4$)$_2$}$_n$. The connectivity change (1-D vs. 2-D) was assigned to the *trans* conformations of the –N = N– 4,4′-azopyridine bridges that leads to the observed zig-zag chain topology. The step-like 1-D chain in {[Cu(II)$_5$(L$_2$)$_4$(pz)$_2$(MeOH)$_3$](ClO$_4$)$_2$·MeOH}$_n$ demonstrated that shorter pyrazine connector ligands would produce the expected extended topology while bringing the individual {Cu(II)$_5$} metallacrowns closer together in the process. Interestingly, however this was only achieved using the 2-(amino)phenylhydroxamic acid (L_2H_2) as no discernible products were obtained via the 2-(dimethylamino)phenylhydroxamic acid (L_1H_2). This observation was attributed to sterics effects; where the less bulky –NH$_2$ fragments in L_2H_2 (*cf.* -NMe$_2$ groups in L_1H_2) allowed the individual {Cu(II)$_5$} units to come close enough together to form the coordination polymer.

Variable temperature magnetic susceptibility studies (χ_MT vs. T) on the discrete metallacrown [Cu(II)$_5$(L$_1$)$_4$(MeOH)$_4$](ClO$_4$)$_2$ and the extended networks {[Cu(II)$_5$(L$_1$)$_4$(4,4′-bipy)$_3$](ClO$_4$)$_2$·(H$_2$O)}$_n$ and {[Cu(II)$_5$(L$_2$)$_4$(pz)$_2$(MeOH)$_3$](ClO$_4$)$_2$·MeOH}$_n$ were indicative of strong intramolecular antiferromagnetic exchange between the Cu(II) ions and $S = ½$ ground spin states in all three materials. All three crystal structures highlighted two separate magnetic exchange pathways between the constituent Cu(II) centres. The first (J_1) represented the Cu(II)$_{outer}$–Cu(II)$_{outer}$ pathway (comprising one Cu(II)–N–O–Cu(II) bridge with angles ranging from 160.46° to 177.04°), while the second (J_2) characterised the exchange between the Cu(II)$_{outer}$–Cu(II)$_{inner}$ ions representing both the Cu(II)–N–O–Cu(II) pathways (angles ranging from 21.25° to 48.16°) and one Cu(II)–O$_{oxime}$–Cu(II) bridge (angles ranging from 113.47° to 121.56°). Using the model given in Fig. 17b and the isotropic spin-Hamiltonian given in Eq. 1, the best-fit parameters obtained for the three complexes are given in Table 1. Fitting the magnetic data of the 1-D coordination polymer {[Cu(II)$_5$(L$_2$)$_4$(pz)$_2$(MeOH)$_3$](ClO$_4$)$_2$·MeOH}$_n$ required a Curie–Weiss parameter (θ) to account for the intermolecular exchange propagated via the axial pyrazine connector ligands.

$$\begin{aligned}\hat{H} = &-2J_1(\hat{S}_1 \cdot \hat{S}_2 + \hat{S}_2 \cdot \hat{S}_3 + \hat{S}_3 \cdot \hat{S}_4 + \hat{S}_4 \cdot \hat{S}_1) \\ &-2J_2(\hat{S}_1 \cdot \hat{S}_5 + \hat{S}_2 \cdot \hat{S}_5 + \hat{S}_3 \cdot \hat{S}_5 + \hat{S}_4 \cdot \hat{S}_5) \\ &+\sum\nolimits_{i=1=5} \left\{\mu_B B g \hat{S}_i\right\} \end{aligned} \quad (1)$$

where: $\hat{S}$ = spin operator, J = pairwise isotropic magnetic exchange between constitutive metal centres; μ_B = Bohr magneton; ~B the external static magnetic field; g = isotropic g-factor of the metal ions; i and j = indices referring to the constituent metal ions ($n = 5$).

Table 1 Magnetic exchange parameters obtained from a family of [Cu_5] 12-$MC_{Cu(II)}$-4 metallacrown complexes [41]

Complex	J_1 (cm^{-1})	J_2 (cm^{-1})	Curie–Weiss constant (θ, K)
$[Cu(II)_5(L_1)_4(MeOH)_4](ClO_4)_2$	−139.77	−295.31	–
$\{[Cu(II)_5(L_1)_4(4,4'\text{-bipy})_3](ClO_4)_2\cdot(H_2O)\}_n$	−48.81	−85.68	–
$\{[Cu(II)_5(L_2)_4(pz)_2(MeOH)_3](ClO_4)_2\cdot MeOH\}_n$	−86.04	−145.15	−0.23

Note g-value fixed at 2.15

Building upon this work, 2019 saw the Jones group investigate the coordination chemistry of novel functionalised mono- and ditopic hydroxamic acids. One such target ligand was (*N*-hydroxy-2-((2-hydroxy-3-methoxybenzyl)amino)benzamide (LH_3) and was successfully synthesised via the one-pot Schiff base coupling and selective imine reduction of 2-amino-phenylhydroxamic acid and ortho-vanillin using the reducing agent sodium triacetoxyborohydride [43]. Surprisingly and despite the elaborate nature of this ligand, its Cu(II) ligation gave rise to the 12-$MC_{Cu(II)}$-4 metallacrown $[Cu(II)_5(LH)_4(MeOH)_2(NO_3)_2]\cdot 3H_2O\cdot 4MeOH$ (Fig. 18a–d) [44]. Here the pentametallic core was constructed by four doubly deprotonated LH^{2-} ligands, each exhibiting the $\eta^1{:}\eta^2{:}\eta^1{:}\eta^1{:}\eta^1$ μ_3-bridging mode (Fig. 18d). The planar $\{Cu(II)_5(LH)_4\}^{2+}$ core was formed via Cu(II) binding at the near planar hydroxamate groups of each LH^{2-} ligand, as observed in previous 12-$MC_{Cu(II)}$-4 metallacrowns. However, unlike other analogues, it was noted that the deliberate addition of the phenolic group provided each ligand with a natural angular topology and allowed these phenolic groups to twist away from the $\{Cu(II)_5(LH)_4\}^{2+}$ plane. The result of which was a final topology whereby each phenolic unit was positioned in an alternating up-down-up-down arrangement with respect to the 12-$MC_{Cu(II)}$-4 inorganic core. Furthermore, these phenolic groups were therefore able to provide long contacts with the four outer Cu(II) ions. It was also noted that two-terminal MeOH ligands effectively sat in a pocket provided by the LH^{2-} phenolic groups (Fig. 18c).

Magnetic susceptibility measurements on $[Cu(II)_5(LH)_4(MeOH)_2(NO_3)_2]\cdot 3H_2O\cdot 4MeOH$ produced a room temperature $\chi_M T$ product of 1.49 cm^3 mol^{-1} K and was indicative of the early onset of intramolecular antiferromagnetic exchange between the Cu(II) metal centres (Fig. 18f). This was supported by a continued decrease in magnetic susceptibility upon cooling. Simultaneous fitting of the magnetic susceptibility and magnetisation data was carried out using the PHI program, the isotropic spin-Hamiltonian in Eq. 2 and the model given in Fig. 18e [45]:

$$\hat{H} = -2\sum_{i,j>i}^{n} \hat{S}_i J_{ij} \hat{S}_j + \mu_B \sum_{i=1}^{n} \vec{B} g_i \hat{S}_i \tag{2}$$

where $\hat{S}$ = spin operator and J = pairwise isotropic magnetic exchange between constitutive metal centres. The best-fit parameters obtained were $J_1 = -115.33\ cm^{-1}$

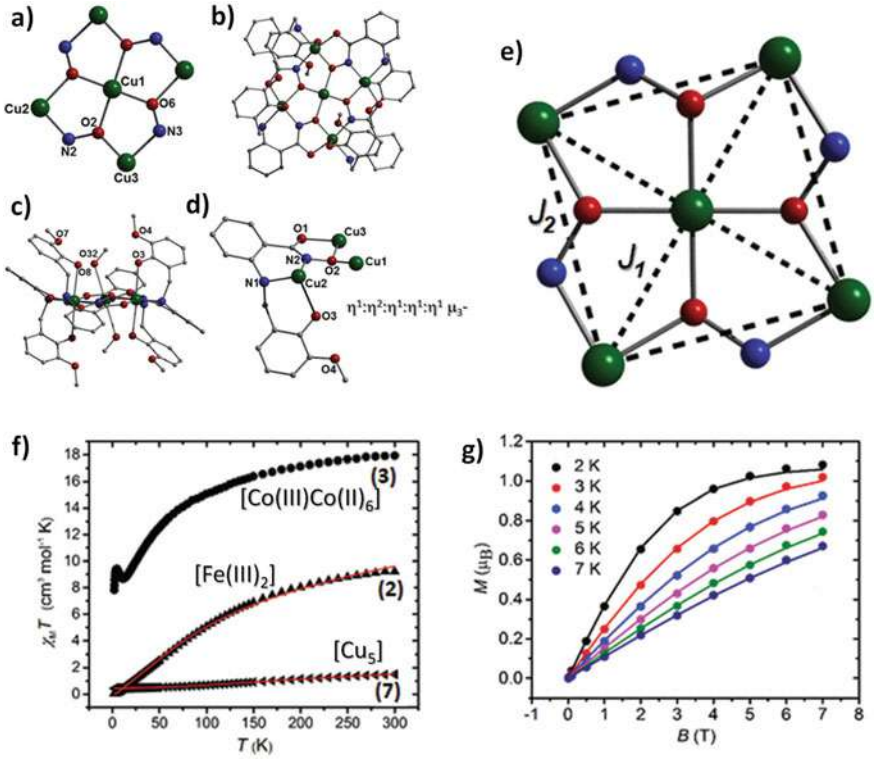

Fig. 18 **a** The inorganic core in $[Cu(II)_5(LH)_4(MeOH)_2](NO_3)_2{\cdot}3H_2O{\cdot}4MeOH$ (**a**) accompanied by its crystal structure as viewed perpendicular (**b**) and parallel (**c**) to the $\{Cu(II)_5\}$ plane. All terminal methanol ligands were removed for clarity (apart from in Fig. c). **d** The bonding motif employed by the LH^{2-} ligands (dark line) shows the elongated Cu–O interaction at a distance of 2.502 Å (Cu2–O3). **e** The magnetic exchange coupling model employed to fit the data in $[Cu(II)_5]$. **f** $\chi_M T$ versus T plots obtained from polycrystalline samples of $[Cu(II)_5]$ (◄) along with the complexes $[Fe(III)_2(2\text{-aphH})_4Cl_2]{\cdot}2MeCN$ (▲) and $[Co(III)Co(II)_6(2\text{-aphH})_8(2\text{-aph})_2(MeOH)_4(NO_3)_2]NO_3{\cdot}3.5H_2O{\cdot}14MeOH$ (●) (2-aphH_2 = 2-(acetoxy)phenylhydroxamic acid). Measurements taken in the T = 300–2 K temperature range and in an applied field (B) of 0.1 T for $[Fe(III)_2]$ and $[Co(III)Co(II)_6]$, and 0.5 T for $[Cu(II)_5]$. **g** Magnetisation ($M/\mu B$) vs. B (T) data obtained from a polycrystalline sample of $[Cu(II)_5]$ measured in the 2–7 K temperature range and 0–7 T magnetic field range. Figures reproduced with permission from [44]. Copyright 2019 Royal Society of Chemistry

and $J_2 = -83.03\,cm^{-1}$ and $g_{Cu(II)} = 2.14$. The J-values obtained were commensurate with those observed in other similarly bridged Cu(II) complexes [41, 46] and gave rise to an isolated $S = 1/2$ ground spin state.

4.2.1 Just Add Water: Deviations from 12-MC-4 Metallacrown Formation

Investigations by McDonald and co-workers on the Ni(II) coordination chemistry of 2-(dimethylamino)phenylhydroxamic acid (L_1H_2) led to the synthesis of the [Ni(II)$_5$] 12-MC$_{Ni(II)}$-4 metallacrowns [Ni(II)$_5$(L$_1$)$_4$(MeOH)$_4$](ClO$_4$)$_2$·2MeOH and [Ni(II)$_5$(L$_1$)$_4$(py)$_5$](ClO$_4$)$_2$·H$_2$O, whose planar {Ni(II)$_5$(L$_1$)$_4$}$^{2+}$ cores were akin to their Cu(II) analogues as described in Sect. 6.3.2 (Fig. 19a–d). Although both complexes comprise the metallacrown core, structural differences between these siblings were observed in terms of the metal coordination spheres. More specifically, the Ni(II) ions in [Ni(II)$_5$(L$_1$)$_4$(MeOH)$_4$](ClO$_4$)$_2$·2MeOH possess a combination of diamagnetic distorted square planar geometries and paramagnetic square-based pyramidal and octahedral arrangements. Likewise, the addition of pyridine at the axial Ni(II) sites in the structure of [Ni(II)$_5$(L$_1$)$_4$(py)$_5$](ClO$_4$)$_2$·H$_2$O effectively converted the majority of the square planar Ni(II) ions to square-based pyramidal and octahedral geometries, thus effectively introducing more paramagnetic centres and activating additional magnetic superexchange pathways within the metallacrown [47].

In order to ascertain the magnetic nature of the square planar and square-based pyramidal Ni(II) ions within [Ni(II)$_5$(L$_1$)$_4$(MeOH)$_4$](ClO$_4$)$_2$·2MeOH and [Ni(II)$_5$(L$_1$)$_4$(py)$_5$](ClO$_4$)$_2$·H$_2$O, DFT calculations were employed using a varying combination of spin states ($s = 0$ vs. $s = 1$) to confirm their electronic structures. As illustrated in Fig. 20a, the outcome from these studies confirmed that three Ni(II) centres within [Ni(II)$_5$(L$_1$)$_4$(MeOH)$_4$](ClO$_4$)$_2$·2MeOH and four metal sites in [Ni(II)$_5$(L$_1$)$_4$(py)$_5$](ClO$_4$)$_2$·H$_2$O were paramagnetic in nature and from this a suitable model for the fitting of the magnetic data was produced. From these foundations, variable temperature magnetic susceptibility measurements were then performed on powdered microcrystalline samples of [Ni(II)$_5$(L$_1$)$_4$(MeOH)$_4$](ClO$_4$)$_2$·2MeOH and [Ni(II)$_5$(L$_1$)$_4$(py)$_5$](ClO$_4$)$_2$·H$_2$O and produced room temperature χ_MT values of 3.55 cm^3 mol^{-1} K and 3.43 cm^3 mol^{-1} K, respectively. These values were lower than expected for three (3.63 cm^3 mol^{-1} K) and four (4.84 cm^3 mol^{-1} K) non-interacting, paramagnetic Ni(II) centres ($g = 2.2$) and suggested antiferromagnetic exchange. These thoughts were supported by the steady decrease in their χ_MT products upon declining temperatures and indicative of dominant intermolecular antiferromagnetic exchange in both complexes. The steeper χ_MT versus T curve in [Ni(II)$_5$(L$_1$)$_4$(py)$_5$](ClO$_4$)$_2$·H$_2$O suggests stronger antiferromagnetic exchange between the Ni(II) centres compared to those in [Ni(II)$_5$(L$_1$)$_4$(MeOH)$_4$](ClO$_4$)$_2$·2MeOH (showing a more shallow χ_MT versus T curve). The models given in Fig. 20b were employed to fit the magnetic properties of both pentametallic complexes. The isotropic magnetic exchange parameter (J_1) was employed to represent the interactions between the central Ni(II) ion and the surrounding paramagnetic metal centres and more specifically associated with 1 × Ni(II)–O–Ni(II) and 1 × Ni(II)–O–N–Ni(II) interaction. The second (J_2) characterised the exchange around the outer ring of the 12-MC$_{Ni(II)}$-4 metallacrown, between the peripheral Ni(II) metal centres connected through Ni(II)–O–N–Ni(II) interactions. The best-fit parameters obtained were $J_1 = -3.51$ cm^{-1} (in [Ni(II)$_5$(L$_1$)$_4$(MeOH)$_4$](ClO$_4$)$_2$·2MeOH) and $J_1 = -16.87$ cm^{-1} and $J_2 = -$

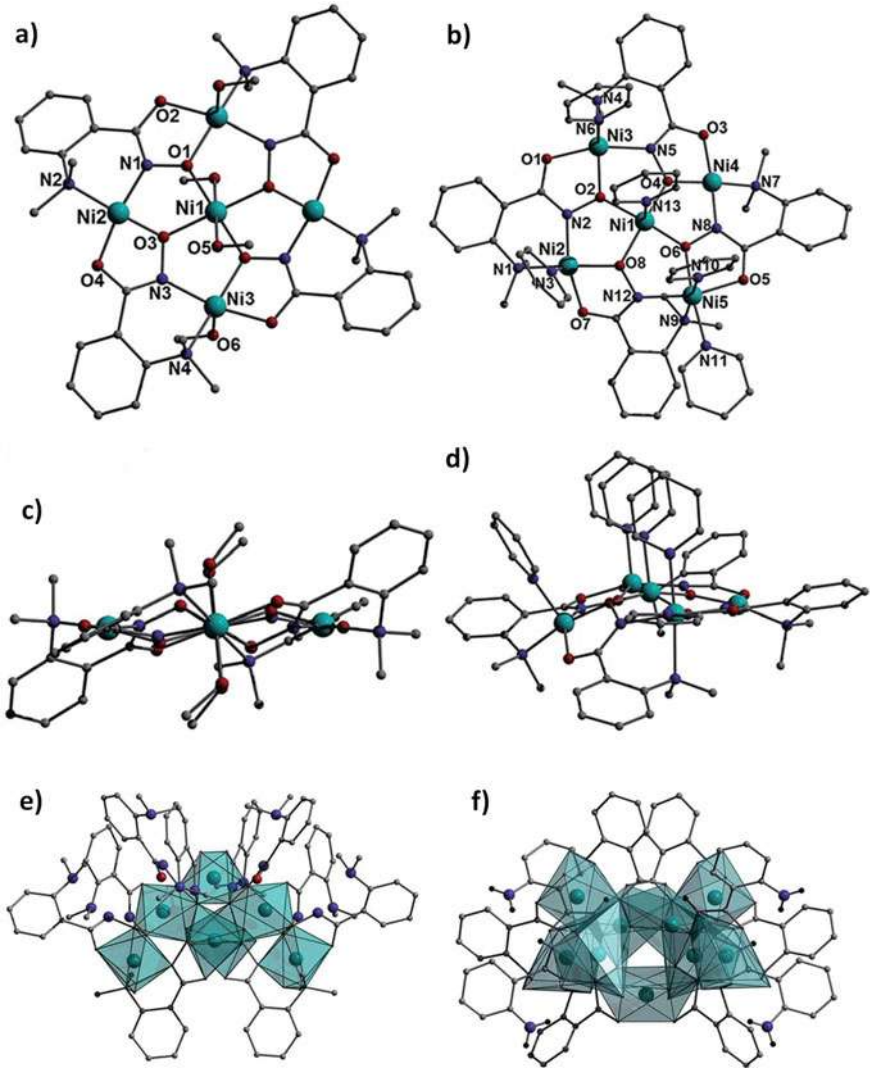

Fig. 19 Crystal structures of $[Ni(II)_5(L_1)_4(MeOH)_4](ClO_4)_2{\cdot}2MeOH$ and $[Ni(II)_5(L_1)_4(py)_5](ClO_4)_2{\cdot}H_2O$ as viewed perpendicular (**a**, **b**) and parallel (**c**, **d**) to their pentametallic 12-$MC_{Ni(II)}$-4 metallacrown cores, respectively. Polyhedral representations of the crystal structures of $[Ni(II)_7(L_1H)_8(L_1)_2(H_2O)_6]SO_4{\cdot}15H_2O$ (**e**) and $[Ni(II)_9(\mu\text{-}H_2O)_2(L_2)_6(L_2H)_4(H_2O)_2](ClO_4)_2{\cdot}2MeOH{\cdot}18H_2O$ (**f**). Hydrogen atoms have been omitted for clarity. Colour code: light blue (Ni), red (O), dark blue (N), grey (C). Figures reproduced with permission from (2014) [47]. Copyright 2014 Royal Society of Chemistry

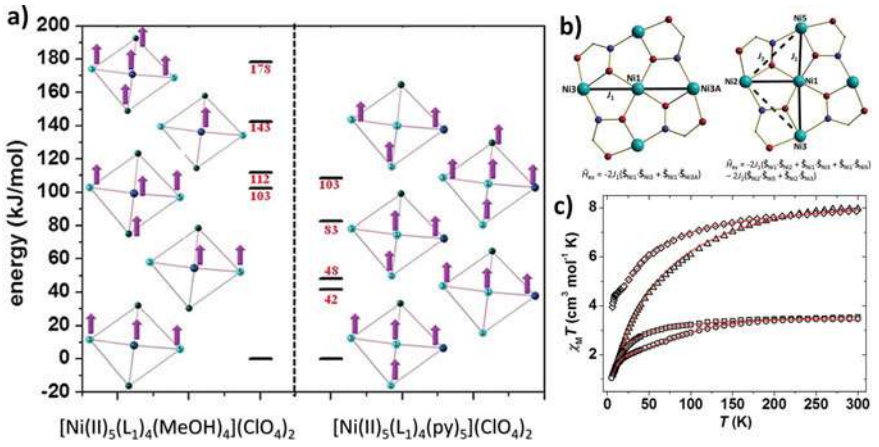

Fig. 20 **a** All possible total spin (*s*) configurations of the individual Ni(II) metal ions in the 12-$MC_{Ni(II)}$-4 metallacrowns $[Ni(II)_5(L_1)_4(MeOH)_4](ClO_4)_2{\cdot}2MeOH$ and $[Ni(II)_5(L_1)_4(py)_5](ClO_4)_2{\cdot}H_2O$ (right), with their respective energies (kJ mol^{-1}). **b** Schematics describing the models used to fit the experimental data for $[Ni(II)_5(L_1)_4(MeOH)_4](ClO_4)_2{\cdot}2MeOH$ (left) and $[Ni(II)_5(L_1)_4(py)_5](ClO_4)_2{\cdot}H_2O$. **c** $\chi_M T$ versus T plots obtained for complexes $[Ni(II)_5(L_1)_4(MeOH)_4](ClO_4)_2{\cdot}2MeOH$ (□), $[Ni(II)_5(L_1)_4(py)_5](ClO_4)_2{\cdot}H_2O$ (○), $[Ni(II)_7(L_1H)_8(L_1)_2(H_2O)_6]SO_4{\cdot}15H_2O$ (◊) and $[Ni(II)_9(\mu\text{-}H_2O)_2(L_2)_6(L_2H)_4(H_2O)_2](ClO_4)_2{\cdot}2MeOH{\cdot}18H_2O$ (Δ). The solid lines represent best-fits of the experimental data. Figures reproduced with permission from [47]. Copyright 2014 Royal Society of Chemistry

7.83 cm^{-1} (in $[Ni(II)_5(L_1)_4(py)_5](ClO_4)_2{\cdot}H_2O$), with $S = 1$ and $S = 2$ ground spin states, respectively (Fig. 20c).

Interestingly, the introduction of water to the reaction of $Ni(II)SO_4{\cdot}6H_2O$, L_1H and NaOH in methanol resulted in a change in topology and an increase in nuclearity in the form of the heptametallic complex $[Ni(II)_7(L_1H)_8(L_1)_2(H_2O)_6]SO_4{\cdot}15H_2O$ (Fig. 19e). Likewise, the nonametallic complexes $[Ni(II)_9(\mu\text{-}H_2O)_2(L_2)_6(L_2H)_4(H_2O)_2]SO_4{\cdot}29H_2O$ and $[Ni(II)_9(\mu\text{-}H_2O)_2(L_2)_6(L_2H)_4(H_2O)_2](ClO_4)_2{\cdot}2MeOH{\cdot}18H_2O$ (L_2H_2 = 2-(amino)phenylhydroxamic acid; Fig. 19f) were produced in the same vein, using $Ni(II)SO_4.6H_2O$ and $Ni(II)(ClO_4)_2.6H_2O$ precursors, respectively. Both complexes were found to comprise μ-bridging H_2O ligands along with singly (L_2H^-) and doubly (L_2^{2-}) deprotonated hydroxamate ligands and thus clearly defined the role water played in their synthon. Indeed, this simple synthetic tweak could allow the synthetic chemist to navigate around the formation of the common and often stable metallacrown cores.

Magnetic susceptibility studies on $[Ni(II)_9(\mu\text{-}H_2O)_2(L_2)_6(L_2H)_4(H_2O)_2](ClO_4)_2{\cdot}2MeOH{\cdot}18H_2O$ were indicative of dominant antiferromagnetic exchange (Fig. 20c), while the data obtained from the heptanuclear complex $[Ni(II)_7(L_1H)_8(L_1)_2(H_2O)_6]SO_4{\cdot}15H_2O$ suggested a combination of ferro- and antiferromagnetic coupling between the Ni(II) centres. The structural complexity of both complexes prevented detailed analysis of their susceptibility data due to the sheer number of different intramolecular magnetic interactions observed within both moieties. Therefore, the

magnitude of the exchange was instead estimated by using simpler models. For both complexes, attempts were made to fit the susceptibility data with just one J value, while assuming all Ni(II)$\cdots$Ni(II) interactions were of similar magnitude. A suitable fit was obtained for $[Ni(II)_9(\mu\text{-}H_2O)_2(L_2)_6(L_2H)_4(H_2O)_2](ClO_4)_2{\cdot}2MeOH{\cdot}18H_2O$ using this approach, affording a J_1 value of -5.27 cm^{-1} (g fixed at 2.2). However, that was not the case for $[Ni(II)_7(L_1H)_8(L_1)_2(H_2O)_6]SO_4{\cdot}15H_2O$ and so two J-values were required. To this end, J_1 described the Ni(II)–O–Ni(II) magnetic pathways while the J_2 parameter described the more elaborate Ni(II)–O–N–Ni(II) bridges. Applying this model gave rise to the best-fit parameters $J_1 = +0.64$ cm^{-1} and $J_2 = -8.94$ cm^{-1} (g fixed to 2.2) (Fig. 20c).

4.3 Inverse Metallacrowns and Inverse Crown Ether Complexes

Attention now turns to a family of complexes that are structurally related to metallacrowns in the form of inverse metallacrowns and Inverse Crown Ether (ICE) complexes. More specifically, inverse metallacrowns simply possess metal ions that are oriented towards the centre of the molecule (a position favoured by O and N-donor atoms in traditional metallacrowns). Inverse Crown Ether complexes, on the other hand, possess the exact opposite arrangement to classic crown ethers with respect to their Lewis acidic and Lewis basic sites (see Sect. 6.4.6).

4.4 Triple Decker Inverse 12-MC$_{\text{Cu(I)-pz}}$-4 Azametallacrowns

In 2017, Guo and co-workers developed the solvothermal synthesis (DMF/EtOH (v/v—1:5); 160 °C) of a family of triple-decker complexes of general formula $\{(MX)_2[Cu(I)_4(pz)_4]_3\}$ (MX = NaCl, NaBr, NaI, KCl, KBr, KI and Hpz = 4-nitropyrazole) [48]. Each complex comprises three $[Cu(I)_4(pz)_4]$ inverse 12-MC$_{\text{Cu(I)-pz}}$-4 azametallacrown units connected into the triple layered array via incorporated halide anions (X = Cl, Br and I) and represent rare examples of metallacrown based multi-decker architectures [46a, 49]. The $\{Cu(I)_4(pz)_4\}$ inverse azametallacrown units comprise four Cu(I) centres arranged into a square-motif through four singly deprotonated μ-bridging pz$^-$ ligands (Fig. 21a) to forge the required –[Cu–N–N]$_n$- linkages. The halide anions sit in-between the inverse azametallacrown units and are held in position through six weak Cu(I)$\cdots$X interactions (e.g. Cu(I)$\cdots$Cl distances in $[(NaCl)_2[Cu(I)_4(pz)_4]_3]$ lie in the 2.593(2)–2.920(3) Å range) and give rise to T-shaped three coordinate geometries at the metal centres (Fig. 21b, c). The charge balancing M$^+$ (M = Na, K) cations lie at the periphery of the structures.

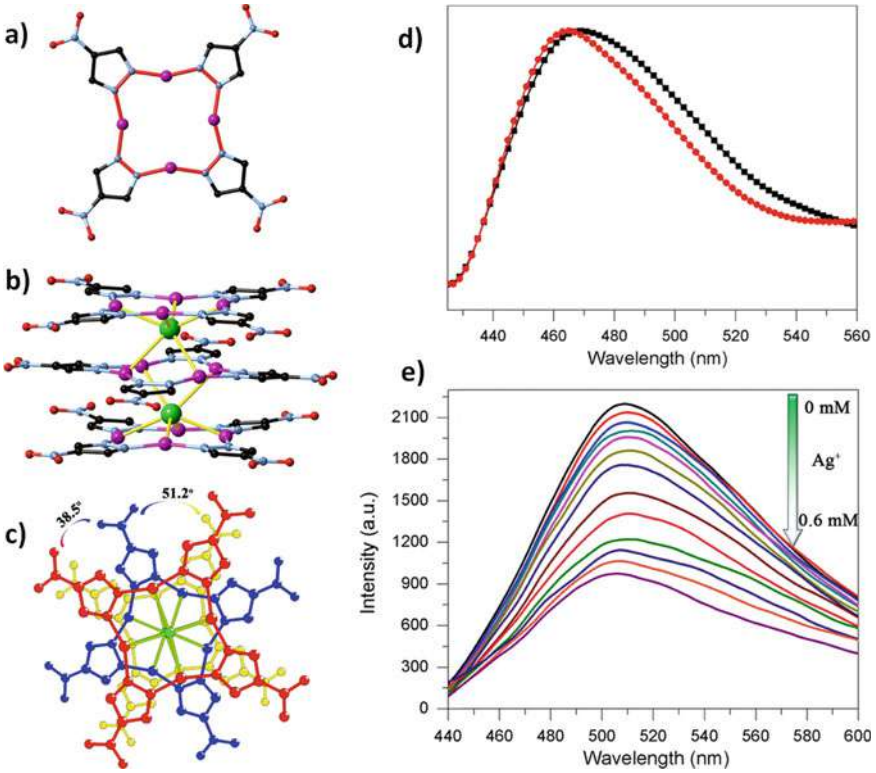

Fig. 21 **a** Crystal structure of the $\{Cu(I)_4(pz)_4\}$ inverse azametallacrown core. Side-on view (**b**) and top view (**c**) of the triple-decker structure comprising three azametallacrowns sandwiched by two Cl^- ions (green spheres). Colour codes: purple (Cu), red (O), light blue (N), Cl (green) and black (C). **d** Solid-state PL spectra of $\{(KI)_2[Cu(I)_4(pz)_4]_3$ (red line) and 4-nitropyrazole (Hpz; black line). **e** Solution state PL studies of $\{(KI)_2[Cu(I)_4(pz)_4]_3$ when introduced to different aqueous concentrations of Ag^+ (0.05 (top), 0.10, 0.15, 0.20, 0.25, 0.30, 0.35. 0.40, 0.45, 0.50, 0.55 and 0.60 mM (bottom)). Figures reproduced with permission from [48]. Copyright 2017 American Chemical Society

After preliminary solid-state measurements were conducted (Fig. 21d), solution state luminescence studies were carried out on $[(KI)_2[Cu(I)_4(pz)_4]_3]$ in order to probe any potential fluorescence sensing properties. It was found that emission intensities decreased linearly upon increasing Ag^+ addition (0 to 0.6 mM) with a limit-of-detection (LOD) of 114 μM (Fig. 21e). Similar studies on analogues $[(KCl)_2[Cu(I)_4(pz)_4]_3]$ and $[(KBr)_2[Cu(I)_4(pz)_4]_3]$ also showed promising Ag^+ detection with LODs of 65.6 and 74.4 μM, respectively. Using cyclic voltammetry studies, all three of these complexes were also found to be excellent electrocatalysts for the reduction of nitrile.

4.5 An Inverse 9-$MC_{Cu(II)}$-3 Metallacrown as Host to an Anti-Inflammatory

Investigations into the Cu(II) coordination chemistry of the ligand phenyl 2-pyridyl ketoxime (PhPyCNOH) by Tarushi and co-workers initially produced the complex $[Cu(II)_3(\mu_3\text{-}O)(PhPyCNO)_3(NO_3)]_2$ (Fig. 22a) [50]. The inorganic core in this hexametallic complex comprises two fused $\{Cu(II)_3(\mu_3\text{-}O)(PhPyCNO)_3(NO_3)\}$ units where the singly deprotonated oxime ligands bridge the Cu(II) centres via the $\eta^1{:}\eta^1{:}\eta^1$ μ-bonding motif. Furthermore, a single $\mu_3\text{-}O^{2-}$ anion sits in the centre of the moiety while also providing a longer contact to the second $\{Cu(II)_3\}$ unit (Cu–O ~2.29 Å). A single NO_3^- anion sits on one face of each triangular unit and satisfies charge balancing requirements. The result in a topological sense is the formation of an inverse 9-$MC_{Cu(II)}$-3 motif, where the metal centres of the repeating –[Cu–N–O–]$_n$– units are oriented towards the centre of the cavity. Indeed, this topology has been observed in a large family of structurally related $[Mn(III)_3]$ [51] and $[Mn(III)_6]$ [52] Single-Molecule-Magnets, themselves constructed using various functionalised salicylaldoxime ligands. Interestingly and as predicted, the anti-inflammatory sodium diclofenac (diclH) was readily incorporated into the 9-$MC_{Cu(II)}$-3 framework in the form of the single-tiered complex $[Cu(II)_3(\mu_3\text{-}OH)(PhPyCNO)_3(dicl)_2]\cdot MeOH\cdot 0.5H_2O$ (Fig. 22b). In this complex a $\mu_3\text{-}OH^-$ lies at the centre of the $\{Cu(III)_3\}$ core and partakes in hydrogen bonding with the two singly bound diclofenate ligands situated above and below the metallacrown unit. An intramolecular H-bond is observed between the proton of the central $\mu_3\text{-}OH^-$ ion (H51O) and the juxtaposed unbound carboxylate oxygen atom (O32) at a distance of 1.97 Å. Indeed this same O atom along with its equivalent located on the other side of the $\{Cu(II)_3\}$ core (O41) partake in intra-ligand H-bonding with nearby imino groups at a distances of 2.19 Å (N31(H31N)$\cdots$O32) and 2.33 Å (N41(H41N)$\cdots$O41) (Fig. 22b).

Variable temperature magnetic susceptibility ($\chi_M T$ vs. T) studies on $[Cu(II)(\mu_3\text{-}OH)(PhPyCNO)_3(dicl)_2]$ $MeOH\cdot 0.5H_2O$ indicated significant intramolecular antiferromagnetic exchange between the three Cu(II) centres. Attempts at fitting these data using both a $1 \times J$-model (assuming an equilateral triangular $\{Cu(II)_3\}$ array) and a $2 \times J$-model (assuming an isosceles triangular $\{Cu(II)_3\}$ motif) were deemed unsatisfactory with emphasis on the lower temperature region (Fig. 22c, d). An alternative model incorporating antisymmetric exchange terms was successfully employed to fit the low temperature magnetic susceptibility and magnetisation data, giving the following parameters: $g_{xy} = g_z = 2.0$ (fixed), $G = 28(1)$ cm^{-1}, $\delta = 32(1)$ cm^{-1} (TIP $= 120 \times 10^{-6}$ emu mol^{-1}) (Eq. 4). EPR studies confirmed the triangular $\{Cu(II)_3\}$ motif was retained in solution and highlighted the presence of isosceles (or lower) magnetic symmetry as well as confirming the presence of antisymmetric exchange through the observed g_{eff} values of 1.17 and 1.78.

$$\hat{H} = -2J_{12}\left(\hat{S}_1 \cdot \hat{S}_2\right) - 2J_{13}\left(\hat{S}_1 \cdot \hat{S}_3\right) - 2J_{23}\left(\hat{S}_2 \cdot \hat{S}_3\right) \quad (3)$$

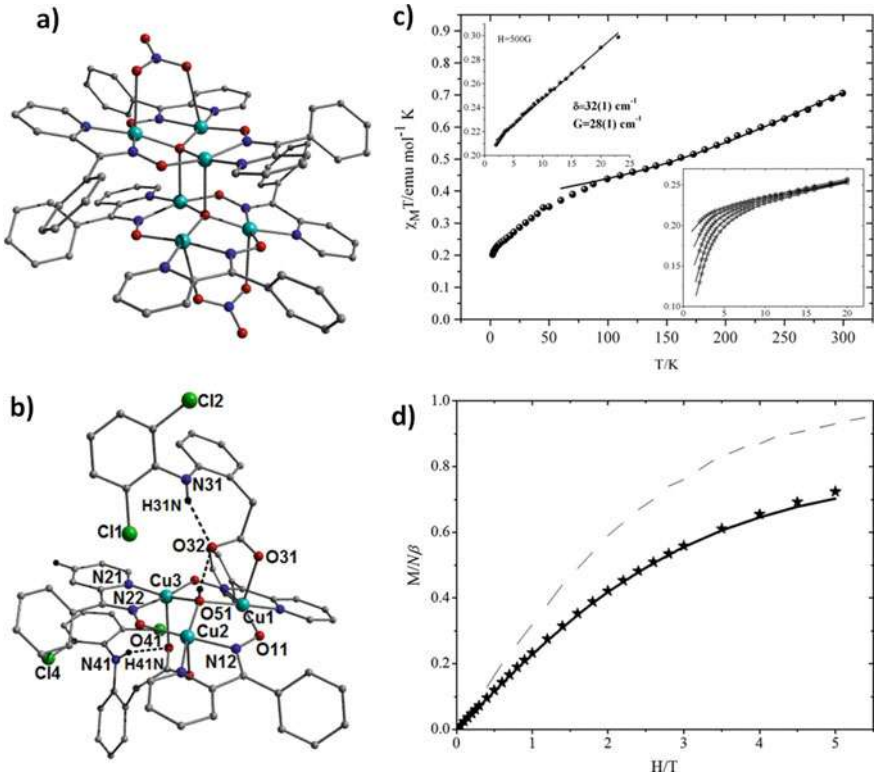

Fig. 22 Crystal structures of the inverse 9-$MC_{Cu(II)}$-3 metallacrowns $[Cu(II)_3(\mu_3\text{-}O)(PhPyCNO)_3(NO_3)]_2$ (**a**) and $[Cu(II)(\mu_3\text{-}OH)(PhPyCNO)_3(dicl)_2]\cdot MeOH\cdot 0.5H_2O$ (**b**). Colour codes: light blue (Cu), dark blue (N), red (O), green (Cl) and grey (C). Dashed lines represent intramolecular H-bonding (N31(H31N)···O32 = 2.19 Å; N41(H41N)···O41 = 2.33 Å and O51(H51O)···O32 = 1.97 Å). **c** Main figure: Variable magnetic susceptibility ($\chi_M T$) versus field studies on $[Cu(II)(\mu_3\text{-}OH)(PhPyCNO)_3(dicl)_2]\,MeOH\cdot 0.5H_2O$ (•). The solid line represents the fitting results described in the main text (Eq. 3). Upper-inset: Low temperature fitting (solid lines) of $\chi_M T$ versus T data at 500 G. The solid lines represent the line of best-fit using the spin-Hamiltonian in Eq. 4. Lower-inset: Fitting (solid lines) of the low temperature $\chi_M T$ versus T data at various external magnetic fields (1.0, 2.0, 3.0, 4.0 and 5.0 T). The solid line of fit obtained using the spin-Hamiltonian in Eq. 4. **d** Magnetisation data for $[Cu(II)(\mu_3\text{-}OH)(PhPyCNO)_3(dicl)_2]\,MeOH\cdot 0.5H_2O$ (0–6.5 T field range) at a temperature of 2 K. The dotted line represents the brillouin function for a $S_T = ½$ system with $g = 2.00$. The solid line represents the product of a modified magnetisation formula with incorporated antisymmetric terms. Figures reproduced with permission from [50]. Copyright 2016 John Wiley and Sons

$$\begin{aligned}\hat{H} = &-2J_0\left(\hat{S}_1\cdot\hat{S}_2+\hat{S}_2\cdot\hat{S}_3\right)-2J_1\left(\hat{S}_1\cdot\hat{S}_3\right)\\ &+G\left(\left[\hat{S}\cdot\hat{S}_2\right]+\left[\hat{S}_2\cdot\hat{S}_3\right]+\left[\hat{S}_3\cdot\hat{S}_1\right]\right).\\ &+g_z\cos\theta+\left(g_{xy}\sin\theta\right)\beta\hat{H}\left(\hat{S}_1+\hat{S}_2+\hat{S}_3\right).\end{aligned}\tag{4}$$

where J_0 and J_1 = isotropic exchange interactions (due to symmetry lowering); G = antisymmetric exchange vector parameter for a two-centre interaction (for more extensive detail please refer to reference 50).

UV-spectroscopy, viscosity measurements, cyclic voltammetry and competitive binding studies (with ethidium bromide (EB) intercalator) on $[Cu(II)_3(\mu_3\text{-}O)(PhPyCNO)_3(NO_3)]_2$ and $[Cu(II)_3(\mu_3\text{-}OH)(PhPyCNO)_3(dicl)_2]$ $MeOH{\cdot}0.5H_2O$ in conjunction with CT (Calf Thymus) DNA were indicative of strong binding through intercalation [50]. Both complexes also demonstrated binding with both Bovine Serum Albumin (BSA) and Human Serum Albumin (HSA) with binding constants of $1.22(\pm0.08) \times 10^5$ and $1.11(\pm0.07) \times 10^5$ M^{-1} ($[Cu(II)_3]_2$) and $2.16(\pm0.10) \times 10^5$ and $2.46(\pm0.15) \times 10^5$ ($[Cu(II)_3]$), respectively. These values were found to be commensurate with previously reported metal-NSAIDs (NSAID = non-steroidal anti-inflammatory drug) complexes and strongly suggested that the presence of the metallacrown topology did not significantly affect binding affinity towards biomolecules.

4.6 Inverse Crown Ether Complexes and Their Solid-State Hosting Abilities

This section focuses on the seminal work of Mulvey and co-workers centred on the design and synthesis of a novel family of organometallic complexes that were coined Inverse Crown Ether (ICE) complexes. These complexes were named as such due to the reversal of the roles normally observed in crown ethers. More specifically, inverse crown ether complexes each comprise s-block metal centres within their ring structures and these motifs capture O, C or H containing anions at its core (Fig. 23), as opposed to the reverse scenario within traditional crown ether complexation. Mulvey and his team went on to show how other metals could be integrated into these ring systems along with their remarkable ability to deprotonate a range of organic guest substrates such as arenes and metallocenes (*vida infra*). We will begin with the discovery that under the correct circumstances, inverse crown ether complexes are effective oxygen scavengers.

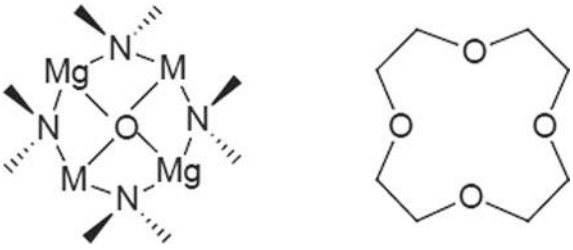

Fig. 23 (**Left**) Generalised structure of an Inverse Crown Ether complex. (**Right**) A schematic of the [12]-crown-4 crown ether. Figure reproduced with permission from [55]. Copyright 1999 Royal Society of Chemistry

4.6.1 Oxide and Peroxide Accommodating Inverse Crown Ether Complexes

In 1998, Kennedy and co-workers documented the elegantly deliberate introduction of molecular oxygen within the inverse crown ether complexes [(O)′ $Li(I)_2Mg(II)_2(tmp)_4$] (tmp = 2,2,6,6-tetramethylpiperidine) (Fig. 24a) and [$(O_2)_x(O)_y$′ $Na(I)_2Mg(II)_2(hmds)_4$] ($x = 0.68$ and $y = 0.32$; hmds = 1,1,1,3,3,3-hexamethyldisilazane) [53]. In both cases a near planar 8-MC-4 inverse crown topology has been formed by alternating Li(I)/Na(I) and Mg(II) metal centres connected through four amine ligands. These cationic $\{Li(I)_2Mg(II)_2(tmp)_4\}^{2+}$ and $\{Na(I)_2Mg(II)_2(hmds)_4\}^{2+}$ cores achieve charge neutrality by accommodating the guest oxide/peroxides. This work was rapidly followed by the synthesis of the analogue complex [$(O_2)_x(O)_y$′ $Li(I)_2Mg(II)_2(hmds)_4$] ($x = 0.715(7)$ and $y = 0.285(7)$), obtained from the dinuclear [Li(I)Mg(II)$(hmds)_3$] starting material [54]. The following year (1999), Kennedy and co-workers expanded on this family of complexes by introducing K^+ metal centres within the inverse crown ether core in the form of the 8-MC-4 inverse crown coordination polymer [(O_2)′ $K(I)_2Mg(II)_2(hmds)_4]_\infty$ [55]. The octagonal rings comprising an alternating $\{K(I)\text{-}N\text{-}Mg(II)\text{-}N\}_2$ topology connect through four singly deprotonated μ-bridging $hmds^-$ ligands and surrounds distorted square planar peroxide guest molecules. The individual {(O_2)′ $K(I)_2Mg(II)_2(hmds)$} units are connected into 1-D chains through intermolecular $K\cdots CH_3(SiMe_2)$ interactions.

In 2008, the Mulvey group further expanded on this family of inverse crown ether complexes by successfully incorporating the first transition metal ions (in place of the Mg(II) centres observed in previous analogues) into their inorganic core topology in the form of [(O)′ $Li(I)_2Mn(II)_2(tmp)_4$] as shown in Fig. 24b [56]. Attempts at synthesising the Na(I) analogue to this structure were fruitless until the ligand tmp was replaced with 1,1,1,3,3,3-hexamethyldisilazane (hmds) to give the inverse crown ether complex [(O)′ $Na(I)_2Mn(II)_2(hmds)_4$]. The analogous structures in [(O)′ $Li(I)_2Mn(II)_2(tmp)_4$] and [(O)′ $Na(I)_2Mn(II)_2(hmds)_4$] exhibit the now familiar near planar octagonal 8-MC-4 inverse crown ether topologies comprising alternating M(I) (M = Li(I) and Na(I)) and Mn(II) ions whose metal centres are connected by μ-bridging tmp^- and $hmds^-$ ligands, respectively. In both cases the eight membered rings surround a guest oxide (O^{2-}) anion of distorted square planar geometry to give M–O (M = Na(I) and Li(I)) bond distances of 1.9334(6) and 2.3262(6) Å, respectively and Mn(II)–O bond distances of 1.9368(3) and 1.9272(2) Å, respectively.

4.6.2 *Metal Anionic Crowns (MACs): Anionic Inverse Crown Ether Complexes*

These findings further piqued interest in such complexes and swiftly resulted in the introduction of a new sub-class of ICE complex in the form of the anionic Metal Anionic Crowns (MACs). More specifically, it was found that reaction of *n*-Butylsodium, hmds and (−)-spartene gave rise to the rather surprising

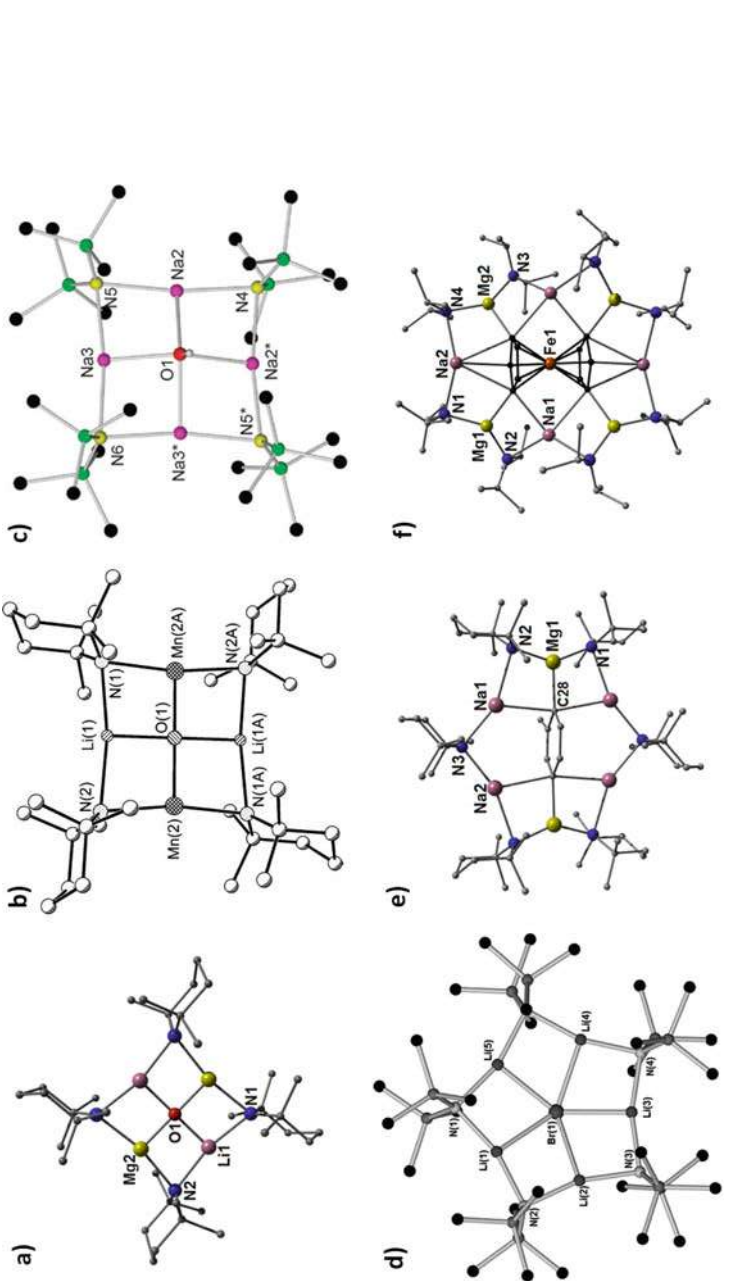

Fig. 24 Crystal structures of the Inverse Crown Ether complexes **a** [(O) ⁄ $Li(I)_2Mg(II)_2(tmp)_4$]; **b** [(O) ⁄ $Li(I)_2Mn(II)_2(tmp)_4$]; **c** [(−)-sparteine$Na(I)(hmds)Na(-)$-sparteine)](OH) ⁄ $Na(I)_4(hmds)_4$]; **d** [{2(R,R)-tmcda}Li(I)][Br ⁄ $Li(I)_5(hmds)_5$]; **e** [$(C_6H_3CH_3)$ ⁄ $(Na(I)_4\ Mg(II)_2(tmp)_6$] and **f** [{$Fe(C_5H_3)_2$} ⁄ $Na(I)_4Mg(II)_4\{^iPr_2N\}_8$]. Figure **a** reproduced with permission from [53]. Copyright 1998 John Wiley and Sons. Figure **b** obtained with permission from [56]. Copyright 2008 Royal Society of Chemistry. Figure **c** obtained with permission from [57]. Copyright 2009 Royal Society of Chemistry. Figure **d** reproduced with permission from [58]. Copyright 2011 John Wiley and Sons. Figure **e** reproduced with permission from [59]. Copyright 1999 John Wiley and Sons. Figure **f** reproduced with permission from [65]. Copyright 2004 American Chemical Society

(but entirely reproducible) species $[Na(I)_2(hmds)((-)\text{-sparteine})_2][(OH)\ /\ Na(I)_4(hmds)_4]$ (Fig. 24c) [57]. The $[Na(I)_2(hmds)((-)\text{-sparteine})_2]^+$ cation comprises two $\{Na(I)((-)\text{-spartene})\}^+$ units connected through a single μ-bridging $hmds^-$ moiety. Each Na(I) centre exhibits distorted trigonal planar geometries. The charge balancing $[(OH)\ /\ Na(I)_4(hmds)_4]^-$ anion comprises a near perfectly planar 8-MC-4 inverse crown ether topology giving rise to a $Na(I)_4N_4$ ring and stabilised through μ-bridging $hmds^-$ ligands. Within this inorganic core lies a disordered OH^- guest anion, held in position through Na–O bonds with mean distance of 2.336 Å. In a similar vein, 2011 saw Kennedy and co-workers subsequently demonstrate through a variety of synthetic pathways the successful encapsulation of both Cl^- and Br^- anions within the lithium lithiate MACs $[\{2(R,R)\text{-tmcda}\}Li(I)][Cl\ /\ Li(I)_5(hmds)_5]$, $[Li(I)_2(\mu\text{-Cl})(Me_6\text{-tren})_2][Cl\ /\ Li(I)_5(hmds)_5]$ and $[\{2(R,R)\text{-tmcda}\}Li(I)][Br\ /\ Li(I)_5(hmds)_5]$ (hmds = 1,1,1,3,3,3-hexamethyldisilazide; tmcda = N,N,N′,N′-(1R,2R)-tetramethylcyclohexane-1,2-diamine; Me_6-tren = tris[2-dimethylamino)ethyl]amine) [58]. As demonstrated in Fig. 24d, each member exhibits a star shaped near planar $\{Li(I)_5(\mu\text{-hmds})_5\}$ ring that surround their five coordinate halide guests. Interestingly and presumably due to size considerations, the bromine atom in $[\{2(R,R)\text{-tmcda}\}Li(I)][Br\ /\ Li(I)_5(hmds)_5]$ was found to sit 0.4 Å above the planar Metal Anionic Crown. Attempts at I^- incorporation instead gave rise to the coordination polymer $[\{Li(I)_2(_\mu\text{-hmds})_2\}\{Li(I)_2(\mu\text{-}I)_2(R,R)\text{-tmcda}\}_2]_\infty$, whose $\{Li(I)_2(_\mu\text{-hmds})_2\}$ and $\{Li(I)_2(\mu\text{-}I)_2(R,R)\text{-tmcda}\}$ units are connected through Li···I intermolecular interactions.

4.6.3 Site Selective Deprotonation of Arene Guest Moieties Accommodated Within Cationic Inverse Crown Ether Complex Hosts.

In further developments upon this theme, Armstrong and co-workers discovered that the combination of *n*BuNa, Bu_2Mg and 2,2,6,6-tetramethylpiperidide (tmp) (1:1:3) gave rise to a 12-membered cationic $[(Na(I)_4Mg(II)_2(tmp)_6]^{2+}$ host complex that was able to template the site selective double deprotonation of guest benzene ($[C_6H_4]^{2-}$) and toluene ($[C_6H_3CH_3]^{2-}$) moieties (added in excess) to give a new family of inverse crown ether complexes in the form of $[(C_6H_4)\ /\ (Na(I)_4Mg(II)_2(tmp)_6]$ and $[(C_6H_3CH_3)\ /\ (Na(I)_4Mg(II)_2(tmp)_6]$ (Fig. 24e) [59]. Close scrutiny of these crystal structures showed a severely distorted 12-atom $\{N_6Na(I)_4Mg(II)_2\}^{2+}$ core topology with a single guest arene sitting approximately perpendicular to the mean plane of the ring structure and bound at the 1,4-positions through four Na-C bonds (including 2 × π bonds) and two Mg-C bonds (effectively replacing the C–H bonds stripped from the guests upon their metalation) (Fig. 24e). This discovery was rapidly followed by the synthesis of an unprecedented 24 membered $[(KNMgN)_6]^{6+}$ ring structure that remarkably was shown to houses six singly deprotonated benzene ($[C_6H_5]^-$) and toluene ($[C_6H_4CH_3]^-$) guests in the form of the complexes $[(C_6H_5)_6\ /\ K(I)_6Mg(II)_6(tmp)_{12}]$ and $[(C_6H_4CH_3)_6\ /\ K(I)_6Mg(II)_6(tmp)_{12}]$, respectively [60]. Due to the sheer size of this cyclic structure, each guest moiety lies away from the central

cavity and is held in position by a combination of ispo Mg-C σ bonds and K-C π bonding interactions.

In 2007, Carella and co-workers successfully replaced the Mg(II) ions in the previously reported inverse crown ether complex $[(C_6H_4)\prime\ (Na(I)_4Mg(II)_2(tmp)_6]$ with paramagnetic Mn(II) centres to produce the analogous complex $[(C_6H_4)\prime\ Na(I)_4Mn(II)_2(tmp)_6]$. This complex represented the first example of transition metal incorporation within the host unit of an inverse crown ether complex [61]. These findings were further exploited by Alborés and co-workers with the successful inclusion of Cr(II) and Fe(II) centres within the inverse crown ether complexes $[(C_6H_4)Na(I)_4Cr(II)_2(tmp)_6]$ and $[(C_6H_4)Na(I)_4Fe(II)_2(tmp)_6]$ (Fig. 25a) [62]. Akin to previous inverse crown complexes housing arene guest anions, in all three cases the doubly deprotonated $[C_6H_4]^{2-}$ guest lie approximately orthogonal to the plane of the inverse crown ether host unit and are locked into position through both M-C (M = Cr(II), Mn(II) and Fe(II)) and Na-C bonding interactions located at the 1,4-arene carbon sites.

Variable temperature magnetic susceptibility ($\chi_M T$) measurements on complexes $[(C_6H_4)\prime\ Na(I)_4Mn(II)_2(tmp)_6]$, $[(C_6H_4)\prime\ Na(I)_4Fe(II)_2(tmp)_6]$ and $[(C_6H_4)\prime\ Na(I)_4Cr(II)_2(tmp)_6]$ each showed a decreasing $\chi_M T$ product with decreasing temperature indicative of varying degrees of antiferromagnetic exchange between the paramagnetic transition metal centres. Fitting of the magnetic data using the spin-Hamiltonian given in Eq. 5 gave rise to the magnetic exchange parameters $J = -0.70\ cm^{-1}$ ($[(C_6H_4)\prime\ Na(I)_4Mn(II)_2(tmp)_6]$), $-2.28\ cm^{-1}$ ($[(C_6H_4)\prime\ Na(I)_4Fe(II)_2(tmp)_6]$) and $-12.09\ cm^{-1}$ ($[(C_6H_4)\prime\ Na(I)_4Cr(II)_2(tmp)_6]$) (Fig. 25c).

The stronger antiferromagnetic coupling between the Cr(II) ions in $[(C_6H_4)\prime\ Na(I)_4Cr(II)_2(tmp)_6]$ was attributed to the stronger overlap between the magnetic orbitals and the benzene orbitals as confirmed using DFT calculations [62].

$$\hat{H} = -2J\left(\hat{S}_1 \cdot \hat{S}_2\right) \tag{5}$$

$\left(\hat{S}_1 = \hat{S}_2 = 5/2\right)$ when M = Mn(II); $\hat{S}_1 = \hat{S}_2 = 2$ when M = Fe(II) and Cr(II).

4.6.4 Pre-Inverse Crowns as Templates Towards Inverse Crown Ether Complex Formation

In 2014, Martínez-Martínez and co-workers successfully synthesised the monoalkylbisamido magnesiates $[Na(I)Mg(II)(tmp)_2{}^nBu]$ and $[K(I)Mg(II)(tmp)_2{}^nBu]$ in a solvent free crystalline form [63]. Moreover, the latter was found to exist in three polymorphic forms (depending on hydrocarbon solvent employed). Namely, a helical polymer with an infinite −K–N–Mg–N− chain, a tetramer comprising a 16-atom $(K(I)NMg(II)N)_4$ ring and a related hexameric 24-atom $(K(I)NMg(II)N)_6$ ring structure. Both magnesiates were found to dissolve in hydrocarbon solvents and devoid of solvent ligation and were therefore likely candidates as precursors to inverse

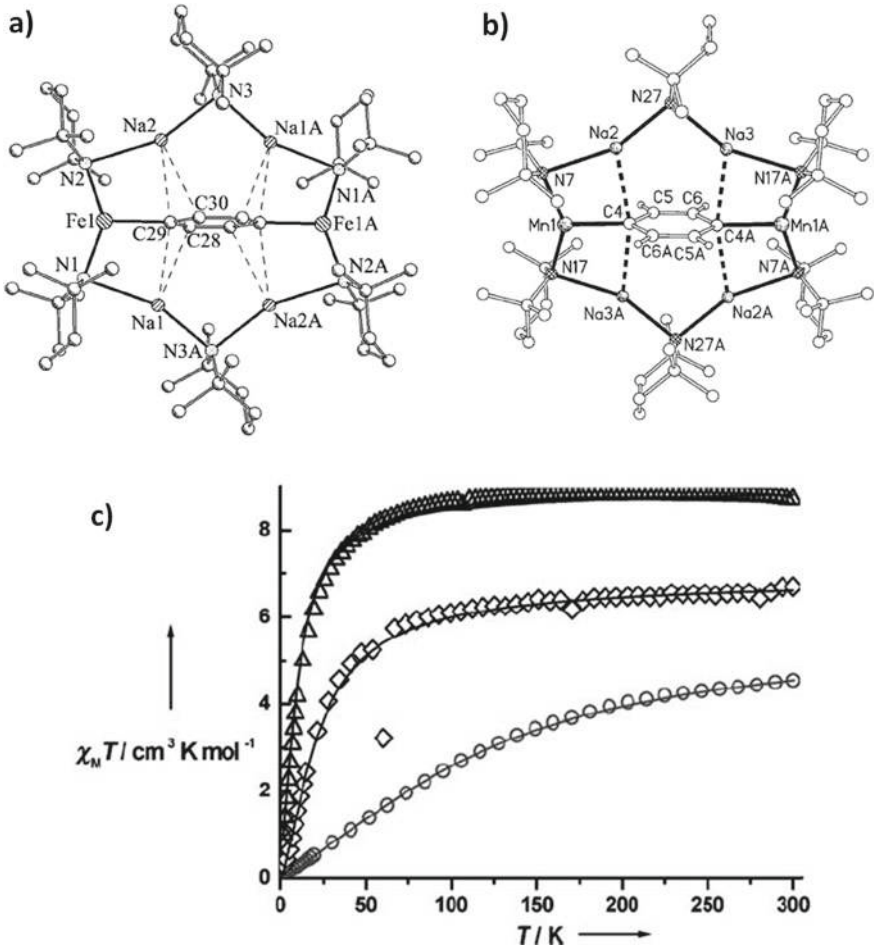

Fig. 25 Crystal structures of **a** $[(C_6H_4)\prime\ Na(I)_4Fe(II)_2(tmp)_6]$ and **b** $[(C_6H_4)\prime\ Na(I)_4Mn(II)_2(tmp)_6]$. **c** Magnetic susceptibility ($\chi_M T$) vs. temperature (K) plots obtained from polycrystalline samples of $[(C_6H_4)\prime\ Na(I)_4Mn(II)_2(tmp)_6]$ (**Δ**), $[(C_6H_4)Na(I)_4Fe(II)_2(tmp)_6]$ (⋄) and $[(C_6H_4)Na(I)_4Cr(II)_2(tmp)_6]$ (○). The solid lines represent the best-fit of the magnetic data. Figures **a** and **c** reproduced with permission from [62]. Copyright 2009 John Wiley and Sons. Figure **b** reproduced with permission from [61]. Copyright 2007 John Wiley and Sons

crown ether complexes. This was indeed found to be the case when reaction of $[Na(I)Mg(II)(tmp)_2{}^nBu]$ and $[K(I)Mg(II)(tmp)_2{}^nBu]$ with benzene and toluene each gave previously obtained inverse crown ether complexes ($[(C_6H_3R)_6\prime\ Na(I)_4Mg(II)_2(tmp)_6]$ and $[(C_6H_3R)_6\prime\ K(I)_6Mg(II)_6(tmp)_{12}]$ (R = H, Me) using a much improved procedure and enhanced yields, thus supporting the premise that metalation was enhanced via the template effect. Moreover, the reaction of both magnesiates with naphthalene ($[C_{10}H_8]$) gave rise to the entirely new complexes $[(2\text{-}C_{10}H_7)_6\prime\ K(I)_6Mg(II)_6(tmp)_{12}]$ and $[(1,4\text{-}C_{10}H_6)\prime\ Na(I)_4Mg(II)_2(tmp)_4(tthp)_2]$ (tthp

= 2,2,6-trimethyl-1,2,3,4-tetrahydropyridide), respectively. Representing the first naphthalene-based inverse crown complex, the structure in $[(2\text{-}C_{10}H_7)_6 \prime K(I)_6 Mg(II)_6(tmp)_{12}]$ (Fig. 26a, b) comprises a macrocyclic 24-atom $\{K(I)NMg(I)N\}_6$ ring system whose puckered nature allows extensive interaction with the singly deprotonated (and thus metalated at the 2-position) $[C_{10}H_7]^-$ guests bound to a single Mg(I) centre and held in position through a number of π-interactions with juxtaposed K(I) metal sites. The structure in $[(1,4\text{-}C_{10}H_6) \prime Na(I)_4Mg(II)_2(tmp)_4(tthp)_2]$ (Fig. 25c) is entirely different to that of its K(I) analogue. Here a 12-atom

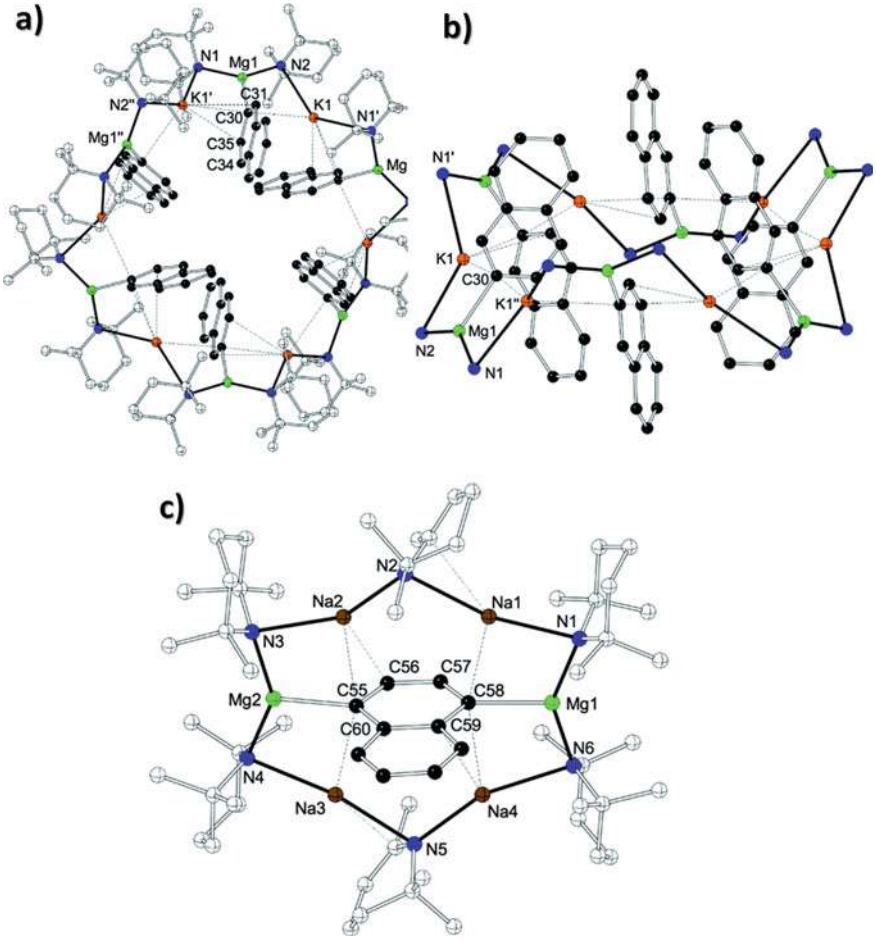

Fig. 26 Crystal structures of the inverse crown complexes $[(2\text{-}C_{10}H_7)_6 \prime K(I)_6Mg(II)_6(tmp)_{12}]$ (**a** and **b**) and $[(1,4\text{-}C_{10}H_6) \prime Na(I)_4Mg(II)_2(tmp)_4(tthp)_2]$ (**c**). Colour code: orange (K), brown (Na), lime green (Mg), blue (N), red (O), green (Cl) and black/colourless (C). The dashed lines in figures **a** and **b** represent K···C interactions. The dashed lines in **c** illustrate Na···C interactions. Figures were reproduced with permission from [63]. Copyright 2014 Royal Society of Chemistry

$\{Na(I)_4Mg(II)_2N_6\}^{2+}$ cyclic structure is forged through a combination of μ-bridging tmp^- and $tthp^-$ ligands, the latter being formed in-situ (and reproducibly) through the loss of methane from two of the six amide (tmp^-) ligands. Once again, the guest naphthalene units (this time unexpectedly doubly deprotonated at the 1,4-positions) lie orthogonal to the host architecture and partakes in a number of Na-C π-bonds (bond range: 2.674–3.265 Å) and Mg-C σ-bonds (mean distance = 2.220 Å) to stabilise the resultant structure.

4.6.5 Selective Deprotonation and Tetrametalation of Metallocene Guests Within Host Inverse Crown Ether Complexes

Using the sterically demanding diisopropylamine ($^iPr_2N$) ligand instead of 1,1,1,3,3,3-hexamethyldisilazide (hmds) or 2,2,6,6-tetramethylpiperidine (tmp), Mulvey and co-workers demonstrated how the cationic 16-MC-8 inverse crown $[Na(I)_4Mg(II)_4(^iPr_2N)_8]^{4+}$ was able to encapsulate metallocene derived $[M(II)(C_5H_3)_2]^{4-}$ (M = Fe, Ru, Os) guest moieties in the guise of the siblings: $[\{M(C_5H_3)_2\}\prime\ Na(I)_4Mg(II)_4(^iPr_2N)_8]$ (M = Fe(II), Co(II), Os(II)) (Fig. 24f) [64]. The severely puckered host inverse crown ether unit is forged through an alternating array of Na(I) and Mg(II) ions separated and connected through eight singly deprotonated μ-bridging $^iPr_2N^-$ ligands. Interestingly, the incorporation of the guest metallocenes represented a new, effective and controlled route towards regioselective tetrametalation through their exclusive deprotonation at the 1, 1′, 3 and 3′ cyclopentandienyl (Cp) positions. The Cp rings of the guest metallocenes lie perpendicular to the plane of the $[Na(I)_4Mg(II)_4(^iPr_2N)_8]^{4+}$ inverse crown hosts and are held in position through a number of M-C (M = Na(I), Mg(II)) interactions with mean bond lengths of 2.670 Å and 2.153 Å, respectively [65]. Interestingly and unlike the benzene and toluene containing inverse crowns (e.g. $[(C_6H_5)\prime\ K(I)_6Mg(II)_6(tmp)_{12}]$ and $[(C_6H_4CH_3)\prime\ K(I)_6Mg(II)_6(tmp)_{12}]$), the Mg-C bonds in $[\{Fe(C_5H_3)_2\}\prime\ Na(I)_4Mg(II)_4(^iPr_2N)_8]$ were found to tilt away from the plane of the aromatic ring at angles of 63.1° and 58.4° for the two independent Mg–C bonds. NMR studies on all siblings confirmed solution stability in arene solvents, while further variable temperature measurements indicated the existence of two distinct interconverting conformers ('Z' ↔ 'W' shaped). 2-D [^{1}H, ^{1}H] Exchange NMR spectroscopy (EXSY) studies clearly demonstrated that slow exchange took place in each solution with exchange rates (at 300 K) of 0.4 ± 0.1 s^{-1} in $[\{Fe(C_5H_3)_2\}Na(I)_4Mg(II)_4(^iPr_2N)_8]$ (forward and reverse had the same rate); 0.32 ± 0.04 s^{-1} (minor to major) and 0.12 ± 0.01 s^{-1} (major to minor) in $[\{Ru(C_5H_3)_2\}Na(I)_4Mg(II)_4(^iPr_2N)_8]$); 0.45 ± 0.05 s^{-1} (minor to major) and 0.16 ± 0.02 s^{-1} (major to minor) in $[\{Os(C_5H_3)_2\}Na(I)_4Mg(II)_4\{^iPr_2N\}_8]$. Variable temperature ^{1}H NMR studies confirmed fluxional behaviour in all three members, giving coalescence temperatures of 370 K ($[\{Fe(C_5H_3)_2\}Na(I)_4Mg(II)_4(^iPr_2N)_8]$), 350 K ($[\{Ru(C_5H_3)_2\}Na(I)_4Mg(II)_4(^iPr_2N)_8]$) and 355 K ($[\{Os(C_5H_3)_2\}Na(I)_4\ Mg(II)_4\ (^iPr_2N)_8]$) [65].

5 Concluding Remarks

It is hoped that this chapter has successfully showcased a number of archetypal and non-archetypal metallacrowns (and azametallacrowns) as well as Inverse Crown Ether complexes, each aesthetically beautiful in their own way while crucially differing in their structural form (e.g. size, shape and topology). Indeed, it is these differences that allow such materials to possess their unique resultant properties. More specifically, these individual families are each endowed with definitive physical and electronic characteristics that allow their controlled engagement with other moieties such as guest ions and molecules (e.g. Na^+, K^+, F^-, ReO_4^-, TcO_4^-, O^{2-}, O_2^{2-}, arenes and metallocenes) or (if required) their pre-designed aggregation into extended network architectures such as 1-D and 2-D coordination polymers or oligomers comprising viable qubits towards potential Quantum Information Processing. Investigations into the enhancement and expansion of these themes continue at a pace and will no doubt produce even more novel functional and multifunctional metallacrown derived materials over the coming years.

References

1. For examples see: (a) Saalfrank, R.W., Bernt, I., Uller, E., Hampel, F.: Template-mediated self-assembly of six- and eight-membered iron coronates. Angew. Chem. Int. Ed. **36**, 2482–2485 (1997). (b) Saalfrank, R.W., Bernt, I., Hampel, F.: Metallocoronates or one-dimensional polymers through self-assembly-influence of templates and hydrogen bonding on product formation. Angew. Chem. Int. Ed. **40**, 1700–1703 (2001). (c) Saalfrank, R.F., Deutscher, C., Maid, H., Ako, A.M., Sperner, S., Nakajima, T., Bauer, W., Hampel, F., Heβ, B.A., van Eikema Hommes, N.J.R., Puchta, R., Heinemann, F.W.: Synthesis, structure, and dynamics of six-membered metallocoronands and metallodendrimers of iron and indium. Chem. Eur. J. **10**, 1899–1905 (2004)
2. (a) Meally, S.T., Karotsis, G., Brechin, E.K., Papaefstathiou, G.S. Dunne, P.W.P. McArdle, P., Jones, L.F.: Planar $[Ni_7]$ discs as double-bowl, pseudo metallocalix[6]arene host cavities. CrystEngComm. **12**, 59–63 (2010). (b) Meally, S.T., McDonald, C. Karotsis, G., Papaefstathiou, G.S., Brechin, E.K., Dunne, P.W., McArdle, P., Power, N.P., Jones, L.F.: A family of double-bowl *pseudo* metallocalix[6]arene discs. Dalton Trans. **39**, 4809–4816 (2010). (c) Meally, S.T., McDonald, C., Kealy, P., Taylor, S.M., Brechin E.K., Jones, L.F.: Investigating the solid-state hosting abilities of homo- and heterovalent $[CO_7]$ metallocalix[6]arenes. Dalton Trans. **41**, 5610–5616 (2012)
3. Jones, L.F., Kilner, C.A., de Miranda, M.P., Wolowska, J., Halcrow, M.A.: A hexacopper fluoro metallacrown cavitand and its alkali-metal complexes. Angew. Chem. Int. Ed. **46**, 4073–4076 (2007)
4. Jones, L.F., Barrett, S.A., Kilner, C.A., Halcrow, M.A.: Ammonium, alkylammonium and amino acid complexes of a hexacopper fluoro-metallacrown cavitand. Chem. Eur. J. **14**, 223–233 (2008)
5. Jones, L.F., Kilner, C.A., Halcrow, M.A.: A cobalt metallacrown anion host with guest-dependent redox activity. Chem. Eur. J. **15**, 4667–4675 (2009)
6. Overgaard, J., Iversen, B.B., Palii, S.P., Timco, G.A., Gerbeleu, N.V., Larsen, F.K.: Host-guest chemistry of the chromium-wheel complex $[Cr_8F_8(^t BuCO_2)_{16}]$: prediction of inclusion

capabilities by using an electrostatic potential distribution determined by modelling synchotron X-ray structure factors at 16 K. Chem. Eur. J. **8**, 2775–2786 (2002)
7. Vitórica-Yrezábal, I.J., Sava, D.F., Timco, G.A., Brown, M.S., Savage, M., Godfrey, H.G.W., Moreau, F., Schröder, M., Siperstein, F., Brammer, L., Yang, S., Attfield, M.P., McDouall, J.J.W., Winpenny, R.E.P.: Binding CO_2 by a Cr_8 metallacrown. Angew. Chem. Int. Ed. **56**, 5527–5530 (2017)
8. Nugent, P., Belmabkhout, Y., Burd, S.D., Cairns, A.J., Luebke, R., Forrest, K., Pham, T., Ma, S., Space, B., Wojtas, L., Eddaoudi, M., Zaworotko, M.J.: Porous materials with optimal adsorption thermodynamics and kinetics for CO_2 separation. Nature **495**, 80–84 (2013)
9. Sava, D.F., Zheng, N., Vitórica-Yrezábal, I.J., Timco, G.A., Winpenny, R.E.P.: Binding of halogens by a Cr_8 metallacrown. Dalton Trans. **47**, 13771–13775 (2018)
10. Xu, Y., Jager, W., Ozier, I., Gerry, M.C.L.: Rotational spectrum, structure, and chlorine nuclear quadrupole coupling constants of the van der Waals complex Ar-Cl_2. J. Chem. Phys. **98**, 3726–3731 (1993)
11. Huber, K.-P.: Molecular Spectra and Molecular Structure: IV. Constants of Diatomic Molecules. Springer Science & Business Media (2013)
12. Vitórica-Yrezábal, I.J., Sava, D.F., Reta, D., Timco, G.A., Winpenny, R.E.P.: Reversible uptake of sulfur-containing gases by single crystals of a Cr_8 metallacrown. Dalton Trans. **48**, 13184–13189 (2019)
13. Larsen, F.K., McInnes, E.J.L., El Mkami, H., Overgaard, J., Piligkos, S., Rajaraman, G., Rentschler, E., Smith, A.A., Smith, G.A., Boote, V., Jennings, M., Timco, G.A., Winpenny, R.E.P.: Synthesis and characterisation of heterometallic Cr7M wheels. Angew. Chem. **115**, 105–109 (2003)
14. Laye, R.H., Larsen, F.K., Overgaard, J., Muryn, C.A., McInnes, E.J.L., Rentschler, E., Sanchez, V. Teat, S.J., Güdel, H.U., Waldmann, O., Timco, G. A., Winpenny, R.E.P.: A family of heterometallic wheels containing potentially fourteen hundred siblings. Chem. Commun. 1125–1127 (2005)
15. Faust, T.B., Heath, P.G., Muryn, C.A., Timco, G.A., Winpenny, R.E.P.: Ceasium ion sequestration by a fluoro-metallacrown [16]-MC-8. Chem. Commun. **46**, 6258–6260 (2010)
16. Timco, G.A., Carretta, S., Troiani, F., Tuna, F., Pritchard, R.J., Muryn, C.A., McInnes, E.J.L., Ghirri, A., Candini, A., Santini, P., Amoretti, G., Affronte, M., Winpenny, R.E.P.: Engineering the coupling between molecular spin qubits by coordination chemistry. Nat. Nanotech. **4**, 173–178 (2009)
17. Whitehead, G.F.S., Moro, F., Timco, G.A., Wernsdorfer, W., Teat, S.J., Winpenny, R.E.P.: A ring of rings and other multicomponent assemblies of cages. Angew. Chem. **125**, 10116–10119 (2013)
18. Timco, G.A., Faust, T.B., Tuna, F., Winpenny, R.E.P.: Linking heterometallic rings for quantum information processing and amusement. Chem. Soc. Rev. **40**, 3067–3075 (2011)
19. Ferrando-Soria, J., Pineda, E.M., Chiesa, A., Fernandez, A., Magee, S.A., Carretta, S., Santini, P., Vitorica-Yrezabal, I.J., Tuna, F., Timco, G.A., McInnes, E.J.L., Winpenny, R.E.P.: A modular design of molecular qubits to implement universal quantum gates. Nat. Commun. **7**, 11377–11386 (2016)
20. Ardavan, A., Bowen, A.M., Fernandez, A., Fielding, A.J., Kaminski, D., Moro, F., Muryn, C.A., Wise, M.D., Ruggi, A., McInnes, E.J.L., Severin, K., Timco, G.A., Timmel, C.R., Tuna, F., Whitehead, G.F.S., Winpenny, R.E.P.: Engineering coherent interactions in molecular nanomagnet dimers. Quantum Inf. **1**, 15012–15018 (2015)
21. Faust, T.B., Bellini, V., Candini, A., Carretta, S., Lorusso, G., Allan, D.R., Carthy, L., Collison, D., Docherty, R.J., Kenyon, J., Machin, J., McInnes, E.J.L., Muryn, C.A., Nowell, H., Pritchard, R.G., Teat, S.J., Timco, G.A., Tuna, F., Whitehead, G.F.S., Wernsdorfer, W., Affronte, M., Winpenny, R.E.P.: Chemical control of spin propagation between heterometallic rings. Chem. Eur. J. **17**, 14020–14030 (2011)
22. Ardavan, A., Rival, O., Morton, J.J.L., Blundell, S.J., Tyryshkin, A.M., Timco, G.A., Winpenny, R.E.P.: Will spin relaxation times in molecular magnets permit quantum information processing? Phys. Rev. Lett. **98**, 057201–057204 (2007)

23. Lee, C.-F., Leigh, D.A., Pritchard, R.G., Schultz, D., Teat, S.J., Timco, G.A., Winpenny, R.E.P.: Hybrid organic-inorganic rotaxanes and molecular shuttles. Nat. Lett. **458**, 314–318 (2009)
24. Ballesteros, B., Faust, T.B., Lee, C.-F., Leigh, D.A., Muryn, C.A., Pritchard, R.G., Schultz, D., Teat, S.J., Timco, G.A., Winpenny, R.E.P.: Synthesis, structure and dynamic properties of hybrid organic-inorganic rotaxanes. J. Am. Chem. Soc. **132**, 15435–15444 (2010)
25. Fernandez, A., Ferrando-Soria, J., Pineda, E.M., Tuna, F., Vitorica-Yrezabal, I.J., Knappke, C., Ujma, J., Muryn, C.A., Timco, G.A., Barran, P.E., Ardavan, A., Winpenny, R.E.P.: Making hybrid [n]-rotaxanes as supramolecular arrays of molecular electron spin qubits. Nat. Commun. **7**, 10240–10249 (2016)
26. Lockyer, S.J., Chiesa, A., Timco, G.A., McInnes, E.J.M., Bennett, T.S., Vitorica-Yrezebal, I.J., Carretta, S., Winpenny, R.E.P.: Targeting molecular quantum memory with embedded error correction. Chem. Sci. **2**, 9104–9113 (2021)
27. Lockyer, S.J., Nawaz, S., Brookfield, A., Fielding, A.J., Vitorica-Yrezabal, I.J., Timco, G.A., Burton, N.A., Bowen, A.M., Winpenny, R.E.P., McInnes, E.J.L.: Conformational flexibility of hybrid [3]- and [4]-rotaxanes. J. Am. Chem. Soc. **142**, 15941–15949 (2020)
28. Piotrowski, H., Polborn, K., Hilt, G., Severin, K.: A self-assembled metallomacrocyclic ionophore with high affinity and selectivity for Li^+ and Na^+. J. Am. Chem. Soc. **123**, 2699–2700 (2001)
29. Piotrowski, H., Hilt, G., Schulz, A., Mayer, P., Polborn, K., Severin, K.: Self-assembled organometallic [12]metallacrown-3 complexes. Chem. Eur. J. **7**, 3197–3208 (2001)
30. Lehaire, M.-L., Scopelliti, R., Piotrowski, H., Severin, K.: Selective recognition of fluoride anion using a Li^+-metallacrown complex. Angew. Chem. Int. Ed. **41**, 1419–1422 (2002)
31. Lehaire, M.-L., Scopelliti, R., Severin, K.: Stabilisation of molecular LiF and LiFHF inside metallamacrocyclic hosts. Inorg. Chem. **41**, 5466–5474 (2002)
32. Lehaire, M.-L., Scopelliti, R. Severin, K.: Encapsulation of molecular Na_2SiF_6 by two metallacrown complexes. Chem. Commun. 2766–2767 (2002)
33. Grote, Z., Lehaire, M.-L., Scopelliti, R., Severin. K.: Selective complexation of Li^+ in water at neutral pH using a self-assembled ionophore. J. Am. Chem. Soc. **45**, 13638–13639 (2003)
34. Lehaire, M.-L., Schultz, A., Scopelliti, R., Severin, K.: Electronic effects in 12-metallacrown-3 complexes: a theoretical and experimental study. Inorg. Chem. **42**, 3576–3581 (2003)
35. Rochat, S., Grote, Z., Severin. K.: Ruthenium-based metallacrown complexes for the selective detection of lithium ions in water and in serum by fluorescence spectroscopy. Org. Biomol. Chem. **7**, 1147–1153 (2009)
36. Hynes, M. J.: J. Chem. Soc., Dalton Trans. 311–312 (1993)
37. Gao, J., Rochat, S., Qian, X., Severin, K.: A simple assay for the fluorometric detection of lithium ions in aqueous solution. Chem. Eur. J. **16**, 5013–5017 (2010)
38. Katsuta, S., Saito, Y., Takahashi, S.: Application of a lithium-ion selective metallacrown to extraction-spectrophotometric determination of lithium in saline water. Anal. Sci. **34**, 189–193 (2018)
39. Kilbas, B., Mirtschin, S., Scopelliti, R., Severin, K.: A solvent-responsive coordination cage. Chem. Sci. **3**, 701–704 (2012)
40. Rodríguez-Hermida, S., Lago, A.B., Pino-Cuevas, A., Hagenbach, A., Cañdillas-Delgado, L., Carballo, R., Abram, U., Vázquez-López, A.: Hexameric cationic copper(II) metallacrown as a pertechnetate and perrhenate scavanger. Chem. Eur. J. **22**, 1847–1853, (2016)
41. McDonald, C., Whyte, T., Taylor, S.M., Sanz, S., Brechin, E.K., Gaynor, D., Jones, L.F.: Progressive decoration of pentanuclear Cu(II) 12-metallacrown-4 nodes towards targeted 1- and 2-D extended networks. Cryst. Eng. Comm. **15**, 6672–6681 (2013)
42. Seda, S.H., Janczak, J., Lisowsky, J.: Synthesis and reactivity of copper(II) metallacrowns with (*S*)-phenylalanine and 2-picolinehydroxamic acids. Inorg. Chim. Acta. **359**, 1055–1063 (2006)
43. Abdel-Magid, A.F., Carson, K.G., Harris, B.D., Maryanoff, C.A., Shah, R.D.: Reductive amination of aldehydes and ketones with sodium triacetoxyborohydride. Studies on direct and indirect reductive amination procedures. J. Org. Chem. **61**, 3849–3862 (1996)
44. Fugu, M.B., Ellaby, R.J., O′Connor, H.M., Pitak, M.B., Klooster, W., Horton, P.N., Coles, S.J., Al-mashhadani, M.H., Perepichka, I.F., Brechin, E.K., Jones, L.F.: Mono- and ditopic

hydroxamate ligands towards discrete and extended network architectures. Dalton. Trans. **48**, 10180–10190 (2019)
45. (a) Chilton, N.F., Anderson, R.P., Turner, L.D., Soncini, A., Murray, K.S.: PHI: a powerful new program for the analysis of anisotropic monomeric and exchange-coupled polynuclear *d*- and *f*-block complexes. J. Comput. Chem. **34**, 1164–1175 (2013). (b) Khan, O.: Molecular Magnetism. VCH, New York (1993)
46. (a) Pavlishchuk, A.V., Kolotilov, S.V., Zeller, M., Thompson, L.K., Fritsky, I.O., Addison, A.W., Hunter, A.D.: A triple-decker heptadecanuclear $(CuII)_{15}(CrIII)_2$ complex assembled from pentanuclear metallacrowns. Eur. J. Inorg. Chem. 4851–4858 (2010). (b) Happ, P., Rentschler, E.: Enforcement of a high-spin ground state for the first 3d heterometallic 12-metallacrown-4 complex. Dalton Trans. **43**, 15308–15312 (2014)
47. McDonald, C.M., Sanz, S., Brechin, E.K., Singh, M.K., Rajaraman, G., Gaynor, D., Jones, L.F.: High nuclearity Ni(II) cages from hydroxamate ligands. RSC Adv. **4**, 38182–38191 (2014)
48. Guo, L.-Y., Su, H.-F., Kurmoo, M., Wang, X.-P., Zhao, Q.-Q., Lin, S.-C., Tung, C.-H., Sun, D., Zheng, L.-S.: Multifunctional triple-decker inverse 12-metallacrown-4 sandwiching halides. Appl. Mater. Inter. **9**, 19980–19987 (2017)
49. Lah, M.S., Gibney, B.R., Tierney, D.L., Penner-Hahn, J.E., Pecoraro, V.L.: The fused metallacrown anion $Na_2\{[Na_{0.5}[Ga\text{-(salicylhydroximate)}]_4]_2(\mu_2\text{-}OH)_4\}$- is an inorganic analog of a cryptate. J. Am. Chem. Soc. **115**, 5857−5858 (1993)
50. Tarushi, A., Raptopoulou, C.P., Psycharis, V., Kontos, C.K., Kessissoglou, D.P., Scorilas, A., Tangoulis, V., Psomas, G.: Copper(II) inverse-[9-metallacrown-3] compounds accommodating nitrato or diclofenac ligands: structure, magnetism, and biological activity. Eur. J. Inorg. Chem. **2**, 219–231 (2016)
51. (a) Cano, J., Cauchy, T. Ruiz, E., Milios, C.J., Stoumpos, C.C., Stamatatos, T.C., Perlepes, S.P., Christou, G., Brechin, E.K.: On the origin of ferromagnetism in oximato-based $[Mn_3O]^{7+}$ triangles. Dalton Trans. 234–240 (2008). (b) Inglis, R., Jones, L.F., Karotsis, G., Collins, A., Parsons, S., Perlepes, S.P., Wernsdorfer, W., Brechin, E.K.: Enhancing SMM properties via axial distortion of $[Mn_3]$ SMMs, Chem. Commun. **45**, 5924–5926, (2008). (c) Inglis, R., Jones, L.F., Mason, K., Collins, A., Moggach, S.A., Parsons, S., Perlepes, S.P., Wernsdorfer, W., Brechin, E.K.: Ground spin state changes and 3-D exchange couples $[Mn^{III}{}_3]$ SMMs. Chem. Eur. J. **14**, 9117–9121 (2008). (d) Inglis, R., Taylor, S.M., Jones, L.F., Papaefstathiou, G.S., Perlepes, S.P., Datta, S., Hill, S., Wernsdorfer, W., Brechin, E.K.: Twisting, bending, stretching: strategies for making ferromagnetic triangles. Dalton Trans. **42**, 9157–9168 (2009)
52. (a) Milios, C.J., Vinslava, A., Wernsdorfer, W., Moggach, S., Parsons, S., Perlepes, S.P., Christou, G., Brechin, E.K.: A record anisotropy barrier for a single-molecule magnet. J. Am. Chem. Soc. **129**, 2754–2755 (2007). (b) Milios, C.J., Inglis, R., Vinslava, A., Bagai, R., Wernsdorfer, W., Parsons, S., Perlepes, S.P., Christou, G., Euan K. Brechin, E.K.: Toward a magnetostructural correlation for a family of Mn_6 SMMs. J. Am. Chem. Soc. **129**, 12505–12511 (2007). (c) Inglis, R. Jones, L.F. Milios, C.J., Datta, S. Collins, A., Parsons, S., Wernsdorfer, W., Hill, S., Perlepes, S.P., Piligkos, S., Brechin, E.K.: Attempting to understand (and control) the relationship between structure and magnetism in an extended family of Mn_6 single-molecule magnets. Dalton Trans. 3403–3412 (2009). (d) Inglis, R., Milios, C.J., Jones, L.F., Piligkos, S., Brechin. E.K.: Twisted molecular magnets. Chem. Commun. **48**, 181–190 (2012)
53. Kennedy, A.R., Mulvey, R.E., Rowlings, R.B.: Remarkable reaction of hetero-S-block-metal amides with molecular oxygen: cationic $(NMNMg)_2$ ring products (M = Li or Na) with anionic oxo or peroxo cores. Angew. Chem. Int. Ed. **37**, 3180–3184 (1998)
54. Kennedy, A.R., Mulvey, R.E., Rowlings, R.B.: Intermetallic lithium-magnesium hexamethyldisilazide: synthesis and structure, discovery of an oxygen-centered variant, and a reaction with benzonitrile that produces a novel amidinate cage compound with a trigonal bipyramidal Li_4MgO core. J. Am. Chem. Soc. **120**, 7816–7824 (1998)
55. Kennedy, A.R., Mulvey, R.E., Raston, C.L., Roberts, B.A., Rowlings, R.B.: 'Inverse crown ether' complexes: extension to potassium through the synthesis of $[\{[(Me_3Si)_2N]_4K_2Mg_2(O_2)\}\infty]$, a peroxo-centred macrocycle linked into infinite chains by intermolecular $K\cdots CH_3(SiMe_2)$ interactions. Chem. Commun. 353–354 (1999)

56. Kennedy, A.R., Klett, J., Mulvey, R.E., Newton, S., Wright, D.S.: Manganese(II)-lithium and –sodium inverse crown ether (ICE) complexes. Chem. Commun. 308–310 (2008)
57. Clark, N.M., Garcia-Alvarez, P., Kennedy, A.R., O'Hara, C.T., Robertson, G.M: Reactions of (−)-sparteine with alkali metal HMDS complexes: conventional meets the unconventional. Chem. Commun. 5835–5837 (2009)
58. Kennedy, A.R., Mulvey, R.E., O′Hara, C.T., Robertson, G.M., Robertson, S.D.: Mixed lithium amide-lithium halide compounds: unusual halide-deficient amido metal anionic crowns. Angew. Chem. Int. Ed. **50**, 8375–8378 (2011)
59. Armstrong, D.R., Kennedy, A.R., Mulvey, R.E., Rowlings, R.B.: Mixed-metal sodium—magnesium macrocyclic amide chemistry: a template reaction for the site selective dideprotonation of arene molecules. Angew. Chem. Int. Ed. **38**, 131–133 (1999)
60. Andrews, P.C., Kennedy, A.R., Mulvey, R.E., Raston, C.L., Roberts, B.A., Rowlings, R.B.: An unprecedented hexapotassium-hexamagnesium 24-membered macrocyclic amide: a polymetallic cationic host to six monodeprotonated arene anions. Angew. Chem. Int. Ed. **39**, 1960–1962 (2000)
61. Carella, L.M., Clegg, W., Graham, D.V., Hogg, L.M., Kennedy, A.R., Klett, J., Mulvey, R.E., Rentschler, E., Russo, L.: Sodium-mediated manganation: direct mono- and dimanganation of benzene and synthesis of a transition-metal inverse crown complex. Angew. Chem. **119**, 4746–4750 (2007)
62. Alborés, P., Carella, L.M., Clegg, W., Garcia-Alvarez, P., Kennedy, A.R., Klett, J., Mulvey, R.E., Rentschler, E., Russo, L: Direct C–H metalation with Chromium(II) and Iron(II): transition-metal host/benzenediide guest magnetic inverse-crown complexes. Angew. Chem. Int. Ed. **48**, 3317–3321 (2009)
63. Martinez-Martinez, A.J., Armstrong, D.R., Conway, B., Fleming, B.J., Klett, J., Kennedy, A.R., Mulvey, R.E., Robertson, S.D., O′Hara, C.T.: Pre-inverse-crowns: synthetic, structural and reactivity studies of alkali metal magnesiates primed for inverse crown formation. Chem. Sci. **5**, 771–781 (2014)
64. Clegg, W., Henderson, K.W., Kennedy, A.R., Mulvey, R.E., O'Hara, C.T., Bowlings, R.B., Tooke, D.M.: Regioselective tetrametalation of ferrocene in a single reaction: extension of the s-block inverse crown chemistry to the d-Block. Angew. Chem. Int. Ed. **40**, 3902–3905 (2001)
65. Andrikopoulos, P.C., Armstrong, D.R., Clegg, W., Gilfillan, C.J., Hevia, E., Kennedy, A.R., Mulvey, R.E., O'Hara, C.T., Parkinson, J.A., Tooke, D.M.: A homologous series of regioselectively tetraprotonated group 8 metallocenes: new inverse crown ring compounds synthesised via a mixed sodium-magnesium tris(diisopropylamide) synergic base. J. Am. Chem. Soc. **126**, 11612–11620 (2004)

Water-Soluble 15-Metallacrown-5 Complexes: Molecular Structures and Properties

Marina A. Katkova and Sergey Yu. Ketkov

Abstract Among numerous metallacrowns, the 15-Metallacrown-5 (15-MC-5) systems represent an exceptional class of heterometallic 3d–4f coordination compounds with unique structures and properties. This chapter considers the advantages of aminohydroximate Ln(III)–Cu(II) 15-MC-5 complexes for the development of water-soluble aqua metallamacrocyclic compounds. In these complexes, the nearly planar neutral metallamacrocycle consists of five [Cu(II)–N–O] repeat units with five hydroximate oxygen atoms surrounding the central Ln^{3+} ion, the open part of the lanthanide coordination sphere being filled with weakly bound inner-shell water molecules. The fundamental structural aspects and synthetic strategies, which are important for the design and control of water-soluble 15-MC-5 systems, are reviewed. The processes of formation of the Ln(III)–Cu(II) 15-metallacrown-5 complexes in solution have been recently investigated by computational methods. The relative stabilities of the complexes under consideration were found to depend on the Cu(II) and Ln(III) coordination surroundings as well as on the ligand mutual orientations. Selected examples demonstrating the beauty and the originality of the crystal structures are discussed. In addition, new opportunities for the potential applications associated with well-defined stable structures bearing an increasing number of water molecules in the Ln(III) inner-sphere are briefly reviewed. Finally, the possible strategies for syntheses of water-soluble 15-MC-5 with some central-cavity metal ions other than lanthanides are outlined.

M. A. Katkova (✉) · S. Yu. Ketkov
G.A. Razuvaev Institute of Organometallic Chemistry RAS, 49 Tropinina, Nizhny Novgorod 603950, Russian Federation
e-mail: marina@iomc.ras.ru

S. Yu. Ketkov
e-mail: sketkov@iomc.ras.ru

C. M. Zaleski (ed.), *Advances in Metallacrown Chemistry*,
https://doi.org/10.1007/978-3-031-08576-5_7

1 Introduction

Since the first description of polynuclear metallamacrocyclic complexes named as metallacrowns (MCs) in 1989 by Pecoraro [1], the 15-Metallacrown-5 presented as an exceptional class of heterometallic 3d–4f coordination compounds with novel topologies. While there are several excellent reviews available in the literature that extensively describe their fascinating architecture and potential applications in various research fields [2–9], the present chapter focuses on water-soluble lanthanide(III)–copper(II) 15-MC-5 complexes bearing aminohydroximate ligands. In these complexes, the planar metallamacrocycle consists of five [Cu(II)–N–O] repeat units with five hydroximate oxygen atoms surrounding a lanthanide central metal. The great fundamental interest of coordination chemists in Ln–Cu complexes is driven by the numerous coordination possibilities of the combination of Cu and Ln metal ions, which differ through their chemical and structural preferences [10]. The importance of water-soluble 15-MC-5 complexes is stimulated also by their biomedical prospects [9, 11–16]. Copper is a bioessential element, which plays significant role in many biochemical processes in living organisms [17]. On the other hand, lanthanides are used in a number of medical diagnostic techniques [18]. The hydroxamic acids and their derivatives are widely employed as particularly constituents of antibacterial, antifungal, anticancer agents, and specific enzyme inhibitors [19]. Furthermore, the beautiful structures of 15-MC-5 metallacrowns continue to reflect a remarkable capability of tailoring metal and ligand choice toward a large number of applications. It should be noted that water as a solvent represents a highly active medium for molecular solvation due to its polar character and hydrogen-bonding ability. This chapter provides a review on the synthetic approaches to the water-soluble 15-MC-5 complexes, the structural features of these systems, the processes of their formation and decomposition, the relaxivity properties relevant to the MRI applications, and pH-dependent spectroscopic properties in solution.

2 15-MC-5 Structural Paradigm

The aminohydroxamic acids present molecular systems that showcase the elegant design strategy based on the chelate ring geometry named as 15-MC-5 Structural Paradigm [4, 20, 21]. The aminohydroximate ligands form subunits with a 108° internal angle (Scheme 1) that is ideal for realizing a flat pentagonal ring (Fig. 1).

Thus, α-aminohydroximate 15-MC-5 complexes with the Cu(II) ring metal ions represent an intriguing class of fivefold symmetric heteronuclear metallamacrocyclic compounds which has received widespread interest in recent years due to their exceptional structures characterized by single-crystal X-ray diffraction analysis (Table 1) [22–56]. However, to describe the process of MC formation, many additional factors including the size and reactivity of the chosen metal, coordination abilities of the ligands, as well as reaction conditions should be considered.

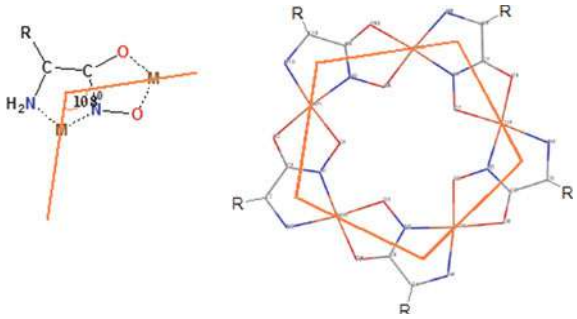

Scheme 1 Rationale for the formation of pentagonal 15-MC-5 bearing α-aminohydroximate ligands: Glycinehydroximate (R = H); Alaninehydroximate (R = CH_3); Phenylglycinehydroximate (R = C_6H_5); Phenylalaninehydroximate (R = $C_6H_5CH_2$); Homophenylalaninehydroximate (R = $C_6H_5CH_2CH_2$); Tyrosinehydroximate (R = C_6H_4OH)

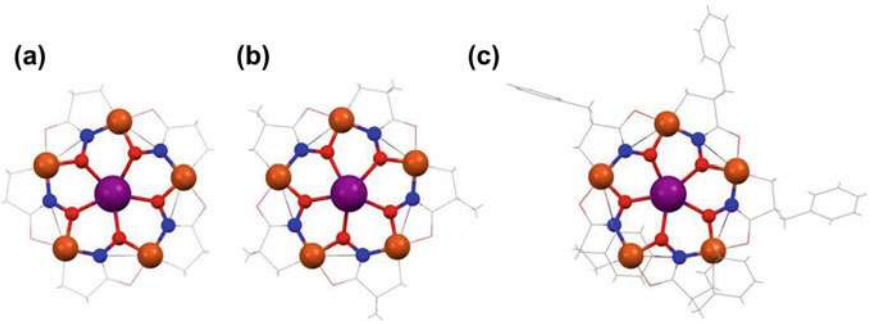

Fig. 1 The flat pentagonal ring images in typical crystal structures of 15-MC-5 metallacrowns based on **a** glycine-, **b** alanine-, and **c** phenylalaninehydroximate ligands. Color code: purple (Ln), brown (Cu), red (O), blue (N), and gray (C)

2.1 Computational Study of the Formation Process

The processes of the 15-MC-5 formation in the solution phase have been investigated by methods of quantum chemistry [58]. A 15-MC-5 Y(III)–Cu(II) complex based on glycinehydroximate ligands was selected as the model compound. The replacement of the lanthanide(III) cation with the lighter rare earth Y(III) ion is widely used for computational modeling of electronic structures of lanthanide complexes. The Y(III) ionic radii are close to Gd(III) ionic radii (1.04 and 1.06 Å, respectively) [59]. Note that glycinehydroxamic acid is the simplest example of aminohydroxamic acids. The optimized structures of GlyhaH_2 (1a), N- and O-deprotonated monoanions (hydroxamates) GlyhaH (1b, 1c), and dianion (hydroximate) Glyha (1d) are shown in Fig. 2 together with the atomic charges calculated within the frames of the Quantum Theory of Atoms in Molecules (QTAIM) [60].

Table 1 Single-crystal structural data of lanthanide 15-MC-5 complexes based on Cu(II) ring metal ions with α-aminohydroximate ligand is available in the Cambridge Crystallographic *Data* Centre (CCDC)

	α-Amino-hydroximate ligand	Central metal	Anion bound to central M	Space group/space group No.	R-factor (%)	Refs.	Refcode
1	Glyha	Y	$C_2H_3O_2$	P-1/2	6.56	[22]	WUZNIQ
2	Glyha	La	–	P-1/2	2.15	[23]	QEXTEV
3	Glyha	La	–	P-1/2	2.85	[22]	WUZNOW
4	Glyha	La	$C_2H_3O_2$	P-1/2	3.58	[24]	OLUZAY
5	Glyha	Ce	–	P-1/2	5.82	[25]	DUVPUH
6	Glyha	Ce	–	P-1/2	7.56	[26]	XITYAD
7	Glyha	Pr	NO_3	P-1/2	7.84	[24]	OLUZOM
8	Glyha	Pr	SO_4	P-1/2	2.88	[27]	UVOFAN
9	Glyha	Pr	CO_3, $C_8H_4O_2$	P-1/2	6.15	[28]	QIFWIO
10	Glyha	Pr	$C_8H_4O_2$	P-1/2	4.07	[30]	PEJPUS
11	Glyha	Nd	NO_3	P-1/2	4.80	[24]	OLUZUS
12	Glyha	Nd	NO_3	P-1/2	1.78	[22]	WUZNEM
13	Glyha	Nd	SO_4	P-1/2	2.24	[27]	UVOFER
14	Glyha	Nd	$C_2H_3O_2$	P-1/2	3.58	[29]	GAMQIX
15	Glyha	Nd	CO_3, $C_8H_4O_2$	P-1/2	3.98	[30]	PEJPIG
16	Glyha	Nd	CO_3, $C_8H_4O_2$	P-1/2	6.17	[28]	QIFVUZ
17	Glyha	Sm	NO_3	P-1/2	4.11	[24]	OMABAH
18	Glyha	Sm	SO_4	P-1/2	5.09	[27]	UVOFIV
19	Glyha	Sm	SO_4, $C_8H_4O_2$	P-1/2	3.62	[28]	QIFWEK
20	Glyha	Sm	$C_8H_4O_2$	P-1/2	5.90	[30]	PEJQAZ
21	Glyha	Eu	NO_3, OH	P-1/2	12.30	[31]	XEBKAQ

(continued)

Table 1 (continued)

	α-Amino-hydroximate ligand	Central metal	Anion bound to central M	Space group/space group No.	R-factor (%)	Refs.	Refcode
22	Glyha	Eu	SO_4	P-1/2	3.77	[27]	UVOFOB
23	Glyha	Eu	SO_4, $C_8H_4O_2$	P-1/2	3.00	[28]	QIFWAG
24	Glyha	Eu	$C_2H_3O_2$	P-1/2	4.49	[32]	XUDWAW
25	Glyha	Eu	$C_8H_4O_2$	P-1/2	5.48	[30]	PEJPOM
26	Glyha	Gd	–	P-1/2	4.05	[33]	RACCAC
27	Glyha	Gd	NO_3	P-1/2	5.19	[34]	YEBQ IG
28	Glyha	Gd	SO_4	P-1/2	3.78	[27]	UVOFUH
29	Glyha	Gd	CO_3	P-1/2	7.05	[35]	GIXRIQ
30	Glyha	Gd	CO_3	P-1/2	3.43	[36]	HOMZUH
31	Glyha	Gd	$C_2H_3O_2$	P-1/2	7.59	[24]	OLUZEC
32	Glyha	Gd	$C_3H_5O_3$	P-1/2	7.97	[22]	WUZNUC
33	Glyha	Gd	$C_6H_5O_7$	P-1/2	2.98	[35]	GIXTAK
34	Glyha	Gd	$C_8H_4O_4$	P-1/2	4.89	[35]	GIXQOV
35	Glyha	Gd	$C_8H_4O_4$	P-1/2	4.76	[35]	GIXQUB
36	Glyha	Gd	$C_8H_4O_4$	P-1/2	4.45	[35]	GIXRAI
37	Glyha	Ho	CO_3	P-1/2	3.34	[36]	HONBEU
38	Glyha	Ho	SO_4	P-1/2	3.09	[27]	UVOGES
39	Glyha	Tb	$C_2H_3O_2$	P-1/2	8.03	[24]	OLUZIG
40	Glyha	Dy	SO_4	P-1/2	2.44	[27]	UVOGAO
41	Glyha	Dy	CO_3	P-1/2	3.07	[36]	HONBAQ
42	Alaha	La	–	P212121/19	4.06	[23]	QEXTIZ

(continued)

Table 1 (continued)

	α-Amino-hydroximate ligand	Central metal	Anion bound to central M	Space group/space group No.	R-factor (%)	Refs.	Refcode
43	Alaha	Nd	OH	P212121/19	3.45	[37]	RAPXUB
44	Phgha	La	$C_6H_4NO_2$	P212121/19	3.79	[38]	BAWWAZ
45	Phgha	La	$C_6H_8O_4$	P21/4	5.14	[39]	GEYREJ
46	Phgha	La	$C_{10}H_4O_4S_2$	P21/4	5.58	[38]	BAWVEC
47	Phgha	Gd	$C_8H_5O_4$	P212121/19	4.35	[38]	BAWVAY
48	Pheha	Y	–	C2/5	6.43	[40]	UBELEU
49	Pheha	Y	NO_3	C2/5	–	[41]	NIXKEL
50	Pheha	La	–	P6222/180	9.35	[42]	SUMSOJ
51	Pheha	La	–	C2/5	4.37	[43]	JOWGOU
52	Pheha	La	–	P1/1	5.07	[44]	NUYJAT
53	Pheha	La	NO_3	P3221/154	0.00	[41]	VIWXUV
54	Pheha	La	NO_3	P3221/154	5.41	[45]	IBODIM
55	Pheha	La	NO_3	P3221/154	5.41	[40]	IBODIM01
56	Pheha	La	NO_3, $C_9H_9O_2$	P21/4	6.56	[46]	KUGYIV
57	Pheha	La	SO_4	P1/1	5.13	[47]	FIKGEO
58	Pheha	La	$C_2H_3O_2$	P1/1	5.47	[43]	JOWGUA
59	Pheha	La	$C_6H_8O_4$	P21/4	10.9	[45]	IBODOS
60	Pheha	La	$C_6H_4NO_2$	P1/1	5.71	[38]	BAWVUS
61	Pheha	La	$C_7H_5O_2$	P4212/90	8.35	[46]	KUGYOB
62	Pheha	La	$C_8H_4O_4$	P1/1	5.23	[38]	BAWWED
63	Pheha	La	$C_5H_5FeC_6H_4O_2$	P212121/19	4.96	[48]	MUYLIC

(continued)

Table 1 (continued)

	α-Amino-hydroximate ligand	Central metal	Anion bound to central M	Space group/space group No.	R-factor (%)	Refs.	Refcode
64	Pheha	La	$Fe(C_6H_4O_2)_2$	I212121/24	3.37	[48]	MUYLOI
65	Pheha	Ce	–	P1/1	7.13	[49]	WAYXAY
66	Pheha	Ce	NO_3	P3121/152	6.17	[40]	UBEKIX
67	Pheha	Ce	SO_4	P1/1	5.59	[26]	XITXUW
68	Pheha	Pr	–	P3121/152	4.62	[40]	UBEKOD
69	Pheha	Nd	–	C2/5	7.80	[40]	UBEKUJ
70	Pheha	Sm	NO_3	P21/4	7.65	[40]	UBEMIZ
71	Pheha	Sm	NO_3	P41/76	5.60	[50]	WUQZUD
72	Pheha	Sm	NO_3	P41/76	5.60	[40]	WUQZUD01
73	Pheha	Sm	NO_3	P43/78	3.87	[50]	WURBAM
74	Pheha	Sm	NO_3	P43/78	3.87	[40]	WURBAM01
75	Pheha	Eu	OH	P41/76	4.09	[51]	FUVJAI
76	Pheha	Eu	OH, NO_3	P41/76	4.24	[40]	UBEMOF
77	Pheha	Eu	NO_3	P21212/18	6.63	[40]	UBELIY
78	Pheha	Eu	$C_7H_5O_2$	P21/4	6.58	[51]	FUVJEM
79	Pheha	Gd	–	P21/4	4.39	[23]	QEXTOF
80	Pheha	Gd	–	C2/5	7.90	[40]	UBELAQ
81	Pheha	Gd	NO_3	P212121/19	4.71	[52]	ABOZIC
82	Pheha	Gd	NO_3	P212121/19	2.97	[52]	ABOZOI
83	Pheha	Gd	NO_3	P41/76	4.39	[40]	UBEMUL
84	Pheha	Gd	NO_3, OH	P43/78	0.00	[41]	VIWYAC

(continued)

Table 1 (continued)

	α-Amino-hydroximate ligand	Central metal	Anion bound to central M	Space group/space group No.	R-factor (%)	Refs.	Refcode
85	Pheha	Gd	NO_3, OH	P43/78	3.68	[41]	NIXJEK
86	Pheha	Gd	NO_3, OH	P43/78	3.68	[40]	NIXJEK01
87	Pheha	Gd	NO_3, OH	C2/5	–	[41]	NIXJIO
88	Pheha	Gd	$C_4H_2O_4$	P21/4	4.87	[53]	UDAYOO
89	Pheha	Gd	$C_6H_4O_4$	P1/1	2.95	[53]	UDAYUU
90	Pheha	Gd	$C_6H_4NO_2$	P1/1	2.24	[54]	DEZFEU
91	Pheha	Gd	$C_6H_8O_4$	P2221/20	5.85	[39]	GEYROT
92	Pheha	Gd	$C_6H_8O_4$	P21/4	6.10	[45]	IBODUY
93	Pheha	Gd	$C_8H_7O_2$	P21/4	2.86	[46]	KUGYER
94	Pheha	Gd	$C_{12}H_6O_4$	P21/4	4.97	[53]	UDAZAB
95	Pheha	Tb	NO_3	P21/4	–	[41]	NIXJOU
96	Pheha	Tb	NO_3, OH	P41/76	–	[41]	NIXKIP
97	Pheha	Tb	NO_3	P21212/18	6.79	[40]	UBELOE
98	Pheha	Dy	NO_3	P41/76	–	[41]	NIXKOV
99	Pheha	Dy	NO_3	P41/76	–	[55]	NIXKOV01
100	Pheha	Dy	NO_3	P21212/18	5.73	[40]	UBELUK
101	Pheha	Dy	NO_3	P41/76	3.17	[40]	UBENAS
102	Pheha	Dy	NO_3, OH	P212121/19	–	[41]	NIXJUA
103	Pheha	Dy	NO_3, OH	P21212/18	–	[55]	NIXJUA01
104	Pheha	Dy	$C_6H_4NO_2$	P1/1	2.93	[54]	DEZFIY
105	Pheha	Dy	$C_7H_5O_2$	P21/4	3.53	[48]	MUYLEY

(continued)

Table 1 (continued)

	α-Amino-hydroximate ligand	Central metal	Anion bound to central M	Space group/space group No.	R-factor (%)	Refs.	Refcode
106	Pheha	Dy	$C_7H_{10}O_4$	P1/1	4.48	[42]	SUMSID
107	Pheha	Ho	NO_3	P41/76	–	[41]	NIXKUB
108	Pheha	Ho	NO_3	P41/76	–	[55]	NIXKUB01
109	Pheha	Ho	NO_3	P21212/18	7.75	[40]	UBEMAR
110	Pheha	Ho	NO_3, OH	P212121/19	–	[41]	NIXKAH
111	Pheha	Ho	NO_3, OH	P21212/18	–	[55]	NIXKAH01
112	Pheha	Ho	NO_3, OH	P41/76	4.97	[40]	UBENEW
113	Pheha	Er	NO_3	P212121/19	5.06	[40]	UBEMEV
114	Pheha	Tm	NO_3	P41/76	3.51	[40]	UBENIA
115	Hphha	La	$C_6H_4NO_2$	P41212/92	9.48	[38]	BAWVOM
116	Hphha	La	$C_8H_4O_4$	P21/4	4.82	[38]	BAWWIH
117	Hphha	Gd	$C_8H_4O_4$	P1/1	3.64	[38]	BAWWON
118	Hphha	Gd	$C_6H_8O_4$	P21/4	2.49	[39]	GEYRIN
119	Hphha	Gd	$C_{10}H_4O_4S_2$	P21/4	5.50	[38]	BAWVIG
120	Tyrha	Gd	–	P-1/2	6.05	[23]	QEXTUL
121	Tyrha	Gd	–	C2/5	5.51	[56]	WIYLUL
122	Tyrha	Gd	–	C2/5	6.49	[56]	WIYMAS
123	Tyrha	Gd	–	C2/5	4.99	[56]	WIYMEW

Abbreviations for α-aminohydroximate ligands [57]: Glyha—glycinehydroximate; Alaha—alaninehydroximate; Phgha (ex Pgha)—phenylglycinehydroximate; Pheha (ex Phalaha)—phenylalaninehydroximate; Hphha (ex Hpheha)—homophenylalaninehydroximate; and Tyrha—tyrosinehydroximate

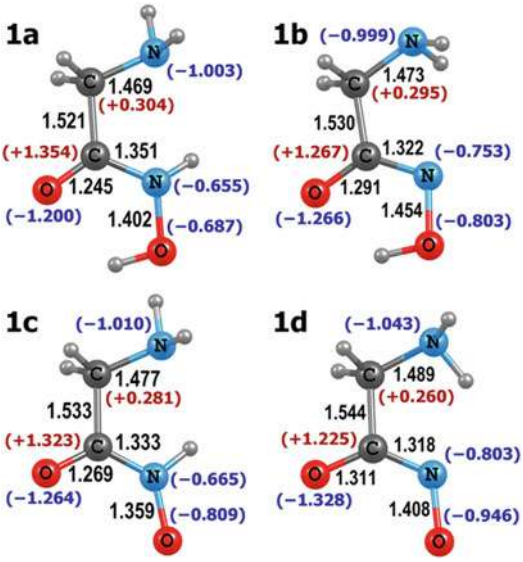

Fig. 2 The optimized structures of glycinehydroxamic acid $GlyhaH_2$ (**1a**), N- and O-deprotonated monoanions GlyhaH (**1b** and **1c**, respectively), and dianion Glyha (**1d**). The atomic QTAIM charges are indicated in parentheses. The bond lengths are given in Å. *Adapted from* Ref. [58] by permission from Springer Nature Customer Service Centre GmbH: Springer, © 2018

Both optimized bond lengths and Wiberg indices obtained from the Natural Bond Orbital (NBO) calculations (Table 2) testify for a single bond character of C–C, C–N(amine), and N–O in $GlyhaH_2$ and the corresponding monoanions and dianions. The C–N(imine) and C–O bond orders are larger (1.2–1.6). In neutral [$GlyhaH_2$], the bond order of C–N(imine) is lower than that of C–O, while in the fully deprotonated ligand $[Glyha]^{2-}$ the situation is reversed (Table 2). The QTAIM analysis supports the formation of the negatively charged N,N- and O,O-chelating sites [58].

Taking into account the structure of anions of glycinehydroxamic acid, three coordination sites, (O,O)Cu(O,O), (N,N)Cu(O,O), and (N,N)Cu(N,N) can participate in the formation of coordination compounds. According to the DFT calculations (Fig. 3), the most stable structures of the glycinehydroxamate copper chelates contain the (N,N)Cu(N,N) coordination sites. This agrees with the X-Ray structure

Table 2 The bond orders in glycinehydroxamic acid and its anions obtained by the NBO analysis (Wiberg bond indexes)

Bond	[$GlyhaH_2$]	$[GlyhaH]^-$	$[GlyhaH]^-$	$[Glyha]^{2-}$
C–C	0.982	0.969	0.972	0.965
C–N(amine)	1.012	1.013	1.001	0.994
C–N(imine)	1.252	1.551	1.356	1.603
C–O	1.528	1.305	1.395	1.233
N–O	1.009	0.970	1.089	1.069

Adapted from Ref. [58] by permission from Springer Nature Customer Service Centre GmbH: Springer, © 2018

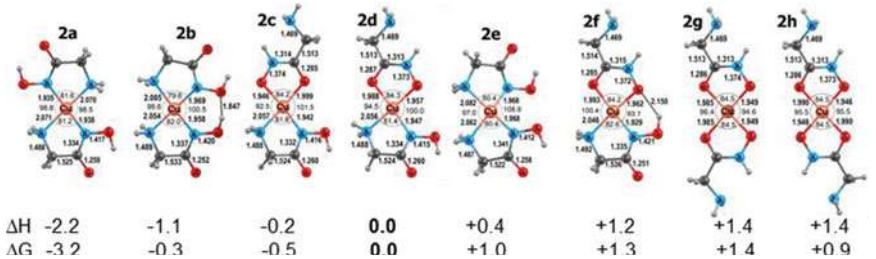

Fig. 3 The optimized structures of the glycinehydroxamate Cu(GlyhaH)$_2$ complexes (**2a–h**). The angles are given in degrees. The calculated enthalpy and free energy changes relative to **2d** are given in kcal/mol. *Adapted from* Ref. [58] by permission from Springer Nature Customer Service Centre GmbH: Springer, © 2018

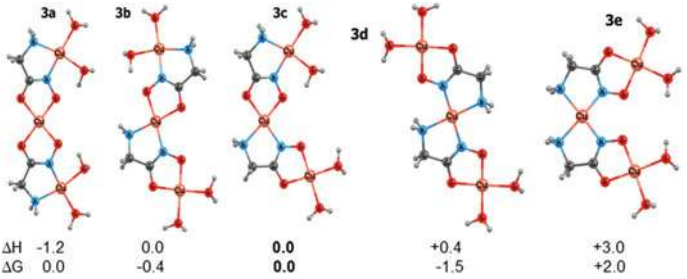

Fig. 4 The optimized structures of trinuclear Cu(II) glycinehydroximate complexes (**3a–e**). The calculated enthalpy and free energy changes are given in kcal/mol. *Adapted from* Ref. [58] by permission from Springer Nature Customer Service Centre GmbH: Springer, © 2018

of Cu(GlyhaH)$_2$ [61] which corresponds to the 2a isomer, the experimental geometry being close to that predicted by DFT [58].

The orders of relative stabilities of hydroxamate species **2a–h** and cationic glycinehydroximates **3a–e** are different (Figs. 3 and 4). In the latter case, the variations in the electronic energy and enthalpy are similar. However, the Gibbs energy changes in a different way. For instance, the **3a** system bearing the cis-(O,O)Cu(O,O) site is favorable by the electronic energy and enthalpy. On the other hand, the **3d** species containing the trans-(N,N)Cu(N,N) fragment possesses the lowest Gibbs energy. The increased contribution of entropy to the relative stabilities of such systems is, therefore, evident.

According to these calculations, the most stable oligomers of copper chelates should start their growth from the (N,N)Cu(N,N) coordination sites via a sequential formation of the (N,N)Cu(O,O) moieties in different directions. However, the presence of a central lanthanide ion specifically prevents the growth of linear and zigzag oligomers based on the copper chelates and provides the dominant growth of the (N,N)Cu(O,O) units forming the desired metallamacrocyclic structure (Fig. 5).

The predicted 15-MC-5 structure (Fig. 6) represents the neutral metallacyclic ring

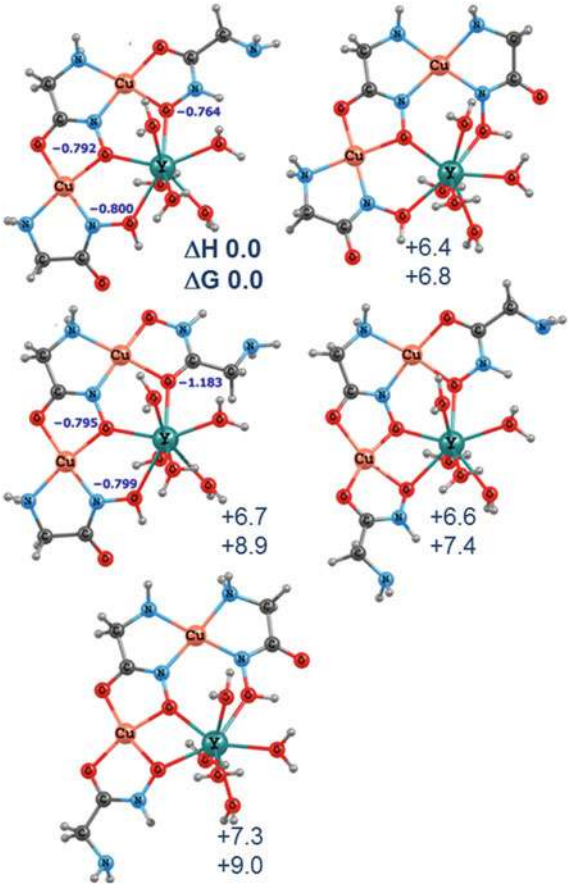

Fig. 5 The calculated enthalpy and free energy changes (kcal/mol) for the heterometallic Y(III)–Cu(II) fragments. *Adapted from* Ref. [58] by permission from Springer Nature Customer Service Centre GmbH: Springer, © 2018

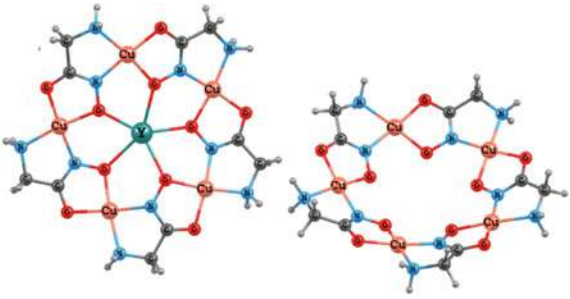

Fig. 6 The structures of the Y^{3+}[15-MC-5] ion and [15-MC-5] scaffold optimized at the B3LYP/DGDZVP (PCM) level of DFT. *Adapted from* Ref. [58] by permission from Springer Nature Customer Service Centre GmbH: Springer, © 2018

Table 3 Comparison of calculated and X-ray crystal structural parameters for the glycinehydroximate Y(III)-Cu(II) complexes

Distances [Å] and angles [°]	Calculated Y[15-MC-5] (from Ref. [62])	SC-XRD Y(OAc)[15-MC$_{Cu(II)Glyha}$-5] (from Ref. [22])
C–C	1.499–1.500	1.505–1.515
C–N(amine)	1.474–1.476	1.472–1.493
C–N(imine)	1.299–1.302	1.285–1.304
C–O	1.270–1.272	1.287–1.302
N–O	1.367–1.370	1.387–1.415
Cu–N(amine)	2.025–2.032	2.008–2.039
Cu–N(imine)	1.987–1.905	1.893–1.911
Cu–O(carbonyl)	1.930–1.935	1.924–1.966
Cu–O(oxime)	1.932–1.945	1.935–1.976
Y–O(oxime)	2.346–2.425	2.372–2.410
O(oxime)–Cu–N(imine)	90.3–91.6	88.3–91.3
O(oxime)–Y–O(oxime)	71.8–73.2	70.5–74.2

since the positive (+2) charges of the copper(II) ions are balanced by the negative (−2) charges of the aminohydroximate ligands. The Y(III) ion is encapsulated at the center of the structure with the formal (+3) positive charge. The calculated structure of Y(III)–Cu(II) complex agrees well with the geometry obtained from the X-ray diffraction experiment for Y(OAc)[15-MC$_{Cu(II)Glyha}$-5] [22] (Table 3).

The N–O, C–C, and C–N(amine) bond lengths in Y^{3+}[15-MC-5] agree well with the single bond character assumed on the basis of the Wiberg indices of 0.98–1.03 (Table 4) [62]. This also correlates nicely with the previous computational analysis of the individual Glyha ligand [58]. The bond orders for the C–O and C–N(imine) bonds are close to 1.3. and 1.5, respectively, which is indicative of the higher π-contribution to the C–N(imine) bonds compared to the C–O bonds in 15-metallacrowns-5.

The large covalent contribution to the ligand bonds is indicated by the QTAIM parameters at the Bond Critical Points (BPCs): the high electron densities $\rho(\mathbf{r}_c)$ (0.252–0.375 a.u.) and negative values of Laplacian $\nabla^2\rho(\mathbf{r}_c)$ (Table 4). For the classification of bonding interactions, the potential to kinetic energy density ratio $|V(\mathbf{r})|/G(\mathbf{r})$ can be used as well [63, 64]. Ionic bonds considered as closed-shell interactions in QTAIM are characterized by $|V(\mathbf{r}_c)|/G(\mathbf{r}_c) < 1$. The $1 < |V(\mathbf{r}_c)|/G(\mathbf{r}_c) < 2$ values correspond to intermediate interactions and $|V(\mathbf{r}_c)|/G(\mathbf{r}_c) > 2$ to covalent bonds. The intraligand interactions are covalent ($|V(\mathbf{r}_c)|/G(\mathbf{r}_c) > 2.30$, see Table 4). The $|V(\mathbf{r}_c)|/G(\mathbf{r}_c)$ ratios decrease on going from C–N(amine) (3.34) to C–N(imine) bonds (2.92–2.97) indicating an increase in the charge separation which agrees with the C(sp^2) atoms being more positive than C(sp^3). The Y–O, Cu–O, and Cu–N interactions are characterized by rather low Wiberg indices (0.22–0.39) and BCP electron density $\rho(\mathbf{r}_c)$ (0.037–0.112 a.u.), the corresponding $\nabla^2\rho(\mathbf{r}_c)$ values are positive (Table 4). The $|V(\mathbf{r}_c)|/G(\mathbf{r}_c) = 1.002$–$1.021$ ratios at the Y–O(oxime) BCPs lie between the

Table 4 NBO and QTAIM (a.u.) parameters of Y^{3+}[15-MC-5]

Bond	Wiberg index	$\rho(\mathbf{r})$	$\nabla^2\rho(\mathbf{r})$	$\lvert V(\mathbf{r})\rvert/G(\mathbf{r})$
C–C	0.98	0.269–0.270	−(0.743–0.742)	5.071–5.080
C–N(imine)	1.47–1.48	0.374–0.375	−(1.207–1.186)	2.922–2.972
C–N(amine)	0.99	0.252–0.254	−(0.590–0.582)	3.339–3.343
C–O	1.31–1.32	0.363–0.365	−(0.583–0.572)	2.300–2.310
N–O	1.02–1.03	0.337–0.340	−(0.433–0.422)	2.495–2.504
Y–O(oxime)	0.24–0.26	0.041–0.049	0.167–0.206	1.002–1.021
Y–O(aq)	0.22–0.24	0.037–0.045	0.160–0.196	0.968–0.992
Cu–O(oxime)	0.29–0.31	0.090–0.093	0.420–0.440	1.190–1.194
Cu–O(carbonyl)	0.33	0.092–0.093	0.436–0.444	1.194–1.196
Cu–N(imine)	0.39	0.110–0.112	0.429–0.441	1.265–1.269
Cu–N(amine)	0.31–0.32	0.083–0.085	0.300–0.305	1.242–1.244

Adapted from Ref. [62] by permission from Springer Nature Customer Service Centre GmbH: Springer, © 2019

intermediate and ionic types of the contacts. The Cu coordination bonds are less polar than Y–O ($|V(\mathbf{r}_c)|/G(\mathbf{r}_c) = 1.190$–$1.269$), the Cu–O interactions being more polar than Cu–N [62].

The presence of the positive Y^{3+} ion at the center of the metallacrown leads to charge redistribution in the [15-MC-5] scaffold, higher electron density being accumulated on the O(oxime) atoms. Correspondingly, the O(oxime) QTAIM charges become more negative when one goes from the "empty" [15-MC-5] scaffold (−(0.678–0.677)*e*) to the yttrium complex Y^{3+}[15-MC-5] (−(0.775–0.765)*e*). Accordingly, the negative charges on the peripheral O(carbonyl) atoms decrease from −(0.150–0.149)*e* to −(0.132–0.131)*e*, while the positive charges on the Cu atoms increase from 0.991–0.992*e* to 1.039–1.047*e* (Table 5).

Table 5 The QTAIM atomic charges (*e*) of complex Y^{3+}[15-MC-5] and "empty" scaffold [15-MC-5]

Atom	Y^{3+}[15-MC-5]	[15-MC-5] scaffold
C(sp^3)	0.273–0.275	0.273–0.274
C(sp^2)	1.291–1.296	1.257–1.258
N(amine)	−(0.965–0.964)	−(0.972–0.971)
N(imine)	−(0.673–0.667)	−(0.683–0.680)
O(carbonyl)	−(1.132–1.131)	−(1.150–1.149)
O(oxime)	−(0.775–0.765)	−(0.678–0.677)
Cu	1.039–1.047	0.991–0.992
Y	2.367	–

Adapted from Ref. [58] by permission from Springer Nature Customer Service Centre GmbH: Springer, © 2018

3 Synthetic Approaches to Aqua Complexes

The first reported glycinehydroximate Eu(III)–Cu(II) metallacrown has been prepared in water by the one-step reaction of glycine hydroxamic acid with copper acetate and europium(III) nitrate in the presence of tetraethylammonium hydroxide [31]. It was supposed that nitrate binding in a bidentate mode to the central Eu^{3+} ion can effectively compete with carboxylate guests, whereas the acetate ions have not been seen to bind to the metallacrown.The second glycinehydroximate Gd(III)–Cu(II) complex structurally characterized by X-ray analysis, has been synthesized in an aqueous solution by the two-step method [34]. The Ln(III)–Cu(II) sulfate complexes were synthesized by the addition of the sodium glycinehydroximate aqueous solution to the solution of Cu(II) sulfate and Ln(III) nitrate [27]. Thus, it could be expected that the different species are formed depending on the reaction conditions and on the Ln(III) and Cu(II) salt used.

Following these results, using Cu(II) acetate, glycinehydroxamic acid, and Ln(III) nitrate in water, various Ln(III)–Cu(II) (Ln = La, Nd, Eu, Y) complexes were isolated and characterized (Fig. 7).

It is interesting that the CH_3COO^- anion coordinated to the central Ln^{3+} cation results in a larger deviation of the metallacrown from the planar geometry compared to the complexes bearing NO_3^-. An H-bonded specific network is responsible for this effect [22, 24, 32]. The crystal structure reveals the presence of hydrogen bonds involving the acetate and amine fragments of the neighboring Eu(OAc)[15-MC-5] molecules (Fig. 8). The acetate anion bound to the central metal ion also forms hydrogen bonds with the water molecules attached to the Cu^{2+} ions. The charge neutrality of the system is achieved due to the NO_3^- ions located in the lattice. It is important to note that they do not interact with the Cu^{2+} ions [32].

Note, that the attempts to investigate the role of water in the syntheses of various glycinehydroximate metallacrowns lead to some different types of aqua complexes: monoaqua, diaqua, triaqua, and tetraaqua [8] (Scheme 2). All of these complexes are stable and well soluble in water.

The tetraaqua Ln(III) metallacrowns have been successfully synthesized using $LnCl_3$, $Cu(CH_3COO)_2$, and glycinehydroxamic acid in water in the absence of nitrate

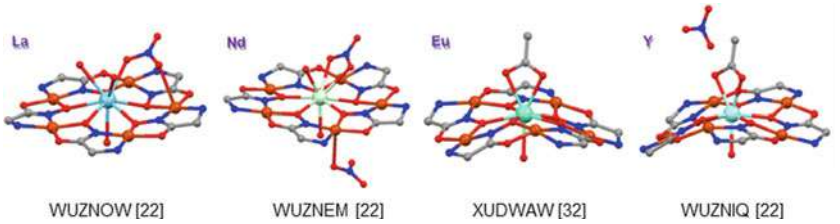

Fig. 7 Molecular structures of glycinehydroximate Ln(III)–Cu(II) (Ln = La [22], Nd [22], Eu [32], Y [22]) complexes. All hydrogen atoms, uncoordinated NO_3^-, and solvate water molecules are omitted for clarity

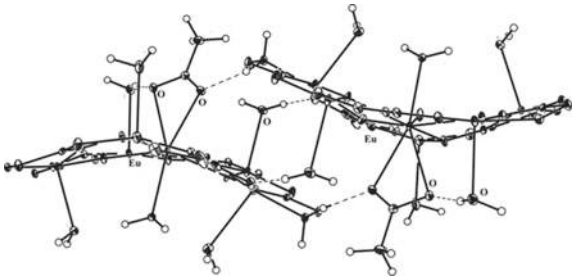

Fig. 8 Fragment of complex Eu(OAc)[15-MC-5] (XUDWAW) packing. (30% thermal ellipsoids probability) Hydrogen atoms are omitted for clarity. *Redrawn from* Ref. [32] with permission from Elsevier © 2014

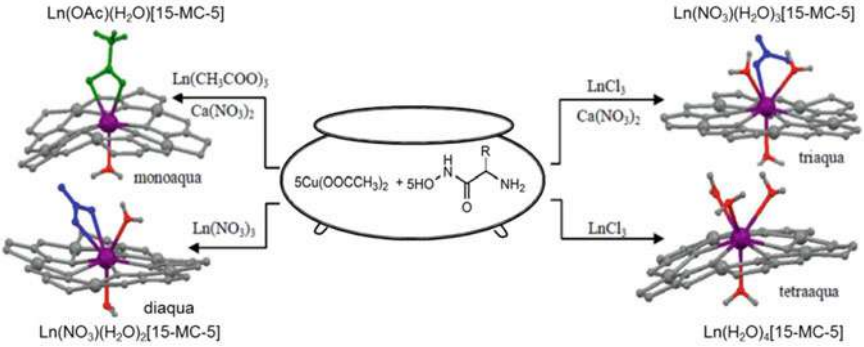

Scheme 2 Synthetic route to aqua Ln(III)–Cu(II) 15-MC-5 complexes

anion [33]. Why is it especially interesting? Because such unique planar disk-like structures with an increasing (up to four) number of exchangeable water molecules on a paramagnetic (e.g. Gd^{3+}) ion have potential applications in magnetic resonance imaging (MRI). It's well known, that the free Gd(III) ion is toxic, and in order to ensure safe clinical use, it is chelated by organic ligands such as DOTA or DTPA. But in general, the polyamino-polycarboxylate ligands are octadentate, therefore, only one H_2O molecule can bind to the free coordination site left. Historically, the design of new efficient contrast agents was directed to increase the hydration number (parameter q in Solomon-Bloembergen-Morgan theory [65]). The efforts to increase the q value lead to only limited success since the complexes became less stable [66]. In addition, the development of specific high-field MRI contrast agents is also in demand since the classic Gd(III) contrast agents decrease substantially their relaxation efficiency as magnetic field strengths increase [67]. The Ln(III) metallacrowns bearing a metallacycle formed by various aminohydroxamic ligands (glycine, α-alanine, α-phenylalanine, and α-tyrosine) and increased number of coordinated water molecules ($q = 3$–4) (Scheme 3) represent good examples to demonstrate the influence of the

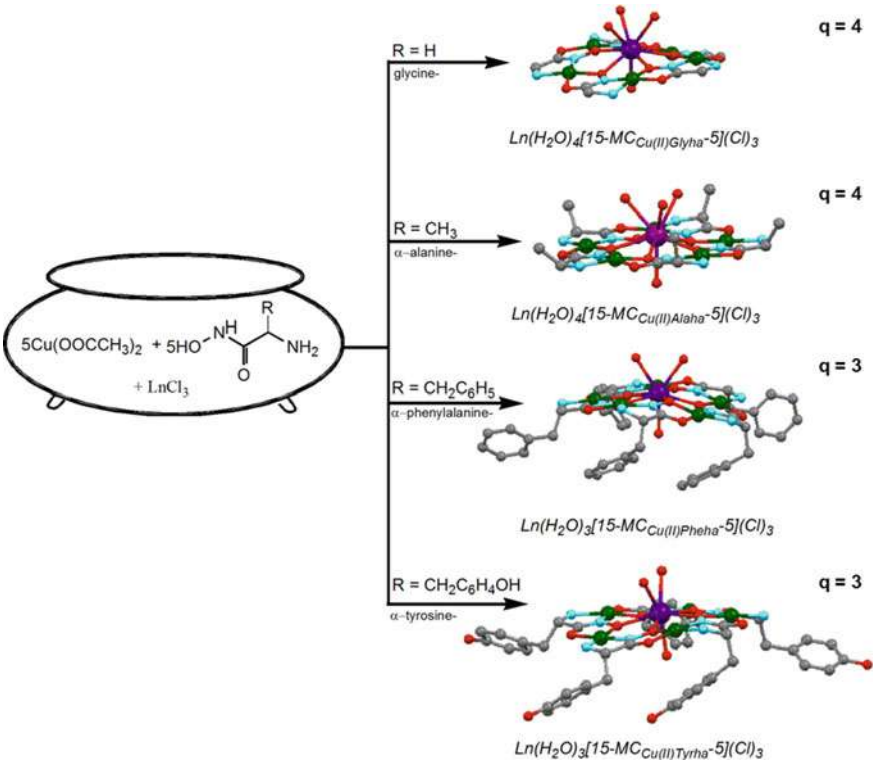

Scheme 3 Synthetic route to the aqua (q = 3,4) aminohydroximate Ln(III)–Cu(II) 15-MC-5 complexes. *Adapted from* Ref. [23] by permission of John Wiley and Sons, © 2018 John Wiley & Sons, Ltd.

ligand structure on the water coordination surrounding of the central Ln(III) ion. All of these complexes are well soluble in water and stable in the air [23].

3.1 Structures of Aminohydroximate Ln(III)–Cu(II) 15-MC-5 Aqua Complexes

According to X-ray diffraction investigations, in the tetra- or tri-aqua aminohydroximate Ln(III)-Cu(II) complexes, the bond lengths and angles are typical for 15-MC-5 metallacrowns (Table 6). The Ln^{3+} ion with the coordination number of 9 (e.g. La^{3+}) is surrounded by five oxygen atoms of the ring and four water molecules (Fig. 9). Three water molecules are located on one side of the metallacrown ring and one H_2O species lies on the opposite side. The Ln–O (aq) distances are not equal and change from 2.5 to 2.6 Å. Moreover, four Cu(II) ions are also coordinated by the water molecules.

Table 6 Comparison of SC-XRD structural parameters for aqua La(III) and Gd(III) metallacrowns based on the Glyha, Alaha, Pheha, and Tyrha ligands

Distances [Å] and angles [°]	La(III)/Glyha QEXTEV	La(III)/Alaha QEXTIZ	Gd(III)/Pheha QEXTOF	Gd(III)/Tyrha QEXTUL
Ln–O (oxime)	2.487(1)–2.581(1)	2.514(6)–2.570(5)	2.373(9)–2.467(9)	2.388(10)–2.449(8)
Cu–O (oxime)	1.926(1)–1.942(1)	1.900(6)–1.928(6)	1.913(8)–1.946(9)	1.912(9)–1.939(11)
Cu–O (carbonyl)	1.951(1)–1.959(1)	1.923(6)–1.963(6)	1.891(9)–1.943(9)	1.884(13)–1.926(8)
Cu–N (imine)	1.906(1)–1.933(1)	1.901(7)–1.912(7)	1.881(11)–1.921(11)	1.866(9)–1.894(12)
Cu–N (amine)	1.991(2)–2.023(1)	1.980(8)–2.015(8)	1.991(11)–2.009(11)	1.997(12)–2.038(13)
Cu–O (aq)	2.383(1)–2.412(1)	2.477(8)–2.85(1)	2.38(1)–2.64(1)	2.54(2)
Ln–O (aq)	2.566(1)–2.648(1)	2.559(6)–2.633(6)	2.373(9)–2.469(9)	2.381(9)–2.55(4)
O(oxime)–Cu–N(imine)	89.88(5)–93.22(5)	90.8(3)–92.6(3)	90.0(4)–91.8(4)	90.3(4)–91.5(4)
O(oxime)–Ln–O(oxime)	67.62(3)–72.86(4)	67.73(19)–69.87(18)	70.1(3)–73.1(3)	70.5(3)–71.9(3)

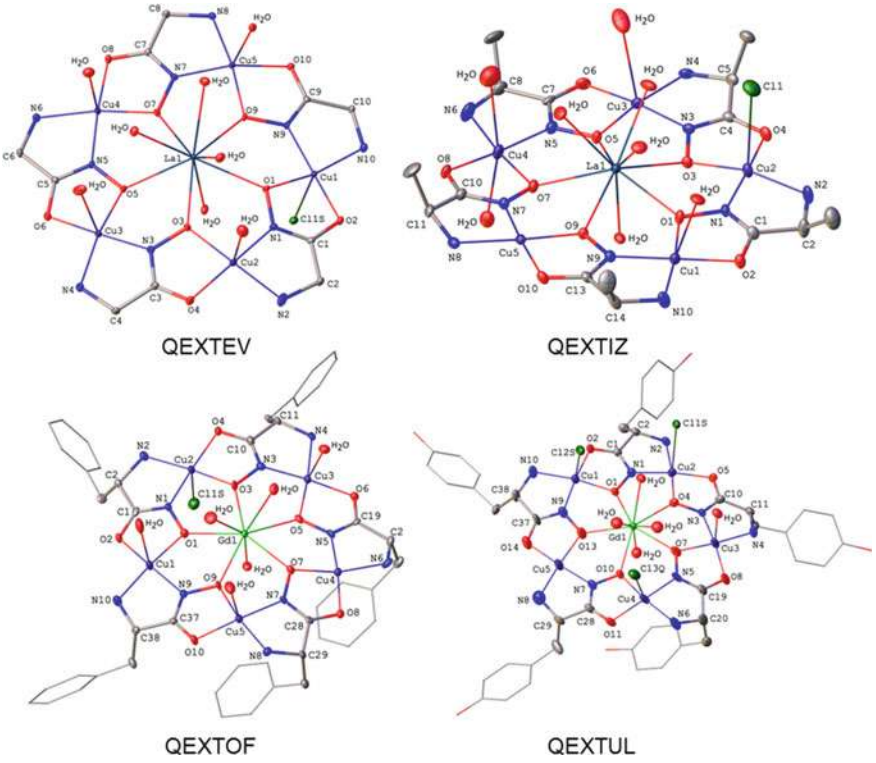

Fig. 9 Molecular structures of aqua aminohydroximate La(III) and Gd(III) complexes based on the Glyha, Alaha, Pheha, and Tyrha ligands. All hydrogen atoms, uncoordinated Cl^- ions, and solvate water molecules are omitted for clarity. *Adapted from* Ref. [23] by permission of John Wiley and Sons, © 2018 John Wiley & Sons, Ltd.

It should be noted that due to the different nature of the 15-metallacrown-5 species, complexes form different packing motifs in crystals, wherein numerous intermolecular interactions with solvated water molecules are revealed. The main motifs as shown in Figs. 10, 11, 12 and 13 are centrosymmetric dimers (in the case of the glycinehydroximate species), one-dimensional chains with a staggered orientation (for the alaninehydroximate species), a jaw-type sandwich (for the phenylalaninehydroximate species), and two-dimensional chains with parallel stacking of the 15-MC-5 rings (for the tyrosinehydroximate species).

4 Solution-State Behavior

The remarkable feature of water-soluble Ln(III)–Cu(II) 15-MC-5 complexes is the deep blue color (Fig. 14). Accordingly, the electronic absorption spectra of these

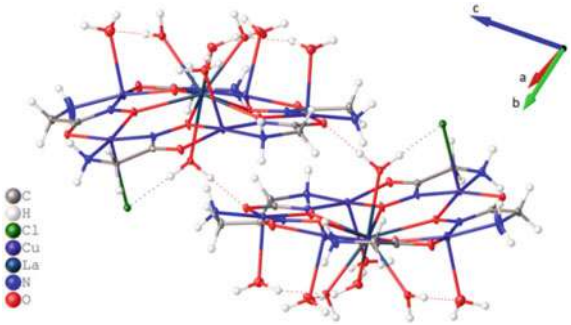

Fig. 10 Fragment of crystal packing of $Ln(H_2O)_4[15\text{-}MC_{Cu(II)Glyha}\text{-}5](Cl)_3$ (QEXTEV). The dashed lines show the short contacts. *Reproduced from* Ref. [23] by permission of John Wiley and Sons, © 2018 John Wiley & Sons, Ltd.

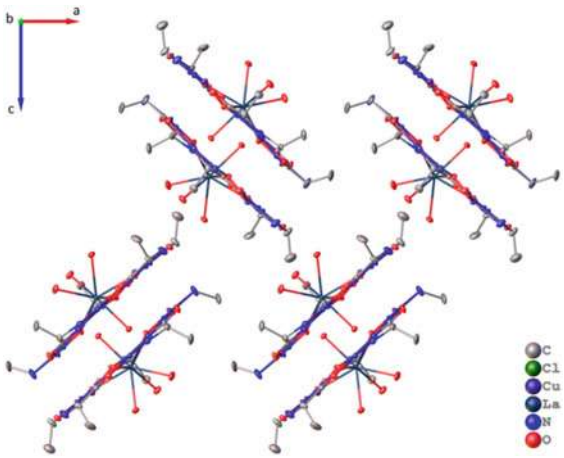

Fig. 11 Crystal packing of $Ln(H_2O)_4[15\text{-}MC_{Cu(II)Alaha}\text{-}5](Cl)_3$ (QEXTIZ). *Reproduced from* Ref. [23] by permission of John Wiley and Sons, © 2018 John Wiley & Sons, Ltd.

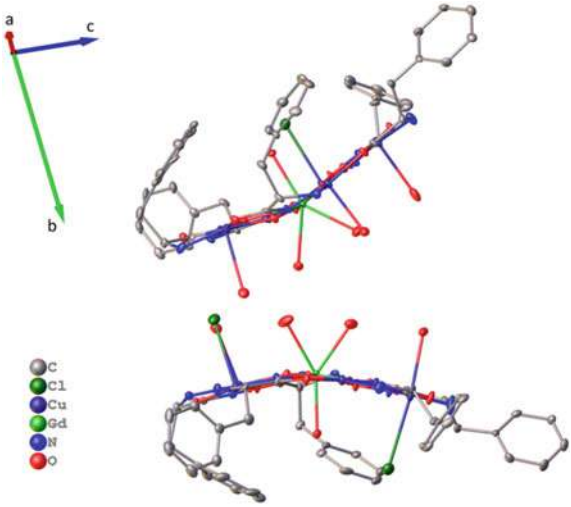

Fig. 12 Fragment of crystal packing of $Ln(H_2O)_4[15\text{-}MC_{Cu(II)Pheha}\text{-}5](Cl)_3$ (QEXTOF). *Reproduced from* Ref. [23] by permission of John Wiley and Sons, © 2018 John Wiley & Sons, Ltd.

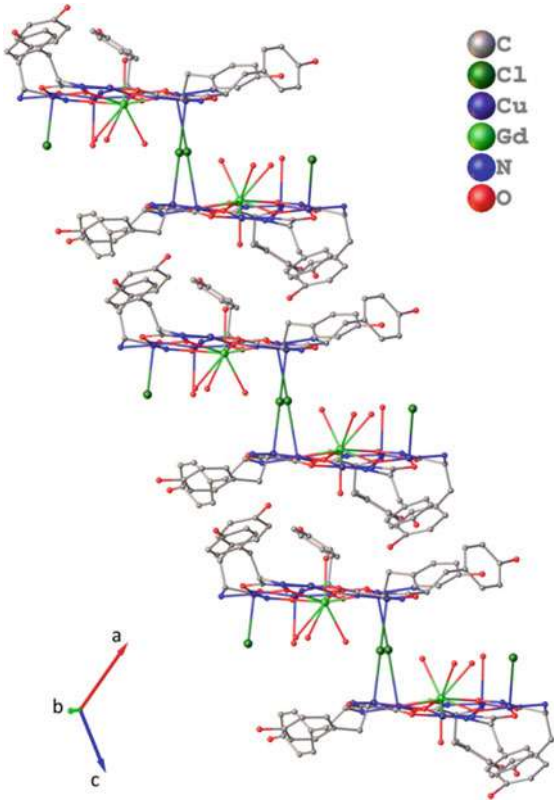

Fig. 13 Crystal packing of $Ln(H_2O)_4[15\text{-}MC_{Cu(II)Tyrha}\text{-}5](Cl)_3$ (QEXTUL). *Reproduced from* Ref. [23] by permission of John Wiley and Sons, © 2018 John Wiley & Sons, Ltd.

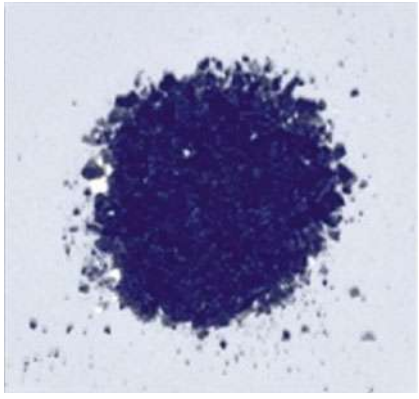

Fig. 14 Complex $La(H_2O)_4[15\text{-}MC_{Cu(II)Pheha}\text{-}5](Cl)_3$ in the powdered form. *Reproduced from* Ref. [43] by permission of John Wiley and Sons, © 2019 Wiley–VCH Verlag GmbH & Co. KGaA, Weinheim

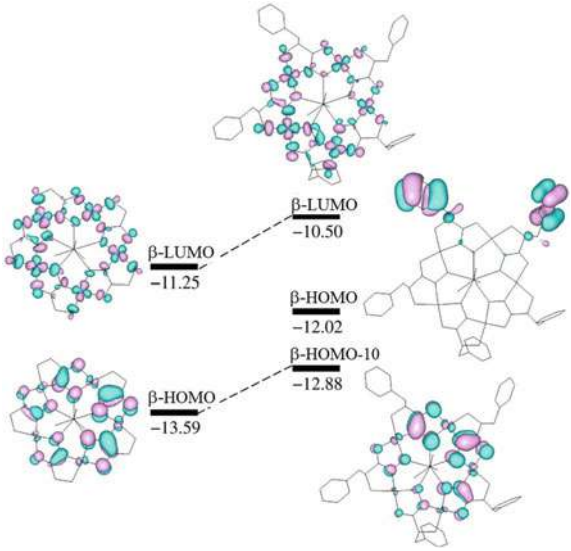

Fig. 15 Isosurfaces (isovalue 0.03) and energies (eV) of molecular orbitals in complexes $\{Y(H_2O)_3[15\text{-}MC_{Cu(II)Glyha}\text{-}5]\}^{3+}$ and $\{Y(H_2O)_3[15\text{-}MC_{Cu(II)Pheha}\text{-}5]\}^{3+}$ calculated at the B3LYP/DGDZVP level. *Reproduced from* Ref. [69] by permission from Springer Nature Customer Service Centre GmbH: Springer, © 2019

complexes show a broad band in the visible region with a maximum at 575 nm ($\varepsilon = 406\ M^{-1}\ cm^{-1}$) which is attributed to the Cu(II) d–d transition [22, 32, 43].

For comparison of the aminohydroximate complexes, a DFT study of Y(III)–Cu(II) 15-MC-5 based on the Glyha and Pheha ligands was performed using the B3LYP functional and split valence double basis set DGDZVP with polarization functions [68, 69]. As shown in Fig. 15, orbital analysis predicts the energy gap of 2.38 eV between the β-LUMO and the highest occupied MO containing contributions of the copper 3*d* orbitals (β-HOMO-10) in the Pheha complex. A similar value (2.34 eV) was found for the glycinehydroximate analogue, where it corresponds to the β-LUMO and β-HOMO energy difference. This energy gap is in good agreement with the position of the *d–d* absorption band at 575 nm (2.16 eV). The α- and β-orbitals of Y(III)–Cu(II) Pheha-metallacrown, which are close in energy and lie between HOMO and HOMO-10, are localized on the benzyl substituents. Thus, the introduction of the $PhCH_2$ group increases the energies of both occupied and vacant orbitals of the metallamacrocycle, as a result of the electron-donating effect of substituents [69].

The stability of tetraaqua La(III)–Cu(II) phenylalaninehydroximate complex (JOWGOU) at various pH was confirmed by recording UV absorption spectra in H_2O (pH 6.8), ammonium buffer (pH 9.2), and acetate buffer (pH 3.8) [43]. No change in the absorption band intensities or positions was observed even after 24–48 h. On the other hand, the electronic absorption spectra of this type of complex are pH-sensitive. As shown in Fig. 16, the absorption bands become weaker as pH decreases [43].

In acidic media, a colorless solution is formed from the dark blue complexes. No further absorbance variations are detected for pH values below 3.3. At the same time,

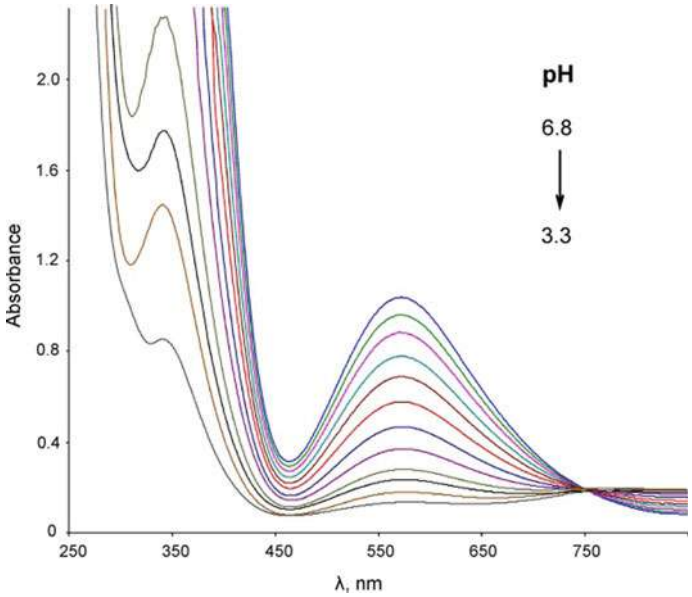

Fig. 16 The pH-dependent UV-visible spectrum of complex $La(H_2O)_4[15MC_{CuPheha}\text{-}5](Cl)_3$ (2.5 mM) in aqueous solution at room temperature. The arrow indicates the intensity variations at different pH values. *Reproduced from* Ref. [43] by permission of John Wiley and Sons, © 2019 Wiley–VCH Verlag GmbH & Co. KGaA, Weinheim

in conrast to the experiments with the Ca(II)–Cu(II) [15-MC-5] complexes [70], the absorption band at ca. 640 nm typical for the Cu[12-MC-4] disassembly species [71, 72] did not appear. These observations are in accord with the previous potentiometric and calorimetric investigations of various acidic Ln(III)–Cu(II) [15-MC-5] solutions detecting only the Ln(III) ions [73]. The discoloration can be associated with the protonation of the aminohydroximate ligands in $La(H_2O)_4[15MC_{CuPheha}\text{-}5](Cl)_3$. [43] The presence of an isosbestic point at ca. 750 nm can be a result of the [CuL] fragment transformation to [CuLH]. The addition of a base causes the original solution to return to a blue color. The reversible color change testifies for the ligand protonation rather than for the complex disassembly proposed for the alaninehydroximate system [73]. Flexible gelatin films were prepared from aqueous solutions of gelatin and La(III)-Cu(II) 15-MC-5. This demonstrates a rare example of incorporation of such type of metallamacrocyclic complexes into a polymeric matrix.. The color of gelatin films, doped with Ln(III)–Cu(II) 15-MC-5, changes when exposed to acidic or alkaline atmospheres. The film color variations (Fig. 17) are reversible and easily monitored with the naked eye [43].

To provide theoretical insights into the reversible halochromic effect associated with protonation/deprotonation of the hydroximate ligands, the DFT modeling was performed for cationic species $\{La(H_2O)_4[15\text{-}MC_{Cu(II)Pheha}\text{-}5]\}^{3+}$ [43]. The calculated Cu–N, Cu–O, and La–O interatomic distances in this molecule correlate very

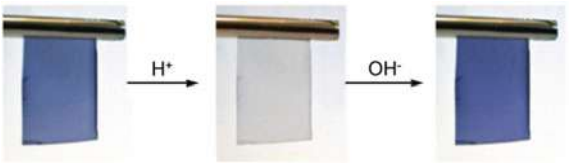

Fig. 17 Color reversibility of the gelatin film dyed with $La(H_2O)_4[15MC_{CuPheha}\text{-}5](Cl)_3$ upon exposure to acidic-alkaline gaseous atmospheres. *Reproduced from* Ref. [43] by permission of John Wiley and Sons, © 2019 Wiley–VCH Verlag GmbH & Co. KGaA, Weinheim

well with the experimental single-crystal X-ray diffraction data (JOWGOU). The DFT calculations show that the N1–C1–C2–N2 dihedral angle is distorted on protonation from 12.76° to 43.61° as a result of the tetrahedral surrounding of the protonated N1 atom (Fig. 18). The protonation also leads to a ~ 0.1 Å increase in the La–O3 distances [43].

Molecular orbital analysis of the model 15-metallacrowns-5 reveals a decrease in the β-HOMO -β-LUMO energy gap ΔE_β on protonation (Fig. 19). The energy gap between the frontier β-orbitals of $La[15\text{-}MC_{Cu(II)Pheha}\text{-}5]^{3+}$ (2.28 eV) correlates well with the absorption spectrum revealing a band at 2.16 eV. The computed decrease in the ΔE_β value by 0.55 eV (from 2.28 to 1.73 eV) on going from $La[15\text{-}MC_{Cu(II)Pheha}\text{-}5]^{3+}$ to $La[15\text{-}MC_{Cu(II)Pheha(H)}\text{-}5]^{4+}$ agrees well with the experimental redshift of the absorption band from 575 to 800 nm which corresponds to the 0.61 eV decrease in the electronic transition energy [43].

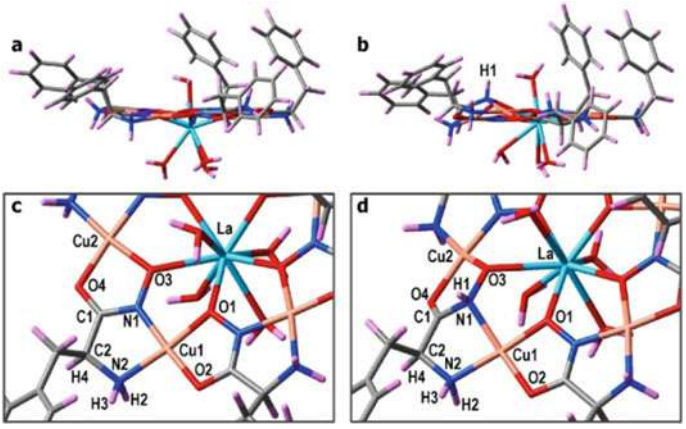

Fig. 18 Optimized geometries of the model metallacrowns $La[15\text{-}MC_{Cu(II)Pheha}\text{-}5]^{3+}$ (**a**) and $La[15\text{-}MC_{Cu(II)Pheha(H)}\text{-}5]^{4+}$ (**b**) and their fragments (**c**, **d**). *Reproduced from* Ref. [43] by permission of John Wiley and Sons, © 2019 Wiley–VCH Verlag GmbH & Co. KGaA, Weinheim

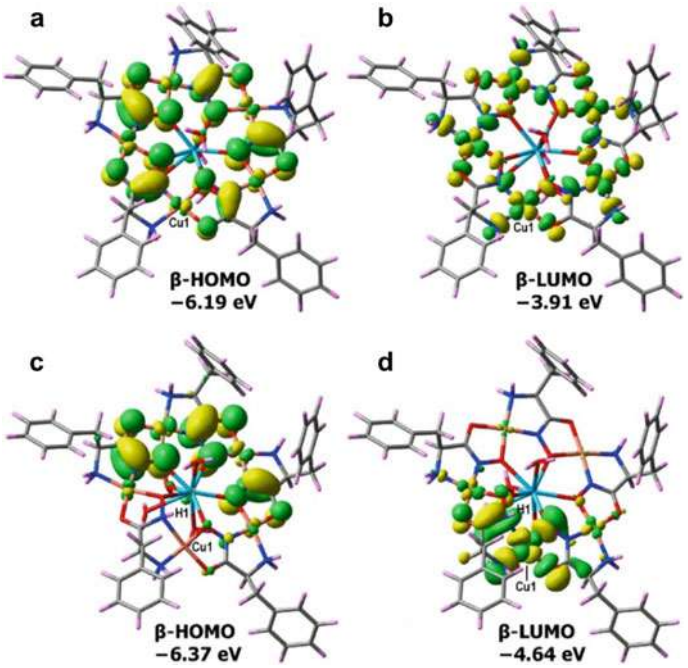

Fig. 19 Isosurfaces of the frontier molecular orbitals (isovalue 0.025) obtained for optimized structures of the La[15-$MC_{Cu(II)Pheha}$-5]$^{3+}$ (**a**, **b**) and La[15-$MC_{Cu(II)Pheha(H)}$-5]$^{4+}$ (**c**, **d**) ions. *Reproduced from* Ref. [43] by permission of John Wiley and Sons, © 2019 Wiley–VCH Verlag GmbH & Co. KGaA, Weinheim

4.1 Toward MRI Applications

Pecoraro and co-workers first described the potential advantage of the 15-MC-5 metallacrown scaffold for MRI applications [31]. Binnemans and co-workers demonstrated [34] that the ^{1}H NMR relaxation dispersion profiles of bis-aqua (q = 2) Gd(III) aminohydroximate metallacrown complexes are similar to the typical line shapes of the classic contrast agents derived from the Gd(III) chelates. For this metallacrown, the experimental water proton longitudinal relaxivities (r_1) in the range of 0.24 mT–1.4 T appear to be twice higher than those of Magnevist™ (Gadolinium DTPA dimeglumine salt). This difference was assigned to the presence of two H_2O molecules in the Gd(III) first coordination sphere in bis-aqua metallacrown complexes compared to one H_2O molecule in Gd–DTPA. The high relaxivity properties ($r_1 > 9.3\ s^{-1}\ mM^{-1}$) of tetraaqua 15-MC-5 complexes [33] at 4.7, 7, and 9.4 T make them suitable for the development of useful high-field MRI contrast agents which can be applied in biological imaging.

In the 15-MC-5 systems, the paramagnetic effect can be provided by two different paramagnetic ions, Cu(II) and Ln(III), coordinated by the water molecules. To

exclude the paramagnetic component from the Ln(III) ion, the complexes of diamagnetic La(III) were chosen, therefore, the paramagnetic effect of complexes should result exclusively from the Cu(II) ions. It was found that the Cu(II)-based relaxivity values of complexes Ln(III)–Cu(II) are negligible [33]. Among the paramagnetic lanthanide ions (Ce(III), Pr(III), Nd(III), Sm(III), Eu(III), Gd(III), Tb(III), Dy(III), Ho(III), Er(III), Tm(III) and Yb(III)), the largest paramagnetic effect would be expected for the Gd(III) ion due to its unique symmetric high-spin electronic ground state (S = 7/2) (Fig. 20).

As compared with the commercial contrast agent Magnevist, the tetraaqua Gd(III) glycinehydroximate complex displays only small differences between relaxivities at the 4.7 T, 7 T, and 9.4 T magnetic fields (Fig. 21) [33].

Note that the relaxivity of the tetra-aqua Gd MC complex decreases in the presence of an excess of lactate anions (Fig. 22). According to X-ray analysis, the bidentate lactate ligand and the water oxygen in the Gd lactate metallacrown (WUZNUC) lie at the apical positions of the Gd(III) coordination environment [22]. The Gd–O(aq) distance to the bottom coordinated water is slightly shorter than that found for the tetraaqua complex.

As mentioned above, in all these structures, the Ln(III) ion coordination sites are open for the inner-sphere water molecules due to the specific ligand environment provided by the metallamacrocycle ring. According to the X-ray diffraction experiments and DFT calculations, the Ln–H(aq) distances (2.96–3.10 Å) are similar to those in commercial contrast agents and in the hydrated Gd(III) ion (3.1 ± 0.1 Å) [74]. The calculated changes in enthalpy that correspond to the removal of an H_2O

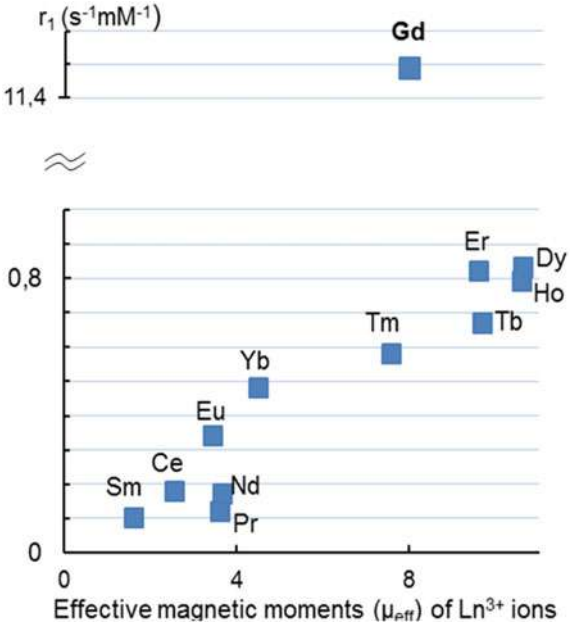

Fig. 20 Influence of the central metal ion on the relaxivities r_1 (18 °C) of $Ln(H_2O)_4[15\text{-}MC_{Cu(II)Glyha}\text{-}5](Cl)_3$ at 9.4 T in water (based on the previously reported data [33])

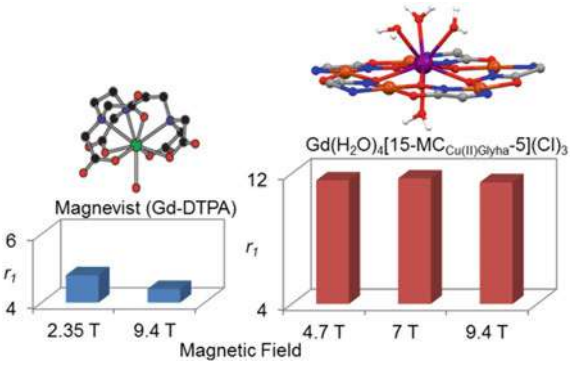

Fig. 21 Comparision of relaxivities of Magnevist and $Gd(H_2O)_4$[15-$MC_{Cu(II)Glyha}$-5]$(Cl)_3$

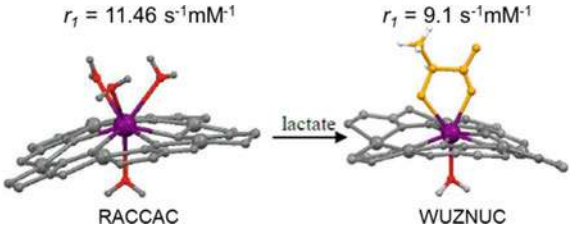

Fig. 22 The change of relaxivity ongoing from $Gd(H_2O)_4$[15-$MC_{Cu(II)Glyha}$-5]$(Cl)_3$ to the 15-MC-5 complex with lactate. *Adapted from* Ref. [33] with permission from Elsevier © 2015

molecule from the nine-coordinated Ln(III) ion in metallacrowns, ΔH_{sol}, are rather small (ca. ± 1 kcal/mol), which provides a facile exchange of the upper water molecules forming the H_2O triad (Fig. 23) [23]. The ΔH_{sol} value is not sensitive to the substituents in the [15-MC-5] metallacycle.

Assuming that the relaxivity of the complexes depends mainly on the inner-sphere molecules the r_1 and r_2 values presented in Table 7 suggest that the molecular weight and the number of the H_2O molecules are directly bound to the Gd(III) ion or ligand substituents have little effect [23]. Therefore, an increase in the number of the H_2O

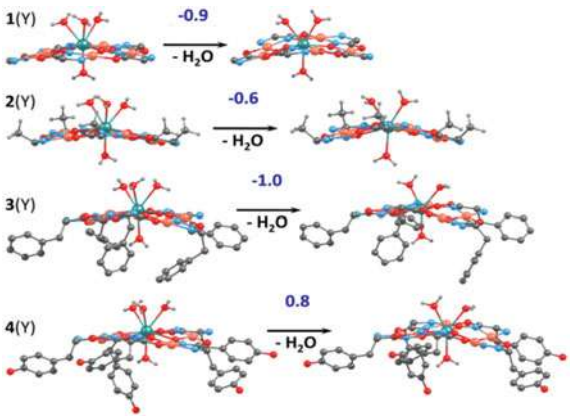

Fig. 23 Enthalpies ΔH_{sol} (kcal/mol) of water detachment from the Y(III) metallacrowns in solution. Hydrogen atoms except those of Me and H_2O in the B3LYP/DGDZVP optimized structures are omitted. *Adapted from* Ref. [23] by permission of John Wiley and Sons, © 2018 John Wiley & Sons, Ltd.

Table 7 High field relaxivities (18 °C, 9.4 T), hydration number, and molecular weights of selected Gd(III)–Cu(II) aminohydroximate complexes

Complex	q	MW_{MC} (Da)	r_1 (s^{-1} mM^{-1})	r_2 (s^{-1} mM^{-1})
$Gd(H_2O)_4$[15-$MC_{Cu(II)Glyha}$-5]$(Cl)_3$	4	987	11.5	11.6
$Gd(H_2O)_4$[15-$MC_{Cu(II)Alaha}$-5]$(Cl)_3$	4	1057	14.8	12.3
$Gd(H_2O)_4$[15-$MC_{Cu(II)Pheha}$-5]$(Cl)_3$	3	1420	13.9	14.2
$Gd(H_2O)_4$[15-$MC_{Cu(II)Tyrha}$-5]$(Cl)_3$	3	1500	12.2	12.2

Adapted from Ref. [23] by permission of John Wiley and Sons, © 2018 John Wiley & Sons, Ltd.

molecules involved in the exchange, as well as the modification of ligand substituents may not be enough to achieve the highest relaxivity in such metallamacrocyclic complexes. As a rule, a significant contribution to the high relaxivity of various systems is made by a rich hydration shell formed by strong hydrogen bonds between bulk H_2O molecules and complexes. [75, 76]. Such a rich hydration shell with close contacts between water molecules and the 15-MC-5 scaffold is a typical feature of the metllacrowns considered.

The enhanced relaxivities of these complexes at ultra-high field (9.4 T) suggest their use as a model for the design of efficient high-field MRI contrast agents. The Gd glycinehydroximate MC complex was applied as a contrast agent for high-field MRI of ischemic stroke in mice [8] and the Gd alaninehydroximate MC complex was used to create contrast in mouse kidneys [23]. The injection dose for Gd MC used was tenfold lower than the Gd-DTPA dose typically used in clinics [23]. Note that the imaging of the anatomically complex kidney of smaller animals such as mice is extremely difficult because of the poor intrinsic contrast without a contrasting agent (Figs. 24 and 25).

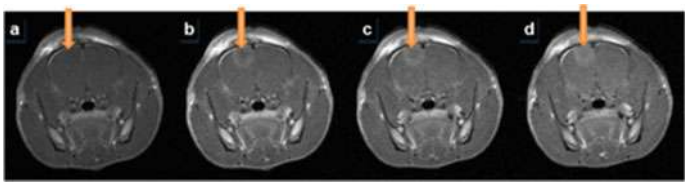

Fig. 24 Investigation of $Gd(H_2O)_4$[15-$MC_{Cu(II)Glyha}$-5]$(Cl)_3$ as a contrast agent for high-field MRI of ischemic stroke in mice: **a** pre-scan without injection of Gd MC; **b** MR image scanned after injection of Gd MC; **c** MR image scanned after 10 min injection; **d** MR image scanned after 20 min injection. *Reproduced from* Ref. [8] by permission from Springer Nature Customer Service Centre GmbH: Springer, © 2018

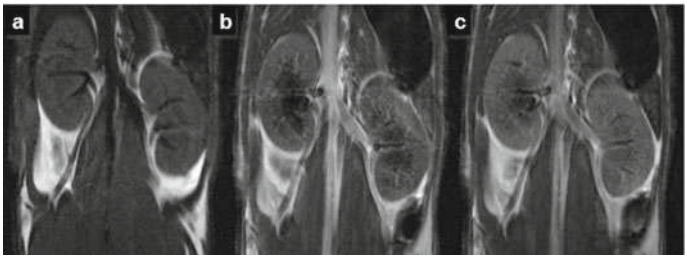

Fig. 25 MR images of $Gd(H_2O)_4[15\text{-}MC_{Cu(II)Alaha}\text{-}5](Cl)_3$ injected mouse kidneys scanned at 9.4 T with different timing: **a** pre-scan without injection of Gd MC; **b** MR image scanned immediately after injection of Gd MC; **c** MR image scanned 40 min after injection of Gd MC. *Reproduced from* Ref. [23] by permission of John Wiley and Sons, © 2018 John Wiley & Sons, Ltd.

4.2 Toward Hydrothermal Single-Source Precursors of Nanomaterials

Among the water-soluble Ln(III)–Cu(II) aminohydroximate metallacrowns, the simple glycinehydroximate complexes are presented as the primary model for studying the thermal stability [25, 29]. Compared with other glycinehydroximate complexes [29], the complexes based on Glyha, Alaha, and Pheha display similar thermal decomposition behaviors [26]. TG-DSC-MS studies revealed that the decomposition of these complexes proceeds through two major stages. The first ill-defined step with a weight loss of 4–5% within 80–150 °C temperature range is associated with the loss of lattice water molecules. The second stage consists of a sharp exothermic dip at 210–250 °C depending slightly on the nature of the central Ln ion (Table 8). The enthalpy of the exothermic process is (−150)–(−200) kcal/mol [29]. Therefore, the Ln(III)–Cu(II) complexes have potential application as a single-source precursor for the low-temperature growth of nanostructured cerium–copper mixed oxides under mild hydrothermal conditions.

Table 8 The influence of the central metal ion on the enthalpy ΔH and temperature T max corresponding to the exothermic dip on the TG-DSC diagrams [29] for glycinehydroximate Ln(III)–Cu(II) 15-MC-5 complexes $Ln(H_2O)_4[15MC_{CuGlyha}\text{-}5]Cl_3$

Ln	ΔH, (kcal/mol)	T max, (K)
Y	−156.8	520.7
La	−180.5	495.3
Ce	−202.5	495.9
Pr	−152.2	514.3
Nd	−149.5	520.6
Sm	−162.6	517.4
Eu	−160.8	516.0
Gd	−158.8	521.9
Dy	−160.6	521.1

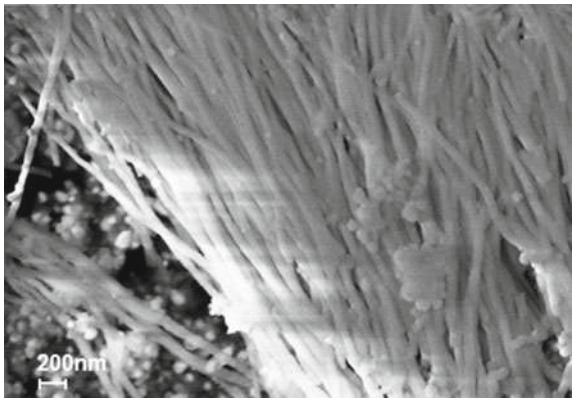

Fig. 26 SEM images of the as-grown silica nanowires. *Reproduced from* Ref. [49] with permission from Elsevier © 2017

It is interesting to note that the hydrothermal treatment of a silicon plate with a Ce(III)–Cu(II) metallamacrocyclic compound at 190 °C for 24 h leads to the formation of bamboo-like silica nanowires with an average diameter of 30–50 nm and a length of 15–20 mm (Fig. 26) [49].

With an idea to explore the unique properties of cerium(III) 15-MC-5 metallacrowns, the water-soluble Ce(III)–Cu(II) aqua-complexes bearing aminohydroximate (Glyha, Alaha, and Pheha) ligands have been tested for preparing a new nanocomposite hybrid material containing multi-walled carbon nanotubes (MWCNTs) and copper/ceria oxides. Relatively mild conditions of hydrothermal synthesis provide MWCNTs being not damaged when obtaining the oxide nanoparticles with a high degree of crystallinity and controllable morphology [25]. An additional crucial factor in the processing of nanocomposites consists of an efficient formation of MWCNT dispersions. Nanotubes tend to form bundles and ropes as a result of a strong van der Waals attraction [77]. Oppositely charged or non-ionic surfactants (e.g., sodium cholate or dodecylbenzene sulfonate and cetyltrimethylammonium bromide) can be employed in order to neutralize these attractive forces. However, the use of traditional surfactants suffers from their unpredictable influence on the toxicity in addition to their irreversible adsorption on the surface, resulting in undesirable changes in the properties of the final material [78]. The water-soluble Ce(III)–Cu(II) aqua-MC complexes bearing aminohydroximate (Glyha, Alaha, and Pheha) ligands appear to display dispersing properties with respect to MWCNTs in water (Fig. 27) [79]. Thus, Fig. 27a, b shows the vials of the aqueous MC-MWCNT dispersions at different time intervals after sonication. As indicated by the different colors of the vials, the amount of nanotubes remaining in the supernatant depends on the nature of the Ce(III)–Cu(II) 15-MC-5 derivatives. The phenylalanine derivative is well recognized among glycine and alanine 15-MC-5 as a good dispersant for MWCNTs. As shown in Fig. 27c, the aqueous phenylalanine derivative-MWCNT dispersion was quite stable over one month. Additionally, the suitability of these Ln(III)–Cu(II) derivatives for MWCNT dispersion and exfoliation in water has been investigated by optical density measurements and scanning electron microscopy.

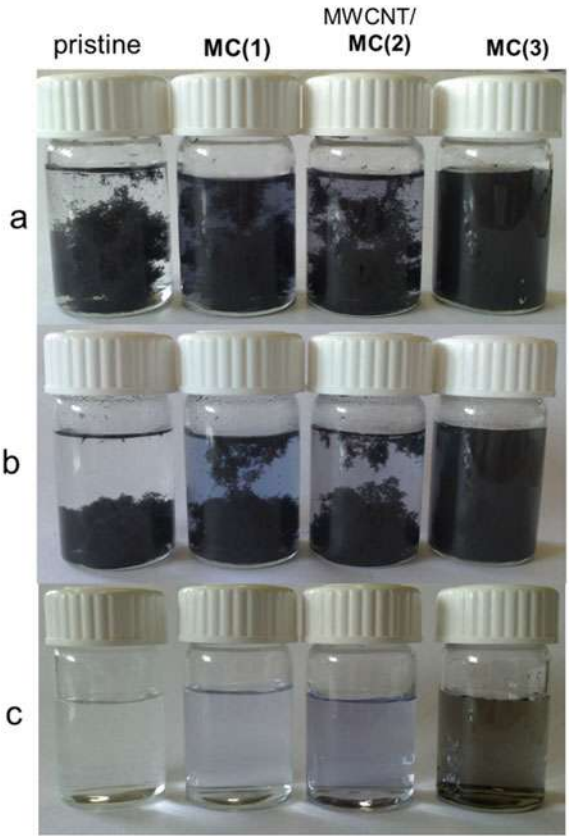

Fig. 27 Vials containing aqueous dispersions of (left to right) pristine MWCNT, MC(1)-MWCNT, MC(2)-MWCNT, MC(3)-MWCNT, after sonication (**a**), after 30 days (**b**), and after centrifugation for 20 min at 6000 rpm (**c**). Metallacrown Ce(III)–Cu(II) bearing Glyha (MC(1)), Alaha (MC(2)), and Pheha (MC(3)) ligands. *Adapted from* Ref. [79] with permission from Elsevier © 2017

The superiority of phenylalanine metallacrown can be attributed to the efficient π–π interaction between the phenylalanine groups of metallacrown and the carbon rings of MWCNTs [79].

The Ce(III)–Cu(II) phenylalanine metallacrown was used as a unique single-source precursor for a facile one-pot, surfactant-free, and template-free synthesis of nano- and mesocrystals with intriguing structures and morphologies (Fig. 28) [26]. The first two microphotographs (Fig. 28a, b) show that the product consists of a large number of necklace-like nanostructures. Spherical particles of CeO_2 in the form of flakes penetrated by carbon nanotubes were investigated using SEM and TEM. Figure 28c–t show exotic nanostructures of hydrothermally grown copper oxides. The nanoparticles of cerium and copper oxides have been synthesized using polynuclear metallamacrocyclic 15-MC-5 complexes and MWCNTs as precursors via the simple hydrothermal method without any surfactant or capping agents in water at 190 °C [26].

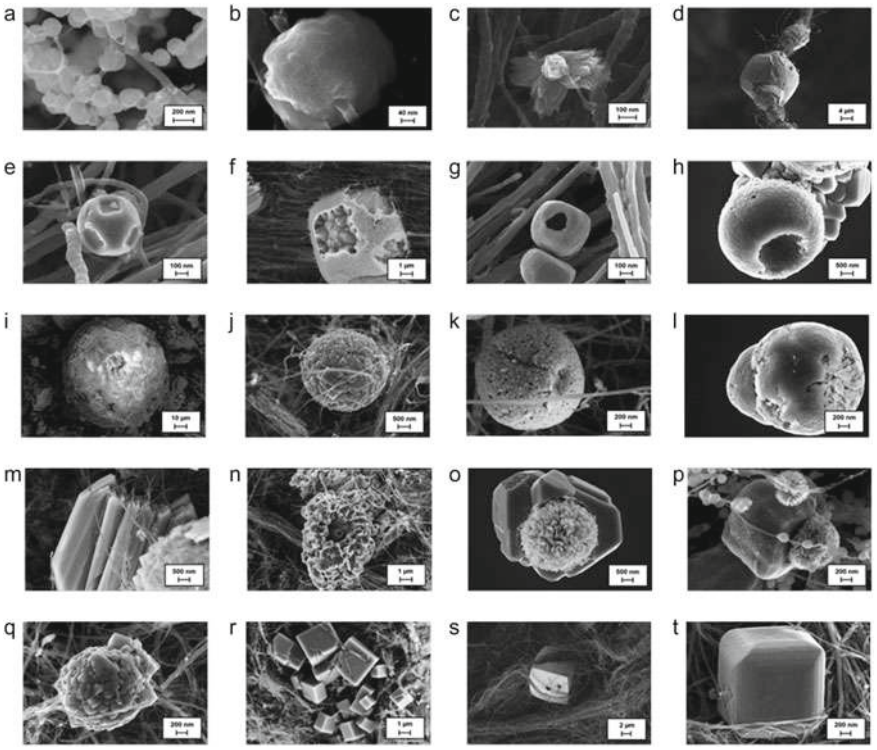

Fig. 28 SEM images of cerium (**a**, **b**) and copper (**c**–**t**) oxides obtained in the hydrothermal synthesis on the basis of water-soluble phenylalanine Ce(III)–Cu(II) 15-MC-5 complexes. *Reproduced from* Ref. [26] by permission of John Wiley and Sons, © 2019 Wiley–VCH Verlag GmbH & Co. KGaA, Weinheim

5 New Similarities and Analogues: Bi(III) Versus Ln(III)

Based on the idea that the identical charges and close ionic radii of Bi^{3+} and La^{3+} cations open up the possibility for the development of Bi(III)-based metallacrowns, a novel example of Bi(III)–Cu(II) hydroximate metallamacrocyclic complex of the 15-MC-5 type has been synthesized [80, 81]. The single-crystal X-ray analysis revealed the classic metallamacrocyclic molecular geometry with the neutral ring formed by five [Cu(II)–N–O] repeating units, the Bi^{3+} ion being encapsulated within the central cavity by the five hydroximate O atoms (Fig. 29).

However, DFT calculations reveal weaker donor–acceptor interactions between the metallamacrocycle and the central Bi^{3+} ion compared to the La(III)–Cu(II) complex. A larger deformation electron density (DED) is accumulated at the axial positions of the pentagonal pyramid formed by the ligand environment of the Bi^{3+} ion which results in the smaller effective positive charge on this metal ion and the smaller

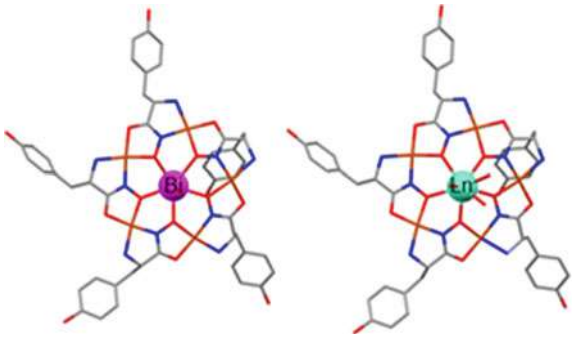

Fig. 29 The molecular structures of Bi^{3+} and Ln^{3+} tyrosinehydroximate 15-metallacrowns-5. *Reproduced from* the open access article [81] (© 2022 by the authors; licensee MDPI, Basel, Switzerland)

negative charges on the oxime O atoms [81]. This effect explains the preferable coordination of the negative OH^- species instead of the H_2O molecule, as well as the unusual structure with the six-coordinated central ion. Significant π-contributions to the interactions between the central ion and metallamacrocycle were revealed for both Bi(III) and La(III) complexes. The larger DED concentration at the axial positions of Bi^{3+} and the π-interactions are nicely visualized by the DED isosurfaces (Fig. 30).

To conclude, following our interest in water-soluble 15-Metallacrown-5 complexes, this new example not only enriches the structural diversity of the 15-MC-5 family, but also offers another approach to the discovery of new polynuclear metallamacrocyclic complexes with unconventional structures and properties.

Concluding Remarks

The synthetic strategies providing a basis for the design of water-soluble 15-MC-5 systems together with the results of quantum chemical modeling were reviewed. The

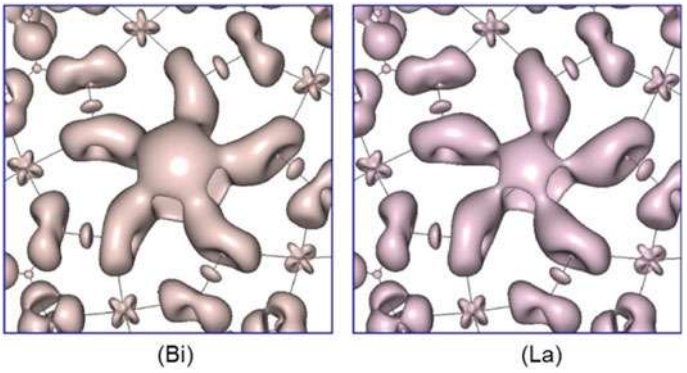

Fig. 30 Deformation electron density isosurfaces at 0.01 a.u. in the region of the central ion and the five oxime oxygen atoms for $[Bi(15\text{-}MC_{Cu(II)Tyrha}\text{-}5)]^{3+}$ (left) and $[La(15\text{-}MC_{Cu(II)Tyrha}\text{-}5)]^{3+}$ (right). The isosurfaces are built at the same scale. *Reproduced from* the open access article [81] (© 2022 by the authors; licensee MDPI, Basel, Switzerland)

relative stabilities of the metallacrowns under consideration were found to depend on the Cu(II) and Ln(III) coordination surroundings as well as on the ligand mutual orientations. New opportunities for the potential applications of the water-soluble 15-MC-5 (including MRT contrast agents) are associated with well-defined stable structures bearing an increasing number of water molecules in the Ln(III) inner-sphere. Low-temperature decomposition of metallacrowns leads to the new nanomaterials based on metal oxides. With the use of synthetic strategies discussed, water-soluble 15-MC-5 systems with some central-cavity metal ions other than lanthanides can be obtained.

Acknowledgements This work was supported by the Russian Science Foundation (project No. 18-13-00356).

References

1. Lah, M.S., Pecoraro, V.L.: Isolation and characterization of $\{Mn^{II}[Mn^{III}$'(salicylhydroximate)$]_4$(acetate)$_2$(DMF)$_6\}$2DMF: an inorganic analogue of M^{2+}(12-crown-4). J. Am. Chem. Soc. **111**, 7258–7259 (1989). https://doi.org/10.1021/ja00200a054
2. Lah, M.S., Pecoraro, V.L.: Development of metallacrown ethers: a new class of metal clusters. Comments Inorg. Chem. **11**, 59–84 (1990). https://doi.org/10.1080/02603599008035819
3. Bodwin, J.J., Cutland, A.D., Malkani, R.G., Pecoraro, V.L.: The development of chiral metallacrowns into anion recognition agents and porous materials. Coord. Chem. Rev. **216–217**, 489–512 (2001). https://doi.org/10.1016/S0010-8545(00)00396-9
4. Mezei, G., Zaleski, C.M., Pecoraro, V.L.: Structural and functional evolution of metallacrowns. Chem. Rev. **107**, 4933–5003 (2007). https://doi.org/10.1021/cr078200h
5. Tegoni, M., Remelli, M.: Metallacrowns of copper(II) and aminohydroxamates: thermodynamics of self assembly and host–guest equilibria. Coord. Chem. Rev. **256**, 289–315 (2012). https://doi.org/10.1016/j.ccr.2011.06.007
6. Ostrowska, M., Fritsky, I.O., Gumienna-Kontecka, E., Pavlishchuk, A.V.: Metallacrown-based compounds: applications in catalysis, luminescence, molecular magnetism, and adsorption. Coord. Chem. Rev. **327–328**, 304–332 (2016). https://doi.org/10.1016/j.ccr.2016.04.017
7. Pavlyukh, Y., Rentschler, E., Elmers, H.J., Hubner, W., Lefkidis, G.: Magnetism of metallacrown single-molecule magnets: from a simplest model to realistic systems. Phys. Rev. B **97**, 214408 (2018). https://doi.org/10.1103/PhysRevB.97.214408
8. Katkova, M.A.: Water-soluble polynuclear metallamacrocyclic copper(II) and lanthanide(III) complexes based on amino hydroxamic acids. Russ. J. Coord. Chem. **44**, 284–300 (2018). https://doi.org/10.1134/S107032841804005X
9. Lutter, J.C., Zaleski, C.M., Pecoraro, V.L.: Metallacrowns: supramolecular constructs with potential in extended solids, solution-state dynamics, molecular magnetism, and imaging. Adv. Inorg. Chem. Cambridge, MA **71**, 177–246 (2018). https://doi.org/10.1016/bs.adioch.2017.11.007
10. Andruh, M., Costes, J.-P., Diaz, C., Gao, S.: 3d–4f combined chemistry: synthetic strategies and magnetic properties. Inorg. Chem. **48**, 3342–3359 (2009). https://doi.org/10.1021/ic801027q
11. Dendrinou-Samara, C., Alevizopoulou, L., Iordanidis, L., Samaras, E., Kessissoglou, D.P.: 15-MC-5 manganese metallacrowns hosting herbicide complexes: structure and bioactivity. J. Inorg. Biochem. **89**, 89–96 (2002). https://doi.org/10.1016/j.ica.2018.09.001

12. Cal, M., Jaremko, L., Jaremko, M., Stefanowicz, P.: The metallacrowns as templates for spontaneous self-assembly of polypeptides into a tetrahelical bundle. New J. Chem. **37**, 3770–3777 (2013). https://doi.org/10.1039/C3NJ00641G
13. Cal, M., Kotynia, A., Jaremko, L., Jaremko, M., Lisowski, M., Cebo, M., Brasun, J., Stefanowicz, P.: Metallacrowns as products of the aqueous medium self-assembly of histidine-hydroxamic acid-containing polypeptides. Dalton Trans. **44**, 11172–11181 (2015). https://doi.org/10.1039/C5DT01267H
14. Rajczak, E., Gluszynska, A., Juskowiak, B.: Interaction of metallacrown complexes with G-quadruplex DNA. J. Inorg. Biochem. **155**, 105–114 (2016). https://doi.org/10.1016/j.jinorgbio.2015.11.025
15. Tarushi, A., Zampakou, M., Perontsis, S., Lafazanis, K., Pantazaki, A.A., Hatzidimitriou, A.G., Geromichalos, G.D., Psomas, G.: Manganese(II) complexes of tolfenamic acid or naproxen in polymeric structures or encapsulated in [15-MC-5] manganese(III) metallacrowns: structure and biological activity. Inorg. Chim. Acta **483**, 579–592 (2018). https://doi.org/10.1016/j.ica.2018.09.001
16. Mathieu, E., Sipos, A., Demeyere, E., Phipps, D., Sakaveli, D., Borbas, K.E.: Lanthanide-based tools for the investigation of cellular environments. Chem. Commun. **54**, 10021–10035 (2018). https://doi.org/10.1039/C8CC05271A
17. Barrya, N.P.E., Sadler, P.J.: Exploration of the medical periodic table: towards new targets. Chem. Commun. **49**, 5106–5131 (2013). https://doi.org/10.1039/C3CC41143E
18. Cotruvo, J.A., Jr.: The chemistry of lanthanides in biology: recent discoveries, emerging principles, and technological applications. ACS Cent. Sci. **5**, 1496–1506 (2019). https://doi.org/10.1021/acscentsci.9b00642
19. Gupta, S.P.: Hydroxamic Acids: A Unique Family of Chemicals with Multiple Biological Activities. Springer-Verlag, Berlin Heidelberg, Germany, (2013). https://doi.org/10.1007/978-3-642-38111-9
20. Chow, C.Y., Trivedi, E.R., Pecoraro, V.L., Zaleski, C.M.: Heterometallic mixed *3d–4f* metallacrowns: structural versatility, luminescence, and molecular magnetism. Comments Inorg. Chem. **35**, 214–253 (2015). https://doi.org/10.1080/02603594.2014.981811
21. Remelli, M., Bacco, D., Dallavalle, F., Lazzari, E., Marchetti, N., Tegoni, M.: Stoichiometric diversity of Ni(ii) metallacrowns with β-alaninehydroxamic acid in aqueous solution. Dalton Trans. **42**, 8018–8025 (2013). https://doi.org/10.1039/C3DT50370D
22. Katkova, M.A., Zabrodina, G.S., Muravyeva, M.S., Shavyrin, A.S., Baranov, E.V., Khrapichev, A.A., Ketkov, S.Yu.: Facile one-pot route toward water-soluble lanthanide–copper–glycinehydroximate 15-metallacrown-5 complexes. Eur. J. Inorg. Chem. **2015**, 5202–5208 (2015). https://doi.org/10.1002/ejic.201500695
23. Katkova, M.A., Zabrodina, G.S., Baranov, E.V., Muravyeva, M.S., Kluev, E.A., Shavyrin, A.S., Zhigulin, G.Yu., Ketkov, S.Yu.: New insights into water-soluble and water-coordinated copper 15-metallacrown-5 gadolinium complexes designed for high-field magnetic resonance imaging applications. Appl. Organomet. Chem. **32**, e4389 (2018). https://doi.org/10.1002/aoc.4389
24. Meng, Y., Yang, H., Li, D., Zeng, S., Chen, G., Li, S., Dou, J.: Synthesis, crystal structure, DNA-binding and magnetism of copper 15-metallacrown-5 complexes based on glycinehydroxamic acid ligand. RSC Adv. **6**, 47196–47202 (2016). https://doi.org/10.1039/C6RA05239H
25. Kremlev, K.V., Samsonov, M.A., Zabrodina, G.S., Arapova, A.V., Yunin, P.A., Tatarsky, D.A., Plyusnin, P.E., Katkova, M.A., Ketkov, S.Yu.: Copper(II)–cerium(III) 15-metallacrown-5 based on glycinehydroxamic acid as a new precursor for heterobimetallic composite materials on carbon nanotubes. Polyhedron **114**, 96–100 (2016). https://doi.org/10.1016/j.poly.2015.11.006
26. Katkova, M.A., Kremlev, K.V., Zabrodina, G.S., Rumyantcev, R.V., Gazhulina, A.P., Gusev, S.A., Ketkov, S.Yu., Fomina, I.G., Eremenko, I.L.: Polynuclear aminohydroximate metallamacrocyclic Cu(II)-Ce(III) complexes: a facile route to intricate nanostructures of copper and cerium oxides. Eur. J. Inorg. Chem. **2019**, 1002–1010 (2019). https://doi.org/10.1002/ejic.201801439
27. Pavlishchuk, A.V., Kolotilov, S.V., Fritsky, I.O., Zeller, M., Addison, A.W., Hunter, A.D.: Structural trends in a series of isostructural lanthanide-copper metallacrown sulfates

(Ln^{III} = Pr, Nd, Sm, Eu, Gd, Dy and Ho): hexaaquapentakis [μ_3-glycinehydroxamato(2-)]sulfatopentacopper(II)lanthanide(III) heptaaquapentakis [μ_3-glycinehydroxamato(2-)]sulfatopentacopper(II)lanthanide(III) sulfate hexahydrate. Acta Crystallogr. Sect. C Cryst. Struct. Commun. **67**, m255–m265 (2011). https://doi.org/10.1107/S0108270111021780
28. Pavlishchuk, A.V., Kolotilov, S.V., Zeller, M., Lofland, S.E., Addison, A.W.: Magnetic properties of Ln^{III}–Cu^{II} 15-metallacrown-5 dimers with terephthalate (Ln^{III} = Pr, Nd, Sm, Eu). Eur. J. Inorg. Chem. **2018**, 3504–3511 (2018). https://doi.org/10.1002/ejic.201800461
29. Makarov, S.G., Zabrodina, G.S., Cherkasov, A.V., Plyusnin, P.E., Arapova, A.V., Katkova, M.A., Ketkov, S.Yu.: Preparation and thermal decomposition of Ln(III)-Cu(II) polynuclear metallamacrocyclic compounds based on glycinehydroxamic acid. Macroheterocycles **9**, 263–267 (2016). https://doi.org/10.6060/mhc160317m
30. Pavlishchuk, A.V., Kolotilov, S.V., Zeller, M., Lofland, S.E., Thompson, L.E., Addison, A.W., Hunter, A.D.: High nuclearity assemblies and one-dimensional (1D) coordination polymers based on lanthanide-copper 15-metallacrown-5 complexes (LnIII = Pr, Nd, Sm, Eu). Inorg. Chem. **56**, 13152–13165 (2017). https://doi.org/10.1021/acs.inorgchem.7b01944
31. Stemmler, A.J., Kampf, J.W., Kirk, M.L., Atasi, B.H., Pecoraro, V.L.: The Preparation, characterization, and magnetism of copper 15-Metallacrown-5 lanthanide complexes. Inorg. Chem. **38**, 2807–2817 (1999). https://doi.org/10.1021/ic9800233
32. Katkova, M.A., Zabrodina, G.S., Muravyeva, M.S., Khrapichev, A.A., Samsonov, M.A., Fukin, G.K., Ketkov, S.Yu.: New experimental insights into the formation of unexpected water-soluble Eu(III)–Cu(II) 15-metallacrown-5 compound with acetate. Inorg. Chem. Commun. **52**, 31–33 (2015). https://doi.org/10.1016/j.inoche.2014.12.008
33. Muravyeva, M.S., Zabrodina, G.S., Samsonov, M.A., Kluev, E.A., Khrapichev, A.A., Katkova, M.A., Mukhina, I.V.: Water-soluble tetraaqua Ln(III) glycinehydroximate 15-metallacrown-5 complexes towards potential MRI contrast agents for ultra-high magnetic field. Polyhedron **114**, 165–171 (2016). https://doi.org/10.1016/j.poly.2015.11.033
34. Parac-Vogt, T.N., Pacco, A., Nockemann, P., Laurent, S., Muller, R.N., Wickleder, M., Meyer, G., Elst, L.V., Binnemans, K.: Relaxometric study of copper [15]metallacrown-5 gadolinium complexes derived from α-aminohydroxamic acids. Chem. Eur. J. **12**, 204–210 (2006). https://doi.org/10.1002/chem.200500136
35. Pavlishchuk, A.V., Kolotilov, S.V., Zeller, M., Thompson, L.K., Addison, A.W.: Formation of coordination polymers or discrete adducts via reactions of gadolinium(III)–copper(II) 15-metallacrown-5 complexes with polycarboxylates: synthesis. Struct. Magn. Prop. Inorg. Chem. **53**, 1320–1330 (2014). https://doi.org/10.1021/ic401928m
36. Pavlishchuk, A., Naumova, D., Zeller, M., Cazorla, S.C., Addison, A.W.: The crystal structures of $\{LnCu_5\}^{3+}$ (Ln = Gd, Dy and Ho) 15-metallacrown-5 complexes and a reevaluation of the isotypic Eu^{III} analogue. Acta Crystallogr. Sect. E Cryst. Commun. **75**, 1215–1223 (2019). https://doi.org/10.1107/S205698901900999X
37. Stemmler, A.J., Barwinski, A., Baldwin, M.J., Young, V., Pecoraro, V.L.: Facile preparation of face differentiated, chiral 15-metallacrown-5 complexes. J. Am. Chem. Soc. **118**, 11962–11963 (1996). https://doi.org/10.1021/ja9622968
38. Jankolovits, J., Lim, C.S., Mezei, G., Kampf, J.W., Pecoraro, V.L.: Influencing the size and anion selectivity of dimeric Ln^{3+}[15-Metallacrown-5] compartments through systematic variation of the host side chains and central metal. Inorg Chem. **51**, 4527–4538 (2012). https://doi.org/10.1021/ic202347j
39. Jankolovits, J., Van-Noord, A.D.C., Kampf, J.W., Pecoraro, V.L.: Selective anion encapsulation in solid-state Ln(III)[15-metallacrown-5]$^{3+}$ compartments through secondary sphere interactions. Dalton Trans. **42**, 9803–9808 (2013). https://doi.org/10.1039/C3DT50535A
40. Zaleski, C.M., Lim, C.S., Noord, A.D.C.V., Kampf, J.W., Pecoraro, V.L.: Effects of the central lanthanide ion crystal radius on the 15-$MC_{Cu^{II}(N)pheHA}$-5 structure. Inorg. Chem. **50**, 7707–7717 (2011). https://doi.org/10.1021/ic200740h
41. Zaleski, C.M., Noord, A.D.C.V., Kampf, J.W., Pecoraro, V.L.: Controlling the polymorph of $Ln^{III}(NO_3)_{3-x}(OH)_x$[15-$MC_{CuII(N)S\text{-}pheHA}$-5] complexes through solvent type and ^{LnI}II ion choice. Cryst. Growth. Des. **7**, 1098–1105 (2007). https://doi.org/10.1021/cg060743h

42. Lim, C.S., Jankolovits, J., Kampf, J.W., Pecoraro, V.L.: Chiral metallacrown supramolecular compartments that template nanochannels: self-assembly and guest absorption. Chem. Asian J. **5**, 46–49 (2010). https://doi.org/10.1002/asia.200900612
43. Katkova, M.A., Zabrodina, G.S., Rumyantcev, R.V., Zhigulin, G.Yu., Ketkov, S.Yu., Lyssenko, K.A., Fomina, I.G., Eremenko, I.L.: pH-responsive switching properties of a water-soluble metallamacrocyclic phenylalaninehydroximate La(III)–Cu(II) complex: insight into tuning protonation ligand states. Eur. J. Inorg. Chem. **2019**, 4328–4335 (2019). https://doi.org/10.1002/ejic.201900536
44. Jankolovits, J., Lim, C.S., Kampf, J.W., Pecoraro, V.L.: Disruption of the La(III)[15-Metallacrown-5] cavity through bithiophene dicarboxylate inclusion. Z. Naturforsch. B Chem. Sci. **65**, 263–272 (2010). http://www.znaturforsch.com/s65b/s65b0263.pdf
45. Cutland, A.D., Halfen, J.A., Kampf, J.W., Pecoraro, V.L.: Chiral 15-metallacrown-5 complexes differentially bind carboxylate anions. J. Am. Chem. Soc. **123**, 6211–6212 (2001). https://doi.org/10.1021/ja015610t
46. Lim, C.S., Kampf, J.W., Pecoraro, V.L.: Establishing the binding affinity of organic carboxylates to 15-metallacrown-5 complexes. Inorg. Chem. **48**, 5224–5233 (2009). https://doi.org/10.1021/ic9001829
47. Zabrodina, G.S., Katkova, M.A., Samsonov, M.A., Ketkov, S.Yu.: Investigation of chromophoric behavior of water-soluble La^{III}-Cu^{II} polynuclear metallamacrocyclic 15-MC-5 complex. Z. Anorg. Allg. Chem. **644**, 907–911 (2018). https://doi.org/10.1002/zaac.201800214
48. Jankolovits, J., Kampf, J.W., Maldonado, S., Pecoraro, V.L.: Voltammetric characterization of redox-inactive guest binding to Ln^{III}[15-metallacrown-5] hosts based on competition with a redox probe. Chem. Eur. J. **16**, 6786–6796 (2010). https://doi.org/10.1002/chem.200903015
49. Katkova, M.A., Zabrodina, G.S., Kremlev, K.V., Gusev, S.A., Kaverin, B.S., Obiedkov, A.M., Fomina, I.G., Lyssenko, K.A., Eremenko, I.L.: Surface modification of silicon plate by hydrothermal treatment with a copper–cerium metallamacrocyclic compound. Mendeleev Commun. **27**, 402–404 (2017). https://doi.org/10.1016/j.mencom.2017.07.029
50. Noord, A.D.C.V., Kampf, J.W., Pecoraro, V.L.: Preparation of resolved fourfold symmetric amphiphilic helices using chiral metallacrown building blocks. Angew. Chem. Int. Ed. **41**, 4667–4670 (2002). https://doi.org/10.1002/anie.200290010
51. Tegoni, M., Tropiano, M., Marchio, L.: Thermodynamics of binding of carboxylates to amphiphilic Eu^{3+}/Cu^{2+} metallacrown. Dalton Trans. 6705–6708 (2009). https://doi.org/10.1039/B911512A
52. Lim, C.S., Jankolovits, J., Zhao, P., Kampf, J.W., Pecoraro, V.L.: Gd(III)[15-Metallacrown-5] recognition of chiral α-amino acid analogues. Inorg. Chem. **50**, 4832–4841 (2011). https://doi.org/10.1021/ic102579t
53. Lim, C.S., Noord, A.C.V., Kampf, J.W., Pecoraro, V.L.: Assessing guest selectivity within metallacrown host compartments. Eur. J. Inorg. Chem. **2007**, 1347–1350 (2007). https://doi.org/10.1002/ejic.200700054
54. Mezei, G., Kampf, J.W., Pan, S., Poeppelmeier, K.R., Watkins, B., Pecoraro, V.L.: Metallacrown-based compartments: selective encapsulation of three isonicotinate anions in non-centrosymmetric solids. Chem. Commun. 1148–1150 (2007). https://doi.org/10.1039/B614024F
55. Zaleski, C.M., Depperman, E.C., Kampf, J.W., Kirk, M.L., Pecoraro, V.L.: Using Ln^{III}[15-$MC_{CuII(N)(S)\text{-pheHA}}$-5]$^{3+}$ complexes to construct chiral single-molecule magnets and chains of single-molecule magnets. Inorg. Chem. **45**, 10022–10024 (2006). https://doi.org/10.1021/ic061326x
56. Cutland, A.D., Malkani, R.G., Kampf, J.W., Pecoraro, V.L.: Lanthanide [15]Metallacrown-5 complexes form nitrate-selective chiral cavities. Angew. Chem. Int. Ed. **39**, 2689–2691 (2000). https://doi.org/10.1002/1521-3773(20000804)39:15<2689::AID-ANIE2689>3.0.CO;2-0
57. A short guide to abbreviations and their use in peptide science. Amino Acids Peptides Proteins **42**, P010–P017 (2017). https://doi.org/10.1039/9781788010627-FP010
58. Zhigulin, G.Yu., Zabrodina, G.S., Katkova, M.A., Ketkov, S.Yu.: Quantum chemical study of formation of Cu^{II}–Y^{III} metallamacrocyclic complexes based on glycinehydroximate ligands. Russ. Chem. Bull. **67**, 1173–1181 (2018). https://doi.org/10.1007/s11172-018-2198-0

59. Shannon, R.: Revised effective ionic radii and systematic studies of interatomic distances in halides and chalcogenides. Acta Crystallogr. Sect. A **32**, 751–767 (1976). https://doi.org/10.1107/S0567739476001551
60. Cortes-Guzman, F., Bader, R.F.W.: Complementarity of QTAIM and MO theory in the study of bonding in donor–acceptor complexes. Coord. Chem. Rev. **249**, 633–662 (2005). https://doi.org/10.1016/j.ccr.2004.08.022
61. De Miranda-Pinto, C.O.B., Paniago, E.B., Carvalho, S., Tabak, M., Mascarenhas, Y.P.: Crystal and molecular structure of a copper(II)-glycinehydroxamic acid complex. Inorg. Chim. Acta **137**, 145–149 (1987). https://doi.org/10.1016/S0020-1693(00)81157-3
62. Zhigulin, G.Yu., Zabrodina, G.S., Katkova, M.A., Ketkov, S.Yu.: DFT studies of the electron density distribution and donor-acceptor interactions in water-soluble aminohydroximate metallamacrocyclic Ca^{II} and Y^{III} complexes. Russ. Chem. Bull. **68**, 743–750 (2019). https://doi.org/10.1007/s11172-019-2481-8
63. Espinosa, E., Alkorta, I., Elguero, J., Molins, E.: From weak to strong interactions: a comprehensive analysis of the topological and energetic properties of the electron density distribution involving X-H$\cdots$F–Y systems. J. Chem. Phys. **117**, 5529 (2002). https://doi.org/10.1063/1.1501133
64. Gibbs, G.V., Cox, D.F., Crawford, T.D., Rosso, K.M., Ross, N.L., Downs, R.T.: Classification of metal-oxide bonded interactions based on local potential- and kinetic-energy densities. J. Chem. Phys. **124**, 084704 (2006). https://doi.org/10.1063/1.2161425
65. Bloembergen, N., Morgan, L.O.: Proton relaxation times in paramagnetic solutions. Effects of electron spin relaxation. J. Chem. Phys. **34**, 842 (1961). https://doi.org/10.1063/1.1731684
66. Werner, E.J., Datta, A., Jocher, C.J., Raymond, K.N.: High-relaxivity MRI contrast agents: where coordination chemistry meets medical imaging. Angew. Chem. Int. Ed. **47**, 8568–8680 (2008). https://doi.org/10.1002/anie.200800212
67. Lawson, D., Barge, A., Terreno, E., Parker, D., Aime, S., Botta, M.: Optimizing the high-field relaxivity by self-assembling of macrocyclic Gd(III) complexes. Dalton Trans. **44**, 4910–4917 (2015). https://doi.org/10.1039/C4DT02971B
68. Zhigulin, G.Yu., Zabrodina, G.S., Katkova, M.A., Ketkov, S.Yu.: Polynuclear glycinehydroximate Cu(II)–Gd(III) metallamacrocyclic complexes: halochromic properties. Russ. J. Coord. Chem. **45**, 356–360 (2019). https://doi.org/10.1134/S107032841905004X
69. Katkova, M.A., Zabrodina, G.S., Zhigulin, G.Yu., Rumyantsev, R.V., Ketkov, S.Yu.: Water-soluble chiral Y(III)–Cu(II) metallamacrocyclic phenylalaninehydroximate complex. Russ. J. Coord. Chem. **45**, 721–727 (2019). https://doi.org/10.1134/S1070328419100014
70. Tegoni, M., Furlotti, M., Tropiano, M., Lim, C.S., Pecoraro, V.L.: Thermodynamics of core metal replacement and self-assembly of Ca^{2+} 15-metallacrown-5. Inorg. Chem. **49**, 5190–5201 (2010). https://doi.org/10.1021/ic100315u
71. Jankolovits, J., Kampf, J.W., Pecoraro, V.L.: Isolation of elusive tetranuclear and pentanuclear M(II)–hydroximate intermediates in the assembly of lanthanide [15-metallacrown-5] complexes. Inorg. Chem. **52**, 5063–5076 (2013). https://doi.org/10.1021/ic302831u
72. Beccia, M.R., Garcia, B., Garcia-Tojal, J., Leal, J.M., Secco, F., Tegoni, M.: The mechanism of the Cu2+[12-MCCu(Alaha)-4] metallacrown formation and lanthanum(III) encapsulation. Dalton Trans. **43**, 9271–9282 (2014). https://doi.org/10.1039/C4DT00557K
73. Dallavalle, F., Remelli, M., Sansone, F., Bacco, D., Tegoni, M.: Thermodynamics of self-assembly of copper(II) 15-Metallacrown-5 of Eu(III) or Gd(III) with (*S*)-α-alaninehydroxamic acid in aqueous solution. Inorg. Chem. **49**, 1761–1772 (2010). https://doi.org/10.1021/ic902146d
74. Caravan, P., Astashkin, A.V., Raitsimring, A.M.: The Gadolinium(III)−water hydrogen distance in MRI contrast agents. Inorg. Chem. **42**, 3972–3974 (2003). https://doi.org/10.1021/ic034414f
75. Caravan, P., Ellison, J.J., McMurry, T.J., Lauffer, R.B.: Gadolinium(III) chelates as MRI contrast agents: structure, dynamics, and applications. Chem. Rev. **99**, 2293–2352 (1999). https://doi.org/10.1021/cr980440x

76. Watanabe, T., Frahm, J., Michaelis, T.: Reduced intracellular mobility underlies manganese relaxivity in mouse brain in vivo: MRI at 2.35 and 9.4 T. Brain Struct. Funct. **220**, 1529–1538 (2015). https://doi.org/10.1007/s00429-014-0742-8
77. Tasis, D., Tagmatarchis, N., Bianco, A., Prato, M.: Chemistry of carbon nanotubes. Chem. Rev. **106**, 1105–1136 (2006). https://doi.org/10.1021/cr050569o
78. Pinna, N., Niederberger, M.: Surfactant-free nonaqueous synthesis of metal oxide nanostructures. Angew. Chem. Int. Ed. **47**, 5292–5304 (2008). https://doi.org/10.1002/anie.200704541
79. Katkova, M.A., Zabrodina, G.S., Kremlev, K.V., Gusev, S.A., Obiedkov, A.M., Kaverin, B.S., Fomina, I.G., Eremenko, I.L.: Effect of Ce(III)-Cu(II) 15-metallacrown-5 compounds on the dispersion of multi-walled carbon nanotubes in aqueous solutions: toward surfactant-free applications. Thin Solid Films **628**, 112–116 (2017). https://doi.org/10.1016/j.tsf.2017.03.029
80. Zabrodina, G.S., Katkova, M.A., Baranov, E.V., Zhigulin, G.Yu., Ketkov, S.Yu.: Synthesis and molecular structure of the first metallamacrocyclic Bi(III)-Cu(II) 15-MC-5 complex derived from pyrazinohydroxamic acid. Macroheterocycles **12**, 300–306 (2019). https://doi.org/10.6060/mhc190866z
81. Katkova, M.A., Zhigulin, G.Y., Rumyantcev, R.V., Zabrodina, G.S., Shayapov, V.R., Sokolov, M.N., Ketkov, S.Yu.: Water-soluble bismuth(III) polynuclear tyrosinehydroximate metallamacrocyclic complex: structural parallels to lanthanide metallacrowns. Molecules **25**, 4379 (2020). https://doi.org/10.3390/molecules25194379

Metallacrown-Based Catalysts for Water Oxidation and CO_2 Conversion

Hua Yang, Jianmin Dou, and You Song

Abstract The problems of the world energy crises and anthropogenic climate change demand renewable energies substitute for fossil energy. The conversion of the earth-abundant small molecules, such as H_2O and CO_2 into energy-rich/value-added compounds serves as the optimal choice to solve energy issues. And a promising strategy is to split water into hydrogen and oxygen to achieve the storage of the excess renewable energies. In nature, the oxidation of water in photosystem II is efficiently catalyzed by a multinuclear Mn_4CaO_5 cluster, oxygen-evolving complex (OEC), which is recognized as a highly active and robust catalyst to supply rapid multielectron transfer and smooth O–O bond formation. Thus, the natural enzymes for small-molecule conversions have encouraged many researchers to pursue this project, and the earth-abundant transition metal ions such as Mn, Fe, Co, and Cu-based multinuclear metal complexes have been widely explored. As a result, the multinuclear metal complexes with definitive structures and coordination environment of metal centers have been recognized as promising candidates for developing efficient artificial catalysts for redox. Metallacrowns (MCs), a kind of metallamacrocycle complexes, have the unique feature, definitive structures, and rich metal ions in such a small volume and display the interestingly catalytic activity of water oxidation and carbon dioxide conversion. The detailed description is given in the following text.

H. Yang (✉) · J. Dou
Shandong Provincial Key Laboratory of Chemical Energy Storage and Novel Cell Technology, College of Chemistry and Chemical Engineering, Liaocheng University, Liaocheng 252059, P. R. China
e-mail: yanghua@lcu.edu.cn

J. Dou
e-mail: dougroup@163.com

Y. Song
State Key Laboratory of Coordination Chemistry, Collaborative Innovation Center of Advance Microstructures, School of Chemistry and Chemical Engineering, Nanjing University, Nanjing 210093, P. R. China
e-mail: yousong@nju.edu.cn

C. M. Zaleski (ed.), *Advances in Metallacrown Chemistry*,
https://doi.org/10.1007/978-3-031-08576-5_8

1 Water Oxidation

Water oxidation process ($2H_2O \rightarrow O_2 + 4H^+ + 4e^-$) is thermodynamically and kinetically unfavorable due to its requirement for the transfer of four electrons and the formation of an O–O bond [1–5]. Consequently, it is crucial for the development of highly active and stable artificial catalysts for water oxidation. In this field, the metal clusters electro/photocatalysts have attracted more and more attention [6–9]. Metallacrowns as one outstanding family of metal clusters have definitive and charming structures and display various physical–chemical properties, such as bioactivity, molecular recognition, catalysis, single-molecule magnets, and so on [10]. They also showed excellent catalytic performance as electro/photocatalysts in water splitting. Masaoka S. and co-authors [11, 12] synthesized a series of pentanuclear scaffold complexes $[M_5(\mu_3\text{-}O)(\mu\text{-}L)_6]^{3+}$ through 3,5-bis(2-pyridyl)pyrazole (Hbpp, LH) ligand and their derivatives. The scaffold structures display a triangular $[M_3(\mu_3\text{-}X)]$ core (M = Fe, Co, Zn, Mn; X = O_2^- or OH^-) wrapped by two $[M(\mu\text{-}bpp)_3]$ units (Fig. 1). Herein, the $[Fe^{II}{}_4Fe^{III}(\mu_3\text{-}O)(\mu\text{-}L)_6]^{3+}$ (**[Fe_5]**) complex was discussed as a representative. In the trigonal–bipyramidal structure, the triangular $[Fe_3(\mu_3\text{-}O)]$ core can be regarded as a 9-MC-3 structural type with [M–N–N] repeat unit, a feature of azametallacrown (azaMC), which is an extension and the second class of MCs. At the apical positions, two iron ions are hexa-coordinated by three L^- ligands to display distorted octahedral geometries, while the triangular three iron ions are penta-coordinated through two L^- ligands and an O^{2-} anion to form distorted bipyramidal geometries. So, the coordinative unsaturated triangular metal ions and the coordinative saturated apical metal ions likely exhibit multiple redox-active centers.

The cyclic voltammogram (CV) of **[Fe_5]** in acetonitrile revealed one reversible reduction wave ($E_{1/2} = -0.55$ V, versus ferrocene/ferrocenium, Fc/Fc^+) and four reversible oxidation waves ($E_{1/2} = 0.13$, 0.30, 0.68, and 1.08 V), corresponding to

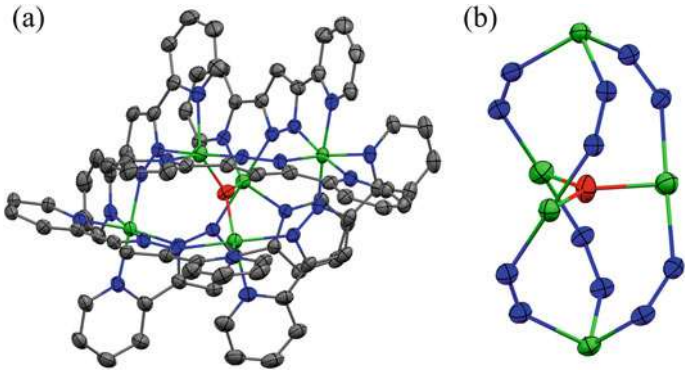

Fig. 1 **a** ORTEP drawings (50% probability ellipsoids) of the structure of cationic moiety of $[Fe_5(\mu_3\text{-}O)(\mu\text{-}L)_6(BF_4)_3]$ (left, hydrogen atoms are omitted for clarity) and **b** the core structure highlighting the azametallacrown connectivity between the iron centers. (HL = 3,5-bis(2-pyridyl)pyrazole.) Color scheme: O = red, C = gray, N = blue, and Fe = green

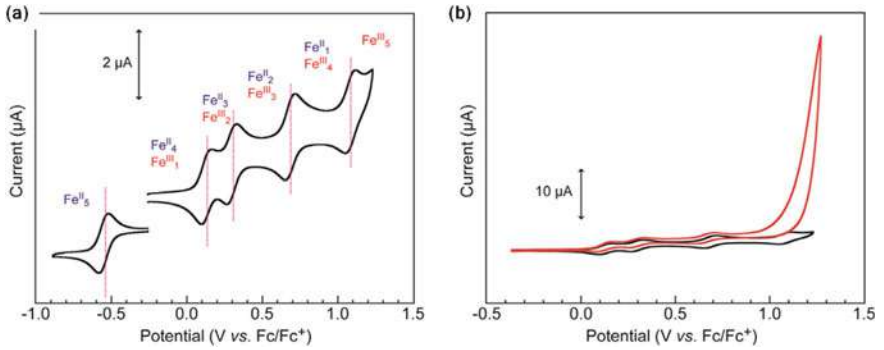

Fig. 2 **a** CVs of **[Fe$_5$]** (0.2 mM) in an acetonitrile solution containing Et_4NClO_4 (0.1 M) at a scan rate of 10 mV s^{-1}. **b** CVs of **[Fe$_5$]** (0.2 mM) in acetonitrile solution containing Et_4NClO_4 (0.1 M) at a scan rate of 10 m V s^{-1} with 5 M of H_2O (red line) and without water (black line, the same data as in **a**). (Reproduced with permission from [11])

five sequentially one-electron transfers in true each of the iron ion Fe^{III}/Fe^{II} couples (Fig. 2a). Thus, the existence of five irons in **[Fe$_5$]** complex makes it to demonstrate the high redox flexibility and attain the high potential to generate four-electron oxidized species. Notably, a large irreversible anodic current (catalytic current) appeared in the profile of the CV when water was added into the system with the potential corresponding to the $[Fe^{III}{}_5]/[Fe^{II}Fe^{III}{}_4]$ redox couple, indicating an electrocatalytic active site for O_2 evolution from water (Fig. 2b). Controlled potential electrolysis (CPE) was conducted to quantify the evolution of O_2 from water with a faradaic efficiency of 96% based on a $4e^-$ process. In electrocatalytic reactions, the pseudo-first-order rate constant κ_{cat}, corresponding to the turnover frequency (TOF) value, was also used to evaluate catalytic activity, and the resulting TOF value can be deduced from Eq. (1) [13–16].

$$\frac{i_{cat}}{i_p} = 2.242 n_{cat} \left(\frac{\kappa_{cat} RT}{F}\right)^{1/2} v^{1/2} \tag{1}$$

where i_{cat} is the catalytic current, i_p is the peak current measured in the absence of substrate, n_{cat} is the number of electrons involved in the catalytic reaction, F is Faraday's constant, κ_{cat} is the effective first-order rate constant, R is the universal gas constant, T is the temperature in Kelvin, and v is the scan rate. The limiting currents were kept unchanged as the scan rates in the range of 1.6–2.6 V s^{-1} (Fig. 3a), and a linear relationship was observed through the plot of the ratio of i_{cat} to i_p as a function of the inverse of the square root of the scan rate (Fig. 3b). The slope of the plot gave the TOF value of 1,900 s^{-1} for water oxidation of **[Fe$_5$]**, which is about 1,000 times greater than that of reported other iron-based water oxidation catalysts [17–23]. Furthermore, the obtained TOF and TON (turnover number) values from the controlled potential electrolysis (CPE) are 140–1,400 s^{-1} and 10^6–10^7 in 120 min, respectively. These values illustrate **[Fe$_5$]** complex can serve as an efficient and

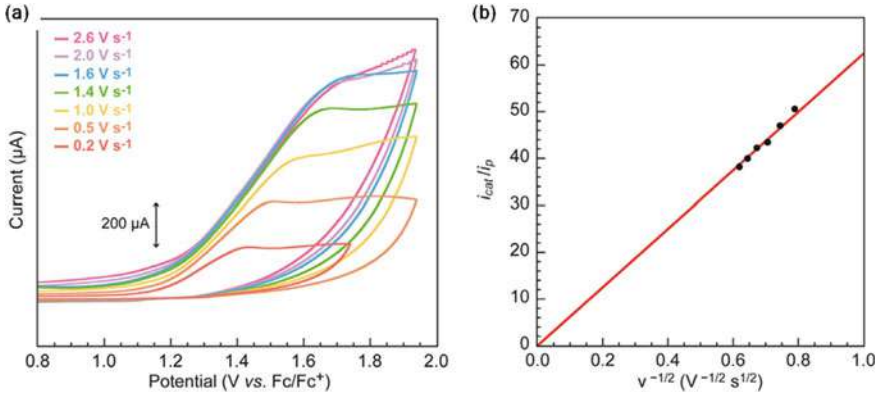

Fig. 3 **a** CV of **[Fe$_5$]** (0.2 mM) in an acetonitrile/water (10:1) mixed solution containing Et_4NClO_4 (0.1 M) at scan rates of 0.2–2.6 V s^{-1}. **b** A plot of the ratio of i_{cat} to i_p as a function of the inverse of the square root of the scan rate v, showing the linear relationship. Data obtained from the measurements with the scan rates (in V s^{-1}) of 1.6, 1.80, 2.00, 2.20, 2.40, and 2.60 were used for the calculation of the TOF. (Reproduced with permission from [11])

robust molecular catalyst for water oxidation. This also reveals a signal that the earth-abundant metal complexes will be the potential candidates for the oxidation of water in the future.

A possible catalytic cycle of **[Fe$_5$]** was forwarded based on the electrochemical measurements and illustrated in Fig. 4. The results revealed that a four-step, one-electron oxidation process occurred and accompanied the transfer of an electron from the initial [$Fe^{II}_4Fe^{III}$] state (S_0 in Fig. 4) to the completely oxidized [Fe^{III}_5] state (S_4). The substrate water molecule linked the S_4 state to form a [$Fe^{III}_5(OH_2)$] species (**A** in Fig. 4), where a Fe^{III} ion in the triangular core possessed a hexa-coordinated geometry. Another water molecule attacked on with sequential or simultaneous deprotonation, and a bis-oxo mixed-valence [$Fe^{II}_2Fe^{III}(Fe^{IV}=O)_2$] species (**B** in Fig. 4) was formed, confirmed at an energy minimum by the calculation. Note that the charge delocalization from triangular core Fe^{III} ions to the apical iron ions led to the formation of the $Fe^{IV}=O$ unit in the angular core. Then, the peroxo species (**C** in Fig. 4) was generated between the co-facial oxo group in **B**, in which O–O bond formation occurred. The quantum chemical calculation also revealed that the O–O bond formation process smoothly proceeded in an intramolecular fashion in **[Fe$_5$]** [24]. Finally, O_2 was released from **C** to regenerate the initial S_0 state, and the whole catalytic cycle was completed. Later, Najafpour M.M. carried out a series of experiments to investigate the true catalyst for water oxidation in the presence of **[Fe$_5$]** complex. The result revealed that **[Fe$_5$]** was not stable, and its decomposition led to the formation of Fe oxide, which was possible one candidate as the true catalyst for water oxidation.[25]

Although **[Fe$_5$]** has high activity and stability as a robust and efficient molecular catalyst for water oxidation, the relatively large onset potential is a drawback. Therefore, decreasing onset potential remains a challenge. Recently, two new complexes

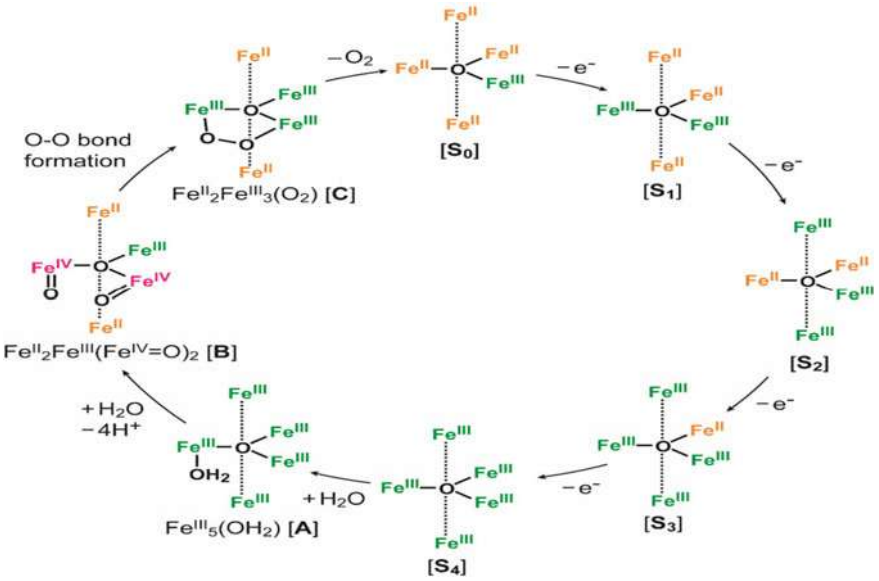

Fig. 4 Catalytic mechanism of **[Fe$_5$]** for O_2 evolution from water. (Reproduced with permission from [11])

[Fe$_5$–Me] and **[Fe$_5$–Br]** (Fig. 5a, b) have been synthesized through Me-Hbpp and Br-Hbpp ligands with the 4-position of the Hbpp ligand replaced by electron-donating Me- and electron-withdrawing Br-groups, and the catalytic activity has been explored and compared with the parent **[Fe$_5$]** [26]. **[Fe$_5$–Me]** and **[Fe$_5$–Br]** demonstrated the same structural motifs as **[Fe$_5$]**, and the bond distances between Fe–N did not change significantly after the introduction of the substituents (either methyl or bromo

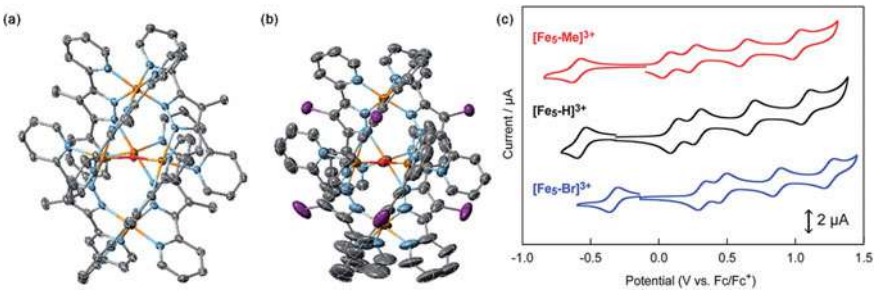

Fig. 5 ORTEP drawings of the cationic moieties of **a [Fe$_5$–Me]**$(PF_6)_3$ and **b [Fe$_5$–Br]**$(BF_4)_3$. **c** CVs of 0.2 mM solution of **[Fe$_5$–Me]** (red line), **[Fe$_5$–Br]** (blue line), and **[Fe$_5$]** (black line). Measurements were carried out in MeCN solution containing 0.1 M TBAP under Ar at a scan rate of 10 mV s^{-1}. Working electrode, glassy carbon; counter electrode, Pt wire; reference electrode, Ag/Ag^+. (Reproduced from [26] with permission from the Royal Society of Chemistry)

groups). The redox properties of **[Fe_5–Me]** and **[Fe_5–Br]** complexes were investigated through CV in dry MeCN with 0.1 M Bu_4NClO_4 under an Ar atmosphere. The results exhibit the five reversible redox processes, similar to that of **[Fe_5]** (Fig. 5c), indicating that the introduction of substituents on the ligands has no influence on the electron transfer ability of the pentanuclear iron scaffold. Noteworthy, all the redox waves of **[Fe_5–Me]** were shifted to more negative potential relative to those of **[Fe_5]**, whereas the redox waves of **[Fe_5–Br]** were positively shifted. These trends are consistent with the electron-donating and electron-withdrawing nature of the methyl and bromo substituents. This result reflects that the substituents on the ligands can tune the redox potentials of the pentanuclear iron complexes.

In order to investigate the water oxidation of **[Fe_5–Me]** and **[Fe_5–Br]**, the electrocatalytic activities were examined in a solution containing 0.2 mM complexes and 5 M H_2O. The result showed a large irreversible current in the >1.0 V region (Fig. 6). CPE confirmed the catalytic activity of the water oxidation, and the faradaic efficiencies of water oxidation reactions based on $4e^-$ process were 92 and 86% for **[Fe_5–Me]** and **[Fe_5–Br]**, respectively. TOF and TON values were 300 s^{-1} and 2×10^6 for **[Fe_5–Me]**, as well as 20 s^{-1} and 1×10^5 for **[Fe_5–Br]**, respectively, which were lower than those of **[Fe_5]**, but higher than those of the other reported iron complexes for water oxidation [17–21].

Carefully comparing the CVs of **[Fe_5–Me]** and **[Fe_5–Br]** complexes in the presence of H_2O, it was found that the electrochemical behavior was different. For **[Fe_5–Me]**, the large irreversible current deriving from the catalytic water oxidation appeared at a potential close to the fourth redox couple (1.08 V) (Fig. 6a). The onset potential (E_{onset}) was determined to be 1.09 V with a corresponding overpotential (η) of 0.65 V at pH = 5. The large catalytic current of **[Fe_5–Br]** was observed at a more negative potential than that of the fourth redox couple (1.27, Fig. 6b), and the E_{onset} and η were 1.15 and 0.71 V, respectively. These values indicated that two pentanuclear iron complexes likely possessed different catalytic mechanisms. In the

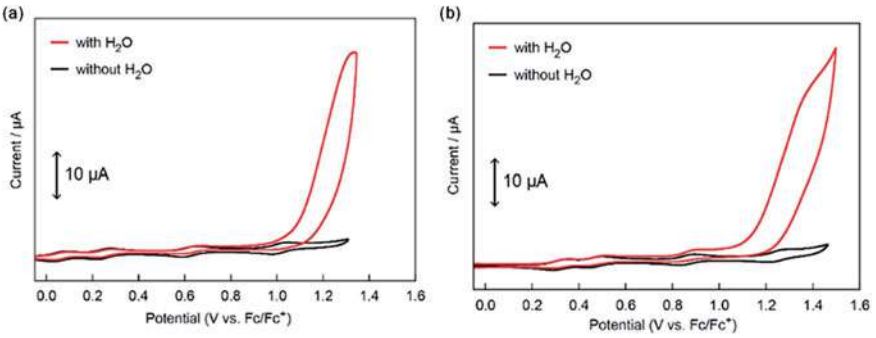

Fig. 6 CVs of 0.2 mM solutions of **a [Fe_5–Me]** and **b [Fe_5–Br]** in acetonitrile containing TBAP (0.1 M) in the absence of H_2O (black lines) and the presence of 5 M H_2O (pH = 5, red lines). The CVs were measured using a GC electrode under an Ar atmosphere at a scan rate of 10 mV s^{-1}. (Reproduced from [26] with permission from the Royal Society of Chemistry)

case of **[Fe$_5$–Me]**, the E_{onset} was situated in a slightly more positive potential than the $E_{1/2}$ of the fourth redox couple (1.01 V). This means the combination of four-electron oxidized species (S_4 state) with one water molecule triggered the catalysis of water oxidation. The electron-donating nature of methyl substituent promoted the formation of the S_4 state at a more negative potential, which makes **[Fe$_5$–Me]** to have a smaller E_{onset} than that of the **[Fe$_5$]** complex. So, a similar catalytic mechanism is proposed as that of **[Fe$_5$]** (Fig. 4). The catalytic current for **[Fe$_5$–Br]** (E_{onset} 1.15 V) was observed between the third (0.87 V) and fourth (1.27) redox waves. This showed that the three-electron oxidized species combined one water molecule to undergo a chemical reaction and further were oxidized at 1.15 V under a concerted chemical and electrochemical process to initiate the catalytic reaction. Thus, a possible catalytic mechanism for **[Fe$_5$–Br]** was proposed as in Fig. 7. First, a sequential, stepwise three-electron oxidation process occurred, where the electronic structures underwent from S_0, S_2 to S_3 states. But, different from the oxidation of S_2 to S_3 states in **[Fe$_5$]** and **[Fe$_5$–Me]**, the oxidation of S_2 to S_3 states in **[Fe$_5$–Br]** involved a two-step intramolecular electron transfer process, namely the oxidation in the triangular core and the reduction at the apical position occurred simultaneously. So, the S_3 state exhibited three Fe^{III} ions in the triangular core, which was different from that of **[Fe$_5$]** and **[Fe$_5$–Me]**. Then, one water molecule attacked on the fully oxidized [$Fe_3(\mu_3$-O)] core of the S_3 state and coupled with a one-electron oxidation process to form the water-bound $Fe_5(OH_2)$ species (**A**). Similar to that in Fig. 4, **A** generated **B** and **C**; lastly, O_2 was released from **C**, accompanying the catalytic process returned

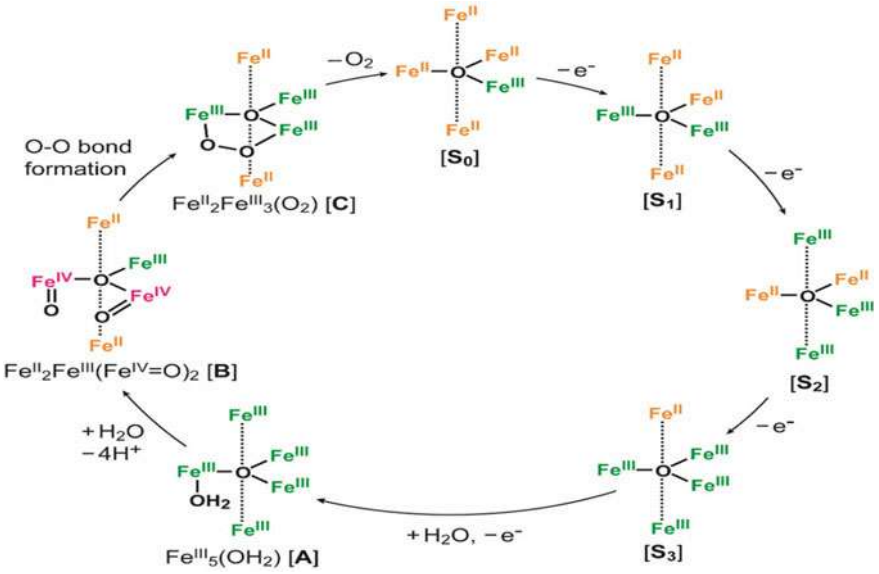

Fig. 7 Catalytic mechanism of **[Fe$_5$–Br]** for O_2 evolution from water. (Reproduced from [26] with permission from the Royal Society of Chemistry)

to the initial S_0 state. In this mechanism, the formation of the S_4 state was bypassed in **[Fe$_5$–Br]**, which can be proved by the lower onset potential in **[Fe$_5$–Br]**-catalyzed process, compared with **[Fe$_5$]** catalysis. Therefore, based on the aforementioned discussion, we can conclude that the tuning of electron structures can control the catalytic reaction, while the substituents not only influence the redox potentials but also change the reaction mechanism.

A tetranuclear, grid nickel complex $[NiL]_4{\cdot}4(NO_3)$ (**[Ni$_4$]**) with metallacrown-like topology and [Ni–O] repeat unit was synthesized through bis-[(E)-N′-(1-(pyridin-2-yl)ethylidene)]carbohydrazide ligand (HL) (Fig. 8). The asymmetric unit of **[Ni$_4$]** complex contains a carbohydrazone ligand, which is coordinated to the Ni^{II} ion as a mono-negative ligand, and a nitrate anion is located beside the complex. In the **[Ni$_4$]** unit, each Ni^{II} ion is hexa-coordinated, distorted octahedral geometry where the coordinated atoms come from two perpendicular carbohydrazone ligands. The ligands in the *mer* configuration link Ni^{II} ions with the oxygen atoms shared by adjacent Ni^{II} ions to exhibit a symmetrical molecular square. The Ni–N and Ni–O bond lengths are in the normal range of reported Ni^{II} complexes. The adjacent Ni–Ni distances are 3.927 Å and the bond angles subtended of Ni–O–Ni are 137.36(15)°. The electrocatalytic activity of water oxidation was investigated in the presence of water with Fluorine-doped tin oxide (FTO) as the working electrode and graphite as the auxiliary electrode (Fig. 9). No oxidation/reduction peaks were observed in pure acetonitrile (Fig. 9a). Under the above condition, adding water, the current of water oxidation increased, accompanying the water oxidation reaction started at 1.6 V and a significant change occurred at 0.12, 0.73, and 1.20 V (Fig. 9b). For the potential ranging from −0.3 to 1.8 V and in the presence of acetonitrile/water (1.5/10) and $LiClO_4$ (0.1 M), the continuous CV measurement exhibited a significant change (0–1.0 V) in catalytic current, indicating that this complex was unstable and decomposed into a Ni oxide compound on the electrode (Fig. 9c). The amperometry showed that the FTO used in the measurement after washing displayed higher activity than a fresh FTO for water oxidation in KOH (0.1 M) (Fig. 9d). This result likely

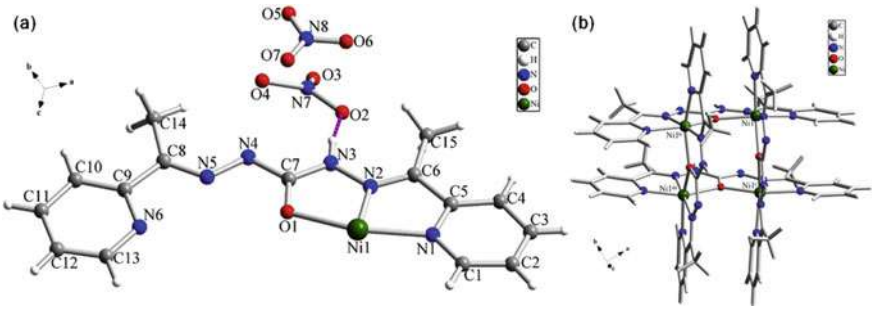

Fig. 8 **a** The asymmetric unit of the grid tetranuclear complex $[NiL]_4{\cdot}4(NO_3)$. **b** Molecular structure of $[Ni_4L_4]^{4+}$ in the crystal structure (the nitrate anions are eliminated for clarity; Symmetry codes: (i) $-x+1/2, y, -z+1/2$; (ii) $x, -y+1/2, z+1/2$; (iii) $-x+1/2, -y+1/2, z$. (Reproduced with permission from [27])

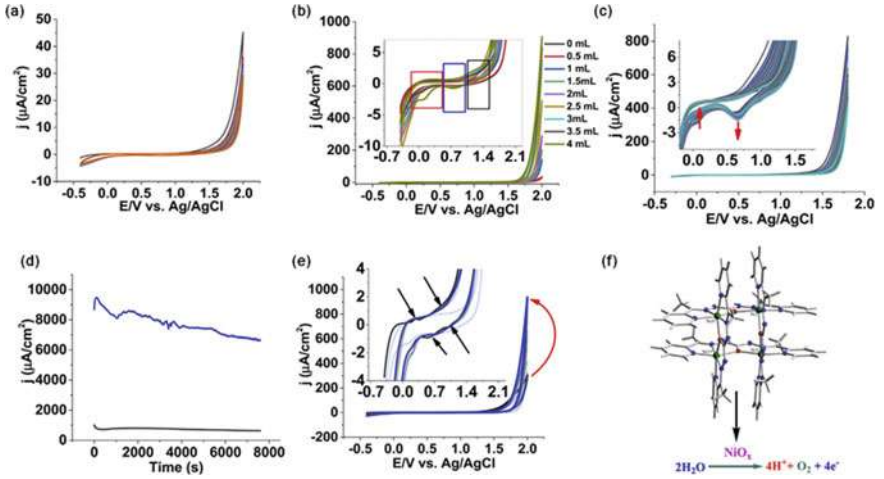

Fig. 9 CVs of **[Ni$_4$]** (0.08 mM) in 20 mL acetonitrile containing $LiClO_4$ (0.10 M) electrolyte. **a** The effect of adding water on **[Ni$_4$]** during CVs in acetonitrile containing $LiClO_4$ (0.10 M) electrolyte. **b** The continuous CVs of **[Ni$_4$]** in $LiClO_4$ (0.1 M) in acetonitrile/water (10/1.5) in the range of (−0.3 V)–(1.8 V). **c** The continuous CVs of **[Ni$_4$]** in acetonitrile/water (90/10) (electrolyte: $LiClO_4$ (0.10 mM)) (0.10 M) in the range of (−0.4 V)–(2.0 V). **d** The amperometry of the operated FTO after operation for 2 h at 1.8 V in the presence of **[Ni$_4$]** (blue) compared to a fresh FTO (black) in KOH (0.10 M) at 1.15 V versus Ag/AgCl. **e** Scan rates were 50 mV s^{-1}. The electrochemical experiments were performed using fluorine-doped tin oxide (FTO) and graphite as the working and the auxiliary electrode, respectively. **f** A proposed model for water oxidation in the presence of **[Ni$_4$]**. (Reproduced with permission from [27])

indicates that the true catalyst comes from the surface of the electrode. The decrease of current is derived from the leaking of the catalyst into the solution. Adding the ratio of acetonitrile/water to 90/10, the catalytic current showed a significant increase in water oxidation, which illustrated a conversion occurring relating to the high amount of acetonitrile (Fig. 9e). The electrode after water oxidation by the **[Ni$_4$]** complex was investigated through various physical–chemical methods, and a proposed model for water oxidation was shown in Fig. 9f. The result showed that the decomposition of the **[Ni$_4$]** complex, a Ni oxide compound on the electrode, could serve as a contributor to the water oxidation reaction under the observed catalysis [27].

An exceptionally stable octacobalt-cluster-based metal–organic framework $[Co_8(OH)_6(bdt)_6(H_2O)_2]$ (**[Co$_8$]**, H_2bdt = 1,4-Benzenedi(1*H*-1,2,3-trizaole)) with perfect facing-facing double-deck 12-MC-4 azametallacrown (azaMC) structural type was reported and the enhanced water oxidation catalysis was investigated under electro-/photodriven, respectively. **[Co$_8$]** cluster consists of a face-centered *fcu* network, connected to 12 adjacent ones through linear *exo*-tetradentate linkers to display cubic topology, and with the help of the linkers of 2-connected bdt^{2-}, it further forms a 3D porous framework (Fig. 10). In **[Co$_8$]** cubic structure, the hydroxyl anion at each face connects four coplanar Co^{II} ions to form a $\{Co_4(\mu_4\text{-OH})\}$ unit,

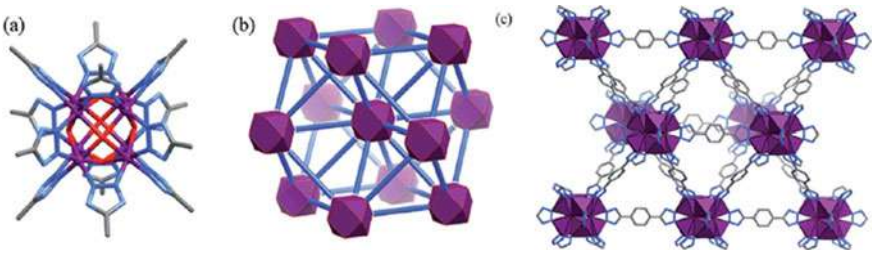

Fig. 10 **a** The structure of $[Co_8(\mu_4\text{-}OH)_6(Rtrz)_{12}]$ ($Rtrz^- = 1,2,3$,-triazolate group) cluster (hydrogen atoms are omitted for clarity). **b** The network topology (octanuclear cluster and bistriazolate ligands are simplified as violet polyhedra and blue sticks, respectively). **c** 3D coordination framework (CoN_3O_3 units are shown as violet polyhedra) of [Co_4-bdt]. (Reproduced from [28] with permission from the Royal Society of Chemistry)

where each Co^{II} ion is located in a hexa-coordinated CoN_3O_3 coordination environment, and the adjacent Co^{II} ions are bridged by N–N donors from the terminal triazole groups to demonstrate 12-MC-4 azaMC structural type. The photodriven water oxidation experiment showed an initial TOF of $3.05 \pm 0.03\ S^{-1}$ under the condition of $[Ru(bpy)_3](SO_4)$ as the photosensitizer and $Na_2S_2O_8$ as the sacrificial electron acceptor with the Clark-type oxygen electrode used to detect in situ the amount of evolved O_2 dissolved in the solution (Fig. 11a). The stability of the structure made the TOF remain $3.05\ S^{-1}$ after 12,000 runs in the photocatalytic water oxidation reaction (Fig. 11b). The electrochemical measurements (Linear sweep voltammetry, LSV) revealed a four-electron process and an overpotential of 352 mV at 2.0 mA cm^{-2}[28].

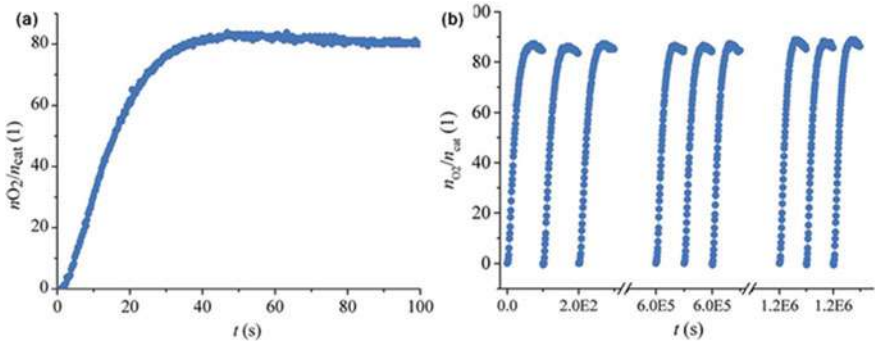

Fig. 11 **a** Kinetics of O_2 formation in the photocatalytic system using [Co_4-bdt] as the catalyst. **b** O_2 production profiles of the repeated photocatalytic water oxidation reactions using [Co_4-bdt] as the catalyst. Reaction conditions: $[Ru(bpy)_3]SO_4$ (0.03 mmol), catalyst (0.5 nmol), borate buffer (pH = 9, 2 mL), $Na_2S_2O_8$ (0.1 mmol), LED light ($\alpha = 450 \pm 5$ nm), and 25 °C. (Reproduced from [28] with permission from the Royal Society of Chemistry)

2 CO_2 Conversion

The excessive use of fossil fuels discharges massive carbon dioxide into the atmosphere and also causes serious environmental pollution issues. To mitigate the energy crisis and greenhouse effect, several categories, such as CO_2 capture, storage, and conversion, have been considered to reduce CO_2 emissions. Although various catalysts, including noble metals and their derived products, metal oxides, single-atom catalysts, Mxenes, carbon-based materials, and so on, have been reported for CO_2 utilization, the metal complexes with distinct structure and coordination number still have attracted considerable attention from the researchers for CO_2 electroreduction or photoreduction.

A pentanuclear cobalt complex $[Co^{II}{}_5OH(bpp)_6](BF_4)_3$ (**[Co$_5$]**, Hbpp = 3,5-bis(2-pyridyl)pyrazole) exhibits the same molecular scaffold as **[Fe$_5$]** with Co ions substitute for Fe ions in trigonal–bipyramidal geometries, where two $[Co(\mu\text{-bpp})_3]$ units are located at the apical positions (Fig. 12a) [29]. Two apical Co ions are in hexa-coordinated environment with distorted octahedral geometries, while triangular three Co ions display penta-coordinated, distorted trigonal–bipyramidal geometries. The average distance between the Co ion and central O atom in the triangular core is 2.009(4) Å, which is larger than that of the **[Fe$_5$]** complex (1.961(3) Å), indicating that the central bridging moiety is OH^-, not O^{2-}, observed in **[Fe$_5$]**. Under the Ar atmosphere, the CV profile displayed two reversible oxidation waves (Co^{III}/Co^{II}) and three reversible reduction waves (Co^{II}/Co^{I}), which indicated **[Co$_5$]** has redox properties suitable for reductive reactions. Therefore, under the CO_2 atmosphere, a large irreversible current was observed at about $E_{pc} = -2.5$ V, and the intensity of the irreversible current significantly increased in the presence of trifluoroethanol as a proton source (Fig. 12b). Meanwhile, the production of CO_2 reduction was confirmed as CO, H_2, and HCOOH through the controlled potential electrolysis. Furthermore, a CO_2-saturated solution, containing **[Co$_5$]**, sacrificial electron donor

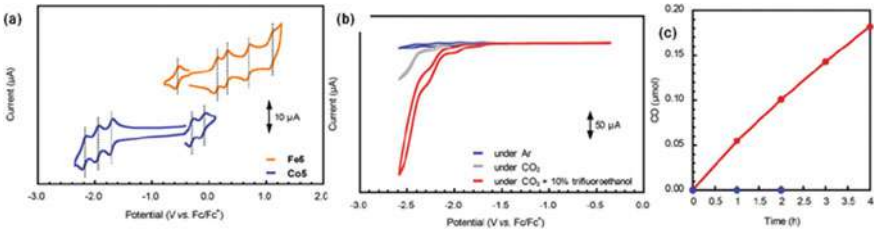

Fig. 12 CVs of 0.2 mM solutions of **a [Co$_5$]** (blue line) and **[Fe$_5$]** (orange line) under Ar atmosphere. **b [Co$_5$]** under Ar (blue line), CO_2 (gray line), and CO_2 in the presence of 10% trifluoroethanol (red line) in acetonitrile containing 0.1 M TBAP. The CVs were measured using a GC electrode at a scan rate of **a** 100 or **b** 50 mV s^{-1}. **c** Photocatalytic production of CO in the presence of 30 μM **[Co$_5$]** (red line) and in the absence of **[Co$_5$]** (blue line) in a CO_2-saturated DMA/TFE (17:3, v/v) solution containing 150 μM $Ir(ppy)_3$ and 0.1 M BIH. (Reproduced from [29] with permission from the Royal Society of Chemistry)

1,3-dimethyl-2-phenyl-2,3-dihydro-1*H*-benzo[d]imidazole (BIH), and photosensitizer $Ir(ppy)_3$ (Hppy = 2-phenylpyridine), was irradiated for 4 h through wavelength 420 nm visible-light, and a resultant production CO (0.18 μmol) was obtained with a maximum TON of 58.4 (Fig. 12c). The isotopic labeling experiments also confirmed that CO originated from the CO_2 reduction[29].

A 12-MC-4 azametallacrown complex $[Ni_4(L)_4(\mu\text{-}OH)_4)](ClO_4)$ (**[Ni_4]**, L = 3,6-di(pyrazol-1-yl)pyridazine) was constructed and exhibited a 12-membered macrocycle with four Ni^{II} ions coplanar and linked together through –N–N– bridging groups to achieve Ni–N–N repeat unit in the ring (Fig. 13a) [30]. Two neutral tetradentate ligands are in a *cis*-isomer arrangement to surround one Ni atom, except that, two hydroxide groups also bridge the same Ni atom. Thus, the coordination atoms of the Ni atom consist of four nitrogen atoms (N1, N3) of two ligands and two oxygen atoms (O1) of hydroxide bridging groups to form hexa-coordinated, distorted octahedral geometries. The CV measurement showed that a reduction peak (E_{pc} = −1.46 V) was observed under the Ar atmosphere, which was attributed to Ni^{II}/Ni^{I} redox couple (Fig. 13b). In the presence of CO_2, a new reduction peak and a current enhancement appeared at $E_{pc} = -1.71$ and −1.97 V, respectively, and an irreversible reduction peak (−2.25 V) was observed (Fig. 13b). These results showed that Ni^{I} centers, reduced product of Ni^{II} ions, were formed, then, CO_2 bond to the Ni^{I} species. CPE experiments displayed a detected amount of CO of 0.17 μmol with a charge passing approximately 1.59 C for comparison of a blank (1.35 C). The result suggests the bimetallic synergistic effect between Ni centers in **[Ni_4]** structure enhances the selectivity for CO_2 to CO conversion. In other words, the **[Ni_4]** structure may possess a more suitable environment and stability for the CO_2 reduction reaction [31]. While the current enhancement may be attributed to CO_2 interaction with **[Ni_4]** complex

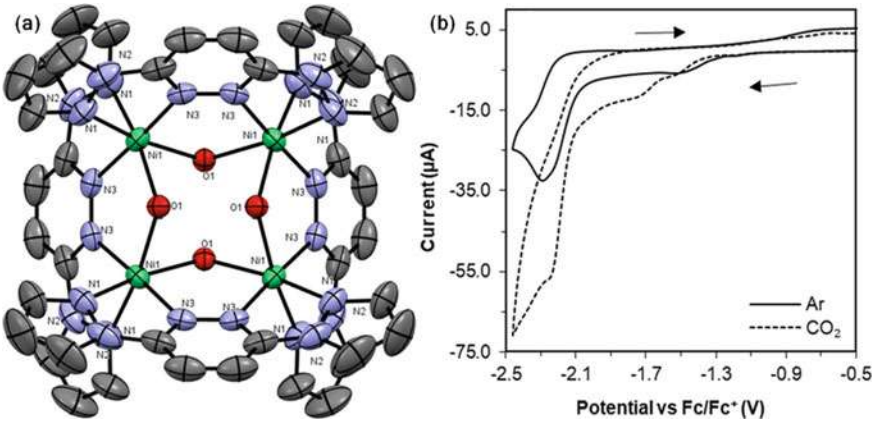

Fig. 13 **a** X-ray crystal structure of 12-MC-4 nickel complex $[Ni_4(L_1)_4(\mu\text{-}OH)_4](ClO_4)_4$ with thermal ellipsoids (50% probability). Hydrogen atoms and four ClO_4^- anions are omitted for clarity. **b** CVs of 0.5 mM 12-MC-4 **[Ni_4]** complex with 0.1 M TBAP in 2 mL DMF under Ar atmosphere (black line) and CO_2 (dashed line) at scan rate of 100 mV s^{-1}. (Reproduced with permission from [30])

and hydrogenation of the aromatic N-heterocyclic ligand under reduction conditions [32].

Two multiple MCs-type complexes $\{Na(H_2O)_4[SmZn_{16}(picha)_{16}(Py)_8]\ (OTf)\cdot 4MeOH\cdot 12H_2O\}$ (**[SmZn$_{16}$]**) and $\{H[DyZn_{16}(picha)_{16}(Py)_8](OTf)_4\cdot 4MeOH\cdot 12H_2O\}$ (**[DyZn$_{16}$]**) have been reported [33, 34]. These two complexes are isostructural and have overall S_8 symmetry. Herein, only **[DyZn$_{16}$]** was discussed. In the crystal structure of **[DyZn$_{16}$]**, a 24-MC-8 unit encapsulates two concave 12-MC-4 subunits, which are linked by an eight-coordinated Dy^{III} ion to form a sandwich configuration (Fig. 14). Interestingly, the two complexes displayed different catalytic activity. **[SmZn$_{16}$]** exhibited excellent catalytic performance in the catalytic conversion of CO_2 to cyclic carbonate with a percent conversion up to 96.3% and selectivity of 98.7%, whereas **[DyZn$_{16}$]** acted as an efficient catalyst for the Knoevenagel condensation reaction with yield up to 97.2%.

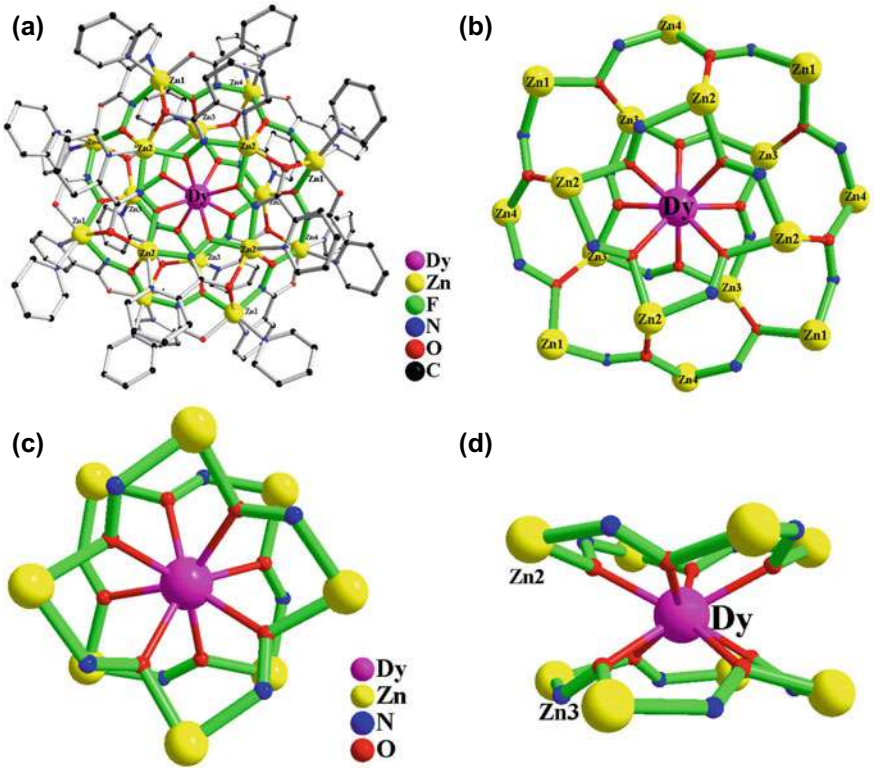

Fig. 14 **a** The Crystal structure of $[DyZn_{16}(picha)_{16}(Py)_8]^{3+}$. (All hydrogen atoms and free ions are omitted for clarity). **b** Metal core of **[DyZn$_{16}$]**. **c** Top view of the inner MC ring about the central Dy^{3+}. **d** Side view of the inner MC ring about the central Dy^{3+}

3 Summary

In summary, in this chapter, we have shown the structures and catalytic activity of a series of metallacrown electro/photocatalysts for water oxidation and CO_2 conversion. Metallacrowns possess definitive and charming structures and rich metal centers exhibiting coordinative saturated or unsaturated. Depending on the unique feature of metallacrowns, they may display multiple redox-active centers. Although $[M_5]$ complexes had a similar pentanuclear scaffold structure, where the triangular $[M_3(\mu_3\text{-}O)]$ cores were wrapped by two $[M(\mu\text{-}L)_3]$ units, different CV profiles and catalytic activity have been observed due to the change of metal centers and substituting groups on ligands. For example, **[Fe_5]** complexes can act as electrocatalysts and exhibit efficient catalytic activity for water oxidation. But the effect of electron-donating and electron-withdrawing substitutes on ligands led to two distinctive catalytic reaction mechanisms. Metal cobalt ions substitution of iron ions in **[Fe_5]** formed a new **[Co_5]** complex, which could reduce CO_2 to CO under photoirradiation in the presence of a photosensitizer. Meanwhile, the other structural type metallacrown catalysts also exhibited excellent catalytic performance in water oxidation or CO_2 conversion fields. Therefore, taking full advantage of the earth-abundant transition metal ions and controlling the ligands to design the desired metallacrowns for high efficient and robust catalysts can be realized. And it is possible to formulate multinuclear metallacrown catalysts for water oxidation or small-molecule conversion to mitigate the energy crisis and solve the environmental issue.

References

1. Kanan, M.W., Nocera, D.G.: In situ formation of an oxygen-evolving catalyst in neutral water containing Phosphate and Co^{2+}. Science **321**, 1072–1075 (2018). https://doi.org/10.1126/science.1162018
2. Seitz, L.C., Dickens, C.F., Nishio, K., Hikita, Y., Montoya, J., Doyle, A., Kirk, C., Vojvodic, A., Hwang, H.Y., Norskov, J.K., Jaramillo, T.F.: A highly active and stable $IrO_x/SrIrO_3$ catalyst for the oxygen evolution reaction. Science **353**, 1011–1014 (2016). https://doi.org/10.1126/science.aaf5050
3. Liu, J., Wang, J.S., Zhang, B., Ruan, Y.J., Lv, L., Ji, X., Xu, K., Miao, L., Jiang, J.J.: Hierarchical $NiCo_2S_4$@NiFe LDH heterostructures supported on nickel foam for enhanced overall-water-splitting activity. ACS Appl. Mater. Interfaces **9**, 15364–15372 (2021). https://doi.org/10.1021/acsami.7b00019
4. Du, J., Li, F., Sun, L.C.: Metal-organic frameworks and their derivatives as electrocatalysts for the oxygen evolution reaction. Chem. Soc. Rev. **50**, 2663 (2021). https://doi.org/10.1039/d0cs01191f
5. Jia, Y., Zhang, L.Z., Gao, G.P., Chen, H., Wang, B., Zhou, J.Z., Soo, M.T., Hong, M., Yan, X.C., Qian, G.R., Zou, J., Du, A.J., Yao, X.D.: A heterostructure coupling of exfoliated Ni-Fe hydroxide nanosheet and defective graphene as a bifunctional electrocatalyst for overall water splitting. Adv. Mater. **29**, 1700017 (2017). https://doi.org/10.1002/adma.201700017
6. Mezei, G., Zaleski, C.M., Pecoraro, V.L.: Structural and functional evolution of metallacrowns. Chem. Rev. **107**, 4933–5003 (2007). https://doi.org/10.1021/cr078200h

7. Li, G.F., Zhu, D.X., Wang, X.L., Su, Z.M., Bryce, M.R.: Dinuclear metal complexes: multi-functional properties and applications. Chem. Soc. Rev. **49**, 765–838 (2020). https://doi.org/10.1039/c8cs00660a
8. Chen, L.J., Chen, G., Leung, C.F., Cometto, C., Robert, M., Lau, T.C.: Molecular quaterpyridine-based metal complexes for small molecule activation: water splitting and CO_2 reduction. Chem. Soc. Rev. **49**, 7271–7283 (2020). https://doi.org/10.1039/d0cs00927j
9. Jin, X.T., Li, X.L., Lei, H.T., Guo, K., Lv, B., Guo, H.B., Chen, D.D., Zhang, W., Cao, R.: Comparing electrocatalytic hydrogen and oxygen evolution activities off first-row transition metal complexes with similar coordination environments. J. Energy Chem. **45** (2022) (online). https://doi.org/10.1016/j.jechem.2021.08.068
10. Kaufhold, S., Petermann, L., Staehle, R., Rau, S.: Transition metal complexes with N-heterocyclic carbene ligands: from organometallic hydrogenation reaction toward water splitting. Coord. Chem. Rev. **304–305**, 73–87 (2015). https://doi.org/10.1016/j.ccr.2014.12.004
11. Okamura, M., Kondo, M., Kuga, R., Kurashige, Y., Yanai, T., Hayami, S., Praneeth, V.K.K., Yoshida, M., Yoneda, K., Kawata, S., Masaoka, S.: Pentanuclear iron catalyst designed for water oxidation. Nature **530**, 465–468 (2016). https://doi.org/10.1038/nature16529
12. Kondo, M., Masaoka, S.: Pentanuclear scaffold: a molecular platform for small-molecule conversions. Acc. Chem. Res. **53**, 2140–2151 (2020). https://doi.org/10.1021/acs.accounts.0c00186
13. Helm, M.L., Stewart, M.P., Bullock, R.M., DuBois, M.R., DuBois, D.L.: A synthetic nickel electrocatalyst with a turnover frequency above 100,000 s^{-1} for H_2 production. Science **333**, 863–866 (2011). https://doi.org/10.1126/science.1205864
14. Barnett, S.M., Goldberg, K.I., Mayer, J.M.: A soluble copper−bipyridine water-oxidation electrocatalyst. Nat. Chem. **4**, 498–502 (2012). https://doi.org/10.1038/NCHEM.1350
15. McCrory, C.C.L., Uyeda, C., Peters, J.C.: Electrocatalytic hydrogen evolution in acidic water with molecular cobalt tetraazamacrocycles. J. Am. Chem. Soc. **134**, 3164–3170 (2012). https://doi.org/10.1021/acsami.7b00019
16. Marinescu, S.C., Winkler, J.R., Gray, H.B.: Molecular mechanisms of cobalt-catalyzed hydrogen evolution. Proc. Natl. Acad. Sci. USA **109**, 15127–15131 (2012). https://doi.org/10.1073/pnas.1213442109
17. Ellis, W.C., Mcdaniel, N.D., Bernhard, S., Collins, T.J.: Fast water oxidation using iron. J. Am. Chem. Soc. **132**, 10990–10991 (2010). https://doi.org/10.1021/ja104766z
18. Fillol, J.L., Codolà, Z., Garcia-Bosch, I., Gómez, L., Pla, J.J., Costas, M.: Efficient water oxidation catalysts based on readily available iron coordination complexes. Nat. Chem. **3**, 807−813 (2011). https://doi.org/10.1038/NCHEM.1140
19. Coggins, M.K., Zhang, M.T., Vannucci, A.K., Dares, C.J., Meyer, T.J.: Electrocatalytic water oxidation by a monomeric amidate-ligated Fe(III)−aqua complex. J. Am. Chem. Soc. **136**, 5531–5534 (2014). https://doi.org/10.1021/ja412822u
20. Wickramasinghe, L.D., Zhou, R., Zong, R., Vo, P., Gagnon, K.J., Thummel, R.P.: Iron complexes of square planar tetradentate polypyridyl-type ligands as catalysts for water oxidation. J. Am. Chem. Soc. **137**, 13260–13263 (2015). https://doi.org/10.1021/jacs.5b08856
21. Kottrup, K.G., D'Agostini, S., Van, L.P.H., Siegler, M.A., Hetterscheid, D.G.H.: Catalytic activity of an iron-based water oxidation catalyst: substrate effects of graphitic electrodes. ACS Catal. **8**, 1052–1061 (2018). https://doi.org/10.1021/acscatal.7b03284
22. Liu, Y., Xiang, R., Du, X., Ding, Y., Ma, B.: An efficient oxygen evolving catalyst based on a μ-O diiron coordination complex. Chem. Commun. **50**, 12779–12782 (2014). https://doi.org/10.1039/c4cc04118f
23. Annunziata, A., Esposito, R., Gatto, G., Cucciolito, M.E., Tuzi, A., Macchioni, A., Ruffo, F.: Iron(III) complexes with cross-bridged cyclams: synthesis and use in alcohol and water oxidation catalysis. Eur. J. Inorg. Chem. **2018**, 3304–3311 (2018). https://doi.org/10.1002/ejic.201800451
24. Liao, R.-Z., Masaoka, S., Siegbahn, P.E.M.: Metal oxidation states for the O-O bond formation in the water oxidation catalyzed by a pentanuclear iron complex. ACS Catal. **8**, 11671−11678 (2018). https://doi.org/10.1021/acscatal.8b02791

25. Mehrabani, S., Bikas, R., Zand, Z., Mousazade, Y., Allakhverdiev, S.I., Najafpour, M.M.: Water splitting by a pentanuclear iron complex. Int. J. Hydrog. Energy **45**, 17434–17443 (2020). https://doi.org/10.1016/j.ijhydene.2020.04.249
26. Praneeth, V.K.K., Kondo, M., Okamura, M., Akai, T., Izu, H., Masaoka, S.: Pentanuclear iron catalysts for water oxidation: substituents provide two routes to control onset potentials. Chem. Sci. **10**, 4628–4639 (2019). https://doi.org/10.1039/c9sc00678h
27. Azadi, G., Zand, Z., Mousazade, Y., Bagheri, R., Cui, J.F., Song, Z.L., Bikas, R., Wozniak, K., Allakhverdiev, S.I., Najafpour, M.M.: A tetranuclear nickel(II) complex for water oxidation: meeting new challenges. Int. J. Hydrog. Energy **44**, 2857–2867 (2019). https://doi.org/10.1016/j.ijhydene.2018.12.059
28. Huang, N.-Y., Shen, J.-Q., Ye, Z.-M., Zhang, W.-X., Liao, P.-Q., Chen, X.-M.: An exceptionally stable octacobalt-cluster-based metal-organic framework for enhanced water oxidation catalysis. Chem. Sci. **10**, 9859–9864 (2019). https://doi.org/10.1039/c9sc03224j
29. Akai, T., Kondo, M., Lee, S.K., Izu, H., Enomoto, T., Okamura, M., Saga, Y., Masaoka, S.: Effect of metal ion substitution on the catalytic activity of a pentanuclear metal complex. Dalton Trans. **49**, 1384–1387 (2020). https://doi.org/10.1039/c9dt04684d
30. Subramaniam, J.D., Lee, S.K., Chinapang, P., Praneeth, V.K.K., Okamura, M., Kondo, M., Masaoka, S., Woi, P.M.: Synthesis and structural characterization of centrosymmettric multinuclear nickel(II) complexes with neutral tetradentate N_6-ligand. Trans. Metal Chem. **46**, 255–262 (2021). https://doi.org/10.1007/s11243-020-00441-5
31. Cao, L.M., Huang, H.H., Wang, J.W., Zhong, D.C.: The synergistic catalysis effect within a dinuclear nickel complex for efficient and selective electrocatalytic reduction of CO_2 to CO. Green Chem. **20**, 798–803 (2018). https://doi.org/10.1039/c7gc03451b
32. Olu, P.Y., Li, O., Krischer, K.: The true fate of pyridinium in the reportedly pyridinium-catalyzed carbon dioxide electroreduction on Platinum. Angew Chem. Int. Ed. **57**, 14769–14772 (2018). https://doi.org/10.1002/anie.201808122
33. Xu, H., Yang, H., Huang, X.Q., Li, D.C., Dou, J.M.: Two $Zn_{16}Ln$ (Ln = Dy, Sm) metallacrowns: synthesis, magnetism and their efficient catalysis for Knoevenagel condensation. Sci. Adv. Mater. **11**, 215–222 (2019). https://doi.org/10.1166/sam.2019.3373
34. Jiang, X.Y., Ding, H.M., Liu, Y., Zhang, H.C., Xin, N.N., He, Q.P.: A novel organic-inorgnic hybrids heterometallic materials: synthesis and highly efficient conversion of CO_2. Sci. Adv. Mater. **11**, 203–207 (2019). https://doi.org/10.1166/sam.2019.3452

A Structural Examination of Metallacrowns with Main Group Elements in the Ring Positions

Jacob C. Lutter and Curtis M. Zaleski

Abstract The aim of this chapter is to highlight recent metallacrown chemistry that utilizes main group elements in the metallacrown ring. Since the first vanadium-based 9-MC-3 was reported in 1989, metallacrown structures have traditionally included transition metal ions in the ring position of metallamacrocycles. These metals have imparted attractive properties to the metallacrowns such as molecular magnetism, catalysis, molecular recognition, and selective guest binding. While one of the first described metallacrowns in 1993 contained the main group element gallium in the ring positions, a 12-MC-4 dimer, little research was directed to these types of elements until recently. Not only has gallium now been incorporated into the metallacrown ring, but the elements aluminum, indium, tin, lithium, sodium, silicon, and tellurium have also been used to generate archetypal metallacrowns with a M–N–O repeat unit and/or azametallacrowns with a M–N–N repeat unit. The resulting metallacrowns have interesting properties including single-molecule magnetism, luminescence, and bioactivity. This chapter will examine the structural diversity of metallacrowns that can be achieved with main group elements and will feature some of the interesting properties and applications of these molecules.

1 Introduction

Since the first reports of metallacrowns (MCs) by Pecoraro in 1989, the field has been dominated by structures that contain transition metal ions in the ring positions of the macrocyclic molecules [1, 2]. These ions can impart particularly interesting

J. C. Lutter (✉)
Department of Chemistry and Biochemistry, University of Southern Indiana, 8600 University Blvd., Evansville, IN 47712, USA
e-mail: jlutter@usi.edu

Department of Chemistry, Wayne State University, 5101 Cass Ave., Detroit, MI 48202, USA

C. M. Zaleski
Department of Chemistry and Biochemistry, Shippensburg University, 1871 Old Main Dr., Shippensburg, PA 17257, USA
e-mail: cmzaleski@ship.edu

C. M. Zaleski (ed.), *Advances in Metallacrown Chemistry*,
https://doi.org/10.1007/978-3-031-08576-5_9

magnetic properties such as single-molecule magnetism and magnetorefrigeration as the unpaired electrons of the ring transition metal ions often couple with a paramagnetic central metal ion, typically either a transition metal or lanthanide ion. In addition, the multiple oxidation states of the metal ions and preferable coordination numbers of particular ions have led to a plethora of structure types and motifs with a variety of applications including catalysis, selective anion binding, bioactivity, proton relaxation enhancement, and luminescence [2–4]. Indeed, the remarkable chemistry of transition metal ions is fully utilized with metallacrown chemistry. However, the use of main group metal ions in the ring positions of MCs has largely been overlooked. In 1993, Lah, Pecoraro, and coworkers described a gallium-based MC and it is one of the first reported MC structures [5]. Then it was not until the early 2000s that main group MCs were again described though the research seemed in a more sporadic fashion with solitary reports. However, in the past 10 years, there has been a more consistent and systematic research approach dedicated to MCs with main group metal ions in the ring position.

One area of interest for the main group metallacrowns is lanthanide-based luminescence. Since the prototypical example in 2016, there have been publications that explore more elaborate compositions that consistently use Ga^{III} as the ring metal [6]. The metallacrown frameworks generally perform well as "antenna" to sensitize the weakly absorbing f–f transitions of central Ln^{III} ions [7]. Furthermore, gallium-based metallacrowns are of interest since they may sensitize both visible and near-infrared emitting lanthanide ions. Examples of these metallacrowns come in a few different configurations including an archetypical 12-MC-4, a bent 12-MC-4, dimerized sets of archetypical 12-MC-4s, and even a [3.3.1.] metallacryptate [6, 8–11]. These structures have been examined for their photophysical properties and have been elaborated for further application. Functional groups including ethynes, maleimides, and iodines have been attached to the dimerized 12-MC-4s to allow for specific coupling of molecules of interest to the MCs, or to enhance the capability of these compounds to provide X-ray computed tomography contrast in conjunction with the Ln^{III} emission [12, 13]. Other luminescence applications such as luminescent nanothermometry and white light emission have also been explored and open up even more possibilities for further study of metallacrown complexes within this field [14, 15].

Another intensely investigated topic of metallacrown research is molecular magnetism. Transition metal metallacrowns have been consistently explored thanks to the paramagnetism of such ions [16]. However, the main group metallacrowns have showed facile routes for the study of lanthanide ion magnetic phenomena. By placing diamagnetic main group elements in the ring, the magnetism of the central lanthanide ion can be studied in an MC framework without complicating factors of magnetic exchange between the central and ring metal species. Trivalent lanthanide ions in particular have a large amount of magnetic anisotropy thanks to the unquenched spin–orbit coupling that is of general interest within the field of single-molecule magnets [17]. Metallacrowns and metallacrypates with lanthanide ions in eight- or nine-coordinate geometries have been studied as single-ion magnets to explore the relationship of the ligand field to the barrier for slow magnetization relaxation [10,

11, 18]. One example, a 16-MC-6, also provided an opportunity to study the interaction of two Ln^{III} ions in close proximity that had some interesting cooperative relaxation processes [19].

Thanks in part to these motivating factors, there has been a renaissance in these types of metallacrowns where gallium, aluminum, tellurium, or tin have been incorporated into the ring positions. In addition, there have been reports with gallium, indium, aluminum, silicon, tin, lithium, and sodium-based azametallacrowns, MCs with a nitrogen–nitrogen bridge between the metal centers. Main group ions have distinct chemistry from the transition metal ions that dominate metallacrown research. Varying extents of Lewis acidity and bonding covalency contribute to a wide range of never-before-seen structural motifs with bespoke –[M–N–O]– or –[M–N–N]– repeating units. The aim of this chapter is to highlight the recent advancements in the main group chemistry of metallacrowns, with a focus on the structural aspects of these compounds.

Please note that many of the figures in this chapter were generated using *Mercury* software from crystallographic data in CIF format (available from the Cambridge Crystallographic Data Centre at www.ccdc.cam.ac.uk) [20]. Figures with crystallographic representations have hydrogen atoms and lattice solvent molecules omitted for clarity. In cases where the geometry about a metal center was ambiguous, continuous shape measure (CShM) values were determined with the *SHAPE* (version 2.1) software [21–23]. Typically, CShM values below or near 1.0 indicate minimal distortions from the ideal shape, and values between 1.0 and 3.0 indicate that the designated geometry is distorted from the ideal but the assignment is still valid, while values over 3.0 indicate significant distortions from an ideal shape [22, 23].

2 Gallium-Containing Metallacrown Complexes

The main group archetypical metallacrown complexes are largely represented by structures that feature trivalent gallium ions as the ring metal. The first example of such a structure was reported in 1993 by Lah, Penner-Hahn, Pecoraro, and coworkers as a set of two 12-$MC_{Ga^{III}N(shi)}$-4 faces that bind to three monovalent sodium ions (Fig. 1) [5]. The two MCs are connected by four μ-$^{-}$OH anions that bridge between the ring Ga^{III} ions of adjacent MCs. The gallium ions are five-coordinate with square pyramidal geometry (CShM range from 0.226–0.407). Each Ga^{III} ion binds two κ^2-salicylhydroximate (shi^{3-}) ligands in a *trans* fashion in the basal plane, where one shi^{3-} binds with the imino nitrogen atom and the phenoxide oxygen atom while the other shi^{3-} binds with the oxime and carbonyl oxygen atoms of the ligand. The shi^{3-} ligands provide the N–O bridges between the Ga^{III} centers; thus, the shi^{3-} ligands form the framework of the metallacrowns. The coordination of the Ga^{III} ions is completed by a μ-$^{-}$OH anion in the apical position. One sodium ion is captured inside the dimer by binding the central cavity of each MC and is eight-coordinate with cubic geometry (CShM = 0.757). The coordination is fulfilled by the eight oxime oxygen atoms of the shi^{3-} ligands that provide the MC framework. The remaining

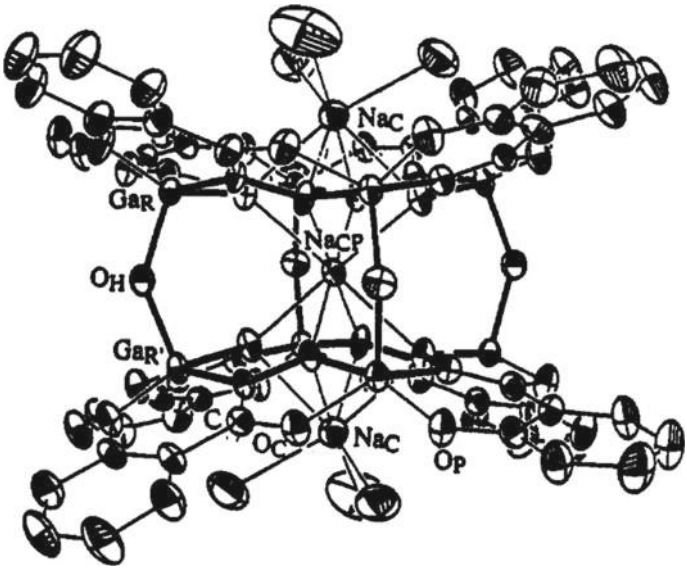

Fig. 1 ORTEP diagram from crystallographic data for the $Na_2\left\{Na_{0.5}\left[12\text{-}MC_{Ga^{III}N(shi)}\text{-}4\right]_2\right\}(\mu - OH)_4$ compound. Reprinted (adapted) with permission from [5]. Copyright 1993 American Chemical Society

two sodium ions cap the ends of the dimer by binding to the central cavity opposite of the encapsulated sodium ion. Each sodium ion is seven-coordinate with a face-capped octahedral geometry (CShM = 2.783). The coordination is comprised of four oxime oxygen atoms of four shi^{3-} ligands and three carbonyl oxygen atoms of three *N,N*-dimethylformamide (DMF) molecules. For about two decades after this report, gallium-containing metallacrowns would remain absent from the frontier of the field. However, since 2015 there has been a renaissance of gallium-containing metallacrown complexes as more metallacrown research has focused on lanthanide ion magnetism and lanthanide-based luminescence using encapsulated trivalent rare-earth ions (Ln^{III}) [3, 4]. The closed shell $3d^{10}$ valence electron configuration of Ga^{III} has become an attractive choice thanks to its diamagnetic and optically silent nature for such applications.

2.1 Gallium 12-MC-4 Structures

One of the first compounds to be reported in this new era of trivalent gallium metallacrown research was an archetypical $\left\{Ln^{III}\left[12\text{-}MC_{Ga^{III}N(shi)}\text{-}4\right](C_7H_5O_2)_4\right\}(C_5H_6N)$ reported by Eliseeva, Petoud, Pecoraro, and coworkers in 2016 [6]. This metallacrown is comprised of one Ln^{III} ion, four Ga^{III} ions, four shi^{3-}, and four benzoate ligands (Fig. 2). The authors

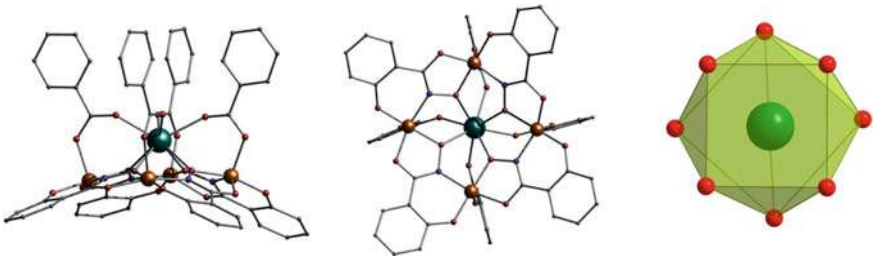

Fig. 2 Representation of the $\{Ln^{III}[12\text{-}MC_{Ga^{III}N(shi)}\text{-}4]\}^{-}$ compound from crystallographic data; side view (left) and down the pseudo-four-fold axis (center). Isolation of the dysprosium ligand field (right). Aqua = dysprosium, orange = gallium, blue = nitrogen, red = oxygen, and gray = carbon. Reprinted (adapted) with permission from [6]. Copyright 2016 American Chemical Society

reported the crystal structure for the dysprosium analogue that has pseudo-four-fold symmetry. The Dy^{III} ion is in an eight-coordinate square antiprism geometry binding to the oxime oxygen of the four shi^{3-} and a carbonyl oxygen of four benzoate ligands. The square antiprism has an average torsion angle of 41.72°. Two of the Ga^{III} are in five-coordinate square pyramidal geometries and the other two Ga^{III} are in six-coordinate octahedral geometries. The five-coordinate Ga^{III} ions have two κ^2-shi^{3-} bound to the basal positions where one shi^{3-} binds with the imino nitrogen and the phenoxide oxygen and the other binds using the oxime and carbonyl oxygens. The apical position is occupied by a carbonyl oxygen from the benzoate. For the six-coordinate Ga^{III} ions, two κ^2-shi^{3-} bind in the equatorial positions where one uses the imino nitrogen and phenoxide oxygen, and the other uses the oxime and carbonyl oxygen atoms. The axial positions are occupied by a carbonyl oxygen from benzoate and a solvent molecule either pyridine or methanol. The metallacrown itself is not planar but instead domed or bowled. This feature leads to the molecule having convex and concave sides of the central cavity. Due to the large ionic radius of the central lanthanide ion, it is situated on the convex side of the central cavity rather than lying in the plane of the cavity. Similar structural features were reported by Boron, Pecoraro, Zaleski, and coworkers in 2014 and 2016 for the related $Ln^{III}[12\text{-}MC_{Mn^{III}(N)shi}\text{-}4]$ molecules with Mn^{III} ions in the ring positions [24, 25]. The $Ln^{III}[12\text{-}MC_{Ga^{III}(N)shi}\text{-}4]$ molecules demonstrate the ability to sensitize emission from many trivalent lanthanide ions including Sm, Eu, Tb, Dy, Ho, Er, Tm, and Yb. The Dy and Sm analogues had emissions in both the visible and near-infrared (NIR) regions. Moreover, the Yb^{III} version of the MC possesses rather a strong emission in the NIR with an observed quantum yield of 5.88% in the solid state.

Another variation of a bent $Ln^{III}[12\text{-}MC_{Ga^{III}(N)shi}\text{-}4]$ has been reported with the general composition of $LnGa_4(shi)_4(H_2shi)_2$ by Eliseeva, Petoud, Pecoraro, and coworkers in 2020 [8]. The authors reported crystallographic data for both the terbium and ytterbium analogues of the compound (Fig. 3). The authors observed a clear difference in the structure of both analogues, likely due to the difference in ionic radius between Tb^{III} and Yb^{III}. The terbium analogue has a nine-coordinate

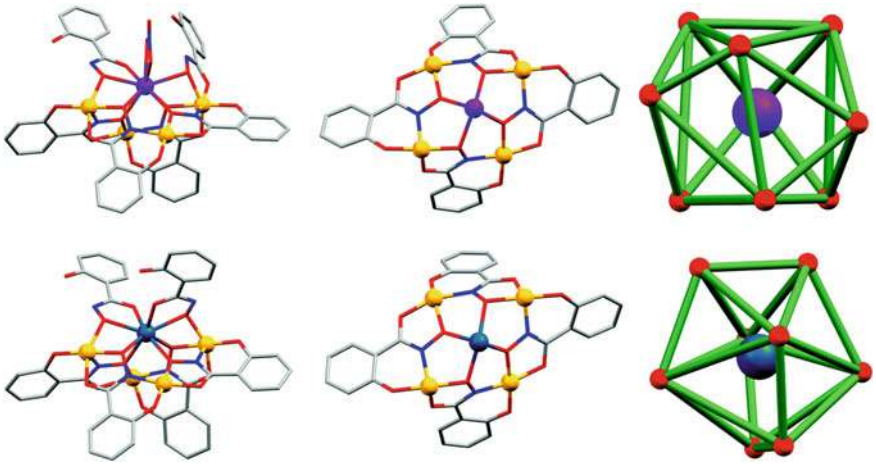

Fig. 3 Top row: representation from crystallographic data for the bent 12-MC-4 terbium analogue (left), the 12-MC-4 component (center), and isolation of the terbium ligand field (right). Bottom row: representation from crystallographic data for the bent 12-MC-4 ytterbium analogue (left), the 12-MC-4 component (center), and the ytterbium ligand field (right). Purple = terbium, aqua = ytterbium, yellow = gallium, blue = nitrogen, red = oxygen, and gray = carbon. Reprinted (adapted) with permission from [8]. Copyright 2020 Royal Society of Chemistry

tricapped trigonal prism geometry around the terbium, where the ion is bound to the oxime oxygen of all four shi^{3-} ligands as well as both H_2shi^-, the carbonyl oxygen of a H_2shi^-, and two oxygens from a bound bidentate nitrate anion. Each Ga^{III} is in a unique ligand field, where three Ga^{III} ions are six-coordinate octahedra, and one Ga^{III} ion is best described as a five-coordinate square pyramid (CShM = 1.379). The gallium coordination pattern about the MC ring is octahedral with Λ stereoisomerism, octahedral with *trans* configuration, octahedral with Δ stereoisomerism, and then square pyramidal. The gallium ion in a propeller conformation with Λ chirality is bound to the oxime and carbonyl oxygens of a κ^2-shi^{3-} and one κ^2-H_2shi^- as well as the imino nitrogen and phenoxide oxygen of a κ^2-shi^{3-}. For the *trans* configuration gallium ion, two κ^2-shi^{3-} are opposite of each other where one is bound using the oxime and carbonyl oxygens while the other is bound using the imino nitrogen and phenoxide oxygen. The coordination is completed by two axially bound *trans* pyridine molecules. The gallium ion with a propeller conformation with Δ chirality is connected to the oxime and carbonyl oxygens of a κ^2-shi^{3-}, the imino nitrogen and phenoxide oxygen of another κ^2-shi^{3-}, the oxime oxygen of a κ^2-H_2shi^-, and a pyridyl nitrogen atom. The square pyramidal gallium ion is bound to two κ^2-shi^{3-} ligands in the basal position using the oxime and carbonyl oxygens of one and the imino nitrogen and phenoxide oxygen of the other and contains a pyridyl nitrogen in the apical position.

The smaller ionic radius of the Yb^{III} ion compared to Tb^{III} leads to significant structural differences [26]. A comparison of average bond lengths for each analogue shows that the terbium analogue has an average Tb–O bond length of 2.420 Å while

the ytterbium analogue has an average Yb–O bond length of 2.296 Å. Also, the Yb^{III} is in an eight-coordinate trigonal dodecahedral geometry comprised of the four oxime oxygens of shi^{3-} ligands and the oxime and carbonyl oxygens of the two H_2shi^- ligands and does not have the nitrate bound. The authors attribute this absence to the slight difference in coordination behavior between the lanthanide ions in the central cavity of the metallacrown. The four Ga^{III} ions are in similar coordination environments to those in the terbium analogue, where three are in six-coordinate octahedra and one is in a five-coordinate geometry best described as a square pyramid (CShM = 0.915), with a similar—propeller Λ, *trans* octahedral, propeller Δ, square pyramidal—pattern about the MC ring as described for the terbium analogue above. In addition, the coordination spheres are analogues to their counterparts in the terbium analogue. In both molecules, the 12-$MC_{Ga^{III}(N)shi}$-4 ring, with H_2shi^{2-} ligands bridging between the ring metal ions and the central Ln^{III} ion, is "bent" to a greater degree than the 12-$MC_{Ga^{III}N(shi)}$-4 structures with benzoate bridging ligands between the Ga^{III} and Ln^{III} ions. In the benzoate MCs, the phenyl rings of neighboring shi^{3-} ligand almost lie in the same plane, while in the H_2shi^{2-} MCs, the phenyl rings of adjacent shi^{3-} are almost 90° relative to each other (Figs. 2 and 3). Like the flatter benzoate 12-$MC_{Ga^{III}N(shi)}$-4, this bent H_2shi^{2-} metallacrown was able to sensitize emission from a wide range of Ln^{III} ions including Tb, Dy, Ho, Er, and Yb. However, this scaffold had generally smaller quantum yields, likely due to the proximity between the Ln^{III} ion and the N–H oscillators from H_2shi^- ligands.

In 2019, an analogous structure was reported by Shao and coworkers for a dysprosium compound that uses 3-hydroxy-2-napthanoic hydroxamic acid (H_3nha) rather than H_3shi (Fig. 4) [18]. This Dy^{III} analogue is more like the Tb^{III} analogue structure reported for the shi-containing compound than the Yb^{III} analogue. The Dy^{III} is in a nine-coordinate tricapped trigonal prism ligand field geometry comprised of six oxime oxygens from four nha^{3-} and two H_2nha^- ligands, a carbonyl oxygen from a H_2nha^-, and two oxygens from a bidentate nitrate anion. Once again, three Ga^{III}

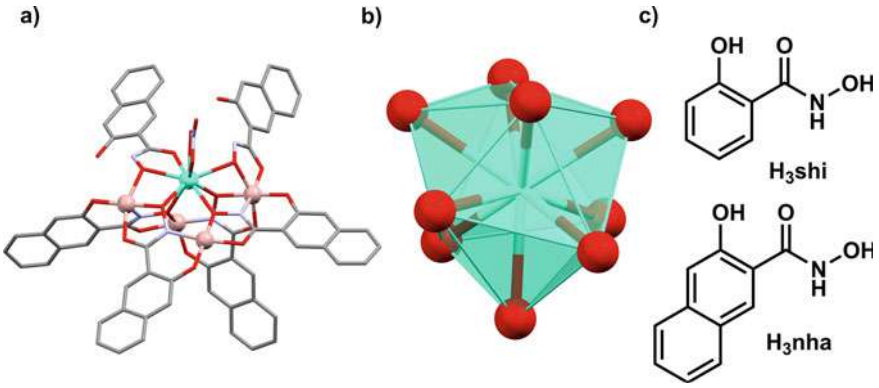

Fig. 4 **a** Representation from crystallographic data for the bent Dy^{III}/nha 12-MC-4 compound, **b** isolated Dy^{III} ligand field, and **c** schematic of H_3shi and H_3nha ligands. Aqua = dysprosium, tan = gallium, blue = nitrogen, red = oxygen, and gray = carbon

ions are in six-coordinate distorted octahedral ligand fields and the fourth Ga^{III} ion is in a five-coordinate square pyramidal geometry (CShM = 1.218). The identity of the atoms that bind to each gallium is the same for each equivalent gallium as the Tb^{III}/shi^{3-} analogue except that the atoms come from nha^{3-} ligands rather than shi^{3-} ligands. The Ga^{III} centers also follow an ordering of—propeller Λ, *trans* octahedral, propeller Δ, square pyramidal—about the MC ring, leading to the bent 12-MC-4 structure. However, the extent of bending is slightly different between the shi^{3-} and nha^{3-} analogues. Measurement of the average Ga^{III}–Ln^{III}–Ga^{III} angle using only the gallium ions with ligands that are folded downwards reveals that the Tb^{III}/shi^{3-} analogue has an angle of 97.02°, the Yb^{III}/shi^{3-} analogue has a similar angle of 97.28°, and the Dy^{III}/nha^{3-} analogue has a slightly more acute angle of 95.32°. This metric suggests that the nha^{3-} analogue has a more severe bend in the structure than its shi^{3-} counterparts. The authors studied the magnetic behavior of this species and were able to determine that the compound is a single-molecule magnet. Values for an effective barrier (U_{eff}) of 26.2 K with a pre-exponential factor (τ_0) of 2.97×10^{-6} s were determined from the fitting of experimental data collected with an applied field of 800 Oe to quench quantum tunneling of the magnetization.

2.2 Gallium 12-MC-4 Dimer Structures

The bowled $Ln^{III}[12\text{-}MC_{Ga^{III}(N)shi}\text{-}4]$ structure with benzoate has also been synthesized such that two of the metallacrowns can be linked to form a dimerized structure when benzoate anions are replaced by a dicarboxylate anion. The prototypical example of such a metallacrown with gallium was reported in 2018 by Eliseeva, Petoud, Pecoraro, and coworkers [9]. This compound is comprised of two 12-MC-4 s that contain one Ln^{III}, four shi^{3-}, and four Ga^{III} in each metallacrown that are connected by four isophthalate (iph^{2-}) linkages (Fig. 5). The authors reported crystallographic data for the dysprosium analogue that shows a rather curious case of disorder in the refined structure where two metallacrowns appear superimposed on top of one another. Metallacrowns will form the –[M–N–O]– motif such that the ordering is either clockwise or anticlockwise about the *z*-axis [27]. So, the disorder observed with this metallacrown is likely due to indiscriminate pairing of clockwise and anticlockwise isomers as the dimers assemble and pack in the crystal lattice. The Dy^{III} ion is in an eight-coordinate square antiprismatic geometry comprised of four oxime oxygens from shi^{3-} and four carbonyl oxygens from the iph^{2-} ligands. The square antiprism has an average torsion angle of 49.28°. The Ga^{III} ions are distributed such that two of the ions are in six-coordinate octahedral ligands fields while the other two are in five-coordinate square pyramidal ligand fields (CShM = 0.330 and 0.536). The six-coordinate Ga^{III} ions bind the two κ^2-shi^{3-} ligands in the equatorial positions using a combination of the imino nitrogen and phenoxide oxygen of one κ^2-shi^{3-} and the oxime and carbonyl oxygens of another. The axial positions are occupied by a carbonyl oxygen from iph^{2-} and an oxygen from a solvent molecule, either water

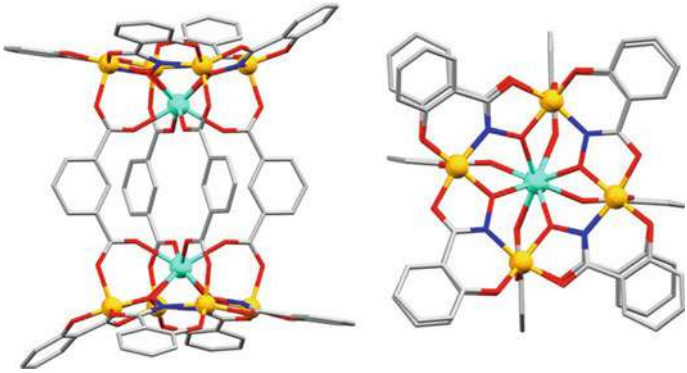

Fig. 5 Representation from crystallographic data for the 12-MC-4 dimer compounds; side view (left) and top-down view (right). Teal = dysprosium, yellow = gallium, blue = nitrogen, red = oxygen, and gray = carbon. Reprinted (adapted) with permission from [9]. Copyright 2017 John Wiley and Sons

or *N,N*-dimethylformamide. The five-coordinate Ga^{III} ions are connected to two κ_2-shi^{3-} in the basal positions that have the same binding configuration as the κ^2-shi^{3-} ligands of the six-coordinate Ga^{III} ions. The apical position for both ions is occupied by a carbonyl oxygen from iph^{2-} anion. This dimerized scaffold was able to sensitize Ln^{III} emission across the visible and near-infrared from ions including Pr, Nd, Sm, Tb, Dy, Ho, Er, and Yb. Compared to the monomeric metallacrown, this scaffold has a smaller quantum yield likely due to Ln–Ln self-quenching effects. However, the inclusion of larger ions such as Pr^{III} and Nd^{III} is rather exciting for metallacrown species.

After this prototypical report, several variations of this structure type have been synthesized and described. In 2019, Pecoraro and coworkers reported a method for orthogonal functional group incorporation onto the shi^{3-} and iph^{2-} anions [12]. The MC framework ligand can be modified to introduce an ethynyl functionality in the fourth position of the benzene ring to produce 4-ethylnylsalicylhydroximate ($eshi^{3-}$). The ethynyl group allows for the coupling of azide-containing organic molecules to the MC ligand via copper-catalyzed alkyne-azide cycloaddition. In addition, the iph^{2-} anion was modified to possess a maleimido group giving 5-maleimidoisophthalate ($miph^{2-}$). This portion of the MC then may undergo coupling with thiols via a Michael addition (Fig. 6). To demonstrate the coupling capability, the $eshi^{3-}$-based MC was coupled with benzyl azide and the $miph^{2-}$-based MC was coupled to cysteamine as a proof of concept. Electrospray ionization time-of-flight mass spectrometry confirmed complete coupling to all eight $eshi^{3-}$ or all four $miph^{2-}$ moieties of the MCs, and UV–visible absorbance and Sm^{III} luminescence experiments were performed to ensure that Ln^{III} sensitization was preserved after each of the coupling reactions. The structure for the Sm^{III} analogue with the $eshi^{3-}$ and unfunctionalized iph^{2-} was reported and differs from the original metallacrown in a few minor ways (Fig. 6). First, the ethynyl version was reported with sodium countercations from sodium

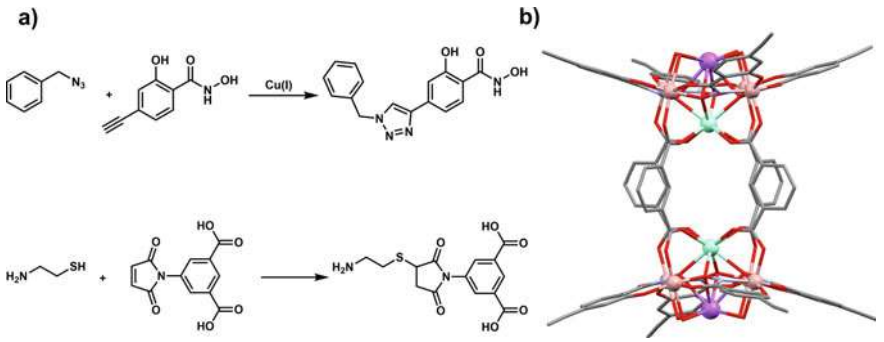

Fig. 6 **a** Schematic of the copper-catalyzed alkyne-azide cycloaddition and Michael addition performed on the metallacrown's ligands, and **b** representation from crystallographic data of the octaethynylmetallacrown. Teal = samarium, pink = gallium, purple = sodium, blue = nitrogen, red = oxygen, and gray = carbon. Reprinted (adapted) with permission from [12]. Copyright 2019 Elsevier

hydroxide used in the synthesis rather than ammonium countercations from ammonium hydroxide in the dimer with only nonfunctionalized ligands. The sodium binds below the metallacrown in a nine-coordinate capped square antiprism geometry using four oxime oxygens from the $eshi^{3-}$ in the 12-MC-4, four water molecules that are also bound to the Ga^{III} ions in the ring (one of these water molecules is 50% disordered with a *N,N*-dimethylformamide molecule), and one solvent water molecule that was refined with half occupancy. Due to the four bound solvent water molecules, each Ga^{III} is in a six-coordinate octahedral ligand field, where two κ^2-$eshi^{3-}$ bind using the familiar combination of imino nitrogen with phenoxide oxygen, and the oxime and carbonyl oxygens in the equatorial position. The axial positions are occupied by a carbonyl oxygen from iph^{2-} and a bound water molecule. Also, the curious case of disorder from indiscriminate clockwise and anticlockwise metallacrowns is not observed in this data set. The Sm^{III} ion does not have significant changes in its ligand field geometry compared to the Dy^{III} ion in the original version beyond slight differences expected from the change in ionic radii of the Ln^{III} ions.

In addition, Eliseeva, Petoud, Pecoraro, and coworkers reported a version of the dimer scaffold that incorporated iodine atoms onto the shi^{3-} and/or iph^{2-} ligands in 2020 (Fig. 7) [13]. Four compositions are mentioned in the article, such that each has differing amounts of iodine atoms on the MC scaffold from 0 to 12 in increments of four. The tetraiodo scaffold has iodine on the iph^{2-} anions only (in the fifth ring position), the octaiodo version has iodine on the shi^{3-} anions only (in the fourth ring position), and the dodecaiodo composition has an iodine on each ligand. Each composition was examined for its photophysics and for X-ray attenuation as a step toward a bimodal imaging agent. The authors report structural data for the Sm^{III} analogue of the tetraiodo and the octaiodo compound with sodium countercations. The tetraiodometallacrown is reminiscent of the ethynyl version reported in 2019 where the metal ions bind in essentially the same equivalent ligand field geometry and donor atom composition (Fig. 7). The systematic disorder from

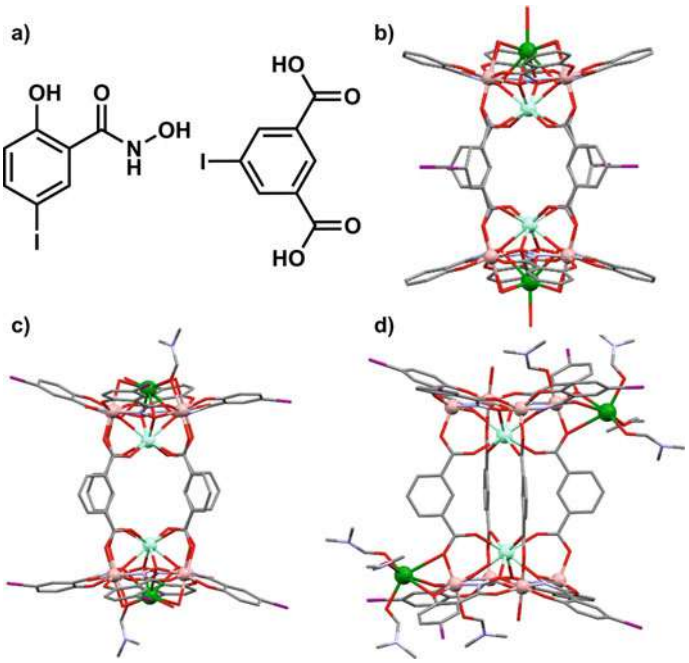

Fig. 7 Schematic of the iodine-containing ligands (**a**), representations from crystallographic data of the tetraiodometallacrown (**b**), the octaiodometallacrown with sodium below the ring (**c**), and the octaiodometallacrown with sodium on the side of the ring (**d**). Teal = samarium, pink = gallium, green = sodium, blue = nitrogen, red = oxygen, purple = iodine, and gray = carbon. Reprinted (adapted) with permission from [13]. Copyright 2020 John Wiley and Sons

combinations of clockwise and anticlockwise metallacrowns is observed in this data set. The octaiodometallacrown crystallized with sodium countercations; however, two distinct binding environments for the sodium were observed on two separate dimer metallacrown molecules (Fig. 7c, d). One of these binding sites is familiar where the sodium binds below the metallacrown ring, but this time the ion is in an eight-coordinate square antiprism geometry. The sodium ion connects to four oxime oxygens from the iodinated shi^{3-} ligand, three solvent waters that are also bound to Ga^{III} ions, and the carbonyl oxygen of one solvent *N,N*-dimethylformamide molecule that is bound to a Ga^{III} ion as well. The geometries and ligand environments of Ga^{III} and Sm^{III} ions do not deviate significantly from the structures of the dimers previously discussed. The second binding mode for the sodium countercation is in a six-coordinate octahedral geometry that is on the side of the 12-MC-4 ring. The ligand field consists of a carbonyl oxygen from an 4-iodoshi^{3-}, a phenoxide oxygen from another 4-iodoshi^{3-}, a carbonyl oxygen from iph^{2-}, and three carbonyl oxygens from solvent *N,N*-dimethylformamide molecules such that solvent and metallacrown oxygen atoms are separated into a *fac*-type isomer. Since the sodium ion is not below the metallacrown ring, the Ga^{III} ions have a mixture of five- and six-coordinate ligand

fields as was observed in the original scaffold. Two of the four Ga^{III} ions have octahedral geometry where the equatorial positions are occupied by two κ^2–4-iodoshi^{3-} that bind using the imino nitrogen and phenoxide oxygen or the carbonyl and oxime oxygens, while the axial positions are occupied by a carbonyl oxygen from iph^{2-} and a solvent oxygen from water or *N,N*-dimethylformamide. The remaining two Ga^{III} ions are in square pyramidal ligand fields (CShM = 0.269 and 0.410) where the basal positions are occupied by two κ^2–4-iodoshi^{3-} ligands using the same binding modes as described for the octahedra, and the apical position is occupied by a carbonyl oxygen from an iph^{2-} anion. Neither composition observed in this data set to display the disorder from clockwise and anticlockwise pairings. The iodo-metallacrowns were examined for their X-ray attenuation coefficient and there was a linear relationship between X-ray attenuation and the amount of iodine atoms in the structure. This observation speaks to the capability to tune the metallacrowns' attenuation predictably, based on rational design tenets that are possible with metallacrown synthesis. Plus, the Ln^{III} and Ga^{III} contribution to X-ray attenuation suggest that such compounds could perform rather well prior to iodine incorporation. Emission from Yb^{III} was observed for each compound, and the overall quantum yields $\left(Q_{Yb}^{L}\right)$ decreased as the iodine content increased, but the observed lifetimes (τ_{obs}) remained constant (Table 1). The authors also noted that the intrinsic quantum yields (Q_{Yb}^{Yb}) increased as iodine content increased, and sensitization efficiency (η_{sense}) decreased with iodine content (Table 1). So, the trend in overall quantum yield is a combination of both parameters as the iodine atoms affect each compound.

In 2019, Rentschler and coworkers reported another dimerized "double-decker" gallium-containing 12-MC-4 structure that captures one Dy^{III} ion between two 12-$MC_{Ga^{III}(N)shi}$-4 frameworks (Fig. 8) [11]. This dimer resembles the first gallium 12-MC-4 dimer, reported in 1993, that captured one sodium ion between two 12-$MC_{Ga^{III}N(shi)}$-4 metallamacrocycles, and two additional sodium ions were bound to the dimer on the outer faces of the MCs [5]. In the dysprosium-containing dimer, both 12-MC-4 frameworks are connected to the central Dy^{III} ion via the oxime oxygens of the shi^{3-} ligands. Each Ga^{III} ion of a MC is connected to a Ga^{III} ion on the other MC via a μ-$^{-}$OH anion, which is analogous to the sodium double-decker compound. The Dy^{III} ion has an eight-coordinate square antiprism geometry (CShM = 1.175) with an average torsion angle of 36.52° that is comprised of the eight oxime oxygens of the shi^{3-}. This geometry is different from the encapsulated sodium of the analogous

Table 1 Photophysical properties of ytterbrium–gallium dimeric 12-MC-4 compounds in DMF solution with increasing iodine content

Number of iodine atoms per dimer	τ_{obs} (μs)	τ_{rad} (μs)	Q_{Yb}^{Yb} (%)	Q_{Yb}^{L} (%)	η_{sense} (%)
0	51.1(2)	295	17	8.6(1)	51
4	51.3(1)	230	22	8.32(4)	37.8
8	50(2)	270	18	4.5(1)	25
12	51(1)	170	30	4.13(8)	13.8

Reprinted (adapted) with permission from [13]. Copyright 2020 John Wiley and Sons

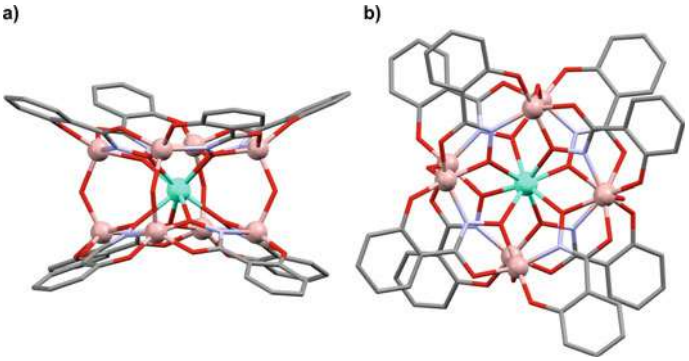

Fig. 8 Representation from crystallographic data for the "double-decker" dimerized metallacrown complex from a side view (**a**) and from a top-down view (**b**). Aqua = dysprosium, pink = gallium, blue = nitrogen, red = oxygen, and gray = carbon

dimer, which had a cubic geometry. Each of the four Ga^{III} is in five-coordinate ligand fields that are best described as square pyramidal geometries (CShM values range from 0.213 to 0.600). The basal positions are occupied by two κ^2-shi^{3-} that bind with either the imino nitrogen and the phenoxide oxygen or the oxime and carbonyl oxygen atoms, and the apical position is occupied by a μ-$^{-}$OH anion. Of the examples with eight-coordinate square antiprism Ln^{III} ligand fields, the one presented in this compound is distinct from other gallium 12-MC-4 compounds. Table 2 summarizes common metrics for this ligand field geometry, and this double-decker dimer is unique where the Ln^{III} is equidistant from oxime oxygen mean plane of each face, has equivalent "magic angles" of 54.3°, is significantly less twisted with respect to the average torsion angle, and also has a nearly perfect compression factor of unity for a cubic antiprism, where the compression factor is the ratio between the height and average side length of the prism. The authors characterized this compound as a single-molecule magnet via alternating current susceptibility measurements with a 1000 Oe applied field. The data were fit using an Arrhenius relationship to have an effective barrier (U_{eff}) of 39.00 K with a pre-exponential factor (τ_0) of 2.27×10^{-8} s.

In addition to these reports, there is also a publication that describes the use of each version of the Dy^{III}/Ga^{III} 12-MC-4 scaffolds with shi^{3-} as a source of white light emission. In 2020, Eliseeva, Petoud, Pecoraro, and coworkers describe how each compound has varying relative intensities of blue and yellow light emissions that may combine to act as a white light source [14]. The authors investigated the archetypical $Dy^{III}(benzoate)_4[12\text{-}MC_{Ga^{III}(N)shi}\text{-}4]$ with sodium and pyridinium countercations, the bent $Dy^{III}(H_2shi^{-})_2[12\text{-}MC_{Ga^{III}(N)shi}\text{-}4]$, the dimerized $\{Dy^{III}[12\text{-}MC_{Ga^{III}(N)shi}\text{-}4]\}_2(iph)_4$, as well as the double-decker $Dy(\mu\text{-}OH)_4[12\text{-}MC_{Ga^{III}(N)shi}\text{-}4]_2$. The emissions that were examined for composite white light emission were the π–π emission originating from the ligand and sharp bands corresponding to Dy^{III} $^4F_{9/2} \rightarrow {}^6H_J$ (J = 15/2, 13/2, and 11/2) transitions. Both the CIE color coordinates and the correlated color temperature (CCT) were measured

Table 2 Metrics for comparison between eight-coordinate Ln^{III} square antiprism species in 12-$MC_{Ga}{}^{III}$-4 individual molecules and dimers

Metallacrown	O_{ox}–Ga d_{MP}/Å	Magic angle with O_{carb}	Magic angle with O_{ox}	Ln–O_{carb} d_{MP}/Å	Ln–O_{ox} d_{MP}/Å	Torsion angle	Compression factor
$DyNa(ben)_4[12\text{-}MC_{Ga}{}^{III}{}_{N(shi)}\text{-}4]$	0.317	60.75°	53.41°	1.142	1.837	41.72°	0.9144
$[NH_4]_2\{Dy^{III}[12\text{-}MC_{Ga}{}^{III}{}_{N(shi)}\text{-}4]\}_2(iph)_4$	0.370	61.05°	53.27°	1.127	1.395	49.26°	0.9139
$\{Sm^{III}Na[12\text{-}MC_{Ga}{}^{III}{}_{N(eshi)}\text{-}4]\}_2(iph)_4$	0.396	63.55°	50.64°	1.052	1.525	41.80°	0.9172
$\{Sm^{III}Na[12\text{-}MC_{Ga}{}^{III}{}_{N(shi)}\text{-}4]\}_2(5\text{-iodo-iph})_4$	0.407	63.26°	51.34°	1.068	1.490	41.17°	0.9084
$\{Sm^{III}Na[12\text{-}MC_{Ga}{}^{III}{}_{N(4\text{-iodo-shi})}\text{-}4]\}_2(iph)_4$, Na below	0.433	64.78°	50.35°	1.006	1.539	41.66°	0.9012
$\{Sm^{III}Na[12\text{-}MC_{Ga}{}^{III}{}_{N(4\text{-iodo-shi})}\text{-}4]\}_2(iph)_4$, Na beside	0.373	63.01°	51.87°	1.085	1.470	49.69°	0.9026
$[n\text{-}Bu_4N]\{Dy(\mu\text{-}OH)_4[12\text{-}MC_{Ga}{}^{III}{}_{N(shi)}\text{-}4]_2\}$	0.342	54.30°	54.30°	1.355	1.355	36.41°	1.0145

for each of the metallacrowns. Due to slight differences in relative band intensities and crystal field effects on the Dy^{3+} ion, each of these compounds showed slightly different behavior. Based on the results, the authors concluded that the $\{Dy^{III}[12\text{-}MC_{Ga^{III}(N)shi}\text{-}4]\}_2(iph)_4$ dimer was the closest to white light emission.

2.3 *Non-standard Gallium-Containing Metallacrowns and Metallacryptates*

In addition to these various examples of gallium-containing metallacrowns, there have been a few other compounds that do not fit the metallacrown archetype exactly, yet still are metallamacrocylic –[M–N–O]–containing molecules. One example of these non-standard metallacrowns is a compound with the general composition of $Ln_2Ga_4(shi)_4(Hshi)_2(H_2shi)_2$ that was reported by Percoraro, Mallah, and coworkers in 2015 (Fig. 9) [19]. This compound is a 16-MC-6 where the ring is formed by –[Ga–N–O–Ga–N–O–Ln–O–Ga–N–O–Ga–N–O–Ln–O]– atoms (Ln^{III} = Gd, Tb, Dy, Er, or Y) and includes both gallium and lanthanide ions in the MC ring. The sequence differs from a standard metallacrown by two –[Ln–O–Ga]– "stutters" that omit a nitrogen atom. The compound lies on an inversion center such that the asymmetric unit is half of the molecule. The Ln^{III} has an eight-coordinate trigonal dodecahedral geometry (*SHAPE 2.1* analysis) comprised of the carbonyl and oxime oxygens of a κ^2-shi^{3-}, carbonyl and phenoxide oxygen atoms of a κ^2-$Hshi^{2-}$, two oxime oxygens from separate shi^{3-} ligands, an oxime oxygen from a H_2shi^-, and an oxygen from a solvent molecule. There are two distinct Ga^{III} centers and both have six-coordinate octahedral geometries. One Ga^{III} ion is bound to the imino nitrogen and oxime oxygen of a κ^2-shi^{3-}, the carbonyl and oxime oxygen of another κ^2-$Hshi^{2-}$, and the carbonyl and oxime oxygens of a κ^2-H_2shi^- in a propeller conformation. This Ga^{III}

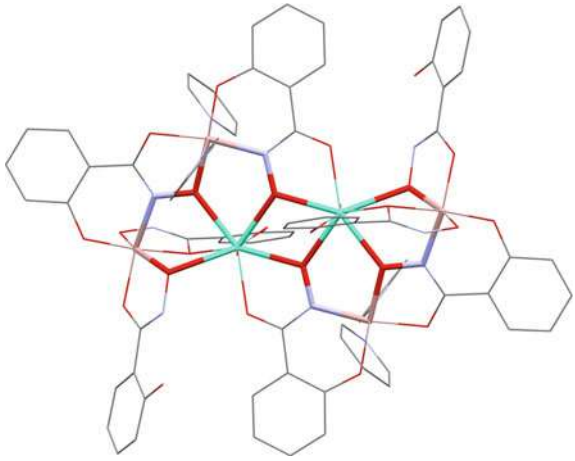

Fig. 9 Highlighted 16-MC-6 motif in the $Ln_2Ga_4(shi)_4(Hshi)_2(H_2shi)_2$ compound from crystallographic data. Aqua = dysprosium, tan = gallium, blue = nitrogen, red = oxygen, and gray = carbon

center is Λ chirality in the asymmetric unit, and the symmetry generated gallium center has Δ chirality. The other Ga^{III} ion is attached to two *trans* shi^{3-} ligands in the equatorial plane bound to the carbonyl and oxime oxygens of one κ^2-shi^{3-} and to the imino nitrogen and phenoxide oxygen of another κ^2-shi^{3-}. The coordination is completed by the two *trans* axial pyridine molecules. The pyridine molecules are at a torsion angle of 96.46°. The shi^{3-} ligands form the MC plane of the molecule, the $Hshi^{2-}$ are perpendicular to this molecular plane and bind on opposite faces of the MC, and the H_2shi^- molecules are twisted about 40° with respect to this molecular plane. The $Dy^{III}{}_2Ga_4$ structure was studied as a single-molecule magnet and yielded interesting observations. First, there are two distinct relaxation processes where one has independent relaxation of the Dy^{III} ion with a barrier of 26 K, and the other process is a coupled pathway where the Dy^{III} ions are interacting with a barrier of 18 K with a 2000 Oe applied field. This coupled relaxation pathway was an interesting observation since weakly interacting paramagnetic species are useful for quantum computing. To explore an isolated Dy^{III} relaxation in the 16-MC-6 ligand field, a compound diluted with Y^{III} was synthesized so that no Dy^{III} ions were likely to be proximal. This compound had an effective barrier (U_{eff}) of 31 K with no applied field and of 107 K with an applied field of 750 Oe. This value is rather large for a single Dy^{III} ion in an applied field.

Another example of a non-standard structure is actually considered a metallacryptate, analogous to organic cryptand ligands just as metallacrowns are related to crown ethers. This compound was reported in 2019 by Eliseeva, Petoud, Pecoraro, and coworkers and is comprised of one trivalent lanthanide ion (Pr, Nd, or Sm–Yb), six Ga^{III} ions, seven shi^{3-}, one $Hshi^{2-}$, and one H_2shi^- (Fig. 10) [10]. One pyridine molecule completes the coordination sphere of a Ga^{III}. The authors reported the crystal structure for the terbium analogue, which will be used for discussion here. The metallacryptate motif is comprised of the Tb^{III}, six Ga^{III}, and seven shi^{3-} such that the six Ga^{III} form a ruffled 18-MC-6 with six of the shi^{3-}. However, two of the Ga^{III} are connected by the seventh shi^{3-} such that the overall –[M–N–O]– motif resembles a [3.3.1] cryptand (Fig. 10c, d). The $Hshi^{2-}$ and H_2shi^- act as capping ligands spanning ring Ga^{III} ions and the central Tb^{III} ion. The Tb^{III} ion is in a nine-coordinate spherical tricapped trigonal prismatic ligand field (CShM = 1.122) though the geometries of a spherical capped square antiprism (CShM = 1.173) and muffin (CShM = 1.508) are comparable. The nine oxygen atoms about the Tb^{III} ion are exclusively comprised of the oxime oxygen atoms from seven shi^{3-}, one $Hshi^{2-}$, and one H_2shi^- ligands. Two of the Ga^{III} ions are five-coordinated with a square pyramidal geometry (CShM = 0.538 and 0.784), while the rest of the gallium ions are in six-coordinate octahedral geometries with propeller conformations. The two five-coordinate Ga^{III} ions have the same basal ligand environment and are bound to two *trans* κ^2-shi^{3-} ligands with the imino nitrogen and phenoxide oxygen from one ligand and with the oxime and carbonyl oxygens of the other ligand. The apical position is occupied by either a nitrogen atom of a pyridine molecule or the phenoxide oxygen of the $Hshi^{2-}$ ligand. The octahedral Ga^{III} either binds three κ^2-shi^{3-} ligands or two κ^2-shi^{3-} as well as a κ^2-H_2shi^- in a propeller confirmation with either Λ or Δ stereoisomerism. The geometry pattern of the Ga^{III} centers about the ruffled 18-MC-6

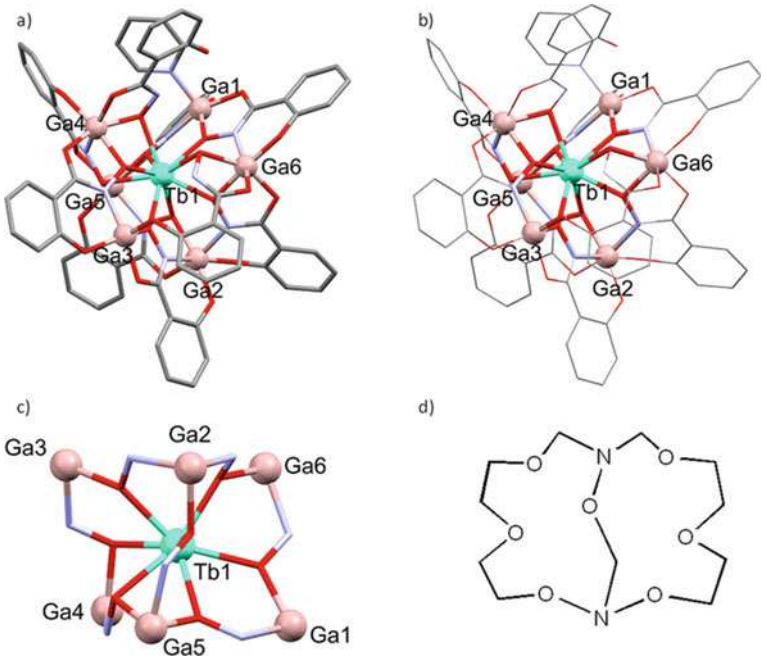

Fig. 10 **a** Representation from crystallographic data for the metallacryptate, **b** highlight of the MNO motif, **c** the isolated metallacryptate motif, and **d** organic cryptand for comparison. Aqua = terbium, tan = gallium, blue = nitrogen, red = oxygen, and gray = carbon. Reprinted (adapted) with permission from [10]. Copyright 2019 John Wiley and Sons

ring is—square pyramid, Δ octahedron, Λ octahedron, square pyramid, Λ octahedron, and Δ octahedron. This metallacryptate demonstrates both lanthanide-based luminescence and single-molecule magnetic properties for certain Ln^{III} analogues. Emission from Ln^{III} including Pr, Nd, Sm, Tb, Ho, Er, and Yb was observed via sensitization from the ligand. Quantum yields and observed lifetimes are suppressed compared to the previous Ln/Ga 12-MC-4 structures likely due to the presence of N–H oscillators near the Ln^{III}. The Dy, Nd, and Yb analogues showed out-of-phase magnetic susceptibility from alternating current experiments in an applied field. Of these analogues, only the Dy^{III} version displayed quenching of quantum tunneling of the magnetization with an applied field. For the Dy version, an effective barrier (U_{eff}) of 12.7 K with a pre-exponential factor (τ_0) of 3.6×10^{-6} was observed in the presence of a 750 Oe applied field.

3 Other Main Group Metallacrown Complexes

In addition to the copious examples of gallium(III) metallacrowns, several other main group ions have been utilized to generate MCs including aluminum, tellurium, and tin. Aluminum is a rational choice since it resides in the same group as gallium and thus should have similar chemistry. Alternatively, tin demonstrates the ability to use a fifth-period metal ion that is a rather uncommon component for metallacrown rings. Lastly, tellurium represents not only another example of a fifth-period ring element, but also an interesting foray into an element that has less metallic character and leads to peculiar guest encapsulation.

3.1 Aluminum-Containing Metallacrowns and Metallacryptates

The first report of aluminum-containing metallacrowns by Zaleski and coworkers in 2020 included both monomeric and dimeric variations of the Ln^{III}[12-$MC_{Al^{III}(N)shi}$-4)] motif that includes aryl carboxylate bridges and sodium as a countercation [28]. The monomeric species uses benzoate as the aryl bridge, and crystallographic data for Ln^{III} = Eu, Gd, Tb, Dy, Ho, Er, Tm, Yb, Lu, and Y were reported. The dimeric species uses isophthalate to link the MCs, and crystallographic data for Ln = Eu, Gd, Tb, Dy, Ho, Er, Yb, and Y were reported. Moreover, just as the gallium–lanthanide structures are luminescent, the aluminum–lanthanide monomers and dimers also emit light in the visible and near-infrared regions [29]. To date, the dimeric terbium–aluminum metallacrown has the highest quantum yield value (43.9%) in the solid state of any terbium-metallacrown. Regarding the structures, each of these structure types has slight nuances that the authors describe in full detail based on the identity of the Ln^{III} in the central cavity. For the sake of comparison to the gallium structures, our discussion will focus on the structure of the dysprosium analogues.

The monomeric Dy^{III}[12-$MC_{Al^{III}(N)shi}$-4] has the Dy^{III} and Na^{I} ions on opposing sides of the MC ring as is typical for a heterotrimetallic form of this motif (Fig. 11). The Dy^{III} is in an eight-coordinate square antiprism geometry comprised of four oxime oxygens of shi^{3-} and four carbonyl oxygens of benzoate ligands. The square antiprism has an average torsion angle of 42.86°. The Na^{I} is in a nine-coordinate capped square antiprism comprised of four oxime oxygens from shi^{3-}, four solvent water molecules, and one solvent *N,N*-dimethylformamide molecule that is disordered about a two-fold axis. Each of the Al^{III} ions is in six-coordinate octahedral ligand fields with two κ^2-shi^{3-} in the equatorial position using the imino nitrogen and phenoxide oxygen or oxime and carbonyl oxygen atoms, and the axial positions are occupied by a carbonyl oxygen from benzoate and a solvent water molecule. Overall, this structure is rather reminiscent of the Ga^{III} analogue, with the caveat that the Ga^{III} version has a pyridinium countercation. Thus, the Ga^{III} ions are five-coordinate as they do not contain a solvent molecule bound in an axial position as

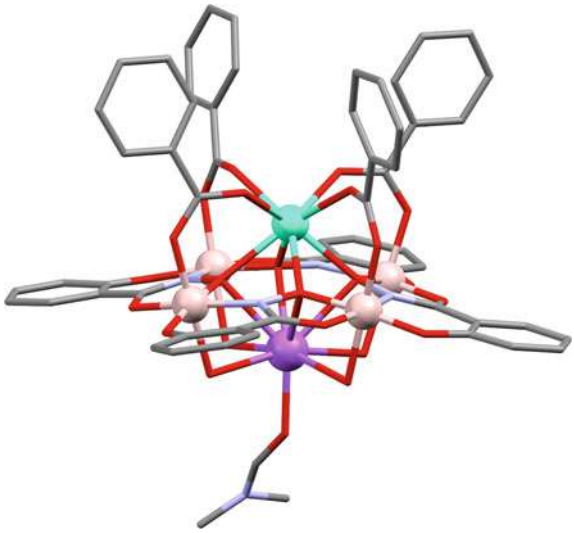

Fig. 11 Representation from crystallographic data of the monomeric aluminum 12-MC-4 compound. Teal = dysprosium, pink = aluminum, purple = sodium, blue = nitrogen, red = oxygen, and gray = carbon

observed for the Al^{III} ions. In addition, the smaller ionic radius of Al^{III} compared to Ga^{III} (0.675 and 0.76 Å, respectively) [26] requires a slightly different positioning of the shi^{3-} ligands. As a result, this MC is slightly less bowled than the Ga^{III} analogue according to the difference in the distance between the oxime oxygen and ring metal ion mean planes, 0.309 Å for the Al^{III} MC and 0.317 Å for the Ga^{III} MC. Finally, the smaller Al^{III} ion also contracts the metallacrown cavity where the distance between cross-cavity oxime oxygen atoms is approximately 3.64 Å for the Al^{III} MC, and the same metric is approximately 3.74 Å with the Ga^{III} MC. This difference in cavity size may explain the absence of reports of Ln^{III} larger than Eu^{III} with the Al^{III} structure that are observed with the Ga^{III} version.

The Al^{III} dimeric scaffold uses shi^{3-} and iph^{2-} ligands with sodium countercations. There are some of the same structural peculiarities as seen with the gallium analogues including whole molecule disorder and two binding modes for Na^{I} ions (Fig. 12). The sodium countercation is either below the metallacrown ring in a nine-coordinate capped square antiprism or bound to the side of the ring in a six-coordinate *fac*-octahedron. The nine-coordinate ligand field is comprised of four oxime oxygens from shi^{3-}, four solvent waters, and one solvent *N,N*-dimethylformamide. The six-coordinate ligand field consists of a phenoxide oxygen from shi^{3-}, a carbonyl oxygen from shi^{3-}, a carbonyl oxygen from iph^{2-}, and three oxygens from *N,N*-dimethylformamide molecules. The Dy^{III} analogue has the sodium ion in the nine-coordinate position. The Dy^{III} ion is in an eight-coordinate square antiprism ligand field geometry with an average torsion angle of 43.36° comprised of four oxime oxygens of shi^{3-} and four carbonyl oxygens of iph^{2-} ligands. The Al^{III} ions are all in six-coordinate octahedra with the same donor atoms as the monomeric version of the dysprosium containing metallacrown. Once again, the smaller ionic radius of aluminum affects the extent of the bowling of the structure, where the oxime

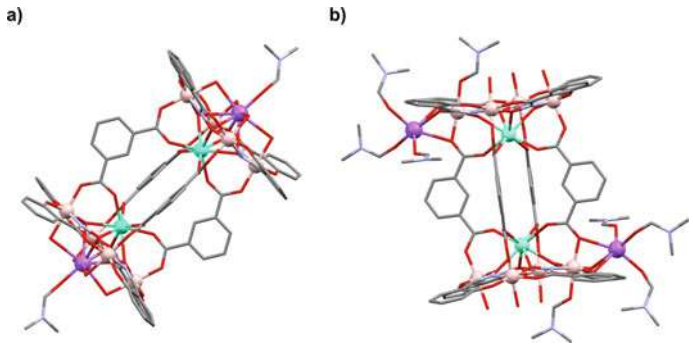

Fig. 12 Representations from crystallographic data for the $\{Al[12\text{-}MC_{Al^{III}(N)shi}\text{-}4\}_2(iph)_4Na_2$ compound with **a** the sodium ion bound below the MC ring and **b** the sodium ion bound to the side of the MC ring. Teal = dysprosium (**a**) or europium (**b**), pink = aluminum, purple = sodium, blue = nitrogen, red = oxygen, and gray = carbon

oxygen mean plane to aluminum mean plane distance is 0.352 Å, compared to the 0.370 Å of the mean plane difference for the gallium version. The cavity size is also contracted from a 3.76 Å cross-cavity oxime oxygen distance in the gallium version to an oxime oxygen distance of 3.67 Å in the aluminum version. Again, no Ln^{III} larger than Eu^{III} is reported for this scaffold, likely due to cavity size restrictions from an approximately 0.1 Å difference between the versions.

Just as was the case for gallium MCs, aluminum-containing compounds are not restricted to the archetypical structural motifs. In 2020, Zaleski and coworkers reported aluminum metallacryptates that can also form extended structures in the solid state [30, 31]. The discrete compound is a [3.3.1] metallacryptate with pyridinium countercations that is reminiscent of the gallium version reported in 2019. The compound is composed of one Ln^{III} (Ln = Gd, Dy, or Yb), six Al^{III}, seven shi^{3-}, two H_2shi^-, two pyridine, and two water solvent molecules. One of the H_2shi^- is disordered with an $Hshi^{2-}$ that binds in a similar fashion as observed for the gallium metallacryptate. Each of these analogues is isostructural, and this discussion will use the Dy^{III} example (Fig. 13). The encapsulated Dy^{III} is in a nine-coordinate capped square antiprism geometry comprised of seven oxime oxygen atoms from shi^{3-} and two oxime oxygen atoms from H_2shi^-. Each of the Al^{III} is in six-coordinate octahedral ligand fields with various donor atom arrangements. Two of the Al^{III} ions have a *trans* configuration of the ligands, while the other four have propeller configurations with either Λ or Δ stereoisomerism. The Al^{III} ions have a similar geometry pattern to that of the gallium metallacryptate, where the pattern about the ruffled 18-MC-6 is *trans*, Δ, Λ, *trans*, Λ, Δ (Fig. 13). The main difference between the aluminum and gallium metallacryptates is that the equivalent Ga ions to the *trans* Al ions are square pyramidal.

The dysprosium [3.3.1] aluminum metallacryptate was also synthesized with sodium countercations that showed two distinct coordination-polymeric 2D sheets in the solid state [30]. The metallacryptate core is slightly altered from the discrete

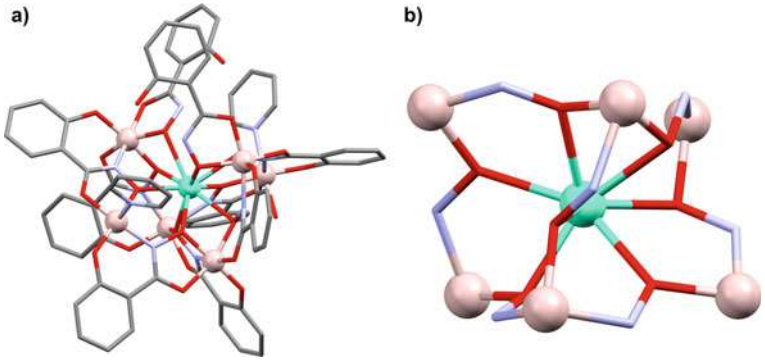

Fig. 13 Representation from crystallographic data of **a** the Dy^{III} metallacryptate and **b** the –[Al–N–O]– motif. Teal = dysprosium, pink = aluminum, blue = nitrogen, red = oxygen, and gray = carbon

compound where the H_2shi^- are now $Hshi^{2-}$ that enable binding to sodium ions on the exterior of the compound, and acetate ligands are included in some of the metal coordination sites. Two polymorphs of the 2D sheets are reported, where one crystallized in *Cc* and the other in *Pc* (Fig. 14). The *Cc* formulation has one metallacryptate within the repeating unit of the coordination polymer, such that each unit is connected to four neighboring compounds. Four sodium ions located at the periphery of each metallacryptate and not part of the MC structure contribute to the linkage between each metallacryptate and four neighboring metallacryptate units. The 2D sheet in *Pc* features a repeating unit with two metallacryptate moieties that use six sodium atoms to form the intermetallacryptate linkages to four dimeric neighbors. In each dimeric unit, the two metallacryptates are enantiomers of each other.

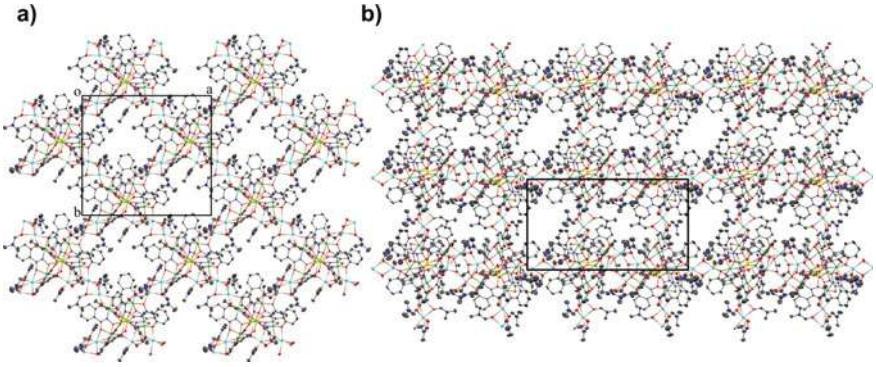

Fig. 14 Extended structures from crystallographic data for **a** the single metallacryptate repeat unit in *Cc* and **b** the paired metallacryptate repeating unit in *Pc*. Yellow = dysprosium, green = aluminum, light blue = sodium, dark blue = nitrogen, red = oxygen, and gray = carbon. Reproduced under an open-access license from Ref. [30]

3.2 Tellurium-Containing Metallacrowns

The first appearance of the metalloid tellurium in the MC ring that follows the –[M–N–O]– motif of metallacrowns was published in 2010 by Vargas-Baca and coworkers [32]. The ring was formed in situ upon the reaction of 1-*tert*-butyl-1-(β-(*N,N*-dimethylcarbamoyl)-telluride)but-1-en-3-one with hydroxylamine-*O*-sulfonic acid to form a macrocyclic set of four 1,2-chalcogenazole oxides (Fig. 15). The structure is described as a "boat" conformation with S_4 symmetry for the 12-MC-4 where the 1,2-tellurazole orientation alternates between "up" and "down" about the MC ring. VSEPR treatment of the Te suggests that it has four valence groups, three σ-bonds to a carbon, nitrogen, and oxygen as well as one lone pair, to form a T-shaped geometry from a square planar configuration such that each lone pair is pointed toward the MC cavity. From this prototypical design, several different host–guest elaborations were explored.

The Vargas-Baca group began to introduce these elaborations in 2016 and 2017 with several guests including Pd^{II}, tetrahydrofuran, and even a C_{60} buckyball, as well as further alterations to the telluride precursor. They reported structures that use a 3-methyl-5-phenyl-1,2-tellurazole 2-oxide building block that has surprising air and moisture tolerance, where the *tert*-butyl of the first MC is replaced by a phenyl, or 5-phenyl-1,2-tellurazole 2-oxide building blocks [33, 34]. The authors demonstrated the ability to synthesize 12-MC-4 and 18-MC-6 compounds with both precursors, however; only the 3-methyl-5-phenyl-1,2-tellurazole 2-oxide building block was used for guest encapsulation and therefore will be the focus for discussion. The 3-methyl-5-phenyl-1,2-tellurazole 2-oxide building block was recrystallized in various solvent mixtures that lead to three distinct structures. The first example was in either a combination of acetonitrile and dichloromethane or acetonitrile and chloroform and the result was an analogous S_4 12-MC-4 construct to the *tert*-butyl

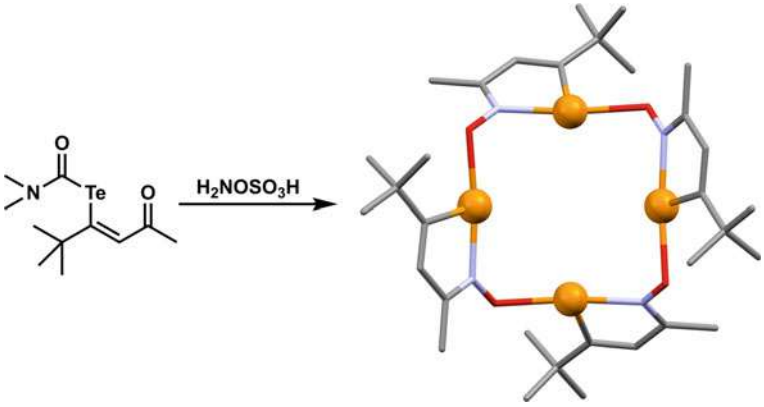

Fig. 15 Reaction scheme for the formation of the tellurium metallacrown. The product is a representation from crystallographic data. Orange = tellurium, blue = nitrogen, red = oxygen, and gray = carbon

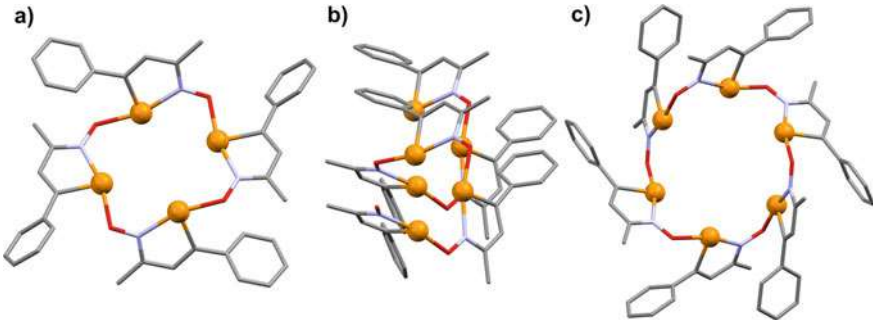

Fig. 16 Representation from crystallographic data of **a** the 12-MC-4, **b** the polymer, and **c** the 18-MC-6 from the 3-methyl-5-phenyl-1,2-tellurazole 2-oxide building block

compound (Fig. 16). The second was recrystallized from benzene and formed a helical polymer rather than a macrocycle (Fig. 16). The third of these structures was recrystallized in a dichloromethane and *n*-hexane mixture that resulted in 18-MC-6 with S_6 symmetry (Fig. 16). While the polymer is too constrained for guest encapsulation, the 12-MC-4 and 18-MC-6 both have examples of guest binding in the solid state.

The 12-MC-4 is able to incorporate two guests, a C_{60} molecule or a Pd^{II} with BF_4^- counteranions (Fig. 17a, b), while the 18-MC-6 encapsulates two tetrahydrofuran molecules (Fig. 17c). The 12-MC-4 observed with the C_{60} guest molecule was formed from the diffusion of the telluride in dichloromethane with a solution of C_{60} in tetrachloroethane. This metallacrown has a slightly different orientation than the apo12-MC-4 where there are asymmetric faces. These faces result from the bias of the ligand to point all of the Te atoms' lone pair toward the same face of a "bowled" structure. The C_{60} guest is situated between two 12-MC-4s, such that it associates with both faces of this metallacrown using Van der Waals interactions. In the case

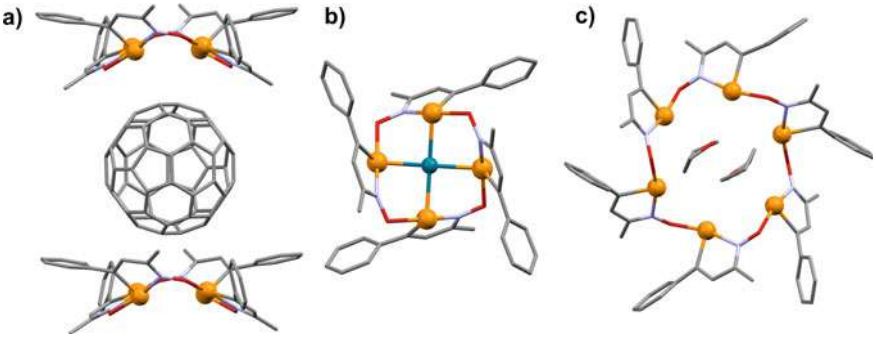

Fig. 17 Representation from crystallographic data for the **a** 12-MC-4 with the C_{60} guest, **b** the 12-MC-4 with Pd^{II}, and **c** the 18-MC-6 with tetrahydrofuran. Teal = palladium, orange = tellurium, blue = nitrogen, red = oxygen, and gray = carbon

of Pd^{II} binding, the "boat" conformation returns and the Pd^{II} is encapsulated in the central cavity. Each Te atom forms a bond with the Pd^{II} to form a four-coordinate square planar ligand field. The Te atoms have four bonds and are best described as a see-saw shape. This observation is rather exciting since there are few examples of metallacrowns that bind a heavy transition metal cation, and the metallacrown is also technically an inverse metallacrown since the Te atoms bind to the central guest. The 18-MC-6 was also recrystallized from tetrahydrofuran, and in this case, two solvent tetrahydrofuran molecules are situated above and below the central cavity of the MC. Each of these examples highlights the range of possible guests with a tellurium metallacrown.

In 2019, more metal ion guests were introduced to the tellurium MCs including Pt^{II}, Rh^{III}, Cu^{I}, Au^{I}, and Ag^{I} [35, 36]. The Pt^{II} MC was formed using a 3-methyl-5-(3,5-di-*tert*-butylphenyl)-1,2-tellurazole 2-oxide precursor to form a 12-MC-4 (Fig. 18b). The Pt^{II} is bound in the central cavity to each Te atom to form a square planar complex. The Te atoms have four bonds and are in a see-saw shape. In addition to the host–guest compound, the authors also observed an apo-18-MC-6 MC with 3-methyl-5-(3,5-di-*tert*-butylphenyl)-1,2-tellurazole 2-oxide. The Rh^{III} 12-MC-4 was formed using 3-methyl-5-phenyl-1,2-tellurazole 2-oxide and each of the four Te atoms bound to the Rh^{III} (Fig. 18a). Again, the Te is in a see-saw geometry with its four bonded partners. The Rh^{III} has a six-coordinate octahedral ligand field comprised of the four Te in the equatorial position and two chloride anions in the axial positions.

The Cu^{I}- and Au^{I}-containing 12-MC-4 s were formed using the 3-methyl-5-phenyl-1,2-tellurazole 2-oxide subunit. The 12-MC-4 with Cu^{I} has the Cu ion in the central cavity much like the Rh^{III}, Pt^{II}, and Pd^{II} MCs; however, the Cu^{I} is five-coordinate with a square pyramidal geometry (CShM = 1.129; Fig. 19a). The four Te atoms from the MC fill the basal positions and the apical position is occupied by an oxygen atom from a trifluoromethanesulfonate anion. The Te atoms are in the familiar see-saw configuration. The 12-MC-4 with Au^{I} has a different binding

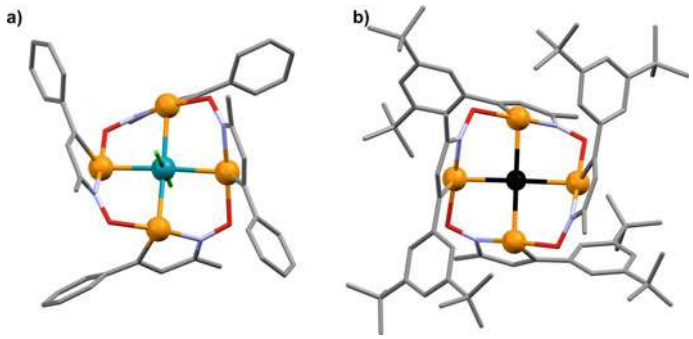

Fig. 18 Representations from crystallographic data for **a** the Rh^{III} metallacrown and **b** the Pt^{II} metallacrown. Teal = rhodium, black = platinum, orange = tellurium, blue = nitrogen, red = oxygen, and gray = carbon

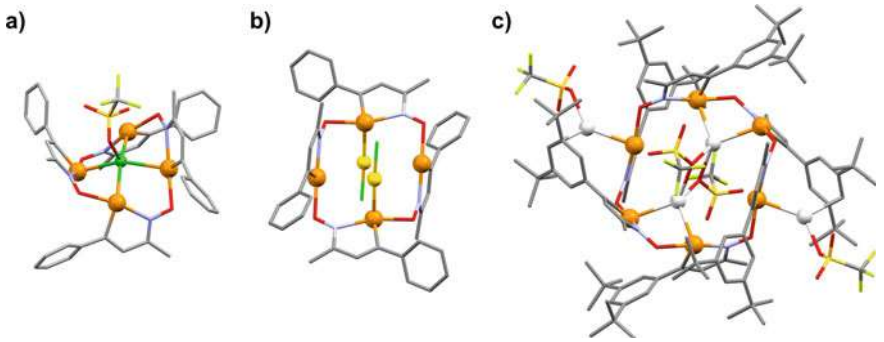

Fig. 19 Representations from crystallographic data of **a** the Cu^{I} 12-MC-4 (green = copper, orange = tellurium, dark yellow = sulfur, pale yellow = fluorine, blue = nitrogen, red = oxygen, and gray = carbon), **b** the Au^{I} 12-MC-4 (yellow = gold, orange = tellurium, lime green = chlorine, blue = nitrogen, red = oxygen, and gray = carbon), and **c** the Ag^{I} 18-MC-6 (white = silver, orange = tellurium, dark yellow = sulfur, pale yellow = fluorine, blue = nitrogen, red = oxygen, and gray = carbon)

motif for the transition metal (Fig. 19b). In this case, two Au^{I} ions bind to the MC, each on opposing sides of the ring. The Au^{I} ions are two-coordinate and linear, where one ligand is Te atom from the MC and the other is a chloride anion. The Te atoms that bind to Au^{I} connect to four atoms in a see-saw geometry, while the unbound Te atoms have three bonds in a T-shape. The Ag^{I}-containing metallacrown is an 18-MC-6 composed of the 3-methyl-5-(3,5-di-*tert*-butylphenyl)-1,2-tellurazole 2-oxide unit (Fig. 19c). Each 18-MC-6 has four Ag^{I} ions that bind in two unique positions. The first position is in the metallacrown cavity such that the silver ion is in a four-coordinate-tetrahedral ligand field. Two metallacrown Te atoms and two oxygen atoms from trifluoromethanesulfonate anions comprise this ligand field. The second site is on the exterior of the metallacrown such that the silver ion is in a three-coordinate trigonal planar ligand field comprised of a Te from the MC, an oxygen from a trifluoromethanesulfonate anion, and an agostic interaction with a C–H bond from the phenyl ring of the precursor ligand.

3.3 Tin-Containing Metallacrowns

The final set for discussion of the main group element archetypical metallacrowns features tin(IV) ions in the metallacrown ring. To date, there are two reports that contain Sn^{IV} metallacrown complexes from Dou and coworkers in 2010 [37, 38]. The initial report describes vacant 12-MC-4 compounds comprised of three organotin centers (R–Sn, R = ethyl, butyl, or phenyl) as the ring metal with shi^{3-} as the framework ligand (Fig. 20). Unlike most 12-MC-4 compounds, these tin-based MCs do not contain a metal ion bound to the central MC cavity. Each six-coordinate octahedral ring Sn^{IV} ion is bound to two κ^2-shi^{3-} in a propeller conformation using the oxime

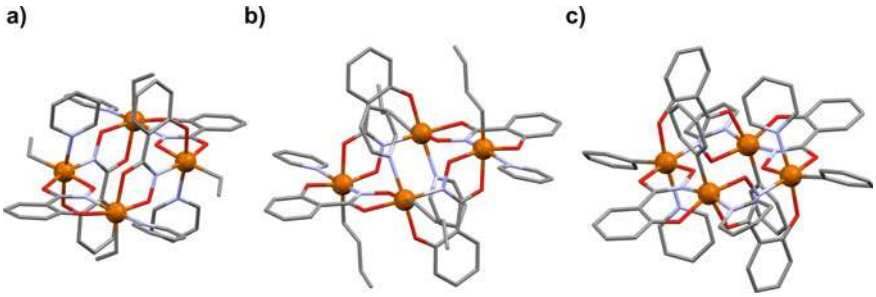

Fig. 20 Representation from crystallographic data for **a** the ethyl organotin 12-MC-4, **b** the butyl organotin 12-MC-4, and **c** the phenyl organotin 12-MC-4. Brown = tin, blue = nitrogen, red = oxygen, and gray = carbon

and carbonyl oxygen atoms of one shi^{3-}, the imino nitrogen and phenoxide oxygen atoms of another shi^{3-}, and the coordination is completed by a pyridyl nitrogen atom and a carbon from the organotin precursor. There are two unique tin(IV) sites in the MC ring, where the stereoisomerism alternates between Λ and Δ chirality about the ring. These 12-MC-4s are also considered to be ruffled structures due to the alternating chiral octahedra. The adjacent shi^{3-} are close to a 90° twist with respect to one another, and the Sn^{IV} ions are not on the same plane since the "vertical" shi^{3-} cause a step-ladder configuration. Shortly after this introductory report, Dou and coworkers expanded on these organotin metallacrowns by using 5-chlorosalicylhydroxamic acid as the framework ligand (Fig. 21). While the structure does not change significantly with the introduction of the chlorine atoms, the authors do note an interesting application for these metallacrown compounds. The chloro-organotin compounds were soluble in DMSO/H_2O mixtures, and in vitro exposure of cancer cells including Bel-7402 and HeLa cells to the chloro-organotin MCs indicated mild tumor-inhibition. The 12-$MC_{Sn^{IV}N(5CI-shi)}$-4 with ethyl groups bound to the tin centers had an IC_{50}

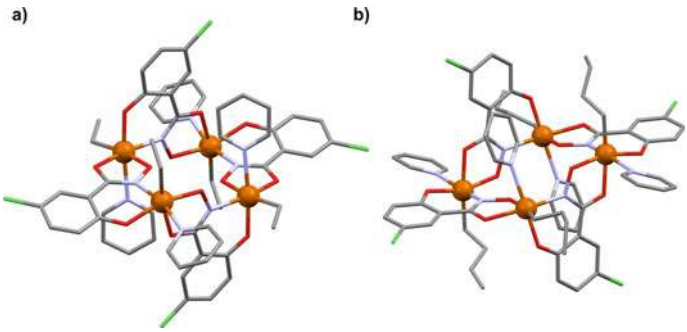

Fig. 21 Representations from crystallographic data for **a** the ethyl organotin 12-MC-4 with an aryl chlorine and **b** the butyl organotin 12-MC-4 with an aryl chlorine. Brown = tin, lime green = chlorine, blue = nitrogen, red = oxygen, and gray = carbon

(the concentration where cell viability decreases by half) value of 15.38 μM for Bel-7402 cells and 12.04 μM for HeLa cells. The butyl version 12-$MC_{Sn^{IV}N(5CI-shi)}$-4 gave comparable IC_{50} values of 15.20 μM for Bel-7402 cells and 11.18 μM for HeLa cells.

4 Azametallacrown Complexes with Main Group Elements

Related to the archetypical metallacrowns with a N–O bridge are a class of macrocyclic molecules known as azametallacrowns (azaMC) with a N–N bridge between the metal centers. These inorganic molecules extend the analogy of MCs to azacrown ethers that contain a nitrogen instead of an oxygen atom in the cyclic repeat unit of the organic macrocycle [39]. Many of the same *p*-block metals that have been used for archetypical MCs have also been used to synthesize azametallacrowns including aluminum, gallium, and tin. However, indium and silicon have also been used to generate *p*-block element azaMCs as well as the *s*-block metals lithium and sodium.

4.1 Gallium and Indium Azametallacrowns

Just as Lah, Pecoraro, and coworkers reported the first gallium MCs, Lah and coworkers reported the first gallium azametallacrowns. In a series of structures with similar but slightly differing pentadentate *N*-acylsalicylhydrazide ligands, Lah and coworkers reported four 18-MC-6 structures where the hydrazide N–N group of the ligand bridges the Ga^{III} ions and generates a macrocycle with six gallium ions per structure (Fig. 22) [40]. The four different ligands used were *N*-formylsalicylhydrazide (H_3fshz), *N*-acetylsalicylhydrazide (H_3ashz), *N*-propionylsalicylhydrazide (H_3pshz), and *N*-lauroylsalicylhydrazide (H_3lshz) (Fig. 23). The Ga^{III} ions are six-coordinate with octahedral geometry. The coordination is composed of two triply deprotonated *N*- acylsalicylhydrazidate ligands and one monodentate solvent molecule (methanol or ethanol). One *N*-acylsalicylhydrazidate ligand binds in a tridentate fashion and provides three atoms (one nitrogen and two oxygen atoms) in a meridional arrangement, while the second ligand binds in a bidentate mode and provides two atoms (one nitrogen and one oxygen). In addition, the binding of the ligands produces chelate rings, and each Ga^{III} ion has a propeller configuration. The stereoconfigurations of the Ga^{III} ions alternate between the Λ and Δ enantiomers about the MC ring. Though the metallamacrocycle has a disk shape, the six Ga^{III} ions are not in a plane but form a chair conformation. The four different ligands used to generate the metallamacrocycles only vary in the side chain of the carbonyl carbon atom: a hydrogen atom for *N*-formylsalicylhydrazide (fshz), a methyl group for *N*-acetylsalicylhydrazide (ashz), an ethyl group for *N*-propionylsalicylhydrazide (pshz), or a $(CH_2)_{10}CH_3$ group for *N*-lauroylsalicylhydrazide (lshz). In the reported structures, the length of the flexible,

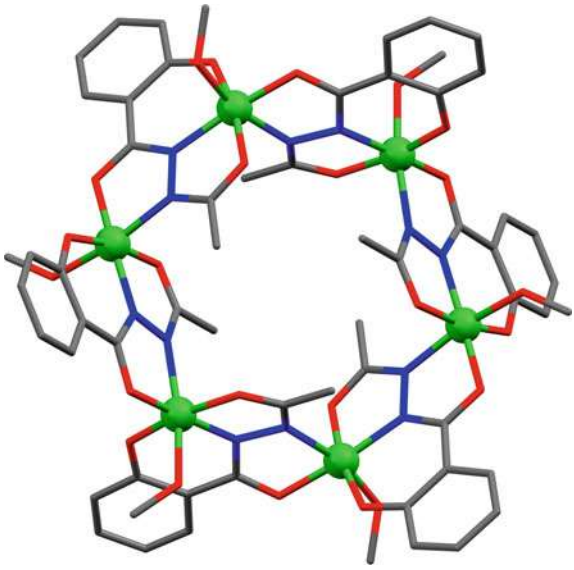

Fig. 22 X-ray crystal structure of the vacant azametallacrown 18-$MC_{Ga^{III}}$-6 with the ligand *N*-acetylsalicylhydrazide. The stereoconfigurations of the Ga^{III} ions alternate between Λ and Δ about the MC ring. Green = gallium, red = oxygen, blue = nitrogen, and gray = carbon

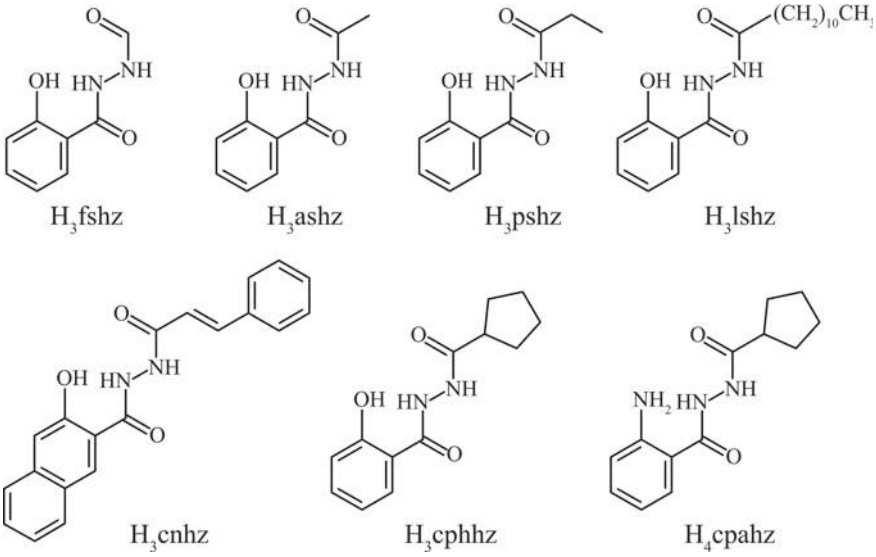

Fig. 23 Sketch of the hydrazide-based ligands used to construct gallium(III) and indium(III) azametallacrowns: *N*-formylsalicylhydrazide (H_3fshz), *N*-acetylsalicylhydrazide (H_3ashz), *N*-propionylsalicylhydrazide (H_3pshz), *N*-lauroylsalicylhydrazide (H_3lshz), N^2-*trans*-cinnamoyl-2-hydroxy-3-naphthoylhydrazide (H_3cnhz), N^2-cyclopentylcarbonyl-2-hydroxybenzoylhydrazide (H_3cphhz), and N^2-cyclopentylcarbonyl-2-aminobenzoylhydrazide (H_4cpahz)

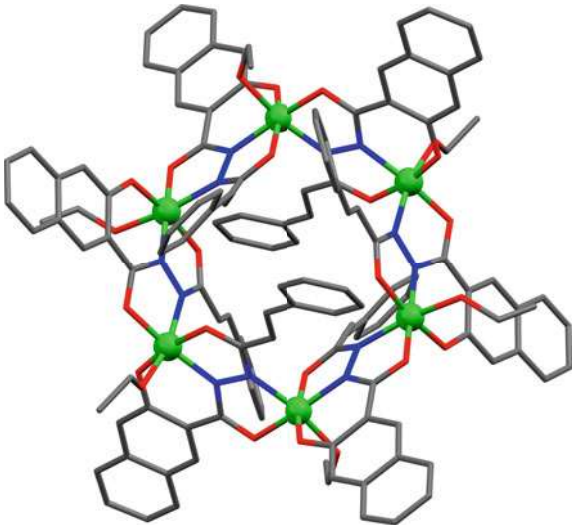

Fig. 24 X-ray crystal structure of the vacant azametallacrown 18-$MC_{Ga^{III}}$-6 with the ligand N^2-*trans*-cinnamoyl-2-hydroxy-3-naphthoylhydrazide. The stereoconfigurations of the Ga^{III} ions alternate between Λ and Δ about the MC ring. Green = gallium, red = oxygen, blue = nitrogen, and gray = carbon

linear alkyl chains did not affect the size of the metallamacrocycle as an aza18-MC-6 compound was generated in each instance. If the side chain of the pentadentate ligand is switched to a bulkier *trans*-cinnamoyl group [N^2-*trans*-cinnamoyl-2-hydroxy-3-naphthoylhydrazide, H_3cnhz], a similar Ga^{III} aza18-MC-6 is produced (Fig. 24) [41]. The Ga^{III} are still octahedral with a similar coordination sphere as described above. In addition, the Ga^{III} ions maintain their propeller configuration, and the stereoconfigurations alternate between Λ and Δ about the MC ring. Besides the differing larger side chain, this hydrazide ligand has a naphthoyl group instead of a phenoxyl group. The steric increase in this region of the ligand also did not affect the size of the macrocycle. However, changing the pentadentate ligand so that the side chain is a bulky cyclopentyl group results in a larger metallamacrocycle [42]. For the two similar ligands, N^2-cyclopentylcarbonyl-2-hydroxybenzoylhydrazide (H_3cphhz) and N^2-cyclopentylcarbonyl-2-aminobenzoylhydrazide (H_4cpahz) ligand, the carbon adjacent to the carbonyl carbon atom is bonded to two carbon atoms and an aza24-MC-8 is generated with both instances (Fig. 25). For the ligands of the aza18-MC-6 molecules, the carbon atom adjacent to the carbonyl carbon atom is only connected to one other carbon atom. Furthermore, the slight variations of the two ligands can lead to different stereoconfigurations for the metal centers. The ligand N^2-cyclopentylcarbonyl-2-hydroxybenzoylhydrazide contains a hydroxyl group in the second position of the phenyl ring of the ligand, and the resulting aza24-MC-8 has octahedral Ga^{III} ions with a similar coordination sphere as the Ga^{III} ions discussed above, where one ligand binds in a meridional fashion, one ligand binds bidentate, and a solvent molecule completes the coordination sphere. In addition, the Ga^{III} stereoconfiguration alternates between Λ and Δ about the MC ring as in metallamacrocycles discussed above. However, if the hydroxyl group in the second position of the phenyl ring is changed to an amino group as in the ligand N^2-cyclopentylcarbonyl-2-aminobenzoylhydrazide,

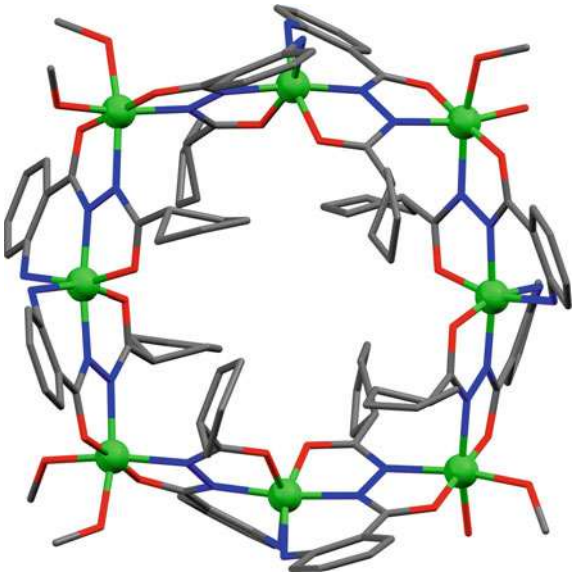

Fig. 25 X-ray crystal structure of the vacant azametallacrown 24-$MC_{Ga^{III}}$-8 with the ligand N^2-cyclopentylcarbonyl-2-aminobenzoylhydrazide. The stereoconfigurations of the Ga^{III} ions alternate between *mer* and Δ about the MC ring. Green = gallium, red = oxygen, blue = nitrogen, and gray = carbon

the stereoconfigurations of the Ga^{III} ions change (Fig. 25). This ligand is only doubly deprotonated as compared to others that are triply deprotonated. This difference in deprotonation causes the N^2-cyclopentylcarbonyl-2-aminobenzoylhydrazide ligand to bind in a slightly different fashion to the Ga^{III} ions. While all of the Ga^{III} ions of the azaMC ring are six-coordinate octahedrons, all do not have a propeller configuration. Half of the Ga^{III} ions are surrounded by two N^2-cyclopentylcarbonyl-2-aminobenzoylhydrazide ligands, and both ligands bind in a tridentate fashion with a meridional stereoconfiguration. For the other Ga^{III} ions, two ligands bind in a bidentate fashion and the coordination sphere is completed by two solvent molecules (in some instances, monodentate nitrate anions can replace the solvent molecules). These octahedra are in a propeller configuration with Δ chirality. As in the other structures, the stereoconfigurations alternate about the MC ring in a pattern of meridional (*mer*)–Δ.

Expanding upon the gallium azaMCs, Lah and coworkers incorporated indium into the metallacycle [43]. As these two metals are in the same family, indium also generated azaMCs with *N*-acylsalicylhydrazide ligands. Using the ligand N^2-cyclopentylcarbonyl-2-aminobenzoylhydrazide with indium though did not generate an aza24-MC-8 as described above. In the gallium azaMCs, the bulky cyclopentyl group generates the larger metallamacrocycle. However, with indium, only the smaller aza18-MC-6 macrocycle was produced (Fig. 26). As in the other structures, the In^{III} ions are six-coordinate and the In^{III} ions have alternating meridional–Δ stereoconfigurations. The alternation stereoisomerism pattern of the In^{III} ions is analogous to the Ga^{III} ions discussed for the larger aza24-MC-6 molecule with half of the In^{III} ions binding two ligands in a tridentate meridional fashion and the other In^{III} ions

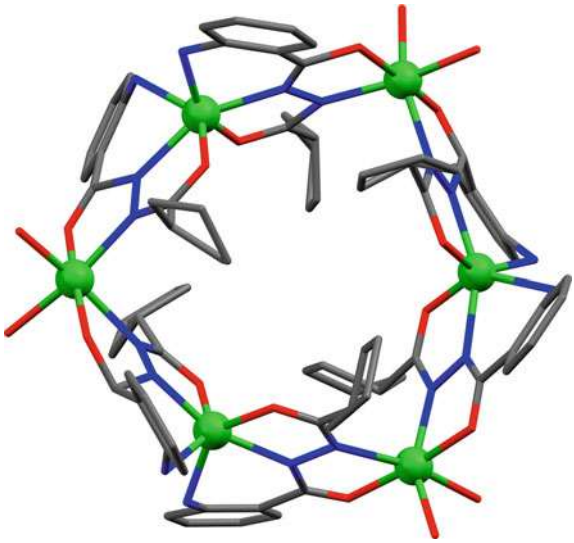

Fig. 26 X-ray crystal structure of the vacant azametallacrown 18-$MC_{In^{III}}$-6 with the ligand N^2-cyclopentylcarbonyl-2-aminobenzoylhydrazide. The stereoconfigurations of the In^{III} ions alternate between *mer* and Δ about the MC ring. Green = indium, red = oxygen, blue = nitrogen, and gray = carbon

with a Δ propeller configuration with two ligands binding bidentate and the coordination sphere completed by either solvent molecules or nitrate anions. While the hexanuclear macrocycle is enthalpically unfavorable compared to the octanuclear system due to the increased ring strain of the hexanuclear system, the hexanuclear macrocycle is entropically favored due to fewer components needed to construct the ring. In addition, the authors believe that the ability of the indium(III) ions to have a larger tolerance for a distorted geometry compared to gallium(III) ions allows the In^{III} ions and the resulting smaller azaMC to compensate for the additional ring strain of the hexanuclear system compared to a potential octanuclear indium-azaMC. Overall, through the systematic alternation of macrocycle components in the described azaMC systems, Lah and coworkers eloquently demonstrate that careful ligand design and metal choice can lead to predictable control of not only the size of the macrocycle but also the stereoconfiguration of the metal centers (Table 3).

4.2 Other p-Block Azametallacrowns—Aluminum, Silicon, and Tin

To date, only one aluminum azametallacrown has been reported, an aza9-MC-3 that also captures an aluminum ion in the central cavity (Fig. 27) [44]. The ring Al^{III} ions are four-coordinate with a tetrahedral shape and are bridged by the hydrazido groups of the ligand 1,1,4,4-tetramethyl-2,3-diazabutadiene. Each ring Al^{III} ion is bound to two hydrogen atoms and two nitrogen atoms of different hydrazido ligands. The aluminum(III) ion captured in the central cavity is six-coordinate and bound to each nitrogen atom of the MC ring. The geometry of the central Al^{III} ion is extremely

Table 3 Comparison of ligand and metal ion type and the resulting azaMC size and metal ion stereoconfiguration

Ligand	Ring metal	azaMC size	Stereoisomer pattern of the metal ions around the MC ring
N-formylsalicylhydrazide (H_3fshz)	Ga^{III}	18-MC-6	ΛΔ…
N-acetylsalicylhydrazide (H_3ashz)	Ga^{III}	18-MC-6	ΛΔ…
N-propionylsalicylhydrazide (H_3pshz)	Ga^{III}	18-MC-6	ΛΔ…
N-lauroylsalicylhydrazide (H_3lshz)	Ga^{III}	18-MC-6	ΛΔ…
N^2-*trans*-cinnamoyl-2-hydroxy-3-naphthoylhydrazide (H_3cnhz)	Ga^{III}	18-MC-6	ΛΔ…
N^2-cyclopentylcarbonyl-2-hydroxybenzoylhydrazide (H_3cphhz)	Ga^{III}	24-MC-8	ΛΔ…
N^2-cyclopentylcarbonyl-2-aminobenzoylhydrazide (H_4cpahz)	Ga^{III}	24-MC-8	*mer*–Δ…
N^2-cyclopentylcarbonyl-2-aminobenzoylhydrazide (H_4cpahz)	In^{III}	18-MC-6	*mer*–Δ…

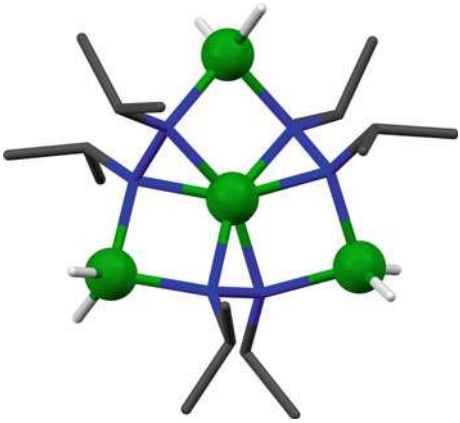

Fig. 27 X-ray crystal structure of the azametallacrown $Al^{III}[9\text{-}MC_{Al^{III}}\text{-}3]$ with the ligand 1,1,4,4-tetramethyl-2,3-diazabutadiene. The central Al^{III} ion binds to each N atom of the MC ring. Green = aluminum, blue = nitrogen, gray = carbon, and white = hydrogen

distorted, likely due to geometric constraints of the diaza ligand. The geometry can best be described as a hexagon (D_{6h}) with a CShM value of 13.270. The next lowest CShM value (14.136) is that of an octahedron (O_h). Both values clearly indicate the geometry of the central aluminum ion is distorted from any ideal shape. The compound is stable in benzene as the ^{27}Al NMR spectrum indicates the presence of both six- and four-coordinate aluminum centers.

Four silicon inverse aza9-MC-3 compounds have been reported, all with the same structure, $[\{SiH(\mu\text{-}pz)_2\}_3\text{-}\mu_3\text{-}O]^+$, where pz^- is a deprotonated 3,5-dimethylpyrazole (Hpz) anion (Fig. 28) [45, 46]. The differences in the structures are the lattice

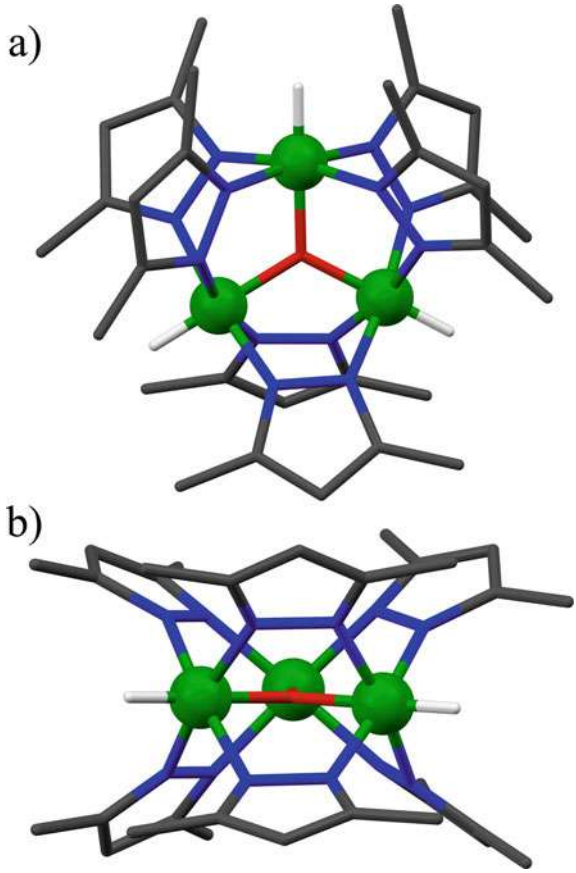

Fig. 28 **a** Top view and **b** side view of the X-ray crystal structure of the inverse azametallacrown 9-$MC_{Si^{IV}}$-3 with an μ_3-oxide anion bound in the central cavity. Two 3,5-dimethylpyrazate anions bridge between each Si^{IV} center. Six 3,5-dimethylpyrazolate anions provide the N–N bridges between the Si^{IV} centers. Green = silicon, red = oxygen, blue = nitrogen, gray = carbon, and white = hydrogen

molecules or the counteranion. In the three structures reported by Kroke and coworkers, the unbound counteranion is chloride but the lattice molecules are either a protonated 3,5-dimethylpyrazole, chloroform, or toluene. For the structure reported by Wagler and Bitto, the unbound counteranion is a $[Si_2Cl_4H_2(\mu\text{-}H)(pz)_2]^-$ unit, and a toluene molecule is located in the lattice. In all four structures, the pyrazolate anions provide the N–N bridge between the Si^{IV} centers, and two pyrazolate anions bridge between each Si^{IV} center to form the aza9-MC-3 framework (Fig. 29). A μ_3-oxide is captured in the central cavity and binds to each ring Si^{IV} center; thus, the macrocycle can be considered an inverse metallacrown as an anion is bound in the central cavity. Each Si^{IV} is six-coordinate with octahedral geometry (CShM values range from 0.879 to 1.315). The equatorial plane of the coordination sphere consists of four nitrogen atoms for four different pz^- ligands and the axial direction consists of the μ_3-oxide anion and a terminal hydride anion.

Four tin azaMCs have been reported thus far. In 2007, Ma and coworkers reported two closely related aza12-MC-4 compounds with the same Schiff-based ligand

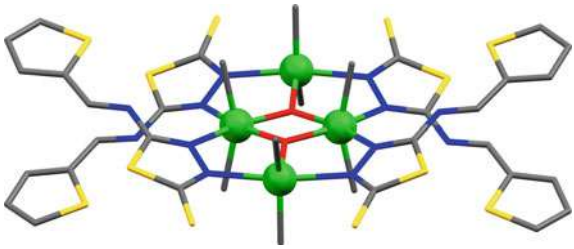

Fig. 29 X-ray crystal structure of the inverse azametallacrown 12-$MC_{Sn^{IV}}$-4 with two μ_3-oxide anions bound in the central cavity. The ligand 4-thiophenelideneamino-1,3,4-thiadiazole-2-thione provides the N–N bridges between the Sn^{IV} ions. Green = tin, red = oxygen, blue = nitrogen, gray = carbon, and yellow = sulfur

4-thiophenelideneamino-1,3,4-thiadiazole-2-thione that provides the N–N linkage between the ring Sn^{IV} ions (Fig. 29) [47]. The only difference between the structures is the lattice solvent molecule: water or methanol. The geometry of the Sn^{IV} centers alternates around the ring between a six-coordinate significantly distorted octahedron (CShM = 4.219 and 4.229) and a five-coordinate trigonal bipyramidal shape (CShM = 0.909 and 1.323). The MCs can be considered inverse MCs as two oxide anions are captured in the central cavity. Each oxide anion forms a μ_3-bridge between one five-coordinate and two six-coordinate Sn^{IV} ions. The six-coordinate Sn^{IV} ions are surrounded by two μ_3-oxide anions and two nitrogen atoms from two different ligands in the equatorial plane and two methyl groups along the axial direction. The coordination of the trigonal bipyramidal Sn^{IV} centers is completed by one μ_3-oxide anion and two methyl groups in the equatorial plane and two nitrogen atoms from two ligands in the axial positions. In addition, the S atoms of the SN_2C_2 five-membered rings of the ligand form long S···S interactions (3.370 Å for the water version and 3.384 Å for the methanol version) that leads to a two-dimensional grid structure (Fig. 30).

Two vacant tin aza24-MC-6 compounds have been reported by Kuang and coworkers in 2020 (Fig. 31) [48]. Both MCs are very similar with the analogous ligands bis(5-chlorosalicylaldehyde) carbazide and bis(5-methylsalicylaldehyde) carbazide used as the framework ligands for the molecule with the carbazide groups providing the N–N linkages between the Sn^{IV} centers. Each MC consists of three six-coordinate and three five-coordinate Sn^{IV} ions with the coordination modes alternating about the MC ring. The six-coordinate tin centers have severely distorted octahedral geometry (CShM values range from 5.313 to 6.458), while the five-coordinate centers are distorted trigonal bipyramids (CShM range from 1.347 to 2.242). The octahedral geometry of the Sn^{IV} center is completed by a nitrogen atom and two oxygen atoms of one ligand in the equatorial plane, the oxygen and nitrogen atoms of a second ligand in the equatorial plane, and two *n*-butyl groups along the axial direction. The five-coordinate geometries consist of two nitrogen atoms and one oxygen atom from the same ligand and two carbon atoms from *n*-butyl groups. The *n*-butyl groups and one of the nitrogen atoms lie in the equatorial plane and the

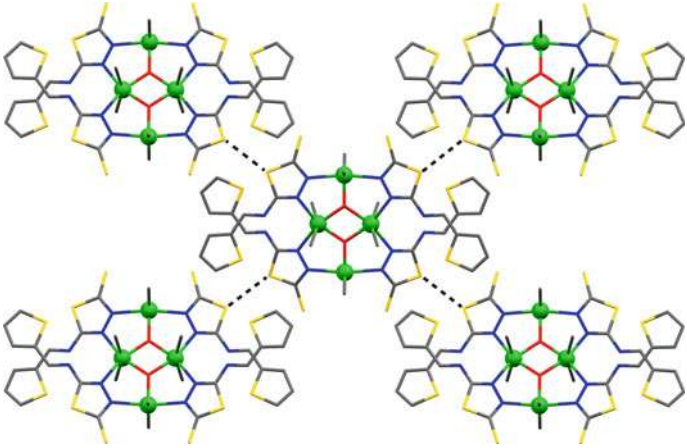

Fig. 30 The azametallacrown 12-$MC_{Sn^{IV}}$-4 forms a two-dimensional sheet via S···S interactions (3.370 Å, represented by the dashed lines) of the ligand. Green = tin, red = oxygen, blue = nitrogen, gray = carbon, and yellow = sulfur

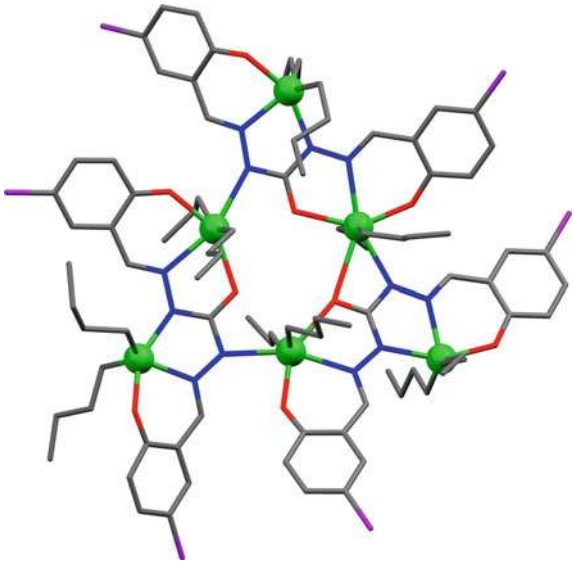

Fig. 31 X-ray crystal structure of the vacant azametallacrown 18-$MC_{Sn^{IV}}$-6 with the ligand bis(5-chlorosalicylaldehyde) carbazide. The coordination geometry of the Sn^{IV} ions alternates between trigonal bipyramidal and octahedral about the MC ring. Green = tin, red = oxygen, blue = nitrogen, gray = carbon, and purple = chlorine

oxygen atom and the other nitrogen atom comprise the *z*-axis. As previous organotin compounds have shown biological activity, the herbicidal properties of the latter two azaMCs were tested on several plant species. Both MCs inhibited the growth of the tested plants as determined by stem and root growth measurements.

4.3 Alkali Metal Azametallacrowns—Lithium and Sodium

While *p*- and *d*-block-based MCs, with either a N–O or N–N linkage, are quite common, MCs with *s*-block metals in the ring are relatively rare. To date, only lithium and sodium have been incorporated in the MC ring positions. The first of these lithium MCs was reported in 2000 as a mixed-metal aza12-MC-4 with alternating Li^{I} and Al^{III} ions in the ring with a –[Li–N–N–Al–N–N]– repeat unit that recurs twice to generate the metallamacrocycle (Fig. 32) [49]. Four pyrazolate anions provide the N–N linkage. The azaMC can be considered an inverse MC as two hydride anions are captured in the central cavity. Each hydride forms a μ_3-bridge between two Li^{I} ions and one Al^{III} ion. Each Li^{I} is four-coordinate by binding to two nitrogen atoms of different pyrazolate anions and to two hydride anions. Each Al^{III} is also four-coordinate by binding with two nitrogen atoms of different pyrazolate anions, a hydride, and a carbon atom of a tris(trimethylsilyl)methyl group, $C(SiMe_3)_3$. Then, in 2002, Russell and coworkers reported two similar lithium-only aza12-MC-4 compounds (Fig. 33) [50]. Both contain bis(imido)phosphine dianion $[RP(N–N = CPh_2)_2]^{2-}$ ligands, which provide the N–N bridge between the Li^{I} ions. The difference between the two structures is the R group of the dianion, as it is either a *n*-butyl or phenyl group. There are two coordination geometries for the Li^{I} ions about the ring, and the geometries alternate about the MC ring. Two of the Li^{I} ions are two-coordinate with a distorted linear geometry (CShM

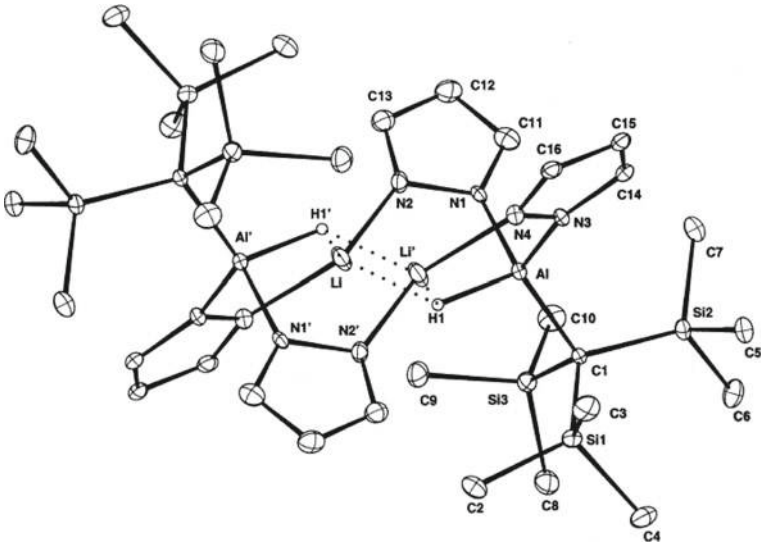

Fig. 32 X-ray crystal structure of the inverse azametallacrown 12-$MC_{Li^{I}/Al^{III}}$-4 with two μ_3-hydride anions bound in the central cavity. Each μ_3-hydride bridges between two Li^{I} ions and one Al^{III} ion. The ligand pyrazolate bridges the N–N bridges between the metal centers. Reprinted with permission from [49]. Copyright 2000 Elsevier

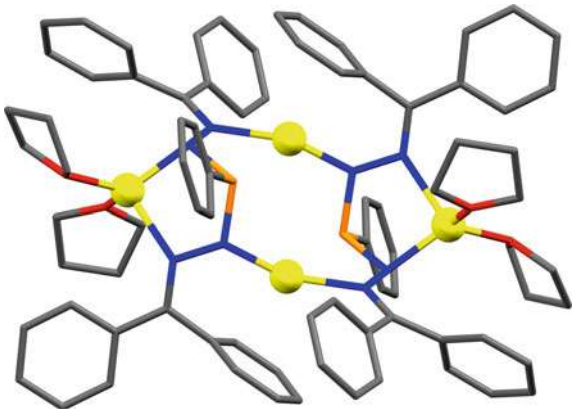

Fig. 33 X-ray crystal structure of the vacant azametallacrown 12-MC_{Li^I}-4 with a bis(imido)phosphine dianion as the bridging ligand between the Li^I ions. The coordination geometry of the Li^I ions alternates between bent and tetrahedral about the MC ring. Yellow = lithium, red = oxygen, blue = nitrogen, gray = carbon, and orange = phosphorous

= 1.918 and 1.972). The Li^I ion binds asymmetrically to two nitrogen atoms of different bis(imido)organophosphine dianions. In addition, the Li^I ions form long-range contacts (~2.5 Å) with carbon atoms of a nearby phenyl ring of the ligands and with the phosphorus center (~2.6 Å). The other two Li^I ions are four-coordinate with tetrahedral geometry (CShM = 1.352 and 1.525). The coordination is completed by two nitrogen atoms from the same bis(imido)organophosphine dianion and two oxygen atoms of solvent tetrahydrofuran (THF) molecules.

In 2015, the Schelter group demonstrated that they could stabilize cerium in the 4 + oxidation state with either Li^I or Na^I ions in the second coordination sphere of the cerium(IV) ion [51]. Using the ligand *N*,*N*′-diphenylhydrazine, which provides the N–N bridges between the Li^I (Fig. 34) or Na^I (Fig. 35) ions, an aza12-MC-4 can be generated with either four Li^I or four Na^I in the MC ring and a Ce^{IV} captured in the central cavity of the macrocycle. In both versions of the azaMC, the Ce^{IV} ion is

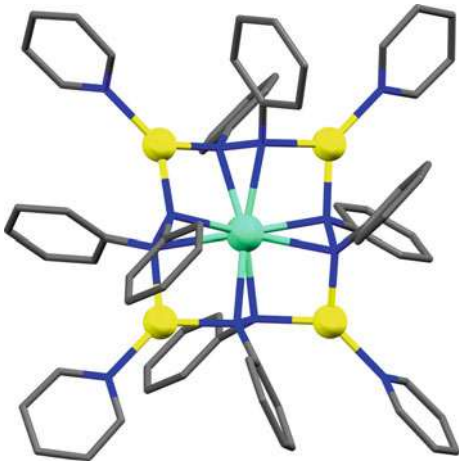

Fig. 34 X-ray crystal structure of the azametallacrown Ce^{IV}[12-MC_{Li^I}-4] with the ligand *N*,*N*′-diphenylhydrazine. The central Ce^{IV} ion binds to each N atom of the MC ring, and each Li^I is three-coordinate with trigonal planar geometry. Yellow = lithium, aqua = cerium, blue = nitrogen, and gray = carbon

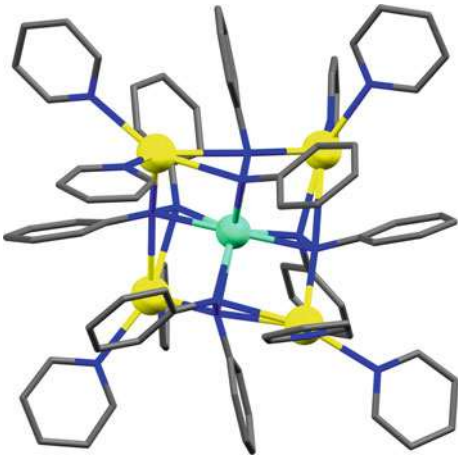

Fig. 35 X-ray crystal structure of the azametallacrown $Ce^{IV}[12\text{-}MC_{Na^I}\text{-}4]$ with the ligand *N*,*N*′-diphenylhydrazine. The central Ce^{IV} ion binds to each N atom of the MC ring, and each Na^I is five-coordinate with square pyramidal geometry. Yellow = sodium, aqua = cerium, blue = nitrogen, and gray = carbon

bound to all eight nitrogen atoms of the MC ring, and the geometry about the Ce^{IV} ion is severely distorted from any ideal shape. In the lithium version of the azaMC, the Ce^{IV} geometry is best described as an octagon (CShM = 10.588), while in the sodium version, the Ce^{IV} geometry is that of a triangular dodecahedron (CShM = 11.993). It is likely the coordination mode of the alkali metal ion affected the position of the nitrogen atoms about the Ce^{IV} ions and these distortions lead to a change in the shape about the central Ce^{IV} ion. In the lithium version of the azMC, the four Li^I ions are three-coordinate with trigonal planar geometry (CShM = 2.167–2.653) and bind to two nitrogen atoms of two different *N*,*N*′-diphenylhydrazine ligands and to the nitrogen atom of a pyridine molecule. In the sodium version of the macrocycle, the four Na^I ions are five-coordinate and bind to two nitrogen atoms of two different *N*,*N*′-diphenylhydrazine ligands and to two nitrogen atoms of two pyridine molecules. Furthermore, each Na^I ion forms a fifth long interaction (~2.8–2.9 Å) with an additional nitrogen atom of one of the *N*,*N*′-diphenylhydrazine ligands to give a severely distorted square pyramidal geometry (CShM = 10.693–12.523). This change in geometry about the alkali metal ion likely leads to a change in geometry for the central Ce^{IV} ion. Subsequent work by the Schelter group produced lithium versions of the azaMC with substituted *N*,*N*′-diarylhydrazine ligands: *N*,*N*′-bis-(4-chlorophenyl)hydrazine (Fig. 36), *N*,*N*′-bis-(3,5-dichlorophenyl)hydrazine, and 3,3′,5,5′-tetrakis(trifluoromethyl)hydrazobenzene [52]. When electron-withdrawing substituents were placed on the phenyl rings of the ligand such as chlorine or trifluoromethyl groups, the expected aza12-MC-4 was synthesized with a Ce^{IV} ion captured in the central cavity. However, if electron-donating substituents such as methyl groups were placed on the ligand, the cerium(IV)-containing azaMC could not be isolated. The cerium(IV)-containing azaMC may have been briefly stable in solution, but it quickly decomposed to brown, unidentified Ce^{III} products. As in the first lithium–cerium azaMC structure, the Li^I ion are three-coordinate with either trigonal planar or vacant tetrahedron geometry (confirmed with *SHAPE 2.1*). While the Ce^{IV} ions

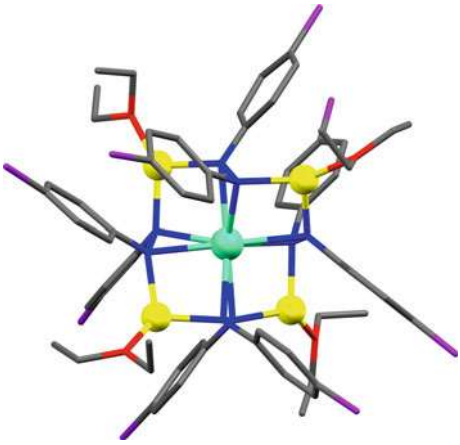

Fig. 36 X-ray crystal structure of the azametallacrown $Ce^{IV}[12\text{-}MC_{Li^I}\text{-}4]$ with the ligand *N*,*N*′-bis-(4-chlorophenyl)hydrazine. The central Ce^{IV} ion binds to each N atom of the MC ring, and each Li^+ is three-coordinate with trigonal planar geometry. Yellow = lithium, aqua = cerium, blue = nitrogen, gray = carbon, and purple = chlorine

are eight-coordinate as in the above structure, the Ce^{IV} ions though have a distorted triangular dodecahedron geometry (CShM = 11.760–12.900). This change in geometry from octagon for the first lithium–cerium azaMC to triangular dodecahedron is likely influenced by the bulkier substituted *N*,*N*′-diarylhydrazine ligands and the bulkier coordination about the Li^I ion. In the original cerium–lithium aza12-MC-4 with *N*,*N*′-diphenylhydrazine, the lithium coordination is completed by a pyridine molecule; however, in the structures with the substituted *N*,*N*′-diarylhydrazine ligands, the pyridine molecule is replaced by a bulkier diethyl ether molecule. Thus, the steric bulkiness of both the diethyl ether molecules and the substituted *N*,*N*′-diarylhydrazine ligands likely influence the geometry about the central Ce^{IV} ion. Not only did the substitution of the phenyl rings of the ligand affect the structural geometry of the azaMCs, but the electron-withdrawing groups also affected the electrochemical properties of the azaMCs. For the azaMC complexes with the electron-withdrawing ligands, it was determined that they were easier to reduce from Ce^{IV} to Ce^{III} compared to the azaMCs containing the unsubstituted *N*,*N*′-diphenylhydrazine ligand.

Two sodium-based azaMCs have been reported thus far with both structures being a vacant metallamacrocycle. The first reported sodium azaMC was a 12-MC-4 (Fig. 37), and the structure of this compound has been reported by two groups, both in 2012 [53, 54]. The ligand *N*-(5-phenyl-1,3,4-oxadiazol-2-yl)-*p*-nitrobenzamide provides the N–N bridge between each sodium ion of the MC ring. Each Na^I ion is five-coordinate with a distorted square pyramidal (CShM = 1.388) geometry and a N_2O_3 coordination environment. Two ligands provide four of the five coordinating atoms about each Na^I ion while the oxygen atom of a solvent methanol molecule completes the square pyramidal geometry. A larger vacant aza18-MC-6 was reported in 2014 by Otten and coworkers (Fig. 38) [55]. A formazanate ligand, which contains a [N–N–C–N–N] backbone, provides the N–N linkage between the sodium ions. In this MC, each sodium ion is four-coordinate with a N_3C coordination environment and a severely distorted shape. The lowest CShM value is for that of a square (9.126)

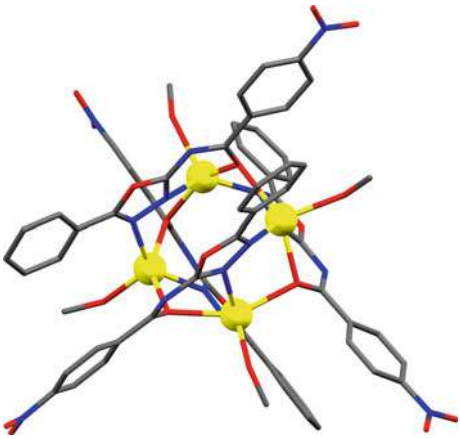

Fig. 37 X-ray crystal structure of the vacant azametallacrown 12-MC_{Na^I}-4 with the ligand *N*-(5-phenyl-1,3,4-oxadiazol-2-yl)-*p*-nitrobenzamide. Each Na^I ion has a square pyramidal geometry. Yellow = sodium, red = oxygen, blue = nitrogen, and gray = carbon

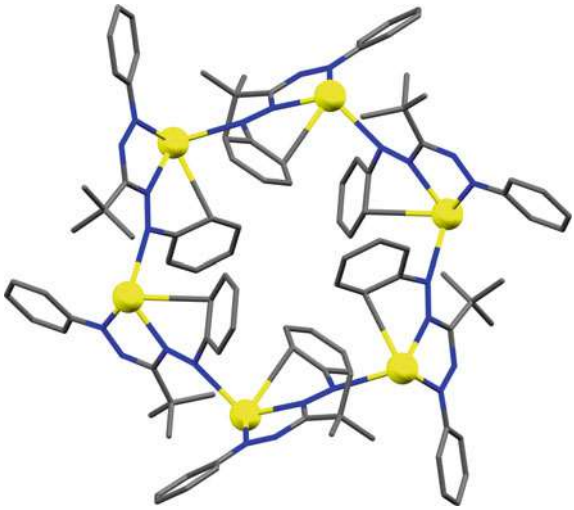

Fig. 38 X-ray crystal structure of the vacant azametallacrown 18-MC_{Na^I}-6 with a formazanate anion as the bridging ligand between the Na^I ions. Each Na^I ion has a severely distorted square geometry. Yellow = sodium, blue = nitrogen, and gray = carbon

with the next lowest being that of a see-saw (15.959). Each sodium ion is bound to two nitrogen atoms and a phenyl carbon atom of one formazanate ligand, and the coordination is completed by a nitrogen atom of a second formazanate ligand. ^{1}H-NMR of the compound in benzene does not clearly indicate if the compound is stable in solution; however, based on its sparing solubility in benzene, the authors believe the metallamacrocycle dissociates in solution.

5 Conclusion

This renaissance of research into main group element-containing metallacrowns showcases several important tenets of this field of research. First, the familiarity of compounds such as the Ga^{III} 12-MC_{shi}-4 with benzoate bridging ligands with reported Mn^{III} structures speaks to the ability to redesign known metallacrown scaffolds rationally by changing the ring metal. This concept is demonstrated over and over throughout the course of this chapter. We also highlighted how amenable known metallacrown structures are to minor alterations of the organic ligand. The bent gallium 12-MC-4 scaffold is possible with both shi^{3-} and nha^{3-}, and the dimerized $Ln_2[12\text{-}MC_{Ga^{III}}\text{-}4]_2$ has been redesigned to include iodo, ethynyl, or maleimido functional groups. In addition, both the 16-MC-6 and [3.3.1] metallacryptate structures are rare in the metallacrown literature and represent exciting possibilities with respect to the wide scope of serendipitous structures that remain undiscovered. The introduction of the tellurium metalloid to the metallacrown analogy results in a new class of compounds where an inverse metallacrown binds metal cations in the central cavity. Overall, these main group metallacrowns and azametallacrowns demonstrate an amazing scope of possible compounds with potential application in a variety of fields including imaging, magnetism, and medicine.

References

1. Pecoraro, V.L.: Structural characterization of [VO(salicylhydroximate)$(CH_3OH)]_3$: applications to the biological chemistry of vanadium(V). Inorg. Chim. Acta. **155**, 171–173 (1989). https://doi.org/10.1016/S0020-1693(00)90405-5
2. Mezei, G., Zaleski, C.M., Pecoraro, V.L.: Structural and functional evolutions of metallacrowns. Chem. Rev. **107**, 4933–5003 (2007). https://doi.org/10.1021/cr078200h
3. Chow, C.Y., Trivedi, E.R., Pecoraro, V., Zaleski, C.M.: Heterometallic mixed *3d–4f* metallacrowns: structural versatility, luminescence, and molecular magnetism. Comments Inorg. Chem. **35**, 214–253 (2015). https://doi.org/10.1080/02603594.2014.981811
4. Lutter, J.C., Zaleski, C.M., Pecoraro, V.L.: Metallacrowns: supramolecular constructs with potential in extended solids, solution-state dynamics, molecular magnetism, and imaging. In: Eldik, R. van, Puchta, R. (eds.) Advances in Inorganic Chemistry, pp. 177–246. Academic Press (2018)
5. Lah, M.S., Gibney, B.R., Tierney, D.L., Penner-Hahn, J.E., Pecoraro, V.L.: The fused metallacrown anion $Na_2\{[Na_{0.5}[Ga(salicylhydroximate)]_4]_2(\mu_2\text{-}OH)_4\}^-$ is an inorganic analog of a cryptate. J. Am. Chem. Soc. **115**, 5857–5858 (1993). https://doi.org/10.1021/ja00066a077
6. Chow, C.Y., Eliseeva, S.V., Trivedi, E.R., Nguyen, T.N., Kampf, J.W., Petoud, S., Pecoraro, V.L.: Ga^{3+}/Ln^{3+} metallacrowns: a promising family of highly luminescent lanthanide complexes that covers visible and near-infrared domains. J. Am. Chem. Soc. **138**, 5100–5109 (2016). https://doi.org/10.1021/jacs.6b00984
7. Bünzli, J.-C.G., Eliseeva, S.V.: Basics of lanthanide photophysics. In: Hanninen, P., Harma, H. (eds.) Lanthanide Luminescence: Photophysical, Analytical and Biological Aspects, pp. 1–45. Springer, Berlin (2010)

8. Nguyen, T.N., Eliseeva, S.V., Chow, C.Y., Kampf, J.W., Petoud, S., Pecoraro, V.L.: Peculiarities of crystal structures and photophysical properties of Ga^{III}/Ln^{III} metallacrowns with a non-planar [12-MC-4] core. Inorg. Chem. Front. **7**, 1553–1563 (2020). https://doi.org/10.1039/C9QI01647C
9. Nguyen, T.N., Chow, C.Y., Eliseeva, S.V., Trivedi, E.R., Kampf, J.W., Martinić, I., Petoud, S., Pecoraro, V.L.: One-step assembly of visible and near-infrared emitting metallacrown dimers using a bifunctional linker. Chem. Eur. J. **24**, 1031–1035 (2018). https://doi.org/10.1002/chem.201703911
10. Lutter, J.C., Eliseeva, S. V., Kampf, J.W., Petoud, S., Pecoraro, V.L.: A unique Ln^{III} {[3.3.1]Ga^{III} Metallacryptate} series that possesses properties of slow magnetic relaxation and visible/near-infrared luminescence. Chem. Eur. J. **24**, 10773–10783 (2018). https://doi.org/10.1002/chem.201801355
11. Athanasopoulou, A.A., Baldoví, J.J., Carrella, L.M., Rentschler, E.: Field-induced slow magnetic relaxation in the first Dy(III)-centered 12-metallacrown-4 double-decker. Dalton Trans. **48**, 15381–15385 (2019). https://doi.org/10.1039/C9DT02432H
12. Lutter, J.C., Lopez Bermudez, B.A., Nguyen, T.N., Kampf, J.W., Pecoraro, V.L.: Functionalization of luminescent lanthanide-gallium metallacrowns using copper-catalyzed alkyne-azide cycloaddition and thiol-maleimide Michael addition. J. Inorg. Biochem. **192**, 119–125 (2019). https://doi.org/10.1016/j.jinorgbio.2018.12.011
13. Lutter, J.C., Eliseeva, S.V., Collet, G., Martinić, I., Kampf, J.W., Schneider, B.L., Carichner, A., Sobilo, J., Lerondel, S., Petoud, S., Pecoraro, V.L.: Iodinated metallacrowns: toward combined bimodal near-infrared and X-ray contrast imaging agents. Chem. Eur. J. **26**, 1274–1277 (2020). https://doi.org/10.1002/chem.201905241
14. Eliseeva, S.V., Salerno, E.V., Lopez Bermudez, B.A., Petoud, S., Pecoraro, V.L.: Dy^{3+} white light emission can be finely controlled by tuning the first coordination sphere of Ga^{3+}/Dy^{3+} metallacrown complexes. J. Am. Chem. Soc. **142**, 16173–16176 (2020). https://doi.org/10.1021/jacs.0c07198
15. Salerno, E.V., Zeler, J., Eliseeva, S.V., Hernández-Rodríguez, M.A., Carneiro Neto, A.N., Petoud, S., Pecoraro, V.L., Carlos, L.D.: [$Ga^{3+}{}_8Sm^{3+}{}_2$, $Ga^{3+}{}_8Tb^{3+}{}_2$] metallacrowns are highly promising ratiometric luminescent molecular nanothermometers operating at physiologically relevant temperatures. Chem. Eur. J. **26**, 13792–13796 (2020). https://doi.org/10.1002/chem.202003239
16. Happ, P., Plenk, C., Rentschler, E.: 12-MC-4 metallacrowns as versatile tools for SMM research. Coord. Chem. Rev. **289–290**, 238–260 (2015). https://doi.org/10.1016/j.ccr.2014.11.012
17. Rinehart, J.D., Long, J.R.: Exploiting single-ion anisotropy in the design of f-element single-molecule magnets. Chem. Sci. **2**, 2078 (2011). https://doi.org/10.1039/c1sc00513h
18. Jiang, X.F., Chen, M.G., Tong, J.P., Shao, F.: A mononuclear dysprosium(III) single-molecule magnet with a non-planar metallacrown. New J. Chem. **43**, 8704–8710 (2019). https://doi.org/10.1039/c9nj01662g
19. Chow, C.Y., Bolvin, H., Campbell, V.E., Guillot, R., Kampf, J.W., Wernsdorfer, W., Gendron, F., Autschbach, J., Pecoraro, V.L., Mallah, T.: Assessing the exchange coupling in binuclear lanthanide(III) complexes and the slow relaxation of the magnetization in the antiferromagnetically coupled Dy_2 derivative. Chem. Sci. **6**, 4148–4159 (2015). https://doi.org/10.1039/C5SC01029B
20. Macrae, C.F., Sovago, I., Cottrell, S.J., Galek, P.T.A., McCabe, P., Pidcock, E., Platings, M., Shields, G.P., Stevens, J.S., Towler, M., Wood, P.A.: Mercury 4.0: from visualization to analysis, design and prediction. J. Appl. Crystallogr. **53**, 226–235 (2020). https://doi.org/10.1107/S1600576719014092
21. Llunell, M., Casanova, D., Cicera, J., Alemany, P., Alvarez, S.: SHAPE, version 2.1 (2013), Barcelona, Spain
22. Cirera, J., Ruiz, E., Alvarez, S.: Continuous shape measures as a stereochemical tool in organometallic chemistry. Organometallics **24**, 1556–1562 (2005). https://doi.org/10.1021/om049150z

23. Casanova, D., Cirera, J., Llunell, M., Alemany, P., Avnir, D., Alvarez, S.: Minimal distortion pathways in polyhedral rearrangements. J. Am. Chem. Soc. **126**, 1755–1763 (2004). https://doi.org/10.1021/ja036479n
24. Azar, M.R., Boron, T.T., Lutter, J.C., Daly, C.I., Zegalia, K.A., Nimthong, R., Ferrence, G.M., Zeller, M., Kampf, J.W., Pecoraro, V.L., Zaleski, C.M.: Controllable formation of heterotrimetallic coordination compounds: systematically incorporating lanthanide and alkali metal ions into the manganese 12-metallacrown-4 framework. Inorg. Chem. **53**, 1729–1742 (2014). https://doi.org/10.1021/ic402865p
25. Boron, T.T., Lutter, J.C., Daly, C.I., Chow, C.Y., Davis, A.H., Nimthong-Roldán, A., Zeller, M., Kampf, J.W., Zaleski, C.M., Pecoraro, V.L.: The nature of the bridging anion controls the single-molecule magnetic properties of DyX_4M 12-metallacrown-4 complexes. Inorg. Chem. **55**, 10597–10607 (2016). https://doi.org/10.1021/acs.inorgchem.6b01832
26. Shannon, R.D.: Revised effective ionic radii and systematic studies of interatomic distances in halides and chalcogenides. Acta Cryst. **A32**, 751–767 (1976). https://doi.org/10.1107/S0567739476001551
27. Pecoraro, V.L., Stemmler, A.J., Gibney, B.R., Bodwin, J.J., Wang, H., Kampf, J.W., Barwinski, A.: Metallacrowns: a new class of molecular recognition agents. In: Karlin, K.D. (ed.) Progress in Inorganic Chemistry, vol. 90, pp. 83–178. Wiley (1997)
28. Travis, J.R., Smihosky, A.M., Kauffman, A.C., Ramstrom, S.E., Lewis, A.J., Nagy, S.G., Rheam, R.E., Zeller, M., Zaleski, C.M.: Syntheses and crystal structures of two classes of aluminum-lanthanide-sodium heterotrimetallic 12-metallacrown-4 compounds: individual molecules and dimers of metallacrowns. J. Chem. Crystallogr. **51**, 372–393 (2021). https://doi.org/10.1007/s10870-020-00861-2
29. Eliseeva, S.V., Travis, J.R., Nagy, S.G., Smihosky, A.M., Foley, C.M., Kauffman, A.C., Zaleski, C.M., Petoud, S.: Visible and near-infrared emitting heterotrimetallic lanthainde-aluminum-sodium 12-metallacrown-4 compounds: discrete monomers and dimers. Dalton Trans. **51**, X–X (2022). https://doi.org/10.1039/D1DT04277G
30. Travis, J.R., Van Trieste III, G.P., Zeller, M., Zaleski, C.M.: Crystal structures of two dysprosium–aluminium–sodium [3.3.1] metallacryptates that form two-dimensional sheets. Acta Cryst. **E76**, 1378–1390 (2020). https://doi.org/10.1107/S2056989020010130
31. Rheam, R.E., Zeller, M., Zaleski, C.M.: Crystal structures of three anionic lanthanide–aluminium [3.3.1] metallacryptate complexes. Acta Cryst. **E76**, 1458–1466 (2020). https://doi.org/10.1107/S2056989020010725
32. Kübel, J., Elder, P.J.W., Jenkins, H.A., Vargas-Baca, I.: Structure and formation of the first $(–O–Te–N–)_4$ ring. Dalton Trans. **39**, 11126–11128 (2010). https://doi.org/10.1039/c0dt01102a
33. Ho, P.C., Szydlowski, P., Sinclair, J., Elder, P.J.W., Kübel, J., Gendy, C., Lee, L.M., Jenkins, H., Britten, J.F., Morim, D.R., Vargas-Baca, I.: Supramolecular macrocycles reversibly assembled by Te$\cdots$O chalcogen bonding. Nat. Commun. **7**, 11299 (2016). https://doi.org/10.1038/ncomms11299
34. Ho, P.C., Rafique, J., Lee, J., Lee, L.M., Jenkins, H.A., Britten, J.F., Braga, A.L., Vargas-Baca, I.: Synthesis and structural characterisation of the aggregates of benzo-1,2-chalcogenazole 2-oxides. Dalton Trans. **46**, 6570–6579 (2017). https://doi.org/10.1039/c7dt00612h
35. Ho, P.C., Bui, R., Cevallos, A., Sequeira, S., Britten, J.F., Vargas-Baca, I.: Macrocyclic complexes of Pt(II) and Rh(III) with iso-tellurazole: N-oxides. Dalton Trans. **48**, 4879–4886 (2019). https://doi.org/10.1039/c9dt00500e
36. Wang, J., Ho, P.C., Britten, J.F., Tomassetti, V., Vargas-Baca, I.: Structural diversity of the complexes of monovalent metal d^{10} ions with macrocyclic aggregates of iso-tellurazole: N-oxides. New J. Chem. **43**, 12601–12608 (2019). https://doi.org/10.1039/c9nj02217a
37. Zhao, X.-J., Li, D.-C., Zhang, Q.-F., Wang, D.-Q., Dou, J.-M.: The novel example of organotin(IV) metallacrowns: syntheses, characterizations and crystal structures of [12-$MC_{[RSn(IV)]N(shi)}$-4] complexes (R=Et, Bu, Ph; Shi=salicylhydroxamic acid). Inorg. Chem. Commun. **13**, 346–349 (2010). https://doi.org/10.1016/j.inoche.2009.12.018

38. Zhao, X.-J., Zhang, Q.-F., Li, D.-C., Dou, J.-M., Wang, D.-Q.: Syntheses, structural characterizations and properties of 12-MC-4 organotin(IV) metallacrowns: [12-$MC_{RSn(IV)N(shi)}$-4] and [12-$MC_{RSn(IV)N(Clshi)}$-4] (R = Et, Bu, Ph; H_3shi = salicylhydroxamic acid; H3Clshi = 5-chlorosalicylhydroxamic acid). J. Organomet. Chem. **695**, 2134–2141 (2010). https://doi.org/10.1016/j.jorganchem.2010.05.027
39. Atkins, T.J., Richman, J.E., Oettle, W.F.: Macrocyclic polyamines: 1,4,7,10,13,16-hexaäzacycloöctadecane. Org. Synth. **58**, 86–98 (1978). https://doi.org/10.15227/orgsyn.058.0086
40. Kim, I., Kwak, B., Soo Lah, M.: A series of nanometer-sized hexanuclear Co-, Fe-, and Ga-metallamacrocycles. Inorg. Chim. Acta. **317**, 12–20 (2001). https://doi.org/10.1016/S0020-1693(01)00361-9
41. Lee, K., John, R.P., Park, M., Moon, D., Ri, H.-C., Kim, G.H., Lah, M.S.: Steric control of the nuclearity of metallamacrocycles: formation of a hexanuclear gallium metalladiazamacrocycle and a hexadecanuclear manganese metalladiazamacrocycle. Dalton Trans. 131–136 (2008). https://doi.org/10.1039/B711686A
42. Park, M., John, R.P., Moon, D., Lee, K., Kim, G.H., Lah, M.S.: Two octanuclear gallium metallamacrocycles of topologically different connectivities. Dalton Trans. 5412 (2007). https://doi.org/10.1039/b710531b
43. Oh, M., Liu, X., Park, M., Kim, D., Moon, D., Lah, M.S.: Entropically driven self-assembly of a strained hexanuclear indium metal–organic macrocycle and its behavior in solution. Dalton Trans. **40**, 5720 (2011). https://doi.org/10.1039/c1dt10220f
44. Uhl, W., Molter, J., Neumüller, B.: Synthesis of aluminum hydrazides by hydroalumination of 2,3-diazabutadienes—formation of an $Al_4(N_2)_3$ cage compound and an $Al_3(N_2)_3$ macrocyclic ligand. Chem. Eur. J. **7**, 1510–1515 (2001). https://doi.org/10.1002/1521-3765(20010401)7:7%3c1510::AID-CHEM1510%3e3.0.CO;2-P
45. Bitto, F., Kraushaar, K., Böhme, U., Brendler, E., Wagler, J., Kroke, E.: Chlorosilanes and 3,5-dimethylpyrazole: multinuclear complexes, acetonitrile insertion and ^{29}Si NMR chemical-shift anisotropy studies. Eur. J. Inorg. Chem. **2013**, 2954–2962 (2013). https://doi.org/10.1002/ejic.201300109
46. Wagler, J., Bitto, F.: (μ_3-Oxo)-hexakis(μ_2-3,5-dimethylpyrazolato)-trihydrido-tri-silicon (μ_2-hydrido)-bis(μ_2-3,5-dimethylpyrazolato)-tetrachloro-dihydrido-di-silicon toluene solvate. CSD Commun. (2014). https://doi.org/10.5517/cc12k1h5
47. Ma, C., Sun, J., Zhang, R., Wang, D.: Self-assembly of organooxotin(IV) clusters with Schiff-base-containing-triazole from hydrolysis or solvothermal synthesis: crystal structures, hydrogen bonds, C-H$\cdots\pi$ stacking and S$\cdots$S interaction. J. Organomet. Chem. **692**, 4029–4042 (2007). https://doi.org/10.1016/j.jorganchem.2007.04.039
48. Feng, Y.-L., Zhang, F.-X., Kuang, D.-Z., Yang, C.-L.: Two novel dibutyltin complexes with trimers and hexanuclear based on the bis(5-Cl/Me-salicylaldehyde) carbohydrazide: syntheses, structures, fluorescent properties and herbicidal activity. Chin. J. Struct. Chem. **4**, 682–692 (2020)
49. Eaborn, C., El-Hamruni, S.M., Hill, M.S., Hitchcock, P.B., Hopman, M., Le Gouic, A., Smith, J.D.: Syntheses of some bulky alkylalanes and alkyltrihydroaluminates: crystal structures of $[Li(THF)_2AlH_3C(SiMe_3)_2(SiMe_2NMe_2)]_2$, $Li(THF)_2Al_2H_5\{C(SiMe_3)_3\}_2$, $(Me_3Si)_3CAlH_2\cdot$THF and the pyrazolato derivative $[LiAlH(C_3H_3N_2)_2C(SiMe_3)_3]_2$ (THF=tetrahydrofuran). J. Organomet. Chem. **597**, 3–9 (2000). https://doi.org/10.1016/S0022-328X(99)00507-0
50. Jack, K.S., Jeffery, J.C., Leedham, A.P., Lynam, J.M., Niedzwiecki, M., Russell, C.A.: Syntheses and structures of bis(imido)organophosphine dianions. Can. J. Chem. **80**, 1458–1462 (2002). https://doi.org/10.1139/v02-144
51. Levin, J.R., Dorfner, W.L., Carroll, P.J., Schelter, E.J.: Control of cerium oxidation state through metal complex secondary structures. Chem. Sci. **6**, 6925–6934 (2015). https://doi.org/10.1039/C5SC02607E
52. Levin, J.R., Cheisson, T., Carroll, P.J., Schelter, E.J.: Accessing relatively electron poor cerium(IV) hydrazido complexes by lithium cation promoted ligand reduction. Dalton Trans. **45**, 15249–15258 (2016). https://doi.org/10.1039/C6DT03154D

53. Yin, G.-J., Zhang, Q., Li, D.: Tetrakis[μ_3-4-nitro-N-(5-phenyl-1,3,4-oxadiazol-2-yl)benzamidato]tetrakis[methanolsodium(I)]. Acta Cryst. **E68**, m570–m570 (2012). https://doi.org/10.1107/S1600536812014791
54. Gao, H., Xu, C., Duan, L.-M., Wang, Z.-Q., Fan, Y.-T.: Crystal structure of methanol[μ-N-(5-phenyl-1,3,4-oxadiazol-2-yl)- 4-nitrobenzamide-κ^2N_1,O_1:κN_2]sodium, $Na(CH_4O)(C_{15}H_9N_4O_4)$. Z. Kristallogr. NCS 227 (2012). https://doi.org/10.1524/ncrs.2012.0086
55. Travieso-Puente, R., Chang, M.-C., Otten, E.: Alkali metal salts of formazanate ligands: diverse coordination modes as a result of the nitrogen-rich [NNCNN] ligand backbone. Dalton Trans. **43**, 18035–18041 (2014). https://doi.org/10.1039/C4DT02578D

Index

C. M. Zaleski (ed.), *Advances in Metallacrown Chemistry*,
https://doi.org/10.1007/978-3-031-08576-5